JP0150081

JAERI-Conf
2000-015

# PROCEEDINGS OF THE WORKSHOP ON SEVERE ACCIDENT RESEARCH, JAPAN (SARJ-99)
NOVEMBER 8-10, 1999, TOKYO, JAPAN

November 2000

(Ed.) Kazuichiro HASHIMOTO

日本原子力研究所
Japan Atomic Energy Research Institute

本レポートは、日本原子力研究所が不定期に公刊している研究報告書です。
入手の問合わせは、日本原子力研究所研究情報部研究情報課（〒319-1195　茨城県那珂郡東海村）あて、お申し越し下さい。なお、このほかに財団法人原子力弘済会資料センター（〒319-1195　茨城県那珂郡東海村日本原子力研究所内）で複写による実費頒布を行っております。

This report is issued irregularly.
Inquiries about availability of the reports should be addressed to Research Information Division, Department of Intellectual Resources, Japan Atomic Energy Research Institute, Tokai-mura, Naka-gun, Ibaraki-ken 〒319-1195, Japan.

© Japan Atomic Energy Research Institute, 2000
編集兼発行　日本原子力研究所

JAERI－Conf 2000－015

# Proceedings of The Workshop on Severe Accident Research, Japan SARJ-99

Organized
by
Severe Accident Research Laboratory
Department of Reactor Safety Research
Nuclear Safety Research Center
Japan Atomic Energy Research Institute
(JAERI)

and

Systems Safety Department
Nuclear Power Engineering Corporation
(NUPEC)

at
Hotel Lungwood
Tokyo, Japan
November 8-10, 1999

Edited by Kazuichiro HASHIMOTO

## Organization of the Workshop

The Workshop was organized by the following staff of JAERI:

I. Takeshita, The Chairman of the Workshop

(Severe Accident Research Laboratory)
K. Hashimoto, H. Nakamura, A. Hidaka, Y. Maruyama, K. Moriyama, T. Kudo, H. Shibazaki, E. Chino, Y. Yuchi, M. Kataoka, T. Naraoka, E. Kato, and M. Shigemoto

and the following staff of NUPEC:

H. Ogasawara, The Cochairman of the Workshop

(Systems Safety Department)
H. Nagasaka, I. Sakaki, M. Ogino, T. Kashiwase, M. Fukasawa, M. Takahashi, H. Noguchi, T. Yamada, Y. Kitajima, S. Miura, M. Sato, T. Hoshokawa, A. Iwamoto

Severe Accident Research Laboratory wishes to express sincere appreciation to Messrs. Y. Sasajima, Director, S. Sato, Ms. S. Kimura, Mr. T. Onawa, Mses. M. Tomita and T. Nishino of the Office of Business Administration of Department of Reactor Safety Research, for their support and assistance to hold the Workshop.

This is a blank page.

JAERI－Conf 2000－015

# Proceedings of the Workshop on Severe Accident Research, Japan (SARJ-99)
November 8-10, 1999, Tokyo, Japan

(Ed.) Kazuichiro HASHIMOTO

Department of Reactor Safety Research
Nuclear Safety Research Center
Tokai Research Establishment
Japan Atomic Energy Research Institute
Tokai-mura, Naka-gun, Ibaraki-ken

(Received September 12, 2000)

The Workshop on Severe Accident Research, Japan (SARJ-99) was taken place at Hotel Lungwood on November 8-10, 1999, and attended by 156 participants from 12 countries. A total of 46 papers, which covered wide areas of severe accident research both in experiments and analyses, such as fuel/coolant interaction, accident analysis and modeling, in-vessel phenomena, accident management, fission product behavior, research reactors, ex-vessel phenomena, and structural integrity, were presented. The panel discussion titled "Link of Severe Accident Research Results to Regulation: Current Status and Future Perspective" was successfully conducted, and the wide variety of opinions and views were exchanged among panelists and experts.

Keywords: Severe Accident, Source Term, Accident Management, Fission Product Behavior, Structural Integrity, In-Vessel Phenomena, Ex-Vessel Phenomena

JAERI－Conf 2000－015

# シビアアクシデント研究ワークショップ(SARJ-99)論文集
1999年11月8－10日，東京

日本原子力研究所東海研究所安全性試験研究センター原子炉安全工学部
（編）橋本　和一郎

（2000年9月12日受理）

1999年11月8日から10日にかけて、ホテル・ラングウッドにおいて、シビアアクシデント研究ワークショップ（SARJ-99）が開催された。このワークショップには、12ヵ国より156名の参加者があった。ワークショップでは、各国における研究の現状、溶融炉心／冷却材相互作用、事故解析及びモデリング、圧力容器内現象、アクシデントマネジメント、FP挙動、研究炉、格納容器内現象、構造健全性など、シビアアクシデントに関する実験及び解析を含む幅広い領域を対象として、合計46件の発表があった。パネルディスカッションでは、「シビアアクシデント研究成果の規制への反映：現状と将来の展望」をテーマに、パネリスト及び会場の専門家により活発な討論が行われ、様々な意見や見解が交換された。

東海研究所：〒319-1195　茨城県那珂郡東海村白方白根2-4

# *FOREWORD*

Severe accidents have been one of the major reactor safety issues especially after the TMI-2 and the Chernobyl accidents. The objectives of severe accident research are first of all to understand physical phenomena associated with severe accidents, to develop analytical methods to predict such phenomena, to quantify the safety margin of nuclear reactors against severe accidents, to evaluate the effectiveness of accident management measures, and finally to increase the level of safety much further.

To meet these objectives, Japan Atomic Energy Research Institute (JAERI) initiated severe accident research in 1985. Wide range of severe accident research activities have been performed in accordance with National Five-year Safety Research Plan established by the Nuclear Safety Commission. On the other hand, Nuclear Power Engineering Corporation (NUPEC) has then conducted Containment Integrity Tests to demonstrate the reactor containment vessel integrity and to respond to mitigative accident management concerns. Based on these activities in Japan, the Workshop on Severe Accident Research, Japan (SARJ) has been held since 1990 to provide results of severe accident research and to exchange information among international participants for more efficient and further progress of the research.

In the Workshop (SARJ-99) held in Tokyo on November 8 - 10, 1999, the topics included overview of research activities, fuel/coolant interaction, accident analysis and modeling, in-vessel phenomena, accident management, fission product behavior, research reactors, ex-vessel phenomena, and structural integrity. The panel discussion titled "Link of Severe Accident Research Results to Regulation: Current Status and Future Perspective" was successfully conducted, and the wide variety of opinions and views were exchanged among panelists and experts.

It is our great pleasure and wish that the information shared at the Workshop will be utilized for further reducing the phenomenological uncertainties and risk of the nuclear reactors associated with severe accidents, for the possible regulatory applications, for future reactor design, for highly enhancing the nuclear safety, and thus finally for the closure of severe accident issues.

Kazuichiro Hashimoto, Editor
Head, Severe Accident Research Laboratory
Japan Atomic Energy Research Institute

This is a blank page.

Contents

1. Plenary Session : Overview of Research Activities ..... 1
Chairpersons: H. Nariai (Tsukuba Univ.), M. Sonnenkalb (GRS)
1.1 Overview of Severe Accident Research at JAERI (K. Hashimoto, JAERI) ..... 3
1.2 Present Status of Containment Integrity Tests at NUPEC (H. Nagasaka, NUPEC) ..... 7
1.3 Practical Lessons from the First Three PHEBUS FP Tests (M.Schwarz et al., IPSN) ..... 11
1.4 Overview of Severe Accident Research at KAERI (H. D. Kim et al., KAERI) ..... 17

2. Session 1: Fuel/Coolant Interaction I ..... 23
Chairpersons: S. Miura (NUPEC), K. Moriyama (JAERI)
2.1 Overview of KAERI Fuel Coolant Interaction Test (S. W. Hong et al., KAERI) ..... 25
2.2 Installation for Low Temperature Vapor Explosion Experiment
(S. Nilsuwankosit and U. Archakositt, Chula Univ.) ..... 30
2.3 COTELS Fuel Coolant Interaction Tests under Ex-Vessel Conditions
(M. Kato et al., NUPEC) ..... 36

3. Session 2: Fuel/Coolant Interaction II ..... 43
Chairpersons: S. Nilsuwankosit (Chula Univ.), M. Kato (NUPEC)
3.1 Three-Component Melt Jet Breakup Model for FCI Analysis
(K. Moriyama et al., JAERI) ..... 45
3.2 Numerical Analysis of Jet Injection Mechanism of Fuel-Coolant Interactions
Using MPS (H. Ikeda et al., Univ. of Tokyo) ..... 52
3.3 Study on the Effect of Subcooling on Vapor Film Collapse on High Temperature
Particle Surface (Y. Abe et al., Yamagata Univ.) ..... 58
3.4 Propagation Calculation for Reactor Cases (Y. Yang et al., Shanghai Jiao Tong Univ.) ..... 68

4. Session 3: Accident Analysis and Modeling I ..... 75
Chairpersons: G. Bandini (ENEA), A. Hidaka (JAERI)
4.1 Status of the ASTEC Integral Code (J.Van Dorsselaere et al., IPSN) ..... 77
4.2 Development Status of Severe Accident Analysis Code SAMPSON
(T. Iwashita and H. Ujita, NUPEC) ..... 83
4.3 ICARE/CATHARE V1 : Application to a PWR 900 MWe Severe Accident Sequence
(M. Zabiego et al., IPSN) ..... 92

5. Session 4: Accident Analysis and Modeling II ..... 99
Chairpersons: J.Van Dorsselaere (IPSN), Y. Maruyama (JAERI)
5.1 TMI-2 Accident Analysis with SCDAP/RELAP5 Code (G. Bandini, ENEA) ..... 101

5.2 Adaptation of the Severe Accident Codes to VVER-440/V213 (V230) Reactor Unit, Their Comparison and Utilisation of the Results (A. Bujan et al., VUJE, a.s.) 107
5.3 Comparison of MAAP4.03 with RELAP/SCDAPSIM/MOD3.2 (T. Kohriyama et al., INSS) 114

6. Session 5: In-Vessel Phenomena 121
Chairpersons: C. Allison (ISS), S. Hong (KAERI)
6.1 Irradiated $UO_2$ Fuel Dissolution by Molten Zircaloy: Some Results from the SCA Corium Interaction Thermochemistry Project (P. Bottomley et al., ITU) 123
6.2 Analysis of Turbulent Natural Convection Heat Transfer in a Lower Plenum during External Cooling Using the COSMO Code (H. Noguchi et al., NUPEC) 130
6.3 Modeling for Water Penetration into Narrow Gap in CAMP Code (Y. Maruyama et al., JAERI) 136
6.4 Identification of Gap Cooling Phenomena from LAVA-4 Experiment Using MELCOR (J. H. Park et al., KAERI) 141
6.5 An Experimental Study on Critical Heat Flux in a Hemispherical Narrow Gap (R. J. Park et al., KAERI) 146

7. Session 6: Accident Management I 153
Chairpersons: Y. Abe (Yamagata Univ.), H. Nakamura (JAERI)
7.1 Development of Hybrid Hydrogen Control System (H. Nakakura and T. Gora, MHI) 155
7.2 Tests on Passive Autocatalytic Recombiner Performance for BWR Application (M. Harada et al., Toshiba) 161
7.3 An Experimental Study on Feasibility of Ex-vessel Cooling through the External Guide Vessel (K. H. Kang et al., KAERI) 167

8. Session 7: Accident Management II 175
Chairpersons: A. Levin (NRC), M. Ogino (NUPEC)
8.1 Experimental Investigation of Thermal-Hydraulic Performance of PCCS with Horizontal Tube Heat Exchangers : Single U-Tube Test (H. Nakamura et al., JAERI) 177
8.2 Analysis of Containment Venting Following a Core Damage At a BWR Mark I Using THALES-2 (S. Widodo et al., BATAN) 185

9. Session 8: Fission Product Behavior I 191
Chairpersons: A. Jones (JRC), A. Watanabe (NUPEC)
9.1 Current Status of VEGA Program and a Preliminary Test with Cesium Iodide (A. Hidaka et al., JAERI) 193
9.2 Quick Look of First VEGA Test and Fabrication Study of Thoria Components (T. Nakamura et al., JAERI) 201

9.3 PHEBUS FPT4: Test Conditions and First Results (F. Serre et al., IPSN) 210
9.4 Studies on Interaction between Cesium Iodide and Type 316 Stainless Steel in WIND Project (T. Kudo et al., JAERI) 216

10. Session 9: Fission Product Behavior II 223
Chairpersons: P. Bottomley (ITU), K. Hashimoto (JAERI)
10.1 Experimental Study on Effects of Boric Acid on Aerosol Revaporization in WIND Project (H. Shibazaki et al., JAERI) 225
10.2 Analyses of CsI Aerosol Deposition Tests in WIND Project with ART and VICTORIA Codes (Y. Yuchi et al., JAERI) 231
10.3 Effects of Radiation and Impurities on Gaseous Iodine Behavior in a Containment Vessel (M. Takahashi et al., NUPEC) 236
10.4 Fission Product Aerosol Removal Test by Containment Spray under Accident Management Conditions (3) (A. Watanabe et al., NUPEC) 244

11. Session 10: Research Reactors 251
Chairpersons: T. Hashimoto (NUPEC), K. Hashimoto (JAERI)
11.1 MINT Research Reactor Safety Program (Mohamad Idris bin Taib, MINT) 253
11.2 Measurements of Radiation Dose Level around 3W1 Beamline of Beijing Electron-Positron Collider (Q. Wang et al., IHEP) 258

12. Session 11: Ex-Vessel Phenomena 265
Chairpersons: S. Koshizuka (Univ. of Tokyo), H. Nagasaka (NUPEC)
12.1 Analysis of Containment Direct Heating (DCH) for 300MWe Nuclear Power Plant (J. Gao, SNERDI) 267
12.2 Improved Hydrogen Combustion Model for Multi-Compartment Analysis (M. Ogino and T. Hashimoto, NUPEC) 272
12.3 Evaluation of Upward Heat Flux in Ex-vessel Molten Core Heat Transfer using MELCOR (S. Y. Park et al., KAERI) 280
12.4 COTELS Ex-Vessel Debris Coolability Tests (I. Sakaki et al., NUPEC) 286
12.5 Numerical Analysis of Molten Core-Concrete Interaction Using MPS Method (S. Koshizuka et al., Univ. of Tokyo) 294

13. Session 12: Structural Integrity 301
Chairpersons: N. Miyazaki (Kyusyu Univ.), Y. Maruyama (JAERI)
13.1 Post-Test Creep Analysis of Piping Failure Tests in WIND Project (E. Chino et al., JAERI) 303
13.2 Modeling of Hot Tensile and Short-Term Creep Strength for LWR Piping Materials under Severe Accident Conditions (Y. Harada et al., MHI) 309

13.3 A Simple Evaluation of Containment Integrity against Ex-Vessel Steam Explosion (H. Nishiura, KEPCO) ..... 315
13.4 Axisymmetric Global Structural Analysis of Prestressed Concrete Containment Vessel beyond Design Pressure (T. Kashiwase and M. Sato, NUPEC) ..... 319

14. Panel Discussion ..... 325
"Link of Severe Accident Research Results to Regulation:
Current Status and Future Perspective"
Chairperson: K. Ishijima (JAERI, Japan)
Panelists: M. Sonnenkalb (GRS, Germany)
A. V. Jones (JRC Ispra, Italy)
H. Nagasaka (NUPEC, Japan)
K. Yahagi (TEPCO, Japan)
J. F. Costello (NRC, USA)

Appendix A Final Program ..... 348
Appendix B List of Participants ..... 357

# 1. Plenary Session

## Overview of Research Activities

**Chairperson:**

H. Nariai (Tsukuba Univ.)

M. Sonnenkalb (GRS)

This is a blank page.

JP0150082



# 1.1 OVERVIEW OF SEVERE ACCIDENT RESEARCH AT JAERI

**HASHIMOTO, Kazuichiro**

Severe Accident Research Laboratory
Department of Reactor Safety Research
Japan Atomic Energy Research Institute
Tokai-mura, Naka-gun, Ibaraki-ken, Japan 319-1195
Phone: +81-29-282-5995, Fax: +81-29-282-5570
E-mail: hashimoto@sarl.tokai.jaeri.go.jp

## ABSTRACT

Severe accident research at Japan Atomic Energy Research Institute (JAERI) aims at the confirmation of the safety margin, the quantification of the associated risk, and the evaluation of the effectiveness of the accident management measures of the nuclear power reactors, in accordance with the governmental five-year nuclear safety research plan. JAERI has been conducting a wide range of severe accident research activities both in experiment and analysis, such as melt coolant interactions, fission product behavior, containment integrity and assessment of accident management measures.Molten core/coolant interaction and in-vessel molten core coolabiliy have been investigated in ALPHA Program. In ALPHA Program, the development of a code, CAMP, is in progress for the analysis of thermo-fluiddynamics of molten debris in a lower plenum of a reactor pressure vessel. A new model for the molten core jet breakup was developed to replace the multiphase-flow based melt model in JASMINE-pre developed at JAERI. In VEGA Program, which aims at FP release from irradiated fuels at high temperature and high pressure under various atmospheric conditions, the facility construction is completed, and the first experiment has been successfully performed in September, 1999. In WIND Project the revaporization of aerosols due to decay heating and also the integrity of the piping under severe accident conditions are being investigated. A test series on FP/structural material interaction has been performed in WIND Project to investigate the interaction between FP simulants and structural materials of reactor coolant piping under severe accident conditions. Code development activities are in progress for fission product behaviors with ART. The experimental analyses and reactor application have made progress by participating international standard problem and code comparison exercises, along with the use of introduced codes, such as SCDAP/RELAP5 and MELCOR. JAERI and Japan Atomic Power Company (JAPC) are jointly performing experiments to ascertain the thermal-hydraulic performance of a passive containment cooling system for ABWR-II. The outcome of the severe accident research will be utilized for the development of more reliable severe accident scenarios, detailed implementation of the accident management measures, and also for the future reactor development, basically through the sophisticated use of verified analytical tools.

**Keywords:** Severe Accident, Accident Management, Melt Coolant Interactions, Fission Product, Containment Integrity, ALPHA, WIND, VEGA

## 1 INTRODUCTION

During a light water reactor(LWR) severe accident various phenomena that threaten the integrity of the pressure vessel and the containment vessel could occur. The occurrence of a severe accident is extremely unlikely since LWRs are designed based on the defense-in-depth concept. However, in order to quantify the safety margin and potential risks of LWRs, severe accident research is of importance. Studies are also required for the evaluation of accident management measures to prevent and mitigate the severe accident. In accordance with current five-year nuclear safety research program (FY1996~FY2000) authorized by Nuclear Safety Commission(NSC), where severe accident research has been selected as one of important research issues, Japan Atomic Energy Research Institute(JAERI) has been conducting a wide range of severe accident research both in experiments and analyses[1]-[2]. In the present paper, recent severe accident research and some related activities at JAERI are described.

## 2 CURRENT RESEARCH STATUS

### 2.1 Integrity of Reactor Pressure Vessel and Containment Vessel

To clarify phenomena affecting containment integrity during a severe accident, ALPHA (Assessment of Loads and Performance of containment in Hypothetical Accident) program has been performed. The program has facilities to investigate (a) melt-coolant interactions[3,4], (b) molten core-concrete interactions, (c) FP aerosol behavior[5], and (d) leak behavior of containment penetrations[6]. Currently in melt-coolant interactions, steam explosion and molten core coolability have been extensively studied. In the frame of ALPHA program, a new model for the molten core jet breakup was developed to replace the multiphase-flow based melt model in JASMINE-pre, the premixing module of the steam explosion simulation code JASMINE[7,8]. The new model was designed emphasizing two aspects: separation of the melt model from the multiphase solver, and giving finer spatial resolution for the melt. The development of a code CAMP, is in progress in ALPHA program for the analysis of thermo-fluiddynamics of molten debris in a lower plenum of a reactor pressure vessel. The code is being developed with objectives to assess boundary conditions for ex-vessel fuel/coolant interactions and the debris coolability in the lower plenum[9]. The CAMP code was applied to the analysis of in-vessel debris coolability experiments performed in ALPHA program.

### 2.2 Source Term Evaluation

VEGA (Verification Experiments of Radionuclide Gas/Aerosol release) program on radionuclide release from irradiated fuels has been initiated. The characteristics of the radionclide release, such as non-volatile FP species, will be examined under high temperature (3273K) and high pressure (1MPa) conditions[10]. Re-irradiation of fuel specimen with NSRR reactor at JAERI will be made to produce short life FPs such as I-131. The test facility was installed into the beta/gamma concrete cell at the Reactor Fuel Examination Facility (RFEF) in JAERI Tokai site in February, 1999. The first fission product release test VEGA-1 was conducted on September 9, 1999 using two PWR pellets at burnup of 47GWd/tU. The fuel pellet of about 10g without cladding tube was heated up to 2500℃ in an inert helium atmosphere at 0.1MPa.

Small-scale basic experiments have been performed with the WAVE (Wide range Aerosol model Verification) facility to investigate aerosol behaviors within a piping. Also efforts have been made for the development and validation of analytical models on aerosol behaviors based on the experimental results[11].

The analysis of the integrity of a steam generator U-tube during secondary system depressurization was performed with SCDAP/RELAP and the JAERI developed FP analysis code, ART. The analysis showed that the potential for steam generator tube rupture after core heat up due to FP deposition cannot be ignored during secondary system depressurization.

### 2.3 Integrity of Piping of Reactor Cooling System

The WIND (Wide range piping INtegrity Demonstration) project has been conducted to evaluate the integrity and safety margin of reactor piping under severe accident conditions. The WIND project consists of tests and analyses related to aerosol behaviors and piping structural integrity[12,13,14].

The aerosol revaporization in piping is being investigated in WIND project[15,16]. The objectives are to characterize the aerosol revaporization from piping surfaces under various thermal-hydraulic conditions and to investigate the effect of boric acid on aerosol revaporization. In the cases that metaboric acid was placed on the test sections, iodine deposition mostly became the same as cesium at the low temperature region during the deposition phase. However, only cesium was deposited onto the high temperature region above approximately 50℃. In the revaporization phase, the experiments showed that the once-deposited cesium and iodide compounds were mostly revaporized when the temperature exceeded the melting points of their compounds.

A test series on FP/structural material interaction has been performed in WIND project to investigate the interaction between FP simulants and structural materials of reactor coolant piping under severe accident conditions. Three tests on the interaction of cesium iodide with type 316 stainless steel in

the various atmospheric conditions were performed.

The deposition phase of aerosol revaporization test series were analyzed by analytical codes for fission product behavior ART and VICTORIA[17]. It was confirmed in the present analysis that similar results on the CsI deposition were obtained between ART and VICTORIA when influences of chemical interactions were negligibly small. The analysis with VICTORIA agreed satisfactorily with the test results in analytical cases that $HBO_2$ was injected into the test section together with CsI to simulate the pre-existence of $HBO_2$.

Thermal and structural responses of the reactor coolant piping under elevated temperature and pressure conditions are being investigated in piping integrity tests in WIND project [18,19,20]. A three-dimensional elasto-plastic creep analysis was performed with ABAQUS code for the test using a nuclear grade type 316 stainless steel pipe, which had an outer diameter of 114.3mm and a wall thickness of 13.5mm. The major material properties at elevated temperature needed for the analysis were measured for specimen sectioned from the test pipe. Based on the measured creep data, a creep constitutive equation including the tertiary stage was developed and incorporated into ABAQUS code.

Based on material testing, the 0.2% proof stress and the ultimate tensile strength above 800℃ were given by the equations of second degree as a function of the reciprocal absolute temperature considering the strength increase due to fine precipitates for the piping materials. The piping materials include type 316 stainless steel, type 316 stainless steel of nuclear grade, CF8M cast duplex stainless steel and STS410 carbon steel. Also the short-term creep rupture time and the minimum creep rate at high-temperature were given by the modified Norton's Law as a function of stress and temperature considering the effect of the precipitation formation and resolution on the creep strength. The present modified Norton's Law gives better results than the conventional Larson-Miller method[21,22].

### 2.4 Collaboration with Other Organizations

JAERI and Japan Atomic Power Corporation (JAPC) are jointly performing experiments to ascertain the thermal-hydraulic performance of a passive containment cooling system (PCCS) using horizontal U-tubes for ABWR-II. The PCCS is used to a long-term cooling of the containment during a severe accident when a containment spray system is in failure. Experiments using a horizontal single U-tube are currently performed in JAERI after August, 1999 to study fundamental condensation heat transfer characteristics of steam with non-condensable gas and flow behavior of condensate and non-condensable gas under assumed severe accident conditions.

In universities wide variety of basic research activities have been conducted, such as experiments and code developments on fuel-coolant interactions, in-vessel melt behaviors, and creep damage analysis of piping, mostly in the joint work between universities and JAERI.

## 3 RELATED ACTIVITIES

NSC has been reviewing the regulatory safety examination guides, such as siting criteria and source terms for the revision based on the state-of-the art knowledge on severe accident research. In November 1995 NSC issued the statement on the accident management that the accident management strategies proposed by utilities are generally reasonable, the implementation of the accident management including operational procedures is to be determined and that further research activities are necessary. Industries are completing the detailed implementation of the accident management measures. Also industries are establishing a self-regulatory document for the containment design of the future reactors.

Since the severe accident research conducted so far has provided many valuable information on phenomenology and contributed to the implementation of accident management strategies, the closure of severe accident issues has been widely discussed. The outcome of severe accident research will be effectively utilized for the revision of regulatory guides, such as siting and source term, for detailed implementation of accident management measures, and also for the industry's self-regulatory document for containment design. If this will be successfully achieved, it will be one major element of closure of severe accident issues. However there still remain some unresolved

phenomena, such as in-vessel coolability, ex-vessel steam explosion, and FP behaviors. Research on these unresolved issues will be continued partly to be reflected for the closure of severe accident issues and partly for the application to future reactor development.

## 4 SUMMARY

Extensive research activities on severe accident are being conducted at JAERI. The research results will be utilized for the revision of safety examination guides and detailed implementation of the accident management measures. It is noted that the international collaboration in severe accident research is of great importance. JAERI has been participating in most of international collaboration and agreement, such as CSARP by USNRC, ACE/MACE by EPRI, and RASPLAV by OECD.

JAERI with NUPEC have been holding Workshop on Severe Accident Research in Japan(SARJ) since 1990 for the effective information exchange. SARJ-99 was tenth and final SARJ meeting, and from 2000 the severe accident research will be discussed in a new workshop which covers safety research activities.

Although a new governmental five-year nuclear safety research plan is under discussion, the severe accident research will probably approach to the closure, along with research results from the world, in next century by contributing to the enhancement of the nuclear safety.

## REFERENCES

[1] Sugimoto, J., Proc. Int. Seminar Heat and Mass Transfer in Severe Accidents, Cesme, Turkey (1995).
[2] Sugimoto, J.(Ed.), Proc. SARJ-98, Yokohama, JAERI-Conf 99-005 (1999).
[3] Yamano, N., et al., Nuclear Engineering and Design, vol.155, Nos.1-2, pp. 369-389 (1995).
[4] Yamano, N. et al., Nuclear Engineering and Design, vol.189, pp. 205-221, (1999).
[5] Kudo, T. et al., Proc. 3rd Int. Conf. Cont. Design & Operation, Toronto, Canada (1994).
[6] Yamano, N. et al., Nucl. Eng. Design, vol. 145, No. 3, pp.365-374 (1993).
[7] Moriyama, K. et al., Proc. Fourth International Conference on Nuclear Engineering (ICONE-4), New Orleans, USA (1996).
[8] Yang, Y. et al., Proc. Seventh International Conference on Nuclear Engineering (ICONE-7), Tokyo, April 19-23 (1999).
[9] Maruyama, Y. et al., Nucl. Eng. Design, Vol.187, pp.241-254 (1998).
[10] Hidaka, A. et al., Proc. SARJ-99, Tokyo, JAERI-Conf 99-005 (1999).
[11] Hidaka, A., et al., Nucl. Sci. Technol. Vol.32, No.10, pp.1047-1053 (1995).
[12] Hashimoto, K., et al., Proc. Third International Conference on Nuclear Engineering (ICONE-3), Kyoto, Japan (1995).
[13] Hidaka, A., et al., Nucl. Eng. Des., Vol.200, No.1-2, pp. 303~315 (2000).
[14] Maruyama, Y., et al., J. Nucl. Sci. Technol., Vol. 36, No. 5, pp. 433-442, (1999).
[15] Igarashi,, M., et al., Proc. Fifth International Conference on Nuclear Engineering (ICONE-5), Nice, France, May 26-30 (1997).
[16] Shibazaki, H., et al., To be published in Nuclear Technology (2000).
[17] Hidaka, A. et al., Proc. NURETH-8, Vol. 2, 595-604, Kyoto, Japan (1997).
[18] Maeda, A. et al., Proc. Fifth International Conference on Nuclear Engineering (ICONE-5), Nice, France, May 26-30 (1997).
[19] Harada, G., et al., 1998 ASME/JSME Joint Pressure Vessel and Piping Conf., USA (1998) .
[20] Maeda, A., et al., Proc. Seventh International Conference on Nuclear Engineering (ICONE-7), Tokyo, April 19-23 (1999).
[21] Harada, Y., et al., J. Nucl. Sci. Technol., Vol.36, No.10, pp.923-933 (1999).
[22] Harada, Y., et al., J. Nucl. Sci. Technol., Vol.37, No.6 (2000).

JP0150083



# 1.2 Present Status of Containment Integrity Tests at NUPEC

**Hideo Nagasaka**
Systems Safety Department, Nuclear Power Engineering Corporation, Japan
Phone:+81(3)4512-2571, Facsimile:+81(3)4512-2599, E-mail:nagasaka@nupec.or.jp

Objectives of Containment Integrity Tests (CIT) conducted at NUPEC are to demonstrate reactor containment vessel integrity during severe accident and to respond to Phase II accident management (AM) concerns regarding uncertainty of phenomena, raised by Japan Atomic Energy Safety Commission. CIT consists of experiments and analysis of debris cooling phenomena, hydrogen combustion behavior, fission products transport behavior and containment structural behavior. The uncertain phenomena regarding Phase II AM (defined as AM after reactor pressure vessel failure) treated at NUPEC are fuel-coolant interaction (FCI) and molten core-concrete interaction (MCCI) phenomena during ex-vessel debris cooling, evaluation of peak pressure during hydrogen combustion, ultimate strength and leakage conditions in the containment vessel and effectiveness of fission products (FP) removal under Phase II AM conditions. Most of these studies have been conducted under the international cooperation including the participation of OECD project.

This paper summarizes the present status of CIT focusing the progress during fiscal year 1998. The major progress is :

a) The effect of pool depth, subcooling and corium falling velocity on FCI in the process of corium falling into water pool was clarified in COTELS Test A. Non-dimensional correlation on the first peak pressure was also developed[1](Fig.1).
b) Long term debris cooling and upper particulate debris bed formation mechanisms against MCCI were evaluated by the structural analysis of cross section of solidified debris and concrete trap in COTELS Test B/C[2](Fig.2).
c) Calculated Nusselt number and maximum temperature better predicted BALI tests results by introducing experimental correlation for turbulent Prandtl number[3](Table1).
d) MELCOR code replaced by new combustion model was verified by NUPEC large scale combustion tests, simulating transient severe accident conditions[4](Fig.3).
e) Pre-test analysis of the ultimate structural behavior for 1/4 scale prestressed concrete containment vessel model was completed[5](Fig.4).
f) GIRAFFE-FP demonstrated effective aerosol FP removal by containment spray under Phase II AM also for additional severe accident scenarios[6](Fig.5).
g) The effect of impurities such as boric acid and silver on iodine chemical behavior in a reactor containment was taken into account in IMPAIR-3 code. The improved code well

predicted the ionic iodine concentration transient in RTF experiments[7](Fig.6).

**Acknowledgements**

This work is sponsored under the contract by the Ministry of International Trade and Industry, Japan

**References**

(1) M. Kato, et al., COTELS Fuel Coolant Interaction Tests under Ex-vessel Conditions, (Session 2).
(2) I. Sakaki, et al., COTELS Ex-Vessel Debris Cooling Tests, (Session 11).
(3) H. Noguchi, et al., Analysis of turbulent natural convection heat transfer in a lower plenum during external cooling using the COSMO code, (Session 5).
(4) M. Ogino, et al., Improved Hydrogen Combustion Model for Multi-Component Analysis, (Session 11).
(5) T. Kashiwase, et al., Axisymmetric Global Structural Analysis of Prestressed Concrete Containment Vessel beyond Design Pressure, (Session 12).
(6) A. Watanabe, et al., Fission Product Aerosol Removal Test by Containment Spray under Accident Management Conditions (3), (Session 9).
(7) M. Takahashi, et al., The Effects of Radiation and Impurities on the Gaseous Iodine Behavior in a Containment, (Session 9).

Table 1 BALI simulation with modified turbulent model

| | | Case A ($Ra'=2.3\times10^{16}$) | | | Case B ($Ra'=7.3\times10^{16}$) | | |
|---|---|---|---|---|---|---|---|
| | | $T_{max}$ (℃) | $Nu_{up}$ | $Nu_{down}$ | $T_{max}$ (℃) | $Nu_{up}$ | $Nu_{down}$ |
| Standard k-ε Model | $Pr_t$=1.0 | 36.4 | 2252 | 1633 | 63.3 | 2257 | 1811 |
| | $Pr_t$=0.6 | 29.0 | 3750 | 2228 | 45.5 | 3939 | 2607 |
| | $Pr_t$=10 | 108 | 494 | 331 | 192 | 490 | 352 |
| $Pr_t$= f(Ri) | | 37.1 | 2815 | 1389 | 56.6 | 2821 | 1648 |
| Test results | | 37.5 | 2690 | 1300 | 54.6 | 3040 | 1832 |

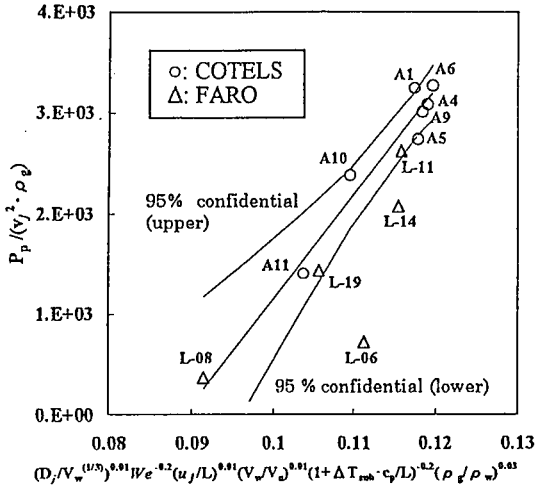



Fig.1 Result of dimensional analysis (COTELS Test A)

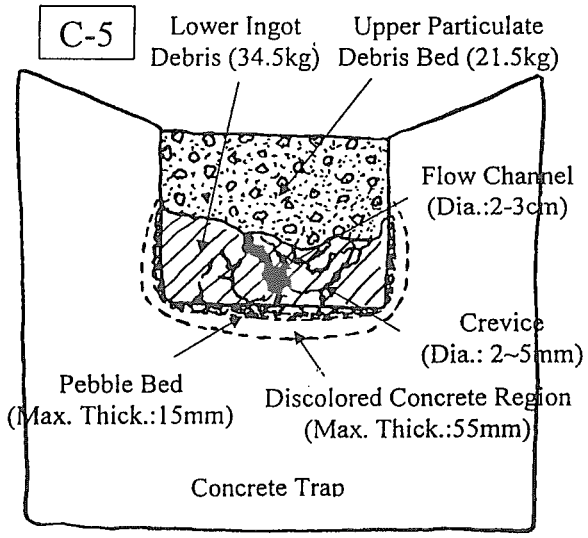



Fig.2 Cross section of solidified debris and eroded concrete

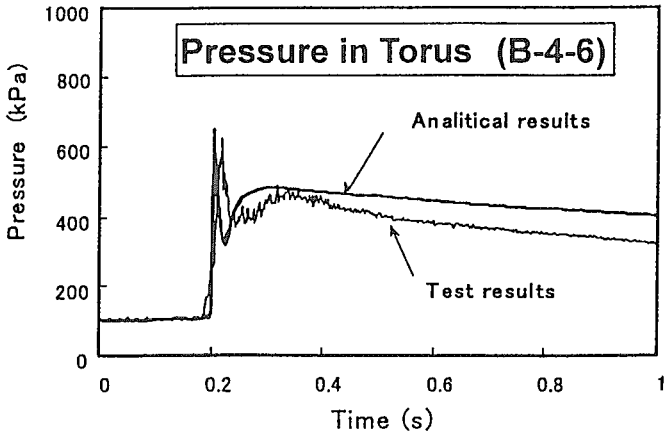



Fig. 3 MCFLASH analytical results comparing with test results (B-4-1)

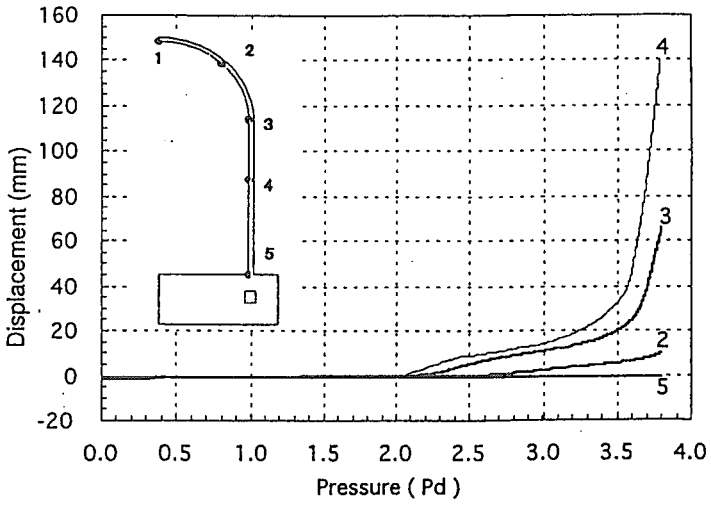



Fig.4 Local displacement versus internal pressure

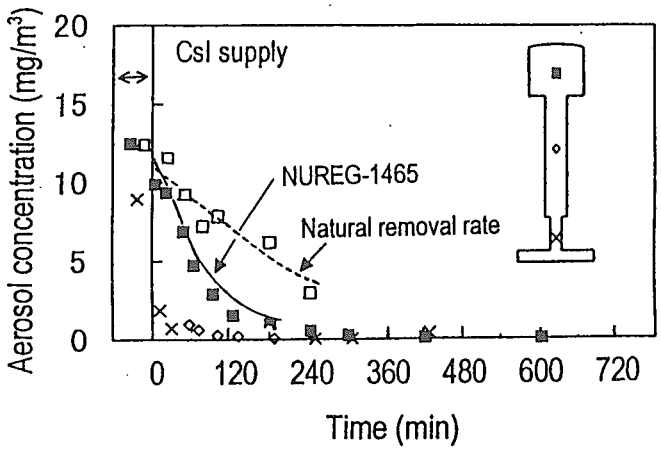



Fig.5 CsI mass concentration in the containment vessel for PWR LOCA sequence

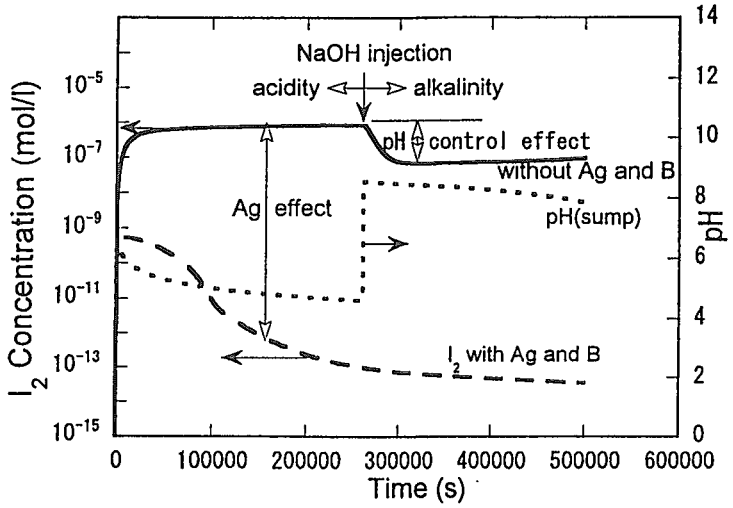



Fig.6. Molecular iodine concentration change in gas phase before and after NaOH injection

JP0150084



# 1.3 Practical Lessons from the First Three PHEBUS FP Tests

M. SCHWARZ and B. CLEMENT
Institut de Protection et de Sûreté Nucléaire - IPSN
Département de Recherches en Sécurité - DRS
CEA CADARACHE - F13108 Saint-Paul-Lez-Durance - France

A.V. JONES
Institute for Systems, Information and Safety - ISIS
European Commission - Joint Research Centre - ISPRA - Italy

## Abstract

The international Phebus FP programme of integral LWR severe accident experiments uses real core materials and scaled, well instrumented primary circuit and containment models. The first tests, FPT0 and FPT1, were performed respectively in December 1993 and July 1996. The experimental conditions were very similar in both tests : low pressure (~0.2 MPa) and steam-rich environment (oxidising conditions), and the test fuel and control rod bundles was brought to a severely degraded state. Test FPT4 measured the releases of low volatile fission products and of actinides from a solid debris bed of irradiated fuel and from a molten pool. Test FPT2 will be performed in mid-2000. An expert group has reviewed the first results, assessed their potential impact on safety studies and accident management strategy, and made recommendations for the future experiments of the programme and for future in-pile programmes as well. In this way guidance was obtained for the analysis of the experimental database and for the conditions of future tests.

**Keywords:** severe accidents; risk assessment; core degradation; fission products; source term; circuit; containment

## Introduction

The international Phebus FP programme [1], in which Japan is represented by both NUPEC and JAERI, provides a unique framework for integral experiments, using real core materials and scaled, well-instrumented primary circuit and containment models, where test fuel can be heated beyond its melting point under different thermal-hydraulic and physico-chemical conditions. The experimental programme is executed by the Institut de Protection et de Sûreté Nucléaire (France). Conditions were very similar in the first two tests: low pressure (~0.2 MPa) and a steam-rich environment (oxidising conditions). The principal difference between these tests was the irradiation of the fuel – nearly fresh in FPT0, medium burnup in FPT1. The most recent experiment, FPT4, was performed in July 1999. The objective was to investigate the release of low volatile fission products and of actinides from a solid debris bed of irradiated fuel and from a molten pool. Test FPT2 will be performed in mid-2000, just a few months after the preceding test, since the experimental circuit was not contaminated during FPT4.

The results of the Phebus FP programme are currently used by the various partners to :

- Validate accident codes
- Refine the reference source term (to containment or to the environment)
- Evaluate accident management features and procedures.
- Assess the safety of next-generation nuclear plants (e.g. EPR).

## The experimental facility

The Phebus FP facility has already been presented in detail [2] and will only be briefly described. Figure 1 illustrates the facility as used in the first two tests.

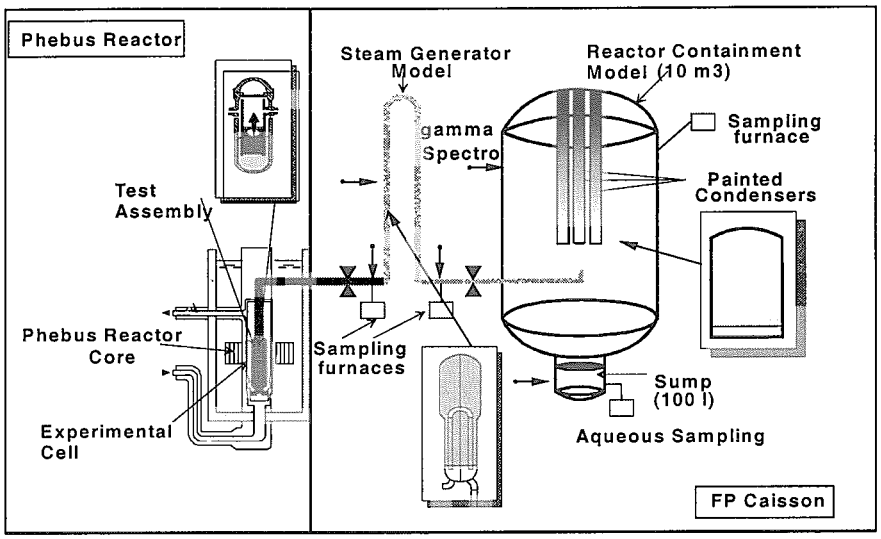



Figure 1: The Phebus-FP Experimental Facility

The test device (rod bundle or debris bed) is inserted into a pressurised water loop, located at the centre of the 40 MW Phebus driver core. The upper plenum above the test fuel bundle is connected, through a hot leg heated at 970 K, to an experimental circuit, including in most tests an inverted U-tube simulating a PWR steam generator and a cold leg heated at 420 K. At the outlet of the cold leg, the steam-hydrogen mixture and radioactive aerosols are injected into a 10 $m^3$ vessel simulating the containment building of a reactor. This configuration is thus typical of a cold leg break. The containment vessel includes scaled painted and condensing surfaces and a water-filled sump to investigate iodine behaviour under realistic conditions. The scaling factor is 1/5000 with respect to a 900 MWe PWR. The facility is equipped with extensive on-line instrumentation and each experiment is completed by PIE and PTA programmes.

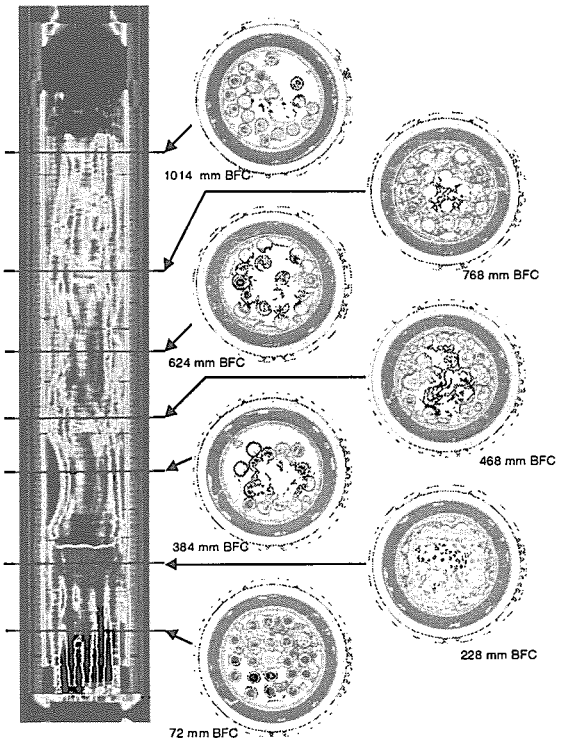



Figure 2: FPT-1 Fuel Degradation illustrated by radiography and tomogrammes

## Overview and status of the experimental programme

The programme comprises six integral experiments, the dates, objectives and main parameters of which are listed in Table 1. Tests FPT0 and FPT1, performed in December 1993 and July 1996 respectively, produced their sources of fission products and other materials to the circuit and containment vessel by degrading an array of 20 cut-down PWR fuel rods with a central silver-indium-cadmium control rod at low pressure in a

flow of steam sufficient to ensure oxidising conditions for nearly the entire transient. The third test, FPT4, was performed in July this year, and studied the release of low volatile fission products, fuel and actinides from a rubble bed which was degraded in a series of temperature plateaux to a molten pool. No circuit or containment were used in this test, the releases being trapped in a series of filters operated sequentially. FPT0 and FPT1, which differed notably in the fuel burnup (see Table 1), achieved an advanced state of degradation - Figure 2 shows the massive material relocation and the formation of a molten pool.

Test FPT2 will be similar to FPT1 but will add boric acid to the steam flow and will reduce the flow to produce a window of reducing conditions. It will also look at the behaviour of recombiner coupons (see below). Test FPT3 will be similar but will have different chemistry because of the presence of a boron carbide control rod. Finally, test FPT5 will examine the effects on degradation and fission product behaviour of air ingress.

Table 1: Phebus-FP test matrix

| No. | Type of fuel | Fuel bundle | Primary circuit | Containment vessel | Date |
|---|---|---|---|---|---|
| FPT-0 | Fresh fuel, 1 Ag-In-Cd rod, 9 d. pre-irrad. | Melt progression & FP release in vapor rich environment | FP chemistry and deposits in non-condensing steam generator. | Aerosol deposition. Iodine radiochemistry at pH 5. | Dec. 2, 1993 |
| FPT-1 | BR3 fuel ~23GWd/tU, 1 Ag-In-Cd rod, re-irrad. | As FPT-0 with irradiated fuel. | As FPT-0 | As FPT-0. | July 26,1996 |
| FPT-2 | As FPT-1 | s FPT-1 under steam poor conditions. | As FPT-1 with effect of boric acid. | $H_2$ recombiner, pH9, evaporating sump, | 2000 |
| FPT-3 | As FPT-1, but with $B_4C$ instead of Ag-In-Cd | As FPT-2 | As FPT-0 | As FPT-2? | 2003 |
| FPT-4 | EdF fuel ~33GWd/tU No re-irradiation. | Low volatile FP & actinide release from $UO_2$ . $ZrO_2$ debris bed, up to melting. | Integral filters in test device Post-test studies on samples | | July 22, 1999 |
| FPT-5 | Pre-irrad. (as FPT-1) | Fuel degradation and FP release in air conditions. | Deposition & chemistry of FPs in air conditions. | As FPT-1 or 2 | 2004-2005 |

## Main findings and evaluation of the results

Interpretation of the test results and the extraction of indications for future tests are pursued as an international effort among the partners in the Scientific Analysis Working Group and its supporting Interpretation Circles [3]. To help keep the test analysis focused on safety-important items an Ad-Hoc group of regulators, utilities and designers [4] has identified and prioritised items where Phebus can make a substantial contribution, Table 2. The items in the table have been used to structure the discussion of Phebus results which follows.

Table 2: Ranking of the remaining key-safety phenomena in LWR severe accidents

| Ranking | Key phenomena | Importance (ad-hoc group) |
|---|---|---|
| 1 | Determination of the iodine forms in the containment : aerosol, molecular, organic | Very important |
| 2 | Chemical forms of iodine transported in the circuits | Important to very important |
| 3 | Production of $H_2$ during late phase and in case of core reflooding | Important to very important |
| 4 | Deposition and late revaporisation of FP, in particular along containment by-pass circuits | Important to very important |
| 5 | Behaviour of $H_2$ recombiner in severe accident condition | Important |
| 6 | Aerosol behaviour inside the containment | Important |
| 7 | Air ingress in core | Important |
| 8 | Mass and composition of corium in lower head plenum for DCH, FCI and CCI | Moderate to important |
| 9 | Amount and composition of FP in a molten pool, and their release | Moderate to important |

### *Iodine behaviour in the containment*

The "classical" model of containment iodine chemistry based on relatively clean separate-effect experiments attributed most of the gaseous iodine to be found in the containment atmosphere to radiolytic reactions in the sump. Phebus with its realistic source showed that under acid conditions iodine in the sump rapidly precipitates and produces little vapour, most probably because of AgI formation and heterogeneous reactions on the surface of silver and silver oxide particles, as confirmed by separate-effect tests. Complementary tests are looking at the radiation stability of silver iodide. The main sources of vapour forms of iodine are found to be the circuit (see below) and the re-emission of organic iodides from painted surfaces exposed to the iodine-containing aerosols. Figure 3 shows an interpretation of test FPT0 including these mechanisms.

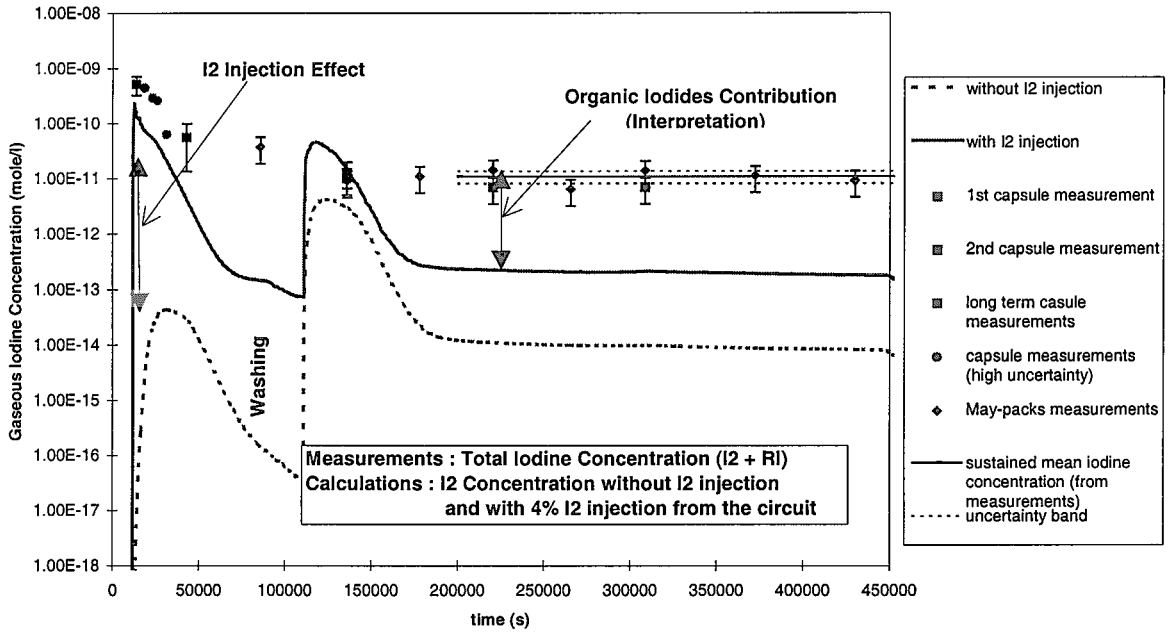



Figure 3: FPT-0 Calculation with IODE 4.1

### *Chemical forms of iodine in the primary circuit*

As mentioned above, it was found but not precalculated that a significant fraction of the iodine was still in vapour form at 150C and so contributed directly to the volatile iodine in the containment atmosphere. Volatile fractions at the circuit outlet were about 30% and 5-10% in FPT0 and FPT1 respectively during the periods of greatest hydrogen production. The difference between the two tests suggests that equilibrium was not attained in the circuit, and non-equilibrium models are being investigated [5].

### *Hydrogen production*

Most codes used for precalculation of FPT0 underestimated the hydrogen production during oxidation runaway by factors up to two. There were two main reasons, both associated with cladding relocation. The codes tended to relocate the cladding to cooler parts of the bundle relatively early, whereas the cladding mostly oxidised in place, and most of the codes did not allow relocated material to continue oxidising. It is clear from the Phebus PIE that oxidation continues simultaneously with relocation. Codes such as ICARE2, ATHLET-CD and MELCOR have been improved on the basis of Phebus results and can now achieve rather good agreement both for temperatures and for hydrogen generation.

### *Fission product deposition and revaporisation*

About 200g of aerosols passed through the circuit in both FPT0 and FPT1. Of this only 10% was trapped in the steam generator tube, although thermophoresis models from separate-effect tests would predict 20-50% trapping. The explanation may lie in the chemistry or in various mechanisms remobilising any deposits. It is clear that Cs was not transported as the hydroxide but possibly as the molybdate, for instance. Another possibility is that deposition did take place, but that the deposits were simultaneously resuspended by the steam flow. There was evidence from FPT0 post-test operations of resuspension. Another mechanism tending to decrease circuit retention is revaporisation, and indeed in FPT1 chemistry-induced revaporisation of Cs was observed late in the test.

### *Recombiners, aerosols in the containment, air ingress*

Recombiners are being installed in several EU countries to reduce the hydrogen risk, and this has stimulated considerable interest in the possible degradation in catalyst performance from their contamination by the fission products and other materials released from the degrading core in a severe accident. In FPT2 small coupons of catalyst produced by various manufacturers will be exposed to the Phebus fission product source and their performance compared with the results of separate effect tests in hydrogen/air mixtures.

Containment aerosols have long been of safety concern for their possible contribution to the environmental source term through leaks or failures. At the moderate humidities of the first Phebus tests it is found that all elements settle at virtually the same rate. The settling is fast, with removal almost complete in 5 hours.

Air ingress, such as could occur through lower head penetration or during a shutdown accident, could have dramatic effects on the release and transport of certain fission products such as Cs, I and Ru. Studies are in progress to define the conditions for test FPT5 which will study these effects.

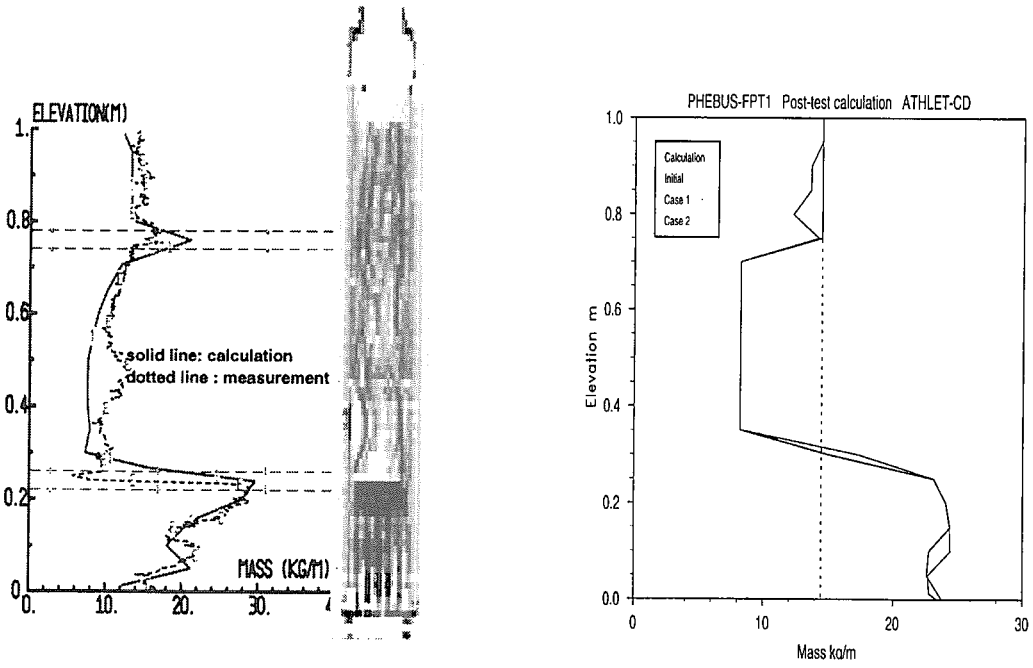



Figure 4: FPT-1 - Measured and calculated (ICARE2 & ATHLET-CD) axial mass distribution

### *Knowledge on corium behaviour*

Fuel relocation in the Phebus bundle (see Figure 4) occurred in FPT0 and FPT1 at a much lower temperature than previously assumed. Corium melting point determinations at JRC Karlsruhe point to a similar conclusion (MP ~2500K), which is tentatively explained by the formation of complex alloys involving Cr and Fe oxides. The IPSN Madrague tests will investigate the mechanisms responsible. The consequences for plant assessment could include faster degradation and relocation and a different melt composition in contact with the lower head.

The first two tests show nearly complete release of the volatile elements (including Te), while release of the less volatiles is influenced by changes in fuel geometry (exposed area) and by the local hydrogen concentration. FPT4 data will clarify the emission of the low-volatile elements that are released by fuel evaporation. There are large uncertainties in the fuel evaporation rate in the existing database.

## Conclusions

Through the first two tests Phebus FP has shown that it can make a significant contribution to our understanding of severe accident issues, to the validation of codes and models, and to improved confidence in NPP safety assessment. One notable example is the new light which Phebus has thrown on iodine chemistry in the containment, where the emphasis is now much more on interactions between fission products and control materials and on organic iodides than on classical radiolytic processes. Future tests and the further analysis of tests already performed such as FPT4 will strengthen and extend the Phebus database to important areas such as low-volatile FP emissions, steam-poor conditions, use of boron carbide control rods, recombiner behaviour, and iodine chemistry in the presence of a non-acidic sump.

It must be stressed that the Phebus data require continued international efforts to analyse them in sufficient depth and to synthesise the results from them in a manner that can be drawn upon by the end users: designers, utilities and regulators. In this effort complementary experiments, code development and validation, and ongoing interaction between the research and user communities all have essential and interlinked roles to play.

## References

[1] von der Hardt, P., Jones, A.V., Lecomte, C., Tattegrain, A., "Nuclear Safety Research. The Phebus FP Severe Accident Experimental Programme", *Nuclear Safety,* Vol. 35(2), July-December 1994, pp. 187-205.
[2] Schwarz, M, Hache, G., Von der Hardt, P. Phebus FP: a severe accident research programme for current and advanced light water reactors. *Nucl. Engineering and Design* v 187, 47-69 (1999)
[3] Schwarz, M., Clément, B., Ktorza, C., Jones, A.V., Zeyen, R., "The Phebus FP International Research Programme on Severe Accidents: Status and Main Findings", *Proc. of the 26th[d] Water Reactor Safety Information Meeting,* Bethesda, Maryland - October 26-28, 1998.
[4] Clément, B., Brisbois, J., "Use of Phébus-FP results for safety evaluation of severe accidents", *CSARP meeting* - Albuquerque, May 1999.
[5] Cantrel, L., Iodine Chemical Kinetic Study Within the Phebus Primary Circuit. *Proc. OECD Workshop on Iodine Aspects of Severe Accident Management,* Vantaa (Helsinki), May 1999.

JP0150085



# 1.4 Overview of Severe Accident Research at KAERI

H.D. Kim, S.B. Kim, S.W. Hong, and D.H. Kim
Korean Atomic Energy Research Institute
P.O. Box 105, Yusong, Taejon, Korea, 305-600
Tel) +82-868-2664 Fax) +82-868-8256 E-mail) hdkim@kaeri.re.kr

**ABSTRACT**

The severe accident research program at Korea Atomic Energy Research Institute, within the framework of governmental 10 year long-term nuclear R&D program, aims at the development of assessment techniques and accident management strategies for the prevention and mitigation of potential risk. The research program includes experimental efforts, development of phenomena specific models and development of an integrated computer code. The results of research program is intended to be utilized for the design of the advanced light water reactor and development of accident management strategies for the operating reactors. The main focused areas of recent investigation at KAERI are experiments on in-vessel core debris retention (SONATA-IV) and fuel coolant interaction (TROI) along with the development of models and integrated computer code (MIDAS).

Keywords: severe accident, in-vessel debris retention, fuel coolant interaction, integrated computer code, and research program

## 1.Introduction

To enhance technological capability and self-sufficiency in nuclear energy supply, the Korean government has established a long-term nuclear R&D program. This program is aimed at developing a wide range of technologies needed for peaceful uses of nuclear energy and also building a foundation for national energy self-sufficiency. In the frame of this long-term program authorized by Ministry of Science and Technology (MOST), severe accident research program has been carried out.

In the phase-II stage (1997-2001), severe accidents research program is directed to the development of assessment techniques and accident management strategies for reduction of the risk through maintaining the integrity of the reactor vessel and the containment(Fig. 1). Two experimental programs have been launched and are in progress. Those are SONATA-IV (Simulation Of Naturally Arrested Thermal Attack - In Vessel) program with the aim of investigating the possibility of in-vessel debris cooling and reactor vessel integrity, and CONVEX (CONtainment integrity Verification EXperiment) program, a corium-water interaction and steam explosion experiment with the aim of

quantifying the impact of such events on containment integrity. Along with the experimental program, development of integral severe accident analysis computer code is being carried out by combining the assessment of currently available integral analysis code and developing new models for unresolved issues. The code is also aimed to be used to assess severe accident sequences for the future reactor, SMART (System integrated Modular Advanced ReacTor), being developed at KAERI.

## 2. SONATA-IV Program

SONATA-IV experimental program, which is to investigate the possibility of gap formation between the debris and the reactor vessel wall and in-vessel debris cooling through the narrow gap, has been launched. A series of experiments called LAVA (Lower-plenum Arrested Vessel Attack) and CHF Experiments in a Hemispherical Gap, are in progress as the first phase of SONATA-IV.

### 2.1 LAVA Experiments

In order to investigate the possibility of in-vessel debris cooling through a narrow gap, a series of experiments called LAVA (Lower-plenum Arrested Vessel Attack) are in progress as SONATA-IV phase-I study(Table 1). A $1/8^{th}$ linear scaled mockup of a lower head vessel was used with $Al_2O_3$/Fe thermite melt (or $Al_2O_3$ only) as a corium simulant. The tests were performed varying the initial conditions such as water subcooling and height, also the material compositions of the melt simulants. In these tests, the lower head vessel experienced deformation and a thin gap formed around the interface between the solidified debris and the vessel due mainly to the thermal load from the termite melt. The results show that there was a significantly rapid temperature reduction of the vessel in the $Al_2O_3$ thermite melt experiments compared with the $Al_2O_3$/Fe thermite melt experiments even though a gap was formed in both cases. It is postulated that in the $Al_2O_3$/Fe thermite melt experiments, the iron melt layer is so dense that water ingression into the gap is difficult due to the high pressure of escaping steam. On the other hand, in the porosity of an $Al_2O_3$ melt layer could enhance water ingression into the gap by giving the flow path of the evaporated steam through the porous media. The water height and subcooling could affect the melt pool formation and the initial thermal attack to the vessel. For clear confirmation of these effects, the tests will be performed with various initial conditions, especially at the saturated and the lower subcooled (approximately 100K) water conditions. In parallel with experimental work, development of computer code, LILAC (Lower Head IntegraL Analysis Code), to simulate overall phenomena for the in-vessel corium retention is on progress.

### 2.2 CHF Experiments in a Hemispherical Gap

A series of experimental investigation on the cooling mechanism in hemispherical narrow gaps has been carried out. A visualization experiment, VISU-II, was done as the first step to get a visual observation of the flow behavior inside a hemispherical gap and to understand the mechanism inducing global dryout. It was observed that the counter-current flow limitation (CCFL) phenomenon prevented water from wetting the heater surface and induced dryout.

CHFG (Critical Heat Flux in Gap) using R-113 has been performed to measure the critical power and to investigate the inherent cooling mechanism in hemispherical narrow gaps. The test results have shown that increases in the gap thickness and the system pressure lead to increase in critical power. Temperature measurements over the heater surface show that the two-phase flow behavior inside the gaps is quite different from the other usual CHF experiments with small-scale horizontal plates and vertical annulus. The measured critical power using R-113 in hemispherical narrow gaps are 60% lower than that using water due to the lower boiling point, which is different from the pool boiling condition.

3. Fuel Coolant Interaction Experiments

Steam explosions have been of concern in the nuclear industry since in hypothetical severe accidents which involve fuel melt down, the extremely fast thermal interactions, and possibly some chemical reactions, between the molten fuel and coolant may cause steam explosion and subsequent containment failure.

As part of the CONVEX program, KAERI launched a intermediate scale fuel coolant interaction (FCI) experiment called as TROI(Test for Real cOrium Interaction with water) using reactor material to investigate the physical mechanism of FCI in the area of explosion and mixing steam explosion experiments. Up to 20kg of the reactor material including $UO_2$, $ZrO_2$, Zr and SS will be poured into water pool inside a pressure vessel. For the melting of reactor material, the cold crucible technology that uses high frequency induction heating in a water-cooled cage will be used. As it offers greater purity and flexibility when working with reactive materials, it is beneficial in terms of composition control compared to the previous technologies. The test facility and relevant instrumentation will be designed and constructed by March 2000. In corporation with university of Wisconsin, three-dimensional FCI computer codes, TEXAS-3D, will be also developed by employing current computational fluid dynamics technology.

4.Code development and Assessments

Along with the experimental program, development of integral severe accident analysis computer code MIDAS (Multi-purposed IntegrateD Assessment code for Severe accidents) is being carried out both by assessing currently available integral analysis codes and by developing new models for unresolved issues. The MELCOR computer code has been selected as a reference code thanks to its flexibility in plant configuration simulation, consideration of momentum conservation and its many updated models for severe accident phenomena. MIDAS will be developed into a two-step approach. MIDAS/TH, which simulates the thermal hydraulic phenomena, is an output in the first step. Then, the behavior of the fission products is modeled and integrated into MIDAS.

The models based upon plant configuration parameters will replace a user specified debris dispersal in the containment during the high-pressure melt ejection sequences. Regarding the molten core-concrete interaction models, a user flexibility is provided for the heat transfer between the molten debris pool and the overlying water. Melt spreadibility in the cavity concrete is also being studied. One of the most important in-vessel retention issues is to identify gap cooling phenomena in the lower head. For this purpose, the SONATA-IV experiments have been simulated by MELCOR and the conceptual gap cooling model is being developed. As the current version of MELCOR has a limitation to describe reactor power history during an ATWS (Anticipated Transient without Scram) sequence, a point kinetics module has been implemented into MIDAS/PK. In addition, MIDAS will be modernized by redefining data structures for the enhanced readability, portability, and flexibility. Eventually, MIDAS is to be used to assess severe accident sequences for the KNGR (Korea Next Generation Reactor) and other future reactor like SMART (System integrated Modular Advanced ReacTor), being developed at KAERI.

## 5. Summary

Severe Accident Research Program at KAERI is toward to develop accident and risk management strategies through maintaining the integrity of the reactor vessel and the containment. For In-vessel debris retention issue resolution and coolability for accident management and improvement of design, SONATA-IV program has well under progression. Series of experiments LAVA, CHFG, CCFL have been performed and demonstrate the gap formation and cooling mechanism. TROI program is focused to investigate the physical mechanism of FCI phenomena using reactor material in the area of triggering and mixing. Melting method using cold crucible has been adopted and possibility of $UO_2/ZrO_2$ mixture melting is confirmed. For quantification of accident management strategy, MIDAS computer code is under developing.

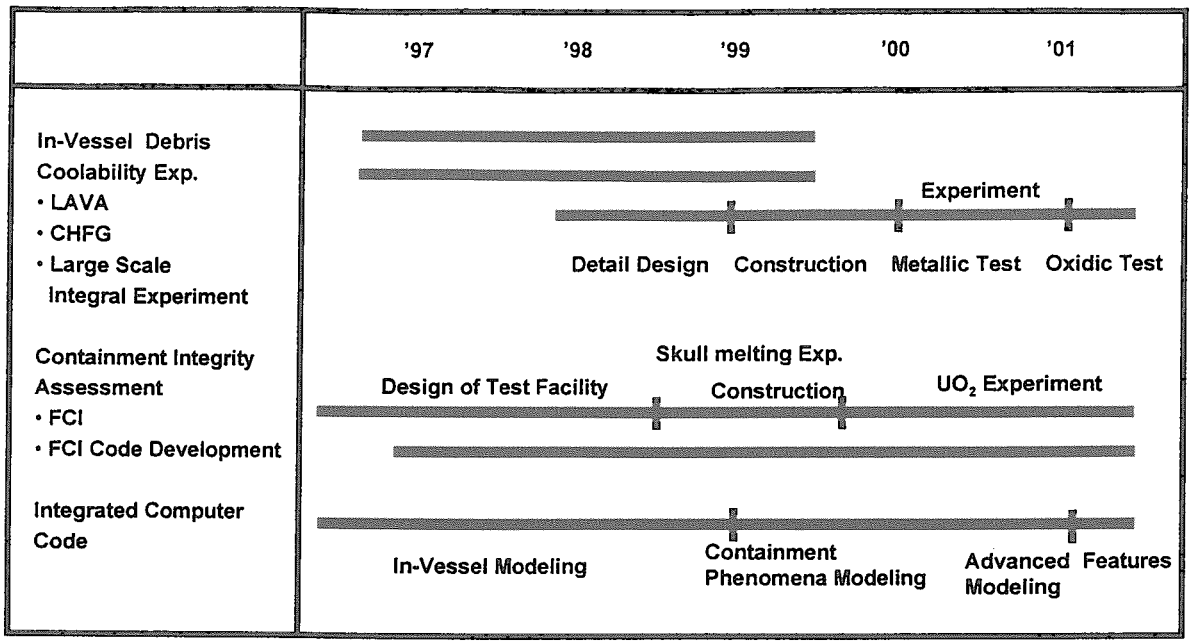



Figure 1. Phase-II of the Severe Accident Research Program

Table 1. LAVA Test Matrix

| Test | Date | Melt Composition & Mass | Water Temperature & Initial Depth | Pressure Load across the LHV |
|---|---|---|---|---|
| LAVA_PRE | '97. 5. 23 | $Al_2O_3$/Fe, 20 kg | 423 K, 45 cm | 0.0 bar |
| LAVA-1 | '97. 7. 24 | $Al_2O_3$/Fe, 40 kg | 418 K, 50 cm | 0.0 bar |
| LAVA-2 | '97. 10.21 | $Al_2O_3$/Fe, 40 kg | 433 K, 50 cm | 16.5 bar |
| LAVA-3 | '97. 12. 9 | $Al_2O_3$, 30 kg* | 433 K, 50 cm | 15.7 bar |
| LAVA-4 | '98. 2. 17 | $Al_2O_3$, 30 kg | 427 K, 50 cm | 16.9 bar |
| LAVA-5 | '98. 9. 28 | $Al_2O_3$, 30 kg | 458 K, 50 cm | 16.9 bar |
| LAVA-6 | '98. 7. 4 | $Al_2O_3$/Fe, 40 kg | 427 K, 50 cm | 16.6 bar |
| LAVA-7 | '98. 11.18 | $Al_2O_3$, 30 kg | 448 K, 50 cm | 17.4 bar |
| LAVA-8 | '99. 2. 8 | $Al_2O_3$, 30 kg | 420 K, 25 cm | 15.4 bar |

*: In LAVA-3, 4, 7 tests, due to the incomplete melt separation, about 3.6 kg, 1.8 kg and 2.9 kg of Fe melt was poured into the Lower Head Vessel, respectively.

Acknowledgement

This project has been carried out under the Nuclear R&D Program by MOST

References

1. S. B. Kim and H.D Kim, "Inherent Cololing of Debris in Reactor Vessel: SONATA-IV Project" OECD/NEA CSNI Special Meeting on In-vessel Debris Coolability and Lower Head Integrity, Nov. 18-19, 1996, Paris, France
2. K. H. Kang, J. H. Kim, S. B. Kim, J. H. Hong, and H. D. Kim., "Experimental Investigations on In-Vessel Debris Coolability through Inhererent Cooling Mechanisms, OECD/CSNI Workshop on In-Vessel Core Debris Retention and Coolability," Garching, Germany, March 3-6, 1998
3. J. H. Jeong, R. J. Park, K. H. Kang, S. B. Kim, and D. H. Kim, "Experimental Study on CHF in a Hemispherical Narrow Gap," OECD/CSNI Workshop on In-Vessel Core Debris Retention and Coolability, Garching, Germany, March 3-6, 1998
4. J.H. Jeong, R. J. Park, and S. B. Kim, "Thermal-hydraulic Phenomena Relevant to Global Dryout in a Hemispherical Narrow Gap," Heat and Mass Transfer 34 (1998), pp321-328.
5. J. H. Kim, K. H. Kang, R. J. Park, S. B. Kim, and H. D. Kim, "Experimental Study on Inherent In-Vessel Cooling Mechanism during a Severe Accident," ICONE-7, Tokyo, Japan, April 19-23, 1999
6. K. Y. Suh, K. H. Kang, J. H. Kim, S. B. Kim, J. S. Cho, and J. E. Chang, "Thermal and Mechanical Behavior of Hemispherical Vessel Lower Head," SMiRT-15, Seoul, Korea, August 15-20, 1999
7. K. I. Ahn, D. H. Kim, S. B. Kim, H. D. Kim, "A Comparative Study on the Reactor Lower Head Models Employed in the Current Severe Accident Codes," NURETH-9, San Francisco, October 3-8, 1999
8. S. W. Hong. J. H. Kim, J. H. Song, M.K. Hwang, B. T. Kim, and H. D. Kim, "An investigation of triggerability and explosivity in fuel coolant interactions", Proceedings of Korean Nuclear Society Spring Meeting, p.213, 1999.
9. S. W. Hong, J. H. Kim, J. H. Song, B. T. Kim, and H. D. Kim, "A feasibility study on UO2/ZrO2 mixture melting using induction skull melting method", Proceedings of Korean Nuclear Society Fall Meeting, 1998

# 2. Session 1

## Fuel/Coolant Interaction I

**Chairperson:**

S. Miura (NUPEC)

K. Moriyama (JAERI)

This is a blank page.

JP0150086



# 2.1 Overview of KAERI Fuel Coolant Interaction Test

S. W. Hong, I. K. Park, C. H. Kim, M. G. Hwang, B. T. Min, J. H. Song, and H. D. Kim
Korea Atomic Energy Research Institute
Dukjin-Dong 150, Yusong-Ku, Taejon, 305-353, KOREA
Tel) 82-42-868-8997 Fax) 82-42-861-2574
E-mail) swhong@nanum.kaeri.re.kr

**Abstract**

Korea Atomic Energy Research Institute (KAERI) started a fuel coolant interaction (FCI) experiment using Corium in 1997. The test facility and relevant instrumentation will be constructed and fabricated by March 2000. The first series of tests are for the investigation of triggering mechanism. The mechanism and role of hydrogen generation and the effect of melt composition will be investigated. The second ones will be on the mixing behavior. The reactor material including UO2, ZrO2, ZR, and SS up to 20 kg will be poured into a water tank inside a pressure vessel. The fuel and water pool geometry is in a multi-dimensional shape. The test facility allows for flexible configuration of the water pool and test section. The cold crucible technology that uses high-frequency induction heating in a water-cooled cage (cold crucible) is going to be used for the corium melting. The preliminary testing for the melting using TiO2 has been completed and the delivery test is under progress.
Keywords: FCI, Cold Crucible

## 1. Introduction

Though the alpha mode failure due to the steam explosion is excluded from the reactor safety issue as discussed in SERG-2 in 1995, there remain FCI issues[1]. They are: localized in-vessel FCI which produces shock loading on the lower head and ex-vessel FCI which produces shock loading of cavity structure. To answer those questions, there have been international efforts on experimental researches, such as, FARO[2], KROTOS[3], ZEREX[4], WFCI[5] and ALPHA[6] program.

Korea Atomic Energy Research Institute (KAERI) launched a intermediate scale fuel coolant interaction (FCI) experiment called as Test for Real cOrium Interaction with water (TROI) using reactor material to investigate the physical mechanism of FCI in the area of explosion and mixing. We also plan to develop three-dimensional FCI computer codes, TEXAS-3D[7], by employing current computational fluid dynamics technology in corporation with university of Wisconsin. The test facility and relevant instrumentation will be designed and constructed by March 2000. We successfully finished preliminary test on the melting and delivery.

## 2. Scope and experimental facility

The reactor material including UO2, ZrO2, ZR, and SS up to 20 kg will be poured into a water tank inside a pressure vessel. A simplified view of the facility is shown in Fig. 1. The test pressure will be

less than 0.5 MPa. The fuel and water pool geometry is in multi-dimensional shape. The test facility is designed to allow flexible configuration of water pool and test section. We believe that the about 3kg used in the KROTOS program might not be enough and that the multi-dimensional effect should be factored into the experimental facilities to simulate reactor conditions [8].

The cold crucible technology[9], which was firstly proposed by Lebedev Physical Institute in 1974, is used for the melting of reactor material. It uses high-frequency induction heating in a water-cooled cage (cold crucible). As it offers greater purity and flexibility when working with reactive materials, it is beneficial in terms of composition control compared to the previous technologies.

## 3. Focus of TROI program

The first series of tests will be focused on the investigation of triggering mechanism. The mechanism and role of hydrogen generation[1] and the effect of metal components, which was mentioned recently [10], will be investigated. The second series of tests will be focused on the mixing behavior. The melt jet water interaction, break up behavior, void fraction distribution will be investigated by using advanced instrumentation including high-speed video [3] and/or X-rays [11]. As there is few data for the multi-dimensional FCI phenomena using reactor material, the results of test will be very helpful in the understanding of the physical mechanism of the FCI. They also can be directly used for the development of multi-dimensional FCI computer codes, TEXAS-3D. The whole program is intended to provide quantitative evaluation of FCI in the area of mixing and explosion.

## 4. Results of preliminary melting and delivery test

Before melting UO2, we performed a preliminary melting and delivery test by using TiO2, which has similar electrical property as the corium. Here we introduce briefly cold crucible design and results of preliminary tests[12].

### 4.1 Cold crucible design

The Fig. 2 shows schematic diagram of cold crucible. The cold crucible consists of 36 copper tubes. The chiller supplies cooling water to the cold crucible and the working coil of R.F generator. The working coil surrounds the cold crucible and generates the magnetic flux to induce the current in the melt. The major design parameters for the cold crucible are the frequency, input power of R.F generator and the cold crucible size. The electrical resistivity of $TiO_2$ is 1.2xE10 Ω.cm at 800 °C. To retain 10kg of $TiO_2$, the cold crucible is sized to have dimension of 15cm diameter and 30cm height. The operating frequency of the cold crucible is approximately 370 KHz. The R.F generator input power has to be determined by considering heat balance between R.F input power and heat loss from the crucible. The heat loss consists of the conduction heat from the sintered layer to the coolant tubes and the radiation heat from melt surface to atmosphere. The sintered layer, which is naturally formed, plays a crucial role in retaining the molten material without direct contact with the cage. Total heat loss is calculated about 13.8kW. The 30kW RF power generator is designed by considering the efficiency of R.F generator.

4.2 Results of preliminary test

The skull melting process includes the basic steps: (1) Melt the material by an R.F field (2) Confine the melt in a solid shell of the same composition as the melt (3) Initiate the melting with the help of a special starting process. Within a few minutes after the induction heating, the melting of the powder in a crucible is initiated by a carbon ring. Due to the oxidation of carbon ring and water entrapped in the powder, the gas is released after several minutes of heating. The majority of $TiO_2$ is melted within 30 minutes after R.F power input. As a hole is made in the powder above the carbon ring to release gas, the center part of the cover crust is collapsed. Therefore, the melt swirling could be seen by a naked eye. The sintered layer of 2 to 3mm is coarsely formed along the wall. Fig 3 shows melt release process. Total 4.7kg of $TiO_2$ powder and debris mixtures is charged into the crucible. The size of hole for melt release is about 8cm, but size of the hole is about 4cm. The amount released through punched hole is about 2.6kg, 60% of initial charged mass.

As we successfully performed preliminary tests, the design methodology and melt release experience will be used for the main test, which is scheduled on the March of 2000.

## 5. Summary

KAERI launched a intermediate scale experimental research program on FCI using reactor material to investigate the physical mechanism in the area of triggering and mixing with the aid of advanced instrumentation. We also plan to develop three-dimensional FCI computer codes, TEXAS-3D[7], by employing current computational fluid dynamics technology in corporation with university of Wisconsin. The facilities are under construction. We successfully performed preliminary tests on the melting and delivery by using cold crucible technology. The results are promising and will be used for the main test.

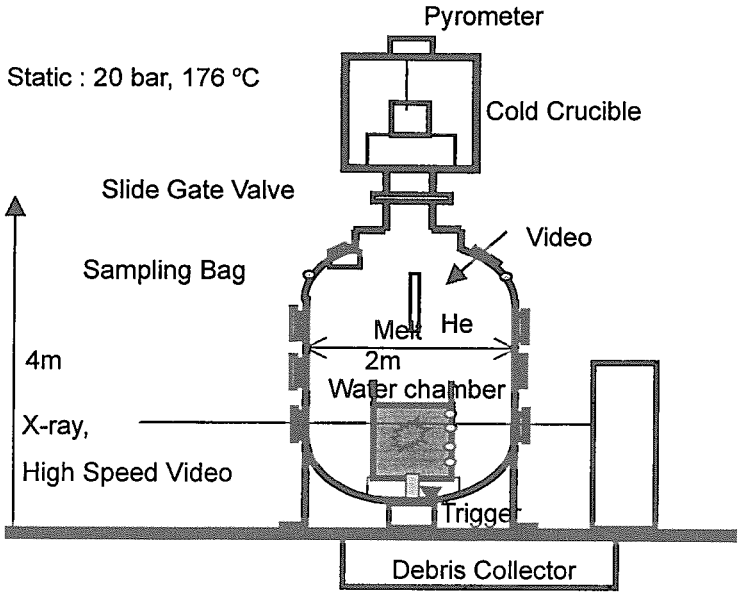



Fig. 1 Schematic Diagram for FCI Test Facility

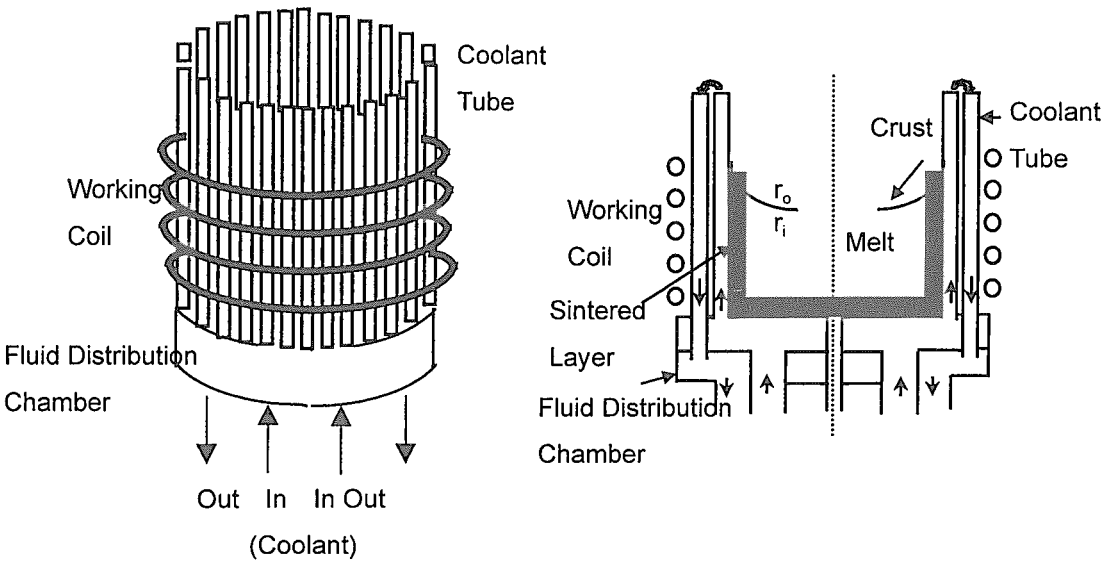



Fig. 2 Schematic Diagram for Cold Crucible

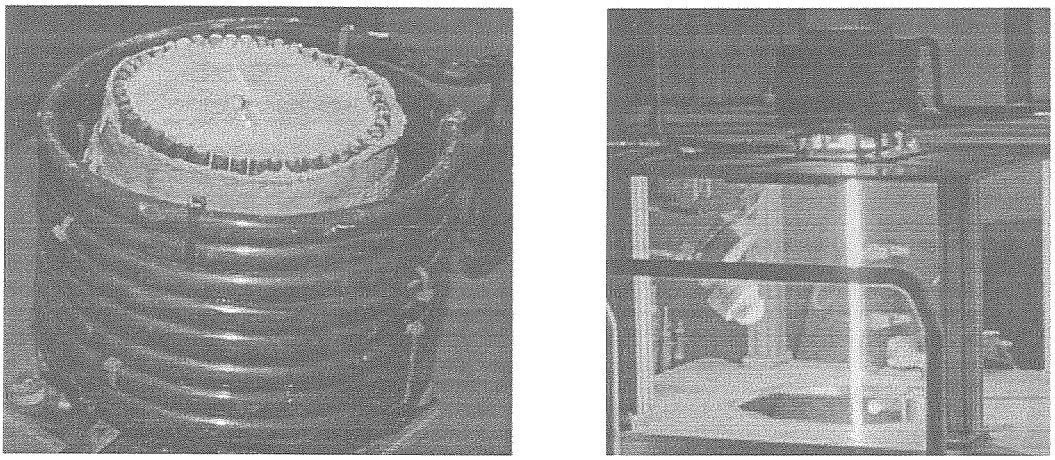


Fig. 3 Melt delivery test

Aknowledgement

This project has been carried out under the Nuclear R&D Program by MOST

References

1. T. P. Speis and S. Basu, Fuel-coolant interaction phenomena in reactor safety: Current understanding and future research needs, Proceedings of final program of CSNI specialist meeting on fuel coolant interactions, 6-7, JAERI-Tokai, Japan, May 19-21, 1997.
2. D. Magallon and I. Huhtiniemi, Corium melt quenching tests at low pressure and subcooling water in FARO, NURETH-9, San-Francisco, California, U.S.A. October 1999.
3. I. Huhtiniemi and D. Magallon, Insight into Steam Explosions with Corium Melts in KROTOS, NURETH-9, San-Francisco, California, U.S.A. October 1999.
4. D. H. Cho, D. R. Armstrong, W. H. Gunther, Experiments on interactions between Zirconium-containing melt and water, NUREG/CR-5372, 1998.
5. H. S. Park, R. Chapman, M. L. Corradini, Vapor explosions in a one-dimensional large scale geometry with simulant melts, NUREG/CR-6623, 1999, draft
6. N. Yamano et. al., Phenomenological studies on melt-coolant interactions in the ALPHA program, Nuclear Engineering and Design, 111, pp.369-389, 1995.
7. J. Murphy et. al., Multi-dimensional modelling of multiphase flow physics: High speed nozzle and jet flows – A case study, NURETH-9, San-Francisco, California, U.S.A. October 1999.
8. S. W. Hong et. al., An investigation of triggerability and explosivity in fuel coolant interactions, Proceedings of Korean Nuclear Society Spring Meeting, p.213, 1999.
9. S. W. Hong et. al., A feasibility study on UO2/ZrO2 mixture melting using induction skull melting method, Proceedings of Korean Nuclear Society Fall Meeting, 1998
10. T.N.Dinh, A.T.Dinh, J.A.Green, and B.R.Sehgal, An assessment of steam explosion potential in molten-fuel coolant interaction experiments, 6th International Conference on Nuclear Engineering, ICONE-6563, May 10-14, 1998.
11. M. C. Baker, R. Bonazza, and M. L. Corradini, Measurements of void fraction in a water-molten tin system by X-ray absorption, NUREG/CP-0160, Proceedings of the OECD/CSNI specialist meeting on advanced instrumentation and measurement techniques, Santa Barbara, California, U.S.A., 1997, pp. 343-352.
12. S. W. Hong et. al., Preliminary Test for Actual Corium Melt and Release in Fuel Coolant Interaction Experiment, Proceedings of Korean Nuclear Society Fall, 1999

JP0150087



## 2.2 Installation for Low Temperature Vapor Explosion Experiment

Sunchai Nilsuwankosit, Urith Archakositt
*Department of Nuclear Technology,*
*Faculty of Engineering*
*Chulalongkorn University*
*Bangkok, Thailand*

**Abstract**
A preparation for the experiment on the low temperature vapor explosion was planned at the department of Nuclear Technology, Chulalongkorn University, Thailand. The objective of the experiment was to simulate the interaction between the molten fuel and the volatile cooling liquid without resorting to the high temperature. The experiment was expected to involve the injection of the liquid material at a moderate temperature into the liquid material with the very low boiling temperature in order to observe the level of the pressurization as a function of the temperatures and masses of the applied materials. For this purpose, the liquid nitrogen and the water were chosen as the coolant and the injected material for this experiment. Due to the size of the installation and the scale of the interaction, only lumped effect of various parameters on the explosion was expected from the experiment at this initial stage.

**Keywords:** Vapor Explosion, Cryogenic Process

### Introduction

In nuclear engineering, one of the major concern in nuclear safety is the result from the fuel-coolant interaction (FCI). The interaction between the molten fuel and the water can result in the very large scale vaporization in a very short time period, the vapor explosion, which can damage the pressure vessel and the containment. To prevent such a consequence, it is necessary to understand the mechanism of the process in order to define the safety parameters.

In addition of its safety application, the process that involves the interaction between the hot material (solid or liquid) and the volatile liquid has also seen its increasing usage for other industrial purposes. As the boiling phenomenon and the mixing process of the materials can be either beneficial or a disadvantage, the information on the interaction between the hot material and the volatile coolant is crucial and is subjected to study.

Due to the limitation in funding and the availability of the heavy industrial applications in the country, there is currently no demand for the large scale research in vapor explosion in Thailand. However, the small scale low temperature experiment on this subject can be valuable. Academically, it offers the fundamental research on the FCI process, albeit at the low temperature. At the same time, it can also be applied to other industrial purposes such as that of the cryogenic or other boiling process. It was for these reasons that the project on the low temperature vapor explosion was proposed.

### Study Plan and Objectives

The main objective of the study was to simulate the interaction between the molten fuel and the volatile cooling liquid without resorting to the high temperature. By observing the outcome of the interaction, it was expected that the mechanism of the interaction can be deduced. However, due to the size of the installation and the expected scale of the explosion, no detailed information was expected at this initial stage and only the lumped effect of various parameters on the explosion was to be correlated.

The aiming at this initial stage of the research was to set up the installation for the experiment. In order to accomplish this task, it was necessary to estimate the scale of the explosion for the desired configuration of the installation. This was done not only to ensure the safety of the installation but, more specifically, to ensure that the explosion could be observed.

In addition to the numerical estimation for the level of the explosion, a limited number of

pre-experiments were also conducted to test the possibility of the vapor explosion in an open environment and in a partly open environment at the room condition. No actual measurement was taken. The observation was done only visually in order to confirm the results.

The last step of this initial stage was to design and construct the installation for the experiment. The installation was designed in a modular fashion so that change or modification could be done for a specific parts of the installation without having to rebuild it from the ground up. In addition, in order to simplify the design, the installation was to be operated mechanically. In the next stage of the research, with the installation working, a number of electronic devices would be incorporated in order to obtained the more detailed and accurate measurement and to automate the operation.

**Numerical Estimation of the Explosion**

In order to estimate the scale of the explosion, a suitable model for the calculation must be used. Even though the actual interaction and the propagation of the explosion were not primarily known, the pressure level and amount of material that interacted might be estimated based on the thermodynamic of the system.

The most fundamental model for the estimation was that of the system in equilibrium. In such case, the fuel, the liquid coolant and the produced vapor were to be at the same temperature. This also implied that the system was at the saturating pressure of the coolant, otherwise the liquid coolant and the produced vapor can not be at the same temperature. With the total mass of the fuel, $m_F$, at the initial temperature of $T_{F0}$ and the initial pressure $P_0$, the initial total mass of the liquid coolant, $m_{f0}$, the initial total mass of the vapor, $m_{g0}$ and with the temperature of the liquid and the vapor being the saturating temperature, $T_{\mathrm{sat0}}$, the total initial heat, $E_{\mathrm{total}}$, carried in the system could be calculated as

$$E_{\mathrm{total}} = m_F i_{F0} + m_{f0} h_{f0} + m_{g0} h_{g0} \tag{1}$$

where $i_{F0}$ was the internal energy at $T_{F0}$ per unit mass of the fuel and $h_{f0}$ and $h_{g0}$ were the enthalpy of the saturated liquid and the saturated vapor at $T_{\mathrm{sat0}}$.

With the assumption that the system was at the equilibrium, no heat loss from the system and no chemical reaction was observed, the total heat of the system could be described as

$$E_{\mathrm{total}} = m_F i_F^* + m_f^* h_f^* + m_g^* h_g^* \tag{2}$$

where $i_F^*$ was the internal energy of the fuel at the final temperature $T^*$ and at the final pressure $P^*$, $m_f^*$ and $m_g^*$ were the final mass of the liquid and the vapor and $h_f^*$ and $h_g^*$ were the enthalpy of the saturated liquid and the enthalpy of the saturated vapor at $T^*$ (it should be noted that $P^*$ was the saturating pressure). Another restriction that must be applied was the conservation of the total mass of the coolant (liquid and vapor). This was described as

$$m_{f0} + m_{g0} = m_f^* + m_g^* \tag{3}$$

To actually solve the above equation, it was also necessary to have the property tables or the correlations that described the relation between the pressure, the temperature and the internal energy and/or the enthalpy of the fuel and the coolant.

The pressure obtained with the above equations was expected for the system that was in equilibrium. In practice, not only the system hardly ever reached the equilibrium in the time scale of the process, the pressure at the equilibrium was expected to be much lower than the pressure observed during the transient. Therefore, while the obtained equilibrium might give the scale of the explosion to be expected, it was still not good enough for the designing purpose.

Another model that was applied was termed the instantaneous explosion model. In this model, the fuel was suddenly quenched to its melting temperature, $T_{Fs}$. The heat content of the fuel was transferred to the coolant and was totally used for vaporization and heating

Table 1: **The expected final pressure ($P''$), liquid nitrogen temperature ($T_f''$) and the void fraction ($\alpha$) as calculated with "EES" for the final water temperature ($T_F''$) from 108-192 K and at the equilibrium (*)**

| $T_F''$(K) | $P''$(kPa) | $T_f''(K)$ | $\alpha$ |
|---|---|---|---|
| 108 | 1252 | 107 | 0.87 |
| 120 | 1315 | 108 | 0.86 |
| 132 | 1346 | 109 | 0.85 |
| 144 | 1359 | 109 | 0.84 |
| 156 | 1361 | 109 | 0.84 |
| 168 | 1354 | 109 | 0.83 |
| 180 | 1339 | 108 | 0.83 |
| 192 | 1319 | 108 | 0.83 |
| 107* | 1247 | 107 | 0.87 |

the produced vapor such that its final temperature was the same as that of the fuel. For the liquid coolant, none of the heat was received and the liquid stayed approximately at its initial temperature with no significant change in its enthalpy while the system was pressurized. In this condition, $i_F^*, m_f^*, m_g^*$, and $h_g^*$ were the internal energy of the fuel at its melting point, the final mass of the liquid, the final mass of the vapor and the enthalpy of the vapor at the melting point of the fuel.

This instantaneous explosion model resulted in a substantially higher pressure level. The model, however, was not realistic. Since, it was more possible that the heat transferred from the fuel was used for the vaporization and the heating of both the liquid and the vapor. Further more, the final temperature of the fuel after the explosion might be either lower or higher than the melting point. This was entirely due to the fuel fragmentation process and the rate at which the heat was transferred from the fuel. Still, the obtained pressure level should define the upper limit for the expected pressure level during the explosion.

With the upper and the lower limit for the pressure level being obtained, it was expected that the actual maximum pressure during the explosion lied some where between these two values. If the pressure and the temperatures of the fuel and the coolant during the explosion were actually observed, it was possible to then calculate the amount of the materials that interacted during the process with the thermodynamic model. For this assumption, $m_f^*, m_g^*, i_F^*, h_f^*$ and $h_g^*$ were the liquid mass, the vapor mass, the fuel internal energy, the enthalpy of the liquid and the vapor, all measured at the given final pressure and temperatures.

In calculating the final pressure and temperatures, the major complication arose from the fact that property tables or correlations must be supplied for the fuel and the coolant. The interpolation of the data and the interation were then expected for the calculation.

With the water as the fuel and the liquid nitrogen as the liquid coolant, a number of calculations were conducted with the computer program "EES." For the calculations, a cylindrical volume with the height of 1.0 m and the inside diameter of 0.1 m was assumed for the system. The initial pressure of the system was 100 kPa. The total mass of water at 300 K was 0.1 kg while the total mass of the saturated liquid nitrogen plus $N_2$ was 1.0 kg. In the specified volume, the initial void fraction was calculated as approximately 0.85.

As "EES" did not have the property of the ice water, the condition of the instantaneous explosion was not calculated. Assume that $N_2$ also had the same final temperature as that of the water while as the liquid nitrogen was at the saturating point, the final pressure, the saturating temperature of the liquid nitrogen and the void fraction were obtained as shown together with that for the equilibrium condition in Table 1. The intermediate pressures were also plotted against the expected temperature of the fuel in Figure 1.

Under the condition as given, the maximum pressure was calculated to be 1361 kPa. Con-
Intermediate Pressure (kPa)

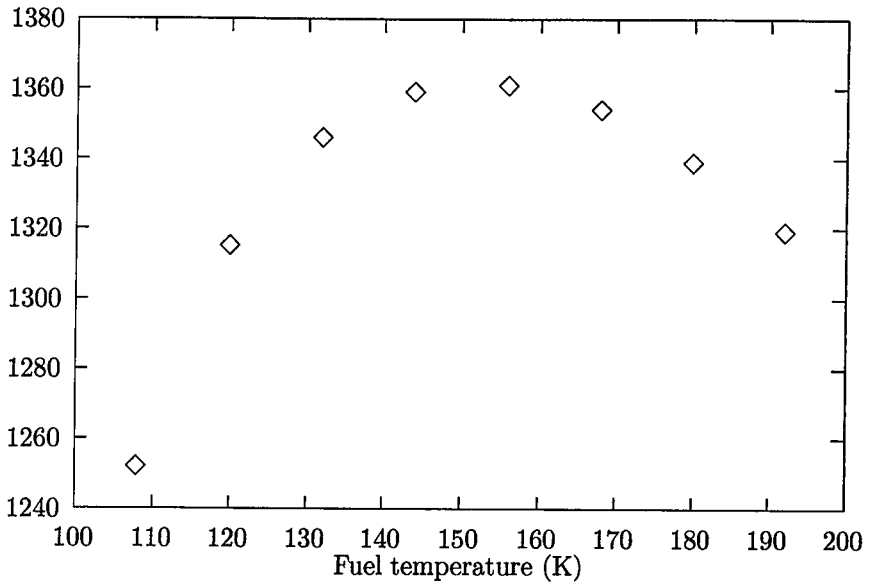



Figure 1: **The calculated intermediate pressure for the expected temperature of the fuel**

sider that the initial pressure in the system was 100 kPa, the system was predicted to be pressurized by ten folds in the process.

**Pre-Experiments**

In order to verify the possibility of the vapor explosion at low temperature, a number of pre-experiments were conducted, visually observed and recorded. These pre-experiments were conducted by simply injecting an amount of water into a volume of the liquid nitrogen in an open container.

Since the experiments were conducted in an open environment, the produced vapor could expand freely. As a result, even though it was observed that the liquid nitrogen was rapidly boiled by the injected water, no explosion was observed in any of these pre-experiments. It might still be possible for the explosion to occur in an open environment, however, if the very large amount of the water and the liquid nitrogen were used in this configuration. The condition as such was not of interest and was not implemented.

For the pre-experiments conducted in the system that was partially open, the pressure build up in the system was observed. Consider that the produced nitrogen gas could get out of the container mainly through the small opening, the free expansion of the produced vapor would not be possible in this configuration. From these results, therefore, it was concluded that one of the possible factors that controlled the pressurization and/or the vapor explosion was the ability of the vapor to expand during the process.

**Design of the Installation**

The installation was designed in a modular fashion. Apart from the connecting pipes and all the control and auxiliary devices, the installation can be divided into four parts. The first one was the container. This part served as a basis platform in which all the other parts could be built and placed up on. Therefore, the part should be strong enough to support the whole structure. To reduce the heat loss rate, the volume inside the container could also be filled with the insulator.

The second part of the installation was termed the "explosion chamber." It was the most critical part of the installation as it was the place where the interaction took place. In general, the explosion chamber was the cylindrical tube with its top end connected to the water injection package. For the liquid nitrogen, it would be filled into the chamber from the bottom. Once the desired level of liquid nitrogen was reached, the valve on the pipe that connected the chamber to the liquid nitrogen tank would be closed so that the water could be injected. As the explosion chamber was the part that experienced the most harsh environment, it should be made with the material that could withstand the low temperature, the chemical attack, the rust and the stress induced by the pressurization. In addition, the inner side fo the chamber should also be insulated in order to reduce the heat transfer from the environment to the coolant.

The third part of the installation was the expansion tube. This part was connected to the explosion chamber and provided the extra volume for the vapor produced by the interaction to expand in to. In one aspect, it provided a safety margin for the explosion so that the system might not be over pressurized. At the same time, the tube also served as a mechanical mean to measure the magnitude of the explosion. This was done by filling the expansion tube with the viscous liquid such as the lubricating oil, the increasing pressure would drive the liquid out of the expansion tube in to the drain storage which was the forth part of the installation. By measuring the volume of the liquid driven out of the expansion tube into the drain storage, the work done by the expansion would then be calculated and correlated in order to obtain the magnitude of the explosion.

An overview drawing that showed the arrangement of the installation, including the connection between the container, the explosion chamber, the expansion tube and the drain storage was also given in Figure 2.

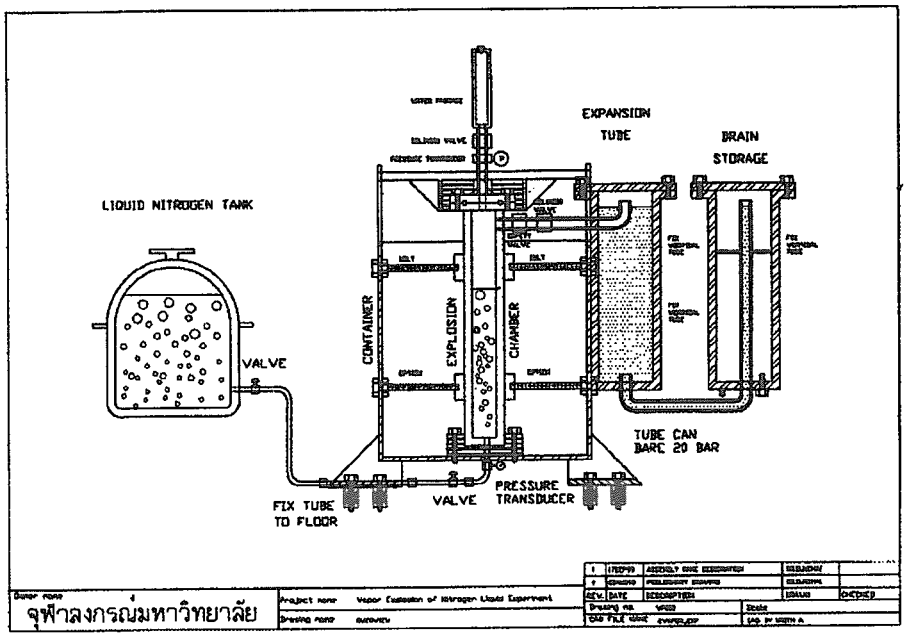



Figure 2: **Overview drawing of the installation**

## Conclusion and Future Plan of Study

From the numerical calculation for the interaction of the liquid water and the liquid nitrogen in a closed volume at room condition, it was estimated that the system could be pressurized by a factor of ten by the interaction between 0.1 kg of water at 300 K and 1.0 kg of liquid

nitrogen. By conducting the pre-experiments in an open environment, no vapor explosion was observed, though the rapid boiling of the liquid nitrogen due to the interaction with the water was clearly seen. The pressure buildup observed in the pre-experiments for a partially open environment confirmed that one condition for the vapor explosion and/or the pressurization was the ability of the vapor to expand in the system during the process.

The design of the installation was done in a modular fashion. There are four separate parts that were connected to each other. The container was the platform in which the whole structure was to be constructed on. The explosion chamber was for conducting the experiment. The expansion tube was designed to provide an extra room for the expansion of the produced vapor. The last part, the drain storage, worked together with the expansion tube to provide a mechanical mean for measuring the expansion work caused by the interaction.

At the time of this writing, the construction of the installation was underway. and was expected to be completed before the end of the year 1999. With the installation ready, the plan was set to conduct the experiments for the system with the configuration similar to that used in the pre-experiments. This was done to obtain the actual reading for the scale for the explosion and/or the pressurization. The larger volume of water and the liquid nitrogen would also be implemented. The interactions between other different materials could also be attempted.

To obtain the information on the progress of the interaction, the more sensitive devices could also be design and incorporated into the installation in order to observe the temperature and the pressure transient during the process. The condition of the system and the materials after the process was concluded should also be observed in order to identify the mechanisms of the interaction and the fragmentation process.

## References

1. M.L. Corradini, J. Murphy, S. Nilsuwankosit, D. Pineau, B. Shamoun, J. Tang and S. Wang, "Fuel-Coolant Interaction Analyses with TEXAS-V Vapor Explosion Model," Nuclear Safety Research Center, Department of Engineering Physics, University of Wisconsin-Madison, USA (1998)

2. S. Nilsuwankosit, K. Moriyama, M. L. Corradini, "Analysis of FARO-L14 Experiment with TEXAS," Proc. NHTC-Houston TX (1996)

3. Chu C.C., M. L. Corradini, "One-Dimensional Transient Model for Fuel-Coolant Interaction Analysis," Nuclear Science Engineering, V.101, P.48-71 (1989)

4. S.A. Klein and F.L. Alvarado, "EES, Engineering Equation Solver," F-Chart Software, USA (1993)

5. B.G.Kyle, "Chemical and Process Thermodynamics," Prentice Hall, USA (1992)

JP0150088



# 2.3 COTELS Fuel Coolant Interaction Tests under Ex-Vessel Conditions

Masami Kato and Hideo Nagasaka
Systems Safety Department, Nuclear Power Engineering Corporation
Phone:+81(3)4512-2572, Facsimile:+81(3)4512-2599, ms-kato@nupec.or.jp

Yuri Vasilyev, Alexander Kolodeshnikov and Vladimir Zhdanov
Institute of Atomic Energy, National Nuclear Center

## ABSTRACT

Extensive efforts have been performed to resolve in-vessel fuel coolant interaction (FCI) concerning $\alpha$-mode failure issue. However, there are several basic differences between in-vessel and ex-vessel FCI conditions. FCI phenomena when a molten corium falls into water pool on containment floor during a sever accident (SA) were experimentally investigated in COTELS Test A. Typical ex-vessel FCI conditions of SA in actual plant were pertinently simulated in the tests based on SA scenario analysis of LWR. In the tests, about 60kg of $UO_2$ mixture was poured into water pool. In most tests conducted, measured pressure in the test vessel reached the first peak value as long as 0.5 s compared with the time observed in steam explosion (SE), then it gradually approached the final quasi-steady state pressure within 10 s. No violent SE was observed in any tests. Most of poured corium was broken up and only small amount of ingot corium was found on the pool bottom. The first peak pressure was well correlated by the corium particle size which was much larger than that usually observed in SE. Measured final quasi-state pressure was larger than that evaluated by the initial stored energy in corium due to non-condensible gas generation as a result of oxidation of metallic components in the corium. The non-dimensional first peak pressure was well correlated by one non-dimensional parameter not only for COTELS data but also for FARO data.

*Keywords: COTELS, Ex-Vessel , $UO_2$ Corium, FCI, Breakup*

## 1. INTRODUCTION

Since in-vessel SE was identified as one of early containment failure scenarios ($\alpha$-mode failure) in WASH-1400, not only FCI researches to understand the fundamental SE phenomena but also a systematic efforts to evaluate a probabilistic approach concerning $\alpha$-mode failure have been extensively performed. These efforts were reviewed by the second steam explosion review group (SERG-2) and it concluded that $\alpha$-mode failure issue was negligibly small from risk perspective[1] and this conclusion was supported by the recent OECD/CSNI specialists meeting at Tokai, Japan[2]. However, ex-vessel SE is still one of remaining issues mainly due to lower pressure condition under which SE is more easily to occur. Recent FARO experiments[3] suggested that metallic Zr in $UO_2$-$ZrO_2$ mixture might enhance a break-up of the corium in pool. KROTOS experiments[4] concluded that an energetic SE was less likely to occur for a few kg of $UO_2$-$ZrO_2$ mixture compared with molten alumina even under low pressure and highly subcooled water conditions. However, there are still a few data available under ex-vessel conditions.

This paper deals with COTELS Test A which focuses on FCI phenomena when a molten corium falls into water pool on containment floor. There are several basic differences between in-vessel and ex-vessel FCI conditions, e.g. ambient pressure and gas composition, corium jet diameter and composition, depth and temperature of water pool and pool bottom material. Typical ex-vessel FCI conditions in actual plant were pertinently simulated in COTELS project based on SA scenario analysis[5]. Dimensional analysis on the first peak pressure due to FCI was conducted based on the evaluation of the test results.

## 2. TEST FACILITY AND TEST CONDITIONS

The test facility (LAVA) mainly consists of an electric melting furnace (EMF), a test vessel and a melt catcher as shown in Fig. 1. The EMF has a capability to melt 60 kg of corium composed of $UO_2$, Zr, $ZrO_2$ and SS by induction heating[6]. Thermocouples and pressure sensors were installed in the test vessel. Gas sampling line was prepared to evaluate $H_2$ gas generation. The diameter of falling corium jet is 5 cm, corresponding to an instrumentation line of reactor pressure vessel (RPV). Pressure difference between EMF and the test vessel can be adjusted to vary corium velocity. Ex-vessel corium includes not only core structures but also structures in a lower plenum, so that the selected corium composition was $UO_2$ (55wt%)+Zr (25%)+$ZrO_2$ (5%)+SS (15%) including more metallic components.

The BWR SA scenario analysis suggested that the existence of water pool on the containment floor before RPV failure was only possible for LOCA sequence and pool depth was shallow. Thus, as reference pool conditions, the temperature is nearly saturated and the depth is 0.4 m. Five cm thickness concrete plate is laid on the melt catcher to examine the effect of interaction among corium, water and concrete considering shallow water pool. As a phase-II AM in Japanese LWRs, a reactor cavity is filled with water before RPV bottom failure to prevent a steel containment shell attack in BWR Mark-I or to suppress a molten core concrete interaction in PWR containment. Pool water is highly subcooled in both cases. In COTELS Test A, these AM conditions were also simulated.

Eight tests including one AM case were carried out. Table 1 summarizes test conditions. Test A1 is a reference case in which test conditions are 56 kg of corium, pure saturated steam conditions at 0.2 MPa, saturated pool water, 0.4 m pool depth and no differential pressure between EMF and the test vessel. Major test parameters are, corium mass (27 kg in A4), non-condensible gas existence in free space (20% of nitrogen gas in A5), pool water subcooling (21 K subcooling in A6), differential pressure between EMF and the test vessel (A8 and A10) and pool depth (0.9 m in A9). It should be noted that the actual differential pressure in A8 might be much smaller than table value because of leakage due to crucible bearing sleeve deformation during the test. Test A11 corresponds to AM condition case, where high

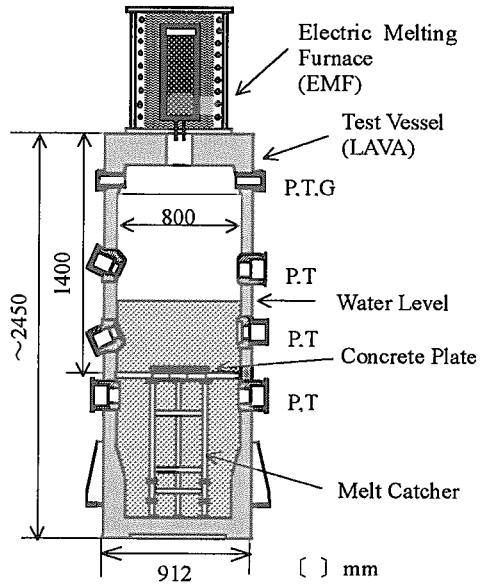



Fig. 1 Test facility of COTELS Test A

Table 1 Summary of initial conditions

| Run No. | A1 | A4 | A5 | A6 | A8 | A9 | A10 | A11 |
|---|---|---|---|---|---|---|---|---|
| Corium mass, kg | 56.3 | 27.0 | 55.4 | 53.1 | 47.7 | 57.1 | 55.0 | 53 |
| Pool depth, m | 0.4 | 0.4 | 0.4 | 0.4 | 0.4 | 0.9 | 0.4 | 0.8 |
| Pool subcooling, K | 0 | 8 | 12 | 21 | 24 | 0 | 21 | 86 |
| Initial pressure, MPa | 0.20 | 0.30 | 0.25 | 0.21 | 0.45 | 0.21 | 0.47 | 0.27 |
| Ambient Gas | Steam | Steam | Steam (*2) | Steam | Steam | Steam | Steam | Ar |
| ΔP, MPa (*1) | 0.03 | 0.03 | 0.01 | ~0 | 0.67(*3) | 0.02 | 0.14 | 0.13 |

Corium composition $UO_2$:55wt%+Zr:25%+$ZrO_2$:5%+SS:15%
*1) ΔP: Pressure difference between EMF and test vessel to increase corium falling velocity
*2) 80 % steam +20 % nitrogen
*3) Actual ΔP might be much smaller because of leakage from deformed crucible bearing sleeve

subcooled and deep pool was established. In this test, a concrete trap with the same dimensions as Test B/C was used instead of the melt catcher.

## 3. EXPERIMENTAL RESULTS

### 3.1 Pressure Transient

Figure 2 shows a typical pressure response in free space. The pressure transient was categorised into three regions. Region 1 is a period from the time of corium contacting with pool surface to the first peak timing. In this region, the pressure rapidly increased and reached to the first peak pressure within 0.5 second. due to steam generation by heat transfer from falling corium particles in the pool. However, a pressure spike typical of steam explosion was not observed. Following to the first peak, the measured pressure temporally decreased in region 2 due to steam condensation by subcooled pool. Then, the pressure gradually approached the quasi-steady state value in region 3 usually in 10 seconds. This was caused by the heat transfer from corium accumulated on the pool bottom. The quasi-steady state pressure was larger than that evaluated by the initial stored energy in corium due to non-condensible gas generation by oxidation of metallic components in the corium in all test cases.

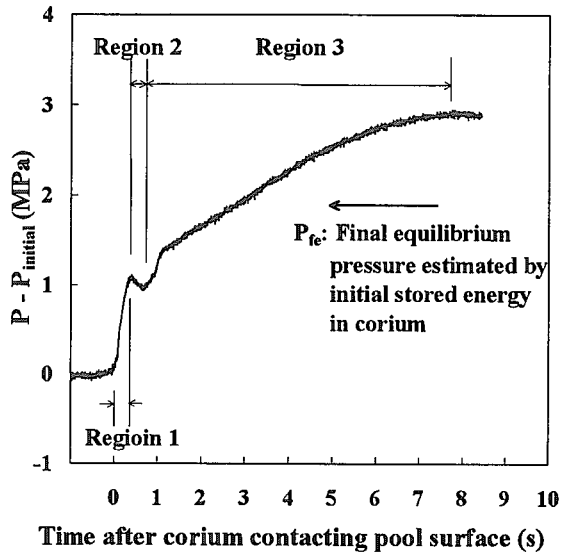



Fig. 2 Typical pressure response in test vessel (A1)

Figure 3 shows some test parameters effect on pressure transient. The initial pressurisation rate was not sensitive to poured corium mass (A4), pool depth (A9) and small pool subcooling change (A5, A6). In fact, the timing of the first peak was shorter than 0.5 second in all cases and this value was smaller than the time required for total drainage of corium from EMF. This suggested that front part of corium jet basically played an important role in region 1. The value of the first peak pressure, occurred in later stage of region 1, was more or less affected by the condensation amount of steam generated during initial phase in region 1. (Dominant mechanism of region 2 was steam condensation) More steam condensation in A5 and A6 due to subcooling, and A9 due to deep pool, caused smaller first peak compared with reference case of A1. The quasi-steady state pressure was lower than that of A1 due to a smaller amount of energy stored in the corium (A4), due to a large amount of pool mass in

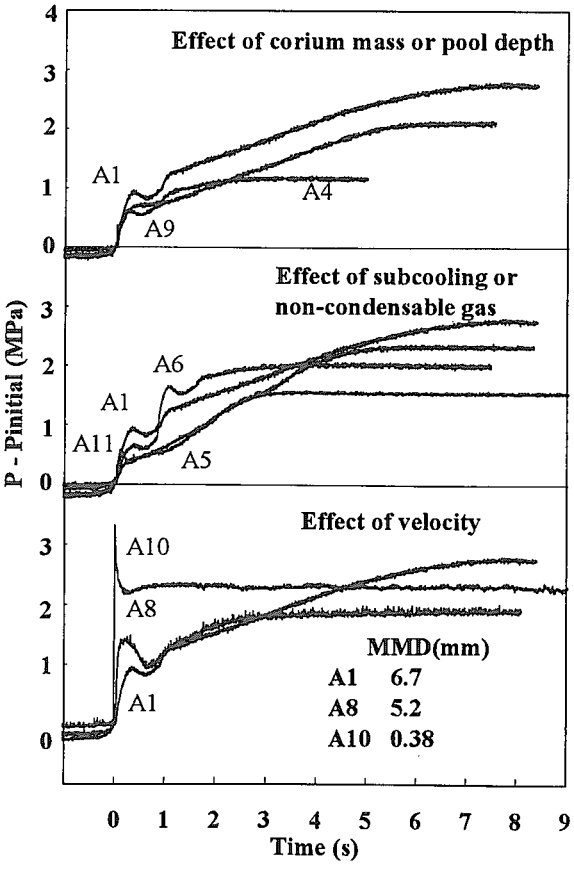



Fig. 3 Comparison of pressure transient

A9 and due to the existence of initial pool subcooling (A5, A6). The first peak pressure was sensitive to corium falling velocity which governed corium particle size. Time required to reach the quasi-steady state pressure was shorter in larger velocity cases, because of predominant initial energy release in region 1. Although higher falling velocity was imposed in AM case A11, the first peak pressure was not so high. This is because coalescence of breakup particles was caused inside of the confined geometry of concrete trap with 36 cm diameter and the generated steam was condensed by high subcooled water.

The first peak pressure in A10 was relatively large and measured mass median diameter (MMD) of particles was a few hundred microns different from any other cases. Figures 4 shows the measured pressure during very short period after corium pouring. A pressure spike typical of steam explosion was not observed in the free space pressure. The shape of small particles in A10 was not spherical. (Spherical shape is usually observed in SE phenomena) These data suggested that the steam explosion did not occur in A10.

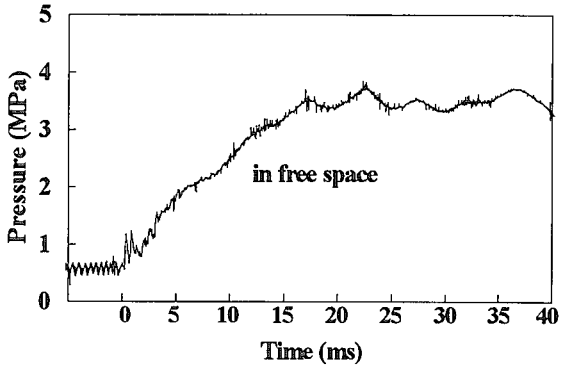



Fig. 4 Short term pressure transient (A10)

### 3.2 Corium Dispersion Characteristics

In all tests, most of poured molten corium was broken up in the pool. Figure 5 summarizes mass of poured corium, mass of ingot corium attached on the concrete plate and breakup ratio defined as (poured corium mass – ingot corium mass)/(poured corium mass). The breakup ratio was ranged from 0.88 to 1.0. Only a few kg corium ingot was observed in most cases. The breakup ratio was all the same except A8 and A10. No ingot corium was found under higher falling velocity (A8 and A10). This demonstrated that, in A11, coalescence of breakup particles was caused due to the 36 cm cylindrical geometry of concrete trap even under higher falling velocity (About 4 kg of ingot corium remained). The ingot corium was easily removed from the concrete floor in all cases except for A5, though the ingot mass was all the same.

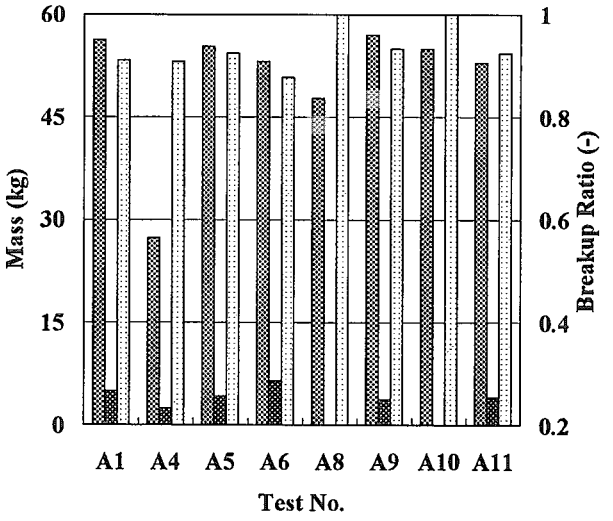



Fig. 5 Breakup ratio

L-11 of FARO, in which 4.1 % of metallic Zr was contained in oxide corium, resulted in complete breakup of the corium jet, while pancake was remained on the pool bottom in other FARO tests without metallic component. CCM tests[7], in which a mixture of $UO_2$, $ZrO_2$ and SS was poured into water, showed shorter breakup length compared with that without metal component. In CCM-6, in which Froud number is close to COTELS reference conditions, (L/D) is about 14 and this corresponds to 0.7 m breakup length in COTELS. These results suggested that metallic components in corium enhanced a corium jet breakup.

Figure 6 shows photographs of particle samples and ingot corium in A1. Size of corium particles was ranged from a few hundred microns to more than 10 mm. The shape was spherical in middle size, while it was irregular in both small and large size. Each particle had many pores not only

on its surfaces but also inside. Micro porosity of particles was about 10 %. These microstructure enhanced debris bed cooling. The bottom surface of ingot corium was also rough and had many small pores. No significant ablation allowed repeated use of the concrete plate. Water penetrated into the gap between the concrete surface and the ingot during quenching process.

Analysis of element concentration of all particle sizes revealed that they did not depend on the particle size. This suggested that the corium was uniformly mixed and melted in EMF before pouring. Particle size was separated by sieving method and measured size distribution was well correlated by Rosin-Rammler distribution, $R$=100 exp{-($x/x'$)$^b$}. Figure 7 shows a comparison of measured particle size distribution. Obtained MMD was similar except for higher velocity cases of A8, A10 and A11 so that initial pressurization rate was all the same. MMD was smaller in higher velocity cases. Figure 8 shows a relation between the first peak pressure and MMD. All data except for A11 was well correlated. Since water subcooling was very large in A11, the peak pressure was extremely suppressed by the high subcooling. Although the largest first peak pressure was observed in A10, it was well correlated with this line. This fact also implied that a SE did not occur in A10 and the first peak pressure was basically caused by heat transfer from corium particles falling in the pool.

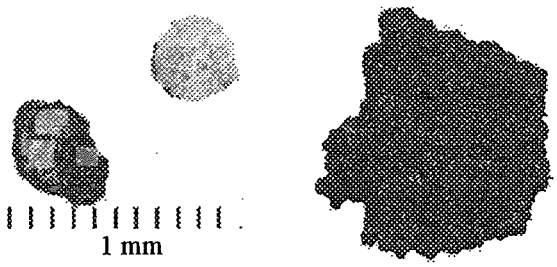



Fig. 6 Photo of particles and ingot corium (A1)

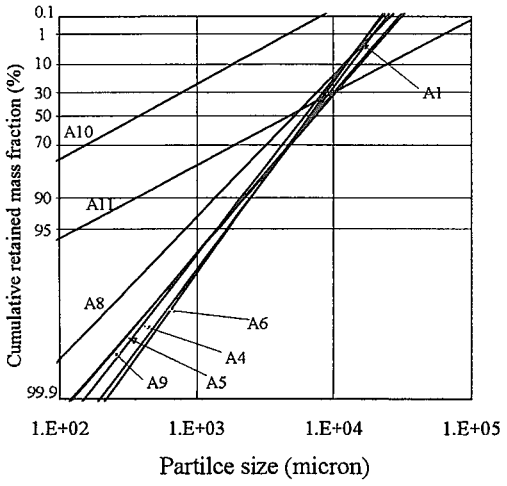



Fig. 7 Comparison of particle size distribution

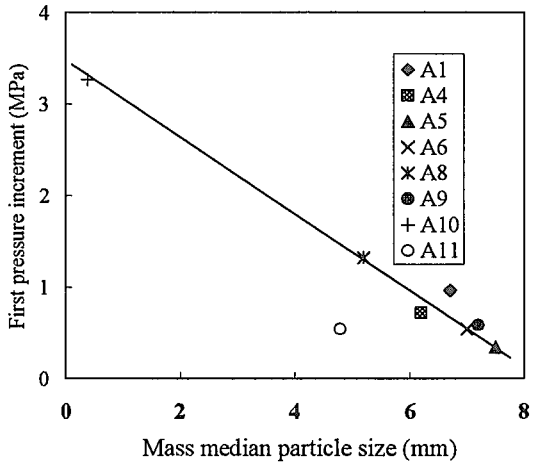



Fig. 8 Relation between MMD and first peak pressure

## 4. DIMENSIONAL ANALYSIS ON FIRST PEAK PRESSURE

In order to investigate the effects of tested parameters on the first peak pressure, dimensional analysis was done. In the analysis, the following assumptions were adopted based on the evaluation of Test A results to reduce the number of independent variables. Since the first pressure increase was mainly controlled by heat transfer from the falling corium particles in the pool before falling corium particles impinging on the concrete floor and dispersed particles size was small, heat conduction effect inside the particle was considered to be small. Hence, thermal conductivity of corium was deleted. Each particle was surrounded by a stable vapor film with large temperature gradient and dominant heat transfer mechanism from corium to water was considered to be radiation so that thermal conductivity and surface tension of water was also deleted. However, emissivity was not included since it was nearly common in the tests and no available data existed. Oxidation of corium components was neglected.

Although gas sampling analysis suggested that metallic components in the corium were oxidized during quenching process, rate constants of oxidations under high temperature have large uncertainty and a reasonable estimation of oxidation during region 1 was difficult.

Based on the above assumptions, the first peak pressure as a dependent variable was correlated by the following 12 parameters, corium specific internal energy (instead of initial temperature and specific heat), density and surface tension, corium jet diameter and falling velocity, water specific heat, latent heat of vaporization, subcooling of water, densities of vapor and water, and volumes of pool and free space. Eight non-dimensional parameters were determined using $\pi$ theorem. One non-dimensional parameter of $(\rho_j/\rho_w)$ was omitted due to quite small effect.

Correlation analysis was applied between a non-dimensional first peak pressure and each independent non-dimensional parameter to determine tentative exponent of each non-dimensional parameter (only COTELS data were used). The best fitting curve of a dimensional correlation based on the tentative exponent values was expressed after trial and error calculations as follows.

$$\frac{P_p}{v_j^2 \cdot \rho_g} = 1.0\times10^5 \cdot X1^{0.01} \cdot X2^{-0.2} \cdot X3^{0.01} \cdot X4^{0.01} \cdot X5^{-0.2} X6^{0.03} - 9.2\times10^3 \quad (1)$$

$\{P_p/(v_j^2 \cdot \rho_g)\}$ is non-dimensional dynamic pressure multiplied by (steam energy/corium energy). $X1$ is $(D/V_w^{(1/3)})$ and a ratio of jet diameter to a reference length of pool volume. Since the first pressure peak occurred in a short time and only limited water near the corium jet in the pool was heated, $X1$ is an indication of local heating of pool water. $X2$ is Weber number $(v_j^2 \cdot \rho_j \cdot D_j/\sigma_j)$ and is an indication of dispersed droplet diameter. $X3$ is a ratio of corium specific internal energy to latent heat of vaporization of water, $(u_j/L)$. $X4$ is a ratio of free space volume to pool volume, $(V_w/V_a)$. $X5$ is Jacob number $(1+\Delta T_{sub} \cdot c_p/L)$ and an indication of subcooling effect. $X6$ is a density ratio of vapor and water, $(\rho_g/\rho_w)$.

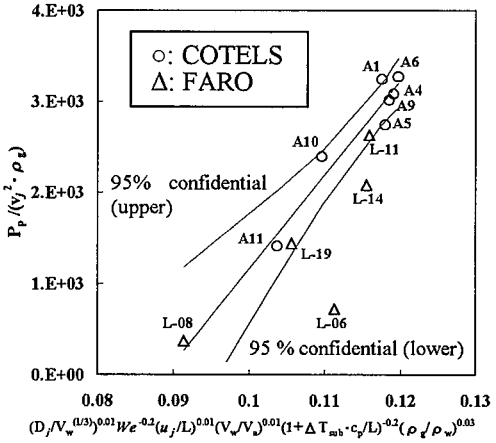



Fig. 9 Result of dimensional analysis

Figure 9 shows the non-dimensional correlation. FARO data was also plotted in this figure. Although most tests of FARO were conducted under high pressure and oxide corium condition (only L11 included 4.1 % Zr) different from COTELS, FARO test results were also well correlated except L-06, in which the pressure increase was low due to small corium mass. This agreement suggested that dominant mechanism of the initial pressure increase was same for both COTELS and FARO, and oxidation process was not significant when SE did not occur. Although the relatively large pressure peak was observed in COTELS A10, good correlation to A10 again confirmed no SE occurrence.

## 5. CONCLUSIONS

(1) Steam explosion was not observed not only under typical ex-vessel severe accident condition but also under AM condition.
(2) Breakup ratio was ranged 88 % to 100 % even under shallow pool. Metallic components in corium enhanced breakup of molten corium jet.
(3) The first peak pressure was well correlated by mass median diameter of breakup corium. This implied that the first peak pressure was mainly controlled by heat transfer from breakup particles.

The first peak pressure was most sensitive to corium falling velocity which governed dispersed corium particle size.

(4) Quasi-steady state pressure after corium quenching was higher than that evaluated by initial stored energy in corium due to oxidization of metallic components in corium.

(5) Water penetrated into gap between ingot corium and concrete floor during quenching process.

(6) Non-dimensional correlation of the first peak pressure derived from COTELS data was well correlated for FARO.

## 6. ACKNOWLEDGEMENTS

This work was sponsored under the contract by the Ministry of International Trade and Industry, Japan.

## NOMENCALTURE

| | | | |
|---|---|---|---|
| $D_j$ | jet diameter | $u_j$ | specific internal energy |
| L | latent heat of vaporization | $v_j$ | velocity of corium jet |
| $P_p$ | first pressure increment | $x$ | particle size |
| R | cumulative particle mass % retained on size $x$ | $x'$ | size parameter |
| $V_a$ | volume of free space | $\Delta T_{sub}$ | water subcooling |
| $V_w$ | volume of water pool | $\rho_g$ | vapor density |
| We | Weber number | $\rho_w$ | water density |
| $c_p$ | specific heat of water | $\rho_j$ | corium density |
| b | distribution parameter | $\sigma_j$ | corium surface tension |

## REFERENCES

1)Basu, S. and Ginsberg, T., "A Reassessment of the Potential for an Alpha-Mode Containment Failure and a Review of the Current Understanding of Broader Fuel-Coolant Interaction Issues", *Second Steam Explosion Review Group Workshop*, NUREG-1524, 1996.

2)Akiyama, M. Yamano, N. and Sugimoto, J., *Proc. of the OECD/CSNI Specialist mtg. On Fuel Coolant Interaction*, Tokai-mura, Japan, 1997.

3)Magallon, A., Zeisberger, A. and Corradini, M., Debris and Pool Formation/Heat Transfer in FARO-LWR, Experiment and Analysis, *Proc. of IN-Vessel Core Debris Retention and Coolability*, Garching, Germany, 1998.

4)Huhtiniemi. I., Magallon, D. and Hohmann, H., Results of Recent KROTOS/FCI Tests: Alimina vs. Corium Melt, *Proc. of the OECD/CSNI Specialist mtg. On Fuel Coolant Interaction*, Tokai-mura, Japan, 1997.

5)Nagasaka, H., Hamazaki, R. and Takahashi, Y., Scenarios of Ex-vessel Debris Cooling as Related to Nuclear Power Safety, *Proc. of Probabilistic Safety Assessment Methodology and Applications*, Seoul Korea, 1995.

6)Nagasaka, H. et al., COTELS Project (1): Overview of Project to Study FCI and MCCI during Severe Accident, *Proc. of OECD/CSNI Workshop on Ex-Vessel Debris Coolability*, Karlsruhe, 1999.

7)Spencer, B. et al., Fragmentation and Quench Behavior of Corium Melt Streams in Water, NUREG/CR-6133, 1994.

# 3. Session 2

# Fuel/Coolant Interaction II

## Chairperson:

S. Nilsuwankosit (Chula. Univ.)
M. Kato (NUPEC)

This is a blank page.

JP0150089



# 3.1 Three-Component Melt Jet Breakup Model for FCI Analysis

Kiyofumi Moriyama, Yu Maruyama,
Hideo Nakamura and Kazuichiro Hashimoto

Severe Accident Research Laboratory
Japan Atomic Energy Research Institute
Tokai-mura, Ibaraki-ken, 319-1195 Japan
phone: +81-29-282-5871, fax: +81-29-282-5570
email: mori@sarl.tokai.jaeri.go.jp

## Abstract

A new molten core jet breakup model was developed to for JASMINE-pre, the premixing module of the steam explosion simulation code developed at JAERI. The new model was designed emphasizing two aspects: separation of the melt model from the multiphase solver, and giving finer spatial resolution for the melt. The model consists of 3 components: jet, pool and particles, and it is designed to be combined with a two-phase flow code to handle the coolant flow field (ACE-3D). The melt jet is solved by 1-D CIP, which is known as a high resolution method, while the pool and particles are handled by 1-D FDM and Lagrangian particle method, respectively. In a simulation of a melt jet breakup experiment in non-boiling conditions (ALPHA-MJB16), the present model qualitatively reproduced the experimental results.

## 1 Introduction

In the framework of ALPHA (Assessment of Loads and Performance of Containment Vessel in Hypothetical Accidents) Program, a steam explosion simulation code JASMINE (JAERI Simulator for Multi-phase Interaction and Explosion) has been developed at Japan Atomic Energy Research Institute since 1994. JASMINE is purposed to simulate FCIs by multiphase thermohydraulics model integrating basic mechanistic models specific to the phenomena as constitutive equations, and as a final goal, to provide a real scale assessment of the influence of the steam explosion in LWR severe accidents. JASMINE has two modules to simulate premixing and propagation/escalation phases. This work is related to the premixing module JASMINE-pre.

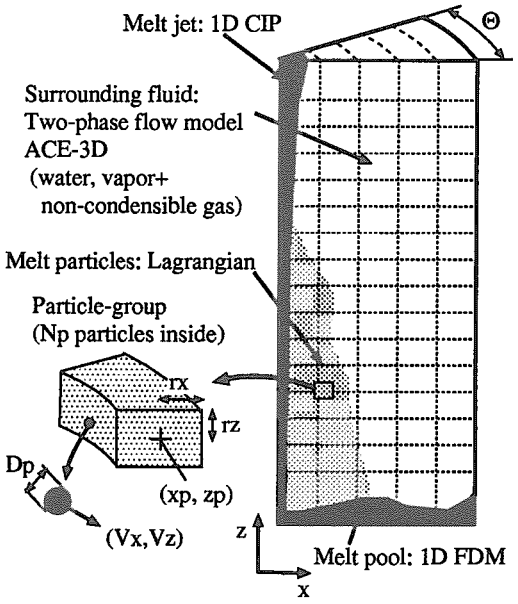



Figure 1: Concept of the new structure of JASMINE-pre

The basic structure of JASMINE-pre has been modified since 1998 [8], to separate the melt model from the multi-field solver for easier development and maintenance, and to give a finer spatial resolution for the melt model.

In the present work, a description of the new melt model and test calculations are given. The calculations here were performed with the melt model alone assuming a constant surrounding fluid conditions.

# 2 Description of the Melt Model

The new structure of JASMINE-pre is schematically shown in Fig. 1. The calculation domain considered is an azimuthal slice of a cylindrical space whose thickness is $\Theta$. The present melt model is a 2-D cylindrical model which satisfies a minimal requirement to handle the phenomena in question. The melt model consists of jet, pool and particle components. The following subsections will describe each component of the melt model.

The surrounding fluid involving water, vapor and non-condensible gases is modeled with a two-phase flow code ACE-3D developed by Ohnuki et al. [9] This part will be coupled later, but was not used in the calculation presented in section 3.

## 2.1 Melt Jet

The jet model was formulated with one dimensional conservation equations in $z$-direction and solved by CIP (cubic-interpolated pseudo-particle) method [13], which is known as a high resolution scheme free from numerical diffusion.

The jet is assumed to reside in the central column of the two-phase flow grid and flowing from the top to the bottom. The grid for melt jet is fit in the $z$-direction grid of two-phase flow model, with a manner that one two-phase flow cell is subdivided into $N_{sub}(\sim 5)$ jet cells to give the jet finer resolution than the coolant flow field.

The basic conservation equations for mass, internal energy and momentum of one dimensional jet are described as below.
Mass:

$$\frac{\partial A_J \rho_J}{\partial t} + v_J \frac{\partial A_J \rho_J}{\partial z} = -\sqrt{2\Theta A_J}\, m_e - A_J \rho_J \frac{\partial v_J}{\partial z} \quad (1)$$

Energy:

$$\frac{\partial e_J}{\partial t} + v_J \frac{\partial e_J}{\partial z} = -\sqrt{\frac{2\Theta}{A_J}} \frac{q}{\rho_J} \quad (2)$$

Momentum:

$$\frac{\partial v_J}{\partial t} + v_J \frac{\partial v_J}{\partial z} = -\frac{1}{\rho_J}\frac{\partial p_a}{\partial z} + K_f(v_a - v_J) + g \quad (3)$$

Where $A_J$, $\rho_J$, $v_J$ and $e_J$ denote the cross section, density, velocity and internal energy of the melt jet. In the momentum equation, pressure $p_a$ is given by the outer fluid field. These equations contains source terms such as $m_e$: mass flux due to droplet entrainment from the jet surface, $q$: heat flux and $K_f$: friction factor, which have to be given by constitutive equations .

To give the mass entrainment from the jet column as particles, the model similar to TEXAS code [2] based on the Epstein-Fauske [3] model considering Kelvin-Helmholtz (K-H) shear flow instability was employed. The primary wave number $k_p$, the corresponding wave length $\lambda_p$ and growth rate $n_p$ are given as follows.

$$k_p = \frac{2\rho_J \rho_a V_r^2}{3\sigma_J(\rho_J + \rho_a)}, \quad \lambda_p = \frac{2\pi}{k_p} \quad (4)$$

$$n_p^2 = \frac{\rho_J \rho_a k_p^2 V_r^2}{(\rho_J + \rho_a)^2} - \frac{\sigma_J k_p^3}{\rho_J + \rho_a} \quad (5)$$

The radial velocity of the particles generated from the wave crests $v_{ex}$ and its mass flux $m_e$ are assumed to be correlated with the wave growth rate as follows.

$$v_{ex} = C_{vx} n_p \lambda_p \quad (6)$$

$$m_e = C_{me} \rho_J v_{ex} \quad (7)$$

Here, $C_{vx}$ and $C_{me}$ are empirical constants. While, the $z$ velocity was assumed to be an average of jet and ambient fluid velocities with a weighting factor $C_{vzwt}$, as

$$v_{ez} = C_{vzwt} v_J + (1 - C_{vzwt}) v_a. \quad (8)$$

The diameter of the melt droplets removed from the jet column was evaluated by a simple Weber number criterion model.

$$d_e = C_{de} \frac{We_{cr}\sigma_J}{\rho_a V_r^2} \quad (9)$$

Here, $V_r$ is the relative velocity between the jet and surrounding fluid, $We_{cr}$ is a critical Weber number which is about 18 considering the force balance between the drag and surface tension at break off of a droplet from a wave crest. $C_{de}$ is an empirical factor.

The friction factor on the jet column was evaluated by a correlation for flow in rough pipes [12], using the primary wavelength and turbulent boundary layer thickness in replace of the wall roughness and the pipe diameter. [8]

Right now, the heat transfer from the jet column to the surrounding fluid is not modeled because it is considered that the melt does not release much heat until it is broken up into particles.

## 2.2 Melt Pool

When the jet column or a particle group reaches the bottom it makes a pool of melt. The melt pool was modeled one-dimensionally in $r$-direction and solved with finite difference method. It resides in a single layer of the two-phase flow grid on the bottom. The pool model uses the same $x$-direction grid with the two-phase flow model.

A conventional upwind scheme and SIMPLE algorithm [10] were applied for numerical solution. This component of melt was built mainly to accommodate the melt agglomerated on the floor as a continuous lump, which is often observed in experiments, and the spatial resolution of this part was not considered very important.

The conservation equations for melt pool can be formulated as follows.
Mass:

$$\frac{\partial w h_P \rho_P}{\partial t} + \frac{\partial (w h_P \rho_P v_P)}{\partial x} = w m_s \qquad (10)$$

Energy:

$$\frac{\partial e_P}{\partial t} + v_P \frac{\partial e_P}{\partial x} = \frac{q}{h_P \rho_P} + \frac{(e_{ms} - e_P)\max(m_s, 0)}{w h_P \rho_P} \qquad (11)$$

Momentum:

$$\frac{\partial v_P}{\partial t} + v_P \frac{\partial v_P}{\partial x} = -\frac{1}{\rho_P}\left[\frac{\partial p_a}{\partial x} + \frac{g}{2}\frac{\partial (h_P \rho_P)}{\partial x}\right] + K_{fa}(v_a - v_P) - K_{fw} v_P$$

Where, $h_P$ and $w(x)(\equiv x\Theta)$ denote the pool height and the arc width of the analysis domain at position $x$, respectively. $m_s$ denotes the mass flux of melt jet or particles falling onto the pool surface which is given by the jet and particle models. $q$, $K_{fa}$ and $K_{fw}$ denote the heat flux at the pool surface, pool-fluid friction factor and pool-floor friction factor. Those variables are presently just set zero, i.e. the heat transfer and friction on the pool are neglected.

When the jet leading edge reaches the bottom of the calculation domain, the mass and energy of the jet flown out is given to the central node of the pool. The momentum of the jet is given to the pool by adding the stagnant impulse due to jet impingement to the central node of the pool.

## 2.3 Melt Particles

A grouped particle method was adopted to enable a practical use of the model. Especially in a large scale such as a reactor simulation, the number of the real debris particle could be too large to directly simulated. The grouped particle method gives a scalability of the model according to computational resources.

A particle group is a group of $N_p$ particles which have uniform properties, and which is assumed to occupy a finite space, i.e. $2r_x$ by $2r_z$ in the $x$-$z$ plain. (see Fig. 1) This assumption is required to move the melt particle volume, force and heat source smoothly among the two-phase flow cells. If a group or a particle was assumed to be a point, the source terms for the two-phase flow model would jump from a cell to another suddenly and cause numerical problems. Other attributes of the group, i.e. the realistic shape of the group, rotation, diffusive feature etc., are stripped off. The motion and heat balance of a representative particle in a group is tracked by Lagrangian method with the basic equations shown below.
Motion:

$$\frac{\partial \mathbf{v}_p}{\partial t} = \mathbf{g} - \frac{\nabla p_a}{\rho_p} + \frac{\mathbf{F}_{hy}}{m_p} \qquad (12)$$

$$\frac{\partial \mathbf{x}_p}{\partial t} = \mathbf{v}_p \qquad (13)$$

Heat balance:

$$\frac{\partial e_p}{\partial t} = \frac{\pi D_p^2 q}{m_p} \qquad (14)$$

$\mathbf{v}_p$, $\mathbf{x}_p$, $m_p$ and $e_p$ denote particle velocity $(v_{px}, v_{pz})$, position $(x_p, z_p)$, mass of a particle and internal energy par unit mass. The hydrodynamic drag force $\mathbf{F}_{hy}$ and heat flux $q$ are given by constitutive equations. The drag is evaluated by a correlation for a sphere subjected to flow [1], with a correction factor to consider the deformation and irregular shape of particles. The heat flux is evaluated by a set of correlations considering convection around a sphere (Ranze-Marchall [11]), film boiling (Epstein-Hauser [4]) and nucleate boiling (Kutateladze [6]). The thresholds of boiling regimes are given by CHF correlation by Zuber [14] and minimum film boiling temperature model by Kondo et al. [5].

This model requires other rules for the interference between groups and between a group and boundaries, as well. Those are defined as below.

Interference between two particle groups:

1. If the sum of the particle volume fractions of two groups in contact is more than the packing limit ($\alpha_{pack} = 0.6$), two groups bounce apart with damping factor $C_{dampar} = 0.5$.
2. If two groups in contact have similar attributes, i.e. temperature, particle size and velocity, they merge into one group.
3. Otherwise, two groups have no interference, i.e. just go through each other.

Particle group-boundary interference:

1. If a group exceeds the central boundary, it is bounced back inside.
2. If a group exceeds upper or side wall, it is bounced back inside with a damping factor $C_{dampwal} = 0.1$.
3. If a group reaches the bottom, it merges into the pool when either of the pool or particle is molten, otherwise piles up on the frozen pool.

When particles are generated on the jet surface, the mass, temperature, size and velocity of particles are given at each jet cell and time step. However, the mass or number of particles generated in one time step at one cell is sometimes not enough to make one particle group. To avoid to generate an empty group or a too small group, the particles just after generated are stored in *pre-particle-group* buffers, and released as a real particle group after it becomes to contain enough mass or number of particles. Each pre-particle-group is attached to each jet cell.

The particles released from the jet are subjected to a turbulence in the boundary layer around the jet, which is considered to give a statistical feature on the particle velocity. In order to take into account this disturbance, the $x$ velocity of the particles $v_{ex}$, originally given from the K-H wave growth rate (see section 2.1), are shuffled with a random number (ranging from 0.02 to 1.0) when the group is released.

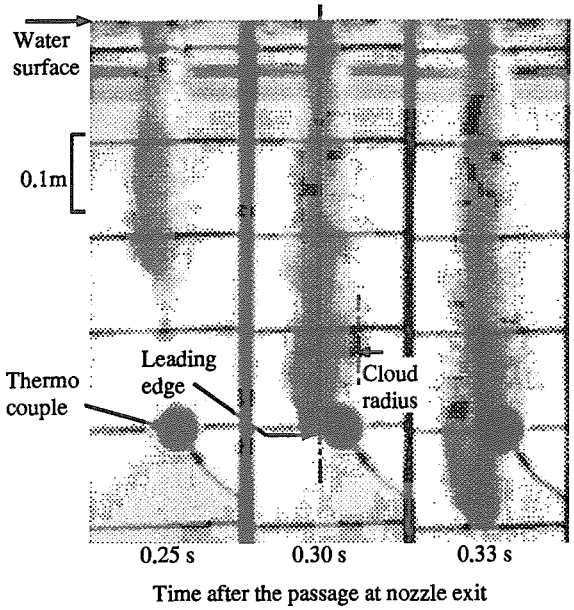



Figure 2: Observation of the melt jet with hight speed video

# 3 Test Calculation

## 3.1 Experimental and Analytical Conditions

A test calculation was performed to see the behavior of the present model, referring a melt jet breakup experiment in non-boiling conditions ALPHA-MJB16. In this experiment, a low melting temperature alloy called "anatomical alloy" (Bi-Sn-Pb-In) at 110 °C was poured into a water vessel of 3 m tall and 80×80 cm cross section, as a jet with diameter 30 mm. The density, surface tension of the melt measured by the authors were $\rho_J = 9400$ kg/m$^3$ and $\sigma_J$ =0.46 N/m. The nominal melting temperature was 60 °C. Water temperature was set at 50 °C. Location of the melt exit was at 2.7 m from the vessel bottom and the water level was 2.3 m. From a simple calculation on the flow in the melt pot and release nozzle, the initial velocity of the jet was 3.5 m/s. With the present set of the initial temperatures of melt and water, the contact interface temperature between two fluids is about 100 °C which causes neither of boiling nor quick solidification upon the contact and gives relatively long time for jet breakup.

Figure 2 shows the melt jet observed by high speed video camera in the experiment. It was observed that the melt jet was totally broken up during flowing down in the water pool making a cloud. The position of the leading edge and the radius of the melt jet and particle cloud, as well as the debris particle size distribution were taken from the experimental result for comparison.

Conditions of the calculation is schematically shown in Fig. 3. The vessel with square cross section was modeled with a cylinder which has a same cross section, and a slice of 0.1 radian wide was taken as the calculation domain. Time step was $5 \times 10^{-4}$ s. The empirical factors involved in the model were tentatively set for this simulation as in Table 1.

## 3.2 Snapshots of the Simulation Result

Fig. 4 shows the snapshots of the simulation results. The profile of the melt jet and pool are indicated with solid and broken lines, respectively. Position of the center of every particle group is plotted with cross dots.

It is seen from the figure that the jet was eroded after entering the water and totally broken up at the height about 1.6 m, the particles made a cloud of radius 0.10~0.15 m, and finally stack on the floor as a debris bed. This result was qualitatively a good reproduction of the phenomena observed in the experiment.

In the simulation, a part of the debris agglomerated to make a continuous lump (or a frozen pool) although which was not the experimental result. The particles are assumed to freeze when its average temperature is 10 K higher than the melting point as in Table 1 but still this result was made. When the criterion was set as $T_{av} < T_{melt}$, the particles totally merged into the pool. Models of surface temperature drop and heat transfer from the pool are

Table 1: Set of empirical factors in MJB16 simulation

| | |
|---|---|
| Jet model | |
| Entrainment $x$-velocity constant $C_{vx}$ | : 0.10 |
| Entrainment $z$-velocity constant $C_{vzwt}$ | : 0.40 |
| Entrainment mass flux constant $C_{me}$ | : 0.15 |
| Entrainment diameter correction factor $C_{de}$ | : 10 |
| Friction constant $C_f$ | : 3.0 |
| Heat transfer coefficient $h$ (W/m$^2$K) | : 0 |
| Pool model | |
| Friction factor with the fluid $C_{fa}$ | : 0 |
| Friction factor with the floor $C_{fw}$ | : 0 |
| Heat transfer coefficient $h$ (W/m$^2$K) | : 0 |
| Particle model | |
| Drag force correction factor $C_{cfrc}$ | : 2.0 |
| Damping factor for particle collision $C_{dampar}$ | : 0.5 |
| Damping factor at walls $C_{dampwal}$ | : 0.1 |
| Tolerance of properties to merge groups | : 20% |
| Pre-particle group release criterion | : $N_p > 100$ or $r_x > \Delta x/4$ |
| Particle freeze criterion | : $T_{av} < T_{melt} + 10\ K$ |

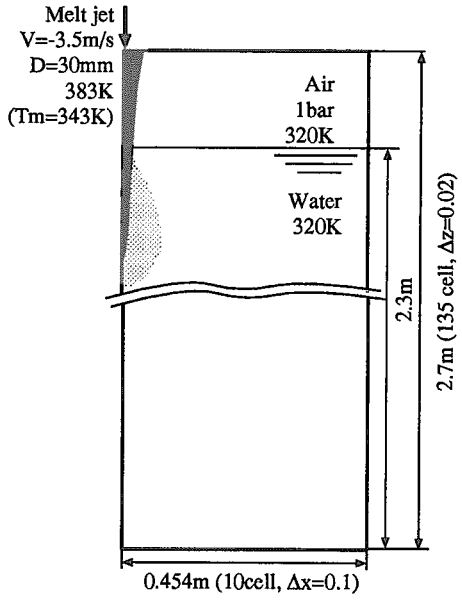



Figure 3: Conditions of MJB16 simulation

probably be responsible and need improvements.

## 3.3 Position of the Leading Edge and Cloud Radius

Figures 5 and 6 show the comparison of simulation (lines) and experimental (dots) results in the jet leading edge position and the radius of the particle cloud.

In Fig. 5, the experimental result shows that the leading edge velocity suddenly slowed at the height 1.6 m, which tells the jet column was totally broken up at this height, and the resulted particles sank making slower envelope below. The solid line, the leading edge of the jet column calculated, stopped at the height 1.6 m and reached a steady state where the mass supplied from the top and eroded in water was balanced. The broken line, the edge of the particle cloud, sank more slowly blow the *breakup height* with the terminal velocity according to the particle diameter. The plot for the particle cloud was made from the average of 5 leading particle groups to moderate the effect of a few groups scattered out from the cloud seen in Fig. 4. The strange stepwise changes in the line is due to one of the leading groups disappeared by merging into the pool.

In Fig. 6, the radius of the cloud observed in the experiment (cross dots) had a tendency to continuously expand, while the simulation result showed a faster expansion in the beginning but rapid saturation later.

The discrepancy between the experiment and simulation observed in the leading edge position and cloud radius is not discussed further in this work because, to some extent, those long term behavior of the particle cloud are related to the fact that the water motion induced by the melt jet flow is not modeled. This aspect will be looked into more detail after the present melt model is coupled with the two-phase flow model.

## 3.4 Debris Size Distribution

Figure 7 shows the cumulative mass fraction curves obtained from the experiment and simulation. The good agreement of the mass median diameter in the

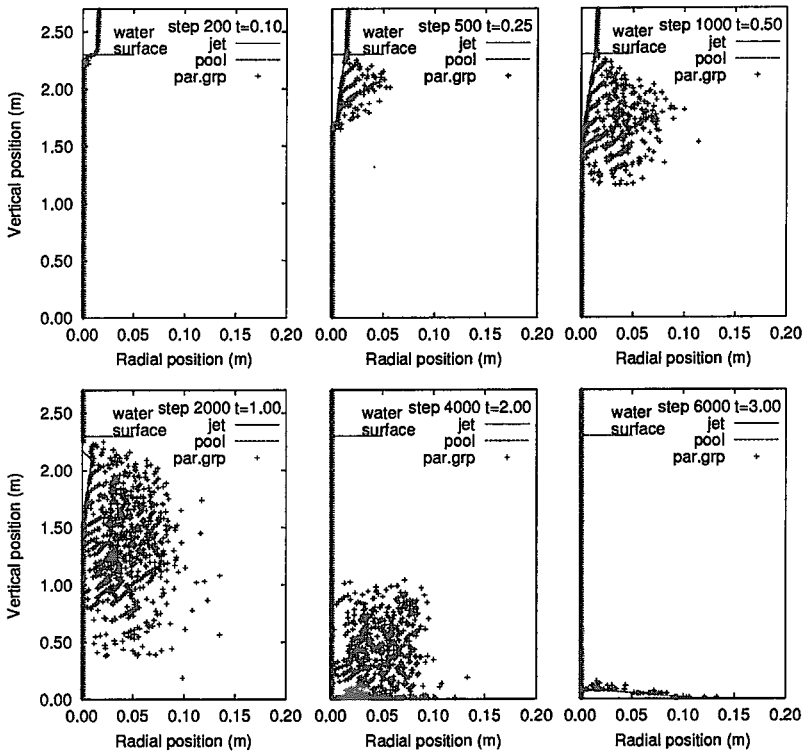



Figure 4: Plot of the simulation result on MJB16

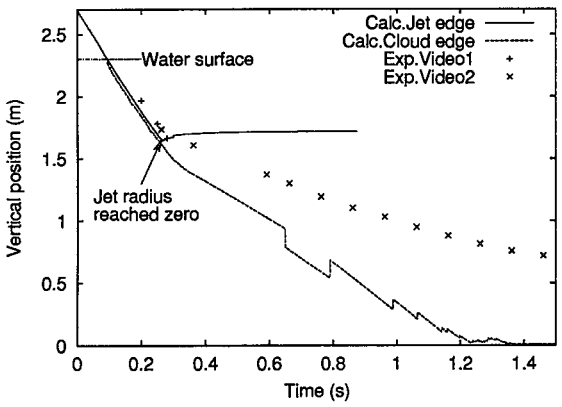



Figure 5: Leading edge position in the simulation and experimental results

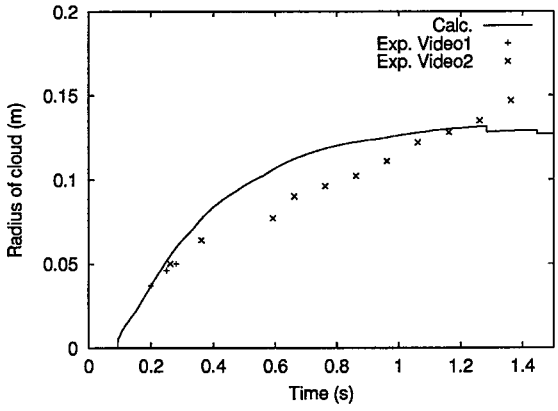



Figure 6: Radius of the particle cloud in the simulation and experimental results

experiment and simulation is the result of setting the correction factor $C_{de} = 10$ (see Table 1). It means that the present model [7] results in an order of underestimation of the diameter without correction. Besides, the distribution of the debris size is too sharp compared with the experiment. Further work is required to improve the model considering the break-off process of the particle more detail.

# 4 Conclusions

A new model for molten core jet breakup was developed for the premixing module of JASMINE, a steam explosion simulation code developed at JAERI. The present model consists of 3 components: jet, pool and particles, and will be combined with a two-phase flow code ACE-3D to handle the coolant flow field.

A simulation of ALPHA-MJB16 experiment was performed with the present model assuming con-

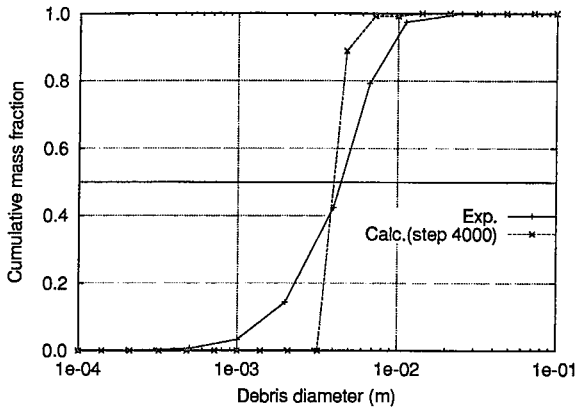



Figure 7: Debris size distribution in the simulation and experiment

stant properties and state variables on the surrounding fluid. From the results of the calculation, the followings were concluded.

- The present model reproduced the phenomena observed in the experiment qualitatively.
- The constitutive correlations for the friction, heat transfer and particle generation adopted here need to be checked in detail and improved after the coupling of the present model and two-phase flow model is completed.

## Acknowledgments

The experimental operation involved in this work was supported by an extensive cooperation of H. Ito, K. Komori, H. Sonobe, M. Nogami of Safety Facility Engineering Services Devision of JAERI, and M. Kojima of Nuclear Engineering, Co. The authors would like to acknowledge their devoted works.

## References

[1] R. B. Bird, W. E. Stewart, and E. N. Lightfoot. *Transport Phenomena*, chapter 6.3. John Wiley & Sons, 1960.

[2] C.-C. Chu, M. L. Corradini, I. Huhtiniemi, J. Murphy, J. Tang, and S. Nilsuwankosit. A code manual for TEXAS-V: One dimensional transient fluid model fuel-coolant interaction analysis. http://silver.neep.wisc.edu/~NSRC/texas/.

[3] M. Epstein and H. K. Fauske. Steam film instability and the mixing of core-melt jets and water. In *ANS Proceefings of 1985 National Heat Transfer Conference, Denver*, pages 277–284, 1985.

[4] M. Epstein and G. Hauser. Subcooled forced-convection film boiling in the forward stagnation region of a sphere or cylinder. *International Journal of Heat and Mass Transfer*, 23:179–188, 1980.

[5] S. Kondo, K. Konishi, K. Morita, N. Shirakawa, and A. Furutani. Fuel-coolant interaction studies at PNC relevant to fast reacter safety. In *Proc. international seminar on the physics of vapor explosions, Tomakomai*, pages 96–109, 1993.

[6] S. S. Kutateladze. Technical Report ACE-tr-3770, US AEC, 1952.

[7] K. Moriyama, Y. Maruyama, H. Nakamura, and K. Hashimoto. Three-component melt jet breakup model for FCI analysis. In *Proceedings of the Workshop on Severe Accident Reseach, Japan (SARJ-99), Tokyo (To be published as JAERI-Conf)*, 1999.

[8] K. Moriyama, Y. Yang, Y. Maruyama, H.-S. Park, and J. Sugimoto. One dimensional molten jet model for integral FCI analysis code. In *Proceedings of the Workshop on Severe Accident Reseach held in Japan (SARJ-98), Tokyo (JAERI-Conf 99-005)*, pages 358–363, 1998.

[9] A. Ohnuki, H. Kamo, and H. Akimoto. Development of multidimensional two-fluid model code ACE-3D for evaluation of constitutive equations. Technical Report JAERI-Data/Code 96-033, Japan Atomic Energy Research Institute, 1996.

[10] S. V. Patankar. *Numerical heat transfer and fluid flow*, chapter 6. Hemisphere publishing corporation, 1980.

[11] W. E. Ranz and W. R. Marshall. *Chem. Eng. Prog.*, 48:141, 1952.

[12] H. Schlichting. *Boundary layer theory*, chapter XX. McGraw Hill, 7 edition, 1979.

[13] T. Yabe and T. Aoki. A universal solver for hyperbolic equations by cubic-polynomial interpolation, I. one-dimensional solver. *Computer Physics Communications*, 66:219–232, 1991.

[14] N. Zuber et al. *Int. Development in Heat Transfer, Part II*, page 230. ASME, 1961. paper 27.

JP0150090

JAERI−Conf 2000−015

# 3.2 Numerical Analysis of Jet Injection Mechanism of Fuel–Coolant Interactions Using MPS

**Hirokazu Ikeda, Seiichi Koshizuka, Yoshiaki Oka,**
*Nuclear Engineering Research Laboratory, The University of Tokyo*
*2-22 Shirane, Shirakata, Tokai-mura, Naka-gun, Ibaraki 319-1106, JAPAN*
*TEL: +81-29-287-8443 (FAX: +81-29-287-8488)*
*E-mail: ikeda@tokai.t.u-tokyo.ac.jp*

**Hyun Sun Park***, and **Jun Sugimoto**
*Severe Accident Research Laboratory, JAERI, JAPAN*

## Abstract

The numerical method used in this study is Moving Particle Semi-implicit (MPS) method which is based on moving particles and their interactions. Grids are not necessary, so that large fluid deformation can be calculated without numerical diffusion. To understand the fundamental physics of the jet penetration, water jet injection into a pool of a denser fluid under non-boiling and isothermal conditions is calculated using the MPS method. The density ratio of the denser fluid (Fluorinert) to water is 1.88. The calculation results are compared with experiments which were conducted in the ALPHA/MUSE facility at JAERI. In three-dimensional calculation, the penetration behavior agrees with the experiment. It is found that the jet penetration process is divided to two stages and, at the first stage, the coolant jet can penetrate deeper than existing correlations of breakup length.

**Keywords** MUSE, MPS, FCI, jet penetration, breakup length

## 1 Introduction

Energetic FCI(Fuel-Coolant Interaction) occurs when a cold liquid comes into contact with a very hot liquid. The hot liquid rapidly releases its internal energy to the cold liquid and excessive amount of vapor is produced with a short time scale. This energetic FCI has been one of the primary safety concerns in nuclear power plants since the integrity of the containment may be damaged by this mechanical energy release. The geometrical contact mode between two liquids such as pouring, stratified, and injection, is an important factor. The injection mode can be classified into coolant injection (CI) and melt injection (MI) modes.

The authors have been developing a new numerical method, Moving Particle Semi-implicit (MPS) method [1], based on moving particles and their interactions. Grids are not necessary, so that fluid fragmentation is calculated without numerical diffusion. In the past studies water jet impingement on a melt pool was calculated as a fundamental process of vapor explosions using the MPS method. The melt was squeezed out of the pool as a filament between two water jets, which was assumed by Ciccarelli and Frost [2] as a fragmentation model. The calculation result also showed that a light fluid jet hardly penetrates into a heavy fluid pool. The behavior mainly depends on the density ratio between the jet and pool fluids [3]-[6].

In this study the MPS method is applied to water jet injection to a pool of a denser fluid in non-boiling and isothermal conditions. The calculation conditions are the same as the experiment named MUSE (MUlti-configuration in Steam Explosions ) in the ALPHA program at JAERI. In MUSE/ALPHA, a set of tests was conducted in non-boiling and isothermal conditions to understand the fundamental physics of the CI mode[7].

## 2 Moving Particle Semi-implicit Method

Governing equations are the mass and momentum conservation equations:

$$\frac{\partial \rho}{\partial t} + \nabla \cdot (\rho \vec{u}) = 0, \tag{1}$$

$$\frac{D\vec{u}}{Dt} = -\frac{1}{\rho}\nabla P + \nu \nabla^2 \vec{u} + \vec{F}. \tag{2}$$

Here $D/Dt$ means Lagrangian differential operator. Only gravity is considered as the external force $\vec{F}$.

In the MPS method a fluid is represented by moving particles. Convection is calculated by the motion of these particles. Thus, numerical diffusion, which is a large problem in the finite difference method, does not take place. The interfaces are always clear even if fragmentation or merging of the fluid occurs.

*Royal Institute of Technology (RIT), Sweden

A weight function is used for all interaction models to restrict the particle interactions within a finite radius of $r_e$:

$$w(r) = \begin{cases} \left(\frac{r_e}{r}\right) - 1 & (r < r_e) \\ 0 & (r \geq r_e) \end{cases} \tag{3}$$
$$r = |\vec{r}_j - \vec{r}_i| \quad .$$

The particle number density $n$ of particle $i$ is defined as,

$$n_i = \sum_{j \neq i} w\left(|\vec{r}_j - \vec{r}_i|\right) \quad . \tag{4}$$

This is in proportion to the fluid density.

Gradient and Laplacian operators involved in the governing equations are transformed to equivalent particle interactions [1]. The following equations are the particle interaction rules applied to particle $i$.

$$\langle \nabla \phi \rangle_i = \frac{Z}{n^0} \sum_{j \neq i} \left[ \frac{\phi_j - \phi_i}{|\vec{r}_j - \vec{r}_i|^2} (\vec{r}_j - \vec{r}_i)\, w\left(|\vec{r}_j - \vec{r}_i|\right) \right] \quad , \tag{5}$$

$$\langle \nabla^2 \phi \rangle_i = \frac{2Z}{\sum_{j \neq i} |\vec{r}_j - \vec{r}_i|^2 w\left(|\vec{r}_j - \vec{r}_i|\right)} \sum_{j \neq i} (\phi_j - \phi_i) w\left(|\vec{r}_j - \vec{r}_i|\right) \quad . \tag{6}$$

A pressure Poisson equation is obtained from the mass conservation equation and the pressure gradient term in the momentum conservation equation:

$$\langle \nabla^2 P \rangle_i^{n+1} = -\frac{1}{\Delta t^2} \left\{ \frac{\rho(\langle n \rangle_i^* - n^0)}{n^0} - \frac{P_i^{n+1}}{c^2} \right\} \quad , \tag{7}$$

where $c$ is the sound velocity. The source term, the right side of Eq.(7), is represented by deviation of the particle number density $n^*$ from $n^0\{1 + P_i^{n+1}/(\rho^0 c^2)\}$, while it is the velocity divergence in the finite difference method.

Motion of fluid particles are calculated with two steps. In the first step all terms in the momentum conservation equation except for the pressure gradient term are explicitly calculated and temporal velocities and positions of the particles are obtained. In the second step, the pressure Poisson equation is solved so as to modify the temporal particle number density $n^*$ to $n^0$. The quantity $n^0$ is constant if the fluid is incompressible or a function of pressure if the fluid is compressible.

# 3 Numerical analysis for MUSE experiment using MPS method

## 3.1 MUSE experiment

To understand the fundamental physical phenomena of water jet injection, a set of tests was conducted in MUSE facility. A water jet was injected into a melt simulant. A schematic of the visualization test is shown in Fig.1. A series of non-boiling isothermal tests was performed in a 100mm-wide and 20mm-deep test section which contains a melt simulant: Fluorinert with a density ratio of 1.88. Here, the density ratio is defined as the ratio of melt simulant to water densities $\rho_p/\rho_j$ at given isothermal conditions. The tests were carried out in two- and three-dimensional geometries. Water jet of 10mm depth was injected into a center of the test section in the two-dimensional geometry.

## 3.2 Two-dimensional calculation

The above experiment is simulated using the MPS method in two dimensions. The calculation arrangement is shown in Fig.2 to simulate the two-dimensional tests. There are 3 types of particles as melt simulant, water, and air. Fluorinert is used for the melt simulant. Calculations without air particles are also conducted to investigate the effects of air. A water jet is initially placed just above the surface of the pool, and is constantly injected from the inflow boundary. Particles near the outflow boundary are constantly deleted so that the total number of particles can be kept constant. The particles are initially arranged like a square grid whose spacing is $2.5 \times 10^{-3} m$. The total number of the particles is initially 6400 for water, air and melt; 3520 of them are water and melt particles. The velocity of the water jet $v_j$ is 3.8, 6 or 9m/s. Viscosity of the water and the melt is $1.09 \times 10^{-3} [kg/m \cdot s]$, and that of air is $1.76 \times 10^{-5} [kg/m \cdot s]$. Surface tension is not considered.

Three calculations including air are carried out in the jet velocity $v_j$ = 3.8, 6, $9 m/s$. In the case of $v_j = 3.8 m/s$, a calculation without air is also carried out. To compare the penetration behavior between the calculation and the experiment, positions at the bottom of the jet are plotted in Fig.3. In the calculation results at 3.8 and 6m/s, the water jet is apparently decelerated at a certain depth. The calculation time may not be enough in 9m/s. One reason for the jet deceleration seem to be a geometrical difference; the depth of the pool is 2cm while that of the water jet is 1cm in the experiment. There are no significant differences between two cases with and without air in this time scale.

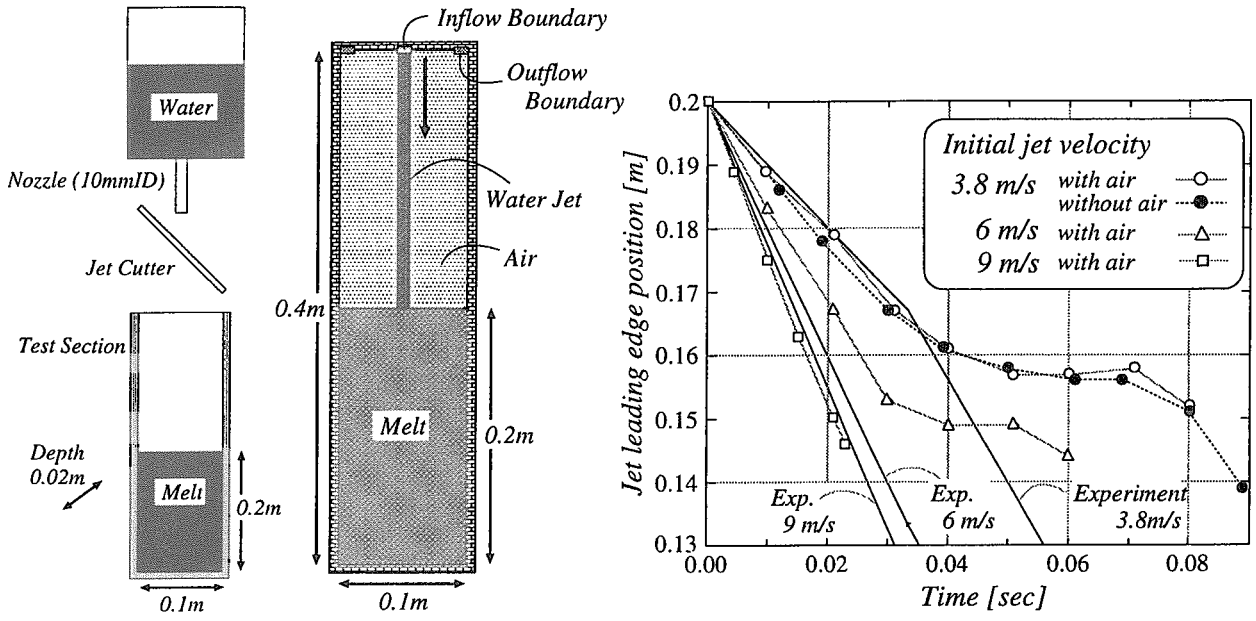



Figure 1: (Left) Schematic diagram of visualization test
Figure 2: (Middle) Calculation arrangement for the test section (2D)
Figure 3: (Right) Jet leading edge position in the results of two-dimensional calculations

### 3.3 Three-dimensional calculation

A three-dimensional calculation of water jet injection is carried out in the actual dimensions of the experiment ( jet depth 1cm ). Figure 4 is the calculation arrangement. Calculation conditions are the same as the experiment. Air is ignored. Depth of the pool is 2cm while that of the water jet is 1cm. Velocity of the water jet is 3.8m/s. The calculation result is shown in Fig.5. The water jet penetrates and forms a hole (0.033sec∼). The experimental result in the same condition is shown in Fig 6, in which each frame is located in an interval of 1/30 sec. The penetration behavior in the three-dimensional calculation is very similar to the experiment.

Figure 7 shows jet leading edge positions in comparison with the two-dimensional results. The three-dimensional calculation agrees with the experiment even where the water jet is decelerated at 0.16m in the two-dimensional cases. Surface levels of the pool at both sides of the wall are shown in Fig.8. We can see good agreement between the experiment and the three-dimensional calculation. The surface level in the two-dimensional calculation is higher since the jet can not penetrate without pushing up the denser pool fluid. This result shows that the difference in the jet arrangement causes the different behavior of the jet penetration.

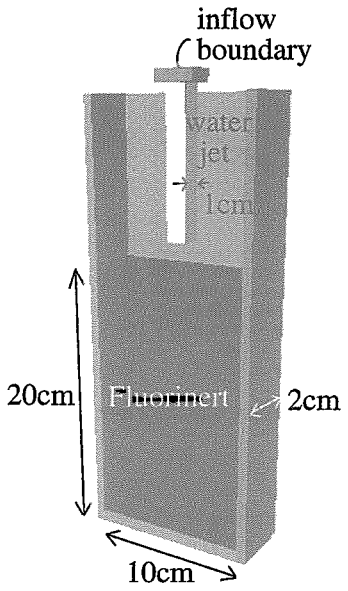
## 4 Consideration of jet penetration length

### 4.1 Basic processes in CI mode

At an early stage of the jet breakup process, the maximum jet penetration depth does not agree with existing correlations for the jet breakup length. It is assumed that CI mode consists of a few processes. At least two basic stages (I) and (II) are observed in the experiments(Fig.9). In the (I) stage, a column of air covers the coolant jet during the penetration. In the (II) stage, jet breakup occurs at a certain depth due to fluid-mechanical instabilities which are caused by a complete liquid-liquid contact. Figure10 shows a schematic of time transition for the jet breakup position. At (I), the jet has a constant velocity which is in proportion to the initial velocity $v_0$. The maximum jet penetration depth $L^{(I)}_{max}$ can be written as $L^{(I)}_{max} = \alpha v_0 t$, where $\alpha$ is a constant. After the air column collapses with a time lag of $\tau$, the breakup position keeps a certain level, which is correlated in a form as

$$\frac{L}{D} = C_{br}\left(\frac{\rho_j}{\rho_p}\right)^{0.5} Fr^{0.5} \quad . \tag{8}$$

Here, $C_{br}$ is a coefficient; $C_{br} = 2.1$ for Saito et al.(1988), $C_{br} \approx 2$ for Schneider et al.(1992), $C_{br} = 1.45$ for Park et al.(1998).



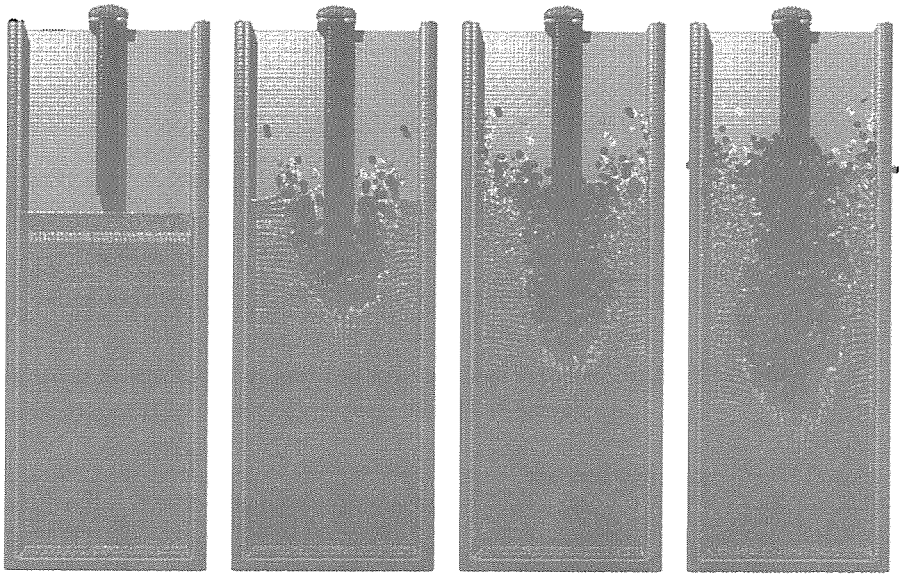




Figure 4: (Left) Calculation arrangement for the test section (3D)
Figure 5: (Right) Calculation result of three-dimensional jet arrangement

## 4.2 Breakup length at the (I) stage

The constant $\alpha$ in the (I) stage is estimated here. Since the jet is mainly decelerated by dynamic pressure of the pool fluid near the leading edge, the jet velocity can be written as follows.

$$\frac{dv_j}{dt} = -\frac{1}{2}\frac{C\rho_p v_j^2}{\rho_j D_0} \quad , \quad v_j = \frac{v_0}{1+\frac{1}{2}C\frac{v_0 t}{D_0}\frac{\rho_p}{\rho_j}} \quad , \tag{9}$$

here, C is a constant. A characteristic time $t^* = D_0/v_0 \cdot (\rho_j/\rho_p)^{\frac{1}{2}}$ which is the time for interaction between two fluids which have different densities is substituted to Eq.(9). Eventually, $\alpha$ is

$$\alpha = \frac{v_j}{v_0} = \frac{1}{1+\beta\left(\frac{\rho_p}{\rho_j}\right)^{\frac{1}{2}}} + \gamma \quad , \tag{10}$$

here $\beta$ and $\gamma$ are constants. A relation between $\alpha$ and a density ratio $\rho_p/\rho_j$ is shown in Fig.11. Here, quasi-2D means the two-dimensional arrangement of MUSE experiments. The constants $\beta$ and $\gamma$ are correlated as $\beta = 0.8$, $\gamma = -0.1$

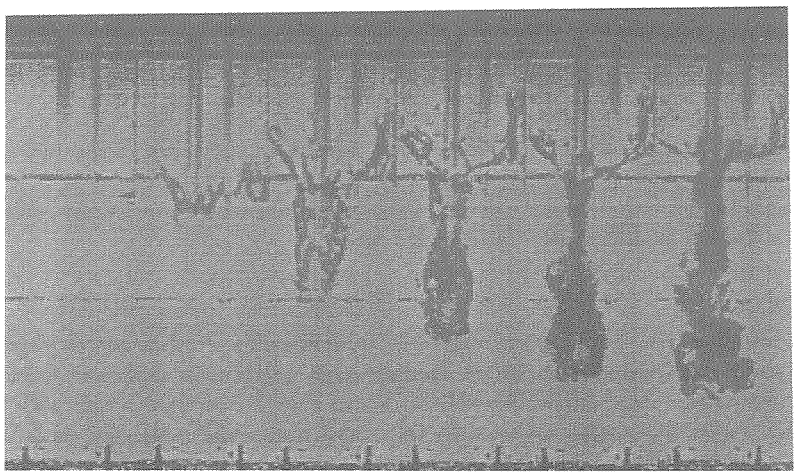


Figure 6: Experimental result of water jet injection, $v_j = 3.8m/s$ (time interval = $1/30sec$)

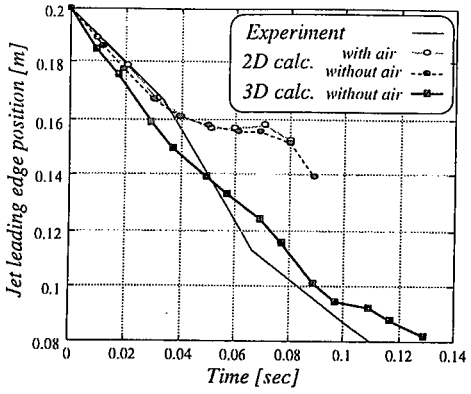



Figure 7: (Left side) Jet leading edge position in the result of three-dimensional jet arrangement

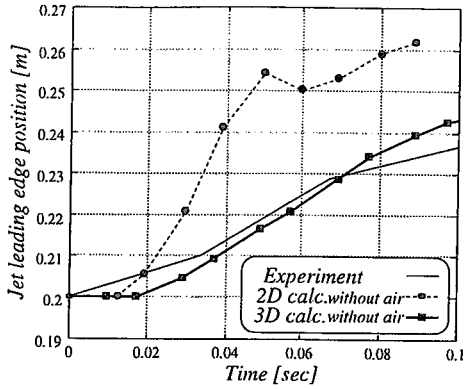
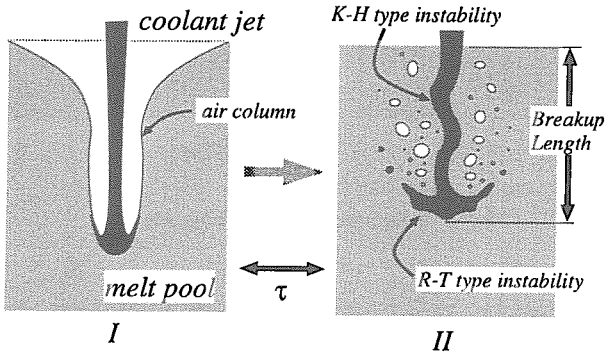



Figure 8: (Right side) Surface level of the melt simulant pool



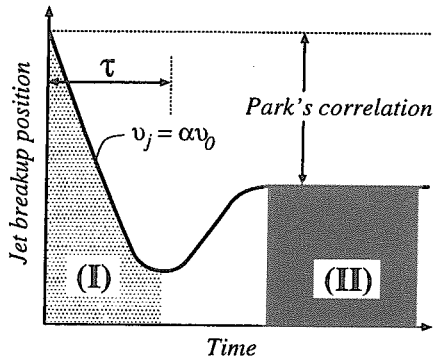




Figure 9: (Left side) Basic processes in CI mode

Figure 10: (Right side) Jet breakup position against time

in quasi-2D, $\beta = 1.2$, $\gamma = 0.1$ in 3D.

The time lag $\tau$ is also estimated. Within the range of the parameters in MUSE experiments, there are no relation between $\tau$ and the initial velocity $v_0$; $\tau \approx 0.12sec$ (3D, $v_j = 3 \sim 5m/s$, $\rho_j/\rho_p = 1/1.88 \sim 1$), $\tau \approx 0.17sec$ (quasi-2D, $v_j = 3.8 \sim 6m/s$, $\rho_j/\rho_p = 1/1.88$). Figure12 shows dependency of $\tau$ on the density ratio (quasi-2D, $v_j = 3.8m/s$) obtained by the MPS calculations. A correlation can be given as

$$\tau_{calc} = 0.04 \cdot \sqrt{\frac{\rho_p}{\rho_j}} + 0.075 \quad . \tag{11}$$

The time lag $\tau$ decreases with increasing density ratio $\rho_j/\rho_p$. This is because the hole created by the jet impact is narrower as the density ratio is higher[6].

The maximum jet penetration depth in (I) process can be estimated by using above correlations as

$$L^{(I)}_{max} = \alpha v_0 \tau_{calc} \qquad (quasi-2D). \tag{12}$$

Relations between the density ratio and the non-dimensional breakup length are shown in Fig.13. Saito's and Park's correlations in the (II) stage are provided for the comparison. CI mode is in the region of $\rho_j/\rho_p < 1.0$, while MI mode is $\rho_j/\rho_p > 1.0$. In CI mode, the jet can penetrate deeper than the steady-state breakup length(Eq.(8)) at the (I) stage, while the column of air collapses at a shallow length in MI mode.

# 5 Conclusions

Water jet injection into a denser liquid is calculated to understand its fundamental physics. In two-dimensional calculations, the water jet is decelerated and the jet leading edge position is shallower than the experiment of ALPHA/MUSE. The penetration behavior in the three-dimensional calculation agrees well with the experiment. This is because the denser liquid should be pushed up more in the two-dimensional geometry. It is found that CI mode can be divided to two stages, and that the coolant jet can penetrate deeper than existing correlations at the first stage.

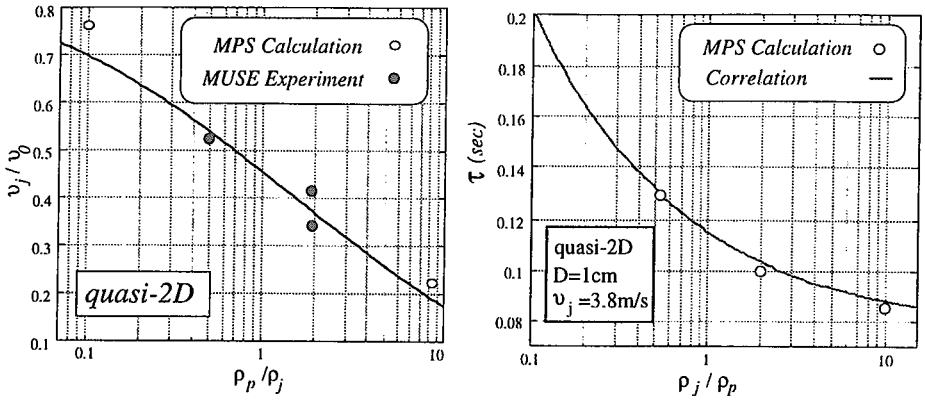



Figure 11: (Left side) Correlation for $\alpha$ against the density ratio
Figure 12: (Right side) Correlation for $\tau$ against the density ratio

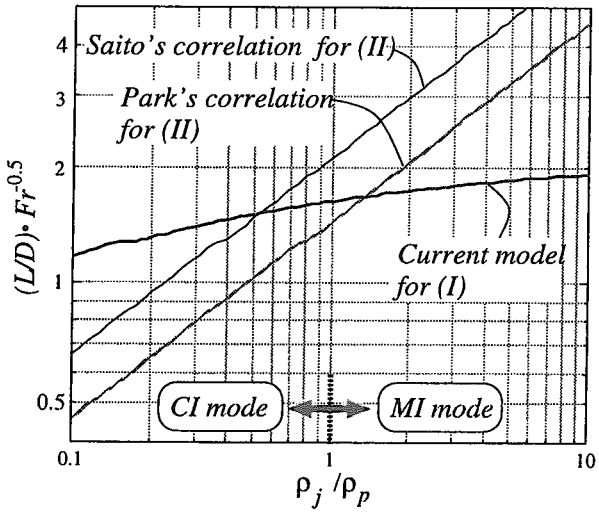



Figure 13: Comparison with the correlations in (I) and (II) stages

# References

[1] S. Koshizuka and Y. Oka, "Moving-Particle Semi-implicit Method for Fragmentation of Incompressible Flow," *Nucl. Sci. Eng.* **123**, 1996, p.421-434.

[2] G. Ciccarelli and D. L. Frost, "Fragmentation Mechanisms Based on Single Drop Steam Explosion Experiments Using Flash X-ray Radiography," *Nucl. Eng. Des.* **146**, 1994, p.109-132

[3] S. Koshizuka, H.Ikeda and Y. Oka, "Numerical Analysis of Fragmentation Mechanisms in Vapor Explosions," *Proc. OECD/CSNI Specialist Meeting on Fuel-Coolant Interactions*, 1997, JAERI-Conf 98-009, p.722-731

[4] S. Koshizuka, H.Ikeda and Y. Oka, "Effect of Spontaneous Nucleation on Melt Fragmentation in Vapor Explosions, " *Proc. Int. Seminar on Vapor Explosions and Explosive Eruptions(AMIGO)*, 1997, p.185–192

[5] S. Koshizuka, H.Ikeda and Y. Oka, "Numerical Simulation of Fragmentation Processes in Vapor Explosions Using Moving Particle Semi-implicit Method," *Proc. Int. Meet. Advanced Reactors Safety(ARS'97)*, 1997, p.872–879

[6] S. Koshizuka, H. Ikeda and Y. Oka, "Numerical Analysis of Fragmentation Mechanisms in Vapor Explosions," *Nucl. Eng. Des.*, **189** , 423-433 (1999)

[7] H.S. Park et al., "Study on Energetic Fuel-Coolant Interaction in the Coolant injection Mode of Contact" *Proc. 6th International Conference on Nuclear Engineering (ICONE6)*, San Diego, USA, 1998, ICONE-6091

[8] H. Ikeda, S. Koshizuka and Y. Oka, "Boiling and Solidification Models for Particle Method to Analyze Molten Core Behavior in Severe Accidents," *Proc. 6th International Conference on Nuclear Engineering (ICONE6)*, San Diego, USA, 1998, ICONE-6233

JP0150091



# 3.3 Study on the effect of subcooling on vapor film collapse on high temperature particle surface

Yutaka ABE, Daisuke TOCHIO and Hiroshi YANAGIDA

Department of Mechanical Systems Engineering, Yamagata University,
Jonan, Yonezawa, Yamagata, 992-8510
Tel & Fax: 0238-26-3221

E-mail: yutaka@mabeken3.yz.yamagata-u.ac.jp

## Abstract

Thermal detonation model is proposed to describe vapor explosion. According to this model, vapor film on pre-mixed high temperature droplet surface is needed to be collapsed for the trigger of the vapor explosion. It is pointed out that the vapor film collapse behavior is significantly affected by the subcooling of low temperature liquid. However, the effect of subcooling on micro-mechanism of vapor film collapse behavior is not experimentally well identified. The objective of the present research is to experimentally investigate the effect of subcooling on micro-mechanism of film boiling collapse behavior.

As the results, it is experimentally clarified that the vapor film collapse behavior in low subcool condition is qualitatively different from the vapor film collapse behavior in high subcooling condition. In case of vapor film collapse by pressure pulse, homogeneous vapor generation occurred all over the surface of steel particle in low subcooling condition. On the other hand, heterogeneous vapor generation was observed for higher subcooling condition. In case of vapor film collapse spontaneously, fluctuation of the gas-liquid interface after quenching propagated from bottom to top of the steel particle heterogeneously in low subcooling condition, On the other hand, simultaneous vapor generation occurred for higher subcooling condition.

And the time transient of pressure, particle surface temperature, water temperature and visual information were simultaneously measured in the vapor film collapse experiment by external pressure pulse. Film thickness was estimated by visual data processing technique with the pictures taken by the high-speed video camera. Temperature and heat flux at the vapor-liquid interface were estimated by solving the heat conduction equation with the measured pressure, liquid temperature and vapor film thickness as boundary conditions. Movement of the vapor-liquid interface were estimated with the PIV technique with the visual observation data.

## 1. Introduction

In the past, large-scale accidents by vapor explosion were occurred in various industrial fields. Thermal detonation model[1] is proposed to describe vapor explosion as shown in Figure 1. The thermal detonation model divides the vapor explosion phenomena into four processes, break-up, pre-mixing, trigger and occurrence of the large-scale vapor explosion. According to the model, vapor film collapse on the pre-mixed high temperature droplet surface is needed to trigger the vapor explosion. In the previous study, it is clarified that the vapor explosion is significantly affected by the subcooling of the low temperature liquid. However, it is not clear how subcooling of the low temperature liquid affect the trigger of the vapor explosion.

Especially, the effect of the subcooling on the micro-mechanism of the vapor film collapse behavior is not well experimentally identified[2], [3], [4]. It is necessary to obtain the experimental information of the micro-mechanism of the vapor film on the high temperature particle surface excluding atmization. The objective of the present research is to experimentally investigate the micro-mechanism of vapor film collapse behavior on the high temperature particle surface.

## 2. Experiment

### 2.1 Experimental apparatus

Figure 2 shows the schematic diagram of the experimental apparatus. Test section is composed of the stainless steel square vessel. Its inner dimension is 54 mm, thickness is 3 mm, and length is 316 mm. Polycarbonate plates for the visual observation are installed on three sides of the test vessel. Strain-gauge type pressure transducers are installed on the center of a rest side in order to measure the pressure and to obtain the trigger signal for high-speed video camera. The sheathed thermocouple to measure the water temperature is the test vessel 30 mm above the center. The pressure pulse generator is located at the bottom of the test vessel. The pressure pulse is generated by hitting the piston with a bullet driven by nitrogen gas. The nitrogen gas flow is operated with electromagnetic valve to obtain good repeatability.

Experimental data are recorded as voltage data into analyzing recorder through amplifier. Those data are transferred to the computer through GP-IB. Visual data are obtained by the high-speed video camera of the maximum speed 40,500 fps. The high-speed video camera starts with trigger signal from the pressure transducer
through analyzing recorder.

The detail structure of the stainless steel ball used in the experiment is shown in Fig. 3. The stainless steel ball of 15 mm diameter is suspended with sheathed thermocouple at the center of the test section. The surface temperature of steel ball is measured by the sheathed thermocouple. The thermocouple is inserted into the ball through a hole drilled with electric discharge processing method. The thermocouple is fixed with wedging in the top of the steel ball. The top of the thermocouple is shaved to be naked at the bottom of the steel ball in order to obtain fast temperature response.

### 2.2 Experimental procedure

Figure 4 shows the experimental procedure. At first, steel ball was heated up to the specified temperature by a burner. Next, the steel ball was submerged into the water to generate the film boiling on the high temperature ball surface. Finally, pressure pulse was generated at the bottom of the test vessel to attack the film boiling on the high temperature ball surface. The vapor film collapse behavior is observed with high-speed video camera.

From the present experimental procedure, the forced vapor film collapse behavior with external pressure pulse is investigated

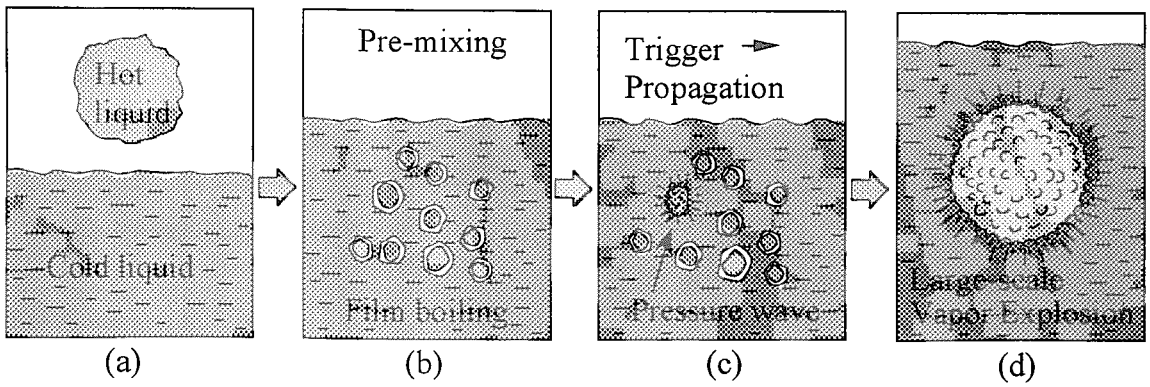



*Fig. 1 Thermal detonation model[1]*

## 2.3 Visual data analysis

The graphic data are captured by using the high-speed video camera (Photoron Ltd. FASTCAM-Ultima). Maximum recording speed of the video camera is 40,500 fps for the frame of 64 pixels by 64 pixels and 4,500 fps for the frame of 256 pixels by 256 pixels. The graphic data are stored in the memory unit as 8-bits digital data. The digital data are transferred to a computer through GP-IB interface and stored in MO-drive. The stored digital graphic data are processed to estimate vapor film thickness on the steel particle surface by using the graphical image data processing software. The schematic diagram of the determination procedure of vapor film thickness is shown in Fig.5. The procedure is follows:

1. Capture graphic data of steel particle without vapor film before experiment.
2. Capture graphic data of vapor film collapse on steel particle.
3. Change the 8-bits digital graphic data into binary information. Turn over the binary information of the graphic data with vapor film.
4. Superimpose two graphic binary data.
5. Count the number of pixels of vapor film.

Divide the number of pixels of vapor film by the length of the particle outer surface to estimate the vapor film thickness. The minimum spatial resolution is estimated as 0.02 mm.

## 3. Results

Figure 6 show the experimental results of pressure and surface temperature. Horizontal axis shows time in ms. It was observed that surface temperature started to decrease when the pressure pulse was arrived.

Symbols of A to F correspond to the pictures below. These pictures were recorded with 4,500 fps. A clear and smooth vapor film was observed at time A before pressure pulse arrived. The peak of the pressure pulse was arrived at time B. At this time, vapor film surface changed white. After the pressure pulse passed away, vapor generation occurred homogeneously all over the surface of the steel particle as shown in C through F.

Figure 7 shows the visual observation results in forced collapse experiment for different subcooling condition. These pictures were recorded with 4,500 fps for subcooling temperature of 8 °C, 18 °C and 25 °C, respectively. In this figure, the arrival time of pressure peak is taken as 0 ms.

Before the arrival of the pressure pulse, clear and smooth vapor film was observed in every condition. The vapor film surface changed white at

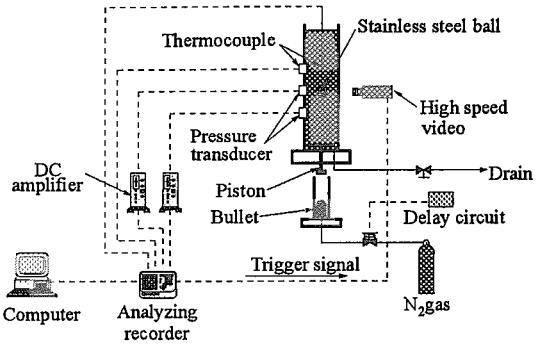



*Fig. 2 Experimental apparatus*

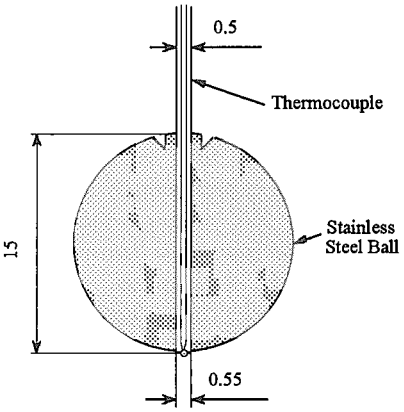



*Fig.3 Structure of steel ball*

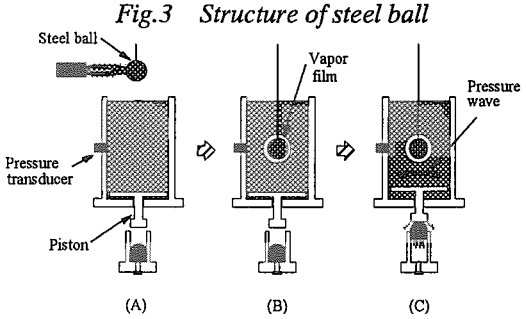



*Fig. 4 Experimental procedure*

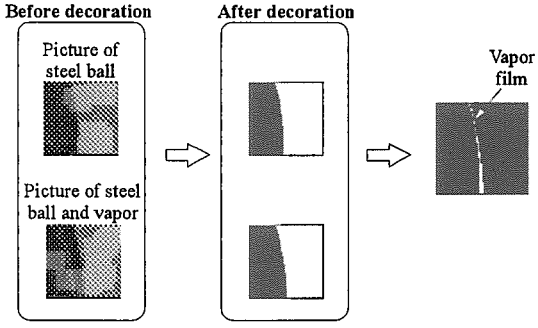



*Fig.5 The determination procedure of vapor film thickness*

time 0 ms in every condition. It was observed that after the time of pressure pulse passing, homogeneous vapor generation was occurred all over the surface of steel particle in low subcooling condition. On the other hand, the heterogeneous

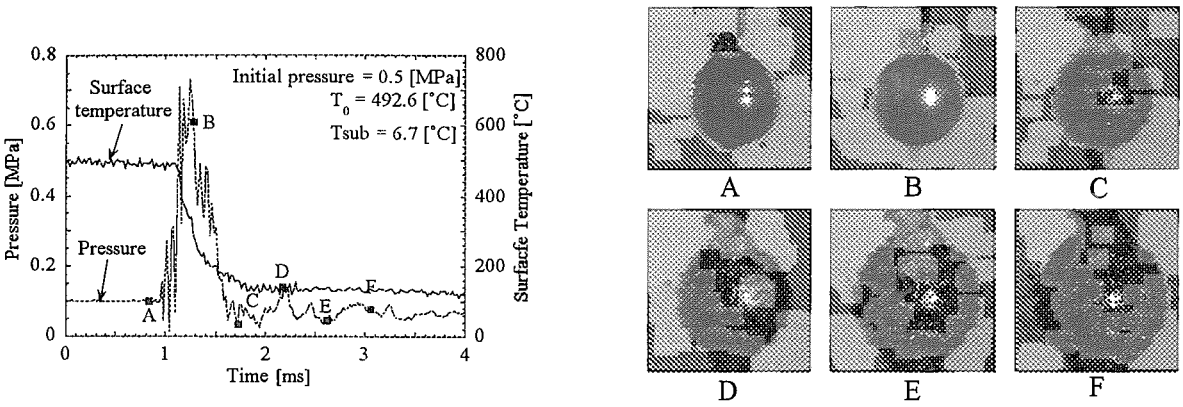



*Fig.6 Surface temperature and pressure in forced collapse experiment*

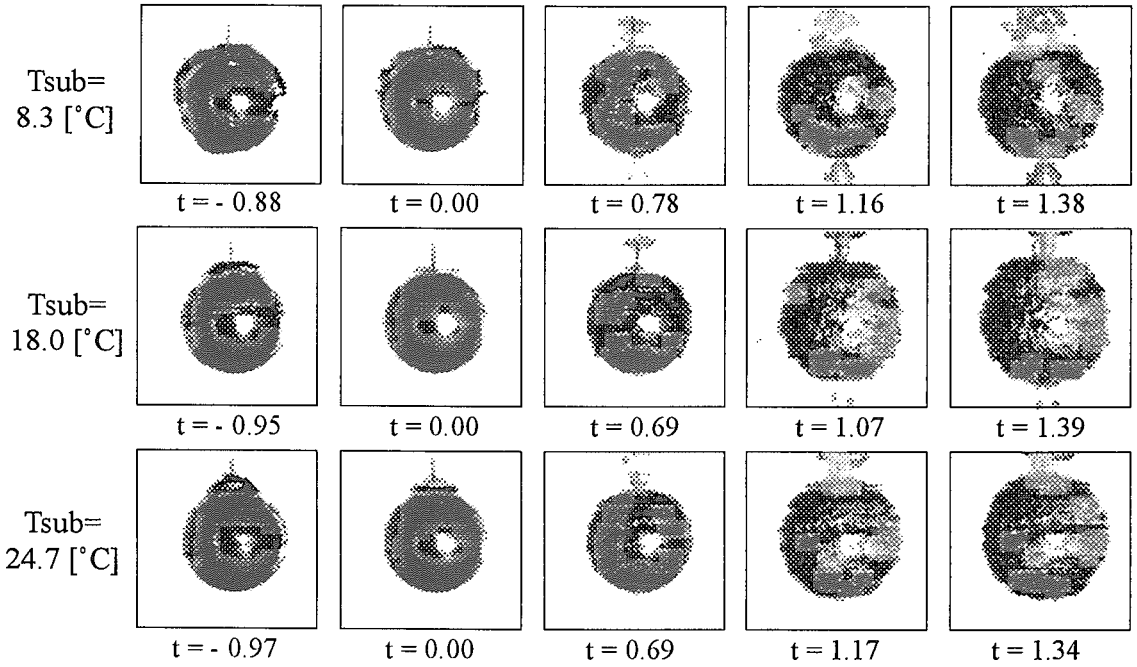



*Fig.7 Observation results in forced collapse experiment (unit: ms)*

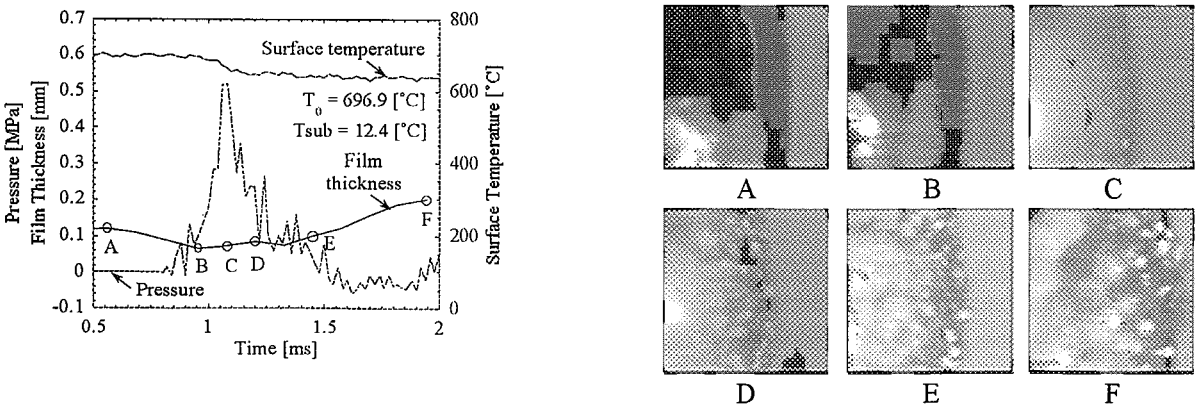



*Fig.8 Surface temperature, pressure and film thickness in forced collapse experiment (Tsub=12.4°C ).*

vapor generation was occurred in high subcooling condition.

Figure 8 show the experimental results of pressure, surface temperature and estimated vapor film thickness. The horizontal axis shows time in ms. Vapor film thickness was estimated from the

visual observation results.

It was observed that surface temperature started decreasing when pressure pulse was arrived. At the time, vapor film thickness decreased to its minimum value. After the estimated vapor film thickness increased quickly.

Symbols of A to F correspond to the pictures below. These pictures were recorded with 40,500 fps. A clear and smooth vapor film was observed before pressure pulse arrived at time A. At time B, vapor film surface changed white as soon as the peak of the pressure pulse was arrived. After the pressure pulse passed away, violent vapor generation occurred as shown in C through F in Fig. 8.

Figure 9 shows the estimated time transient of the vapor film thickness on the steel particle surface for the different subcooling. Symbols of circle, triangle and rectangular show the vapor film thickness for subcooling temperature of 12 °C, 19 °C, and 27 °C, respectively. In Fig. 9, 0 ms is the arrival time of pressure peak.

Before the arrival of pressure pulse, the vapor film thickness for high subcooling condition is lower than that in low subcooling condition. After the arrival of pressure pulse, the vapor film thickness was increased quickly for every subcool condition after the vapor film thickness kept its minimum value for a few milliseconds.

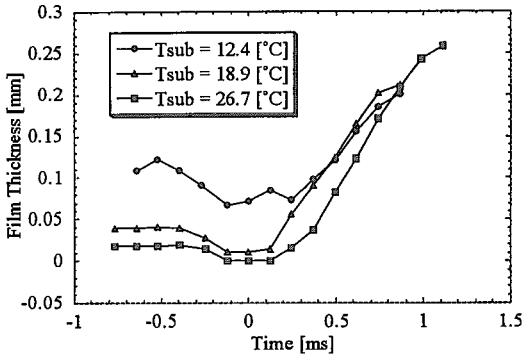



*Fig.9 Time variation of film thickness in forced collapse experiment*

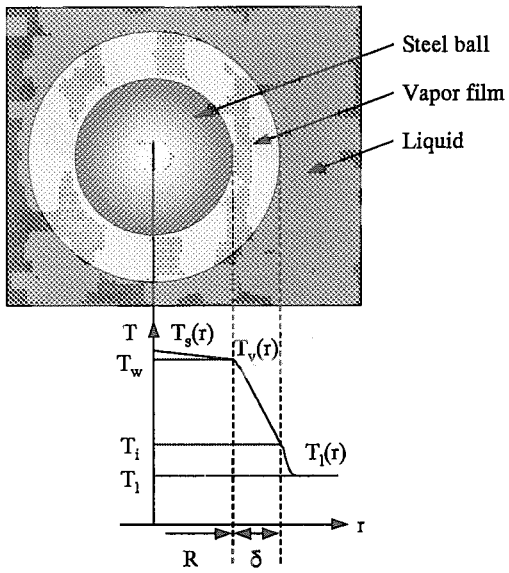



*Fig. 10 Schematics of heat conduction analysis*

## 4. Discussion

### 4.1. Heat conduction analysis

### (1) Configuration and procedure of analysis

In order to estimate the vapor-liquid interface, following heat conduction equation is numerically solved.

$$\frac{\partial T}{\partial t} = \kappa \frac{1}{r^2}\frac{\partial}{\partial r}\left(r^2 \frac{\partial T}{\partial r}\right), \qquad (1)$$

where r is distance from the center of the particle, t is time, $\kappa$ is thermal diffusivity and T is temperature distribution defined as:

$$T(r) = \begin{cases} T_s(r) & (0 < r < R) \\ T_v(r) & (R < r < R+\delta), \\ T_l(r) & (R+\delta < r) \end{cases} \qquad (2)$$

where $T_s(r)$ is the temperature distribution in steel particle, $T_v(r)$ is the temperature distribution in vapor film and $T_l(r)$ is the temperature distribution in liquid. The schematic diagram of the present analysis system is shown in Fig. 10. The system consists of steel particle, vapor film and liquid phase. Complete spherical geometry and homogeneous material properties are assumed in the present analysis. The schematic temperature distribution is also shown in Fig. 10. In the present study, the particle surface temperature $T_w$, bulk liquid

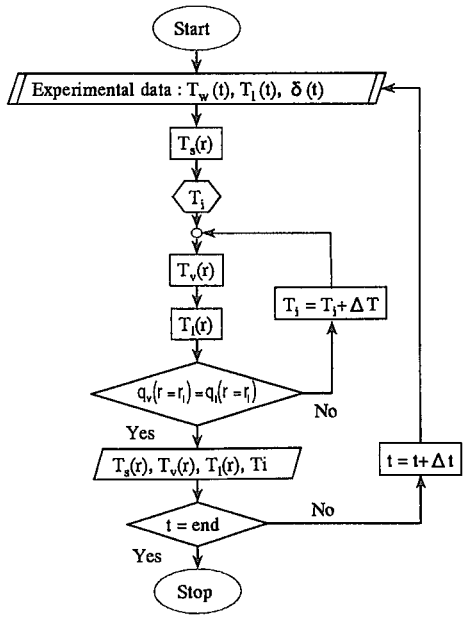



*Fig. 11 Flowchart of heat conduction analysis*

temperature $T_l$ and vapor film thickness $\delta$ were experimentally obtained. Those three data of $T_w$, $T_l$ and $\delta$ were used as boundary conditions to solve the heat conduction equation. The numerical calculation procedure of the heat conduction equation (1) is shown in Fig. 11 as a flow chart. Once the temperature distributions are obtained, the vapor-liquid interface temperature and heat flux can be estimated.

The detail of the solution procedure is as follows:

1. Time transient data of particle surface temperature $T_w$, liquid temperature $T_l$ and vapor film thickness $\delta$ are input as boundary conditions.
2. The temperature distribution in steel particle $T_s(r)$ is calculated.
3. The provisional vapor-liquid interfacial temperature $T_i$ is assumed.
4. The temperature distributions in vapor film $T_v(r)$ and in liquid $T_l(r)$ are calculated.
5. Judged to the heat flux in vapor film is equal to the heat flux in liquid at the vapor–liquid interface.
6. If heat conduction is discontinuous, vapor-liquid interfacal temperature is changed. And the temperature distributions in vapor film and in liquid are calculated again.
7. The procedure 3 through 6 are repeated until the condition of vapor- liquid interfacial heat flux is satisfied.
8. If the condition is satisfied, time step is advanced.

## (2) Results of the heat conduction analysis

Figure 12 shows the temperature distribution in steel particle, vapor film and liquid phase. In Fig. 12, the allow lines show the positions of the particle surface and the vapor-liquid interface for different time. The arrival time of pressure peak is taken as 0 ms.

The particle surface temperature was input data obtained from the present experiment. The vapor-liquid interface temperature was not influenced by the change of the particle surface temperature during this short transient period in the present heat conduction calculation.

Figure 13 shows time transient of heat flux at steel particle surface and at vapor-liquid interface. The upper of Fig. 13 shows the time transient of heat flux at particle surface and the lower of Fig. 13 shows that of the vapor-liquid interface. In Fig. 13, the arrival time of pressure peak is as 0 ms.

Heat flux at vapor-liquid interface was estimated three order smaller than that at particle surface. Heat flux was increased quickly at both

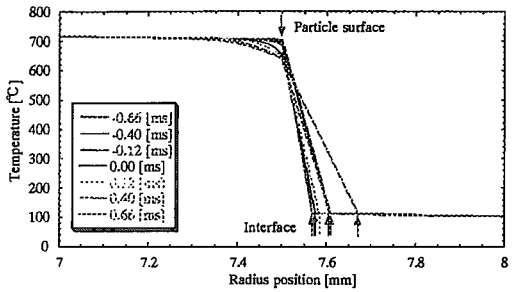



*Fig. 12 Temperature distribution in steel particle, vapor film and liquid*

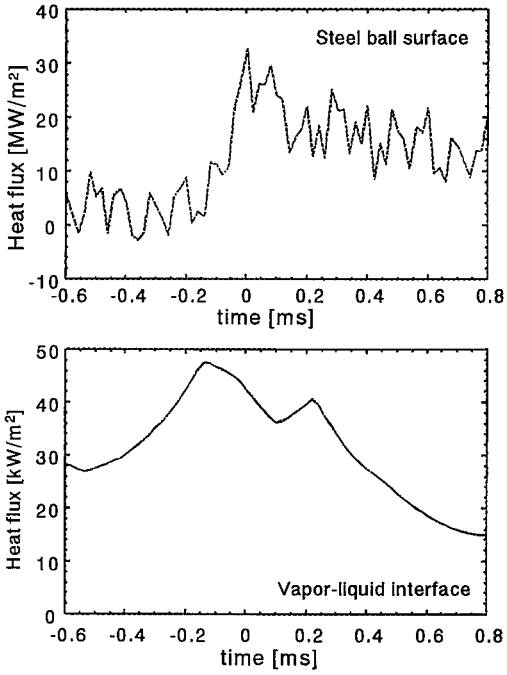



*Fig. 13 Time transient of heat flux*

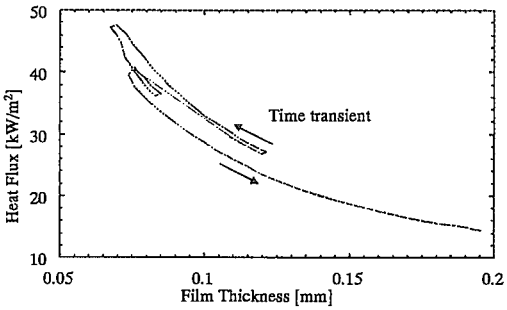



*Fig. 14 Relationship between film thickness and heat flux at vapor-liquid interface*

sites as soon as the pressure peak arriving. The maximum value of heat flux at particle surface was much higher than that of critical heat flux in pool boiling. Heat flux was gradually decreased at both sites after pressure pulse was passed.

Figure 14 shows relationship between heat flux at vapor-liquid interface and estimated vapor

film thickness. Vertical axis shows heat flux at vapor-liquid interface, horizontal axis shows vapor film thickness. In Fig. 14, allow lines show the time merching. At first, heat flux increased with decreasing vapor film thickness. Then, heat flux decreased with increasing vapor film thickness. In the present heat conduction calculation, heat flux at the vapor-liquid interface
is in inverse proportion to the film thickness.

Figure 15 shows the comparison between the present data and existing boiling curve. Solid line shows the estimated heat flux from heat conduction analysis. The dash line shows the existing correlation heat flux, heat flux of nucleate boiling by Jons-Lottes[5], burn-out heat flux by Kutateladze[6], minimum heat flux of film boiling by Zuber[7] and heat flux of film boiling by Bromley[8].

It is shown from Fig. 15 that the estimated heat flux from the present experiment is much higher than the existing correlation.

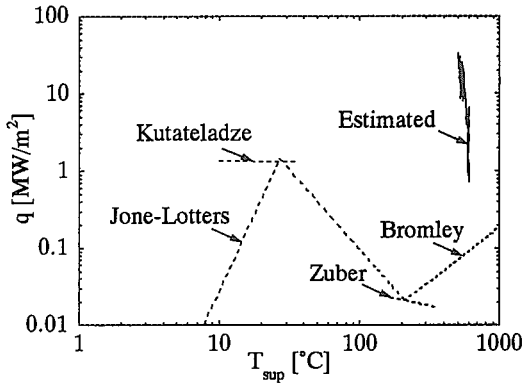



*Fig. 15 Comparison with existing boiling curve*

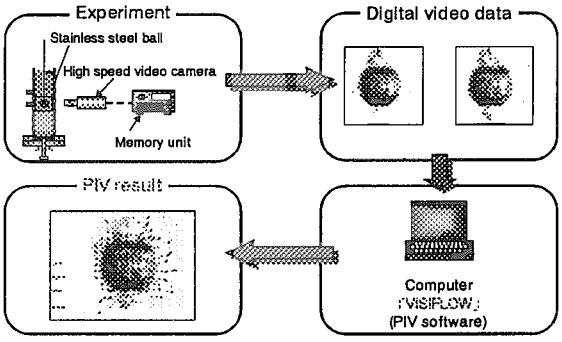



*Fig. 16 PIV analysis system*

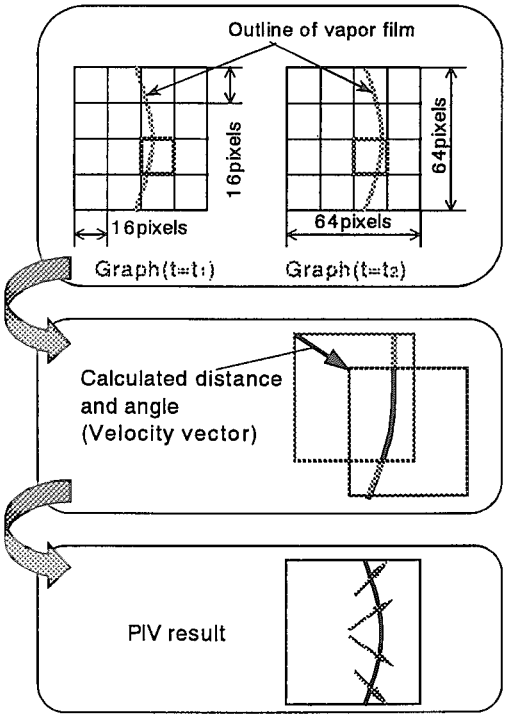



*Fig. 17 Procedure of PIV analysis*

## 4.2 PIV analysis

### (1) Schematic and procedure of PIV analysis

In order to investigate the movement of the vapor-liquid interface, PIV technique was applied to the obtained visual data at the vapor liquid interface in the present experiment.

Figure 16 shows PIV analysis system in the present study and procedure to obtain the PIV analysis results. At first, digital video data was recorded with high-speed video camera of the maximum speed 40,500 fps. Secondly, time continuous two video data were analyzed with PIV software "VISIFLOW". As the result, velocity vector information is produced with the difference between two digital video data.

Figure 17 shows the schematic diagram of the PIV analysis algorithm. The algorithm is as follows:

1. Outline of vapor film taken for continuous time $t = t_1$ and $t = t_2$ are divided into 16 regions, respectively.
2. Each divided region of two pictures is moved a little in all direction to overlap between two pictures at time $t=t_1$ and $t=t_2$.
3. If two pictures are matched, the moving distance and angle are estimated. Then the velocity vector of the vapor-liquid interface movement is determined for one divided region.
4. These procedures are applied for all 16 regions. Finally, the velocity vector at the vapor-liquid interface movement are obtained for all regions.

### (2) Results of the PIV analysis

One of the summaries of the analytical results of velocity field with PIV technique is shown in Fig. 18. Figure 18 shows the results in case that particle surface temperature is 1,000 °C and 600 °C, and subcooling are 10 °C and 60 °C. Vapor film was not established for the subcooling 60 °C at particle surface temperature 600 °C.

It is very difficult to estimate movement of the vapor-liquid interface by PIV technique, since the transient time of the phenomena is very short and view region is very narrow. Figure 18 shows the possibility that the vapor-liquid interface movement can be qualitatively followed by the present PIV technique.

## 4.3 Synthesis of heat conduction analysis and PIV analysis

Figure 19 shows the synthesis results of heat conduction analysis and the PIV analysis. All the data obtained in the present study are summarized in Fig. 19, that is, measured pressure and estimated vapor film thickness, measured particle surface temperature, saturation temperature estimated from the measured pressure and interfacial temperature estimated by the heat conduction analysis, visual information, and velocity vector of the vapor-liquid interface estimated with the PIV analysis.

The upper figure in Fig. 19 shows time transient of pressure and vapor film thickness. In this figure, vertical axes show pressure and vapor film thickness, and horizontal axis shows time in millisecond.

The middle figure in Fig. 19 shows time transient of interfacial temperature, saturation temperature and particle surface temperature. In this figure, vertical axes show interfacial temperature, saturation temperature and particle surface temperature, and horizontal axis shows time in millisecond. In both figures, the arrival time of pressure peak is taken as 0 ms. The lower figure in Fig. 19 shows picture taken from the visual observation, and the outline of vapor film and the velocity vector of the vapor-liquid interface movement. Symbols A to E correspond to figures above in Fig. 19.

Before the arrival of pressure wave, at time A, interfacial temperature was estimated higher than saturation temperature. And a clear and smooth vapor film was observed. Vapor film was not fluctuated.

When pressure pulse arrived, at time B, vapor film thickness reached its minimum value. Outlook of the vapor film changed white at time B. At this time, saturation temperature exceeded the interfacial temperature. Vapor film did not move in horizontal direction in PIV analysis.

The peak of pressure pulse was arrived at time C. The vapor film remained being white. Vapor film thickness was almost same as time B. Saturation temperature increased higher than the interfacial temperature. At this time, PIV result showed the vapor film moved toward the outside.

The pressure peak passed at time D. The boiling started on particle surface from visual information. At this time D, saturation temperature decreased across the vapor-liquid interfacial temperature. Vapor film moved toward particle surface in horizontal direction.

After the pressure pulse passed away, violent

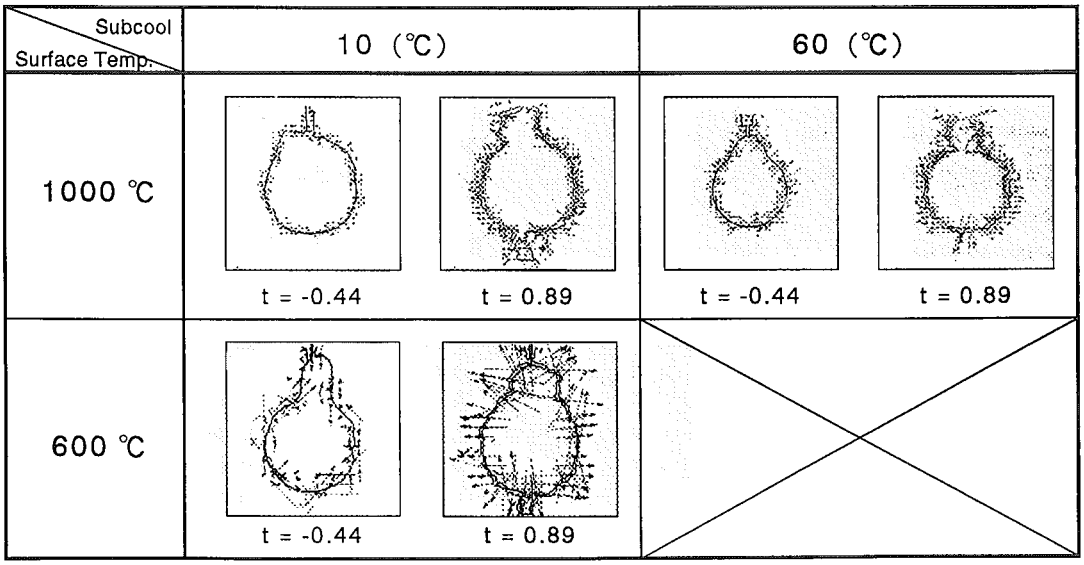



*Fig. 18 Summaries of PIV analysis (unit: ms)*

boiling was observed on particle surface at time E. The estimated vapor film thickness increased quickly. Correspondingly, estimated vapor-liquid interface with the PIV technique moved outward in horizontal direction. The estimated vapor-liquid interfacial temperature with heat conduction analysis became higher than the saturation temperature again.

## 5. Conclusions

1. The time transient of pressure, particle surface temperature, water temperature and visual information were simultaneously measured in the vapor film collapse experiment by external pressure pulse.
2. Film thickness is estimated by visual data processing technique with the pictures taken by the high-speed video camera.
3. Temperature and heat flux at the vapor-liquid interface were estimated by solving the heat conduction equation with the measured pressure, liquid temperature and vapor film thickness as boundary conditions.
4. Movement of the vapor-liquid interface were estimated with the PIV technique with the visual observation data.
5. Stable film boiling changed at the arrival time of pressure pulse. At the time, vapor-liquid interfacial temperature was estimated lower than the saturation temperature by the heat conduction analysis.
6. The estimated interfacial temperature exceeded again the saturation temperature after the pressure pulse passed away, and violent boiling started on the particle surface.

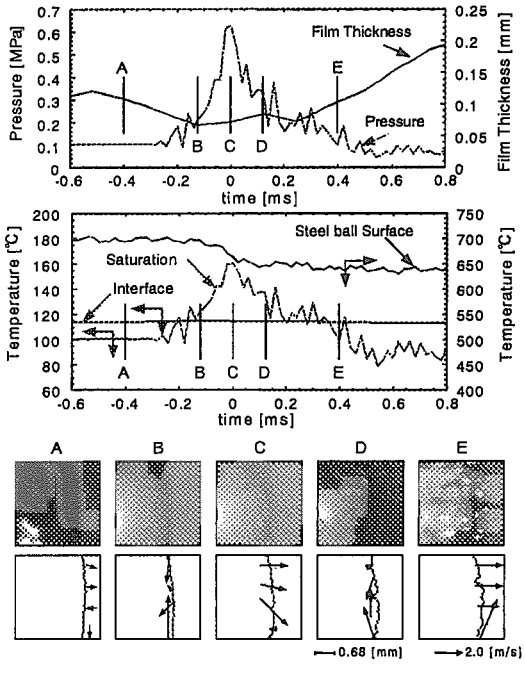



*Fig. 19 Synthesis results from experiment and Analysis*

## Nomenclature

| | | |
|---|---|---|
| $C_p$ | : Specific heat at constant Pressure | $[J/kg\cdot K]$ |
| D | : Steel particle diameter | $[m]$ |
| g | : Gravitational acceleration | $[m/s^2]$ |
| L | : Latent heat of vaporization | $[J/kg]$ |
| p | : Pressure | $[N/m^2]$ |
| Pr | : Prandtl number | $[-]$ |
| q | : Heat flux | $[W/m^2]$ |
| R | : Steel particle radius | $[m]$ |
| r | : radial position | $[m]$ |
| T | : Temperature | $[°C]$ |
| t | : Time | $[s]$ |

## Greeks

| | | |
|---|---|---|
| $\delta$ | : Vapor film thickness | $[m]$ |
| $\kappa$ | : Thermal diffusivity | $[m^2/s]$ |
| $\nu$ | : Dynamic viscosity | $[m^2/s]$ |
| $\sigma$ | : Surface tension | $[N/m]$ |
| $\lambda$ | : Thermal conductivity | $[W/m\cdot K]$ |
| $\rho$ | : Density | $[kg/m^3]$ |

$\Delta\rho$ : $= \rho_l - \rho_v$

## Subscripts

l : Liquid
S : Steel particle
sat : Saturation
sup: Superheating
v : Vapor
w : Steel particle surface

## Reference

[1] Board, S.J., Hall, R.W., Hall, R.S.:Nature, 254, 319 (1975)
[2] M. Yagi, Y. Abe, et. al., "Study of film collapse behavior during vapor explosion.", J. JSME, Ser. B, 65(636), pp.245-251(1999)
[3] Y. Abe and T. Kobayashi, "Study on vapor film collapse behavior on high temperature particle surface (1st report : Measurement of vapor film collapse pressure).", J. JSME, Ser. B, in printing.

[4] Y. Abe and D. Tochio, "Study on vapor film collapse behavior on high temperature particle surface (2nd report : Effect of subcooling on micro-mechanism).", J. JSME, Ser. B, in printing.
[5] W. H. Jens and P. A. Lottes, AEC Report, ANL-4627 (1951).
[6] S. S. Kutateladze, Zh. Tekh. Fiz., 20, p.1389 (1950).
[7] M. Zuber and M. Tribus, UCLA Report, 58-5 (1958).
[8] L. A. Bromley, Chem. Eng. Prog., 46-5, p.221, (1950).

## Appendix

Theoretical heat flux in Fig. 15 is plotted with equations as follows:

(1) Mean heat flux of nucleate boiling by Jens-Lottes[5]

$$q_{Nu} = 2.56 \cdot T_{sup}^4 \cdot \exp\left(\frac{p}{1.6954 \cdot 10^6}\right) \quad (A,1)$$

(2) Burn-out heat flux by Kutateladze[6]

$$q_{Bo} = 0.16 \cdot L\rho_v \cdot \left(\frac{\sigma g \Delta\rho}{\rho_v^2}\right)^{1/4} \quad (A,2)$$

(3) Minimum heat flux of film boiling by Zuber[7]

$$q_{Bo} = 0.157 \cdot L\rho_v \cdot \left(\frac{\sigma g \Delta\rho}{\rho_l^2}\right)^{1/4} \quad (A,3)$$

(4) Mean heat flux of film boiling by Bromley[8]

$$q_{Fi} = \frac{\lambda_v}{D} \cdot Nu_{Fb} \cdot T_{sup} \quad (A,4)$$

$$Nu_{Fb} = 0.62 \times \left\{\frac{g \cdot \Delta\rho \cdot D^3 \, Pr_v \cdot \left(L + 0.5 \cdot C_{pv} \cdot T_{sup}\right)}{C_{pv}\rho_v \cdot T_{sup} \cdot \nu_v^2}\right\}^{1/4} \quad (A,5)$$

Cross points between (A,1) and (A,2), and (A,3) and (A,4) are calculated. Then, these points interpolated linearly to reproduce transition region.

JP0150092

JAERI−Conf 2000−015

# 3.4 Propagation Calculation for Reactor Cases

Yang Yan-hua
*School of Power and Energy Enginering*
*Shanghai Jiao Tong University, Shanghai, China*

K.Moriyama, Y.Maruyama, H. Nakamura and K. Hashimoto
*Japan Atomic Energy Research Institute*
*Tokai-mura, Naka-gun, Ibaraki-ken, 319-11, JAPAN*

## 1 Introduction

The purpose of this study is to investigate the ability of the computer code JASMINE-pro in assessing the propagation of steam explosion under reactor geometry and conditions. Similar geometric and thermal conditions as that in one real reactor were employed as an example for the real reactor calculation. The ex-vessel steam explosion is considered, which is described as follow: during the accident of reactor core meltdown, the molten core melts a hole at the bottom of reactor vessel and causes the higher temperature core fuel being leaked into the water pool below reactor vessel. During the melt-water mixing interaction process, the high temperature melt evaporates the cool water at an extreme high rate and might induce a steam explosion. A steam explosion could experience first the premixing phase and then the propagation explosion phase. The current work focuses only on the second one. However, the initial conditions of this phase require the results from the calculation of the first phase. Unfortunately, we have still do not finish the modeling for the first phase at present. Thus, all the initial conditions used in this calculation are based on analyses from some simple assumptions and the observation from the experiments. The deviation because the uncertain assumptions are also investigated in this calculation.

For a propagation calculation, we should know the information about the initial fragmentation time, the total melt mass, premixing region size, initial void fraction and distribution of the melt volume fraction, and so on. But, even for the first condition, i.e., the initial fragmentation time, we have no proper model. In our study, thus, several time instants, accounted from core leakage, are investigated independently, to treat as the possible initial fragmentation time. By analysis of the leakage rate of the melt jet and a jet penetration speed, we obtained the total mass of the poured melt and the perpetration depth. Then the size of the jet was assumed, to determine a reasonable width for the pouring region and then the possible mixture region. By these assumptions, the volume fraction of melt can be determined. The initial void fractions were selected by several limit values based on the experiment observation. The initial fragmentation triggering location is assumed arbitrarily.

Calculation was two-dimensional with a cylindrical coordinate. Both the height axis and radius axis were equally divided by given mesh numbers. About 10 base cases were performed for different initial conditions and several other cases are performed for investigating the sensitivity of the grid division and the calculation method.

## 2 Geometric Size and Mesh Division

The water pool below the reactor has a height of 4.95 m and a diameter of 6 m, with the initial water level at 4 m. The computational mesh number is basically 33 in height and 20 in radius (1.5 cm width in each side). A summary for these conditions is listed in the follow:

| | | | | | |
|---|---|---|---|---|---|
| height | 4.95 | m | mesh number | 33(H) × | 20(R) |
| diameter | 6 | m | | | |
| water level | 4 | m | mesh size | 0.015(H)× | 0.015(R) $m^2$ |

A check for the effect on the mesh division was performed by change the mesh to 30 and 15 in radius (0.01, 0.02 m each cell) and to 50 and 25 in height (0.01, 0.02 m in each cell), respectively.

### 2.1 Propriety of melt material

The fuel material in the reactor of TMI-II was used for the calculation. The fuel is the oxides mixture of Uranium( 78%$UO_2$ + 17%$ZrO_2$) in that reactor. Its major properties are listed in Table 1.

Table 1: Physical properties of melt fuel in the calculation

| | Solid | Liqud |
|---|---|---|
| Melt Temp., $T_m$ (K) | 3123 [3000 in cal.] | |
| Solidification Temp., $T_{sol}$ (K) | 2830~2850 | |
| density, $\rho_m$ (kg/m$^3$) | 9430 | 7960 |
| Special Heat, $C_p$ (J/kg·K) | 400 | 650 |
| Thermal Conductivity, $\lambda$ (W/m·K) | 8 | 2.88 |
| Latent Heat of Fusion, $L$ (KJ/kg) | 362 | |
| Viscosity, $\mu$ (Pa·s) | | $0.5\times 10^{-6}$ |
| Surface Tension, $\sigma$ (N/m) | | 0.45 |

In the calculation, the initial temperature of melt is assumed to be 3000°C, which is related to the state of liquid.

## 3 Initial Conditions

Initial conditions include the size of initial mixture region, initial void fraction of vapor, initial volume fraction of melt in the mixture region, and the initial fragmentation time and location. Other conditions are the initial

pressure, water subcooling condition and the melt temperature, etc..

## 3.1 Initial fragmentation time

As mentioned above, there is no proper model for the initial fragmentation time. Thus, the possible explosion processes from several given initial fragmentation time instants were investigated in this calculation. The initial time is accounted from the release of core melt from the reactor vessel. Three time instants were chosen, which are 1 s, 3.5 s and 9.98 s. The last one was treated as the base case condition, which is associated to release the total core 70t melt.

## 3.2 Initial mixture region size

### 3.2.1 Jet and melt droplets distribution in mixture region

The size of initial mixture region is dependent on the jet size history at the exit of the breakup role on the bottom of reactor vessel and the jet penetration history inside the water pool. It was assume that the breakup diameter is began from 0.03 m, which is equal to the size of one penetration channel in the reactor. This size is enlarged with time because of steel melt at the breakup exit. The injected jet size inside the water is dependence of the size of the inlet jet size history and the resistance of the water. The later reduces the jet penetration speed and then cause the accumulation on the jet front. Thus, both the jet enlarge at the inlet and the accumulation at the jet front have the effects which the average jet size increases with the time. However, instead of a detail calculation, a simply assumption of that the jet size inside water pool being almost equal to the size of injected jet at the breakup exit on the bottom of reactor vessel at the considering time instant was used. This assumption considers that the enlarge rate of the breakup role size has the same order as that of the jet increase inside the water, which is due to the water resistance if there is no jet breakup. The total mass of melt inside the water can then be decided by the integration of the mass flux at the water surface:

$$M_{m,tot} = \frac{\pi \rho_J u_{J,exit}}{4} \int_0^t (D_{J0} + \dot{D}_{J,exit} t)\mathrm{d}t \qquad (1)$$

$$= \frac{\pi \rho_J u_{J,exit}}{12 \dot{D}_{J,exit}} \left[ (D_{J0} + \dot{D}_{J,exit} t)^3 - D_{J0}^3 \right]$$

where the constant rate of the enlarge of breakup role is used. In calculation, we used $\dot{D}_{J,exit} = 0.0346$ m/s. For jet velocity, $u_J$, it is determined by the pressure difference between the inner and extra vessel and the gravity function,

$$u_J = \sqrt{\frac{2\Delta p}{\rho_J} + 2hg} \qquad (2)$$

where the resistance is ignored. If assume the pressure difference is about 20 bar, the velocities are about 22 m/s at the vessel exit and 22.8 m/s at the water surface. By this velocity, the total mass is 321 and 70,000 kg for time at 1 and 9.98 s.

If the $u_{J,w}$ indicates the penetrate velocity in the water, the penetration distance is

$$L_{jet} = u_{J,w} t_{rel} + \frac{1}{2} g t_{rel}^2 \qquad (3)$$

Assume the resistance of the water makes the velocity reduce to about 80% of the inlet velocity, we have $u_{J,w} \approx$ 17 m/s for $u_{J,exit} = 22$ m/s. Thus, for a pool with a depth of 5 meter, the time of the jet front reached to the pool bottom is about 0.22 s. Thus, in all considered three time instances, the jet has reached to the bottom of the water pool. Exception of the accumulation of the melt at the bottom part, the total melt mass in the mixture region with the equivalent jet diameter as that at the water surface are determined by the jet diameter and the mixture region depth

$$M_m = \frac{\pi \rho_m u_{jet,ws}}{4} \int_{t-t_p}^{t} (D_{J0} + \frac{\partial D_J}{\partial t} t)^2 \mathrm{d}t, \qquad (4)$$

where $t_p$ is the time need for the jet penetrates the total pool length $L_p$.

$$t_p = \frac{L_p}{u_{J,w}} \qquad (5)$$

or $u_{J,w} = 17$m/s, and $L_{mix} = 4$m, $t_p = 0.24$ s. The melt mass in mixture region are 103.2 and 3.516 kg for time at 1 s and 9.98 s, respectively (when the jet diameters are 0.0646 and 0.375 m, respectively).

During the jet penetration, it gradually breaks into melt droplets at its surface and front. The Saito jet breakup model is employed to determine the breakup fraction. This model assumes that the jet can keep a length, called Saito jet breakup length, during its penetration, which is defined by

$$L_s = 2.1 \left(\frac{\rho_J}{\rho_c}\right)^{0.5} \left(\frac{D_J}{g}\right)^{0.5} u_J \qquad (6)$$

and the jet diameter is linearly reduced along this length due to the jet breakup. The value is $L_s = 10.58$ and 25.5 m for$D_J = 0.0646$ and 0.375 when $u_J = 22$ m/s. By this assumption and considering also the limit depth of the pool, indicated by $H_p$, the total jet surface is

, the volume of the total melt along the length is

$$V_m = \frac{\pi}{4} D_J^2 L_p \qquad (7)$$

and the volume of the jet is

$$V_J = \begin{cases} \frac{\pi}{12} D_J^2 L_s & L_p \le L_s \\ \frac{\pi}{12} D_J^2 L_p \left[ 3 - 3\frac{L_p}{L_s} + \left(\frac{L_p}{L_s}\right)^2 \right] & L_p > L_s \end{cases} \qquad (8)$$

Thus the breakup fraction is

$$\beta = \frac{V_m - V_J}{V_m} = \begin{cases} 1 - \frac{L_s}{3L_p} & L_p \le L_s \\ \frac{L_p}{L_s}\left(1 - \frac{L_p}{3L_s}\right) & L_p > L_s \end{cases} \qquad (9)$$

$$S_{jet} = \frac{\pi}{2} D_J H_p \left(2 - \frac{H_p}{L_s}\right) \sqrt{1 + \left(\frac{D_J}{2L_s}\right)^2}. \qquad (10)$$

The remained melt mass is assumed having been broken into the melt droplets. Thus the total volume of the broken melt drops is

$$V_{m.d} = \frac{\pi}{4} D_J^2 \frac{H_p^2}{L_s} \left(1 - \frac{H_p}{3L_s}\right) \qquad (11)$$

which gives the total surface of the melt droplets

$$S_{m.d} = \frac{6V_{m,d}}{d_m} = \frac{3\pi}{2}\frac{D_j^2 H_p^2}{d_m L_s}\left(1 - \frac{H_p}{3L_s}\right). \quad (12)$$

The total melt surface is therefore the sum of the jet surface and the droplet surface

$$S_m = S_{jet} + S_{m.d} \quad (13)$$

The equivalent diameter of the droplet is assumed by treat all the melt media as the droplets with the same surface as the total surface at the real condition. Thus, the equivalent diameter is given by

$$d_m = \frac{6V_m}{S_m} \quad (14)$$

which relative to 0.019 and 0.1119 m for the time instances at 1 s and 9.98 s. The diameter of the broken droplet is equal to about 4 mm.

Summary above discussion for calculation, we have :

| | | |
|---|---|---|
| pressure difference beside leakage existence | 20 | bar |
| the enlarge rate of the breakup role | 0.0346 | m/s |
| jet velocity at the exit | 22 | m/s |
| jet velocity at water surface | 22 | m/s |
| jet velocity inside the water | 17 | m/s |
| time of no breakup jet reach to water pool bottom | 0.2 | m |

And the melt conditions associated with the release time instances are listed in Table 2.

Table 2: Melt conditions at the considered melt release time

| time (s) | melt mass [kg] | melt in mix. rg. [kg] | melt surface [m$^2$] | ave.mlt drop size [m] | jet dia. [m] | Saito length [m] |
|---|---|---|---|---|---|---|
| 1.0 | 319.2 | 103.2 | 7.086 | 0.011 | 0.0646 | 10.58 |
| 9.98 | 70,000 | 3,516 | 103 | 0.0258 | 0.375 | 25.5 |

## 3.3 Initial melt volume fraction and void fraction

The initial volume fraction of melt is dependent on the total released melt mass and the size of mixture region. A region averaged volume fraction was employed in calculation.

$$\alpha_{m0} = \frac{6M_{m,mix}}{\pi D_{mix}^2 L_p \rho_m} \quad (15)$$

The volume fraction in considered cases are listed in Table 3.

Table 3: Initial condition in mixture region

| Time (s) | Region | $D_J$ [m] | $D_{mix}$ [m] | $\alpha_{m0}$ | $\alpha_{v0}$ | Cases |
|---|---|---|---|---|---|---|
| 1 | $D_J + 0.4$ | 0.0646 | 0.4646 | 0.019 | 0.2, 0.3, 0.5 | 5-7 |
| | $10D_J$ | | 0.646 | 0.01 | 0.3 | 8 |
| 9.98 | $D_J + 0.4$ | 0.375 | 0.775 | 0.234 | 0.2, 0.3, 0.5 | 1-3 |
| | $10D_J$ | | 3.75 | 0.01 | 0.3 | 4 |

In calculation, a little bit adjust on mixture region size as well as the volume fraction was done to obtain an average value at the region boundary cell. The real used values are listed later in the tables for case conditions.

The void fraction has been judged in the range of 0.2 to 0.5. Thus three points are tested: 0.2, 0.3 and 0.5, inside, 0.3 is taken as the base case problem. The used value is listed in the above table too.

## 3.4 Initial Trigger Conditions

It is still difficult to know where and under what conditions, the first trigger occurs. Avoid this judgement, we simple assumed that at the consider time instants, the melt in one cell begin to fragment and keeps continuous. The fragmentation strength depends to the velocity difference between the melt drop and the coolant in this cell. We used two ways for determining the velocity difference. One way assumes that the velocity difference is induced by the evaporation at the surface of the droplets. Thus, it depends on the heat transfer ability of the melt drop and the coolant. However, since the initial heat transfer around the melt drops is moderate, it takes a longer time to induce a propagation for the fragmentation by this method. Another way is assuming a constant large velocity for the initial trigger cell in fragmentation calculation. For example, 200 m/s was assumed in calculation. The used of this method is because we found that for some low melt volume fraction cases, the velocity difference at the boundary cells surround the initial trigger cell is so small as not to be able to support a fragmentation propagation. Anyway, in all cases, our purpose is to obtain an initially continuous fragmentation propagation results. Of cause, this consideration is not really correct. But, since there is no available initial trigger model, considering a more severe condition is reasonable.

Two condition of the initial trigger were used:

| | |
|---|---|
| I : by a real $\Delta u_{cm}$ from calculation | Case 1-4 |
| II: by a constant $\Delta u_c$ (= 200 m/s in calculation) | all cases |

## 3.5 Initial fragmentation location

The initial fragmentation locations were arbitrarily selected. Two locations, one being at the middle and one being at the bottom of the mixture region, were considered at the present calculations. Since it can be expected that the location at middle of the mixture region may cause higher energetic explosion, this condition is taken as the base case.

## 3.6 Fragmentation Condition

The critical Weber number of melt is used to judge the fragmentation conditions. Two assumption were tested. One was based on the Weber number of melt drop, and the other was based on the Weber number of melt fragments. The difference on the both conditions is at the order about $10^3$. Although this difference is large, the difference of the Weber number before and after the fragmentation is always above at this order. Thus, the value only affects for the time beginning of the fragmentation, The second assumption can avoid the fragmentation outer of the region where propagation pressure has

been reached. In the present calculation, for the first assumption, the $We_{crit,d_m} = 300$ was used and for the second, the $We_{crit,d_f} = 1$ and 20 were used.

# 4 Results and Discussion

## 4.1 Grid effects

First, how many grid number at least should be used to assure an allowable deviation on grid selection. The Case I is used for this verification, in which, the trigger position is at the vessel bottom. Grids of 50×15, 50×30 and 25×15 were tested. Figure 1 shows the results. It should be noted that in these calculations the initial triggering was calculated not by the local real velocity, which is weak so that the effect of the trigger condition is evidently. For larger cell, case I-a4 with a cell of 2x2 $cm^2$, the propagation is fast mostly due to the larger numerical diffusion, thus the pressure wave is weak and induce a weaker explosion. For small cell, case I-2 with a cell of 1x1 $cm^2$, the numerical diffusion is small, which can keep the shock wave front sharp as to induce an energetic explosion.

Figure 2 shows result for Case 3 with an initial void fraction of 0.5. Case 3-a5 is with a cell of $1x2^2$ and Case 3-e2 with a cell of 1.5x1.5 $cm^2$. The results show the same effect as Case I..

The grid effect seems very important. We should test much to sure which is available. Anyway, in the present stage, for the reason of saving time, we adopted a coarse mesh: 33x15 with which one cell is 1.5x1.5 $cm^2$. The further study will be carried out in the next time.

## 4.2 Effects of critical Weber number

Three values for critical Weber number based on the diameter of fragments ($d_f = 0.07$ mm) were used: 0.37, 1, and 20. The first one is actually related to the Weber number of 300 on the diameter of melt drop ($d_m = 25.8$ mm). This value was used in other's code, such as MC3D. However, the result by this value is largely dependence of the determination of melt-drop diameter, for which, actually we used an equivalent value to include the surface of jet so that it is not the exact value. On the other hand, for larger drop condition, the deform of the drop makes the fragmentation almost independent to the melt size. Thus, the Weber number based on the size of fragment is much more reasonable than that based on droplet.

Figure fig:We1 to fig:We3 show the effects of the critical Weber number on Case 1, 3, 4 and III.. It is evident that at the conditions with high melt volume fraction, this parameter is not sensitive. But with low volume fraction, this value becomes sensitive. It has been found that at higher melt volume fraction condition, the fragmentation is so strong as that the local Weber number is much large than the order of $10^2$. At the lower melt volume conditions, the fragmentation is not so strong and most of the local Weber number in fragmentation region is possible just located in the range between 1 to 20, such as in the Case 4 and III.

The conclusion is that the correct value for critical

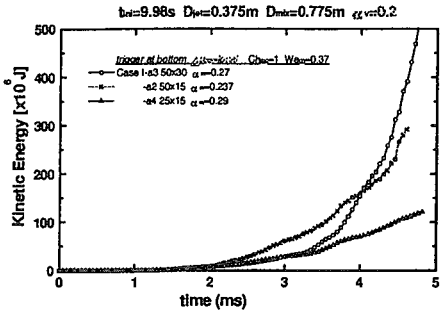



Figure 1: Effect of Grid: t=9.98s, $\alpha_v = 0.2$, $D_{mix} = D_J + 0.4$, trigger location at bottom

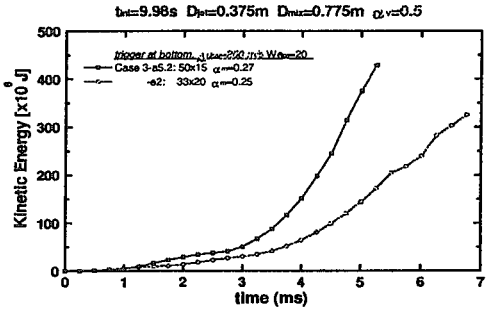



Figure 2: Effect of Grid: t=9.98s, $\alpha_v = 0.5$, $D_{mix} = D_J + 0.4$, trigger location at middle

Weber number is necessary for moderate fragmentation condition.

## 4.3 Effect of heat transfer with melt droplet

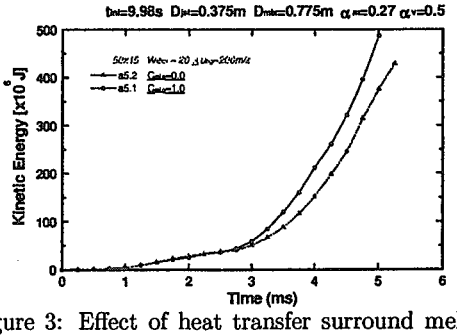



Figure 3: Effect of heat transfer surround melt droplet : t=9.98 s, $\alpha_v = 0.5$, $D_{mix} = D_J + 0.4$

We have found that the vaporization at the surrounding of melt droplet could be possible to induce the fragmentation before the triggering pressure wave arrived, if the Weber critical number is taken small. Thus, a test for the heat transfer is performed in Case 3. Figure 3 shows the results. The difference exist, comparing with the grid effect, this is not severe. And also, it is not enough to overcome the self-induced fragmentation phenomena. At the later calculations, we took this value

be zero.

### 4.4 Effect of initial void fraction

The investigation for initial void fraction is tested for the narrow mixture region conditions, i.e. the Case 1-3 and 6-8. The results are shown in Figure 4 to 7 . For lower initial void fraction, the fragmentation region is propagated faster so that the pressure peak is reached early. However, the influence on the peak value is small for different initial void fraction. This is because, once the fragmentation occurs, the local initial vapor is compressed almost to zero due to the rise of the pressure. Thus, the effect of the initial void is influent on the propagation speed only. This analysis is confirmed by the Figure 6, where the calculation can be continued after the appearance of the peak pressure due to the lower melt volume fraction. It is failed for the higher melt volume since the calculation stopped before the peak pressure reached (see Figure 4). The conclusion is that the deviation due to the uncertain initial void fraction is not so big since the difference on the peak pressure time is not very important.

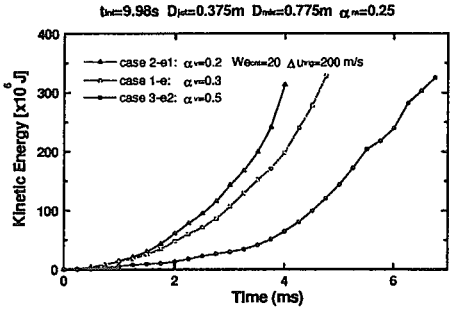



Figure 4: Effect of initial void fraction: t=9.98 s, $D_{mix} = D_J + 0.4$

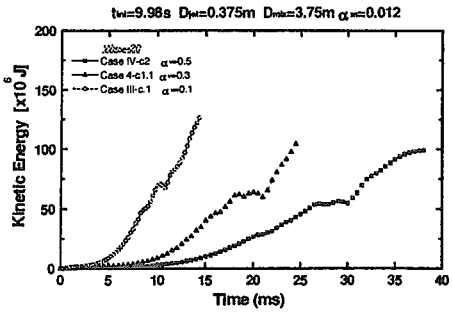



Figure 5: Effect of initial void fraction: t=9.98 s, $D_{mix} = D_J \times 10$

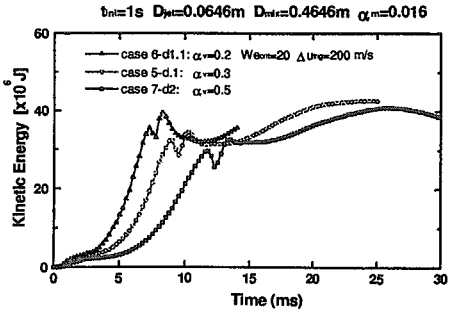



Figure 6: Effect of initial void fraction: t=1 s, $D_{mix} = D_J + 0.4$

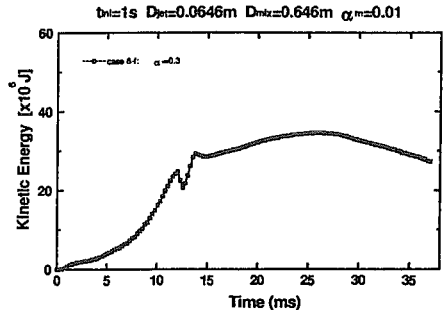



Figure 7: Effect of initial void fraction: t=1 s, $D_{mix} = D_J \times 10$

### 4.5 Effects of initial mixture region size

The differences on the initial mixture region size mainly affect the local melt volume fraction if assume the total melt mass being same. Figure 8 and 9 show the effects on 1 s and 9.98 s cases. This effect is the same as to change the melt volume fraction. Thus , the most important parameter in initial conditions is the melt volume fraction, that is, the initial fragmentation time or the mixture region size.

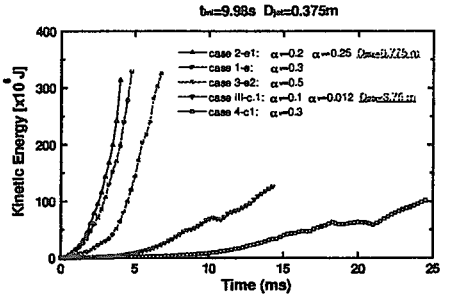



Figure 8: Effect of initial mixture region size: t=1 s, $\alpha_v = 0.3$

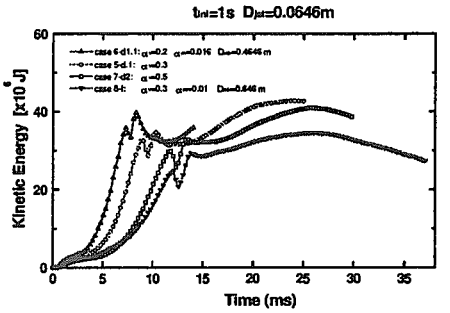



Figure 9: Effect of initial mixture region size: t=9.98 s, $\alpha_v = 0.3$

### 4.6 Pressure at the pool bottom

For the pressure reached to the pool bottom in the 7 basic cases are shown in Figure 10 to 16.

## 5 Conclusion

The propagation explosion for real reactor geometry and condition were investigated. The results show that the most important parameter for the initial condition of this phase is the total mass and its initial distribution. This

gives the requirement for a premixing calculation. On the other hand, for higher melt volume fraction case, the fragmentation is strong so that the local pressure can exceed over the EOS maximum pressure of the code ( It is 1000 bar in EOS model of the JASMINE-pro module), which lead to the incorrect calculation or divergence of the calculation. We expect to make the improvement of the EOS model and reduce also the computation time step to extent the calculation range of the time.

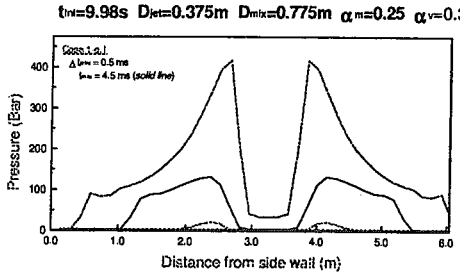



Figure 10: Pressure at the water pool bottom in Case 1: $t = 9.98$ s $\alpha_v = 0.3$, $D_{mix} = D_J + 0.4$

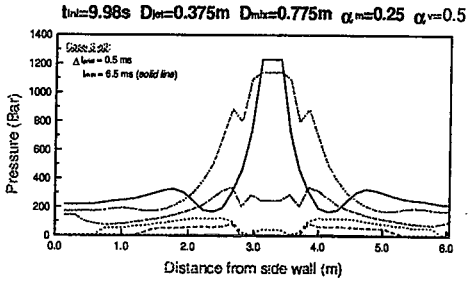



Figure 11: Pressure at the water pool bottom in Case 3: $t = 9.98$ s $\alpha_v = 0.5$, $D_{mix} = D_J + 0.4$

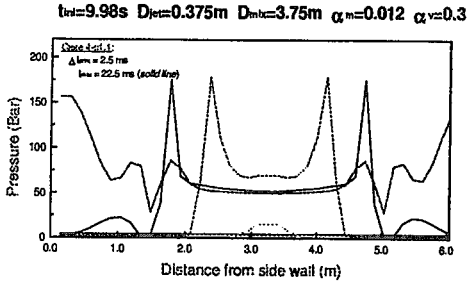



Figure 12: Pressure at the water pool bottom in Case 4: $t = 9.98$ s $\alpha_v = 0.3$, $D_{mix} = D_J \times 10$

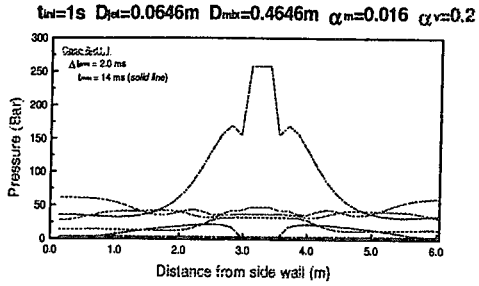



Figure 13: Pressure at the water pool bottom in Case 6: $t = 1$ s $\alpha_v = 0.2$, $D_{mix} = D_J + 0.4$

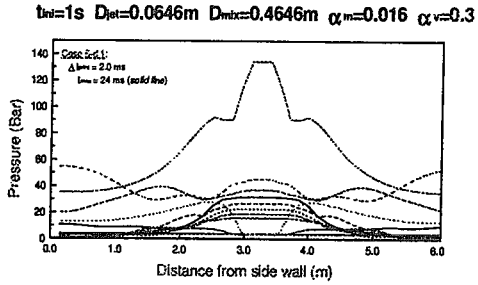



Figure 14: Pressure at the water pool bottom in Case 5: $t = 1$ s $\alpha_v = 0.3$, $D_{mix} = D_J + 0.4$

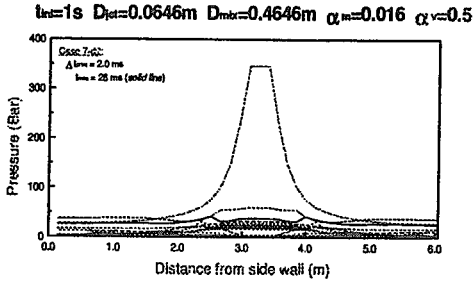



Figure 15: Pressure at the water pool bottom in Case 7: $t = 1$ s $\alpha_v = 0.5$, $D_{mix} = D_J + 0.4$

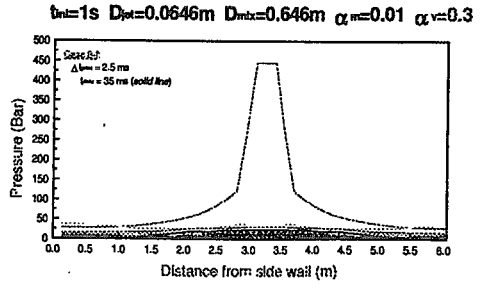



Figure 16: Pressure at the water pool bottom in Case 8: $t = 1$ s $\alpha_v = 0.3$, $D_{mix} = D_J \times 10$

This is a blank page.

# 4. Session 3

# Accident Analysis and Modeling I

## Chairperson:

G. Bandini (ENEA)
A. Hidaka (JAERI)

This is a blank page.

JP0150093



# 4.1 STATUS OF THE ASTEC INTEGRAL CODE

J.P. Van Dorsselaere, Institut de Protection et de Sûreté Nucléaire, DRS/SEMAR,
33-4-42-25-38-16, e-mail: j-pierre.vandorsselaere@ipsn.fr

F. Jacq , Institut de Protection et de Sûreté Nucléaire, DRS/SEMAR,
33-4-42-25-37-67, e-mail: fjacq@cea.fr

H.J. Allelein, Gesellschaft für Anlagen- und Reaktorsicherheit, Köln,

49-221-2068-888, e-mail : sts@grs.de

Abstract

The ASTEC integrated code is developed since 1997 in close collaboration by IPSN and GRS to predict an entire LWR severe accident sequence from the initiating event up to Fission Product (FP) release out of the containment. The applications of such a code are source term determination studies, scenario evaluations, accident management studies and Probabilistic Safety Assessment level 2 (PSA-2) studies.
The version V0 of ASTEC is based on the RCS modules of the ESCADRE integrated code (IPSN) and on the upgraded RALOC and FIPLOC codes (GRS) for containment thermalhydraulics and aerosol behaviour.
The latest version V0.2 includes the general feed-back from the overall validation performed in 1998 (25 separate-effect experiments, PHEBUS.FP FPT1 integrated experiment), some modelling improvements (i.e. silver-iodine reactions in the containment sump), and the implementation of the main safety systems for Severe Accident Management. Several reactor-applications are under way on French and German PWR , and on VVER-1000, all with a multi-compartment configuration of the containment.
The total IPSN-GRS manpower involved in ASTEC project is today about 20 men/year.
The main evolution of the next version V1, foreseen end of 2001, concerns the integration of the front-end phase and the improvement of the in-vessel degradation late-phase modelling.

Keywords : Integrated code – Severe accident – ASTEC – PSA2 – Source term

## 1 Introduction

The integrated code ASTEC (Accident Source Term Evaluation Code) is being developed by IPSN (Institut de Protection et de Sûreté Nucléaire), France, and GRS (Gesellschaft für Anlagen- und Reaktorsicherheit), Germany, since 1994 */1/*. The aim of this close co-operation of both companies is the creation of a fast running integrated code which allows the calculation of the entire sequence of a severe accident in a light water reactor from the initiating event up to the release of fission products into the environment, covering all important in-vessel and ex-vessel phenomena. The main fields of application of this code are probabilistic safety analysis level 2 studies, accident sequence studies, uncertainty and sensitivity studies and support to experiments.

Since the 1980s, a two tier approach has been applied by IPSN and GRS based on the simultaneous but independent development of both integrated and detailed mechanistic codes. During this time IPSN has developed the integrated code ESCADRE, and GRS has modelled the containment behaviour using two codes, RALOC for the thermal hydraulics and the hydrogen distribution and FIPLOC for the aerosol behaviour. For the first ASTEC version (called V0), it has been decided to gather in the same system the best candidates which can be provided by the two companies. Thus, ASTEC V0 consists in a combination of some modules of ESCADRE (for the reactor cooling system, core degradation, fission product release and transport, corium ejection from the vessel, direct containment heating and iodine chemistry in the containment), and of the module CPA (Containment Part of ASTEC), which combines the RALOC and FIPLOC codes.

## 2 Status of ASTEC V0

The first version V0.1 was used intensively in 1998 by IPSN and GRS. A general feed-back came from multi-compartment reactor calculations and from the overall validation on 25 separate-effect experiments (see the validation matrix in Fig.1), and on the FPT1 experiment of the Phebus.FP programme implying most of the code modules in a coupled mode */2/*.

This intensive use led to a recent version, V0.2, released in October 1999 to IPSN and GRS users, which includes the following modules:

- VULCAIN 7.1: RCS thermal hydraulics and core degradation, up to vessel lower head failure. The late-phase degradation simulates corium pool formation and evolution, corium slump into the lower head and (with more crude modelling) corium behaviour in the lower head and vessel failure.
- ELSA 1.1 rev.2: FP release from the fuel rods. The semi-empirical approach deals with three FP classes in an intact geometry : volatile, semi-volatile and non-volatile FPs. When the geometry becomes degraded, the modelling switches from ELSA to a CORSOR-type one.
- SOPHAEROS 1.1 rev.1: FP vapour and aerosol transport in the RCS. With twelve families of species and five states (suspended aerosols, vapour on walls, etc.), the main phenomena are modelled : aerosol deposition (thermophoresis,...), aerosol coagulation (gravitational,...), vapour interactions (condensation on aerosols,...).
- RUPUICUV 1.1: DCH (Direct Containment Heating). This module predicts the ex-vessel corium discharge into the cavity (vessel blow-down, cavity pressurisation) and the potential corium oxidation and entrainment from the cavity to the containment.
- WECHSL 3.5: molten-core concrete interaction (MCCI) in the cavity. It assumes either well-mixed or stratified (oxide, metal) corium, and calculates concrete ablation and corium oxidation.
- CPA, consisting of two main sub-modules :

  - THY for thermal hydraulics inside the containment. It describes phenomena such as gas distribution, pressure build up, hydrogen combustion, behaviour of safety systems etc. It is based on the containment code RALOC Mod4 and the thermal hydraulic part of FIPLOC.

  - AFP for aerosol and FP behaviour in the containment. The models for the aerosol and FP behaviour (transport and depletion) are based on the corresponding models of FIPLOC. The FP transport model FIPHOST is included. The aerosol transport through water pools is simulated with the pool scrubbing model SPARC-B.
- IODE 4.2 for iodine behaviour in the containment (sump and gas phase), including for instance the silver-iodine reactions in the sump.
- ISODOP: decay of FP and actinide isotopes. It starts the calculation using an initial isotope inventory generated by the CEA code PEPIN and allows decay heat and activity in the core, in the

RCS, in the containment and in the environment to be estimated. It is based on a CEA database containing a description of all isotopes.

- SYSINT: management of engineered safety features (for instance spray,...).

The whole documentation of the V0.2 is now ready, and gathered on a Web site: description of all the physical models, on-line hypertext user's manual, minimal validation report.

As for informatics, the ASTEC modules communicate with each other through a database. This allows two different running modes :

- stand-alone mode for running each module independently, useful for module validation,
- coupled mode where all (or a subset) of the modules are run sequentially within a macro-time step. This mode allows explicit feed-back between modules.

The computer interface includes :

- automatic data checkers for pre-processing,
- on-line visualisation tool, including a specific development for visualisation of RCS,
- post-processing of the graphical files with the TIC tool,
- coupling to the statistical analysis tool SUNSET (developed by IPSN) , in order to provide the confidence the user may expect from the code results.

Improvements are under way in order to lead to the version ASTEC V0.3 mid-2000, mainly on extension of the IODE module to deal with several compartments and on integration of the latest version of the SOPHAEROS module (gas phase chemistry, homogeneous nucleation, aerosol mechanical resuspension,...).

## 3 ASTEC V0 applications

Several reactor applications are currently being performed :

- on the one hand to "consolidate" the code through numerous reactor applications, in order to check all models and their coupling in various conditions and ranges of physical parameters, as well as the activation and correct behaviour of main safety systems.
- on the other hand to compare its results with reference integrated codes such ESCADRE (former IPSN integrated reference code), MELCOR on German Konvoï PWR 1300 MWe and on VVER-1000, and MAAP4 on VVER-440.

As an example of current operationality application, the results of a high-pressure reactor-case for a French 900 MWe PWR are presented in the Figures 3 to 5. The reactor nodalization is (Fig.2) : 24 axial meshes and 5 radial rings for the core, 35 volumes for RCS, and 11 compartments for containment.

The scenario is a TMLB sequence, characterized by a total loss of SG feedwater, PORV regulation, no accumulator discharge, and ECCS not available. The hydrogen and steam source is injected in the compartment where is the pressurizer relief tank zone (number C10 on Fig.2). The results show that different models are now operative, mainly DCH after vessel lower head rupture, activation of spray system, first in direct mode then in recirculation mode, and transport of FP and aerosols through the containment compartments.

## 4 Development of ASTEC V1

A main drawback of ASTEC V0 is the absence of a model for the front end phase of a severe accident, i.e. the phase from the initiating event through vessel blow-down up to the beginning of core uncovery. This leads to the necessity of calculating the RCS behaviour during the front end with an adequate thermalhydraulic code, like CATHARE or ATHLET, in order to obtain the initial conditions at the beginning of core uncovery and the sources to the containment during the front end phase.

The development activities for the ASTEC version V1 are concentrated on overcoming this drawback. Feasibility studies have led to replace the VULCAIN module, dealing with the primary circuit thermal hydraulics and core degradation in version V0, by two new modules, CESAR (**C**ircuit **E**volution under **S**evere **A**ccidents in **R**eactors) and DIVA (**D**egradation **I**n-**V**essel during **A**ccidents).

The module CESAR is based on a plant simulator French code. This module covers the 2-phase thermal hydraulics in the reactor coolant system. It is based on a lumped parameter approach with zero- and one-dimensional nodes and with 5 conservation equations for the liquid and gas mass and energy and for the mixture momentum.

The module DIVA is based on ICARE2 V3, the mechanistic reference code for core degradation during severe accidents at IPSN. To fulfil the fast running requirements of ASTEC, CPU-time intensive models of ICARE2 will be replaced by simple models if necessary.
Efforts are currently focusing on coupling both modules, testing different strategies.

Additionally, the ASTEC version V1 will bring improvements in the following areas:

- updates of the modules ELSA (release of fission products from degraded geometry), SOPHAEROS (pool scrubbing) and IODE (formation of iodides from painted walls),
- improvements of ex-vessel models (MCCI) and containment models (H2 combustion, catalytic recombiner models,...).
- standardisation of material properties through a common material data bank.

## 5 External use and validation of ASTEC

The international distribution of ASTEC V0 has already been initiated, with a release to ENEA (Italy), VUJE (Slovaquia), KI and GAN (Russia).

A larger international contribution to the ASTEC code validation is expected within the 5th EC framework programme, in the frame of a shared cost action entitled EVITA (European Validation of the Integrated Code ASTEC). The integrated code ASTEC will be distributed to European partners (16 partners from 8 countries plus JRC Ispra) in order to apply on this code the risk-oriented validation strategy issued from the VASA project (4th EC framework programme, just ended).

Key experiments and severe accidents sequences, which form the basis of analysis, will be selected and defined. A guidance for the ASTEC validation process fitting for specific end-user needs as well as for research requirements will be established. Furthermore, plant applications with ASTEC for the severe accident sequences defined before will demonstrate the capability for studying accident management measures.

EVITA will increase the extension and quality of the ASTEC validation considerably. The validation status reached and the needs for further ASTEC development will be defined by the partners with special attention to specific end-users needs. Beyond the project, the final intention is to dispose of a well validated European integrated code for the simulation of severe accident sequences in nuclear power plants.

## 6 Outlook

High efforts are currently devoted to the development and validation of the integrated code ASTEC: the total amount of manpower involved at IPSN and GRS represents about 20 men per year.

The reactor applications will continue in 2000 on PWR (German 1300 MWe, French 900 MWe in support to IPSN PSA2) and on VVER. These will allow fruitful comparisons with reference codes such as ESCADRE, MELCOR and MAAP4.

The EVITA Project, devoted to ASTEC validation by European partners, will be an important step in the code progress.

In parallel to ASTEC V0 use and improvement, milestones in the development of the next version ASTEC V1, including the front-end phase, are the release end of 2000 of a first version including all new modules for IPSN-GRS use, and the release end of 2001 of a version for external use.

## 7 References

[1] F. Jacq, W. Plumecocq, J.P. Van Dorsselaere, C. Bassi, H.J. Allelein, W. Klein-Hessling, J. Bestele,
ASTEC integral code. Status of development and validation. First application to PHEBUS.FP
CSARP 98, Washington, - May 1998

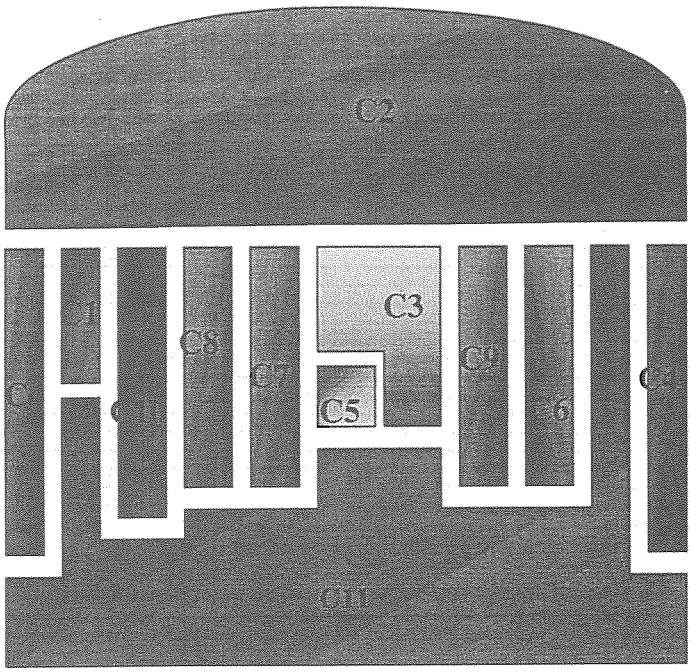
[2] W. Plumecocq, F. Jacq, J.P. Van Dorsselaere, J. Bestele, H.J. Allelein
ASTEC application to FPT1
PHEBUS.FP Information Meeting, Aix-en-Provence - October 1998

## Figure 1: ASTEC V0 - Basic Validation Matrix 15.4.98

| | HDR E11.2 E11.4 | HDR E12.3 | BMC Gx4 | VANAM M3 | KAEVER 148-149, 151 | NUPEC M7.1 | PHEBUS /TH/ | PITEAS SPIPA1 | ORNL Hydrolysis | SREAS Radiolysis | ACE RTF 3B | PHEBUS RTF3 | PHEBUS RTF5 | HIVI 1-6 | HÉVA 6 | VERCORS 4 | VERCORS 1-2 | CORA 13 | PHEBUS B9* | PBFSFD 1.4 | LOFT FP2 | ACRR MP2 | PHEBUS FPT0 FPT1* |
|---|---|---|---|---|---|---|---|---|---|---|---|---|---|---|---|---|---|---|---|---|---|---|---|
| CPA-THY-RALOC | | | | | | | | | | | | | | | | | | | | | | | |
| $H_2$ Combustion | | O,D | | | | | | | | | | | | | | | | | | | | | |
| Pass.Autocat Recomb. | | | O | | | | | | | | | | | | | | | | | | | | |
| Temperature distribution | O | O,D | O | O,D | | O,D | O | | | | | | | | | | | | | | | | V |
| Light gas distribution | O | | O | O,D | | O,D | | | | | | | | | | | | | | | | | V |
| Steam distribution | O | | O | O,D | | O,D | O | | | | | | | | | | | | | | | | V |
| Convection pattern | O | | O | O,D | | O,D | O | | | | | | | | | | | | | | | | V |
| Steam cond. on wall | O | | O | O,D | O,V | O,D | O | O, V | | | | | | | | | | | | | | | V |
| Sensible heat transfer | O | O,D | O | O,D | O,V | O,D | O | O, V | | | | | | | | | | | | | | | V |
| Spray system | O | | | | | O,D | | O,V | | | | | | | | | | | | | | | |
| Sump evaporation | O | | | | | O,D | O | | | | | | | | | | | | | | | | V |
| FP decay heating | | | | | | | | | | | | | | | | | | | | | | | V |
| Boiling | | | | | | | | | | | | | | | | | | | | | | | |
| CPA-AFP-PIPLOC | | | | | | | | | | | | | | | | | | | | | | | |
| Agglomeration | | | | O,D | O,V | | | | | | | | | | | | | | | | | | V |
| Sedimentation | | | | O,D | O,V | | | | | | | | | | | | | | | | | | V |
| Diffusion deposition | | | | O,D | O,V | | | | | | | | | | | | | | | | | | V |
| Diffusiophoresis | | | | O,D | O,V | | | | | | | | | | | | | | | | | | V |
| Condensation on aerosols | | | | O,D | O,V | | | | | | | | | | | | | | | | | | V |
| Condensation on hygros. aerosols | | | | O,D | | | | | | | | | | | | | | | | | | | V |
| Multi-comp. effects | | | | O,D | | | | | | | | | | | | | | | | | | | |
| Turbulent diffusion | | | | | | | | | | | | | | | | | | | | | | | |
| Resuspension | | | | | | | | | | | | | | | | | | | | | | | |
| CPA-IODE | | | | | | | | | | | | | | | | | | | | | | | |
| Thermal reactions in water | | | | | | | | | O | | | | | | | | | | | | | | V |
| Radiolytic Reactions in sump | | | | | | | | | | O | O,D | V | V | | | | | | | | | | V |
| Reactions AgI in Sump | | | | | | | | | | | | V | | | | | | | | | | | V |
| Radiolytic reaction atmosphere | | | | | | | | | | | | | | | | | | | | | | | V |
| Uorganic iodides | | | | | | | | | | | | | | | | | | | | | | | |
| Oganic iodides | | | | | | | | | | | O,D | V | V | | | | | | | | | | V |
| Sump-atm. volatile mass transfer | | | | | | | | | | | O,D | V | V | | | | | | | | | | V |
| Deposition on solid surfaces | | | | | | | | | | | O,D | V | V | | | | | | | | | | V |
| Efect of steam cond. on walls | | | | | | | | | | | | | V | | | | | | | | | | V |
| Water droplets-atmosphere mass transfer | | | | | | | | | | | | | | | | | | | | | | | |
| Particulate iodine behaviour | | | | | | | | | | | | | | | | | | | | | | | V |
| Multi compartments aspects | | | | | | | | | | | | | | | | | | | | | | | |
| VULCAIN | | | | | | | | | | | | | | | | | | | | | | | |
| Clad ballooning | | | | | | | | | | | | | | | | | | | | V | V | | V |
| Oxidation | | | | | | | | | | | | | | | | | | | | V | V | | V |
| Eutectic melts | | | | | | | | | | | | | | | | | | | | V | V | | V |
| Fuel dissolution | | | | | | | | | | | | | | | | | | V | M | V | V | | V |
| Ceramic melts | | | | | | | | | | | | | | | | | | | | V | V | M | V |
| Particulate debris | | | | | | | | | | | | | | | | | | V | | V | V | M | |
| Molten pool | | | | | | | | | | | | | | | | | | | | V | | M | V |
| Core reflooding | | | | | | | | | | | | | | | | | | V | | | V | | |
| Crust failure | | | | | | | | | | | | | | | | | | | | V | | M | |
| Structure ablation | | | | | | | | | | | | | | | | | | | | | | | V |
| FP release and transport | | | | | | | | | | | | | | | | | | | | V | V | | V |
| ELSA | | | | | | | | | | | | | | | | | | | | | | | |
| Volatile FP | | | | | | | | | | | | | | O | D | D | O,M | | | | | | V |
| Low volatile FP | | | | | | | | | | | | | | O | D | D | O,M | | | | | | V |
| No volatile FP | | | | | | | | | | | | | | | | | | | | | | | |

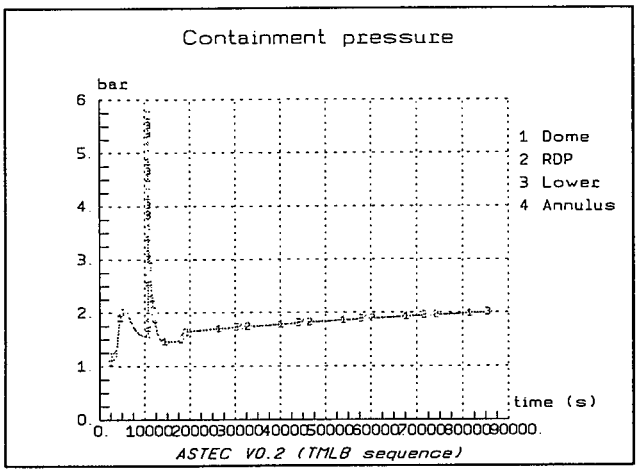
| | ACE L2/5/7 | BETA 1.8 | ANL U2 | ANL U1A UB | ANL IET3 | ANL IET7 | SNL IET4 | SNL IET6 IET10 | SNL IET8B | SNL IET11 | KAERI | TUBA TT28 | TUBA TD7 | DEVAP 08 | AERODEVAP 04 | TRANSAT TR2 | FALCON 18 | PHEBUS FPT0, FPT1* |
|---|---|---|---|---|---|---|---|---|---|---|---|---|---|---|---|---|---|---|
| RUPUICUV | | | | | | | | | | | | | | | | | | |
| Prototypic corium | | | O,D | O,D | | | | | | | V | | | | | | | |
| $H_2$ burning | | | O,D | | | | O | O | | M | V | | | | | | | |
| Scale effect | | | | | | O | | O | | | V | | | | | | | |
| Entrainment (driving press.) | | | O,D | O,D | O | O | O | O | | | V | | | | | | | |
| Cavity water mitigation. | | | | | | | | | M | | | | | | | | | |
| Insulat.disrupt.mitig. | | | | | | | | | | M | | | | | | | | |
| SOPHAERO | | | | | | | | | | | | | | | | | | |
| Aerosols settling | | | | | | | | | | | | | | | | M | | V |
| Laminar diffusion | | | | | | | | | | | | M | | | | | | V |
| Turbulent diffusion | | | | | | | | | | | | | | | | M | | V |
| Eddy impaction | | | | | | | | | | | | | | | | M | | |
| Bend impaction | | | | | | | | | | | | | | | | M | | V |
| Thermophoresis | | | | | | | | | | | | M | | | | | | V |
| Diffusiophoresis | | | | | | | | | | | | | D | | | | | V |
| Vapor FP cond./evap. on walls | | | | | | | | | | | | | | O | M | | D | V |
| Vapor FP cond./evap on aerosols | | | | | | | | | | | | | | | M | | | V |
| Sorbtion | | | | | | | | | | | | | | O | M | | D | V |
| WECHSL/CALTHER | | | | | | | | | | | | | | | | | | |
| Zirconium content | O,D | O,D | | | | | | | | | | | | | | | | |
| R H C upper surface | | O,D | | | | | | | | | | | | | | | | |
| 2 layers (oxide/metal) | | O,D | | | | | | | | | | | | | | | | |
| 1layer (mixed) | O,D | | | | | | | | | | | | | | | | | |
| Siliceous concrete | O,D | O,D | | | | | | | | | | | | | | | | |
| Limest. sand concrete | O,D | O,D | | | | | | | | | | | | | | | | |

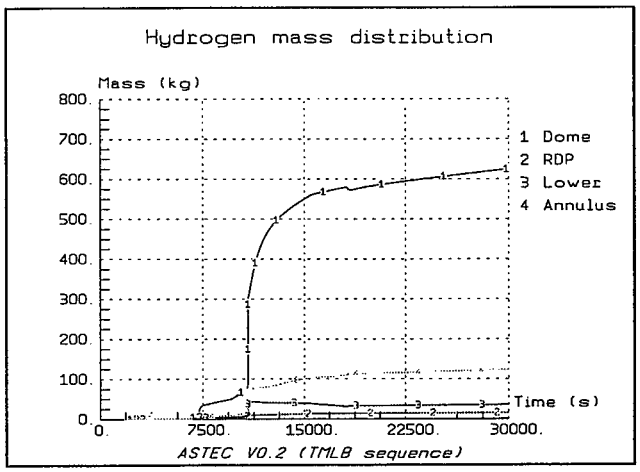
O : means validation performed with an old (stand alone) version
D : means valid. calculation performed with ASTEC V0 as ***Delivering Case*** which were performed until the delivering of ASTEC V0;
M: ***Minimum Validation stage*** to be performed to allow first reactor applications for instance for PSA. Milestone mid 1998
V : means complementary validation calculations intended for ASTEC V0 , but not necessarily until mid 1998
* : global validation calculation for PHEBUS FPT0, FPT1, and TMI2 which serves simultaneously as demonstration calcul

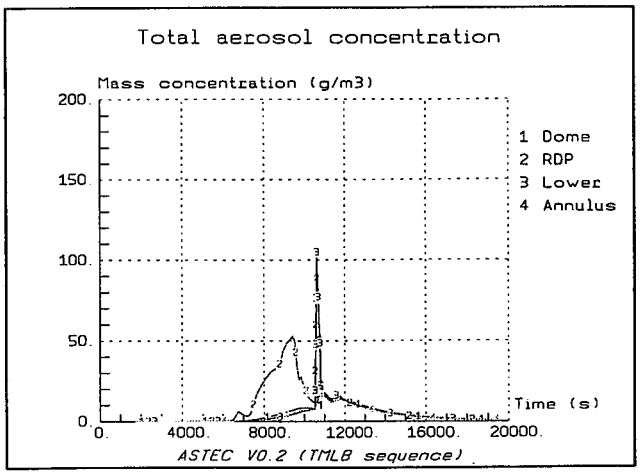



C1 : pressurizer zone
C2 : dome
C3 : discharge pool zone
C4 : annular space
C5 : lower zone
C6 : vessel upper head zone
C7 : loop n°1 zone
C8 : loop n°2 zone
C9 : loop n°3 zone
C10 : pressurizer relief tank zone (RDP)
C11 : zone around loops

Figure 2 : Containment nodalization for an operationality ASTEC calculation on a French PWR 900 MWe




Figures 3 to 5 : Containment results of an operationality ASTEC calculation on a French PWR 900 MWe

JP0150094



# 4.2 Development Status of Severe Accident Analysis Code SAMPSON

Tsuyoshi IWASHITA, Hiroshi UJITA
Advanced Simulation Systems Department, Nuclear Power Engineering Corporation
Fujita Kanko Toranomon Bldg., 6F, 17-1, 3-chome Toranomon, Minato-ku, Tokyo 105-0001
JAPAN
Tel:+81-3-3434-2410, Fax:+81-3-5470-5544, E-mail:ujita@nupec.or.jp

## ABSTRACT

The Four years of the IMPACT, 'Integrated Modular Plant Analysis and Computing Technology' project Phase 1 have been completed. The verification study of Severe Accident Analysis Code SAMPSON prototype developed in Phase 1 was conducted in two steps. First, each analysis module was run independently and analysis results were compared and verified against separate-effect test data with good results. Test data are as follows: CORA-13 (FZK) for the Core Heat-up Module; VI-3 of HI/VI Test (ORNL) for the FP Release from Fuel Module; KROTOS-37 (JRC-ISPRA) for the Molten Core Relocation Module; Water Spread Test (UCSB) for the Debris Spreading Model and Benard's Melting Test for Natural Convection Model in the Debris Cooling Module; Hydrogen Burning Test (NUPEC) for the Ex-Vessel Thermal Hydraulics Module; PREMIX, PM10 (FZK) for the Steam Explosion Module; and SWISS-2 (SNL) for the Debris-Concrete Interaction Module. Second, with the Simulation Supervisory System, up to 11 analysis modules were executed concurrently in the parallel environment (currently, NUPEC uses IBM-SP2 with 72 process elements), to demonstrate the code capability and integrity. The target plant was Surry as a typical PWR and the initiation events were a 10-inch cold leg failure. The analysis is divided to two cases; one is in-vessel retention analysis when the gap cooling is effective (In-vessel scenario test), the other is analysis of phenomena event is extended to ex-vessel due to the Reactor Pressure Vessel failure when the gap cooling is not sufficient (Ex-vessel scenario test). The system verification test has confirmed that the full scope of the scenarios can be analyzed and phenomena occurred in scenarios can be simulated qualitatively reasonably considering the physical models used for the situation.
The Ministry of International Trade and Industry, Japan sponsors this work.

**Keywords** Severe accident analysis, Mechanistic model simulation, Parallel processing, In-vessel retention, Ex-vessel phenomena

## I. INTRODUCTION

IMPACT (Integrated Modular Plant Analysis and Computing Technology) is the name of a program and of specific simulation software, which will perform full-scope and detailed calculations of physical and chemical phenomena in a nuclear power plant for a wide range of scenarios [1-2]. The main analysis objectives are to show that light water reactors (PWR/BWR) maintain safety margin under hypothetical severe accident conditions and to investigate realistic measures of accident management by simulating the accident in detail and on a reasonable time frame using a parallel computer. To satisfy the objectives, it is required to calculate various behaviors of the fuel cladding damage, fuel melting, candling, crust forming, molten debris cooling, fission products release, etc., and to evaluate reactor vessel and containment structural integrity. Because these phenomena are difficult to investigate experimentally, analytical evaluations of the safety margin must be relied upon. To satisfy these analytical needs, computer simulations based upon fundamental physics principles and sophisticated modeling technologies are required. Separate software modules for micro-, meso-, and macro-scale modeling will be developed which may be combined in the most systematically efficient manner in a parallel environment.

The four years of the IMPACT project Phase 1 have been completed. At the end of the phase, demonstration simulations by combinations of up to 11 analysis modules developed for severe accident analysis in the SAMPSON Code (Severe Accident Analysis Code with Mechanistic, Parallelized Simulations Oriented towards Nuclear Field)

were performed and verified [3-6]. The Basic Single-, Two-, and Multi- Phase Flow Analysis Modules (PLASHY: Parallel Large scales Analysis System for HYdrodynamics) have been Parallelized in various coordinate systems [7]. The physical models in the Boiling Transition Analysis Code (CAPE: Critical power Analysis code with Parallel Environment) have been completed and verified for both BWR fuels critical power and PWR fuels DNB prediction capabilities by comparison with fundamental experimental results [8]. The Fluid-Structure Interaction Analysis Code (FLAVOR: FLuid structure interaction Analysis code for VORtex induced vibration) was developed and verified for both 2 dimensional cross flow fluid-structure interaction analysis and 3 dimensional flow induced vibration analysis [9].

## II. MODULE VERIFICATIONS

The verification study of the code was conducted in four steps. First, each analysis module was run independently and analysis results were compared against separate-effect experiment data. Verification analyses included: CORA-13 (FZK) for the Fuel Rod Heat-up Module; HI/VI Test-VI-3 (ORNL) for the FP Release from Fuel Module; KROTOS-37 (JRC-ISPRA) for the Molten Core Relocation Module; Water Spread Test (UCSB) for the Debris Spreading Model and Benard's Melting Test for Natural Convection Model in the Debris Coolability Module; Hydrogen Burning Test (NUPEC) for the Containment Thermal Hydraulics Module; FARO-L14 (JRC-ISPRA) for the Steam Explosion Module; and SWISS-2 (SNL) for the Debris Concrete Reaction Module. Second, module combination tests for dominant phenomena were performed to improve the compatibility of related analysis modules with each other. Third, with the Analysis Control Module, these analysis modules were executed concurrently in the parallel computing environment (IBM-SP2 with 72 processing elements), to demonstrate the code capability and integrity for an in vessel event. The reference plant was Surry as a typical PWR and the initiating event was a 10-inch cold leg failure LOCA. The system analysis was performed to investigate in-vessel retention when water cooling option was adopted and gap cooling was effective (In-vessel scenario test). Fourth, the analysis was extended to the ex-vessel. The reactor pressure vessel failed when steam-cooling options was used and gap cooling was not sufficient (Ex-vessel scenario test).

### 1. Separate Effect Test Analyses

The 10 test analyses were performed to check programming of the 9 modules, shown in Fig.1.

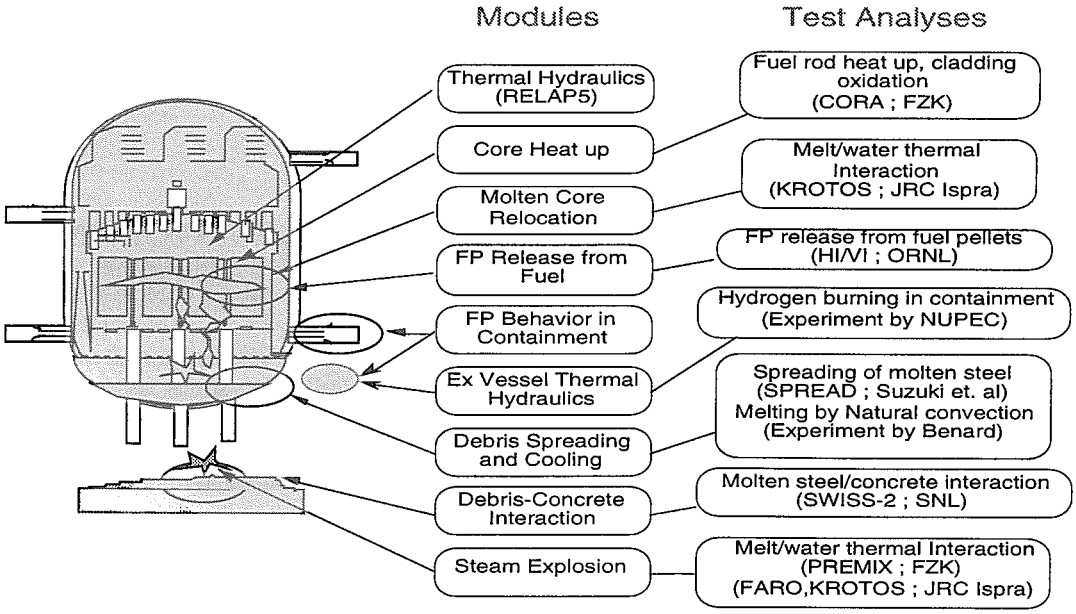



Figure 1 Modules and Test analyses for verification

CORA-13 TEST data were used for Heat up module validation. Fig.2 shows the comparison results. In experimental data, rod surface temperature history is divided into two parts. The first is heat up phase up to 1000 degrees and the second is Zr-water reaction phase with rapid heat generation. Calculation result shows good agreement with experimental data in both phases. But in hydrogen gas generation rate, there are some differences between calculation and experimental data. The module calculates hydrogen generation in the lower temperature region. After 4000second, hydrogen gas generation increase rapidly same as experimental data. The decrease of hydrogen gas generation was caused by lack of metal zirconium. That is end of Zr-water reaction. The peak of hydrogen generation in experiment was caused by reflooding.

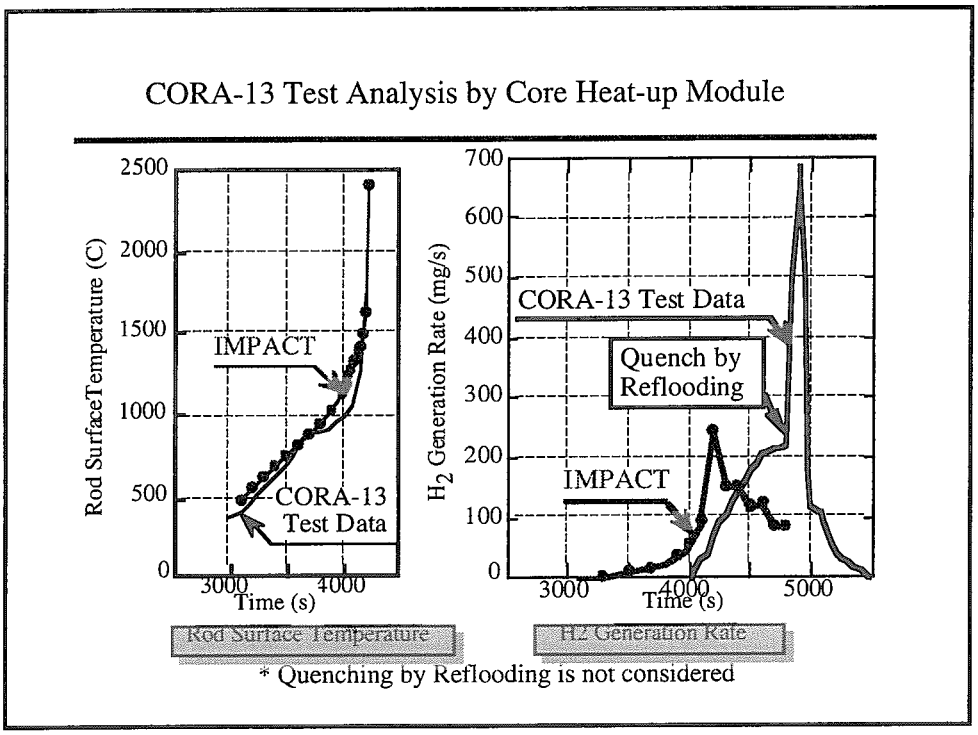



Figure 2 Comparison results of CORA-13 test analysis by the core heat up module

The molten core relocation module solves multi-phase multi-components thermo-hydraulic equations. This module can deal with these number of equations. The left hand side of Figure 3 shows pressure behaviors. The calculation pressure rises faster than that of experiment because of large amount of heat exchange caused by faster fragmentation of molten corium. The discrepancy on this region is caused by neglecting the heat losses in experiment. The right hand side figure shows position of melt front. This model calculates slow penetration speed.

Figure 4 shows calculation results of Kr release compared with experimental data and data obtained by correlation. In experiment, as fuel temperature goes up, Kr release rate is increasing. Both calculation and correlation results of Kr release are nearly the same agreement with experimental data. The Calculation result shows strong influence of fuel temperature change. In this calculation FP release due to grain growth was considered.

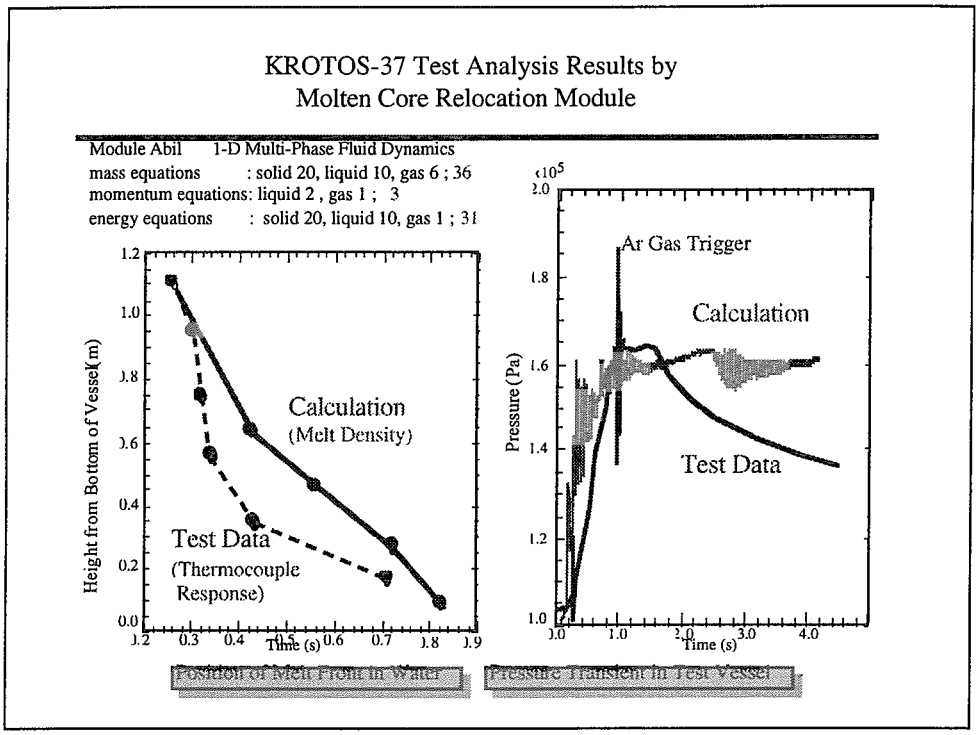



Figure 3 KROTOS-37 Test Analysis by the Molten Core Relocation Module

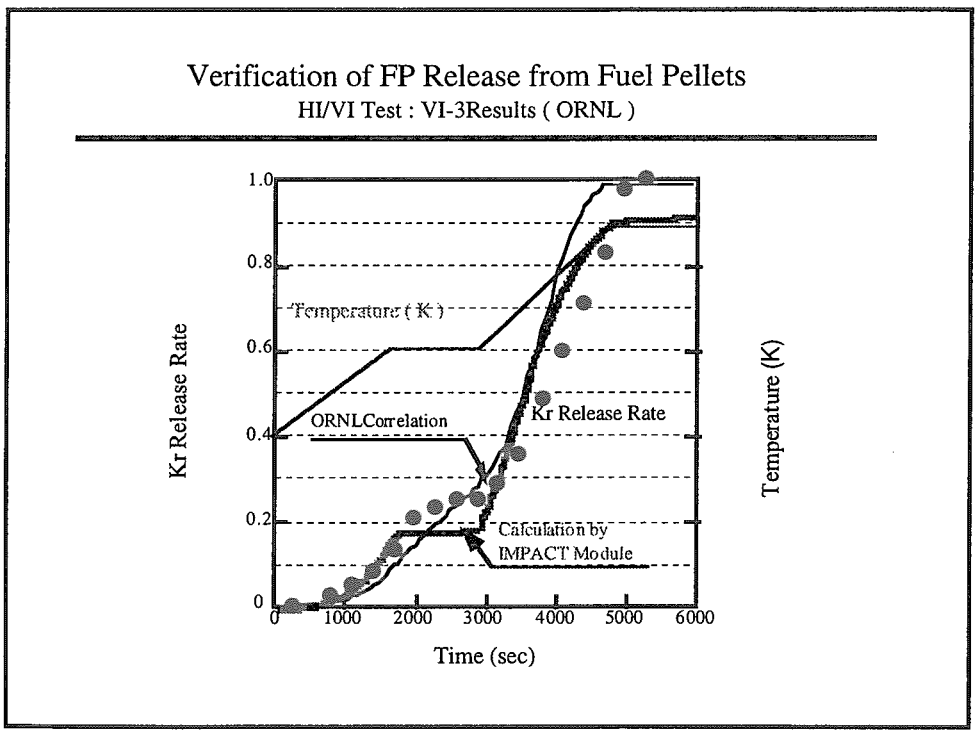



Figure 4 HI/VI Test Analysis

In severe accident, after core melt ,molten debris go down to the lower plenum. And then spread and cooled. For debris spreading two dimensional Cartesian Nabier-Stokes equations are solved. And we have two type of models for debris cooling, 2D natural convection model and Simplified bulk model. For debris bed cooling we use 1D Lipinski model, and 3D heat conduction model for reactor vessel heating. Creep rupture is evaluated by Larson Miller parameter. Both spreading and cooling models were examined by test data.

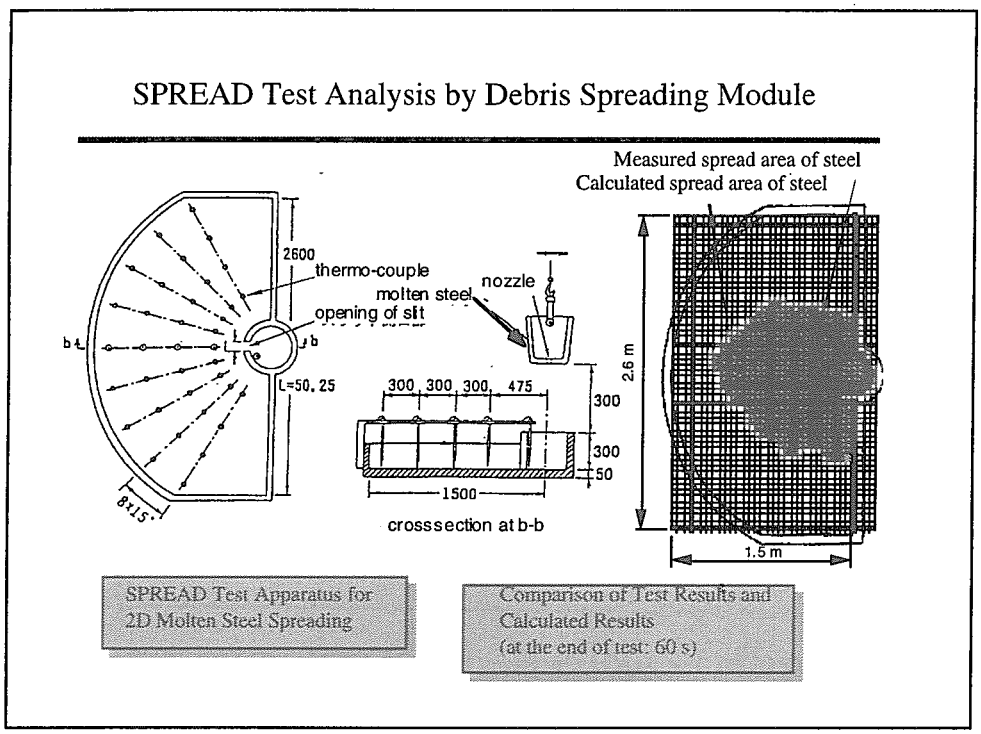



Figure 5 the SPREAD Test Analysis by Debris Spreading Module

The Spreading model was tested by the SPREAD TEST date. Figure 5 shows test sections. Molten steel falls down on this point and then spread through the opening slit. Calculation result shown on this figure with experimental data. The Calculated Spreading area and distance intend to be larger than that of experiment. But differences are not so large.

In case of pressure vessel rupture occurred, debris concrete interaction is need to be evaluated. The SWISS-2 test used for verification of the debris concrete interaction analysis modul. In the teat, Sus304 was heated by induction heating, and the top surface was cooled by water. Figure 6 shows the results. Ablation depth and top surface heat flux were compared with experimental data. Up to 30 minutes calculation result shows good agreement with experimental data, but after that it shows under estimation. And not only this, there is another difference. Experimental data go up exponentially after 30 minutes, while calculation results increase linearly. So ablation model needs to be modified. About heat flux , except immediate after water injection region calculation result shows good agreement with experimental data. The difference may be caused by subcooling effect.

Fig.7 shows the verification results of fine fragmentation propagation model in steam explosion module. The explosion initiated at an elevation of 0.15 m, as in the experiment and the prototype code correctly calculated propagation upward.

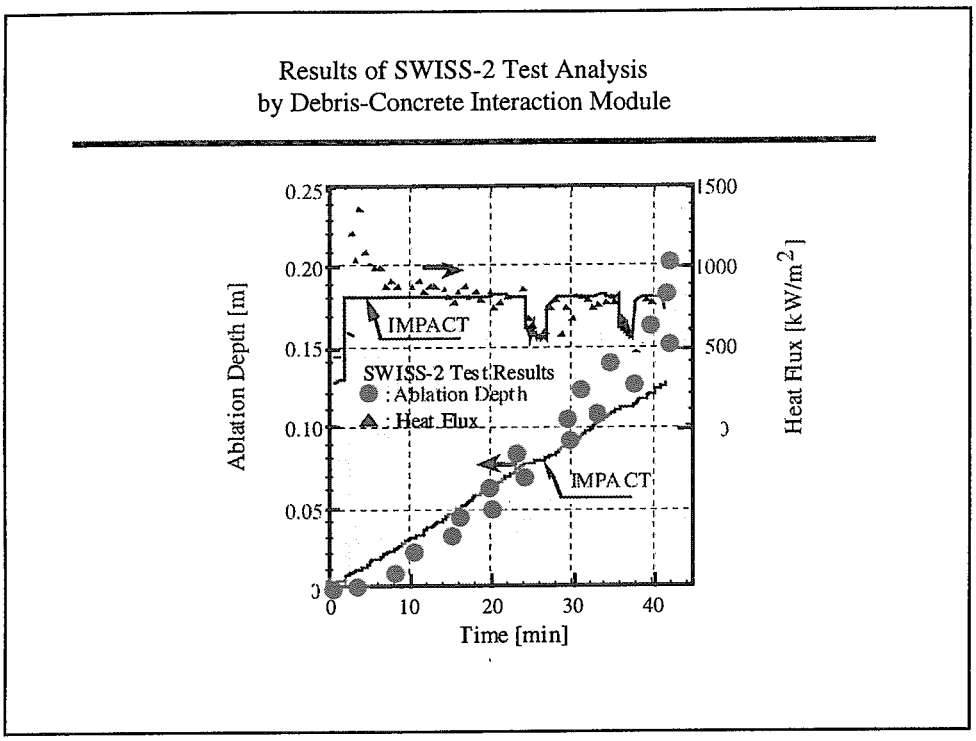



Figure 6 the SWISS-2 Test Analysis by Debris Concrete Interaction Module

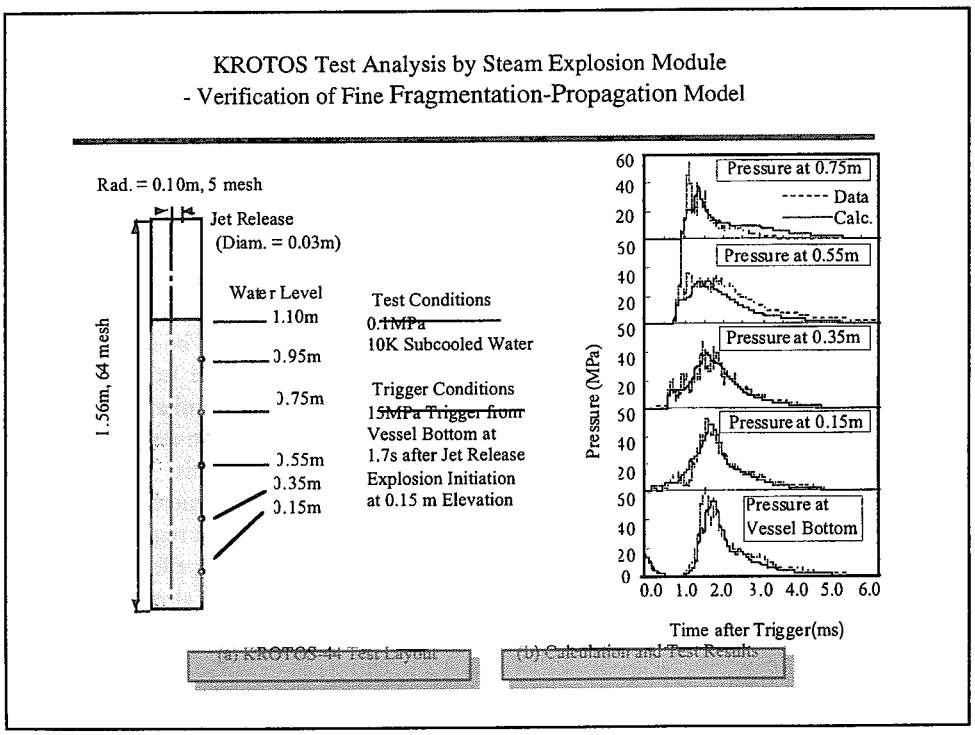



Figure 7 the KROTOS Test Analysis by Steam Explosion Module

## III. IN-VESSEL SCENARIO TEST

For the initial quasi-steady state period, the SSS activated the Thermal Hydraulics in primary system Analysis Module and the Fuel rod Heat-up Analysis Module. Normal and transient thermal hydraulics results obtained here were same as usual transient analysis. Upon transient initiation, the FP Release from Fuel Analysis Module and the Thermal Hydraulics in Containment Analysis Module were called. Additional modules were activated and others terminated according to the change in event. The analysis will be terminated when vessel wall temperature decreases and becomes steady state.

### 1. Core Melt

After the cladding failure at 715s, core melt and relocation behavior was analyzed until 1400s with FRHA and MCRA. The cladding maximum temperature increases to 1500K, upon which the Steam-Zircaloy reaction begins, and then rapidly increases to exceed the fuel failure temperature condition of 2100K.

The fuel melt behavior is shown in Fig. 8. The fuel region is divided into 5 channels and 10 nodes. The second fuel node from the top (node 9) in center channel (channel 1) was melted first at 1114s and then the molten region spread to surrounding nodes. Fuels in Channel 3 were not melted until 1250s while ones in channel 4 has already started to melt, because steam velocity in channel 3 was high compared with other nodes in channel 4 due to the effect of 1 dimensional model (cross flow among channels can not be simulated) and cooling was very effective while fuel temperatures were high. A total of 23 fuel nodes were melted (melt fraction was 1/3), while the fuel in Channel 5 is still intact at 1400s. Pressure in the vessel decreased slowly, and spike occurred after 1114s due to fuel failure.

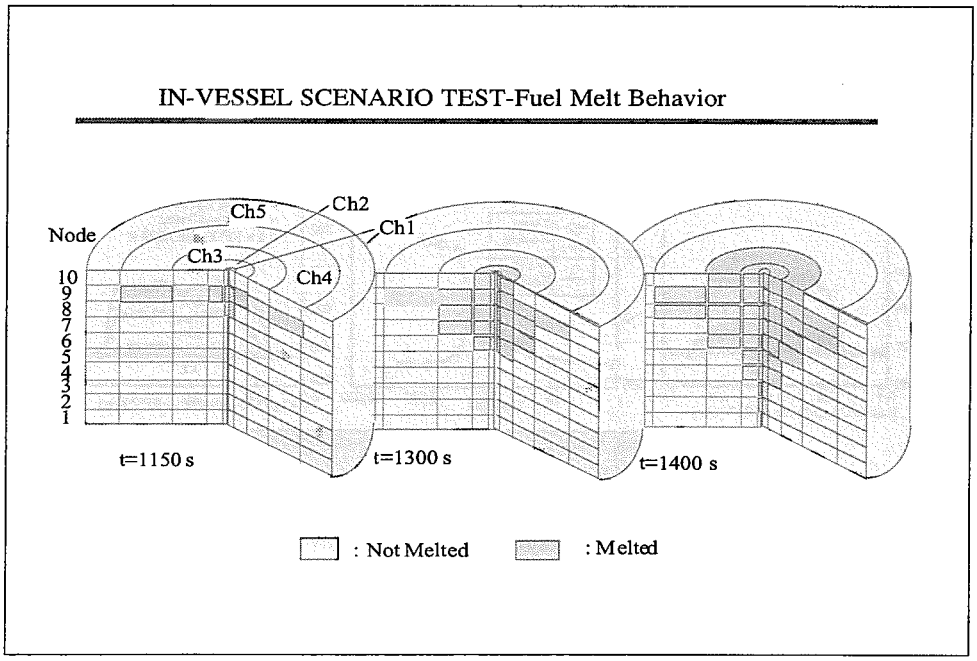



Figure 8 In-Vessel scenario test, Fuel melt behavior

Melt and particle fraction became large when fuel melted and fell from the upper region nodes, and the vapor fraction increased when the node itself melted and fell into lower plenum. Volumetric flow rates of melt content from channel 2 into lower plenum major parts are of fuel particle in this case due to the fuel failure criteria modeled. Total 22 ton of melt have been fallen at time 1400s, over one third of the mass was fallen from Channel 3.

### 2. Debris Cooling

When the molten debris falls into lower plenum for the first time, debris-spreading model starts and the falling is

stopped then natural convection model starts. The time interval of debris falling continued 130s and total 2.0*10^4kg of molten debris was piled on the lower plenum. Therefore, debris-spreading analysis continues to 130s, when steam gap cooling was effective, and then debris-cooling analysis by natural convection model, to 3600s, when gap cooling was effective since water remained in the bottom of vessel. Vessel walls temperature increased while spreading and then decreased while natural convection cooling as shown in Fig. 9.

Outer region was solidified first and crust was formed, because the cooling water was available at the top of molten fuel and between crust and vessel side-wall. Firstly, the debris was solidified due to cooling by the water covering the upper surface and in the gap. Next, solidification advanced upon the inner debris pool by heat transfer at the melt front. After all the debris was solidified, the heat conductivity calculation of the debris was continued. The RPV wall temperature decreased near the fluid temperature at 300s due to cooling by the gap water because it was assumed that the temperature of water in the gap was limited to the saturation point. The removal heat at the gap was added to the water over the upper surface in the models. The vessel wall temperature decreased rapidly compared with molten debris temperature to the level of cooling water temperature at 300s and stayed in steady state till 3600s by gap cooling, as shown in Fig. 9. The in-vessel retention was achieved in this case scenario.

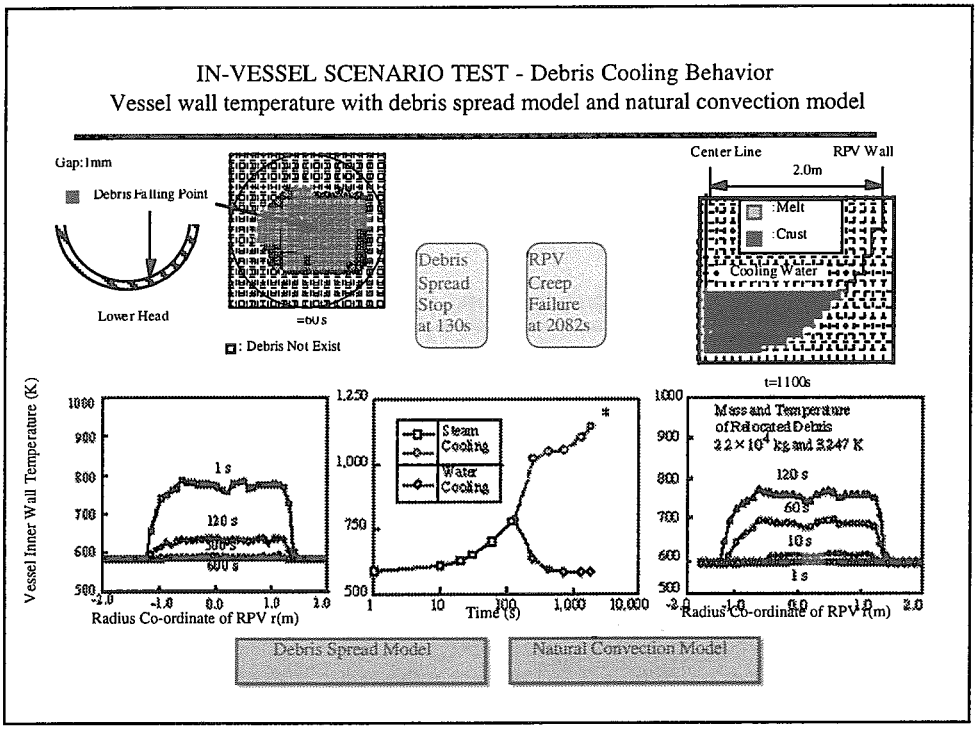



Figure 9 Vessel wall temperature with natural convection model

## IV. EX-VESSEL SCENARIO TEST

The fuel heat up, core melt and relocation, and debris cooling phenomena were also analyzed in the ex-vessel scenario test as same as in the in-vessel scenario test. The system integrated analysis continued through RPV failure to long term debris concrete interaction in the containment vessel, upon which the Simulation Supervisory System ended the calculation 1h after the debris concrete interaction.

### 1. Reactor Pressure Vessel Failure

After spreading is stopped at 130s, the natural convection model analyzes debris-cooling behavior. Outer region was solidified first and crust was formed, because the cooling water was available at the top of molten fuel and

steams existed between crust and vessel side wall. Melt pool and crust regions are separated after 300s and then the state is maintained. In the scenario, cooling water was not available and the capability of steam cooling in gap between crust and vessel side wall was lower than water cooling at the gap cooling model, then vessel wall temperature increased as shown in Fig. 9, and finally vessel creep failure occurred at lower part of vessel of the highest temperature at 2082s.

**2. Debris Spreading**

When the vessel fails and the molten debris falls into primary containment vessel floor at the first time, Debris Spreading Module starts and the spreading is stopped then Debris Concrete Interaction Module starts. Spreading speed was rather high (spreads 1.8m at 30s) than in pressure vessel bottom because floor is flat. Concrete floor temperature increases according to debris spreads.

**3. Debris Concrete Interaction**

One dimensional analysis system of vertical dimension is 2m water depth, .23m debris thickness and 5m limestone concrete thickness with 3.2m wide, and horizontally 3.2m thick concrete. Ablation depth of lower concrete by debris was 8.2cm and side, 4.7cm respectively at 60min, because the lower direction heat transfer coefficient between molten debris and concrete floor is higher than side direction one between debris and concrete wall. Both upward heat flux from debris and its temperature decreased as ablation proceeded, to 160kW/m^2 and 2010K respectively at 60min. Flammable gas release rate increased according to the ablation rate due to concrete decomposition and gas interaction with molten debris, and the final amounts of CO and H2 were 200kg and 11kg respectively until 60min after the molten debris fell onto the floor.

The system verification test has confirmed that the full scope of the scenarios can be analyzed and phenomena occurred in scenarios can be simulated qualitatively reasonably considering the physical models used for the situation. In-vessel scenario test has shown the possibility to evaluate in vessel retention, while Ex-vessel scenario test the ability to calculate whole scope of severe accident.

## VII. CONCLUSIONS

Four years of the IMPACT project Phase 1 have been completed with financial sponsorship from the Japanese government's Ministry of International Trade and Industry. At the end of the phase, demonstration simulations by combinations of up to 11 analysis modules developed for the SAMPSON Code were performed and verified.

The verification study of the SAMPSON was conducted in two steps. First, each analysis module was run independently and analysis results were compared against separate-effect experiment data with good agreement. Second, with the Simulation Supervisory System, these analysis modules were executed concurrently in the parallel environment, to demonstrate the code capability and integrity. The target plant was Surry as a typical PWR and the initiation event was a 10-inch cold leg failure. The system analysis is divided to two cases; one is in-vessel retention analysis (In-vessel scenario test), the other is analysis of phenomena when the event is extended to ex-vessel due to the Reactor Pressure Vessel failure (Ex-vessel scenario test). Through test analyses, the Simulation Supervisory System called and terminated analysis modules as appropriate according to the progression of plant phenomena, controlled the parallel processing, and the analysis modules showed qualitatively good responses.

## REFERENCES

[1] Ujita, H. et. al., Proc. 2nd CSNI Specialist Mtg. on Simulators and Plant Analyzers, Espoo, Finland, 9/1997.
[2] Naitoh, M. et. al., NURETH8, Kyoto, Japan, September 1997.
[3] Morii, T. et. al., Fuel Rod Heat-up and FP Release Behavior Modules, ICONE-7,1999.
[4] Satoh, N. et. al., Molten Core Relocation Module, ICONE-7,1999.
[5] Ujita, H. et. al., Debris Coolability Module, ICONE-7,1999.
[6] Vierow, K. et. al., The Japan Society of Multiphase Flow, Vol. 12 No. 3, September, 1998.
[7] Nagata, S. et. al., AESJ Fall Mtg., Fukui, Japan, September, 1998 (in Japanese)..
[8] Naitoh, M. et. al., NTHAS98 at Pusan, Korea.
[9] Andoh, Y. et. al., ANS 1998 Winter Mtg. at Washington, D. C.

JP0150095



# 4.3 ICARE/CATHARE V1 Application to a PWR 900 MWe severe accident sequence

**Magali Zabiégo[1], Florian Fichot[1], Valia Guillard[1], Marc Barrachin[1], Bertrand Lefèvre[2], Stéphane Mélis[1], Patrick Chatelard[1], Francine Camous[1]**

1. Commissariat à l'Energie Atomique, Institut de Protection et de Sûreté Nucléaire, DRS/SEMAR/LECTA, Centre d'Etudes de Cadarache 13108 St-Paul-Les-Durance Cédex, France.

2 Communications et Systems, Bât. 151 Centre d'Etudes de Cadarache 13108 St-Paul-Les-Durance Cédex, France.

***Abstract:*** In the first part of this paper, a brief description of the V1 version of the ICARE/CATHARE software is presented. The new models developed by IPSN are described here.
An application of this version to a French PWR 900 MWe is then shown. Although a description of the whole circuit is possible with ICARE/CATHARE V1, the present application is restricted to the reactor vessel. The results show the progression of the core degradation and the relocation of an important amount of corium in the reactor lower head.
This calculation demonstrates the capacity of the code to provide a physically grounded simulation of the whole scenario.

***Keywords:*** ICARE/CATHARE V1, PWR, H2 sequence, core degradation.

## 1 Introduction

The ICARE/CATHARE computer code is developed by IPSN to calculate a severe accident sequence in a pressurized water reactor. The V1 version presented here and released in July 1999 is based on the latest version (V3mod0.4) of the ICARE2 core degradation code coupled with the V1.3L_1 version of the CATHARE2 thermal hydraulics code.
The latest models developed by IPSN in ICARE2 are briefly presented in the first part of this paper (See ref.1 for all the details).

A description of the whole circuit is now possible with ICARE/CATHARE V1; this version was used in some applications such as TMI2 (phase 1 and 2), a Large Break LOCA in a PWR 900 MWe, the LOFT LP-FP2 experiment. However, the application presented in the second part of this paper is restricted to a PWR 900 MWe reactor vessel. A total loss of feed water accidental sequence, in which the core uncovery leads to a large degradation, is simulated with the ICARE2 code (stand-alone version). After describing the boundary conditions of this scenario (resulting from a CATHARE2 calculation), we show the repartition of material distribution in the system at different instants.

## 2 ICARE2: new models and capabilities

### *2.1 Core description*

In the ICARE2 code, the meshing is 2-dimensional and cylindrical.
In the previous versions of the code, the available geometrical objects were vertical structures (shrouds), fuel rods, control rods, grids and a fluid field.

In the V3mod0.4 version the following new elements are available:

- horizontal structures (plates),
- core former plates (in the reactor bypass),
- the lower and upper heads of a reactor vessel.

In addition to these elements, different fields are pre-defined over the whole domain and appear during the transient: debris and magma field.

Figure 1 shows an application of a reactor modeling with ICARE2.

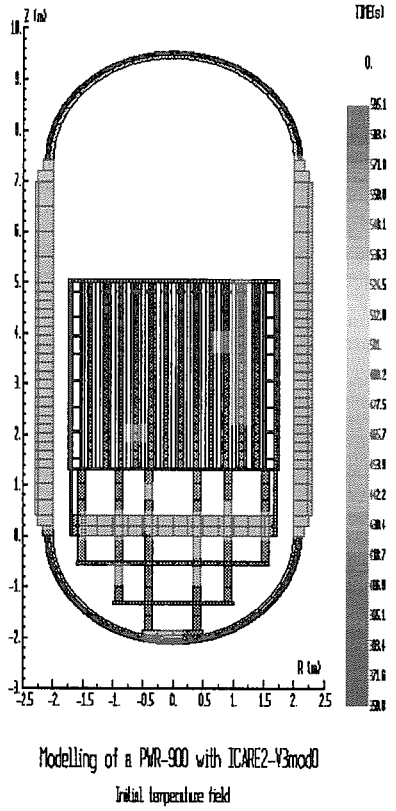



Figure 1: Example of meshing in a reactor case

### *2.2 Dynamic transition to a debris bed*

When the rod cladding fails, according to user-defined mechanical criteria, the pellets located inside the cladding can be instantaneously transformed into debris particles. The size distribution of the particles may either be pre-defined by the user or calculated by a fragmentation model.
Once the debris are generated, it is possible to calculated their collapse. In this version of the code, no mechanical calculation is performed and the debris bed collapse is triggered by some user-defined criteria on porosity, temperature, time and fraction of solid corium around the particles.
The debris fall is stopped by plates and may be stopped by grids. The compaction rate of the spherical particles can be calculated by a model or imposed by the user.

### *2.3 Melting, relocation and pool formation*

To calculate the relocation of the molten materials, a 2-dimensional model was implemented, based on a porous medium approach of the whole system: the medium is supposed to be homogeneous with specific features such as porosity (presence or not of solid components: rods, debris, grids...) and permeability (that takes into account a wall friction averaged on the mesh). This model has also been extrapolated to describe the flow along the lower head, in the bypass or the corium spreading on a plate.
Simultaneously, convective heat exchanges are evaluated so the melt temperature can be estimated as it flows. Given this temperature, the solid fraction present within the corium can be calculated and the viscosity of the flow updated.
When an important mass of molten materials relocates, a molten pool may appear. A mesh is supposed to belong to the pool when it contains no debris or solid structures and when the liquid fraction in this mesh is equal to 1.

### 2.4 *Radiation within the cavity*

The new model implemented in the ICARE2 code allows to calculate the radiative heat flux across cavities (upper and lower plena and large cavities that can appear during the degradation). The code retrieves the faces of the cavity and calculates the view factors between all the faces and the corresponding heat fluxes. The faces of the cavity may be rods, plates, shrouds, debris or pool upper surface.

### 2.5 *Fission products and residual power*

The code can deal with an initial inventory of up to 40 species of fission products (FPs) as well as a reference table for the decay heat.
The mass of each FP specie in each mesh of the system is then retrieved and the power generated in each mesh is calculated. Since the fission products are followed during all the processes involved in the core degradation, the residual power distribution changes according to the FPs relocation.
Four correlations were available in the ICARE2 code to calculate the release of fission products. With the new coupling to the ELSA V1.12 code it is now possible to compute the release in a more accurate way. However, this model is limited to pellet geometry and does not perform any release from debris and/or magma geometry.
$UO_2$ volatilization is also calculated by ELSA V1.12 but there is no feedback to ICARE2 yet.

### 2.6 *Chemical reactions and phase diagrams*

The presence of zircaloy in the particles of the debris bed can lead to oxidation reactions when steam flows through the debris bed. A model similar to the oxidation model for *Zr* claddings was implemented in this version of the code.
The dissolution of $UO_2$ particles or $ZrO_2$ particles by a liquid mixture can also be calculated. In the first version of this model, the reaction is supposed to be instantaneous.

*Computation of material properties:*
To evaluate the physical properties of a mixture, the user can choose between two options:

- In the first approach, a phase diagram is tabulated and interpolations between the tabulated points are performed. These tabulated points come from THERMODATA / IPSN calculations. The enthalpy, the heat capacity and the liquid fraction of a *U-Zr-O* mixture are obtained from the ternary phase diagram. In this case, mixing energy is taken into account.
- In the second approach, all the properties of a mixture are computed as a linear combination of the properties of each material.

### 2.7 *Description of the fluids*

Four different kinds of thermohydraulics (TH) are now available in the ICARE2 code.

- A 1D gaseous TH that deals with a mixture of steam and only one non-condensable gas through a bank of tubes enclosed within a shroud. In this case, it is possible to define a set of parallel channels without any cross-flow.
- A 2D gaseous TH, where the fluid is defined over the structured grid that covers the whole vessel.
- A 1D, 2 phase TH allowing to deal simultaneously with liquid and gaseous phase through a bank of tubes enclosed within a shroud. In this case, the gaseous phase is composed of three fields, vapor and two non-condensable gases. This modeling deals with several parallel channels without cross flow.
- It is now possible to describe a liquid water level in the reactor code and to calculate the decrease of the level. This model is monodimensional with several parallel channels. At the top and at the bottom of each channel, mass transfer is calculated to ensure equal pressure. Heat exchanges with structures and debris are calculated as well as an evaporation rate in each mesh where the temperature exceeds the saturation one. The swollen level is also determined, which gives an axial void fraction profile.

### 2.8 *Coupling with CATHARE2*

In the coupled version, ICARE2 calculates the thermal hydraulics within the core whereas CATHARE2 calculates the rest of the primary circuit.
In the example shown in the second part of this paper, an ICARE2 (stand-alone) calculation is performed so that the lower head of the reactor and some internal structures (plates, support columns) can be represented. This way, the flow of corium in the lower head and the melt of the lower structures and plates could be observed.

Such a scenario can not be modeled with the current ICARE/CATHARE coupled version, in which the lower head is a CATHARE2 element.

# 3 Application of the ICARE2 stand alone version to a PWR 900 MWe "H2" sequence

## *3.1 Brief description of the scenario*

The so called H2 sequence has been selected to test the operationality of the ICARE2 stand alone module with a complex input deck.
This transient is initiated by the total loss of feedwater. At the beginning of the scenario, the water level in the steam generator decreases due to loss of feed water and the pressure of the primary system increases because of lack of cooling. The H2 operating procedure then asks the operator to open the safety valves of the pressurizer to decrease the primary system pressure. The water in the core decreases because the emergency core cooling system (ECCS) does not operate and cannot compensate the loss of water through the safety valves. The core starts to uncover at about 3800 s from the beginning of the transient. The accumulators inject water into the core when the primary system pressure decreases to their setpoint. The lower part of the fuel rods is reflooded but will uncover again due to vaporization.

## *3.2 Boundary conditions*

To perform a severe degradation calculation some boundary conditions must be provided to the ICARE2 code. The water level evolution is simulated with a boundary condition by applying a time dependent flooding axial zone on the metallic structure. Indeed, the liquid water model is not used since it does not allow to simulate reflooding.
The steam mass flow rate is given as a boundary condition as well as the pressure in the core (these conditions were previously calculated with the CATHARE2 code and reported in the ICARE2 input deck).
The residual power within the core region is calculated directly from the fission product inventory at each time step.

## *3.3 Results and discussion*

The calculation presented here shows a satisfactory behavior of the V3mod0.4 version of the ICARE2 code.
Following the scenario, the reactor core starts to uncover 3800 seconds after the beginning of the transient. The oxidation runaway occurs at about 8000 s (see figure 2) and the first rupture of the core baffle (≈ 9000 s) leads to a flow of corium in the bypass. This corium is located above the core former plates and, since it is solidified, it can not flow through the holes of the plates and remains in place (see figure 3, at 10000 s). Note that the figures that represent the material distribution actually shows a filling rate of the meshes with debris or corium (liquid or solid). Full meshes are completely dark, empty meshes are white. These pictures do not allow to distinguish solid from liquid corium.
The core barrel melts down, at an elevation close to 4 meters, at about 12000 s and a little amount of molten material flows down to the lower head of the reactor vessel. A cavity appears in the core (≈14000 s) and rapidly gets wider as more debris melt down.
The lower core plate starts to heat up (≈15500 s) due to the downward progression of the melt front. This causes the temperature of the support structures in the lower head to raise (conduction with the plate).
In the meantime, a small molten pool appears in the core region (≈ 16500 s) and extends radially.
At 18500 s, the lower core plate is molten and corium flows down to the lower head along the lower columns (heating them up) and through the holes of the plates located in the lower head.
Due to radiative heat losses, a small crust can be observed on the top of the molten pool at 19000 s.
At that time, the upper part of the support columns has disappeared as well as part of the lower core plate. The cavity in the core region has grown wider and the molten pool has extended (see figure 4).
At 21000 s, the bottom plate and the lowest support plate are covered by corium. These plates are heated up and start to swell.
Between 22000 and 23000 s, the core barrel and shield almost completely disappear and corium keeps flowing down to the lower head, covering the three lowest plates. The corium present in the lower head is mainly solidified.
At the end of the transient (23000 s, see figure 5), the total mass of debris and corium generated during the degradation is close to 90 tons (see figure 6) and almost 350 Kg (see figure 2) of hydrogen was produced.

## 4 Conclusions

This calculation shows the description with the ICARE2 code of an accidental sequence ending at the lower head failure. The results demonstrate the capacity of the code to provide a physically grounded simulation of the whole scenario. A large debris bed was generated as well as a molten pool in the core region. We could observe molten corium flowing through the former plates in the bypass and through the core plates and arrive in the lower head.
For the future of the ICARE2 code, a 3D, two-phase treatment of the thermalhydraulics is planned through the coupling with the 3D module of CATHARE2 V1.S. A more precise description of the corium behavior in the lower head (jet fragmentation, metal-oxide separation) will be implemented. It is also foreseen to calculate additional material interactions (such as corium/structure interaction, corium oxidation, $B_4C$ oxidation) and to develop models for quenching calculation.

## 5 References

/1/ F. Fichot, F. Babik, M. Barrachin, P. Chatelard, V. Guillard, S. Mélis, M. Zabiégo, B. Lefèvre
ICARE2 V3mod0, Description of the physical models
Note technique IPSN/DRS/SEMAR 98/123, 1999.

## 6 Figures

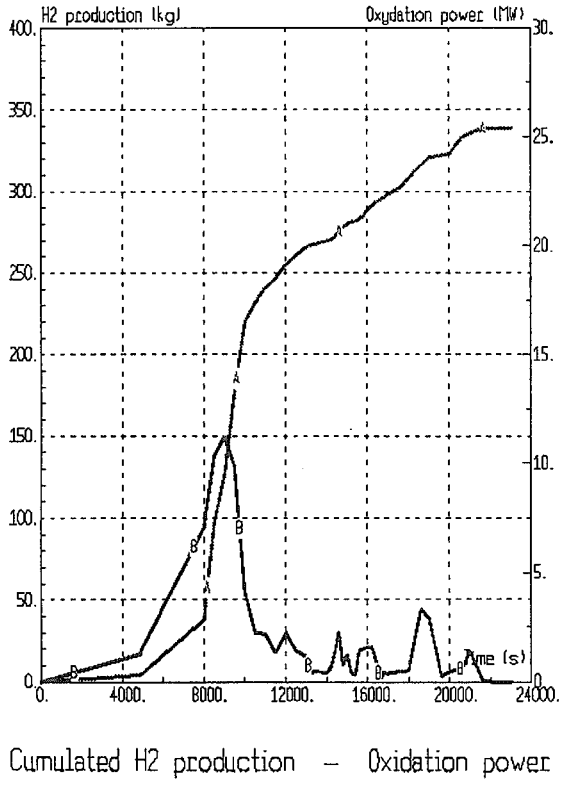



Figure 2: Cumulated H2 production (curve A), oxidation power (curve B)

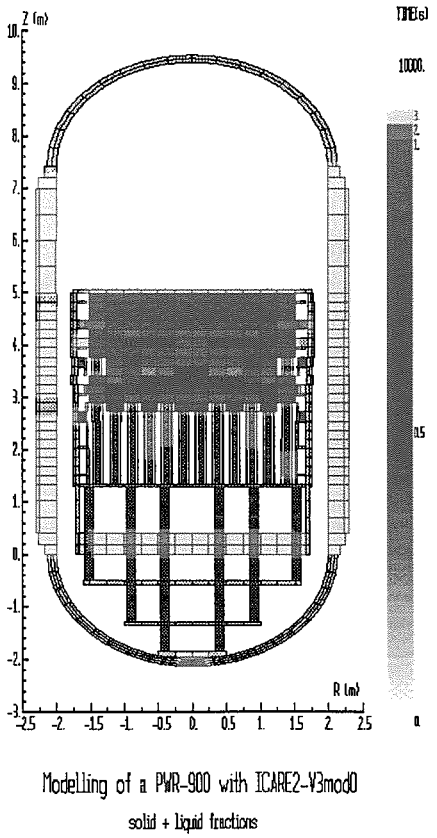



Figure 3: Material distribution at 10000 s

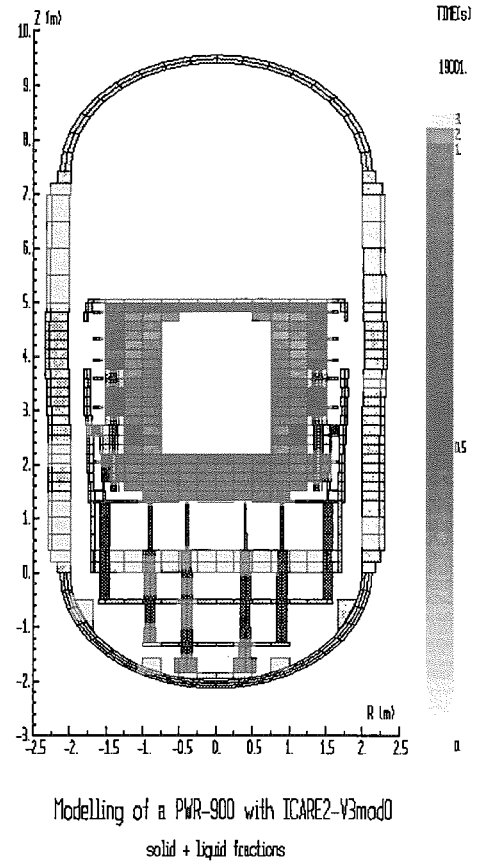



Figure 4: Material distribution at 19000 s.

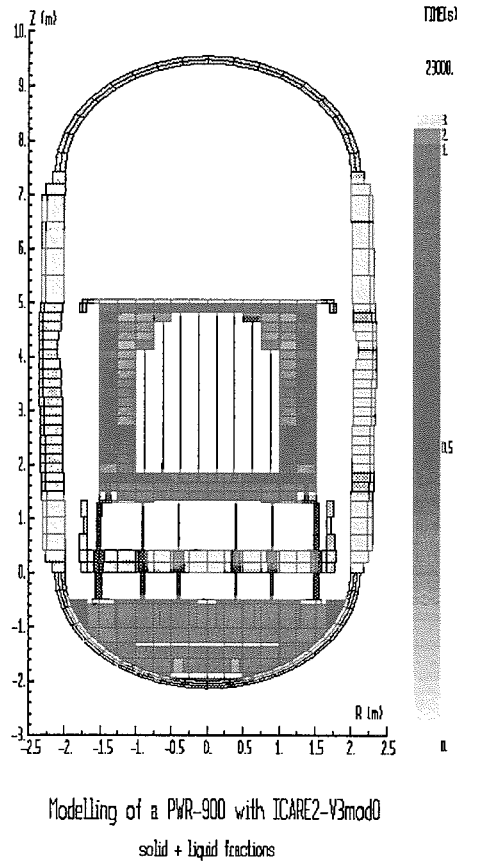



Figure 5: Material distribution at 23000 s.

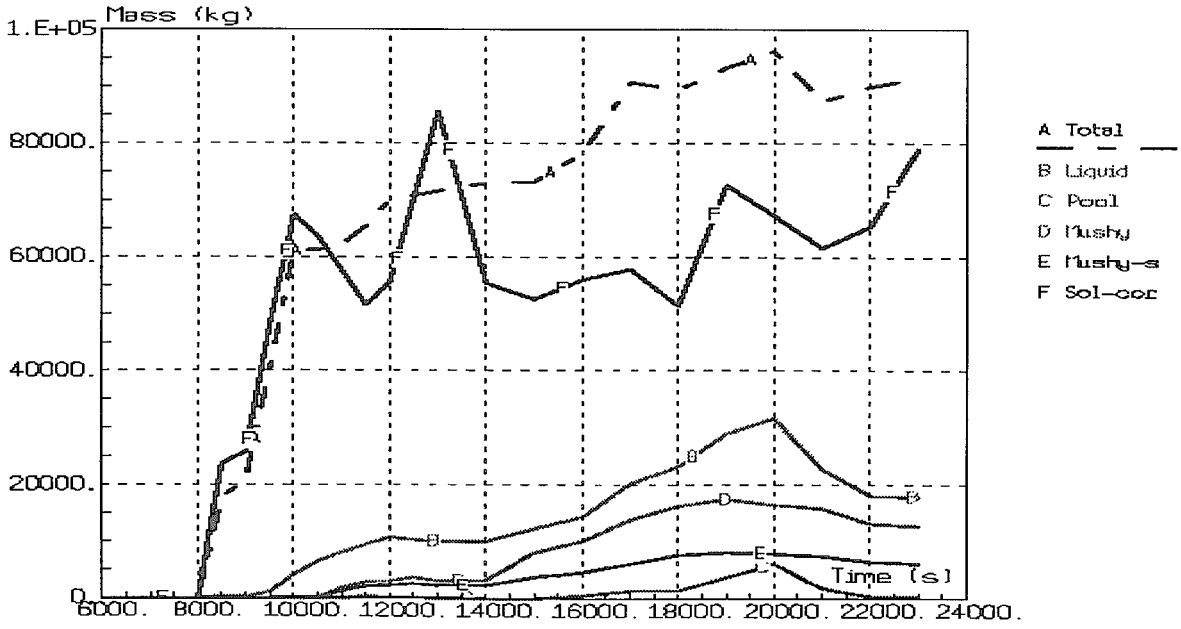



Figure 6: Mass of debris and corium evolution

This is a blank page.

# 5. Session 4

# Accident Analysis and Modeling II

Chairperson:
J. Van Dorsselaere (IPSN)
Y. Maruyama (JAERI)

This is a blank page.

JP0150096



# 5.1 TMI-2 ACCIDENT ANALYSIS WITH SCDAP/RELAP5 CODE

**Giacomino Bandini**
ERG-SIEC-SISTE
Ente per le Nuove Tecnologie, l'Energia e l'Ambiente (ENEA)
Via Martiri di Monte Sole n. 4, 40129 Bologna, Italy
Tel: +39 051 6098669, Fax: +39 051 6098279
e-mail: bandini@bologna.enea.it

## ABSTRACT

Analysis of the TMI-2 accident has been performed using the SCDAP/RELAP5/MOD3.2 system code, which is being developed by INEEL for the U.S. NRC.

The nodalization of the TMI-2 plant included a detailed modeling of the primary coolant system with the reactor pressure vessel, the two coolant loops with once-through steam generators and main coolant pumps, the pressurizer with surge-line and pilot operated relief valve. The nodalization of the secondary system was limited to the secondary side of steam generators. The boundary conditions for the calculations were fixed according to the OECD TMI-2 Analysis Exercise.

The first three phases of the accident including small break LOCA, core heat-up and melting, and core reflood were adequately modeled with SCDAP/RELAP5. Hydrogen generation and relevant primary system pressure increase were well predicted during both core heat-up and reflood.

The code predicted the formation of a large molten pool in the central region of the core and complete quenching and fragmentation of embrittled fuel rod in the upper part of the core, in reasonable agreement with the TMI-2 accident scenario. No molten core material slumping to the lower head was computed by the code in the late phase of the accident.

## Keywords

TMI-2 accident, SCDAP/RELAP5 code, core reflood, hydrogen generation, molten pool formation

## 1. INTRODUCTION

The accident that occurred at the Unit 2 of Three Mile Island (TMI-2) nuclear power plant in 1979 resulted in severe core damage with extensive oxidation and melting of the core (Ref. 1). About 20 tons of molten core material relocated in the lower plenum of the reactor pressure vessel in the late phase of the accident.

The TMI-2 accident provides a unique opportunity to enhance the current understanding of core melt progression, and compare code calculations with the progression of a real accident for code validation.

The TMI-2 accident was initiated by a sudden pressure increase in the secondary system followed by turbine and main feed-water pump trip. The subsequent increase in the primary system pressure caused the scram of the reactor. The opened pressurizer pilot operated relief valve (PORV) failed to close and started a small break loss of coolant accident.

Commonly, four phases can be distinguished in the TMI-2 accident scenario:

- the loss of coolant (0-100 min), characterized by the loss of primary water through the PORV;
- core heat-up and melting (100-174 min), characterized by core uncovery and significant fuel rod oxidation and melting;
- pump transient and core reflood (174-200 min), characterized by the restart of one of the two B-loop main coolant pumps and enhanced hydrogen generation during the quenching of the core;
- high pressure injection (HPI) actuation and molten core material relocation in the lower plenum (200-300 min).

The analysis of the TMI-2 accident has been performed within the COBE project of the 4$^{th}$ Framework European Programme on Nuclear Fission Safety (Ref. 2), for the first two phases of the accident, up to the restart of the 2B pump. The accident analysis has been successively extended to the phases 3 and 4, in order to evaluate the capability of the SCDAP/RELAP5 code to predict hydrogen generation during reflood and core melt progression in the late phase.

## 2. THE SCDAP/RELAP5 CALCULATION

The analysis of the TMI-2 accident has been performed using the SCDAP/RELAP5/MOD3.2 system code (Ref. 3), which is being developed by INEEL for the U.S. NRC. The code is designed to describe the overall reactor coolant system thermal-hydraulic response and core damage progression during a severe accident in light water reactors.

### 2.1 TMI-2 Plant Modeling

The TMI-2 primary and secondary systems were modeled according to the ICARE/CATHARE calculation performed by CEA/IPSN (Ref. 4). Axial an radial discretization of the core was defined in agreement with the INEEL TMI-2 analysis (Ref. 3), as well as axial and radial distribution of the core decay power in the representative fuel rods.

The nodalization of the TMI-2 plant is shown in Fig. 1. The nodalization for the SCDAP/RELAP5 code includes a detailed modeling of the primary coolant system with the reactor pressure vessel, the two coolant loops with once-through steam generators (OTSGs) and main coolant pumps, the pressurizer with surge-line, PORV, spray-line and valve. The nodalization of the secondary system is limited to the secondary side of OTSGs and main steam isolation valves (MSIVs).

The core is represented by five parallel flow channels with cross-flow junctions. One representative fuel rod and one control rod are modeled in each channel. The core baffle and barrel are represented by SCDAP structures. The core by-pass is modeled as an embedded flow channel between the two structures.

### 2.2 Initial and Boundary Conditions

The initial and boundary conditions for the SCDAP/RELAP5 calculation were defined according to the OECD TMI-2 Analysis Exercise (Ref. 5). The initial conditions at the instant of turbine trip in the primary and secondary systems were attained through a steady-state calculation lasting five minutes. The computed initial conditions in the primary system (pressurizer pressure and level, hot and cold leg temperatures, etc.) and the secondary system (OTSG pressures, steam temperatures, etc.), were in good agreement with the TMI-2 data.

Boundary conditions for the primary system include the letdown, HPI and make-up flow rates, and the electrical power of the pressurizer heaters. OTSG pressures and levels in the secondary system were controlled during the whole transient through MSIVs operation and water injection from the auxiliary feed-water (AFW) system, accordingly to TMI-2 data.

The SCDAP/RELAP5 analysis of the first two phases of the TMI-2 accident performed by ENEA (Ref. 2)

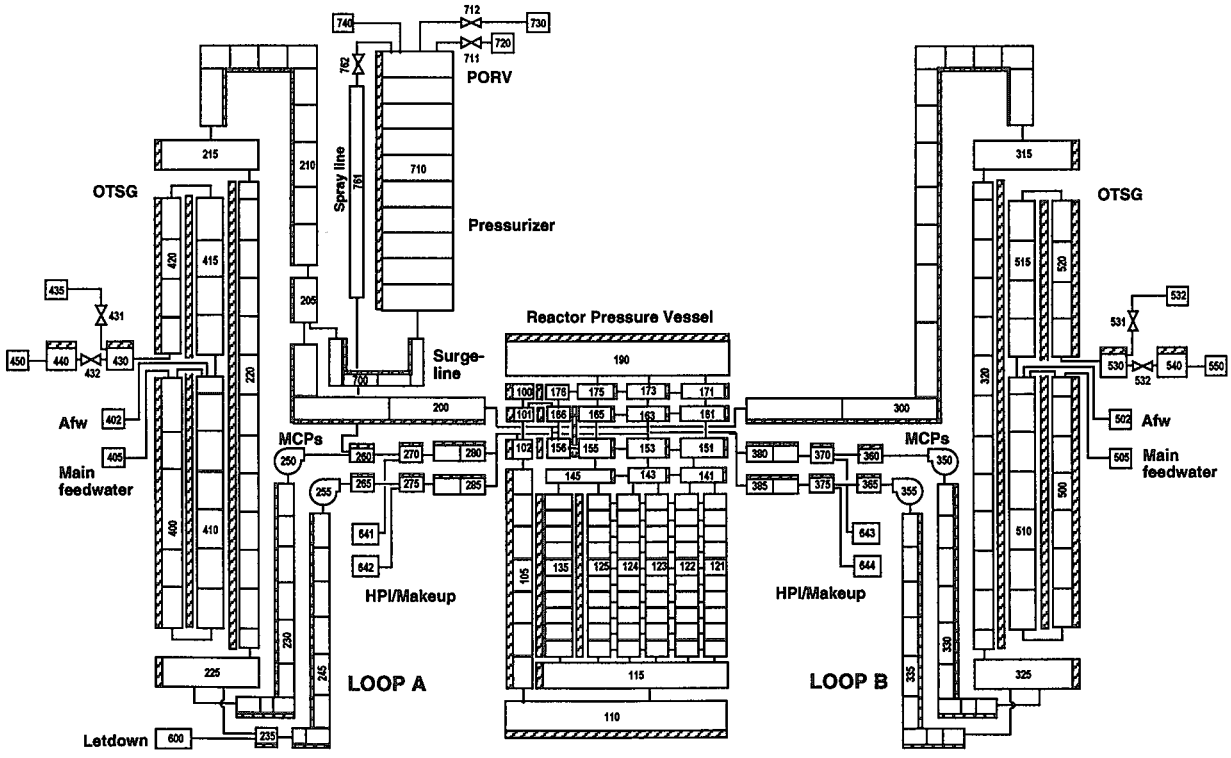



*Fig. 1 – SCDAP/RELAP5 nodalization of the TMI-2 plant*

showed that hydrogen generation and core melting at the end of phase 2 significantly depend on residual water level in the core and clad oxide shell failure criteria. In the present analysis, the make-up flow rate was reduced to 50% after 100 minutes to better evaluate the core water level during the core heat-up and melting phase, accordingly to TMI-2 data as inferred from bottom crust location in central fuel assemblies. The integrity of the fuel rod oxide shell was assumed to be lost when the clad temperature exceed 2300 K and the fraction of clad oxidation is below 60%. The double-side clad oxidation model was switched off in order to avoid too enhanced fuel rod heat-up in the upper part of the core.

## 3. RESULT ANALYSIS

The results of SCDAP/RELAP5 calculation are presented and discussed in this section. The TMI-2 accident transient has been analyzed up to 238 min, some minutes beyond the instant of estimated core material slumping in the TMI-2 accident scenario (around 225 min).

The OTSG pressures and levels (see Figs. 2 and 3) were well controlled during the whole transient calculation, according to the TMI-2 data. The dry-out of OTSGs (block valves were left closed in the AFW system prior to plant startup) was computed by the code in less than two minutes. The opening of AFW block valves by the operator at 8 min restored the capability of OTSGs to remove heat from the primary system.

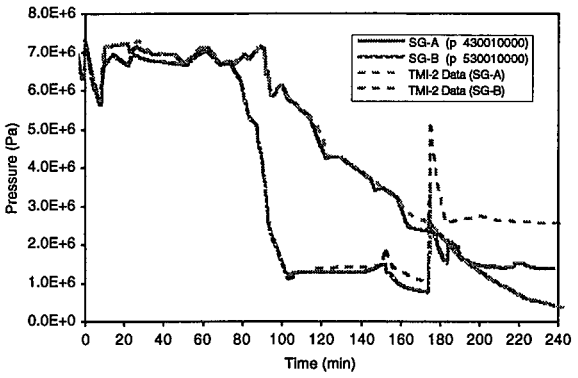



*Fig. 2 - Steam generators A and B secondary side pressure*

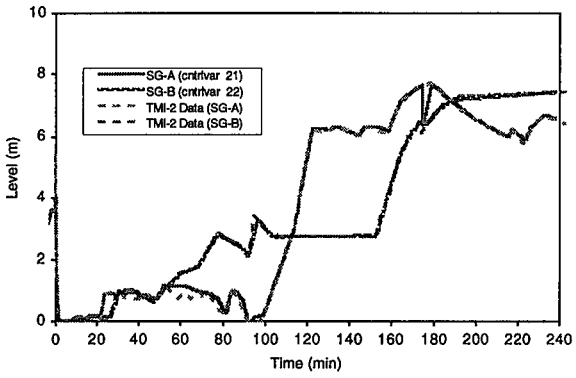



*Fig. 3 - Steam generators A and B water levels*

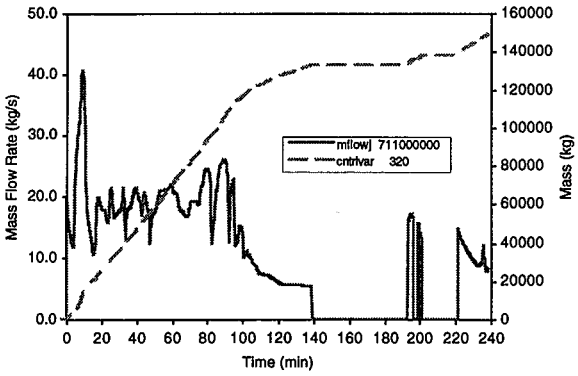



*Fig. 4 – Water mass leakage through the PORV valve*

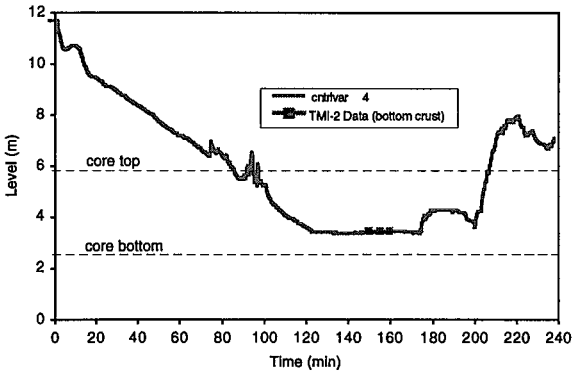



*Fig. 5 – Collapsed vessel water level*

Water leakage through the opened PORV continued up to 139 min when the operator closed the valve. By this time, more than 130 tons of water were computed to be lost from the primary system, that is more than the half of the total water inventory in the primary system. The PORV was re-opened in the late phase of the transient to reduce the primary system pressure.

The Fig. 5 shows the collapsed vessel water level computed by the code. Core uncovery started after all primary pumps were shut down (B-loop pumps at 74 min and A-loop pumps at 100 min, due to vibration) at the beginning of the phase 2. The residual water level in the core was almost constant during phase 2 and in good agreement with TMI-2 data as inferred from bottom crust location in central fuel assemblies. The level increased about 1 m after 2B-loop pump restart at 174 min. The core was completely covered by water after HPI actuation at 200 min.

Fuel rod temperature history at middle and top of the core in the different radial channels is shown in Figs. 6 and 7. Core heat-up started after core uncovery during phase 2. Significant temperature escalation was computed by the code at the core top around 140 min (Fig. 7). During this phase total control rod degradation and partial fuel rod degradation occurred in the upper part of the core. Molten material relocated in colder regions of the core near the water level. Fuel rods at core top were partially cooled during core reflood, and completely cooled after HPI actuation. No significant temperature escalation was computed at core middle (Fig. 6). Fuel rod melting temperature (about 2830 K) was exceeded in the central core region after 160 min, where a molten pool formed. In that region, fuel rod cooling was completed during reflood. Sudden temperature increase in the late phase in channels 3 and 4 is relevant to radial spreading of molten pool.

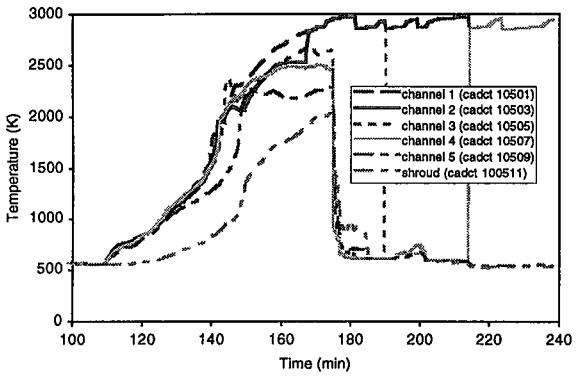



*Fig. 6 – Fuel rod temperature at core middle*

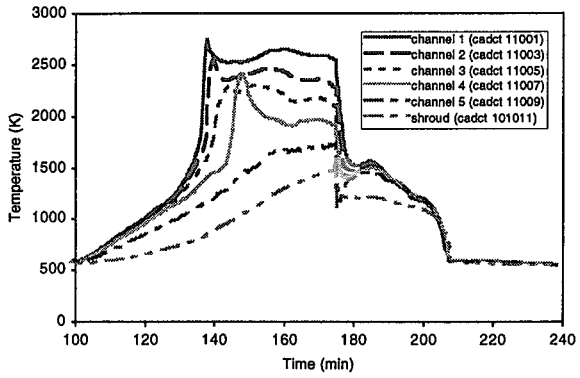



*Fig. 7 – Fuel rod temperature at core top*

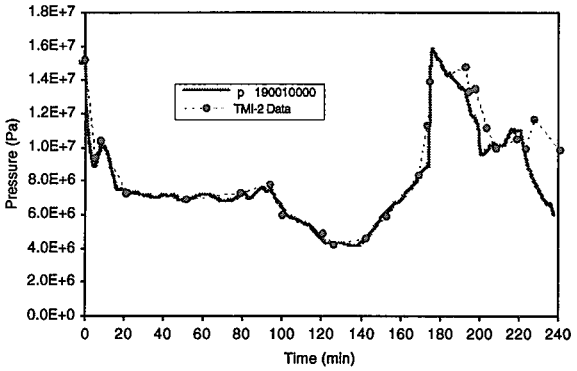



*Fig. 8 – Primary system pressure*

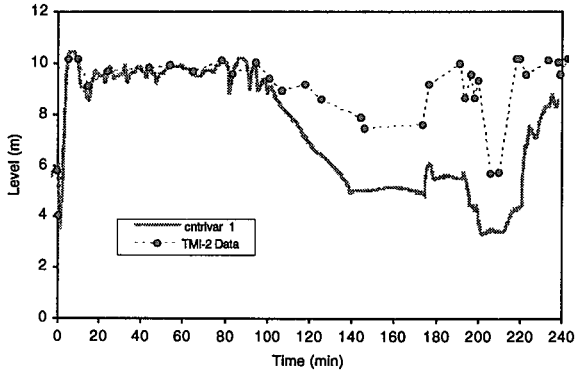



*Fig. 9 – Pressurizer level*

In Figs. 8 and 9, primary system pressure and pressurizer level are compared to TMI-2 measurements. Pressure increase during core heat-up, which was mainly governed by the hydrogen generation, was well predicted by the code (Fig. 8). Pressure increase during reflood was slightly overestimated. The computed pressure continued to decrease at 225 min (PORV was opened at 221 min) with respect to TMI-2 data as core material slumping was not predicted by the code in the late phase. The pressurizer level history was well computed by the code during the phase 1 (Fig. 9). Water hold-up in the pressurizer at the beginning of the phase 2 was not predicted by the code that computed almost constant level decrease up to PORV closure at 139 min. In the following of the transient, pressurizer level behavior was quite well captured by the code.

The hydrogen generation during core heat-up and reflood is compared to TMI-2 estimations in Fig. 10. The amount of hydrogen computed just prior to core reflood was 301 g, in good agreement with TMI-2 data. The restart of 2B pump at 174 min resulted in about 30 $m^3$ of water entering the vessel through the

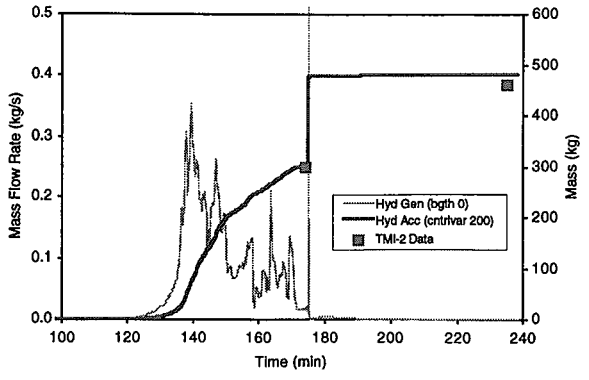



*Fig. 10 – Total core hydrogen generation*

2B-loop. The advancement of the quench water front in the core was about 4 cm/s at the beginning of the reflood phase. The SCDAP/RELAP5 code computed clad oxide shattering and renewed clad metallic surfaces exposed to oxidation during core reflood. The amount of hydrogen computed during reflood was 177 kg, about 10% overestimated with respect to TMI-2 data.

As already mentioned above, the molten pool formation started in the central upper part of the core by the end of the phase 2 (see Fig. 11). The molten pool spread downwards and radially towards the periphery of the core. The molten material in the pool at the end of the phase 2, just prior to core reflood, amounted to about 15 tons.

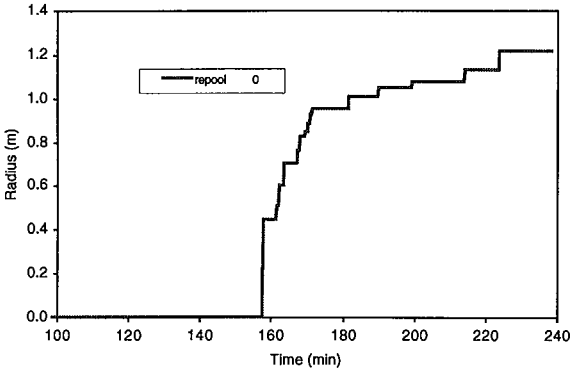



*Fig. 11 – Effective radius of in-core molten pool*

**Core Degradation Map**

I = intact fuel component
P = porous debris
L = partially liquefied porous debris
M = molten or frozen ceramic pool
V = Relap fluid volume now void of fuel

| Fuel rod component # | 1 | 3 | 5 | 7 | 9 |
|---|---|---|---|---|---|
| Axial node # | | | | | |
| 10 | P | P | P | P | I |
| 9 | P | P | P | P | P |
| 8 | V | V | L | L | P |
| 7 | V | V | V | L | P |
| 6 | V | V | V | V | P |
| 5 | xxMxx | xxMxx | xxMxx | xxMxx | P |
| 4 | xxMxx | xxMxx | xxMxx | P | P |
| 3 | P | L | P | I | I |
| 2 | I | I | I | I | I |
| 1 | I | I | I | I | I |
| Relap vol, at bottom | 121010000 | 122010000 | 123010000 | 124010000 | 125010000 |

*Fig. 12 – Conditions of in-core molten pool at 238 min*

The molten pool continued to heat-up and enlarge during phases 3 and 4, after core reflood and HPI actuation. The final state of the core at the end of the calculation is shown in Fig. 12. The code computed fragmentation of embrittled fuel rod in the upper part of the core and the formation of a large porous debris region. The molten mass in the pool at the end of the calculation was around 30 tons. Although the code did not compute collapse of upper debris bed, the weight of upper debris upon the top crust was taken into account to

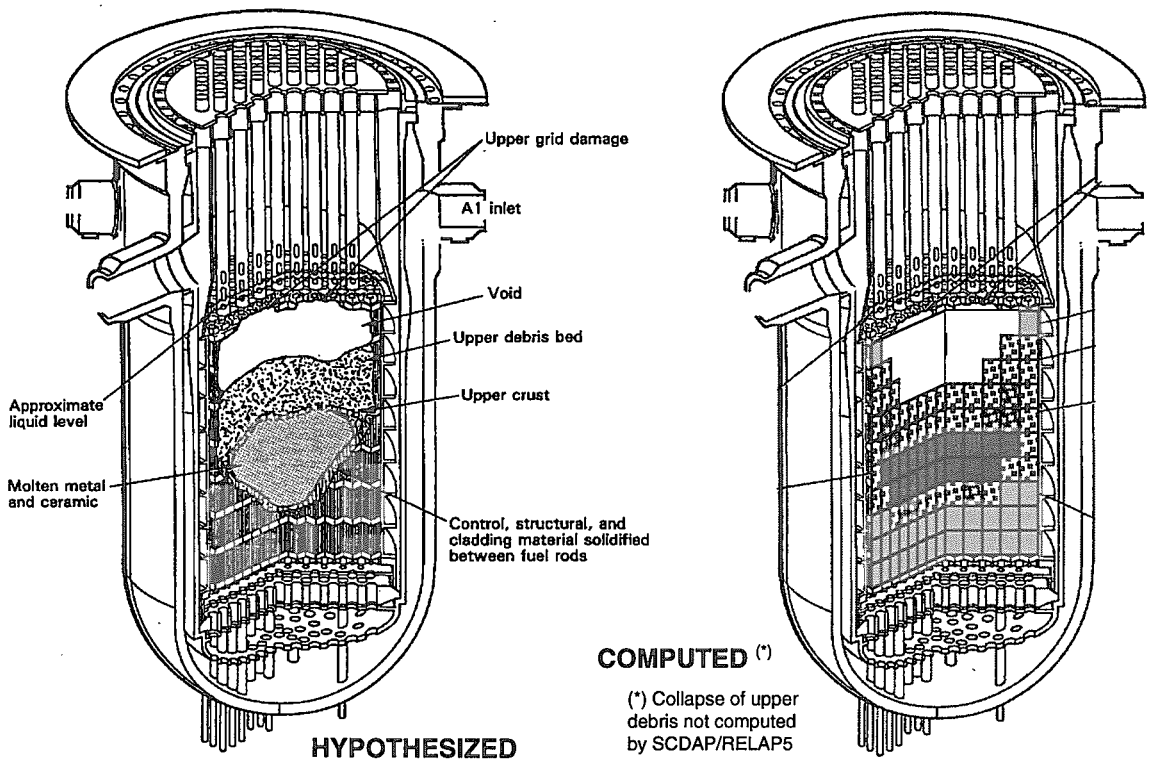



*Fig. 13 – Core Configuration at 225 min (prior to core relocation)*

verify the integrity of the molten pool crust. Thermal and mechanical loads on the molten pool crust at the end of the calculation did not result in crust failure. Therefore, core material slumping to the lower plenum was not computed by the code during the phase 4.

In Fig. 13, the hypothesized core configuration at 225 min, just prior to core relocation, is compared to the computed one (collapse of upper debris bed onto the top crust of molten pool was not computed by the code). Four main regions can be distinguished: the lower intact core zone, the central molten pool region, the upper debris bed, and the void region. The location of the molten pool was well computed by the code, but the amount of molten material seemed underestimated.

## 4. CONCLUSIONS

The analysis of the TMI-2 accident with SCDAP/RELAP5 code was performed beyond the time of estimated core slumping that occurred in the phase 4 of accident scenario.

The first three phases of the TMI-2 accident were adequately modeled with SCDAP/RELAP5. Hydrogen generation and relevant primary system pressure increase were well predicted by the code during both core heat-up and reflood. Molten pool formation and spreading was computed by the code in the late phase, as well as the fragmentation of embrittled fuel rod in the upper part of the core.

The core configuration in phase 4, just prior the estimated core slumping, was reasonably well predicted by the code. The formation of the molten pool, debris bed and void region was computed in substantial agreement with the hypothesized TMI-2 accident scenario.

Large uncertainties still exist in the evaluation of the integrity of the in-core molten pool crust. No crust failure and molten core material slumping to the lower plenum was computed by the code in the late phase.

## REFERENCES

1. Broughton, J. M., et al.: "A Scenario of the Three Mile Island Unit 2 Accident", Nuclear Technology, Vol. 87, 34-53 (1989).
2. Shepherd, I. et al.: "Investigation of Core Degradation (COBE). Final Report", INV-COBE(99)-P10, EUR 18982 EN, (1999)
3. SCDAP/RELAP5 Development Team: "SCDAP/RELAP5/MOD3.2 Code Manual, NUREG/CR-6150, INEL-96/0422, Vol. I－V, (1997)
4. Melis, S. et al.: "Analysis of the TMI-2 Accident using the ICARE/CATHARE Code", SARJ Meeting, Tokyo, (1998)
5. TMI-2 Analysis Exercise Task Group: "TMI-2 Analysis Exercise. Final Report", OECD Report, NEA/CSNI/R(91)8, (1992).

JP0150097



# 5.2 Adaptation of the Severe Accident Codes to VVER-440/V213 (V230) Reactor Unit, Their Comparison and Utilisation of the Results

Albert Bujan, Igor Kubik, Jozef Slaby
VUJE Trnava, Inc.
Okružná 5, 91864 Trnava, Slovak Republic

Tel. +421 805 599 1288 (1423)
Fax +421 805 599 1169
E-mail : bujan@vuje.sk

**ABSTRACT**

This paper presents an application and comparison of the computer codes, devoted for severe accident analysis of PWR up to source term evaluation, to a VVER-440/V213 and V230 NPP. The basic results of selected sequences are described and some physical parameters predicted by different codes are compared. The comparison is deliberated mainly on the timing of main primary circuit events and fission products behaviour up to source term evaluation. Utilisation of the results of the severe accident analysis for development of the emergency procedures for rapid assessment of barriers status and source term category is shortly described, too.

## 1. INTRODUCTION

The systematic study of severe accident phenomena and computer analysis by utilisation of the codes started in VUJE (Nuclear Power Plant Research Institute, Inc.) Trnava in the year 1988 when the mainframe version of STCP [2] (Source Term Code Package) was installed. The modified version STCP-M[1] (which has been able to take into account specific features of VVER) was developed and verified in the frame of IAEA Regional Projects RER/9/004 during the time period of 1988 - 1992 years. The utilisation of the STCP-M was finished at the end of the year 1996, when the codes MELCOR1.8.3 [3] and ESCADREmod1.0 [4] were installed and basic computer models for reactor unit with VVER-440/V213 (3rd and 4th unit of NPP Bohunice and 1st unit of NPP Mochovce) have been developed and validated.

The computer code MAAP4/VVER [5] has been adopted and computer model of reactor unit with WWER-440/V213 (3rd unit of Bohunice NPP) has been validated in the framework of project Phare 4.2.7.a – "VVER-440/V213 Beyond Design Basis Accident and Accident Management", which was solved during the years 1996-98. The computer model for V230 reactor unit (1st and 2nd unit of NPP Bohunice) after gradual reconstruction has been developed and verified since the year 1998.

The last version of the ESCADRE [6] code system (Mod 1.2) has been adopted in the VUJE Trnava in the year 1998 in the framework of bilateral contract with IPSN (Institut de Protection et de Surete Nucleaire) which was devoted to perform work on the ability of ESCADRE mod1.2 software to simulate severe accident sequences on VVER-440/V213 type of reactor.

The main goals of this paper have been as follows:

- to show the application of different codes for severe accident analysis on the reactor unit with VVER-440/V213 (V230),
- comparison of important physical parameters predicted by these codes and to explain of the differences,
- practical utilisation of the results of the codes application.

## 2. VVER DESIGN SPECIFIC FEATURES

In the core , the most important differences from western PWR (from a severe accident viewpoint), are as follows :

- Canned fuel assemblies with the shrouds from Zr-alloy,

- Moveable fuel/absorber assemblies (the number is 37) are of tandem construction (after reactor shutdown, the control-absorption parts made from borated steel are inserted into the core and fuel parts are pushed out into the reactor vessel (RV) lower plenum). Due to this fact ≈11% of decay heat is localised in the RV lower plenum and not inside the core.

Another specific features :

- Horizontal steam generators (SGs).
- Confinement system (model **V213**) which consists from interconnected compartments with bubbler/condenser (B/C) tower. B/T tower is connected to the SG boxes by tunnel with large flow area and consists of vertically mounted water trays (12 floors) connected with 4 airlocks by check valves.

The older model **V230** has check (blow off) valves at the boundary of hermetic zone instead of B/C tower and the circulation condensers have been installed in the emergency water storage tank (EWST) after gradual reconstruction (1st and 2nd unit of Bohunice NPP) to reduce pressure spike especially in the cases of medium and large break LOCA (Loss of Coolant Accident).

## 3. SHORT DESCRIPTION OF THE MODELS

Before explanation of the discrepancies in the results predicted by compared codes, the main differences in the models can be summarized as follows :

**MAAP4/VVER** – integrated code system with fixed reactor coolant system (RCS) nodalisation scheme (15 volumes in the case of VVER model), generalised (user – specified) noding of containment and with availability to model all VVER specific design features. RCS thermalhydraulic (t-h) uses two – fluid model based on the concept that liquid and vapour are separated by swell level. Advanced core degradation model which include simulation of molten pool formation and behaviour (i.e. heat/mass transfer between adjacent molten nodes, breach of crust around the pool is based on time – at – temperature and stress calculation) and with the possibility to calculate lateral corium slump to RV lower plenum before core support plate failure. RV bottom head failure calculation is based on the Larson-Miller material creep model. Model of molten corium – concrete interaction (MCCI) in the reactor cavity is based on the assumption that oxides and metals are homogeneously mixed.

**MELCOR 1.8.3** – integrated code system with availability to model all VVER specific design features. In comparison with MAAP4, the RCS nodalisation is not fixed and can be more detailed. Molten pool formation and lateral corium slump are not modeled. Core support plate failure is predicted when surface temperature reaches the value defined by the user (the same is valid for RV lower head failure). Model of MCCI is based on the assumption that oxides and metals are separated (3 layers : heavy and light oxides and metals).

**ESCADRE mod1.2** – integrated (through "macro time step") system of codes with nodalisation scheme of RCS and confinement defined by user and with the simulation of molten pool formation. There are the following basic limitations in comparison with MAAP4 (MELCOR) :

- missing the two – phase flow t-h in the RCS (i.e. the beginning of the sequence up to the time which correspond, as a rule, to the start of core uncovery, has to be analysed by using another code),
- simple model of the corium behaviour in RV lower plenum which does not take into account interaction with water (i.e. the time margin from start of corium slump to vessel failure is very short),
- it is not possible to model fuel followers in RV lower plenum after shutdown (VVER feature).

Model of MCCI supposes that oxides and metals are either separated (2 layers : oxides and metals) or homogeneously mixed (user choice).

**STCP-M** – the oldest system of codes for severe accident analysis up to source term evaluation, which has a lot of limitations, e.g. :

- very simple - fixed model of primary (1 volume) and secondary (1 volume) circuit,
- simple model of core degradation without molten pool formation,
- fission product (FPs) trasport calculated after thermohydraulic analysis of RCS and confinement e.t.c.

## 4. COMPARISON OF THE CODES ON SELECTED SCENARIA

The following basic three severe accident sequences [7, 8, 9] for VVER-440/V213 reactor unit have been selected for comparison of the codes :

- The medium break LOCA from cold leg (equivalent inner diameter $d_e$=100mm) combined with station blackout, i.e. neither high and low emergency core cooling system (ECCS) nor hermetic boxes spray system (SS) has been available (marked as **S1B** in this paper).
- The same scenario as previous one, but without station blackout and with availability of one train (from 3 independent) of spray system (marked as **S1D**).
- "Transient blackout" sequence characterized by high pressure in the reactor coolant system (RCS) during in-vessel phase (marked as **TB**).

Common basic assumptions for all codes have been as follows :

- from passive ECCS, only the function of 2 hydroaccumulators (HA) from 4 has been supposed,
- axial core thermal power distribution corresponds to burnup fuel (end of 4$^{th}$ cycle) with the maximum in the upper part of core,
- 2-loops model of RCS (i.e. 1 broken loop + 5 unbroken loop) excluding STCP-M (1-volume model),
- confinement nodalisation scheme : 12 – control volumes in MELCOR1.8.3, 14 – in MAAP4/VVER, 3 – in STCP-M and 4 – volumes in ESCADRE mod1.2,
- confinement leak rate through permanent untightness has been taken into account on the level of 16%vol./day under design overpressure (0.15 MPa) with direct leak to the environment,
- the limestone concrete composition (> 30% of $CaCO_3$ and $Ca(OH)_2$ ) of the reactor cavity has been supposed.

**Note 1** : The initial conditions at the "start of core uncovery " have been defined for ESCADRE code system according to STCP-M prediction in the cases of S1B and S1D sequences and according to MAAP4 prediction in the case of TB sequence.

**S1B sequence**

The timing of main (key) primary circuit events is given in Table 4.1.

During the initial blowdown phase the faster start of core uncovery predicted by MAAP4 in comparison with MELCOR is mainly due to relatively simplified RCS t-h model used in MAAP4, which influences through primary pressure calculation the injection of water from HAs. Prediction of the simplest model used in STCP-M is between MAAP4 and MELCOR results.

Despite of the differences in the models the MAAP4 and MELCOR predictions agree to a reasonable extent during the later phase – core heat-up and relocation. Sequence progression is according to MAAP4 slightly faster in comparison with MELCOR. The main reasons are the modeling of molten pool formation in MAAP4 code and also the shift from blowdown phase. Slightly higher in-vessel hydrogen production according to MELCOR code corresponds to longer time up to RV lower head failure. The STCP-M results are in the extent of MAAP4 and MELCOR predictions besides cumulative production of hydrogen, which is underestimates due to very simple core degradation and oxidation models.

According to ESCADRE, the accident progression is slower in comparison with all other codes. The main reason is lesser decay heat (in the range of 15-20%) calculated by the code (Note : At the time when the calculation was performed only approximative inventory of isotopes in the core was used for decay heat calculation, but not from viewpoint of source term calculation).

**Note 2** : In the case of S1D sequence, the timing of key in-vessel events and hydrogen generation differ from S1B sequence in the range of 5 – 10% for individual codes.

Table 4.1 Timing of main events in the reactor coolant system – **S1B** sequence

| EVENT | **STCP-M** [min] | **ESCADRE--Mod1.2** , [min] | **MAAP4/VVER** [min] | **MELCOR1.8.3** [min] |
|---|---|---|---|---|
| Start of core uncovery [1)] | 35,5 | 35,5 | 30,9 | 39,2 |
| Start of FP release from fuel | 54,0 | 48,0 | 39,8 | 71,6 |
| Start of U-O-Zr melting [2)] | 58,7 | 59,3 | 49,5 | 81,2 |
| Melting pool formation | No model | 134,9 | ≈80,0 | No model |
| $1^{st}$ lateral corium slump into → →the reactor vessel lower head | No model | 247,5 | 131,5 | No model |
| Core support plate failure | 141,3 | Not predicted | Not predicted | 153,5 |
| Lower head vessel failure | 260,0 | 248,1 | 244,7 | 285,4 |
| $H_2$ mass produced (in-vessel) | 222,8 kg | 291,3 kg | 316,9 kg | 325,0 kg |

There are no significant differences in confinement pressure and temperature response up to RV lower head failure. After this event, the confinement long term pressurization is influenced mainly by the amount of non-condensible gases which are produced during MCCI. The comparison of produced amount for S1B sequence (differences for S1D sequence are in the range of ± 15%) and of final total pressures inside the SG compartments at time of 120000.0 s from accident start is given in the Table 4.2.

Table 4.2 Non-condensable gases generation and total pressure in SG compartments (**S1B** sequence)

| | **STCP-M** | **ESCADREmod1.2** | **MAAP4/VVER** | **MELCOR1.8.3** |
|---|---|---|---|---|
| Generation of **$H_2$** , [kmol] | 447,0 | 280,0 | 924,0 | 286,0 |
| Generation of **CO** , [kmol] | 245,0 | 171,0 | 682,0 | 518,0 |
| Generation of **$CO_2$** , [kmol] | 134,0 | 95,0 | 14,0 | 6,0 |
| Total amount , [kmol] | **826,0** | **546,0** | **1620,0** | **810,0** |
| Total pressure – **S1B**, [MPa] | 0,196 | 0,122 | 0,209 | 0,179 |
| Total pressure – **S1D**, [MPa] | 0,138 | 0,110 | 0,164 | 0,131 |

The main reasons of discrepancies in the results are different models which are used by individual codes and also differences in corium composition (mass of free metals at the start of MCCI). The most intensive MCCI is predicted by MAAP4 code, the least one in the case of ESCADRE (the least decay heat and also the mass of free metals in corium at the start of MCCI). The cumulative production of gases corresponds to final values of total pressures predicted by individual codes.

**TB sequence**

TB sequence calculation results of the four codes deviate more than the LOCA results.

During the initial phase SGs cool the primary system providing the heat sink. Heat transfer to SGs is sustained until their inventory decreases below the tubing level, then the heat transfer quenches. Sooner SG depletion in the MELCOR prediction is also caused by ≈15% lesser initial water inventory in

comparison with MAAP4 calculation and the difference in start of core uncovery is mainly a consequence of the shift in SGs depletion. Results of STCP-M are strongly influenced by very simple one volume model of RCS and secondary heat sink.

Discrepancies in timing for predictions of fuel melting, core relocation to the lower head and RV lower head failure are twofold - on one hand especially the accumulated differences during the previous phases, on the other hand also the differences of the models as melting pool formation and RV lower head creep failure model in the MAAP4. Detailed analysis of MELCOR result regarding the substantially later RV lower head failure prediction (based on temperature criterion – 1700 K) showed that the reason is pushing part of water from circulation loops (seals) to lower head after core support plate failure and also intensive heat transfer from core debris by convection to the steam. This is also the main reason of higher in-vessel hydrogen production in the case of MELCOR.

According to ESCADRE, the accident progression is slower after start of fuel melting in comparison with MAAP4 prediction. The main reason is lesser decay heat as has been already mentioned.

Due to a simple RCS t-h model in STCP-M, the start of core uncovery is predicted substantially later in comparison with MELCOR and MAAP4 codes and this shift delais all other key events. $H_2$ in-vessel production is underestimated due to simple core degradation and oxidation models.

Table 4.3 Timing of main events in the reactor coolant system – **TB** sequence

| EVENT | **STCP-M** [min] | **ESCADRE--Mod1.2** , [min] | **MAAP4/VVER** [min] | **MELCOR1.8.3** [min] |
|---|---|---|---|---|
| SGs dry-out | 305,7 | - | 396,0 | 268,3 |
| Start of core uncovery | 562,0 | 454,2 | 454,2 | 387,5 |
| Start of FP release from fuel | 591,1 | 465,6 | 473,5 | 401,3 |
| Start of U-O-Zr melting | 603,2 | 493,0 | 536,6 | 423,7 |
| Melting pool formation | No model | 605,5 | ≈570,0 | No model |
| 1st lateral corium slump into → → reactor vessel lower head | No model | 677,5 | 600,5 | No model |
| Core support plate failure | 706,3 | Not predicted | Not predicted | 514,9 |
| Lower head vessel failure | 725,2 | 677,9 | 625,2 | 1526,0 |
| $H_2$ mass produced (in-vessel) | 211,9 kg | 317,6 kg | 344,6 kg | 524,0 kg |

The comparison of produced amounts of non-condensible gases during MCCI and final total pressures in the SG compartments at time of 200000.0 s from accident start is given in the Table 4.4.

Table 4.4 Non-condensable gases generation and total pressure in SG compartments (TB sequence)

| | **STCP-M** | **ESCADREmod1.2** | **MAAP4/VVER** | **MELCOR1.8.3** |
|---|---|---|---|---|
| Generation of **$H_2$** , [kmol] | 455,0 | 347,0 | 990,0 | 243,0 |
| Generation of **CO** , [kmol] | 254,0 | 167,0 | 803,0 | 451,0 |
| Generation of **$CO_2$** , [kmol] | 103,0 | 242,0 | 20,0 | 5,0 |
| Total amount , [kmol] | **812,0** | **756,0** | **1813,0** | **699,0** |
| Total pressure , [MPa] | 0,197 | 0,123 | 0,192 | 0,207 |

Cumulative leakages of fission products to the environment (source terms - ST), expressed in the relation to MAAP4 predictions, are presented in the Tables 4.5, 4.6 and 4.7. It should be stressed that there is a lot of factors (e.g. RCS and confinement t-h response, models of FP release from fuel and behaviour in the RCS and containment volumes e.t.c.) which influence source term. In spite of this fact the agreement in ST prediction is relatively good (especially for MAAP4 and MELCOR) except the following discrepances, where differences are higher than one order of magnitude :

- **MAAP4** overestimates leakage of **Mo** in comparison with **MELCOR** in spite of similar release from fuel in the case of S1D and TB sequences due to lesser efficiency of SS (S1D) and lesser retention in pressurizer (TB). The same effects cause slightly higher release of **Sr** according to MAAP4, inspite of the release from fuel is for all scenaria more than ≈10 times lesser in comparison with MELCOR. The situation is opposite for S1B (ST is ≈7 times higher according to MELCOR).

- Overestimation of the leakage of all FP aerosol groups in the case of **ESCADRE** in comparison with MAAP4 (MELCOR) for TB sequence is mainly due to **no** retention in RCS (Note : it was not possible to use SOPHAEROS code for calculation of FPs retention in the RCS in the case of release through pressurizer RV at the time when analysis was performed).

Table 4.5 Comparison of the source terms – **S1B** sequence

| Fission product group | STCP-M | ESCADRE mod1.2 | MAAP4/VVER | MELCOR1.8.3 |
|---|---|---|---|---|
| **Noble gases (Xe, Kr)** | 0.93 | 0.48 | 1.0 | 0.98 |
| **I (CsI) , Cs (CsOH)** | 1.47 | 0.69 | 1.0 | 0.96 |
| **Te** | 0.48 | 0.13 | 1.0 | 0.97 |
| **Sr** | **48.1** | 2.89 | 1.0 | 7.28 |
| **Mo** | **0.0002** | 0.17 | 1.0 | 0.25 |
| **La** | 3.79 | 1.13 | 1.0 | 1.01 |
| **Ce** | 0.76 | 0.25 | 1.0 | 3.59 |
| **Ba** | 2.39 | 0.98 | 1.0 | 1.09 |

Table 4.6 Comparison of the source terms – **S1D** sequence

| Fission product group | STCP-M | ESCADRE mod1.2 | MAAP4/VVER | MELCOR1.8.3 |
|---|---|---|---|---|
| **Noble gases (Xe, Kr)** | 0.83 | 0.41 | 1.0 | 0.88 |
| **I (CsI) , Cs (CsOH)** | 0.77 | 2.32 | 1.0 | 0.35 |
| **Te** | 0.26 | 0.34 | 1.0 | 0.40 |
| **Sr** | 3.18 | 9.70 | 1.0 | 0.94 |
| **Mo** | **0.0004** | 0.78 | 1.0 | **0.03** |
| **La** | 0.22 | 5.50 | 1.0 | 0.10 |
| **Ce** | 0.05 | 0.95 | 1.0 | 0.37 |
| **Ba** | 0.59 | 4.05 | 1.0 | 0.15 |

Table 4.7 Comparison of the source terms – **TB** sequence

| Fission product group | STCP-M | ESCADRE mod1.2 | MAAP4/VVER | MELCOR1.8.3 |
|---|---|---|---|---|
| **Noble gases (Xe, Kr)** | 0.65 | 0.76 | 1.0 | 0.78 |
| **I (CsI) , Cs (CsOH)** | 0.38 | **14.3** | 1.0 | 1.18 |
| **Te** | 4.16 | **140.0** | 1.0 | 5.46 |
| **Sr** | **173.0** | **44.2** | 1.0 | 0.59 |
| **Mo** | **0.0006** | **26.0** | 1.0 | **0.031** |
| **La** | **48.2** | **86.1** | 1.0 | 0.37 |
| **Ce** | 4.47 | **22.0** | 1.0 | 0.96 |
| **Ba** | **59.6** | **145.0** | 1.0 | 0.42 |

• Leakage of **Mo** is strongly underestimates according to **STCP-M** (RU groupe) due to the small release from fuel (2 – 3 order lesser in comparison with all codes).

## 5. CONCLUSION

The codes MAAP4/VVER, MELCOR1.8.3 and ESCADREmod1.2 are compared on the analyses of three basic scenaria for VVER-440 /V213 reactor unit up to source term evaluation. For illustration, the results are also compared with predictions of the oldest code system STCP-M. Since uncertainties in the fenomenology remain, it is to be expected that different codes will not predict identical accident progression. It can be concluded that reasonable agreement between codes MAAP4 and MELCOR has generally been demonstrated and the reasons for specific differences observed between these codes and also in relation to ESCADRE have been understood.

It should be noted that more than 100 severe accident sequences have been analysed for reactor units V213 and V230 during last 5 – 6 years mainly by using STCP-M and MAAP4/VVER codes (partly also by using of MELCOR and ESCADRE codes) in VUJE Trnava. The results have been (or are being) utilised as follows :

• Emergency planning and preparation of the drills.

• Creation and renewing of knowledge database for emergency procedures (EPs) which have been developed for use by the Emergency Response Centre of the Slovak Nuclear Regulatory Authority [10]. These EPs are devoted for rapid assessment of barier status and source term based on plant data and are used also in the 1st version of the expert system ESPRO PRTY 1.0 [11] developed in VUJE Trnava.

• Supporting analyses for PSA Level-2 of Bohunice NPP.

• Preliminary supporting analyses for Severe Accident Management Guidelines (SAMGs) development or modification of Westinghouse SAMGs (project is under preparation).

Regarding the near future, the adaptation of the ASTEC_V02 code (developed in co-operation IPSN/GRS) to VVER-440/V213 reactor unit has been already started in co-operation with IPSN and also the version of MELCOR 1.8.4 code will be probably adapted during the next year.

## References

1. *Gieseke J.A. et al.* : STCP - User's Guide. NUREG/CR 4587, BMI-2138, USA, Jul 1986.
2. *Z.Techy, J.Dienstbier et al.,* MARCH3-M, TRAP-MELT3M, NAUAM, THCCAM – Modified versions of the codes for VVER-440 type reactors. Interim report of IAEA Project RER/9/004, Moscow, June 1990.
3. MELCOR Computer Code Manuals, Reference manual NUREG/CR 6119, SAND93-2185, Sept. 1994.
4. *D.Tarabelli et al.* : THE ESCADRE CODE SYSTEM, Version mod1.0, SHORT DESCRIPTION OF COUPLINGS BETWEEN CODES. NOTE TECHNIQUE SEMAR 95/55.
5. *M. Van haesendonck, R.Prior,* MAAP4/VVER USER GUIDE. Westinghouse Energy System Europe S.A.. , WENX 93/25, Revision 1, March 1996.
6. *J.P. Van Dorsselaere :* ESCADRE mod1.2, General presentation. NOTE TECHNIQUE SEMAR 98/98.
7. *I. Kubik et al.* : The modelling of fission products transport in the code MELCOR 1.8.3. Report VUJE No. 242/98, October 1998, (in Slovak).
8. *A. Bujan* : The analysis S1B, S1D and TB sequences by using MAAP4/VVER code. Interim report VUJE – ZOV 710/0897/001, August 1997.
9. *A. Bujan* : Recalculation of the sequences S1B, S1D and TB by using ESCADRE mod1.2 code. Interim report VUJE – ZOV 710/1099/01, October 1999.
10. *Bujan A. et al. :* The Estimation of Suorce Term and Introduction of Countermeasures Based on Dominant Conditions of Accident Progression. Radiation Protection Dosimetry, Vol. 73, (1997).
11. *Duranova T. et al.* : ESPRO – An Expert System for the Evaluation of Source Term and Determination and Suggestion of Protective Measures. ANS 7th Topical Meeting on Emergency Preparadness and Response. Santa Fe, New Mexico, USA, 14-17 September 1999.

JP0150098



# 5.3 Comparison of MAAP4.03 with RELAP/SCDAPSIM/MOD3.2

T. Kohriyama(1), M. Ohtani(2), A. Ezzidi(3) and H. Morota(4)

(1)(2) Technical Support Project, Institute of Nuclear Technology,
Institute of Nuclear Safety System, Incorporated
Tel: 0770-37-9112, Fax: 0770-37-2009
E-mail: (1) kohriyama@inss.co.jp, (2) ohtani@inss.co.jp
(3)(4) Computer Software Development Co., Ltd.
Tel: (3) 03-3225-6554, (4) 03-3225-6437, Fax: 03-3225-7145
E-mail: (3) alex@csd.co.jp, (4) morota@csd.co.jp

Abstract

The MAAP4.03 code has been widely used for analyses of severe accident phenomena. It is, however, a system level code applying simpler models and could show phenomenological uncertainties. In order to support MAAP4.03 by a more detailed mechanistic code such as RELAP/SCDAPSIM/MOD3.2, code-to-code comparisons are performed. For a typical 4 loop PWR, analyses of two severe accident sequences were executed. Both codes predicted similar tendencies until the beginning of core melt. MAAP4.03 showed earlier slumping of molten core to a lower head of a reactor pressure vessel than RELAP/SCDAPSIM/MOD3.2. MAAP4.03 considers only axial flows of molten core and crusts suddenly breach by Creep Rupture. RELAP/SCDAPSIM/MOD3.2 treats axial and radial spreads by repeated cycles of melting, flowing and freezing. Bottom crusts can be supported by intact fuel rods. By these more realistic RELAP/SCDAPSIM/MOD3.2 models, MAAP4.03 could be supported maintaining conservatism.

Keywords: severe accident, MAAP, RELAP/SCDAPSIM, comparison, melt, molten core, slump

## 1. Introduction

The MAAP4.03 code has been widely used for analyses of severe accident phenomena. For actual plants, the code can evaluate accident management strategies and analyze accidents concerning PSA Level 2. The MAAP4.03 code is, however, a system level code applying simpler models and the possibility exists that it will show phenomenological

uncertainties, although they can be treated by sensitivity studies. In order to support the system level MAAP4.03 code by a more detailed mechanistic code such as RELAP/SCDAPSIM/MOD3.2, code-to-code comparisons are performed.

The RELAP/SCDAPSIM/MOD3.2 code utilizes the US NRC models of SCDAP/RELAP5/MOD3.2 [1] and has been developed under the international cooperative program SDTP (SCDAP Development and Training Program) focusing on the development of more reliable and user friendly tools. Because the requirements for the accuracy of accident management and PSA Level 2 evaluations have been increased, Institute of Nuclear Safety System, Incorporated (INSS) decided to join SDTP for the practical use and development of RELAP/SCDAPSIM/MOD3.2.

## 2. Model Comparisons

Nodalization schemes for the both codes are shown in Figure 1. In MAAP4.03 fixed 13 nodes are applied for the PWR primary system and momentum equations are replaced by simple calculations. The secondary system is treated as the boundary conditions for the MAAP4.03 calculations. In RELAP/SCDAPSIM/MOD3.2 it is more flexible and detailed because the code utilizes the models of RELAP5/MOD3.2 [2]. Momentum equations are resolved and the nodalization includes the secondary system. The reactor pressure vessel (RPV) is also precisely modeled as shown in Figure 2.

The concept of core damage progression is illustrated in Figure 3. In MAAP4.03 it seems to be macroscopic, while the physical process of the molten core spread model in RELAP/SCDAPSIM/MOD3.2 is microscopic and more dynamic.

## 3. Analytical Conditions

Analyses of two severe accident sequences for a typical 4 loop PWR were executed. Focusing on In-Vessel Cooling Effects, the reactor pressure vessel outer surface assumed to be adiabatic. The first case is an ADC (Large Break LOCA + ECCS Failure + Containment Spray Failure) sequence. The recovery of High Pressure Injection was assumed 1.5 hours after the slump of core materials to the RPV lower head. In this sequence the primary pressure decreases rapidly. Released mass and energy has an impact on the integrity of a containment vessel. The second case is a TML (Loss of Main Feed Water + Auxiliary Feed Water Failure + ECCS Failure) sequence. The intentional depressurization of the primary system was assumed by opening Pressurizer Power Operated Relief Valves 10 minutes after the beginning of core melt. The recovery of HPI

was also assumed 10 minutes after the slump of core materials to the RPV lower head. In this case the primary pressure is maintained relatively high during early phase of the accident. It has an impact on the integrity of a RPV.

4. Comparisons of Analytical Results

The major events of the core damage progression for ADC and TML sequences are compared between MAAP4.03 and RELAP/SCDAPSIM/MOD3.2 in Table 1. The events are Start of core uncovery, Accumulator injection, Total core uncovered, Beginning of core melt, Slump of molten core material to RPV lower head, and RPV failure. This comparison shows that both codes predicted similar tendencies for accident progression until beginning of core melt. However, MAAP4.03 predicted early slump of core materials to the RPV lower head than RELAP/SCDAPSIM/MOD3.2, due to different models of core damage progression in the two codes.

Table 1. Comparisons between MAAP4.03 and RELAP/SCDAPSIM/MOD3.2

| Sequence | Events | MAAP4.03 | RELAP/SCDAPSIM/MOD3.2 |
|---|---|---|---|
| ADC | Start of core uncovery | 11 sec | 10 sec |
| | Accumulator injection | 11 sec | 12 sec |
| | Total core uncovered | 9 min | 10.8 min |
| | Beginning of Core Melt | 28 min | 28 min |
| | Slump to Lower Head | 47 min | 1h 02 min |
| | RPV Failure | No | No |
| TML | Start of core uncovery | 29 min | 33 min |
| | Total core uncovered | 59 min | 63 min |
| | Beginning of Core Melt | 1h 36 min | 1h 33 min |
| | Accumulator injection | 2h 21 min | 2h 14 min |
| | Slump to Lower Head | 2h 05 min | 3h 13 min |
| | RPV Failure | No | No |

In the ADC sequence, Figure 4 shows the transients of core maximum surface temperature by the both codes. Figure 5 includes the core slump ratio in MAAP4.03 and the core degradation map in RELAP/SCDAPSIM/MOD3.2. In the map, 5 fuel rod components with 10 axial nodes are modeled and the slump to the lower head is shown to begin defined by the molten core reaching to the lower part of the core. The transient of the RELAP/SCDAPSIM/MOD3.2 core degradation can be illustrated in Figure 6 by considering the symmetry in the model. In spite of high power density in the center of the core, the periphery of the core shows severer damage due to more zircaloy oxidation by a larger supply of steam into larger volumes. Figure 7, 8 and 9 are similar for the TML sequence.

5. Discussion on Melt Progression Models

In MAAP4.03, when the core starts to melt, the molten material flows to lower core

nodes. In these colder nodes, crust is formed by freezing melt and fails by Creep Rupture resulted in the spread of the molten core into nodes below as shown in Figure 10. In RELAP/SCDAPSIM/MOD3.2, if the region around the molten material is significantly cooler than the freezing temperature of the molten material, then a stable crust is formed holding the molten material in place. Otherwise, the gravity force causes the melt to spread axially downward and radially sideward. When the volume of molten pool is larger and its temperature hotter, it melts the crust at its boundary and spreads. The model for calculating the rate of spread of molten material is based on the concept of a sporadically moving crust by repeated cycles of melting, flowing, and freezing. After the molten material penetrates some distance into the porous debris, its leading edge is cooled and frozen, the spread temporarily stops. The physical process of the spread model is shown in Figure 11.

## 6. Conclusion

Both codes predicted similar tendencies until the beginning of core melt. MAAP4.03 showed earlier slumping of molten core to a RPV lower head than RELAP/SCDAPSIM/MOD3.2. MAAP4.03 considers only axial flows of molten core to lower core nodes and crusts suddenly breach by Creep Rupture. In RELAP/SCDAPSIM/MOD3.2, molten core spreads axially and radially by repeated cycles of melting, flowing and freezing. Bottom crusts can be supported by intact fuel rods. By these more realistic RELAP/SCDAPSIM/MOD3.2 models, MAAP4.03 could be supported maintaining conservatism.

## Acknowledgments

The authors would like to thank Dr. C. Allison and R. Wagner (both of Innovative Systems Software, L.L.C.) for assisting the RELAP/SCDAPSIM/MOD3.2 code running.

## References

[1] The SCDAP/RELAP5 Development Team, "SCDAP/RELAP5/MOD3.2 Code Manual", NUREG/CR-6150 Revision 1, Volume I - V, October 1997.

[2] The RELAP5 Code Development Team, "RELAP5/MOD3 Code Manual", NUREG/CR-5535, Volume I - V, June 1995.

MAAP4.03

RELAP/
SCDAPSIM/
MOD3.2

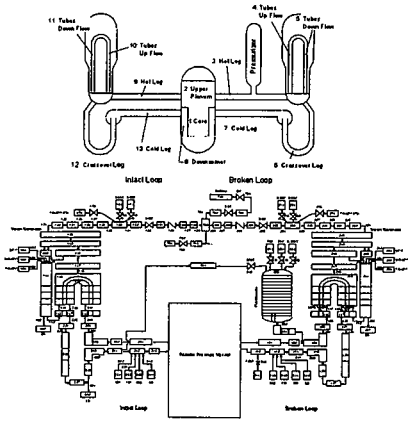


Figure 1 Primary & Secondary System Nodalization

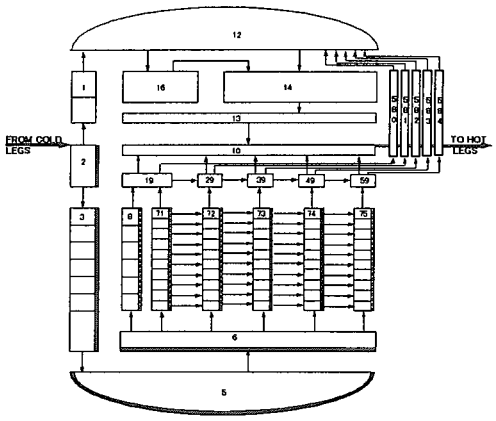



Figure 2 RPV Nodalization in RELAP/SCDAPSIM/MOD3.2

MAAP4.03

RELAP
/SCDAPSIM
/MOD3.2

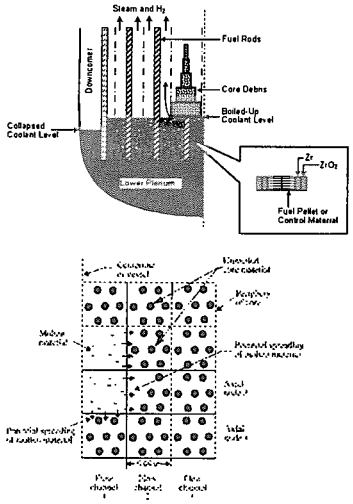



Figure 3 Melt Progression Modeling

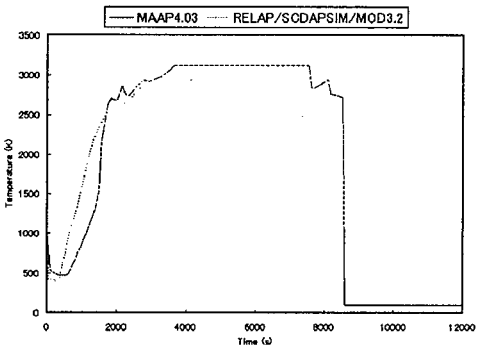



Figure 4 Core Maximum Surface Temperatures in ADC Sequence

MAAP4.03

RELAP
/SCDAPSIM
/MOD3.2

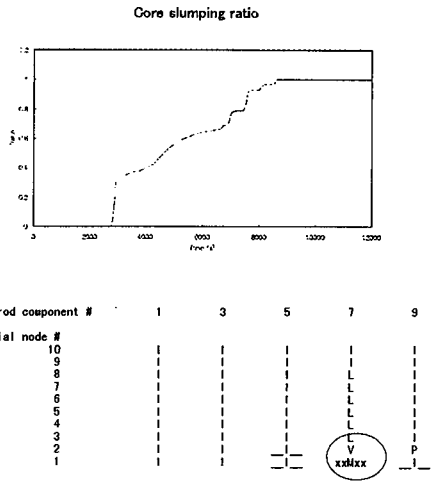



Figure 5 Core Degradation in ADC sequence

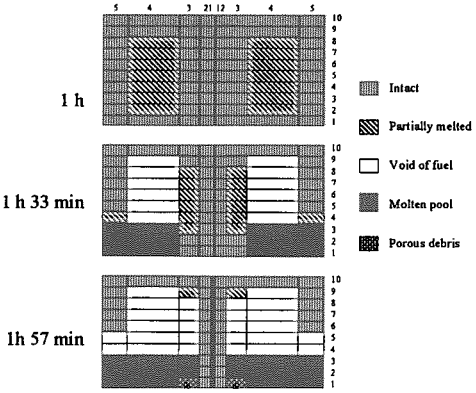



Figure 6 Transient of Core Degradation by RELAP/SCDAPSIM/MOD3.2 in ADC

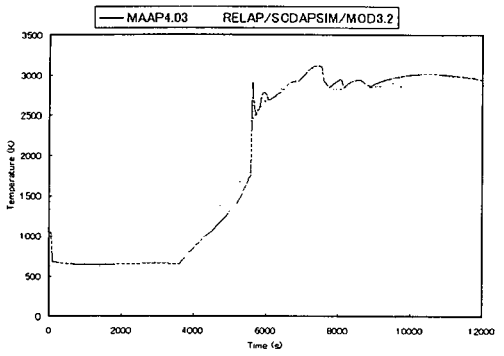



Figure 7 Core Maximum Surface Temperatures in TML Sequence

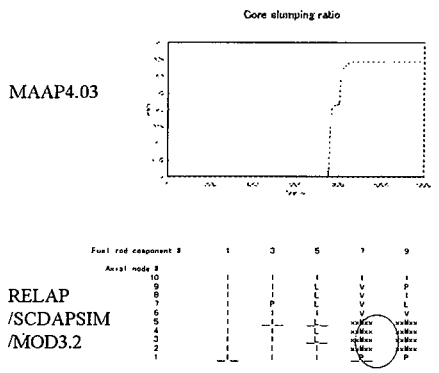



Figure 8 Core Degradation in TML Sequence

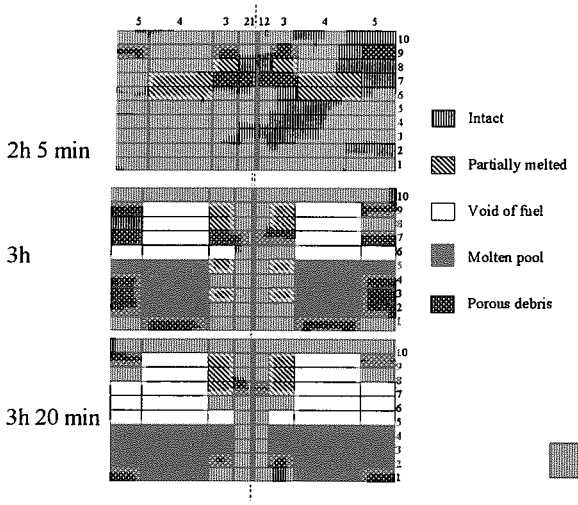



Figure 9 Transient of Core Degradation by RELAP/SCDAPSIM/MOD3.2 in TML

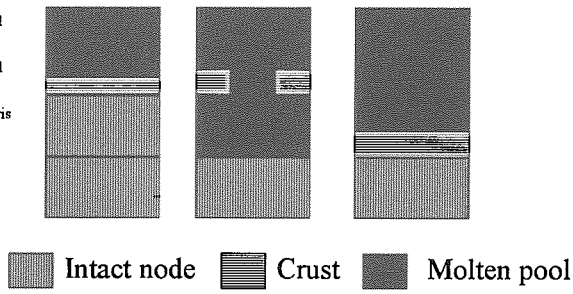



Figure 10 Core Damage Progression Models of MAAP4.03

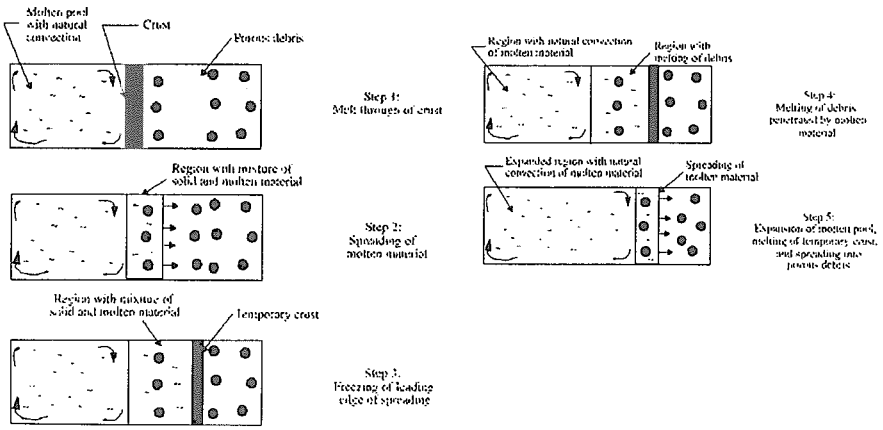



Figure 11 Spread Model in RELAP/SCDAPSIM/MOD3.2

This is a blank page.

# 6. Session 5

## In-Vessel Phenomena

Chairperson:
C. Allison (ISS)
S. Hong (KAERI)

This is a blank page.

JP0150099



# 6.1 Irradiated $UO_2$ Fuel Dissolution by molten Zircaloy: Some Results from the SCA Corium Interaction Thermochemistry Project

P.D.W. Bottomley[1], J-P. Glatz[1] and M. Barrachin[2].
[1] ITU Karlsruhe, [2] IPSN Cadarache

**Keywords: Irradiated Fuel, $UO_2$ Dissolution, $UO_2$-Zircaloy Interactions**

**Abstract**

After preliminary testing, a test series was carried out in the hot cells using cladded segments of 3mm height of both natural $UO_2$ and irradiated $UO_2$ (54 GWd/tU burn-up) heated to 2000°C for durations of upto 200s in a direct electrical heating furnace under inert (Ar) atmosphere.
The attack by the molten zircaloy cladding appeared macroscopically to be faster for the irradiated samples. The non-irradiated samples underwent a slower break-up whereas the irradiated samples broke into smaller irregular pieces due to the pre-existing cracking. Microprobe analysis showed that the melt was composed of two main phases: a metallic Zr-rich α-(Zr,U)O phase and a U-rich $(U,Zr)O_2$ ceramic phase. However the irradiated fuel showed a very high porosity as fission gas bubbles were formed and released. This causes a larger, melt/fuel interface and hence in an increased interaction rate compared with non-irradiated fuel. This implies similar dissolution rates may be expected in the irradiated fuel at over 100°C lower.

## 1 Introduction

The Corium Interactions Thermochemistry (CIT) project is one of the Nuclear Fission Safety In-Vessel Cluster of Shared Cost Action projects that were carried out under the fourth Framework Programme of the European Commission. The 3 year programme (that was completed in June'99) had 12 partners and was co-ordinated by IPSN Cadarache. The work programme included: (i) literature reviews, (ii) experimental tasks on interactions and kinetics of liquid Zircaloy (Zry) and structural material with $UO_2$ fuel; determination of corium viscosity and its variation with composition, as well as (iii) modelling studies of the liquid Zry/$UO_2$ interaction and of a thermodynamic database for the characterization of in- and ex-vessel corium. ITU's task in the CIT project was to examine the interaction of liquefied Zircaloy with irradiated $UO_2$ fuel to obtain data for understanding the behaviour of irradiated materials under severe accident conditions.

## 2 Experimental Method

### *2.1 Scoping tests*

Preliminary scoping tests were carried out using segments of 8mm diameter non-irradiated (depleted) $UO_2$ fuel and zircaloy cladding for different sample heights (from 11mm (whole pellet) to 2mm height)). These were at 2200°C for 6 min. for the 2,3,4 and 5mm height samples and 10 min. for the 11mm high sample under gently flowing argon ($2000ml.mn^{-1}$). The heat –up took 5-7 seconds to reach 1500°C and approximately 20 seconds to reach the maximum temperature (2200°C). The temperatures were determined by an optical pyrometer with an expected precision of +/- 40°C.
There is a uniform temperature domain for the samples of ≤ 5 mm height, whereas the 11 mm height (pellet) sample is too large to be heated uniformly. The melt appeared to mainly 2-phase: a lustrous metallic phase and darker ceramic phase. There was also a considerably altered structure to the fuel that contained much porosity and metallic precipitates. The ceramic-phase rich zones seemed to be more viscous with gas bubbles and fuel fragments. Between the graphite crucible and the melt a metallic phase was seen. This was thought to be a ZrC phase from reaction with the graphite crucible.

### *2.2 Second series of tests*

The second series of dissolution experiments in the direct electrical heating oven was carried out with 3mm high segments of cladded irradiated fuel in graphite crucibles under an flowing inert atmosphere (Ar at 2000ml.mn$^{-1}$) at 2000°C (approx. 800A at 6 V) for various times upto 200 secs. The samples were of high enrichment fuel (8.3% U-235) and had a burn-up of 53GWd/tU. For comparison, similar tests were also carried out with 3mm high, depleted (i.e. non-irradiated) $UO_2$ segments with Zircaloy-4 cladding in good contact with the fuel. The times were measured upon reaching a temperature of 1800°C. The sample times, weights, temperatures and the approximate extent of attack is given in Table 1.

*Table 1: Irradiated $UO_2$ interaction with molten zircaloy: sample and experimental details*

| | Status | Sample weight/g | Interaction time/s | Temp./°C | Extent of dissolution |
|---|---|---|---|---|---|
| 1 | a)fresh fuel | 1.71 | 25 | 2000 | small fraction dissolved |
| | b)irradiated fuel | 2.30 | 25 | 2000 | complete |
| 2 | a)fresh fuel | 1.68 | 49 | 2000 | complete reaction but porous |
| | b)irradiated fuel | 1.65 | 49 | 2000 | complete |
| 3 | a)fresh fuel | 1.70 | 73 | 2000 | --- |
| | b)irradiated fuel | 1.31 | 73 | 2000 | complete |
| 4 | a)fresh fuel | 1.70 | 190 | 2000 | one-quarter dissolved |
| | b)irradiated fuel | 2.66 | 190 | 2000 | three-quarters dissolved |
| 5 | irradiated fuel | 1.72 | 600 | 1740 | fuel attack initiated |

Conditions :segment approx. 2-3 mm thick Atmospheres :1-4 : Ar gas, 5 : He gas
Irradiated fuel burn-up : 53 Gwd/tU (initial enrichment 8.26 %)

A single, low temperature test with a 3 mm irradiated $UO_2$ fuel segment with cladding was made in a $ZrO_2$ crucible in a large W crucible that acted as a susceptor in an HF induction oven at about 1750°C for about 10 min. under inert atmosphere

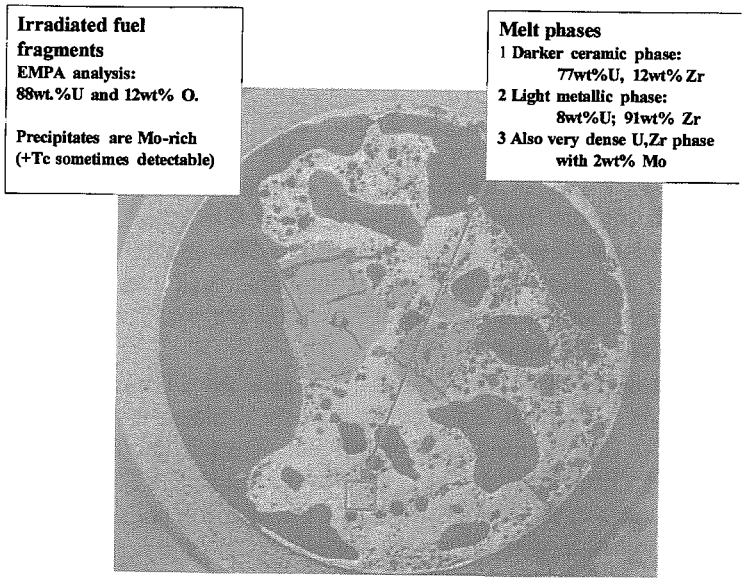



*Fig 1 Macro-photograph of an irradiated fuel segment after 190s at 2000°C under inert Ar atmosphere (5x mag).*

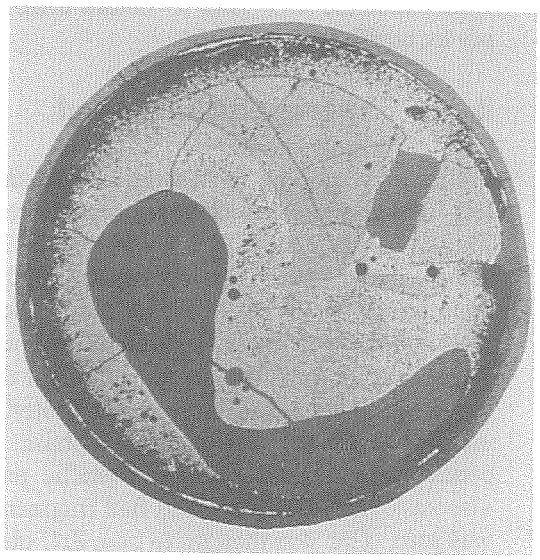


*Fig .2 Macro-photograph of a non-irradiated fuel segment after 190s at 2000°C under inert Ar atmos. (5x mag).*

# 3 Results

## *3.1 Microscopic Examination*

The macrographic photos of the tests at 2000°C showed that the irradiated fuel appeared to dissolve faster than the non-irradiated fuel, with irradiated fuel samples dissolved already at 25s. The irradiated fuel is also moresusceptible to rapid break-up and into smaller pieces, due to the pre-existing cracks (Fig. 1). The non-irradiated fuel breaks up into geometric shapes (Fig. 2).

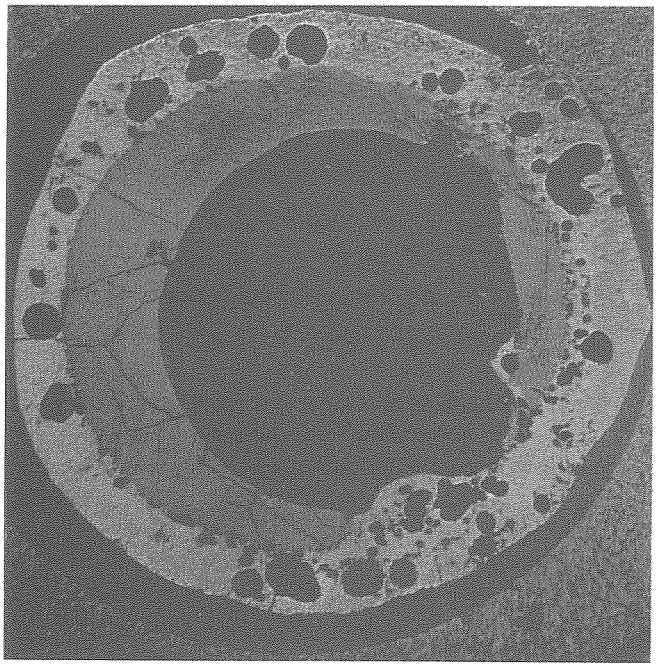


*Fig 3 Macrograph of the low temperature irradiated fuel segment after heating for 600s to 1740°C under inert He atmosphere. The cladding swelling and fuel interaction is evident. (5xmag.)*

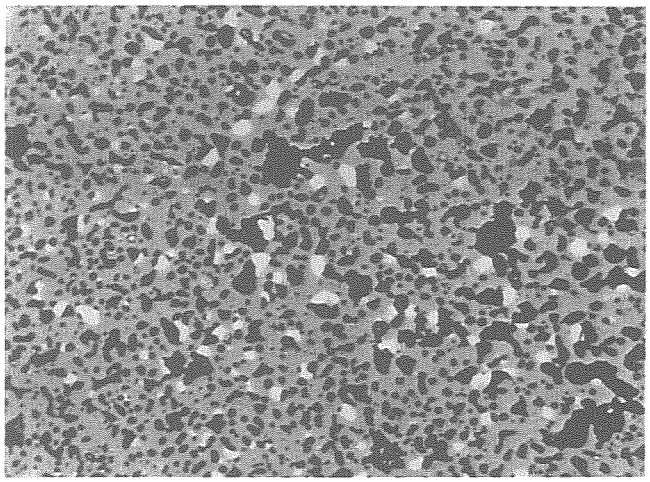


*Fig.4 Microgaph of highly porous irradiated fuel remnant after heating for 190s to 2000°C under inert Ar atmosphere (200x mag.).*

Moreover the interfaces appeared to be linear, compared to the irregular interfaces of the irradiated fuel. The macrographs of the low temperature test revealed a melting and swollen cladding that has 2 phases and has started to attack the $UO_2$ fuel. The fuel also appears highly porous after the thermal annealing (Fig. 3), moreover a large fission gas release had been observed after 5 min (also indicative of an interaction). The porosity in the irradiated fuel at 2000°C is considerable and reaches 30% (unlike the non-irradiated fuel). This is due to the fission gases and volatiles collecting in bubbles and grain boundary pores (see Fig. 4). The fission gas releases increase the interface, and hence the fluxing action. This will cause an acceleration of the irradiated fuel dissolution with time compared to the uniform fuel dissolution of non-irradiated fuel. Metallic precipitates were also seen in the irradiated fuel but not in the non-irradiated fuel (presumed to be the 5 metal fission product precipitates: Mo, Tc, Pd, Ru, Zr). These had evidently precipitated during the heating at the same time as the gases.

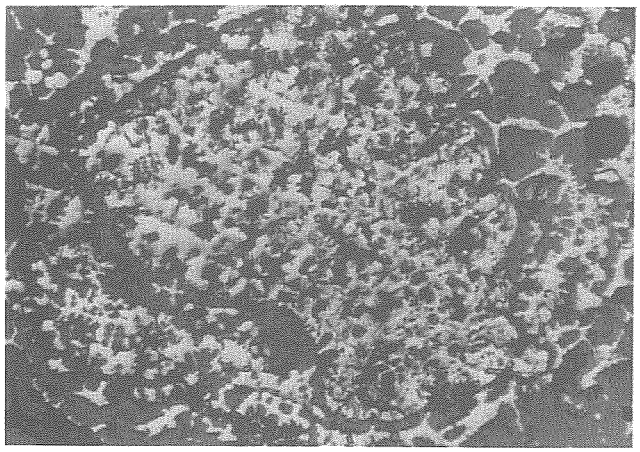


*Fig 5 Micrograph of irradiated fuel segment after 190s at 2000°C under inert Ar atmos.. A darker, U-rich, ceramic phase is seen as well as the bright, Zr-rich metallic phase.(α-Zr(O)). (200x mag.)*

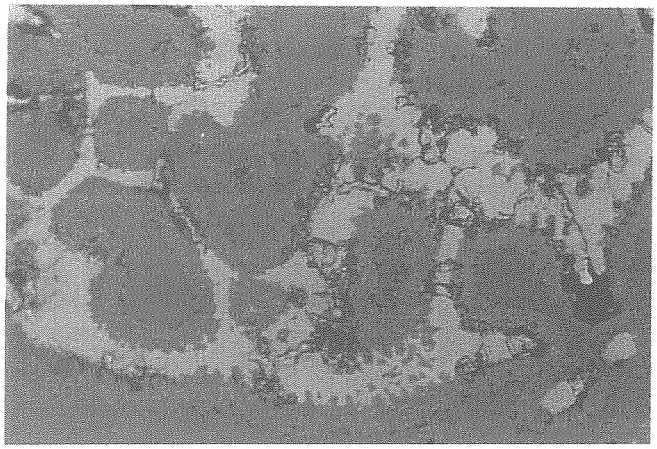


*Fig.6 Microgaph irradiated fuel melt after heating for 190s to 2000°C under inert Ar atmosphere, showing secondary (mixed) precipitates between the ceramic and the metallic phases (200x mag.).*

The corium showed the 2 main phases a bright metallic phase and a darker ceramic phase, along with some porosity (Fig. 5). It is seen that locally, the phase ratios can vary considerably between metallic - rich and ceramic -rich phases. Secondary (mixed) precipitates could sometimes be seen lying inbetween these phases (Fig.6).

### *3.2 Microprobe Analyses*

Microprobe analysis of the irradiated melt revealed the metallic phase to be Zr-rich α-Zr,U(O) (with ~85/90 $^{w}/_{o}$ Zr content) while the darker ceramic phase was 75/80 $^{w}/_{o}$ U in a mixed $(U,Zr)O_2$ oxide (see Figs.1 & 5); occasionally U-rich metallic precipitates were seen The irradiated fuel remnants however, were found to be pure $UO_2$ with no Zr present. Although the metallic precipitates were too small to analyse accurately, local concentrations of Tc, Mo or Pd were found. This supported the idea that these were the noble metal (or 5 metal) precipitates. The EMPA analyses of the phase of the 2000°C/25s

*Table 2 Microprobe analysis of melts from an irradiated $UO_2$ + cladding sample heated to 190 s at 2000 °C*

| | Composition $^{w}/_{o}$ (± 2σ) | | | | | |
|---|---|---|---|---|---|---|
| **Melt phases** | **U** | **Zr** | **Mo** | **Total** | **Composition $^{a}/_{o}$** | **Possible phases** |
| **1. Darker ceramic phase** | 77.39 (±0.44) | 11.53 (±0.18) | 0.02 (±0.01) | 88.94 (±0.48) | 28.4$^{a}/_{o}$U-11.1$^{a}/_{o}$Zr-60.5 $^{a}/_{o}O^{\#}$ | $(U,Zr)O_2$+Zr(O) |
| **2. Light metallic phase** | 8.29 (±0.84) | 90.79 (±1.03) | 0.02 (±0.02) | 99.10 (±1.33) | 3.4 $^{a}/_{o}$ U-96.6$^{a}/_{o}$Zr-0.02$^{a}/_{o}$Mo | α-Zr |
| **3. Brighter centres of light metallic phase** | 7.18 (+0.65) | 87.29 (±0.31) | 0.02 (±0.02) | 94.49 (±0.72) | 3.1$^{a}/_{o}$U-96.9 $^{a}/_{o}$ Zr -0.02 $^{a}/_{o}$ Mo | α-Zr |
| **4. Very dark phase** | 84.55 (±1.30) | 8.68 (±0.36) | 2.60 (±0.18) | 95.83 (±1.36) | 74.3 $^{a}/_{o}$U-19.9 $^{a}/_{o}$Zr-0.06 $^{a}/_{o}$ Mo | (U, Zr) metal |
| **Mean of melt compositions** | 44.4 | 49.6 | 0.66 | 94.6 | | |
| **Fuel Phase** | 88 | 0 | 0 | 88* | 33 $^{a}/_{o}$U – 67 $^{a}/_{o}$ O | $UO_2$ |

*O content measured as 12-14 %  $^{\#}$O estimated by subtraction

irradiated fuel sample gave similar analyse, but with slightly lower 'contaminant' values: thus the metallic phase a-Zr(O) has 92/94 $^{w}/_{o}$ Zr and the ceramic phase has 75$^{w}/_{o}$ U. The results of the analyses for the irradiated segments heated to 2000°C for 190s are given in Table 2. .Image analysis was used to calculate the proportion of the ceramic (U-rich) & metallic (Zr-rich) phase, although in some cases the reaction appeared complete and in others,was incomplete. Nevertheless the samples' average values for the metallic (Zr-rich)/ ceramic (U-rich) phases showed that the ratios fall with time for both irradiated and non-irradiated fuels with the latter showing the lower ratios. This implies that more $UO_2$ is in the melt for non-irradiated fuel.
This however does not take account of compositional differences between each melt. These compositional values have then been cross-multiplied with the % phase area calculated from the micrographs by image analysis. From these the total U, Zr and O melt contents have been estimated. These were then compared with melt data derived by ICP-MS analysis of non-irradiated $UO_2$ at 2000 & 2100°C (Zircaloy rod dissolution of $UO_2$ crucibles produced by AECL-Canada /FZK Karlsruhe under Task 2.3 of the project [4]). In addition our estimates of the oxygen contents were inserted in the AECL/FZK data, since they had given no oxygen measurements, so as render them more comparable to the ITU results.
Moreover the low temperature test at 1740°C gave an effectively similar analysis of the interacted cladding and fuel with metallic Zr-rich phases and darker U-rich ceramic. The U-rich ceramic phase on the inner edge contained approx. 3:1 U:Zr, while the metallic Zry-rich phase was α-Zr(O) with 1-2$^{a}/_{o}$ U. This compares with between 3:1 and 2:1 U:Zr ratio for the ceramic phase of the 2000°C/25s and the 2000°C/190s samples and metallic α-Zr(O) with 2-3$^{a}/_{o}$ content.
A micrograph (Fig. 7) shows large porosity at the cladding/fuel interface, while the swollen cladding displays the ceramic and metallic phases within the cladding with a decreasing proportion of the ceramic phase towards the outside of the cladding from a pure ceramic phase at the inside (Fig. 8). This suggests a U concentration gradient existed at temperature. The cladding was 0.64mm thick after irradiation but is now about 1.1mm thick after interaction: this 72% increase is probably due more to the cladding slumping than to the porosity in the cladding. Again the fuel is very porous and shows metallic phases that are presumed to be 5-metal precipitates. The compositions for the low –temperature data were also cross-multiplied by the % phase values and plotted on the U & Zr content graphs for the melt in Fig. 9

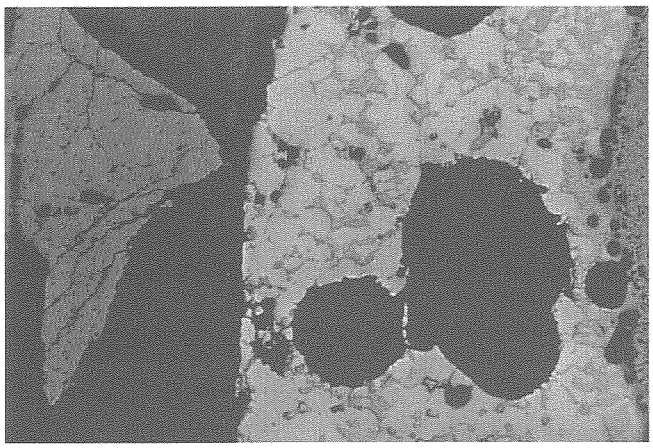


*Fig. 7 Micrograph of interacted cladding and irradiated fuel after 600s at 1740°C in inert atmosphere (He), (50x mag.)*

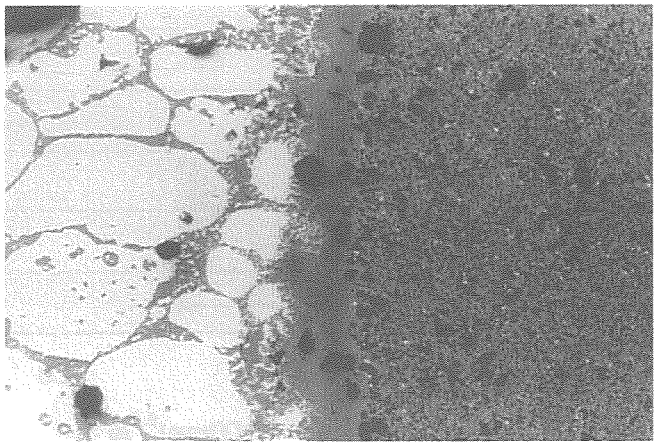


*Fig. 8 Micrograph of interacted cladding and irradiated fuel after 600s at 1740°C in inert atmosphere (He), (200x mag.)*

## 4 Discussion

The comparison of the combined microprobe data with the ICP-MS analysis of the non-irradiated UO2 data from AECL-FZK indicates a more rapid U dissolution at 2000°C for irradiated $UO_2$ fuel than for non-irradiated fuel at 2100°C (Fig. 9), and nearly as fast as non-irradiated fuel at 2200°C. The irradiated $UO_2$ fuel at 2000°C reaches 56 $^{w}/_{o}$U in 190 secs (13.8 s $^{1/2}$) and the AECL non-irradiated fuel at 2100°C reaches approx. 41 $^{w}/_{o}$U in the same time. This would imply irradiated fuel dissolves at 2000°C at rates

equivalent to those for 150°C higher for non-irradiated fuel. Furthermore, no saturation phenomenon was noted, as seen by various workers in non-irradiated fuel [3 - 6]; longer duration tests would be required in irradiated fuel to observe this.
The low temperature values also lie very close to the AECL/FZK data. However after 600s duration the U-rich ceramic phases observed on the outer edge of the cladding probably represent a saturation value (58 % U) for this temperature (ca.1750°C). This compares to 64 % U for AECL/FZK data at 2000°C/600s [4]. Nevertheless this comparison is blurred by the substantial differences in geometry since the AECL/FZK work uses larger samples and has a higher $UO_2$/Zry weight ratio (=10.9) than our samples ($UO_2$/Zry = 4.6) corresponding to CANDU fuel and LWR fuel rod respectively. Both these ratios lie above the total LWR reactor inventory ($UO_2$/Zry=2.14 by weight), but this was done with the intention of examining the kinetics of fuel rod dissolution. The contact SA/Volume ratio is also important, for AECL this was quoted as 750 $m^{-1}$ (Zry or $UO_2$?) for the ITU it was about 1480 $m^{-1}$ for Zry. The higher SA/volume ratio of the ITU geometry would be expected to favour more rapid dissolution.
A further factor is that the accuracy of the temperature determination for ITU: the accuracy of the pyrometer was ± 40 °C, dependent on maintaining the pyrometer window clean. For AECL/FZK this is better at about ± 15-20 °C.
The timing is also difficult (ie to know exactly when the Zircaloy melts) which makes comparison of the times, especially the shorter times, difficult. In both cases the zero time was taken as the Zircaloy melting point. However for AECL/FZK the heat-up time was 60-120s (7$Ks^{-1}$ initial heat-up rate) for durations upto 1600s whereas for ITU it was 10-15s to temperature ( about 200 $K.s^{-1}$ initial rate) but was examining shorter time spans (upto 200-600s), but would have had smaller errors than AECL in this range.

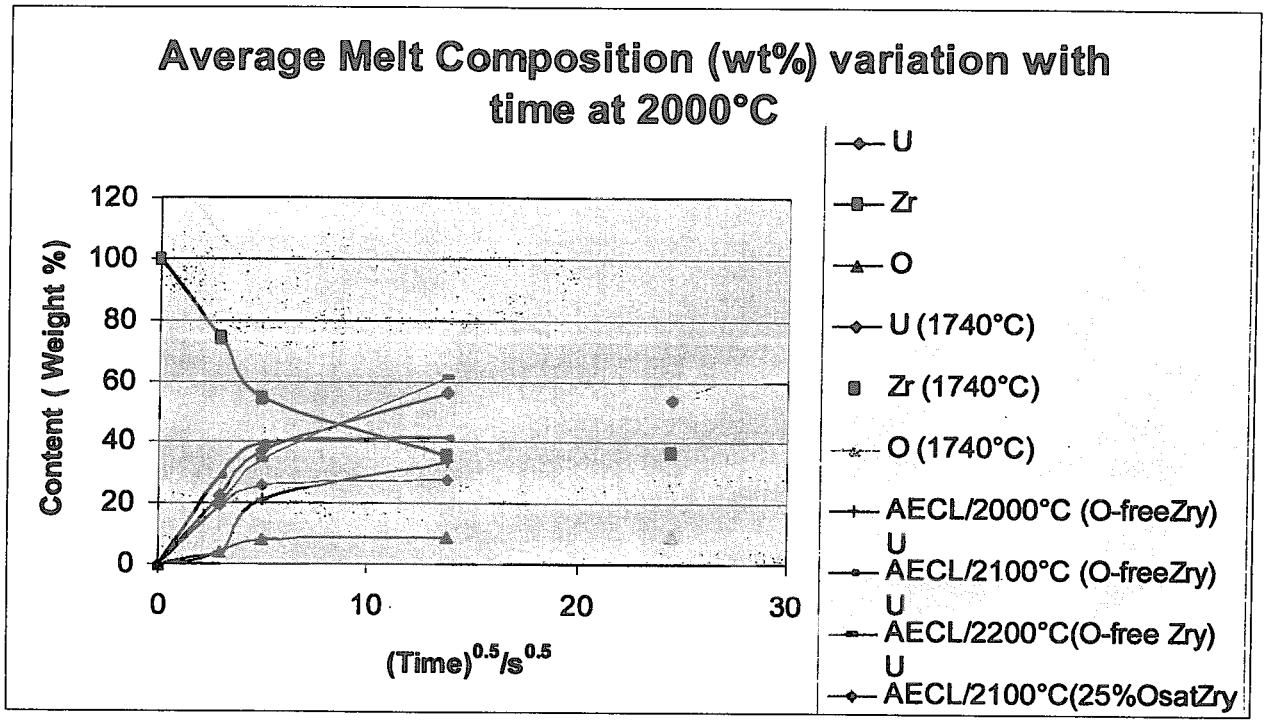



*Fig. 9 Variation of $UO_2$ and Zircaloy content (by weight) in the melt phase with time at 2000°C(AECL Data[2-pt.1])*

## 5 Conclusions

1. The interaction between $UO_2$ fuel and the zircaloy cladding is rapid particularly at 2000°C-2300°C where most testing has been done. Initial low temperature test indicates it commences with irradiated fuel directly upon the zircaloy melting, i.e. degradation could be significant from 1800°C onward.

2. The tests at 2000°C with irradiated and non-irradiated fuel show substantial differences in the macro-photography with a more rapid dissolution of the irradiated fuel. This is attributable to
   i) the additional cracks and fissures of the irradiated material (the non-irradiated fuel breaks up into larger, more geometric pieces)
   ii) the fission gas is released as the irradiated fuel is dissolved and so increases the contact surface between melt and fuel and so increases the dissolution rate.

3. Although the image analysis of the irradiated and non-irradiated fuel, did not confirm this greater reactivity of the irradiated fuel. The combined image analysis and EMPA phase analysis yielded overall melt compositions that could be compared with the non-irradiated dissolution data from AECL/FZK (Task 2.3). Despite being different geometries, the comparison implied a considerably faster dissolution of the irradiated fuel with a rate at 2000°C for irradiated fuel that lay near to that expected (by interpolation) for non-irradiated fuel at 2150°C. Whereas saturation kinetics were observed for non-irradiated fuel, the ITU tests did not extend to sufficiently long times to establish if this was true of irradiated fuels.

4. The tests showed that although graphite crucible interaction had been feared, only in one case of non-irradiated fuel were carbide phases seen. In the irradiated fuels no traces of carbon were detected in the melt by the EMPA analysis.

5. The above conclusions are preliminary but form the basis for future work. This indication of an effective difference in dissolution rates between irradiated and non-irradiated fuel of about 150°C at 2000°C could nevertheless be useful for severe accident code modellers.

## 6 References

1) M. Barrachin and D. Bottomley, Corium Interaction Thermochemistry Shared Cost Action (SCA) Project Status Report: Task 1.1: Dissolution of irradiated $UO_2$ fuel by molten Zircaloy June 1998

2) M. Barrachin and D. Bottomley, Corium Interaction Thermochemistry Shared Cost Action Project Interim Report: Task 2.2: Dissolution of irradiated $UO_2$ fuel by molten Zircaloy (INV-CIT(98)-P016) Sept. 1998.

3) M.S. Veshschunov, P.Hofmann, A.V. Berdyshev., Critical Evaluation of Uranium Oxide Dissolution by molten Zircaloy, J. Nucl. Mater. 231 (1996) 1

4) P. J. Hayward and I.M. George, Dissolution of $UO_2$ in molten Zircaloy: parts 1-4: J Nuc. Mater. 208 (1994) 35, 43; J. Nucl. Mater. 232 (1996) 1, 13

5) K.T. Kim and D.R. Olander, Dissolution of Uranium Dioxide by molten Zircaloy, J: Nucl. Mater. 154 (1988) 85, 102

6) P. Hofmann, H. Uetsuka, A. N. Wilhelm, and E.A.Garcia, Proc. Int. Symp. On Severe Accidents in Nuclear Power Plants, Sorrento, Italy, March 21-25, 1988 (IEAE-SM-296/1) 3

JP0150100



# 6.2 Analysis of Turbulent Natural Convection Heat Transfer in a Lower Plenum during External Cooling Using the COSMO Code

H. Noguchi*, Y. Sawatari and T. Imada**
*Systems Safety Department, Nuclear Power Engineering Corporation, JAPAN
Tel: +81-3-4512-2570, Fax: +81-3-4512-2599
**Fuji Research Institute Corporation, JAPAN

ABSTRACT

The behavior of a large volumetrically heated melt pool is important to evaluate the feasibility of in-vessel retention by external flooding as an accident management. The COSMO (Coolability Simulation of Molten corium during severe accident) code has been developed at NUPEC to simulate turbulent natural convection heat transfer with internal heat source. The COSMO code solves thermal hydraulic conservation equations with turbulent model and can simulate melting and solidification process.

The standard k-ε model has a limitation to describe the turbulent natural convection in the very high Rayleigh number condition ($10^{16}$~$10^{17}$) assumed to occur in a lower plenum of RPV during a severe accident. This limitation results from the assumption of an analogy of momentum and energy transfer phenomena in the standard model. In this paper the modified turbulent model in which the turbulent number is treated, as a function of the flux Richardson number derived from the experiment, has been incorporated and verified by using the BALI experiments. It was found that the prediction of averaged Nusselt number became better than that of the standard model.

In order to extend the COSMO code to the actual scale analysis under the external flooding conditions, more realistic boundary condition derived from the experiments should be treated. In this work the CHF correlation from ULPU experiment or the heat transfer coefficient correlation from CYBL experiment have been applied. The preliminary analysis of an actual scale analysis has been carried out under the condition of the TMI-2 accident.

keywords: *natural convection, Nusselt number, turbulent model, external flooding, Richardson number, turbulent Prandtl number*

## 1. INTRODUCTION

It is important to relevantly assess heat removal from molten corium in a lower plenum in evaluating the feasibility of 'in-vessel retention' by external flooding as a severe accident management. Although level-2 PSA code like MELCOR or MAAP could analyze these phenomena, the incorporated models basically consist of simple modeling and empirical correlations. Hence, these models cannot apply to the conditions beyond the expected parameter ranges. To estimate heat removal from molten corium, it is necessary to develop the mechanistic thermal hydraulic code that could describe pertinently turbulent natural convection and crust formation.

## 2. TECHNICAL APPROACH

### 2.1 Governing equations

Mass, momentum and energy conservation equations are solved as the governing equations. Buoyancy term was treated by Bussinesq approximation. In high Rayleigh number condition, COSMO code can handle standard k- ε turbulent model. Whether the region is solidified or melted is calculated by simple heat balance equation.

### 2.2 Turbulent model

A high Reynolds number type k-ε turbulent model is incorporated in the COSMO code. Eddy diffusivity $a_t$ is calculated by using the turbulent Prandtl number $Pr_t$ and eddy viscosity $\nu_t$. It means turbulent thermal field is assumed analogical with turbulent velocity field. However it is difficult to use fixed value as the turbulent Prandtl number in such system that stable and unstable stratified layer coexist. In a stable stratified layer, flow becomes laminarized then the turbulent Prandtl number should increase.

In this model, the flux Richardson number is utilized as the magnitude of buoyancy. In the transport equation of turbulent energy, two types of production term are observed in natural convection turbulence.

$$\frac{Dk}{Dt} = P + G + D - \varepsilon$$

$$Ri = G/P$$

One is the production term by shear stress ($P$), the other is the production term by buoyancy ($G$). The flux Richardson number $Ri$ is defined as a ratio of these production terms. In a stable stratified layer, the flux Richardson number becomes minus, and flow becomes laminarized if the flux Richardson number decreases. In this model, the turbulent Prandtl number as a function of the flux Richardson number according to the experiments [1].

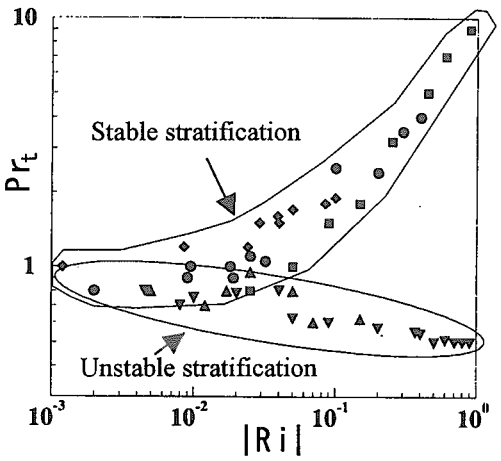



Fig. 1: Dependence of $Pr_t$ on $Ri$

### 2.3 Boundary condition

Basically isothermal boundary condition is used for the experiment analysis like BALI. In order to extend the COSMO code to the plant scale analysis or under the external flooding conditions, more realistic boundary should be treated. At the upper surface of corium pool, film boiling or radiation model was installed. At the lower surface, on the other hand, heat conduction in lower head material and boiling heat transfer for downward facing curved wall derived from CYBL or ULPU experiment [2, 3] were installed.

### 2.4 Solution procedure

The fundamental scheme of the COSMO code is a conservation of finite volume method with staggered meshing in 2-dimensional cartesian coordinate system. The 2nd order QUICK scheme for convection term treatment, the semi-implicit time integral procedure and the SIMPLEST velocity-pressure coupling algorithm have been utilized. The curved wall or the solid obstacles and/or crust are simulated by porous medium approximation. The phase interface tracking method has been utilized. Each mesh has the fraction of solid phase, the direction of the phase interface and the distance to the phase interface. The calculations were carried out on the Compaq alpha workstations.

## 3. ANALYSYS

### 3.1 BALI simulation

BALI experiments were carried out at CEA/DRN in France in order to assess heat removal from reactor vessel during external flooding [4]. Test section modeled the lower plenum with full scale and the 2-dimensional slice model. Two electrodes were placed on the each side, and volumetric heating was achieved by direct current heating. The prototypical high Rayleigh number up to $10^{17}$ was achieved. The isothermal boundary condition was realized by ice crust formation along the cooled wall. The calculation mesh was showed as Fig. 3. Isothermal boundary condition was used. Nusselt number and maximum temperature were time averaged after reaching steady state. Two test cases, $Ra'=2.3\times10^{17}$ (case A) and $Ra'=7.3\times10^{17}$ (case B), were simulated.

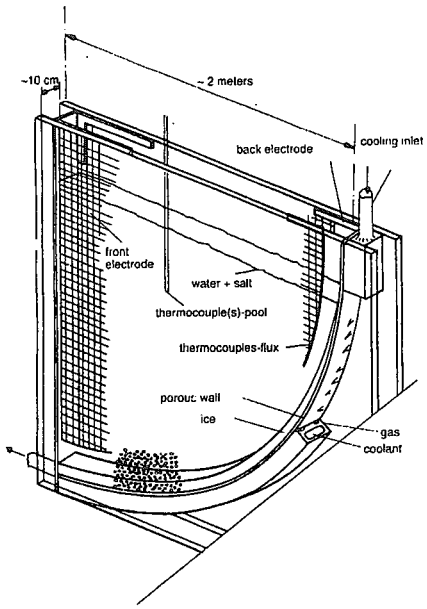



Fig. 2: Test facility of BALI

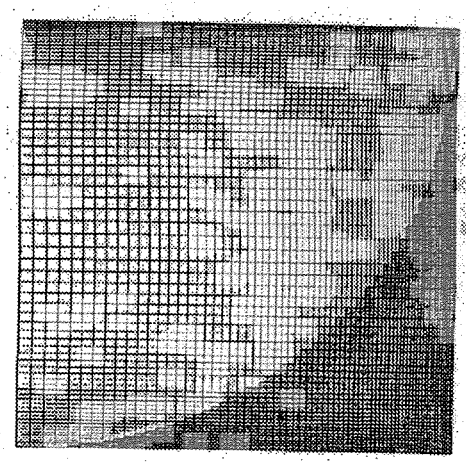


Fig. 3: Calculation mesh

#### 3.1.1 Simulation by the fixed turbulent Prandtl number model

Three types of turbulent Prandtl number, one, point six or ten, were utilized. Figures 4

and 5 are the time averaged velocity and temperature fields in Case A, $Pr_t$=1. Stable stratification was observed in bottom region, and temperature in upper region was almost uniform.

According to Table 1, decrease in the turbulent Prandtl number resulted in increase in Nusselt number and decrease in maximum temperature, because turbulent energy transport was more enhanced rather than turbulent momentum transport. But, point six as the turbulent Prandtl number seemed to be too small especially for downward Nusselt number. Increase in the turbulent Prandtl number, on the other hand, resulted in laminarization. Anyway, to use fixed value as the turbulent Prandtl number in whole region is not appropriate.

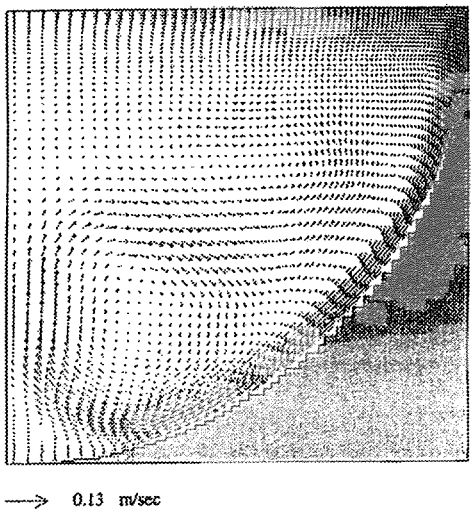



Fig. 4: Velocity Field

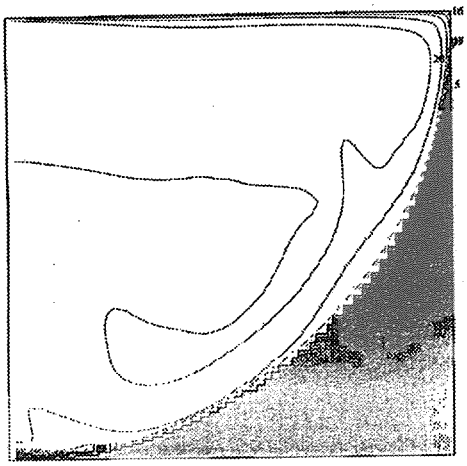


Fig. 5: Temperature Field

3.1.2 Simulation by modified model

The model in which the turbulent Prandtl number is as a function of magnitude of buoyancy should be considered. According to Table 1, predicted Nusselt number and maximum temperature became better than by the standard model with any turbulent Prandtl number.

Table. 1:Calculation Results

| | | Case A | | | Case B | | |
|---|---|---|---|---|---|---|---|
| | | $T_{max}$ (℃) | $Nu_{up}$ | $Nu_{down}$ | $T_{max}$ (℃) | $Nu_{up}$ | $Nu_{down}$ |
| Standard Model | $Pr_t$=1.0 | 36.4 | 2252 | 1633 | 63.3 | 2257 | 1811 |
| | $Pr_t$=0.6 | 29.0 | 3750 | 2228 | 45.5 | 3939 | 2607 |
| | $Pr_t$=10 | 108 | 494 | 331 | 192 | 490 | 352 |
| Modified Model | | 40.0 | 2758 | 1526 | 62.8 | 2956 | 1748 |
| Test results | | 37.4 | 2550 | 1430 | 54.6 | 3040 | 1832 |

3.2 Plant scale analysis

For the plant scale analysis, the various kinds of heat transfer model as the boundary condition were incorporated into the COSMO code. At the upper surface of corium pool, for example, film boiling or radiation could be utilized. At the lower surface, heat conduction in a lower head and boiling at outer surface could be simulated. In this model, the CYBL or ULPU experimental results were used. The material properties were modeled based on the MATPRO. After these models were incorporated, the preliminary calculation under TMI-2 accident condition was carried out.

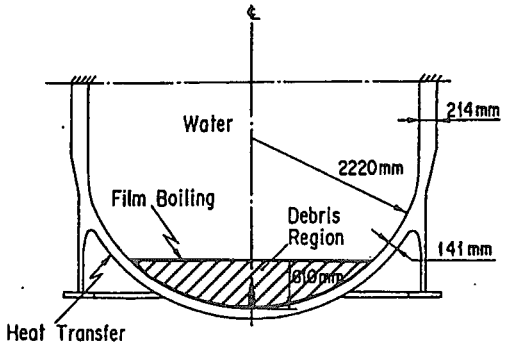


Fig. 6: Calculation region

The calculation region shows as the hatched area in Fig. 6. The debris component is 82% of $UO_2$ and 18% of $ZrO_2$. The initial temperatures and velocities condition of corium were 3000K and 0m/s, respectively. The upper surface was cooled by film boiling. At the lower surface, heat conduction in the lower head and nucleate boiling by external flooding based on CYBL were used. The uniform calculation mesh was used. The simulation was conducted during 2 hours for reaching steady state.

The velocity field and temperature field at the end of the calculation were shown in Fig. 7 and Fig. 8. Crust formation observed along the cooled surface. Maximum temperature of corium region was 2789K. Minimum temperature, on the other hand, was 865K. Minimum temperature of a lower head was 500K.

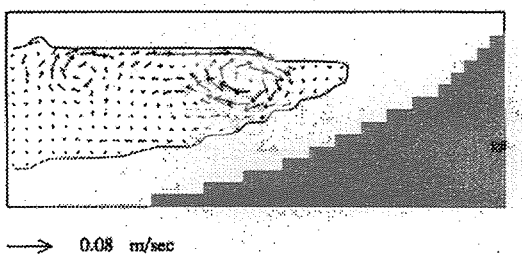
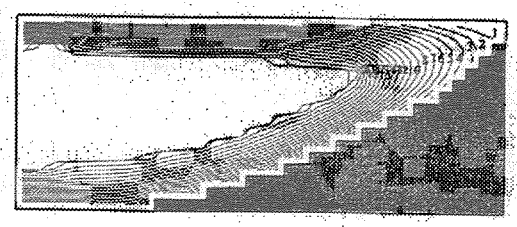


Fig.7: Velocity field (at 7200s)


Fig. 8: Temperature field (at 7200s)

4. CONCLUSIONS

In BALI simulation, the standard turbulent model has a limitation to describe turbulent natural convection heat transfer in whole region under prototypical Rayleigh number. The experimental correlation for the turbulent Prandtl number based on the flux Richardson number was incorporated. In this model, the turbulent Prandtl number increases, if the flux Richardson number is negative and decrease. Predicted Nusselt number and maximum temperature by the

modified model became better than by the standard model.

In the preparation of the plant scale analysis, the boundary conditions for external flooding were incorporated. And the preliminary calculation has been carried out under the condition of the TMI-2 accident.

ACKNOWLEDGMENTS

This work was performed under the contract by the Ministry of International Trade and Industry, Japan.

REFERENCES

[1] A. Ph. Polyakov, "Single phase mixed convection", Convective Heat Transfer, Moklous, Vilnius, 1989 (in Russian)..

[2] T. Y. Chu, J. H. Bentz, S. E. Slezak, W. F. Pasedag, "Ex-vessel boiling experiments: laboratory- and reactor-scale testing of the flooded cavity concept for in-vessel core retention. Part II: Reactor-scale boiling experiments of the flooded cavity concept for in-vessel retention", Nuclear Eng. Des. 89-99, 169, 1997.

[3] T. G. Theofanous, S. Syri, "The coolability limits of a reactor pressure vessel lower head", Nuclear Eng. Des. 59-76, 169, 1997.

[4] J. M. Bonnet, "Thermal hydraulic phenomena in corium pool: the BALI experiment", SARJ-98, Tokyo, 4-6 Nov. 1998.

JP0150101



# 6.3 MODELING FOR WATER PENETRATION INTO NARROW GAP IN CAMP CODE

Y. Maruyama, K. Moriyama, H. Nakamura, K. Hashimoto and M. Hirano

Japan Atomic Energy Research Institute
Tokai-mura, Naka-gun, Ibaraki-ken, 319-1195, Japan
Phone: +81-29-282-5854, Fax: +81-29-282-5570
E-mail: maruyama@sarl.tokai.jaeri.go.jp

K. Nakajima

Research Organization for Information Science and Technology
1-18-16 Hamamatsucho, Minato-ku, Tokyo, 105-0013, Japan

## ABSTRACT

An analytical code, CAMP, is being developed at JAERI for thermo-fluiddynamics of a molten core in the lower plenum of the reactor pressure vessel (RPV). Models for the water penetration into narrow gaps based on the flooding of a two-phase flow have been recently incorporated in CAMP code. The in-vessel debris coolability experiments performed at Japan Atomic Energy Research Institute (JAERI), where an $Al_2O_3$ melt was poured into a water-filled lower head experimental vessel and the interfacial gap between the solidified $Al_2O_3$ and the vessel was supposed to form, were analyzed with CAMP code. It was found that temperature histories at the vessel outer surface were qualitatively reproduced using the water penetration model. The analysis also implied that an appropriate flooding correlation are needed to increase the predictability of CAMP code and that the steam generation in the interfacial gap, which largely influences on the flooding, was dominated by thermal radiation from the surface of the solidified $Al_2O_3$ To the penetrating water.

**Keywords**: Severe accident, CAMP, Lower head, Molten core, Gap formation, Water penetration

## 1. INTRODUCTION

A molten core formed in a reactor core relocates to and may penetrate through a lower head of an RPV during a severe accident of a light water reactor if a sufficient cooling is not maintained. In fact, a severe damage of the reactor core followed by the molten core relocation to the lower head was realized in the Three Mile Island Unit 2 (TMI-2) accident[1]. It was identified through activities in the OECD TMI-2 Vessel Investigation Project (TMI-VIP) that approximately 20 tons of the molten core was accumulated on the lower head[2]. The lower head of the TMI-2 RPV, however, was maintained intact during the accident, resulting in the retention of the molten core within the RPV.

A mitigative accident management measure has been proposed to retain a large amount of the molten core within the RPV, in which the reactor cavity of the reactor containment vessel (RCV) is flooded by water to remove the decay heat from the lower head. In this situation, however, the occurrence of steam explosions due to thermal interactions between the molten core and the water could become a safety concern if the lower head fails. Several conditions for the molten core release to the RCV are needed for the evaluation of the influence of the ex-vessel steam explosions on the RCV integrity, including mass and temperature of the molten core, and location and initial area of failure at the lower head. A code for the analysis of thermo-fluiddynamics of the molten core within the lower plenum, CAMP (Coolability Assessment for Melt Pool) [3], is being developed at JAERI with the main objective to obtain aspects on those conditions for the ex-vessel steam explosions.

The in-vessel debris coolability experiments performed at JAERI[4] was analyzed with CAMP code. In the experiments, the molten $Al_2O_3$ was poured into a water-filled steel vessel simulating a lower head. It was indicated in the experiments that the interfacial gap was formed between the solidified $Al_2O_3$ and the vessel wall, and water subsequently penetrated into the gap. Therefore, analytical models related to the water penetration into narrow gaps were recently incorporated into CAMP code. The present paper summarizes major findings obtained from the analysis of the in-vessel debris coolability experiments with CAMP code.

## 2. DESCRIPTION OF EXPERIMENTS

The conceptual diagram of the in-vessel debris coolability experiments is illustrated in Fig. 1. The in-vessel debris coolability experiments were

performed in a model containment vessel with an inner volume of approximately $50m^3$. The experimental apparatus included a thermite melt generator, a lower head experimental vessel and water and nitrogen supply systems. The structure and dimension of the lower head experimental vessel are also shown in Fig. 1. The vessel was mainly made of carbon steel and composed of hemispherical and cylindrical parts with an inner radius of 0.25m. A stainless steel liner with a thickness of 2mm covered the inner surface of the hemispherical part. A layer of thermal insulator was provided on the outer surface of the vessel for the minimization of a heat loss to the atmosphere of the model containment vessel. Only an $Al_2O_3$ melt produced by the thermite reaction was employed as a molten core simulant and gravitationally poured into the water-filled lower head experimental vessel.

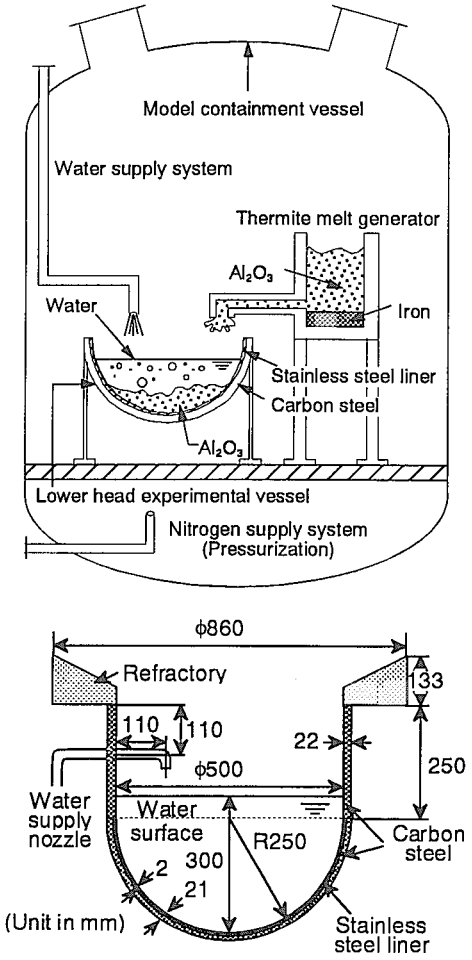



Fig. 1 Conceptual diagram of in-vessel debris coolability experiments and structure of lower head experimental vessel

Two in-vessel debris coolability experiments were performed with an experimental parameter of a mass of the $Al_2O_3$ melt. The model containment vessel was pressurized to approximately 1.3MPa during the experiments to suppress the occurrence of a spontaneous steam explosion. Temperature and level of a water layer in the experimental vessel at the entry of the $Al_2O_3$ melt were similar in the two experiments, which were approximately 450K and 0.3m, respectively. An approximately 30kg of $Al_2O_3$ melt in the first experiment (IDC001) or 50kg in the second (IDC002) was poured into the vessel.

The results on a thermal transient of the lower head experimental vessel showed the formation of an interfacial gap between the solidified $Al_2O_3$ and the vessel wall. It was supposed that the interfacial gap acted as a thermal resistance during an initial phase of the experiments and subsequently became a path for the water penetration to cool down the $Al_2O_3$ melt and the vessel, which supported a hypothesis by Henry and Dube[5] for a debris cooling mechanisms in the TMI-2 accident. The interfacial gap formation was identified in other experimental programs including FARO[6], LAVA[7] and experiments organized by Fauske and Associates, Inc.[8].

## 3. ANALYTICAL MODELS

The present version of CAMP can be basically applied to the analysis for laminar and turbulent convection of the fluids with internal heat generation and solid-liquid phase change. It has capabilities of treating heat conduction of a vessel containing the fluid, vessel deformation due to thermal expansion and elastic strain, and water penetration into narrow gaps. A finite volume scheme for the spatial discretization is employed in CAMP code to solve thermo-fluiddynamics. A finite element method is used for the calculation of vessel deformation based on the temperature distribution of the vessel and the pressure load onto the vessel. The formation of the interfacial gap and the enlargement of the gap width were evaluated from the predicted displacement of the vessel.

In the present analysis, the stainless steel liner with a thickness of 2mm at the inner surface of the experimental vessel was substituted by a 3mm thick carbon steel since thermal conductivity was higher in carbon steel than stainless steel by approximately 50% at an elevated temperature. A depth of the $Al_2O_3$ melt and the overlying water layer was 114mm and 186mm for IDC001, and 160mm and 140mm for IDC002. The initial temperatures of the $Al_2O_3$ melt, the overlying water and the vessel wall were chosen as 2500 K, 468 K and 440K, respectively. The temperature at the inner surface of the vessel in contact with the overlying water was fixed at the saturation temperature of water at 1.3 MPa. Other surfaces of the vessel were assumed to be adiabatic boundaries. The initial gap between the $Al_2O_3$ melt and the vessel was set at 0.2mm so as to be consistent with the temperature increase rate of

the vessel wall.

A boiling heat transfer was assigned for the upper surface of the $Al_2O_3$ melt. Kutateladze correlation for a nucleate boiling[9] and Berenson correlation for a film boiling regime[10] were employed. Critical and minimum heat fluxes were calculated with Zuber[11] and Berenson correlations, respectively. Heat flux in a transition boiling regime was evaluated by linearly interpolating the critical and minimum heat fluxes in a logarithmic plot.

The model for the water penetration into narrow gaps is one-dimensional and is based on the flooding phenomena of a counter-current two-phase flow. The following flooding correlation could be formulated from the experiments by Koizumi, et al.[12] for gaps with a width between 1mm and 5 mm,

$$j_g^{*1/2} + 0.25 j_l^{*1/2} = 0.33 \qquad (1)$$

where,

$$j_g^* = v_g \left[ \frac{\rho_g}{g D_{eq} (\rho_l - \rho_g)} \right]^{1/2} \qquad (2)$$

$$j_l^* = v_l \left[ \frac{\rho_l}{g D_{eq} (\rho_l - \rho_g)} \right]^{1/2} \qquad (3)$$

where, v, g, ρ and $D_{eq}$ are superficial velocity, gravitational acceleration, density and hydraulic equivalent diameter of the gap, and subscript g and l indicate gas and liquid phases, respectively.

A water penetration depth into the interfacial gap is explicitly calculated in CAMP code with the above flooding correlation and the following mass and energy balances at the entrance of the gap,

$$\rho_g v_g = \rho_l v_l \qquad (4)$$

$$q_{vsl} A_{vsl} + q_{deb} A_{deb} = A_{gap} \rho_g v_g h_{fg} \qquad (5)$$

where, $q_{vsl}$, and $q_{deb}$ are the boiling heat flux at the surface of the vessel and the solidified $Al_2O_3$, $A_{vsl}$ $A_{deb}$ are the surface area in contact with penetrating water, $h_{fg}$ is the latent heat of vaporization. The schematic diagram of the water penetration model is illustrated in Fig. 2.

In the water penetration model, boiling heat flux to the penetrating water is necessary. Unfortunately, a complete boiling curve for a narrow gap covering nucleate, transition and film boiling regimes was not currently available. The boiling curve similar to that for the upper surface of the $Al_2O_3$ melt was used. Heat conduction and thermal radiation through the steam were considered for locations of the interfacial gap below the leading edge of the penetrating water. In the film boiling regime, influence of thermal radiation from surfaces with high temperature to water was added to heat conduction through the steam layer.

The initial temperature of the $Al_2O_3$ melt was based on a separate measurement with a pyrometer using a 3 kg of thermite[13]. Same material properties of $Al_2O_3$ as those in a scaling calculation for the in-vessel debris coolability experiments[3] are used in the present analysis.

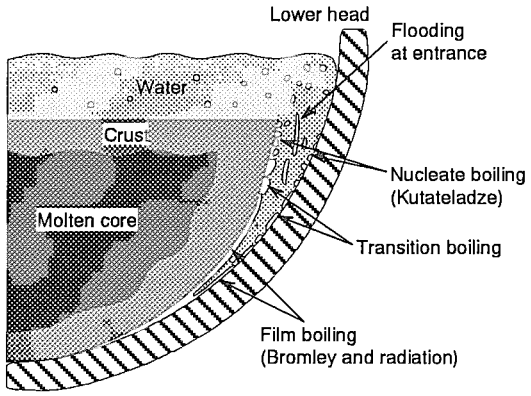



Fig. 2 Conceptual scheme of analytical model for water penetration into interfacial gap

## 4. RESULTS AND DISCUSSIONS

The comparison of the analysis with the in-vessel debris coolability experiment (IDC002) is plotted in Fig. 3 for the temperature history on the outer surface of the lower head experimental vessel. Location compared was at 30 degrees from the center axis of the vessel. The experimental results are plotted for three different circumferential locations.

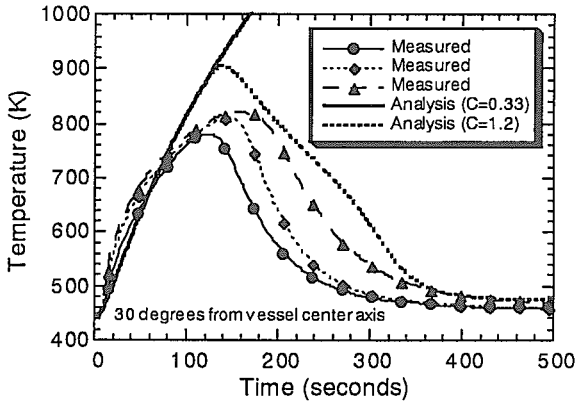



Fig. 3 Comparison of temperature history on vessel outer surface at 30 degrees from vessel center axis for IDC002

It was found that, when the flooding correlation expressed as Eq. (1) was used, the rapid temperature decrease observed in the experiment was not reproduced. The flooding experiments by Koizumi, et al. were performed using vertical annuli with a fixed inner diameter of the outer pipe at 100 mm,

and isothermal air and water were used as upward gas and downward liquid phases, respectively. It was supposed, therefore, that an annular type two-phase flow was developed when the flooding condition was established.

The geometry of the in-vessel debris coolability experiments was different from the flooding experiments by Koizumi, et al. In addition, significant boiling on the solidified $Al_2O_3$ surface, as downward facing heat transfer surface, could produce significant amount of steam and develop a stratified type two-phase flow in the interfacial gap. In the stratified two-phase flow, an interfacial surface area for gas-liquid momentum exchange could be much smaller than that in the annular type two-phase flow, implying easier water penetration into the interfacial gap under the conditions of the in-vessel coolability experiments.

With the consideration mentioned above, several sensitivity analyses were performed with larger value of the constant in the right hand side of Eq. (1). The analytical results with the constant of 1.2 were also plotted in Fig. 3. A qualitative agreement with the experimental results was obtained in the analysis. This agreement was obtained for the temperature history on the vessel outer surface at 60 degrees from the vessel center axis. However, at the center axis (the botom of the vessel), the analysis overestimated the maximum temperature by approximately 200K. Similar findings were obtained in the analysis for IDC001. The temperature history on the vessel outer surface at 30 degrees from the center axis is plotted in Fig. 4 for IDC001. It is noted that coarse analytical mesh was used in the analysis of IDC001 compared with the IDC002 analysis.

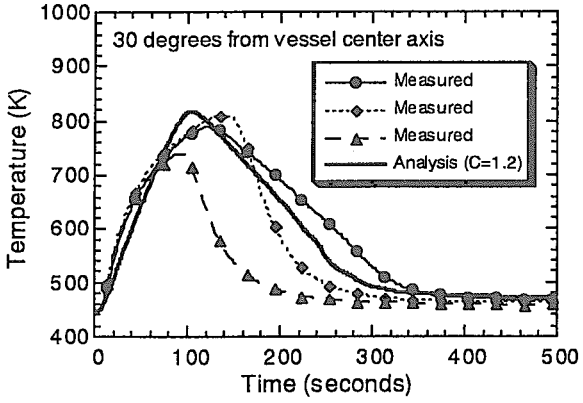



Fig. 4 Comparison of temperature history on vessel outer surface at 30 degrees from vessel center axis for IDC001

As described in the previous section, CAMP has capability of calculating the vessel deformation associated with the formation of the interfacial gap and the gap enlargement. The displacement of the experimental vessel analyzed with CAMP code for IDC002 is shown in Fig. 5. The initial position of the vessel inner surface corresponds to the outer surface of the solidified $Al_2O_3$. For the convenience, the horizontal displacement was intentionally magnified by 10. It was identified in the plot that, due to the vessel deformation, the interfacial gap was formed and the gap width changed with time, that is with the temperature distribution of the vessel. The width at the entrance of the interfacial gap was predicted to be from 1mm to 2mm at the specified time shown in the plot.

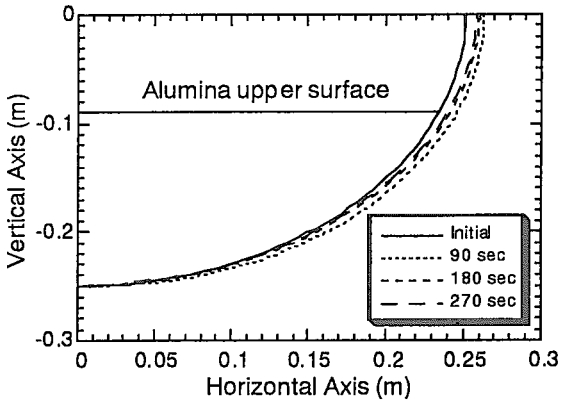



Fig. 5 Predicted displacement of experimental vessel

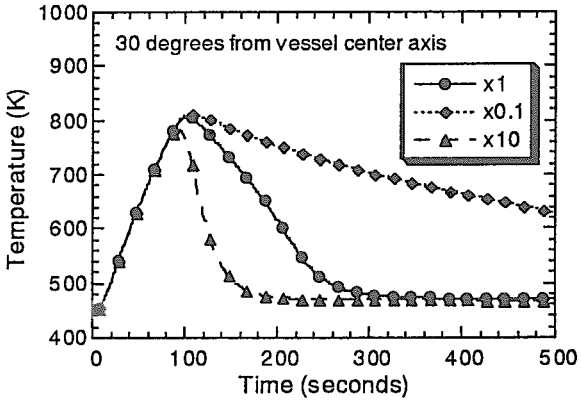



Fig. 6 Results of sensitivity study on influence of boiling heat flux in interfacial gap (temperature history on vessel outer surface at 30 degrees from vessel center axis)

In the present water penetration model, steam production within the interfacial gap is one of key phenomena since it limits the amount of water penetrating into deeper locations of the gap. A sensitivity study was conducted to clarify the influence of the steam generation by boiling on the water penetration behavior since information on boiling in barrow space are quite limited. The results of the sensitivity study on the temperature history on the vessel outer surface are plotted in Fig. 6. The

heat flux obtained from the default boiling curve was multiplied by 0.1 or 10. Thermal radiation heat flux in film boiling regime was not decreased or increased. The radiation emmisivity of the solidified $Al_2O_3$ was fixed at 0.8. The analytical results indicated that the temperature reduction rate was largely influenced by the boiling heat transfer since nucleate boiling was predicted to occur on the inner surface of the vessel. On the other hand, the maximum temperature and the timing that the temperature reduction was initiated were almost same in the three cases. This finding implied that the steam production within the interfacial gap and resulted limitation of the water penetration were dominated by the thermal radiation from the solidified $Al_2O_3$.

## 5. CONCLUSIONS

For the analysis of thermo-fluiddynamics of a molten core in the lower plenum of the RPV, CAMP code is being developed at JAERI. The analytical models were recently incorporated into CAMP code, which were associated with the formation and the enlargement of the gap at the interface between the molten core and the lower head, and the subsequent water penetration into the interfacial gap. The water penetration model is based on the flooding phenomena of a counter-current two-phase flow.

The present version of CAMP code was applied to the analysis of the in-vessel debris coolability experiments performed at JAERI. The $Al_2O_3$ melt produced by a thermite reaction was poured into a water-filled steel vessel, and the formation of the interfacial gap between the solidified $Al_2O_3$ and the vessel was implied in the experiments. It was found through the analysis that the thermal responses of the vessel wall could be qualitatively reproduced by using the models on the vessel deformation and the water penetration into the interfacial gap. However, the analysis also indicated a strong influence of the flooding correlation on the water penetration behavior. Further investigation is thus needed in order to obtain a physically adequate flooding correlation applicable to a realistic conditions and geometry of severe accidents. The additional finding was that the steam production within the interfacial gap, which is important for the prediction of a rate of the water penetration, was dominated by thermal radiation from the downward facing solidified $Al_2O_3$ surface to the penetrating water.

In order to evaluate a thermal load imposed on the lower head, the turbulent natural convection of the molten core with internal heat generation must be predicted with a reasonable accuracy. A low Reynolds number type two-equation turbulence model was recently incorporated into CAMP code, and the validation of the model with the related experiments is currently in progress.

## REFERENCES

(1) J. M. Broughton, et al., A Scenario of the Three Mile Island Unit 2 Accident, Nucl. Technol. 87(1), pp. 34-53, 1989.
(2) J. R. Wolf, et al., TMI-2 Vessel Investigation Project Integration Report, NUREG/CR-6197 TMI V(93)EG10 EGG-2734, March 1994.
(3) Y. Maruyama, et al., Quench of Molten Aluminum Oxide Associated with In-Vessel Debris Retention by RPV Internal Water, Proc. OECD/CSNI Workshop on In-Vessel Core Debris Retention and Coolability, Garching, Germany, March 3-6 1998.
(4) Y. Maruyama, et al., Experimental Study on In-Vessel Debris Coolability in ALPHA Program, Nucl. Eng. Des, 187, pp. 241-254, 1999.
(5) R. E. Henry and D. A. Dube, Water in the RPV: A Mechanism for Cooling Debris in the RPV Lower Head, Proc. Specialist Meeting on Selected Containment Severe Accident Management Strategies, pp. 93-104, Stockholm, Sweden, June 13-15 1994.
(6) D. Magallon, et al., Debris and Pool Formation/Heat Transfer in FARO-LWR: Experiment and Analysis, Proc. OECD/CSNI Workshop on In-Vessel Core Debris Retention and Coolability, Garching, Germany, March 3-6 1998.
(7) K. H. Kang, et al., Experimental Investigations on In-Vessel Debris Coolability through Inherent Cooling Mechanisms, Proc. OECD/CSNI Workshop on In-Vessel Core Debris Retention and Coolability, Garching, Germany, March 3-6 1998.
(8) R. E. Henry, A Scaling and Experimental Approach for Investigating In-Vessel Cooling, Proc. Twenty-Fourth Water Reactor Safety Information Meeting, Vol. 2, pp. 141-159, Bethesda, MD, October 21-23 1996.
(9) S. S. Kutateladze, Heat Transfer in Condensation and Boiling, AEC-Translation-3770, USAEP Tech. Info. Service, 1952.
(10) P. J. Berenson, Film boiling heat transfer from a horizontal surface, J. Heat Transfer, 83, pp. 351-358, 1961.
(11) N. Zuber and M. Tribus, USAEC Report, AECU-2931, 1958.
(12) Y. Koizumi, et at., Gravitational Water Penetration into Narrow-Gap Annular Flow Passages with Upward Gas Flow, Proc. Eighth International Topical Meeting on Nuclear Reactor Thermal-Hydraulics, Vol. 1, pp. 48-52, Kyoto, Japan, September 30-October 4 1997.
(13) Y. Maruyama, et al., Evaluation of Specific Heat and Temperature of Thermite Melt Used in Melt Coolant Interaction Test of ALPHA Program, JAERI-M 93-096 (in Japanese), March 1993.

JP0150102



# 6.4 Identification of Gap Cooling Phenomena from LAVA-4 Experiment Using MELCOR

Jong-Hwa Park, Dong-Ha Kim, See-Darl Kim,

Sang-Baik Kim, Hee-Dong Kim (KAERI, KOREA)

Korea Atomic Energy Research Institute

Dukjin-Dong 150, Yusong-Ku, Taejon, 305-353, KOREA

Tel) 82-42-868-2655

Fax)82-42-861-2574

E-mail) jhpark3@nanum.kaeri.re.kr

## ABSTRACT

During the severe accident, whether the hot debris in lower head will be cool-down or not is the important issue concerning the plant safety. KAERI has launched the "LAVA" experimental program to examine the existence of initial gap and its effect on the cooling of hot debris. The objective of this study is to identify the gap cooling phenomena from the analysis of simulation results on LAVA-4 experiment using MELCOR1.8.4 code. Three parameters on the debris coolability in MELCOR are the quenching heat transfer coefficient for the interaction between molten $Al_2O_3$ and water, the heat transfer coefficient from debris to wall and the diameter of the particulate debris for calculating the available heat transfer area with water. The sensitivity study was performed with these three parameters. However it was believed that there must be a gap between debris and inside wall during the transient. MELCOR1.8.4 does not consider these gap-cooling phenomena. Therefore a conceptual gap-cooling model has been developed and implemented into the lower plenum model in MELCOR to take into account the gap effect in the lower plenum. When the "gap model" is implemented, the peak temperature of the vessel wall was reduced and its cooling rate was increased.

## INTRODUCTION

A new concept of gap cooling mechanism has been suggested to explain the cooling phenomena between the hot debris and the lower head, which was expected to occur in the TMI-2 accident [1]. If molten corium relocates into the lower plenum filled with coolant, a contact resistance may be formed due to strong vaporization of trapped water in a small gap between debris and the wall. As the temperature of the wall is increased more than 800K, the vessel wall weakens and it could be elongated by the stress resulting from the internal pressure and the debris weight itself. The contact resistance and elongation may create a certain path for water to ingress; we called it a gap. This gap may play an important role in cooling down the vessel wall and debris.

KAERI has launched the "LAVA" experimental program to examine the existence of the initial gap and its effect on the cooling of debris [2]. The LAVA-4 experiment was performed by dropping the molten $Al_2O_3$ from thermite reaction into the lower vessel head filled with water. The relocated molten $Al_2O_3$ mass was 30 Kg and the water temperature in lower head was reached at 429.15 K just before the relocation. The radius of hemispherical head was 0.25m and its thickness was 0.025m. The available measured data were as follows; outer surface wall temperature, debris temperature at two points(upper, lower), water temperature(bottom, middle, top), outer surface and atmosphere temperature of test vessel respectively.

The cooling of the relocated molten debris was treated with three different phases in the MELCOR [3]. The first is the falling debris quench phase. During this first phase, molten debris become to cool down rapidly and also the large amount of steam will be produced immediately. All the molten $Al_2O_3$ entering the water were assumed to be converted to the spherical particulate debris, which has the same diameter specified by user. The available surface area for this quenching heat transfer was calculated based on the surface area of this particulate debris. The second is the transition phase between the end of quenching and the beginning of the stable particulate debris bed formation. During this second phase, the leveling of the particulate debris was performed by the time constant for spreading in radial direction. In this phase, decay factor was applied to link the quenching phase to the heat transfer phase from stable particulate debris smoothly. When the decay factor value decrease at 0.01, it is assumed that the stable debris was formed completely. The last is the heat transfer phase from stable particulate debris bed. During this phase, maximum heat transfer rate to the water was limited by the dryout heat flux from "Lipinski zero dimensional model" [4].

## DESCRIPTION OF THE ACTUAL WORK

The Figure 1 shows the LAVA-4 experimental facility. The experimental facility was modeled with the following control volumes; source volume for injecting nitrogen gas, core volume for melting $Al_2O_3$, lower plenum volume for capturing the debris, and two additional volumes for the test vessel and the building. A heater and two valves were added to control the water temperature in the lower plenum as required and to keep track of pressure increase after strong reaction between water and molten $Al_2O_3$, respectively. The Figure 2 shows the nodalization and modeling of LAVA-4 test for MELCOR.

In the MELCOR calculation, the heat transfer coefficient from debris to vessel wall was determined based on the assumption of complete contact. The rapid temperature increase rate on the vessel wall just after relocation of molten $Al_2O_3$ into the lower head was well predicted from Figure 3. The wall temperature was reached at 1000 K maximum and thereafter it decreases slowly. But the measured data shows that the maximum temperature was at most 800 K and it was quenched rapidly after passing this maximum points. The reason for this rapid cooling phenomena could not be identified from our current measured data. But the possible scenario can be made as follows. The wall may have kept completely contact with debris during the short period after relocation because the measured data on wall temperature was well matched with the calculation result based on the complete contact between debris and wall. But as the temperature of carbon steel close to the 800K, carbon steel starts to be deformed. A contact resistance can be created by imperfect wetting between debris and wall. This contact resistance can retardate the temperature increase of inside wall and may play as a way for water ingression. Actually the rapid quenching after peak temperature can be explained only by the sudden water ingression. But in spite of cooling down of the wall, the debris was remained at relatively high temperature as we can see in Figure 4. The possible reason for the debris keeping high temperature may attribute to the existence of dense layer on the outer region of the debris. This dense layer in outer region of debris may play as a strong barrier against the water, therefore debris at TC location could have kept the high temperature until the formation of crack in outer dense layer results in an abrupt water ingression.

To simulate properly this rapid cooling phenomena in LAVA-4 test, three cases were considered to perform the sensitivity study with changing the values of important parameters concerning the debris coolability. The parameter for the first case is the quenching heat transfer coefficient for the interaction between molten $Al_2O_3$ and water in lower vessel head during the first phase. The parameter for the second case is the heat transfer coefficient from debris to wall over the transient. Now, MELCOR1.8.4 can not consider the gap between debris and wall. They were modeled under the condition of complete contact. The parameter for the last case is the diameter of the particulate debris for calculating the available heat transfer area with water.

In case of considering the quenching phenomena during the relocation, Figure 5 shows that the peak temperature of the out surface of the wall was well predicted. But the rapid cool down of wall temperature after peak point still could not be predicted properly. In the second case, the HTC value from debris to wall was reduced from 1330 $W/m^2K$ to 500.0 $W/m^2K$ This reduced HTC value means the existence of gap resistance between debris and wall. From Figure 6, the calculation results with 500 $W/m^2K$ shows that the wall temperature increase rate became slow compared to the case with complete contact. In the last, the size of the diameter of particle was selected to modify the available heat transfer area with water. The reduced diameter means that the available area for heat transfer with water become to increase. The Figure 7 shows that the cool down rate for the wall and the debris were increased. Consequently the quenching in wall and the high temperature on the debris, which

was occurred in LAVA-4 test, could not be simulated with the current model in MELCOR. However, from this study, it was believed that there must be a gap between debris and inside wall during the transient.

For now, MELCOR1.8.4 does not consider these gap-cooling phenomena. Therefore a conceptual gap-cooling model has been developed and implemented into the lower plenum model in MELCOR to take into account the gap effect in the lower plenum. Figure 8 shows the concept of gap model. The basic concept of this model assumes that the heat fluxes from the outer surface of the lower crust and the inside lower head are large enough to vaporizes the water within gap immediately and only the remaining heat from the debris reaches the inside vessel wall. Currently, total amount of heat loss from gap boiling was modeled to be limited by the experimental data on the critical heat flux from Monde.

The LAVA-4 experiment was simulated using MELCOR with and without "gap model" respectively. From Figure 9, when the "gap model" is implemented, the peak temperature of the vessel wall was reduced and its cooling rate was increased. But the rapid cool-down rate after peak temperature was not estimated properly.

## RESULTS

The COR module in MELCOR has been used to simulate the small-scale experiment related to the debris coolability in lower head. The important parameters such as the quenching HTC , the diameter of particulate debris and the HTC from debris to wall concerning the cooling of $Al_2O_3$ are identified and evaluated. From this sensitivity study, the quenching phenomena occurred in LAVA-4 test could not be simulated properly with current MELCOR model. A parametric gap-cooling model was developed and implemented into MELCOR code. But the current "gap model" does not have a model to simulate the phenomena such as limitation of water ingression into the gap due to rapid steam generation and the effect from gap size change. Also the user should supply the heat transfer coefficient values used in the model. These limitations will be studied further to develop a more analytical model. The possible scenario for the LAVA-4 test could be made from these simulation results. For the next series of test, it needs that the water level just after the end of the test should be measured to get the bounding value on the total amount of heat transfer during the test.

## REFERENCES

1. Kune Y. Suh, Robert E. Henry," Integral Analysis of Debris Material and Heat Transport in Reactor Vessel Lower Plenum ", Nuclear Engineering and Design 151 (1994) 203-221.
2. H.D.Kim, S.B.Kim,"Overview of severe accident research and SONATA-IV phase-I experiment at KAERI",CSARP, Bethesda MD, May 4-7 1998.
3. " MELCOR computer code manual : NUREG/CR-6119", vol 1&2,July 1997.
4. Ronald J. Lipinski,"A Model for Boiling and Dryout in Particle Beds", NUREG/CR-2646,1982.

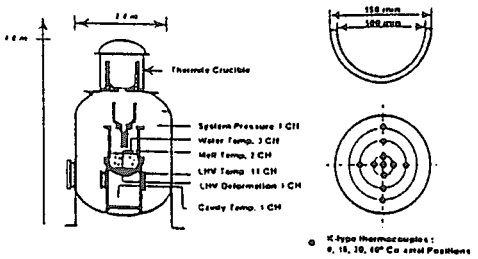


Fig 1 Description of LAVA-4 Experimental Facility

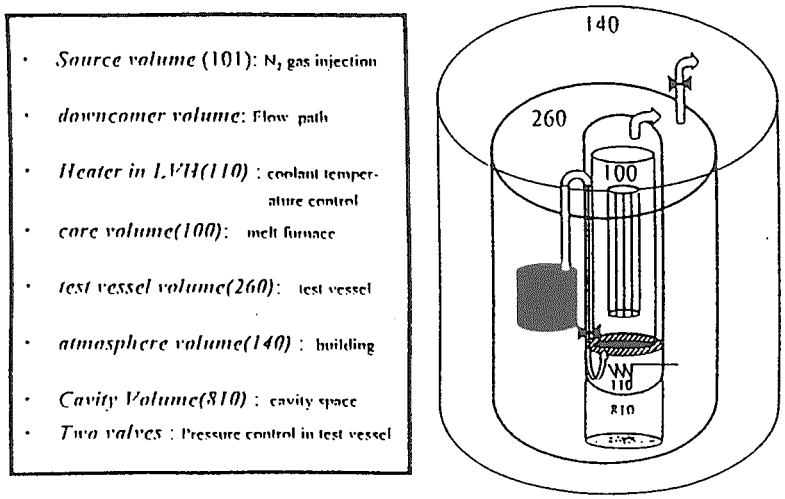



Fig 2 Input Description for Simulating the LAVA-4 Test

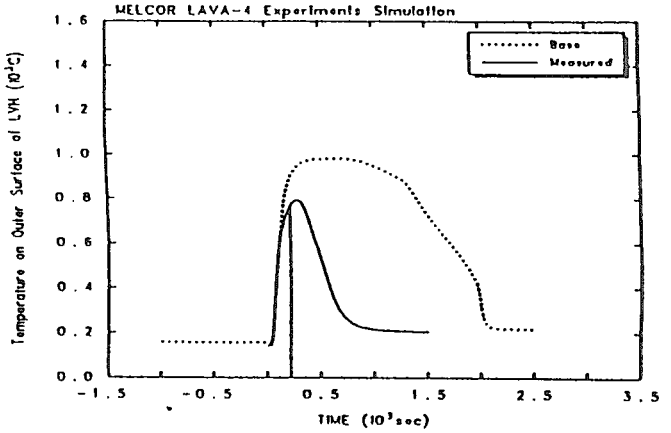



Fig 3 Outside-wall Tempertaure in LAVA-4 test

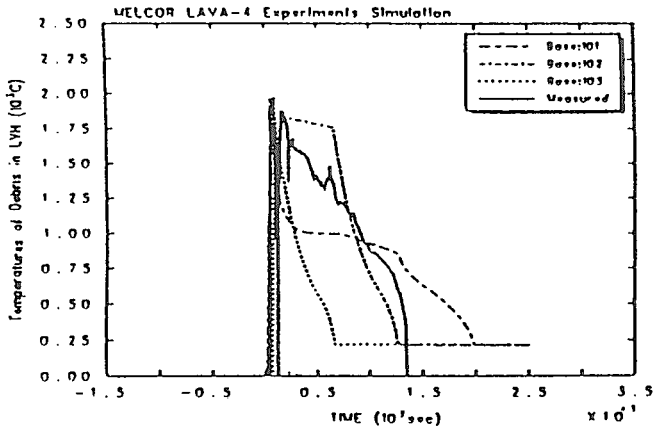



Fig 4 Debris tempertaure in LAVA-4 test

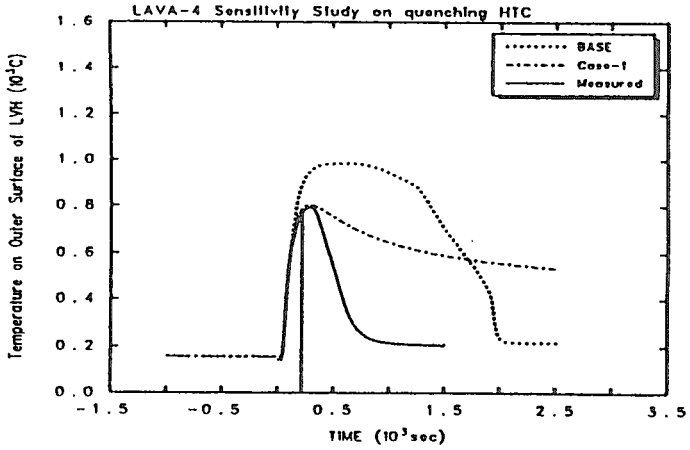



Fig 5 Outside-wall Tempertaure in LAVA-4 test

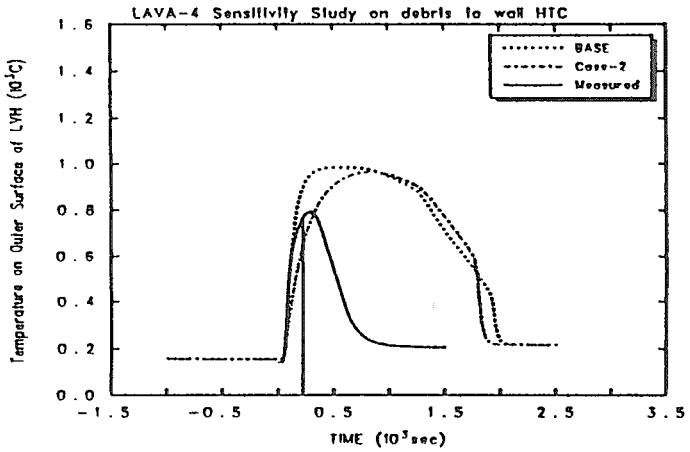



Fig 6 Outside-wall Tempertaure in LAVA-4 test

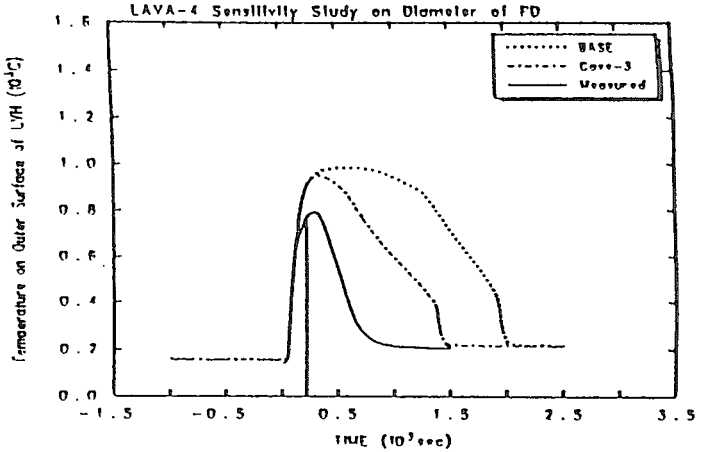
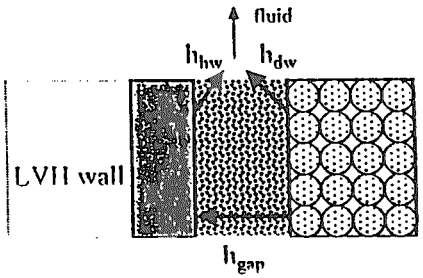



Fig 7 Outside-wall Tempertaure in LAVA-4 test




Bottom-most debris layer

$$q_{dw} = \left[\begin{array}{c}\text{heat loss from debris}\\ \text{to water in gap}\end{array}\right] + \left[\begin{array}{c}\text{heat loss from debris}\\ \text{to inside wall}\end{array}\right] = h_{dw} A_d (T_d'' - T_w) + h_{gap} A_d (T_{h,n}'' - T_{h,n}'')$$

Inner-most wall layer

$$q_{dw} = \left[\begin{array}{c}\text{Heat gain from debris}\\ \text{to inside wall}\end{array}\right] + \left[\begin{array}{c}\text{Heat loss from inside wall}\\ \text{to water in gap}\end{array}\right] = h_{gap} A_d (T_d'' - T_{h,n}'') - h_{hw} A_h (T_{h,n}'' - T_w)$$

Fig 8 Picture of gap cooling model

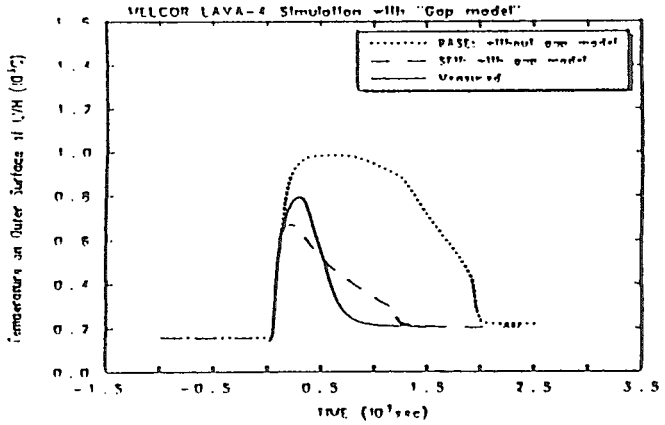



Fig 9 Outside-wall Tempertaure in LAVA-4 test

JP0150103



# 6.5 An Experimental Study on Critical Heat Flux in a Hemispherical Narrow Gap

R. J. Park, S. J. Lee, K. H. Kang, J. H. Kim, S. B. Kim, H. D. Kim
Korea Atomic Energy Research Institute
Dukjin-Dong 150, Yusong-Ku, Taejon, 305-353, KOREA
Tel) 84-42-868-8937
Fax) 82-42-861-2574
E-mail) rjpark@nanum.kaeri.re.kr

J. H. Jeong
Chonan College of Foreign Studies
An-seo-Dong 150, Chun-an, 331-180, KOREA

## ABSTRACT

An experimental study of CHFG (Critical Heat Flux in Gap) has been performed to investigate the inherent cooling mechanism using distilled water and Freon R-113 in hemispherical narrow gaps. As a separate effect test of the CHFG test, a CCFL (Counter Current Flow Limit) test has been also performed to confirm the mechanism of the CHF in narrow annular gaps with large diameter. The CHFG test results have shown that an increase in the gap thickness leads to an increase in critical power. The pressure effect on the critical power was found to be much milder than predictions by CHF correlations of other studies. In the CCFL experiment, the occurrence of CCFL was correlated with the Wallis parameter, which was assumed to correspond to the critical power in the CHFG experiment. The measured values of critical power in the CHFG tests are much lower than CCFL experimental data and the predictions made by empirical CHF correlations.

**Keywords:** CHFG, inherent cooling mechanism, CCFL, critical power, narrow gap

## 1. Introduction

During the TMI-2 accident, molten corium was kept inside the reactor vessel and cooled down without vessel failure, which means that there might be inherent cooling mechanisms that are not known yet clearly. In order to explain the safe cool-down of the relocated corium, a gap-cooling mechanism between relocated corium and reactor pressure vessel is considered to be a plausible one that plays a major role in corium cooling. In order for gap cooling to be effective, the gap size should be large enough and water continue to be supplied through the gap. The maximum power of a heat source removable through boiling is the critical power. At the critical power, the whole of heated surface will be dried off. Therefore, a critical power in hemispherical narrow gaps should be determined to assess effectiveness of the gap cooling mechanism. An experimental study of CHFG has been performed to investigate the inherent cooling mechanism. The objectives of the CHFG test are to measure a critical power using distilled water and R-113 with experimental parameters of system pressure from 1 to 10 atm and gap thickness of 0.5, 1.0, 2.0, and 5.0 mm.

From the visualizing experiments in the hemispherical narrow gap, it was observed that the CCFL phenomena prevented water from wetting the heater surface and induced dryout[1]. That is, CCFL determines the upper limit of cooling capability through gaps that might be formed. In this regard, the CCFL experiments in annular passages with large

diameter are needed. As a separate effect test of the CHFG, a CCFL test has been also performed to confirm the mechanism of the CHF in narrow annular gaps with large diameter. In the CCFL experiment, the occurrence of CCFL was correlated with the Wallis parameter, which was assumed to correspond to the CHF in the CHFG experiment. The measured values of critical power in the CHFG tests are compared with the CCFL experimental data and the predictions made by empirical CHF correlations.

## 2. Test Section

Figure 1 shows the CHFG experimental facility, which consists of an electric heater, a pressure vessel, a heat exchanger and a coolant control system. Four units of stainless steel outer pressure vessel were manufactured to provide gap sizes of 0.5, 1.0, 2.0 and 5.0 mm between the copper shell and the pressure vessel itself. The experiments were performed using de-mineralized water and Freon R-113. The measurements of critical power were made in the range of 1 to 10 atm. The heat generated by the electric heater is removed in a heat exchanger, which takes a role in system pressure regulation as well. A level gauge is installed in the pressure vessel to confirm that the heater is always covered with water during the experiments. The occurrence of dryout was noticed by 66 K-type thermocouple readings. More detailed information on test facility and procedure of CHFG are shown in Reference [2].

Figure 2 shows the schematic diagram of CCFL test facility, which consists of a water supply system, an air supply system, and a test section. The cylindrical test section consists of two walls. The diameter of inner wall is 498 mm and the length of annular gap is 250 mm. The gap sizes are 0.5, 1.0, 2.0, 5.0 mm to correspond to the CHFG test, and the operating pressure is 1 atm. The test section is made of acrylic resign to allow visual observation on the two-phase flow behaviors inside annular gaps. The measuring parameters are water mass flow rate, steam flow rate, and differential pressure between top and bottom of the inner wall. The occurrence of CCFL was defined by a rapid increase of the differential pressure and an increase of water level in the upper part of the inner wall. More detailed information on test facility and procedure of CCFL are shown in Reference [3].

## 3. CHFG Test Results

In the CHFG tests, the dryout region always started from the upper left edge because of CCFL phenomenon. The temperature of this region remains slightly higher than 100°C. The wetted region shrinks and the dryout region expands with time increase. The velocity of the dryout expansion and temperature increase rate of the dryout region get larger with time. This is because the local heat flux at the wetted region increases due to extra heat transferred from the dryout region by conduction. When the dryout region expands to the bottom of the copper shell, the temperature increase of that location is so fast that the heater power should cut off immediately for heater protection. This heat flux with which the dryout region undergoes self-expansion is defined as the critical power.

Figure 3 shows CHFG test results on critical power using water and R-113. As shown in Fig. 3, an increase in gap size from 0.5 mm to 1 mm almost doubles the critical power but that from 1 mm to 2 mm affects critical power just a little. Namely, an increase in the gap thickness leads to an increase in critical power. The measured critical power using R-113 are 60 % lower than that using water due to the lower boiling point, which is different from the pool boiling condition. An increase in pressure leads to small increase in critical power.

Figure 4 shows the comparison of the CHFG test results on critical power with other studies of CHF experiments in gaps of rectangular channels and horizontal plates. Chang & Yao carried out CHF experiments with test sections of vertical annulus at atmospheric pressure and developed the following correlation[4]:

$$\frac{q_{CHF}}{\rho_g h_{fg}} \cdot \sqrt{\frac{\rho_g}{gD\Delta\rho}} = \frac{0.38}{\left(1+\sqrt[4]{\rho_g/\rho_l}\right)^2 \cdot (L/s)} \qquad (1)$$

where, $q_{CHF}$, $g$, $D$, $\rho_l$, $\rho_g$, $h_{fg}$, $L$ and $s$ are the critical heat flux, gravitational

acceleration, diameter, liquid density, gas density, latent heat of evaporation, heated length and gap size, respectively. Monde et al.[5] carried out the CHF experiment at atmospheric pressure in vertical rectangular channels. They reported the following empirical correlation:

$$\frac{q_{CHF}}{\rho_g h_{fg}} \cdot \sqrt[4]{\frac{\rho_g^2}{g\sigma\Delta\rho}} = \frac{0.16}{1+6.7\times10^{-4}(\rho_l/\rho_g)^{0.6}(L/s)} \qquad (2)$$

where, $\sigma$ is the steam-water surface tension.

For comparison, we put the parameters of the present experiments into the above correlations and the gap size was assumed to be 1 mm. Koizumi et al.'s CCFL measurements[6] are also compared. They carried out CCFL experiments in narrow-gap annular passages and presented their experimental data. Since they did not suggest any CCFL correlation, we did some regression analysis to develop the following CCFL correlations:

$$j_g^{*1/2} + 0.23 j_l^{*1/2} = 0.32 \quad \text{for 2 mm gap} \qquad (3)$$

$$j_g^{*1/2} + 0.35 j_l^{*1/2} = 0.35 \quad \text{for 1 mm gap} \qquad (4)$$

where, $j_k^* = j_k \cdot \sqrt{\frac{\rho_k}{gD_{eq}\Delta\rho}}$, $D_{eq} = D_o - D_i$

In order to present them in Fig. 4, superficial velocities are changed into corresponding heat flux that can produce the same mass flow of steam. Koizumi et al.'s CCFL correlation seems to be close to the present measurements in terms of value and pressure trend, while Chang & Yao and Monde et al`s correlations predict much higher. The reason is thought to be that, in the present experiments, CCFL prevents water from penetrating into the top end of the gap and global dryout occurred at lower heat fluxes. Compared with those two empirical CHF correlations, the pressure effect of the present results seems to be quite small. As those two CHF correlations were developed based on the data measured under atmospheric pressure, the pressure trend predicted by them might not be correct. Especially, Monde et al.'s correlation shows rapid increase in CHF with system pressure. It does not seem to be appropriate to use at an elevated pressure.

## 4. CCFL Test Results

In the CCFL experiment, water was accumulated with constant level in the upper plenum and differential level in the upper plenum and differential pressure across gap was very small in normal condition. When CCFL occurs, significant increase in the differential pressure and in the water level was observed.

In the previous studies, the CCFL test data were presented by following Wallis parameter[7] and Kutateladze number[8].

$$j_g^{*1/2} + m_w j_l^{*1/2} = C_w \qquad (5)$$

$$K_g^{*1/2} + m_k K_l^{*1/2} = C_k \qquad (6)$$

where,

$$j_k^* = j_k \sqrt{\frac{\rho_k}{gD(\rho_l-\rho_g)}}, \quad K_k^* = j_k \sqrt[4]{\frac{\rho_k^2}{g\sigma(\rho_l-\rho_g)}} \qquad (7)$$

As shown in Fig. 5, the occurrence of CCFL in the CCFL test was correlated with Wallis parameter in the gap thickness of 1.0 mm, as follows:

$$j_g^{*1/2} + 0.384 j_l^{*1/2} = 0.613 \qquad (8)$$

Figure 6 shows CCFL test results with other correlations, which were Chang & Yao and Monde's. The CCFL test data were assumed to correspond to the following CHF in the CHFG experiment, namely, the superficial velocities in the CCFL test are changed into corresponding heat flux that can produce the same mass flow of steam.

$$\frac{q_{CHF}}{\rho_g h_{fg}} \cdot \sqrt{\frac{\rho_g}{gD\Delta\rho}} = \frac{S}{D} \bullet \frac{2C_w{}^2}{\left(1 + m_w \bullet \sqrt[4]{\rho_g / \rho_l}\right)^2} \qquad (9)$$

As shown in Fig. 6, the CCFL experimental data are much higher than the measured values of CHFG tests on critical power. The variation trend, however, are similar. The higher value of critical power in the CCFL experiment will be evaluated using more CCFL experimental data on other gap sizes of 0.5, 2.0, 5.0 mm.

## 5. Conclusion

The CHFG(Critical Heat Flux in Gap) tests have been performed to identify heat transfer characteristics. As a separate effect test of the CHFG test, a CCFL test has been also performed to confirm the mechanism of the CHF in narrow annular gaps with large diameter. The CHFG test results have been shown the measured critical power values were found to be lower than those measured in planar and annular gaps. The pressure effect on the critical power was found to be much milder than predictions by CHF correlations of other studies. An increase in the gap thickness leads to an increase in critical power in the CHFG experiment. The measured values of CHFG tests on critical power are much lower than CCFL experimental data. It is necessary to test the CHFG with large gap thickness and the CCFL with variable gap size. Finally, CHFG correlation will be developed using the CCFL test data.

## ACKNOWLEGMENTS

This study has been carried out under the Nuclear R&D Program by the Korean Ministry of Science and Technology.

## REFERENCES

(1) J. H. Jeong, R. J. Park, and S. B. Kim, "Visualization Experiments of the Two-Phase Flow Inside a Hemispherical Gap," Int. Commu. Heat & Mass Transfer, Vol. 25, No. 5, pp. 693-700, 1998
(2) J. H. Jeong, R. J. Park, S. B. Kim, "Thermal-Hydraulic phenomena relevant to global dryout in a hemispherical narrow gap," Heat and Mass Transfer 34, 321-328, 1998
(3) S. J. Lee, R. J. Park, S. B. Kim, K. H. Kang, J. H. Jeong, "An Experimental Study on the CCFL in Narrow Annular Gaps with Large Diameter," Proc. of KNS Spring, Meeting, Pohang, Korea, May 28-29, 1999
(4) Y. Chang and S. Yao, "Critical Heat Flux of Narrow Vertical Annuli with Closed Bottoms," J. of Heat Transfer 105, pp. 192-195, 1983
(5) M. Monde., H. Kusuda, and H. Uehara, "Critical Heat Transfer during Natural Convective Boiling in Vertical Rectangular Channels Submerged in Saturated Liquid," J. Heat Transfer 104, pp. 300-303, 1982
(6) Y. Koizumi, H. Nishida, H. Ohtake, and T. Miyashita, "Gravitational Water Peneration into Narrow-gap Annular Flow Passages with Upward Gas Flow," Proc. of NURETH-8, Vol. 1, pp. 48-52, 1997
(7) G. B. Wallis and S. Makkenchery, "The Hanging Film Phenomenon in Vertical Annular Two-Phase Flow," J. Fluids Engineering 96(3), pp.297-298, 1974
(8) S. S. Kutateladze, "Heat Transfer in Condensation and Boiling," USAEC Rep-tr 3770, 1952

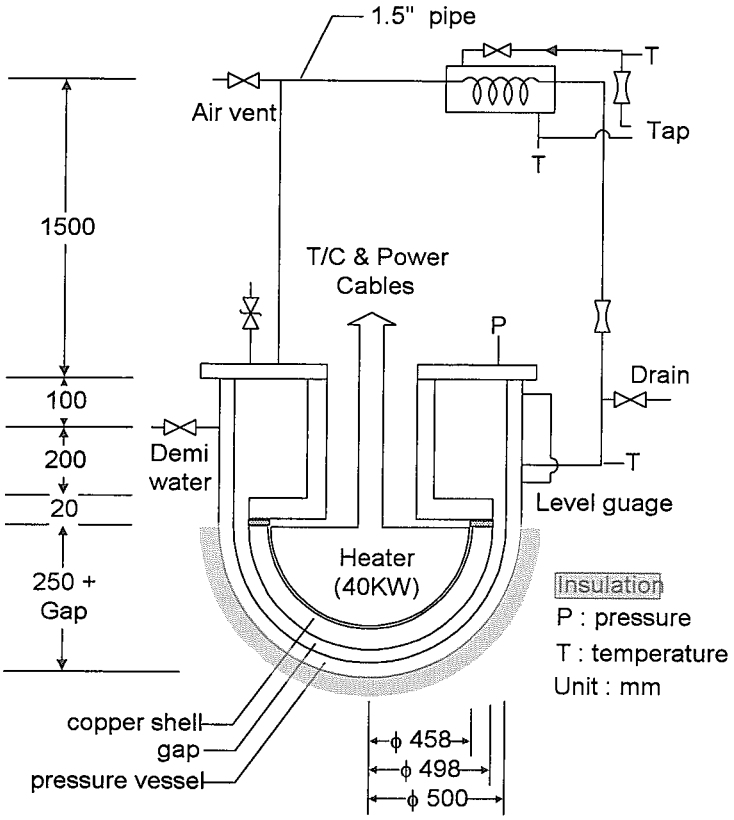



Fig. 1 Schematic diagram of the CHFG test facility.

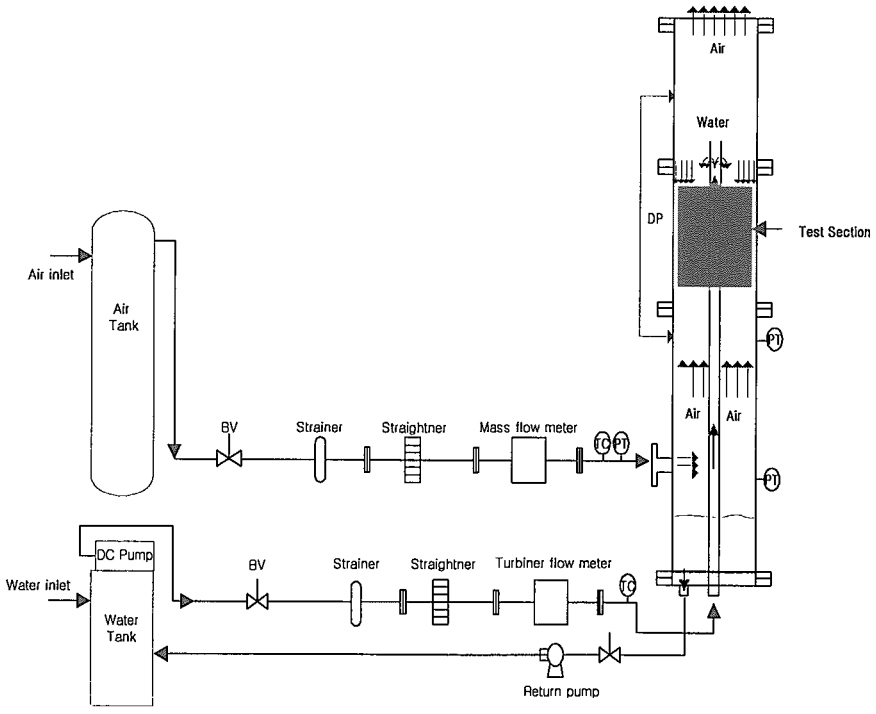



Fig. 2 Schematic diagram of the CCFL test facility.

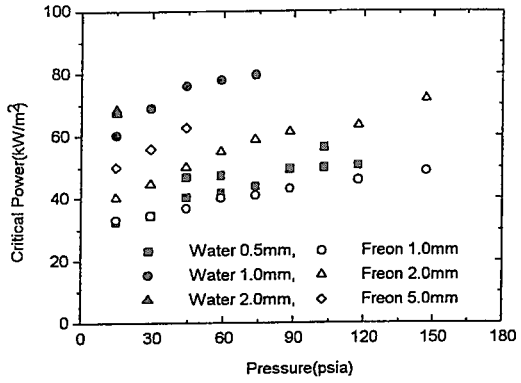



Fig. 3 CHFG test results.

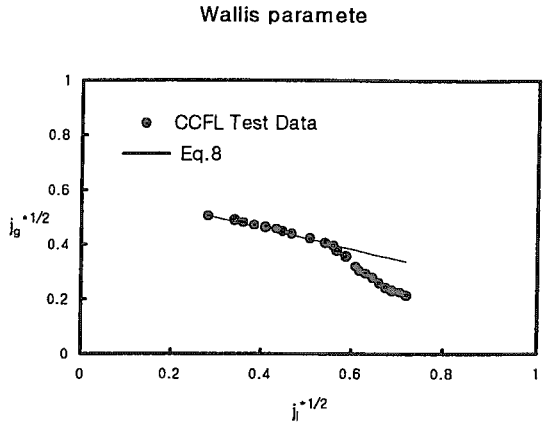



Fig. 5 CCFL test results using Wallis parameter.

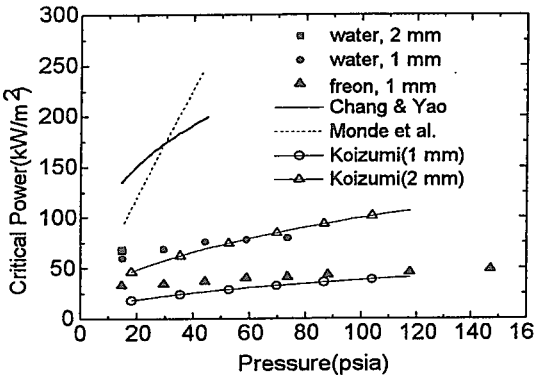



Fig. 4 Comparison of CHFG test results with other correlations.

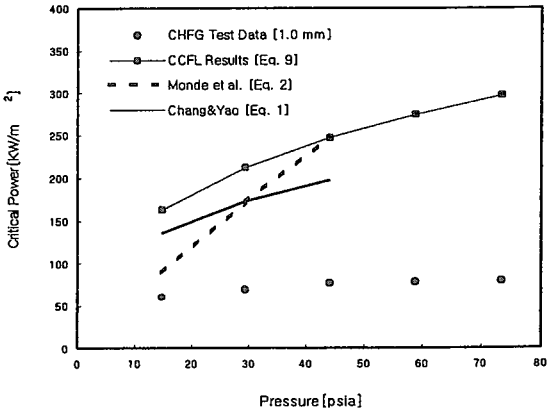



Fig. 6 Comparison of CCFL test results with CHFG test results and other correlations.

This is a blank page.

# 7. Session 6

# Accident Management I

## Chairperson:

Y. Abe (Yamagata Univ.)
H. Nakamura (JAERI)

This is a blank page.

JP0150104



# 7.1 Development of Hybrid Hydrogen Control System

Hiroyuki Nakakura* and Tetsuo Gora**

** Nuclear Fuel & Core Safety Engineering Department, Kobe Shipyard & Machinery Works*
*Mitsubishi Heavy Industries, Ltd.*
*1-1-1, Wadasaki-cho, Hyogo-ku, Kobe 652-8585 Japan*
*Phone:81(78)672-2563 Fax:81(78)672-3479*
*E-mail:nakakura@ncore.kobe.mhi.co.jp*
*** Combustion & Heat Transfer Laboratory, Takasago R&D Center*
*Mitsubishi Heavy Industries, Ltd.*
*2-1-1 Shinhama Arai-cho, Takasago, Hyogo Pref. 676-8686 Japan*
*Phone:81(794)45-6769 Fax:81(794)45-6089*
*E-mail:gora@wl.trdc.mhi.co.jp*

## *Abstract*

Catalytic recombiners disposing of hydrogen in severe accidents of nuclear power plants generally has a weak property for poison and steam environment. Spherical catalyst is robust for poison because of porosity with large specific area, but relatively weak for steam because of easily condensing steam by capillary phenomenon. Plate-type catalyst is conversely thought to be robust for steam but weak for poison. Hybrid hydrogen control system that consists of catalytic layers filled with spherical catalyst, barlike heater penetrating catalytic layers and covering box improves weakness of spherical catalyst by heating and also has function of an igniter.

We first investigated the relation between resistance to steam and material sort with diameter of spherical catalyst to develop hybrid hydrogen control system. We verified that Pt in a small diameter was superior as recombiner catalyst. We successively carried out integrated tests by optimized catalytic layer shape to verify performance of hybrid hydrogen control system as a recombiner and an igniter. Hybrid hydrogen control system is prospected to be applied to commercial nuclear power plants.

*Keywords* : severe accident, hydrogen, recombiner, igniter, catalyst

## 1.INTRODUCTION

In the case where severe accident occurs in nuclear power plant, amount of hydrogen is generated by water-Zr reaction and water radiorosis in containment vessel. Because reach of hydrogen concentration to 13 volume % is very dangerous to detonate, hydrogen control system is required for nuclear power plants especially in small containment vessel. Among hydrogen control system, catalytic recombiner and glowplug-type hydrogen igniter are widely introduced to commercial nuclear power plants.

Catalytic recombiners disposing of hydrogen in severe accidents of nuclear power plants generally has a weak property for poison and steam environment. Spherical catalyst is robust for poison but relatively weak for steam, because it is porous and has a large specific area. Pore easily condenses steam by capillary phenomenon. Plate-type catalyst is conversely thought to be robust for steam but relatively weak for poison.

## 2.HYBRID HYDROGEN CONTROL SYSTEM(HHCS)

Heater enhances robustness of spherical catalyst for steam by evaporating water in pore. Hybrid hydrogen control system that consists of catalytic layers filled with spherical catalyst, barlike heater penetrating catalytic layers and covering box improves weakness of spherical catalyst by heating and also has function of an igniter. After all, hybrid hydrogen control system recombines at low hydrogen concentration such as 2%, and ignites hydrogen at middle hydrogen concentration such as 8%. The representative design condition is that HHCS recombines hydrogen at the rate of 0.2g/s(temporary value) in 4% hydrogen concentration on 80% saturated steam condition and ignites hydrogen below 8% hydrogen concentration on 50% saturated steam condition. Figure-1 shows a schematic of hybrid hydrogen control system. Mixed gas flows in cover box, and hydrogen is recombined to generate heat. Combustion gas is accelerated in cover box by chimney effect and flows out.

## 3.TESTS

We carried out various tests shown in Table-1. We carried out 3 kinds of tests. We first investigated steam absorption characteristics for spherical catalysts of Pt and Pd. We successively investigated recombination performance for spherical catalysts of Pt and Pd after steam absorption. We last estimated HHCS performance as a recombiner and an igniter through integrated tests. Figure-2 shows test specimen of catalytic layer and Figure-3 shows a combustion test facility.

Table-1 Test Matrix

| CASE | CATALYST | | $C_{H2}$ | $C_{H2O}$ | TEMP. | HEATER | TEST RESULTS(Fig-NO) |
|---|---|---|---|---|---|---|---|
| STEAM ABSORP-TION | Pt, Φ1mm/Φ4mm | | 0% | 1% | 20℃ | OFF | 10% MASS INCREASE(Fig-4) |
| | | | | 80% | 94℃ | OFF | 70%/40% INCREASE(Fig-5) |
| | | | | 12% | 50℃ | OFF | 30%/27% INCREASE(Fig-5) |
| | Pd, Φ4mm | | 0% | 80% | 94℃ | OFF | 40% MASS INCREASE |
| RECOMBI-NATION* | Pd, Φ4mm | | 2% | 12% | 50℃ | OFF | NO REACTION(Fig-6) |
| | Pd, Φ4mm | | 4% | 12% | 50℃ | OFF | REACTION(LATE) |
| | Pt, Φ4mm | | 2% | 12% | 50℃ | OFF | NO REACTION |
| | Pt, Φ4mm | | 2% | 80% | 94℃ | OFF | REACTION(LATE) |
| | Pt, Φ4mm | | 2% | 0% | 50℃ | OFF | REACTION(EARLY) |
| | Pd, Φ4mm | | 2% | 0% | 50℃ | OFF | REACTION(EARLY) |
| | Pt, Φ1mm | | 2% | 80% | 94℃ | OFF | REACTION(Fig-7) (VERY LATE) |
| | Pt, Φ1mm | | 2% | 0% | 50℃ | OFF | REACTION(EARLY) |
| | Pt, Φ1mm | | 2% | 80% | 94℃ | ON | REACTION(EARLY)(Fig-8) |
| INTEG-RATED | RECOM-BINER | Pt, Φ1mm 5PLATES | 2,4,6% | 0,80% | 50,94℃ | ON | $H_2$ REDUCTION RATE(Fig-9) 0.2g/s : 50 SHEETS** |
| | IGNITER | | 2%～10% | 0,30, 50% | 50,70,82 ℃ | ON | IGNITED ON (Fig-10) $H_2$ : 3%～10% |

(under atmospheric pressure)
(*:test on wet condition were carried out after full steam absorption)
(**:size of catalytic layer=100mm×250mm×5mm)

### 3.1 Steam Absorption Test

We carried out steam absorption test on atmospheric condition and saturated steam condition. Figure-4 shows steam absorption test result of Pt spherical catalyst in 4mm and 1mm diameter on atmospheric condition. Mass increase of spherical catalyst by steam absorption on atmospheric condition is about 10% regardless of diameter. Figure-5 shows saturated steam absorption test result of Pt spherical catalyst in 4mm and 1mm diameter. Mass increase of spherical catalyst by saturated steam absorption depends on steam concentration more than diameter. Mass increase ratio of spherical catalyst by saturated steam absorption is about 70% for 1mm and 40% for 4mm in diameter. By other tests, we confirmed that saturated steam absorption of spherical catalyst was the same with Pt and Pd.

### 3.2 Recombination Tests

We carried out recombination tests with various condition of catalyst material, diameter, saturated steam concentration and heater power on/off condition.

Figure-6 shows recombination test result of Pd spherical catalyst on 2% hydrogen concentration under 50℃ saturated steam condition without heater power. We averaged temperature in three parts of catalytic layer in upper, middle and lower stream section. Before the test, spherical catalysts were adequately made absorb steam under 94℃ saturated steam condition. This test result shows no increase of temperature in catalytic layer, which means no recombination on 2% hydrogen concentration under 50℃ saturated steam condition after full steam absorption. By other tests, we confirmed temperature increase on 94℃ saturated steam condition or 4% hydrogen concentration.

Figure-7 shows recombination test result of Pt spherical catalyst on 2% hydrogen concentration under 50℃ saturated steam condition without heater power. Figure-8 shows the same recombination test result with catalytic layer heated by a heater. Before the tests, spherical catalysts were also adequately made absorb steam under 94℃ saturated steam condition. The test result without heater power shows very late increase of temperature in catalytic layer, while the test result with catalytic layer heated by a heater shows prompt increase of temperature in catalytic layer. These test results show a heater enhances performance of spherical catalyst to recombine immediately after hydrogen injection.

By other tests, we confirmed that small diameter catalyst had good resistance to steam. We chose Pt in 1mm diameter as spherical catalyst.

### 3.3 Integrated test

Figure-9 shows integrated test results for recombiner performance which were carried out under dry condition in 50℃ and wet condition in 94℃ saturated steam of 80% concentration. We tested with 5 sheets of catalytic layers in height of 100mm×width of 100mm×depth of 5mm with space of 5mm. These test results show spherical catalyst recombines on wet condition less than on dry condition especially at higher hydrogen concentration such as 6%.

Figure-10 shows integrated test results for igniter performance. This test result shows that the heater of HHCS ignites on low hydrogen concentration at low steam concentration. And the heater can ignite on 10% hydrogen concentration at the flammability limit of 50% steam concentration.

## 4. Conclusions

We confirmed that spherical catalyst decreases recombination performance after steam absorption and heater enhances recombination performance of spherical catalyst through various tests. We also confirmed HHCS had suitable performance of a recombiner and an igniter to dispose hydrogen generated in severe accident of nuclear power plants. HHCS is effective for robustness of catalytic recombiner against severe steam condition and prospected to be applied to commercial nuclear power plants.

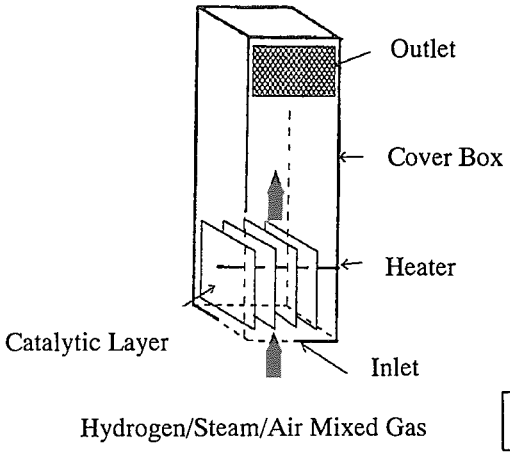



Figure-1 Hybrid Hydrogen Control System

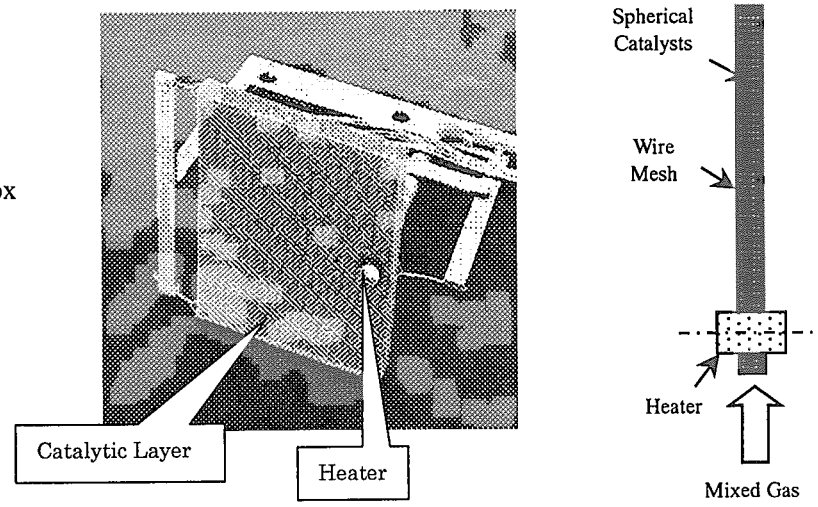



Figure-2 Test Specimen Of Catalytic Layer

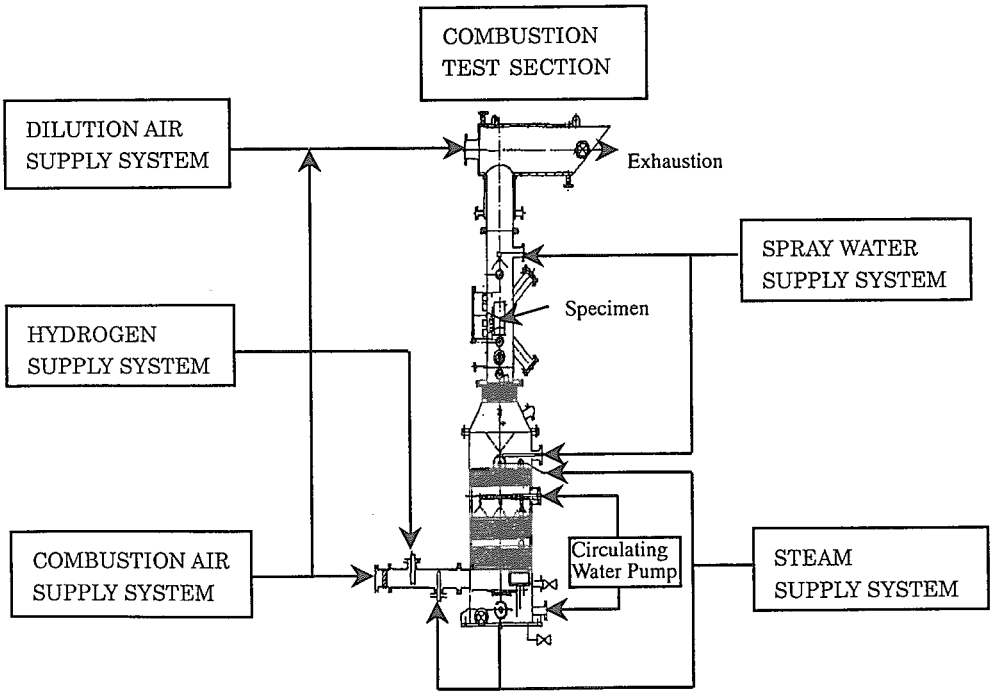



Figure-3 Test Facility

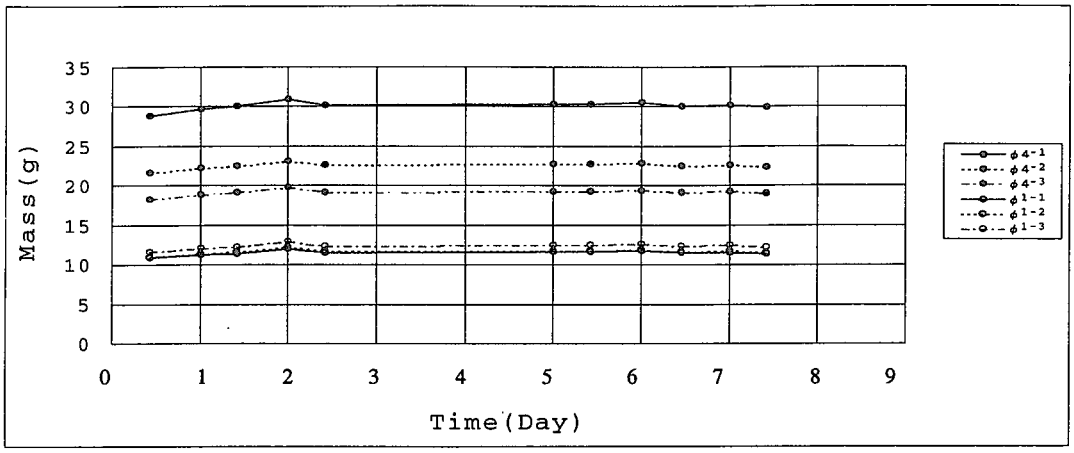



Figure-4 Steam Absorption Test(Atmospheric Condition)

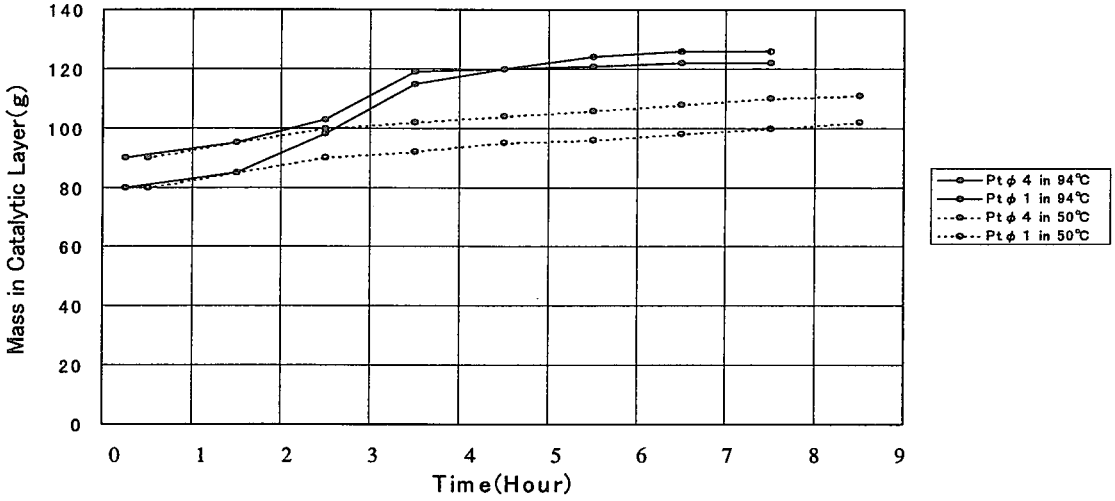



Figure-5 Steam Absorption Test(Saturated Steam Condition-50&94℃)

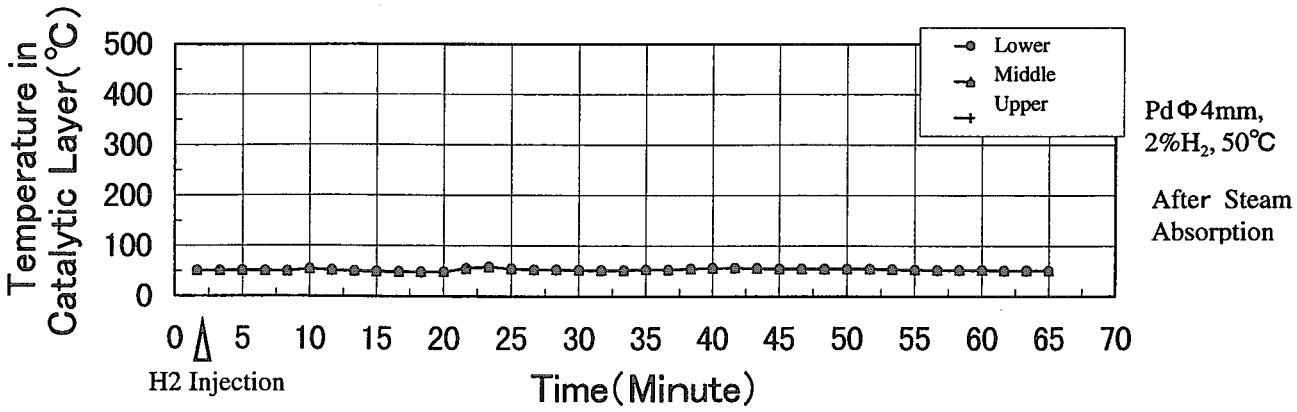



Figure-6 Recombination Test After Saturated Steam Condition

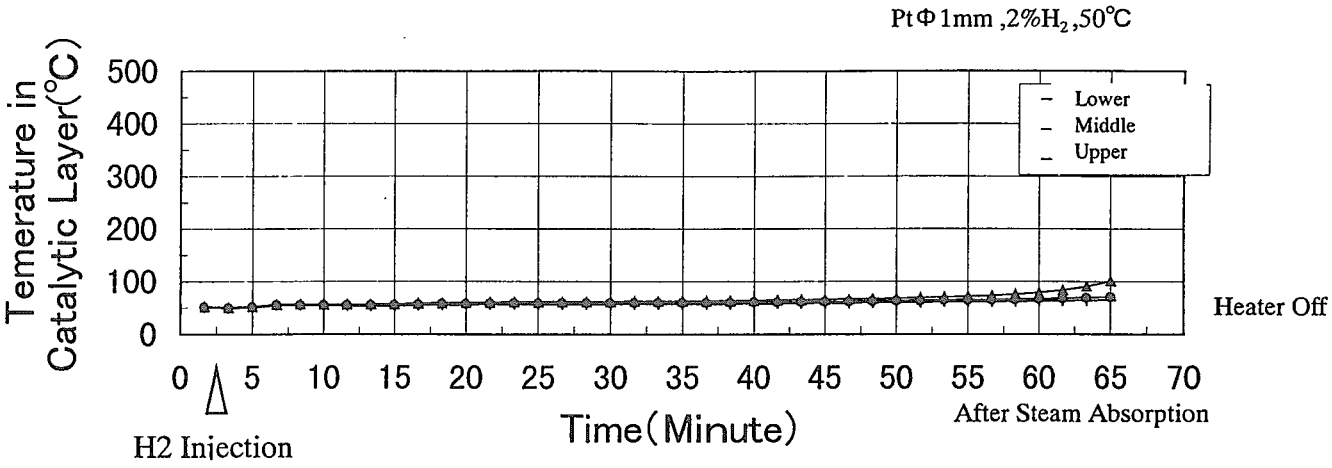



Figure-7 Recombination Test without Heater power

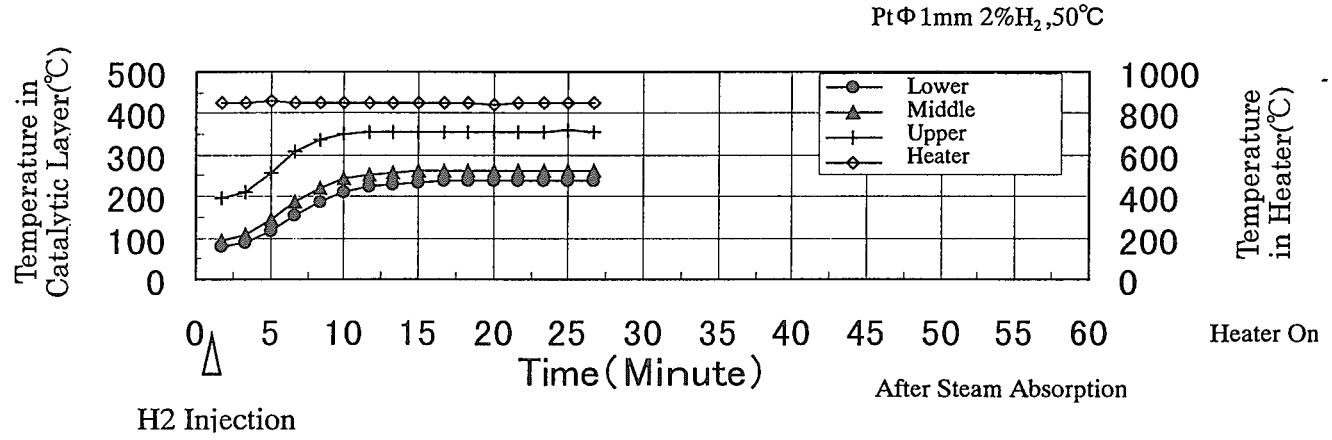



Figure-8 Recombination Test with Catalytic Layer Heated by Heater

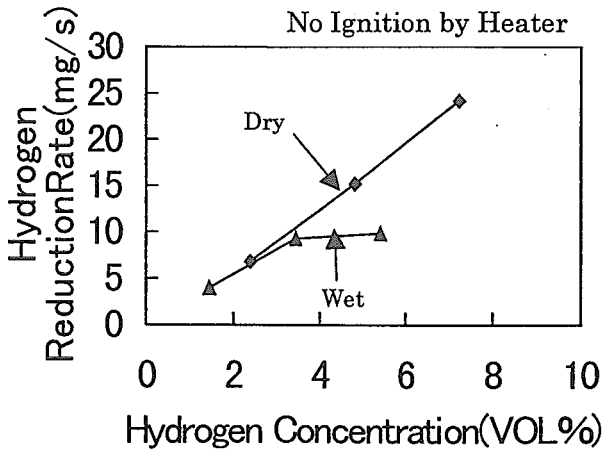



Figure-9 Hydrogen Reduction Rate of Recombiner

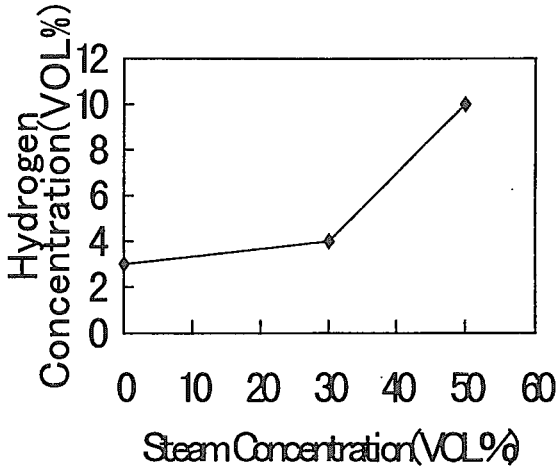



Figure-10 Hydrogen Ignition Concentration of Heater

JP0150105



# 7.2 TESTS ON PASSIVE AUTOCATALYTIC RECOMBINER PERFORMANCE FOR BWR APPLICATION

**Makoto Harada, Yuji Yamamoto, Hirohide Oikawa*,**
*Toshiba Corporation,*
*8, Shinsugita-cho, Isogo-ku, Yokohama 235-8523, Japan*
*Phone: + 81-45-770-2060, Fax: + 81-45-770-2179*
*E-mail: hirohide.oikawa@toshiba.co.jp*

**Shozo Yamanari,**
*Hitachi Works, Hitachi, Ltd.*

**Takeyuki Inagaki, and Toshiyuki Zama**
*Tokyo Electric Power Company*

## ABSTRACT

This paper describes overview of the test program to confirm passive autocatalytic recombiner performance for BWR application, and the first result obtained from the initial part of the test program. The program consists of separate effect test using catalyst test loop to investigate recombiner performance under various atmospheric conditions, and test for startup behavior and recombiner capability in the scaled test vessel. The catalyst test loop is designed so that inlet/exit gas concentration and gas/catalyst temperature can be measured, varying flow rate, gas content or presence of poisoning material. As the first stage, a series of tests was conducted, simulating natural circulation flow rate inside containment, inert (low oxygen concentration) atmosphere, and poisoning material concentration assumed in the conventional licensing evaluation of radiological consequence. The test data suggest that catalytic recombiner has sufficient performance in the BWR specific (inert) condition, and under presence of poisoning material postulated in hypothetical accident condition. The effect of low oxygen concentration or containment spray water on startup behavior and recombiner performance will be investigated in the following vessel test series.

**Keywords:** hydrogen, flammable gas, catalytic recombiner

## 1. INTRODUCTION

The catalytic recombiner performs its function passively and has advantages such as the robustness during accident, easy maintenance and low cost compared with the conventional active recombiner. Although several experiments[1-3] have been performed to investigate catalytic recombiner behavior and establish its performance evaluation basis, most of those experiments focused on PWR specific condition.

Japanese BWR industry has been also conducting study on catalytic recombiner application to light water reactor. The feasibility study on applicability of the catalytic recombiner developed by German manufacturers (Siemens and NIS) to the current product line plant, was started in 1996. After the feasibility study, it was decided to proceed to the next study phase focused on experimental investigation considering BWR specific condition.

This paper describes overview of the test program to confirm passive autocatalytic recombiner performance for BWR application. The program consists of separate effect test using catalyst test loop to investigate recombiner performance under various atmospheric conditions, and test for startup behavior and recombiner capability in the scaled test vessel. The first result obtained from the initial part of the test program is also presented.

## 2. PROGRAM OVERVIEW

The overall test program of current phase consists of two types of experiment. The first part is separate effect test using catalyst test loop to investigate recombiner performance under various atmospheric conditions. A reaction chamber in the test loop contains typical unit cell (a pair of catalyst plate and flow channel between the two plates) of full size PAR. This loop test is aiming at observation of catalyst fundamental behavior under postulated post-accident condition, and provides database for correlation of recombination reaction.

The second part is test for startup behavior and recombiner capability in the scaled test vessel. This test is just started in the second half of 1999, and the effect of low oxygen concentration or containment spray water on startup behavior and recombiner performance will be investigated in this vessel test series.

## 3. CATALYST TEST LOOP AND EXPERIMENTAL RESULT

### (1) Experimental Facility

Schematic diagram of the catalyst test loop, and structure of test section (chamber and catalyst cartridge plate) are shown in Figure 1 and Figure 2, respectively. The test loop is designed so that inlet/exit gas concentration and gas/catalyst temperature can be measured, varying flow rate, gas content or existence of poisoning material in the flow. Two pieces of scaled (full height and reduced width) cartridge, which contain catalyst particles supplied by NIS, are installed in the test section. Mixture of steam, nitrogen, oxygen and hydrogen, simulating typical post accident atmospheric condition inside BWR containment, are supplied from upstream of test section. Material that acts as potential poison against catalytic reaction, such as iodine, can be added to the gas content. The inlet and exit gas (hydrogen and oxygen) concentration is measured periodically using gas chromatograph. Thermocouples are located in the flow channel, and embedded in the catalyst cartridge along the flow direction. Iodine concentration at the inlet and exit of test section is measured by a spectroscope.

### (2) Test Items and Conditions

As the first stage, a series of tests was conducted, simulating natural circulation flow rate inside containment, inert (low oxygen concentration) atmosphere, and poisoning material concentration assumed in the conventional licensing evaluation of radiological consequence. Major test items to be performed in the separate effect test at the catalyst loop are listed in Table 1, and typical test conditions are listed in Table 2.

### (3) Test Result

The first result obtained from the initial part of the program is described below. Figure 3 shows the effect of hydrogen concentration on the hydrogen depletion rate. In these test cases, inlet oxygen concentration was set to 3.5 %, and hydrogen concentration was varied from 0.5% to 3.5%. The reaction occurs even at the lowest hydrogen concentration (0.5%) and saturated steam environment, and depletion rate increases gradually with increase of the concentration. Fischer[1] et al. have been proposed empirical hydrogen depletion rate correlations, typically in the following form.

$$DR = \alpha C^{\beta} (P/T) \quad (1)$$

Where,

DR : depletion rate
C : hydrogen concentration
P : pressure
T : temperature

These existing correlations do not account depletion rate dependency on the oxygen concentration, or only provides simple constant reduction factor for low oxygen concentration. As can be seen from figure, observed hydrogen depletion rate lies between

predictions with and without simple reduction factor for low oxygen concentration, and close to the full capability physically limited by the amount of hydrogen inflow. The result demonstrates that catalytic recombiner performs its function with high (> 80%) efficiency even at low hydrogen and oxygen concentration, and reduction factor in the existing correlation is conservative under typical oxygen concentration in inerted BWR containment.

The effect of oxygen concentration on the hydrogen depletion rate is shown in Figure 4. Inlet hydrogen concentration is fixed at 3.5% in these cases, and the effect of oxygen concentration was examined between the range from 0.5% to 3.5%. This result implies that depletion rate clearly depends on oxygen concentration, and catalytic recombiner has better potential performance (for oxygen concentration > 1 %) than those predicted by existing correlation with constant reduction factor for low oxygen concentration. (For oxygen concentration lower than 1 %, the performance is limited by the amount of oxygen inflow.)

Temperature distributions of catalyst plate and flow channel at typical condition are shown in Figure 5. The catalyst centerline temperature reaches the maximum of 280℃ at about 1/3 of total catalyst cartridge length from the inlet, and gradually decreases through the rest of cartridge. This temperature distribution suggests that catalyst retains potential margin against degradation caused by poisoning material. Gas temperature reaches around 200℃ at the exit of flow channel.

Figure 6 is an example of long term catalyst performance under presence of iodine. In this test, the concentration of poisoning material is based on the assumption in the conventional licensing evaluation of radiological consequence (TID-14844). The catalyst performance was kept as much as the initial level over 20 hours even under hypothetical poisoning material (iodine) concentration.

## 4. CONCLUSIONS

The overview of the test program, aiming at confirmation of passive autocatalytic recombiner performance for BWR application, was summarized. As the first stage, a series of tests was conducted at the catalyst test loop, simulating natural circulation flow rate inside containment, inert (low oxygen concentration) atmosphere, and presence of poisoning material. The recombiner performed its function from the conditon of low (0.5%) flammable gas concentration and saturated steam environment. For most of test cases, observed catalyst performance was higher than prediction by existing correlation assuming simple constant reduction factor for low oxygen concentration. The catalyst initial performance was kept over 20 hours even under hypothetical poisoning material (iodine) concentration. The data suggest that catalytic recombiner has sufficient capability in the BWR specific (inert) condition, and under presence of poisoning material postulated in hypothetical accident condition.

## ACKNOWLEDGMENT

This program has been mutually supported by Japanese BWR industry. The authors also express their gratitude for fruitful comments from engineers who joined technical discussion.

## REFERENCES

1. K.Fischer, "Qualification of a Passive Catalytic Module for Hydrogen Mitigation," Proc. Int. Conf. on New Trends in Nuclear System Thermohydraulics, Vol.2, May 1994.
2. O.Braillard et al., "Tests of Passive Catalytic Recombiners (PARS) for Combustible Gas Control in Nuclear Power Plants," Proc. 2nd Int. Topical Mtg. on Advanced Reactors Safety (ARS '97), June 1997.
3. T.K.Blanchat and A.Malliakos, "Performance Testing of Passive Autocatalytic Recombiners," NUREG/CR-6580, June 1998.

Table 1 Test items
(Separate effect test in the catalyst loop)

| |
|---|
| Effect of hydrogen concentration |
| Effect of oxygen concentration |
| Effect of gas velocity |
| Effect of poisoning material ($I_2$ etc.) |

Table 2 Typical test conditions

| | |
|---|---|
| Pressure | 0.13 MPa |
| Inlet gas flow temperature | 60 ℃ |
| Inlet gas flow rate | 0.2 - 0.4 m/s |
| Hydrogen concentration | 0.5 - 3.5 % |
| Oxygen concentration | 0.5 - 3.5 % |
| Iodine concentration | 40 mg/m$^3$ |

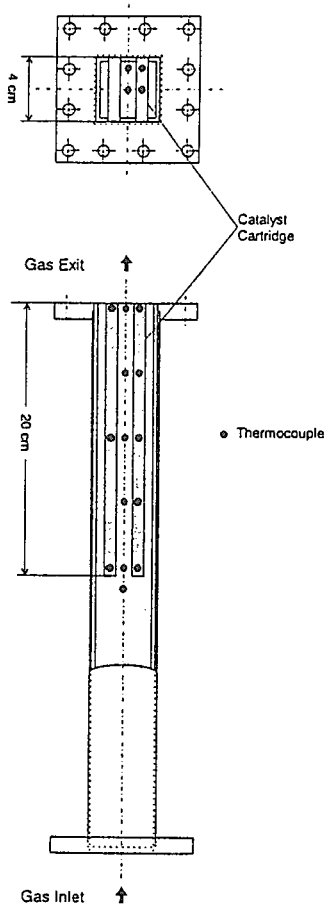



Fig.2 Test section
(Catalyst plate and chamber)

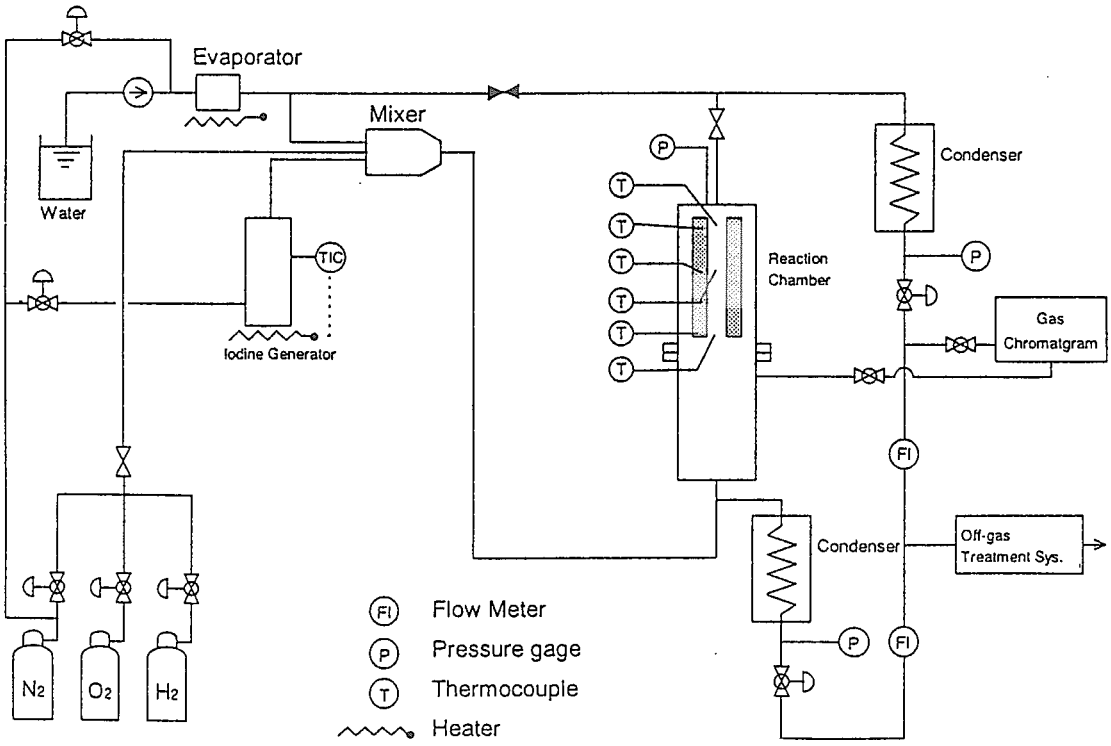



Fig.1 Schematic diagram of the catalyst test loop

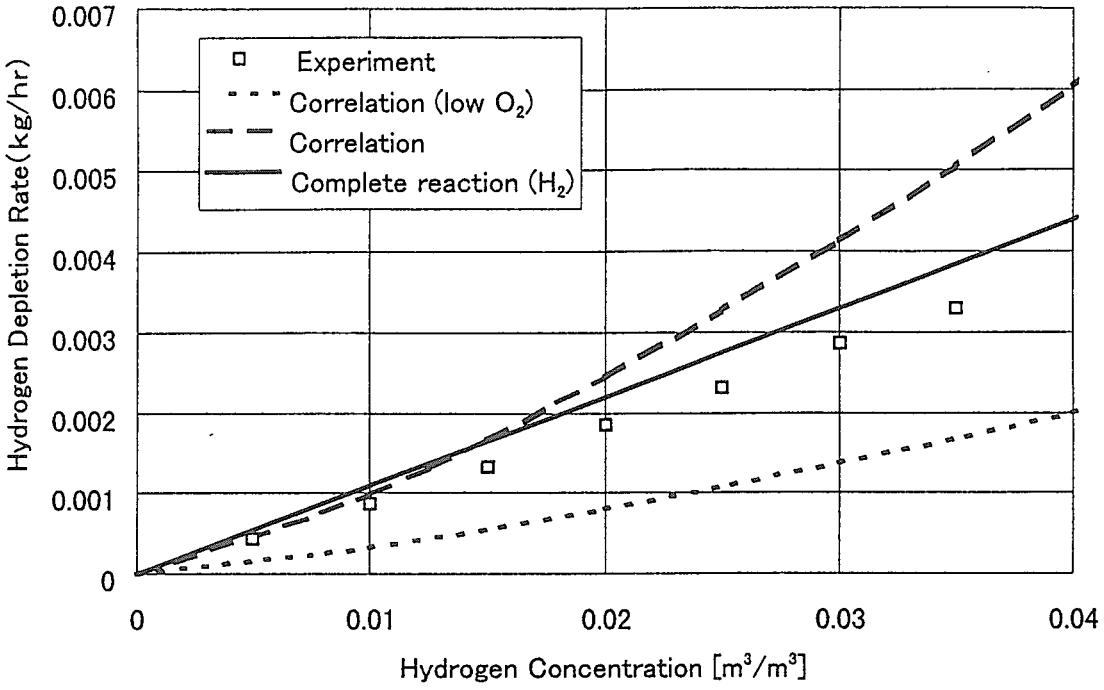



Fig.3 Hydrogen depletion rate (Effect of hydrogen concentration)

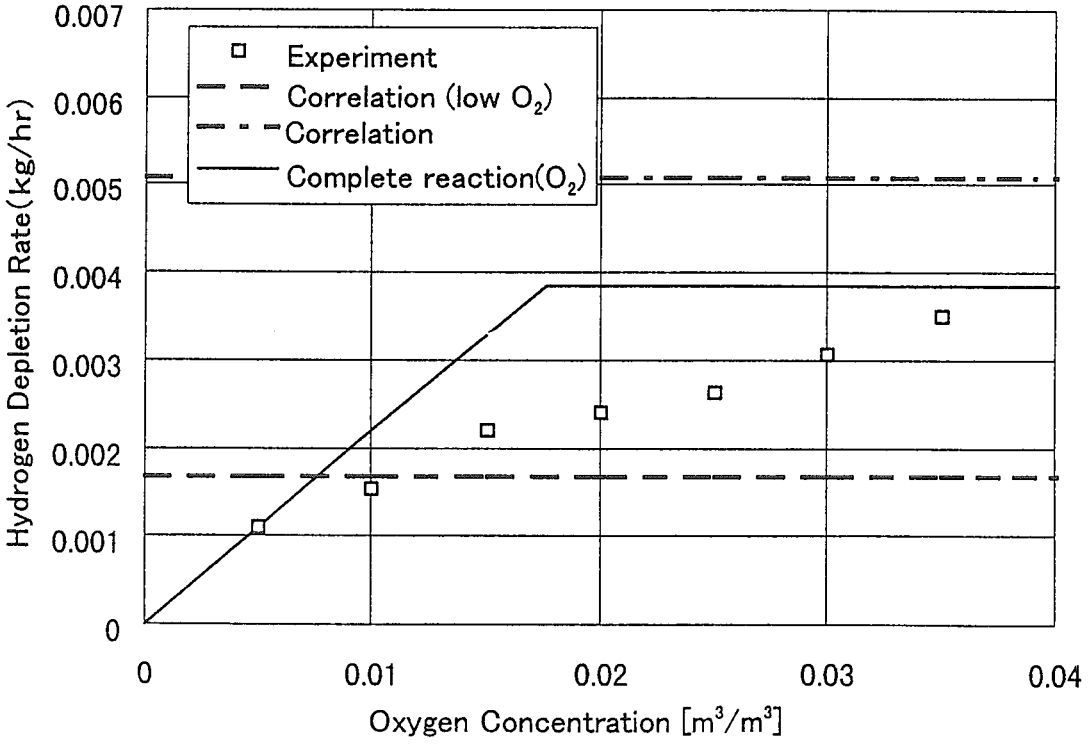



Fig.4 Hydrogen depletion rate (Effect of oxygen concentration)

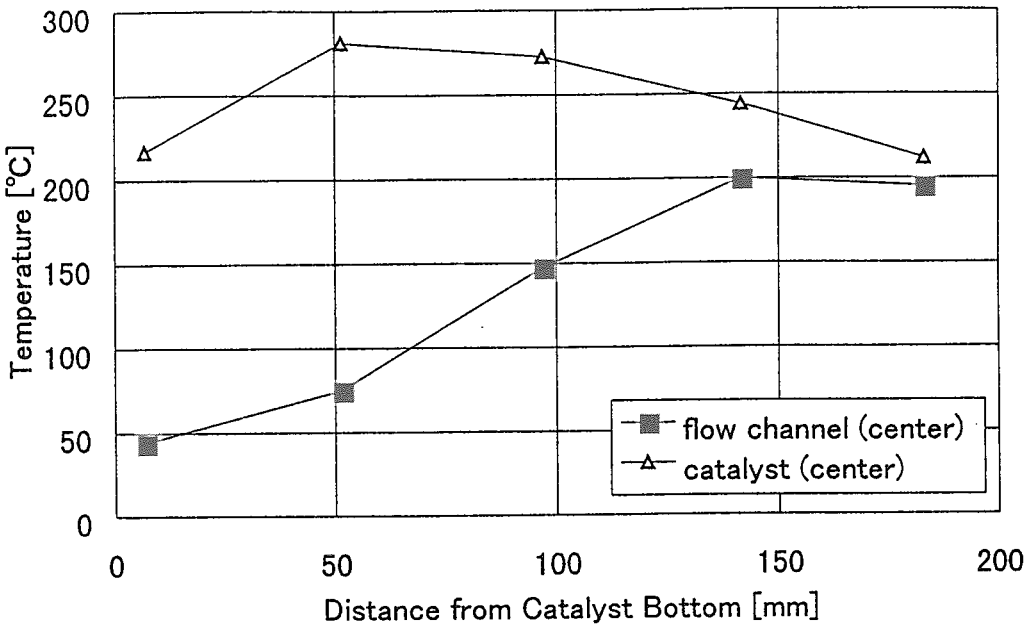



Fig.5 Temperature distribution of catalyst plate and flow channel

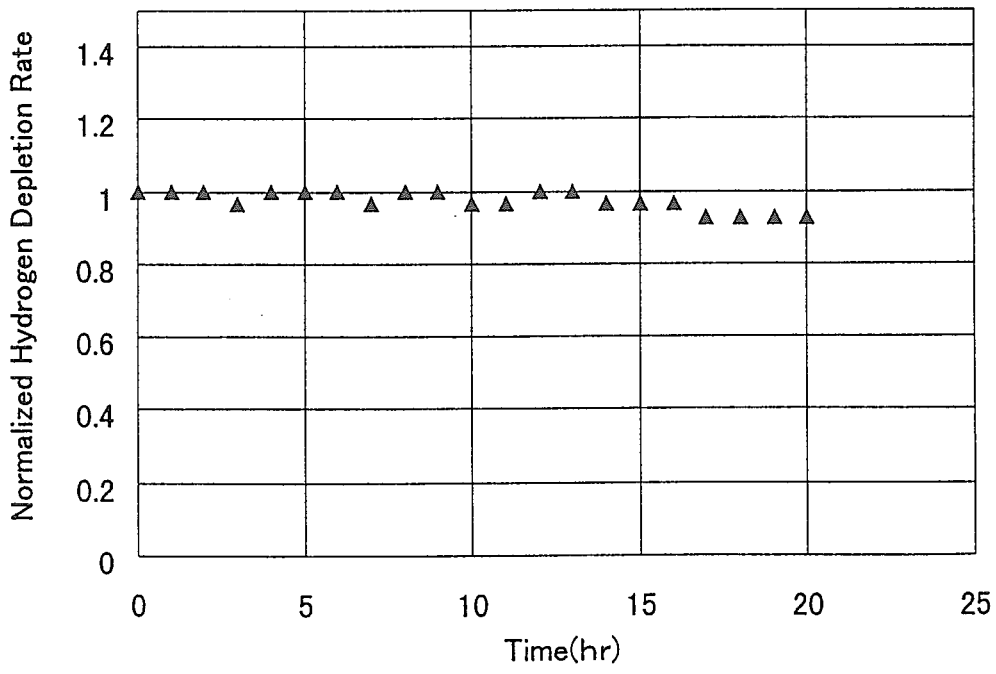



Fig.6 Catalyst performance under presence of iodine

JP0150106



# 7.3 An Experimental Study on Feasibility of Ex-vessel Cooling through the External Guide Vessel

**Kyoung-Ho Kang, Jong-Hwan Kim, Rae-Jun Park and Sang-Baik Kim**

Korea Atomic Energy Research Institute

150 Dukjin-dong Yusong-gu, Taejon 305-353, Korea

Tel) 82-42-868-2665, Fax) 82-42-861-2574, E-mail) khkang@nanum.kaeri.re.kr

**Abstract**

This paper presents the results of a series of experiments for assessing the efficacy of ex-vessel cooling through the external guide vessel during a severe accident. Four tests were performed in the LAVA test facility at KAERI, varying the boundary conditions at the outer surface of the vessel. The first test was a dry condition test conducted without cooling the outside of the vessel. On the other hand, in the second test, the cooling of the vessel surface was produced by gravity-driven forced injection of water along the annular gap of 25 mm between the vessel and the external guide vessel. Water flow rate was about 0.85 kg/s and total mass of available water was 300 kg. For the evaluation of the water flow rate effect, the third test was performed with a pool type cooling in the annulus without any circulation of water. These two external cooling tests were performed under elevated pressure of about 1.6 MPa. Finally, the fourth test was conducted under atmospheric pressure to evaluate the effect of system pressure on boiling heat transfer characteristics. In the dry test and the pool type ex-vessel cooling test performed under atmospheric pressure, the vessel was failed by a melt penetration at about 40 degree upper position from the vessel bottom, which is coincident with the boundary of the $Al_2O_3$/Fe melt separated layers. On the other hand, in both of the ex-vessel cooling tests conducted under elevated pressure of about 1.6 MPa, the vessel didn't fail. Compared with the pool boiling test, the vessel experienced effective cooling due to the inlet flow in the forced flow test. Synthesized the results of the tests, it was shown that the heat removal with ex-vessel cooling through the guide vessel is feasible, but the additional evaluations should be performed to guarantee enough thermal margin.

**Key words :** Ex-vessel Cooling, External Guide Vessel, Melt Separation, Heat Removal

## 1. Introduction

In-vessel Retention (IVR) is one of the severe accident management strategies that have been adopted by operating nuclear power plants and advanced designs. One viable means for IVR is the

method of the external cooling of the reactor vessel by flooding the reactor cavity during a severe accident. The success of the external cooling concept depends on the effectiveness of the ex-vessel boiling process in dissipating the decay heat imposed by the molten core on the reactor vessel bottom. Also, for allowing the reactor cavity to flood, the availability of water to contact the outside of the lower head should be evaluated. For this reason, the studies performed so far were mainly designed to investigate downward-facing boiling phenomena in connection with the external cooling concept[1,2,3,4,7]. Despite many relevant studies have been performed so far, use of definite conclusion for any specific application is not up to the mark due to the uncertainties in the boiling heat transfer characteristics at the outer surface of the vessel. Also, an individual light water reactor differs in the power density, the materials in the core and the shape of the lower head, all of whose factors will influence the heat flux required to be removed with the external cooling. Therefore, the feasibility of that measure in the existing plants is highly plant-specific. Recently, I. S. Hwang et al. proposed an ex-vessel cooling measure using an artificial guide vessel named COASISO (Corium Attack Syndrome Immunization Structures Outside) to facilitate the rapid wetting of the lower head[5]. To concretize this methodology, however, the parametric evaluations on the dimension of the gap structure and the water mass flow rate for the effective cooling should be preceded.

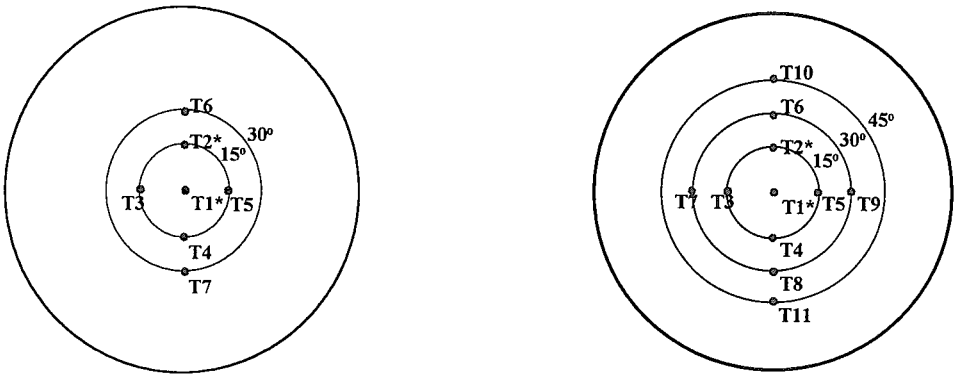
This paper presents the results of a feasibility experiment for assessing the efficacy of ex-vessel cooling through the external guide vessel proposed by the concept of COASISO. Experiments have been conducted in the LAVA test facility at KAERI, using a 1/8 linear scale mockup of a lower plenum[6]. The molten corium in the lower plenum was simulated using $Al_2O_3$/Fe thermite melt. In this study, four tests were performed varying the boundary conditions at the outer surface of the vessel.

## 2. Descriptions of Experiments

The experiments were performed in which the reactor vessel lower head was simulated with a 1/8 linear scale mock-up. This hemispherical test vessel made of commercial carbon steel (SA516-Gr.70) had a 50 cm diameter with a 2.5 cm wall thickness. To create the necessary high heat fluxes, up to 40 kg of molten $Al_2O_3$/Fe thermite was simulated as molten core. The $Al_2O_3$/Fe thermite melt achieves temperatures of about 2400 K. For disrupting the potential of the jet impingement effect of the high-temperature melt, the thermite melt reaction is initially generated in the lower head vessel.

Four tests were performed varying boundary conditions at the outer surface of the vessel. The first dry test was conducted without cooling the outside of the vessel. On the other hand, in the second test, the cooling of the vessel surface was produced by gravity-driven forced circulation of water along the annular gap of 25 mm between the vessel and the external guide vessel. Water flow rate was about 0.85 kg/s and total mass of available water was 300 kg. For the evaluation of the water flow rate effect, the third test was performed with water pool in the annulus without any circulation of water. The dry test was

performed in open space at ambient pressure condition for visual observations on the sequences of the reaction. The other external cooling tests, however, were conducted inside the pressure vessel (LAVA facility) under elevated pressure of about 1.6 MPa. The initial water subcooling was similar in both tests by 180 K. In this study, another pool type ex-vessel cooling test was conducted under atmospheric pressure condition to evaluate the effect of system pressure on boiling heat transfer characteristics.




(a) Dry Test　　(b) Ex-vessel Cooling Test

**Figure 1. Thermocouples Locations**

The occurrence of vessel failure and the thermal behavior of the vessel have been measured by K-type thermocouples embedded in the 3 mm depth of the vessel outer surface, as shown in Figure 1. The additional K-type thermocouples were embedded in the 20 mm depth of the vessel outer surface in the dry test and 13 mm depth of the vessel outer surface in the other ex-vessel cooling tests, respectively at marking points to calculate the conduction heat flux through the vessel wall.

### 3. Experimental Results

In the dry test, after about twenty-eight seconds from the thermite ignition, the vessel was heated to cause a complete melt penetration at about 40 degree from the apex of the vessel bottom. Figure 2 shows the configuration of the vessel failure and the calculated heat flux variations at T1, T2 thermocouple locations. According to the Figure 2 the imposed heat flux through the vessel exceeds 1.5 $MW/m^2$, which indicates that the heat flux generated from thermite melt in this study is quite conservative compared with the TMI-2 case even though decay heat effect isn't considered right now.

The $Al_2O_3$/Fe thermite melt is mixture of alumina ($Al_2O_3$) and iron (Fe). And since the iron is denser than the alumina, the separation of melt components occurred during the thermite reaction and so the first material to contact with the inner surface of the vessel was molten iron. The melt separation process occurred at about 40 degree from the apex of the vessel bottom, which is coincident with the

location of the vessel failure. This result shows that the natural convection flow inside the melt pool and the melt separation process cause the formation of the hot spot and successive melt penetration.

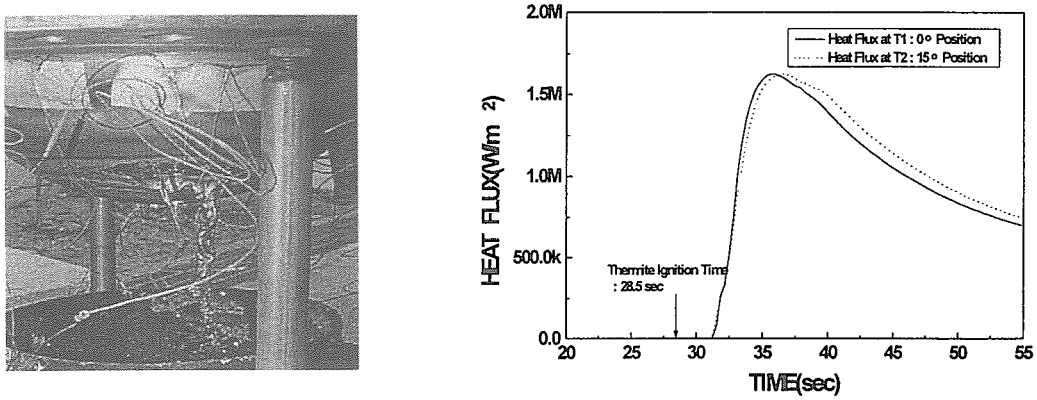
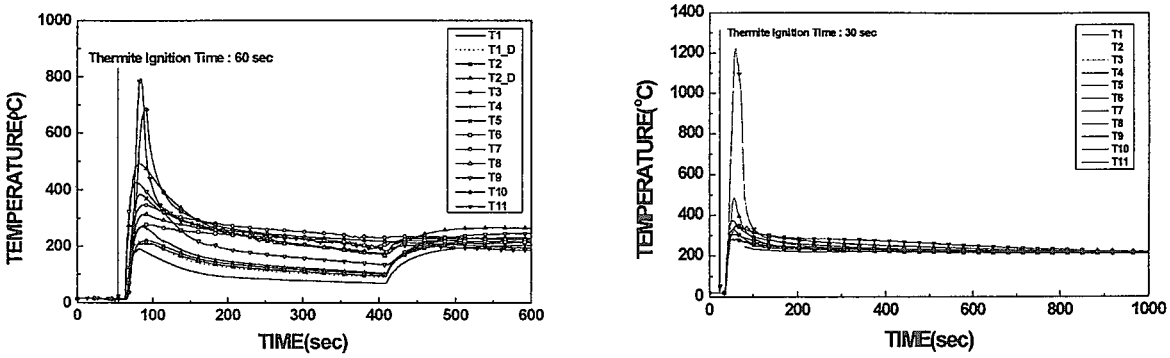



**Figure 2. Configuration of the Vessel Failure and Calculated Heat Flux Variations in the Dry Test**

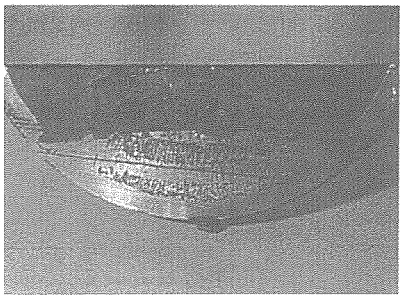
On the contrary to the results of the dry test, in both of the ex-vessel cooling tests performed under elevated pressure of 1.6 MPa, the vessel didn't fail. Figure 3 shows the temperature histories of the vessel in both of the tests. Compared with the pool type test, the vessel experienced effective cool down due to the inlet flow in the forced flow test. According to the cross-sectional view of the vessel in Figure 4, however, the iron welded to the inner surface of the vessel resulting in significant ablation at about 40 degree from the apex of the vessel bottom where the melt separation occurred. This result implies again the leading effect of the melt separation process on the thermal attack to the vessel. In the pool type ex-vessel cooling test conducted under atmospheric pressure, the vessel failed at similar timing and position to the case of the dry test. Figure 5 shows the configuration of the vessel failure.



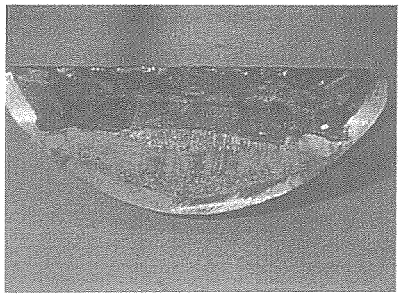

(a) Forced Flow Ex-vessel Cooling Test

(b) Pool Boiling Ex-vessel Cooling Test

**Figure 3. Temperature Histories of the Vessel in the Ex-vessel Cooling Test**

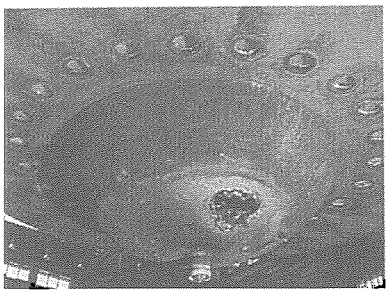


(a) Forced Flow Ex-vessel Cooling Test



(b) Pool Type Ex-vessel Cooling Test

**Figure 4. Cross-sectional View of the Vessel**



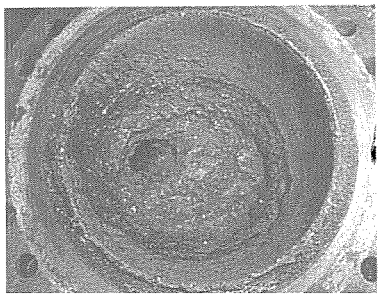


**Figure 5. Configuration of the Vessel Failure in the Pool Boiling Ex-vessel Cooling Test Performed under ambient Pressure**

Unlike to the result of the forced flow ex-vessel cooling test, in the pool type ex-vessel cooling test, the configuration of the vessel ablation was quite asymmetric, which could be found in the temperature histories of the vessel in Figure 3 also. This result implies that the heat transfer in the pool type ex-vessel cooling test could be asymmetric depending on the initial conditions such as melt generation process etc.. On the other hand, in the forced flow ex-vessel cooling test, the uniform cooling of the vessel along the same latitude could be achieved by means of forced inlet water flow at the bottom of the vessel.

Figure 6 shows the calculated heat flux and the heat transfer coefficients from the vessel outer surface to the adjacent water in the forced flow ex-vessel cooling test. According to the heat flux in Figure 6 it is shown that the upper position of the vessel experienced severer thermal attack but the heat flux decreased with time because of the increasing conduction length as the melt solidified inside the vessel. The averaged heat transfer coefficients at T1, T2 were 6000 $W/m^2K$, 8000 $W/m^2K$, respectively which indicate that the vessel effectively cooled down by nucleate boiling at the surface of the vessel.

Figure 7 shows the calculated heat flux and the heat transfer coefficients from the vessel outer surface to the adjacent water in the pool type ex-vessel cooling test performed under elevated pressure of 1.6 MPa. In this test, the heat flux at 15 degree from the apex of the vessel bottom is slightly less than that

of the forced ex-vessel cooling test and the averaged heat transfer coefficients at T1, T2 were 3000 W/m$^2$K, 4000 W/m$^2$K, respectively. According to Figure 6 and 7, in the forced flow test, the heat removal capacity at the vessel surface is larger than the case of the pool boiling test due to the gravity-driven forced inlet water flow.

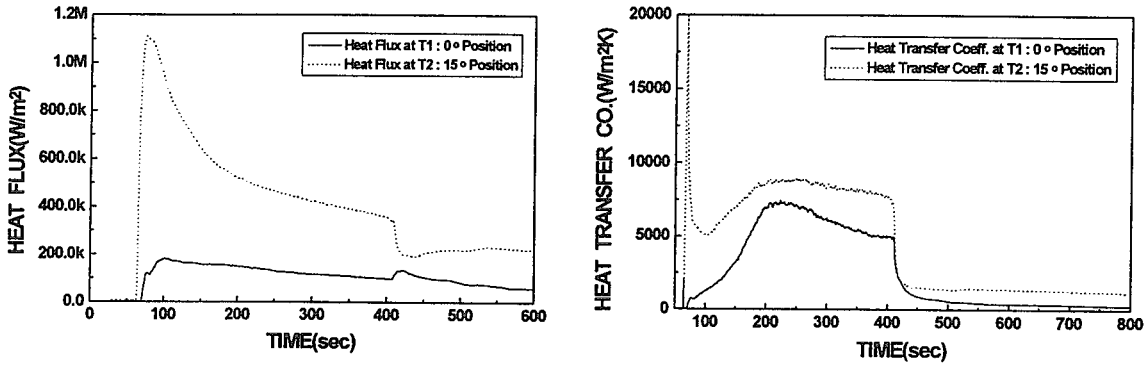



**Figure 6. Calculated Heat Flux and Heat Transfer Coefficients in the Forced Flow Ex-vessel Cooling Test**

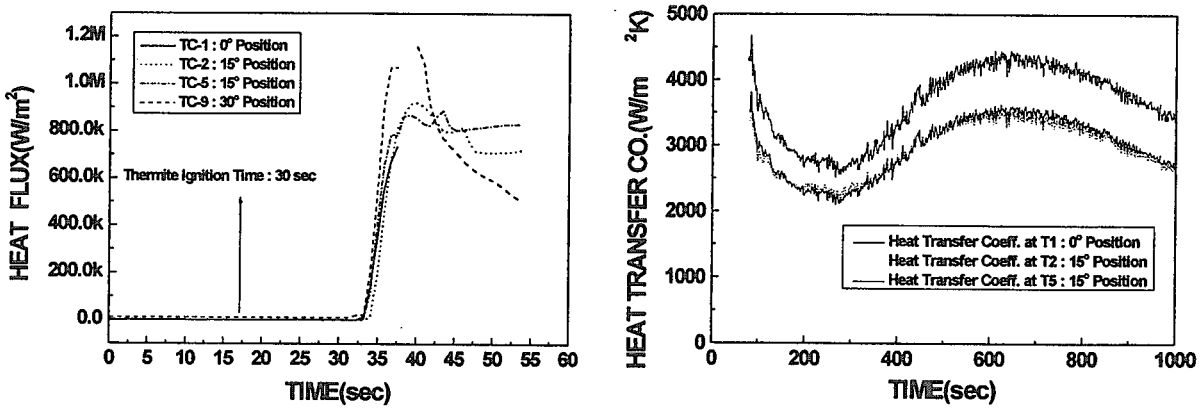



**Figure 7. Calculated Heat Flux and Heat Transfer Coefficients in the Pool Boiling Ex-vessel Cooling Test performed under 1.6 MPa**

## 4. Conclusions

A series of experiments for assessing the efficacy of ex-vessel cooling through the external guide vessel were performed in the LAVA test facility at KAERI, varying the boundary conditions at the outer surface of the vessel. In the dry test and the pool type ex-vessel cooling test performed under atmospheric pressure, the vessel failed by a melt penetration at about 40 degree upper position from the vessel bottom,

which is coincident with the boundary of the $Al_2O_3$/Fe melt separated layers. On the other hand, in both of the ex-vessel cooling tests conducted under elevated pressure of about 1.6 MPa, the vessel didn't fail. Compared with the pool type test, the vessel experienced effective cooling due to the inlet flow in the forced flow test.

As the feasibility study of the ex-vessel cooling through the external guide vessel, the results of this study couldn't fully guarantee the applicability of the pool type ex-vessel cooling measure. However, if the forced flow ex-vessel cooling could be achieved at the outer surface of the vessel, even though the formation of hot spot at the upper portion of the vessel, the vessel could effectively cool down by heat removal with ex-vessel cooling. To concretize the feasibility of the ex-vessel cooling through the guide vessel in this study, the additional tests varying the flow rate of water and the gap size should be performed. Also, the thermal-hydraulic experiments to quantify the coolability limits of the reactor vessel lower head by external cooling measure will be conducted at KAERI in late 1999.

## ACKNOWLEDGEMENT

This study has been carried out under the nuclear R&D program by the Korean Ministry of Science and Technology.

## REFERENCES

1. Robert E. Henry et al., "Cooling of Core Debris within the Reactor Vessel Lower Head," Nuclear Technology, Vol. 101, pp 385 - 399(1993).

2. T. Y. Chu et al., "Ex-vessel Boiling Experiments : Laboratory and Reactor Scale Testing of the Flooded Cavity Concept for In-vessel Core Retention," Nuclear Engineering and Design, Vol. 169, pp 77 - 88(1997).

3. F. B. Cheung et al., "Critical Heat Flux(CHF) Phenomenon on a Downward Facing Curved Surface : Effects of Thermal Insulation," NUREG/CR-5534(1998).

4. T. G. Theofanous et al., "In-vessel Coolability and Retention of a Core Melt," Nuclear Engineering and Design, Vol. 169, pp 1 - 48(1997).

5. I. S. Hwang, et al., "The COASISO Design(II) : Proof-of-principle Demonstration," The 14th KAIF/KNS Annual Conference, Seoul, Korea, April 7-9, 1999.

6. K. H. Kang, et al., "Experimental Investigation on In-vessel Debris Coolability through Inherent Cooling Mechanism, OECD/CSNI Workshop on In-Vessel Core Debris Retention and Coolability, Garching, Germany, March 3-6, 1998.

7. Yang, S. H., Baek, W. P. And Chang, S. H., " An Experimental Study of the Pool-boiling CHF on Downward Facing Plates ", Journal of the Korean Nuclear Society, V. 26(4), p493-501, 1994

This is a blank page.

# 8. Session 7

# Accident Management II

## Chairperson:

A. Levin (NRC)
M. Ogino (NUPEC)

This is a blank page.

JP0150107



# 8.1 Experimental Investigation of Thermal-Hydraulic Performance of PCCS with Horizontal Tube Heat Exchangers: Single U-Tube Test

**Hideo NAKAMURA, Yoshinari ANODA,**

Dept. of Reactor Safety Research
**Japan Atomic Energy Research Institute (JAERI)**
Tokai, Ibaraki, 319-1195 , Japan
e-mail: *nakam@lstf3.tokai.jaeri.go.jp*

**Hiroaki TABATA, Hiroyuki OBATA,**

Research and Development Dept.
**The Japan Atomic Power Company (JAPC)**
Ohtemachi Bldg.
6-1, 1 Ohtemachi, Chiyoda-Ku,
Tokyo, 100-0004 Japan

**Kenji ARAI and Tomohisa KURITA**

Nuclear Engineering Lab.
**Toshiba Co.**
4-1 Ukishima, Kawasaki-ku,
Kawasaki, 210-0862, Japan

*Keywords; Passive Containment Cooling System, PCCS, Severe Accident, Depressurization, Steam Condensation, Heat Transfer, Fundamental Experiment, Horizontal Heat Exchanger, U-tube, Degradation, Non-Condensable Gas, Condensate, Drain, RELAP5 Code*

## Abstract

JAERI and JAPC started a cooperative study to verify performance of a PCCS using horizontal heat exchanger for next-generation BWR in 1998. A test facility with a horizontal single U-tube was constructed in JAERI in 1999 to investigate fundamental condensation behavior under influences of non-condensable gas. Preliminary pre-test analyses were performed using RELAP5/ MOD3.2.1.2 code to expect the experimental outcomes by incorporating a correlation for condensation degradation because of non-condensable gas by Ueno et al. for better prediction. Preliminary results from both experiments (shakedown) and pre-test analyses indicated that the PCCS using horizontal U-tube heat exchanger is promising. Steam generated under assumed severe accident conditions; steam generation rate ≈ 1% core power, non-condensable gas concentration of 1% and simulated containment vessel pressure of 0.7 MPa, was totally condensed with a small differential pressure across inlet and outlet plenum. Experimental data will be accumulated to develop models and correlations for a better prediction of responses of the PCCS using horizontal heat exchanger during postulated severe accidents.

## 1. Introduction

A passive containment cooling system (PCCS)[1-7] is under planning to be used for a long-term cooling of primary containment vessel (PCV) of next-generation BWRs during a severe accident in case that residual heat removal (RHR) systems are in failure. The pressure of the PCV will be maintained as low as possible by condensing steam with no active components.[Δ] JAERI and JAPC have agreed and started to jointly study the availability of the PCCS using a horizontal U-tube heat exchanger in 1998.

Fundamental experiments using a horizontal single U-tube were started in August, 1999 in JAERI to study condensation heat transfer characteristics for steam/non-condensable gas mixture and flow behavior of condensate and non-condensable gas under postulated severe accident conditions. Parameter experiments are planned to perform changing tube geometry and flow conditions. The experimental results will be used to prepare correlations to predict steam condensation behavior under severe accident conditions by the aid of code analyses.

Preliminary pre-test analyses of the condensation heat transfer in the horizontal U-tube were performed using RELAP5/ MOD3.2.1.2 code to expect the experimental outcomes. A correlation to predict degradation of steam condensation by non-

[Δ] Non-condensable gases such as hydrogen and carbon-oxide are generated by the interaction of high-temperature corium with water and concrete of containment base mat, and oxidation of zirconium of core cladding, and will be stored in wetwell with nitrogen gas. The PCCS is not intended to mitigate the pressurization by such gas generation.

condensable gas was incorporated into the code.

This paper summarizes such current experimental and analytical efforts to clarify the thermal-hydraulic performance of the horizontal heat exchanger for PCCS as well as an overview of the whole investigation plan.

## 2. PCCS

### 2.1 Heat Removal Performance

PCCS using heat exchangers have been proposed for SBWR/ESBWR and SWR1000.[1-4] For the SBWR, heat exchangers for isolation condenser (IC) were considered conveniently usable as those of PCCS.[6] Following international developmental study for the SBWR/ESBWR, a vertical in-tube heat exchanger has been recongized to be applicable for a next-generation BWR in JAPAN[5] too as a quasi-proven component. A conventional horizontal U-tube heat exchanger, however, has emerged as another candidate based partly on the consideration of seismic-proof and possibility for cost reduction as a system including PCCS water pool, while it has been considered unsuitable primarily because of lack in the experiences about the in-tube steam condensation behavior; i.e. condensate drain with non-condensable gases.

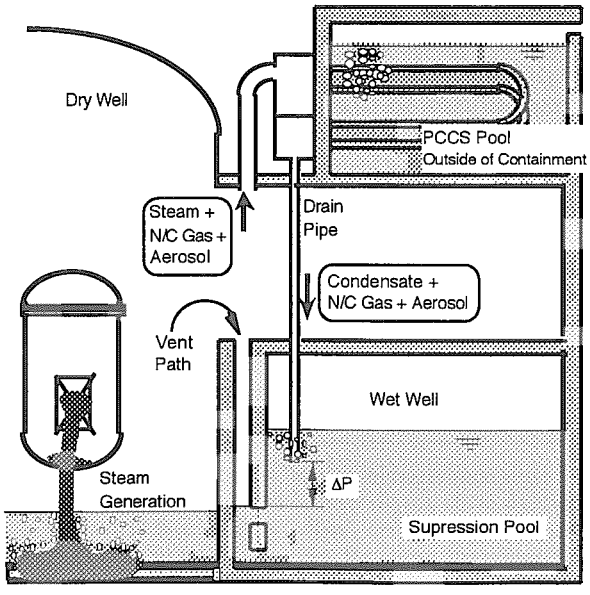



Fig. 1 Schematic of PCCS Operation

PCCS of interest is a once-through system that directly connects drywell (DW) to wetwell (WW) as shown in **Fig. 1**. There is no return line to DW, which was included in the SBWR design with GDCS (gravity drain cooling system). Steam generated in DW is driven through the PCCS heat exchanger with non-condensable gases by the pressure difference between DW and WW; namely by the water head difference ΔP between two elevations: the top of main vent pipe opening and the bottom of PCCS drain pipe. PCCS removes heat by steam condensation in the heat exchanger, and drains condensate and non-condensable gas into WW suppression pool (S/P) respectively by gravity and pressure difference. During severe accidents, aerosols including fission products would enter the PCCS heat exchanger, being drained with condensate.

Since the driving force for the PCCS operation (ΔP, **Fig. 1**) is limited by the plant geometrical configuration, the differential pressure across the heat exchanger should be less than a limiting value; i.e. ~2 kPa. Steam-gas mixture in DW enters WW through main vent line when the DW-WW pressure difference far exceeds this condition. Please note that most of steam enters WW through the main vent line during LOCA blowdown phase or at the incipience of lower head failure by high-temperature melt when the steam generation rate in DW is large. During such transients, steam flows through PCCS at maximum flow rate possibly by transporting uncondensed steam into WW S/P. Heat input to S/P through the main vent will be switched off when the DW-WW pressure difference becomes lower than the above criterion following the decrease in the steam generation rate in DW. PCCS pool is a final heat sink under such conditions.

The pressure difference across the vertical heat exchanger designed for ESBWR/SBWR has been known to be small because it is composed of large diameter short tubes.

### 2.2 In-Tube Condensation Behavior for Horizontal Heat Exchanger

Many researchers have investigated in-tube condensation for horizontal tubes.[9-16] However, there were no investigations that fully cover the PCCS conditions of interest

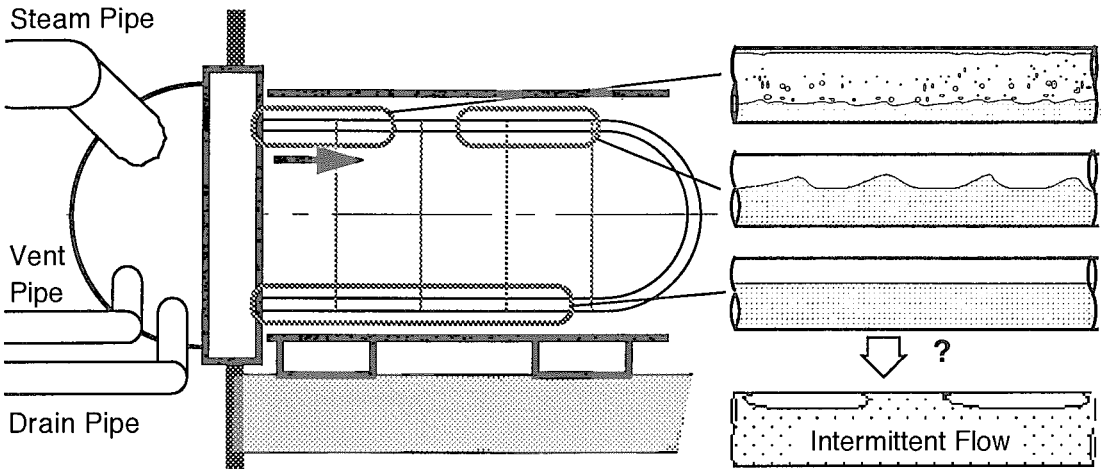



Fig. 2 Expected Flow Regimes in PCCS

where steam condensation takes place at pressures ranging from atmospheric to 0.7 MPa under influences of non-condensable gas.

Several flow regime maps have also been proposed based on experiments, but only for pure steam system where gas phase vanishes at the tube exit in most cases.[17-20] Flow regimes would be different from such observation because non-condensable gas would stagnate near the tube exit and in the outlet plenum in the PCCS of interest, even when pure steam enters the tubes. Typical flow regimes would be annular and/or annular mist, wavy and smooth stratified according to the gas velocity which decreases along the length of the tube as shown in **Fig. 2.**

One of the major concerns here have been the flow regime transition from separated flows such as wavy and/or smooth stratified to intermittent flows such as plug and slug in the tubes, since it may degrade the PCCS heat removal performance greatly because of an increase in the pressure loss across the water-plugged tubes and a oscillative pressure response. Lack in such fundamental knowledge about the heat exchanger performance may have limited the applicability of the horizontal heat exchanger to PCCS.

### 2.3 Approach of Investigation

Based on the survey of investigation status above, JAERI started to study the total performance of horizontal heat exchanger for the PCCS as shown in **Fig. 3.** First, JAERI performed RELAP5 code analyses to obtain preliminary information about the fundamental experiments based on assumed PCCS operation conditions. In parallel, JAERI performed design and manufacture of the test facility for the fundamental experiments, and performed air/water two-phase flow visualization experiments to study the flow response in the U-bend part, because the condenser tube of the test facility for fundamental experiments is SUS-made.

In the fundamental experiments, parameter experiments will be performed to observe in-tube condensation and hydraulic behavior in a single horizontal U-tube co-axially cooled by subcooled coolant. The influence of secondary boiling and gas vent behavior will be studied as separate-effect tests by slightly modifying the test facility. As such, data base will be prepared for model development for better predictions of the perfor-

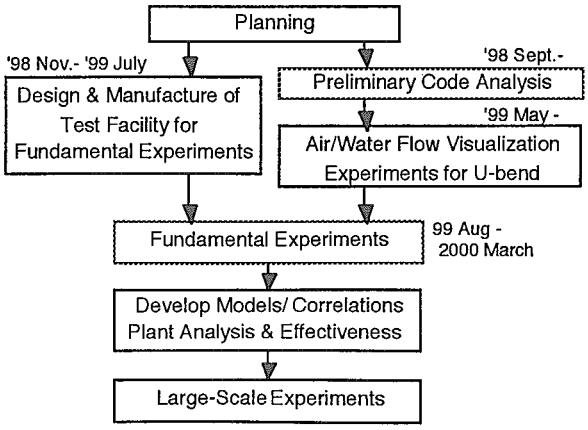



Fig. 3 Investigating Plan

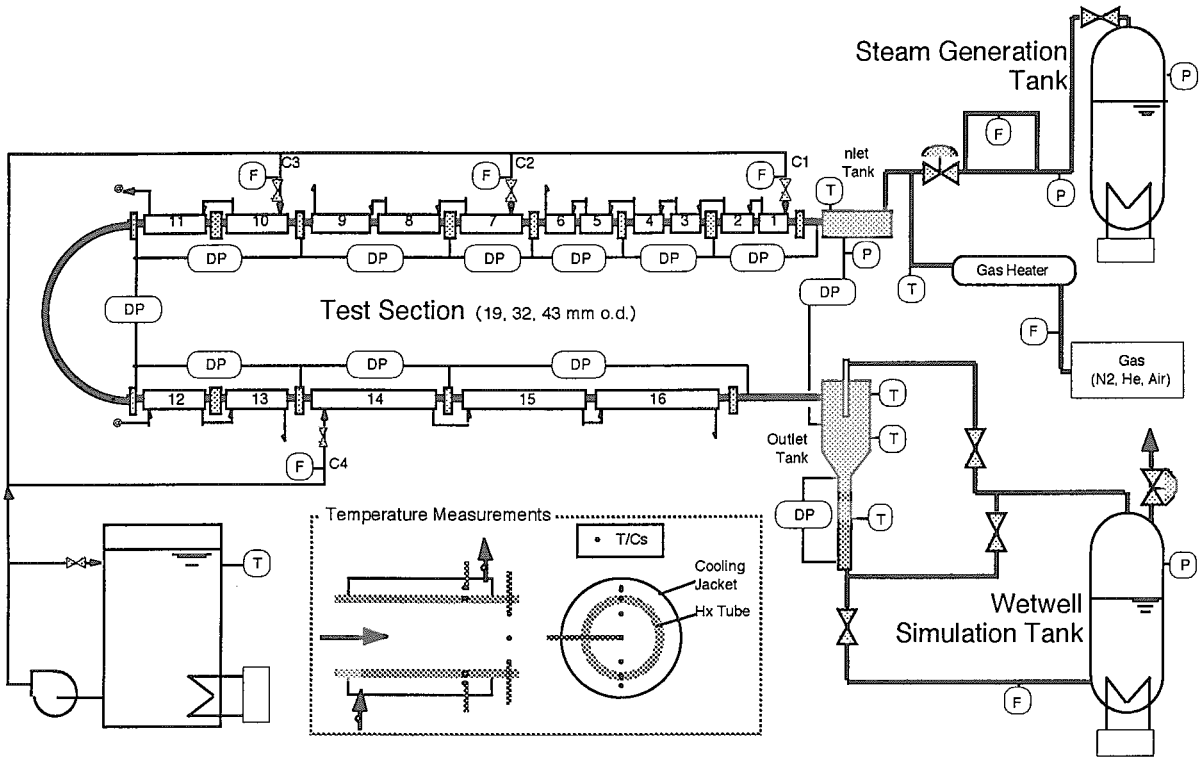



Fig. 4 Schematic of Test Facility for Fundamental Condensation Experiments

mance of the horizontal heat exchanger of PCCS by the aid of code analyses.

A large-scale tube bundle experiment will be performed once the horizontal heat exchanger is recognized feasible from the fundamental experiments and predictive analyses by computer codes being modified by the developed models.

## 3. Experiment

### 3.1 Facility

The facility is located in the ROSA-V/LSTF in JAERI with three test sections made of SUS304 with different tube outer diameters of 19.0, 31.8 and 42.7 mm. Schematic of the facility is shown in **Fig. 4**. Steam generated in 5 $m^3$ tank is provided to the test section inlet tank after slightly superheated by a couple of valves and trace heaters (not shown). Non-condensable gas such as nitrogen ($N_2$) and/or helium (He) to simulate hydrogen ($H_2$) was mixed with steam after temperature control through a gas heater. Flow rates of steam and gas were measured using eddy flowmeters and mass-flowmeters respectively.

The test section was composed of 16 segments with a co-axial cylindrical cooling jacket. Total cooling length was 4 m for both upstream and downstream horizontal legs. Length of cooling jacket (0.25, 0.5 and 1 m) was increased along the test section considering the decrease in condensation rate. The test section was divided into four groups of segments, each of which had an individual secondary flow control for better simulation of cooling in a water pool. Slightly pressurized subcooled water (< 60 °C) was provided to the cooling jacket to measure the amount of removed heat in each jacket. The influence of secondary boiling condition in a tube bundle such as enhancement by flow turbulence and/or degradation by steam blanketing will be investigated by using a special segment where primary steam is routed and injected into the secondary coolant. Horizontal level of the test section tube was carefully checked by using a transparent vinyl tube U-manometer.

Condensate and non-condensable gas drained first into an outlet tank and then travelled down to wetwell simulation tank (5 $m^3$) through a drain piping. Demineralized water was used for both primary and secondary sides.

In each cooling jacket, primary and secondary coolant and wall surface temperatures were measured at nine locations in total. As for primary side, three sheathed thermocouples (T/Cs, 1.6 mm o.d.) were inserted from top, side and bottom of tube on the same plane normal to the flow axis. Center T/C was inserted such that the tip is located on the flow axis. Two other T/Cs were inserted into the tube by ~5 mm from the wall. To measure the tube outer surface temperatures, two sheathed T/Cs (0.5 mm o.d.) were embedded in the tube wall at the tube top and bottom such that the sheath surface was flush to wall outer surface which faces to secondary coolant. The tip of T/Cs was brazed to the tube wall on the same plane as the secondary coolant T/Cs. The secondary coolant temperature was measured by four sheathed T/Cs at the inlet and outlet of the jacket and at two locations adjacent to the wall surface T/Cs. These T/Cs were in-situ calibrated by furnishing steam to the test section at several pressures under adiabatic (vacant secondary) conditions.

Heat loss of the test section was confirmed to be very low from the amount of condensate in such characterization experiments.

### 3.2 Experimental Conditions

Major experimental parameters were the tube geometry, primary fluid and secondary cooling conditions as shown in **Table 1**.

**Figure 5** shows a typical temperature data obtained in shakedown tests using 31.8 mm tube under nominal conditions; 0.7 MPa, 1% decay power (≈ 100 kW/tube), 1% $N_2$ gas partial pressure. Steam-gas mixture velocity at tube inlet was ~19 m/s. Steam was totally condensed in ~6 m* in this experiment. (*Note: Distance from Tube Inlet = Hx/jacket + non-Hx tube length)

Table 1 Experimental Conditions

| Geometrical Conditions | | Parameters for RELAP5 Code Analyses |
|---|---|---|
| Tube O.D. (mm) | 19.0, 31.8, 42.7 | 31.8 |
| Hx Length (m) | 4 x 2 = 8 | Same |
| U-bend Radius (m) | 0.3 | Same |
| U-bend Inclination | -5°, -45°, -90° | 0°, -5°, -90° |
| Flow Conditions | | |
| Primary Pressure (MPa) | 0.2 - 0.7 | 0.7 (exit) |
| Inlet Gas Velocity (m/s) | 10 - 30 (31.8 mm tube) | 20 |
| Gas Concentration (%) | 0 - 20 (partial press.) | 1 |
| Secondary Coolant Temperature (K) | 333 (Inlet) | Same |
| Secondary Boiling Condition in a Bundle | Special segment with steam injection | N/A |

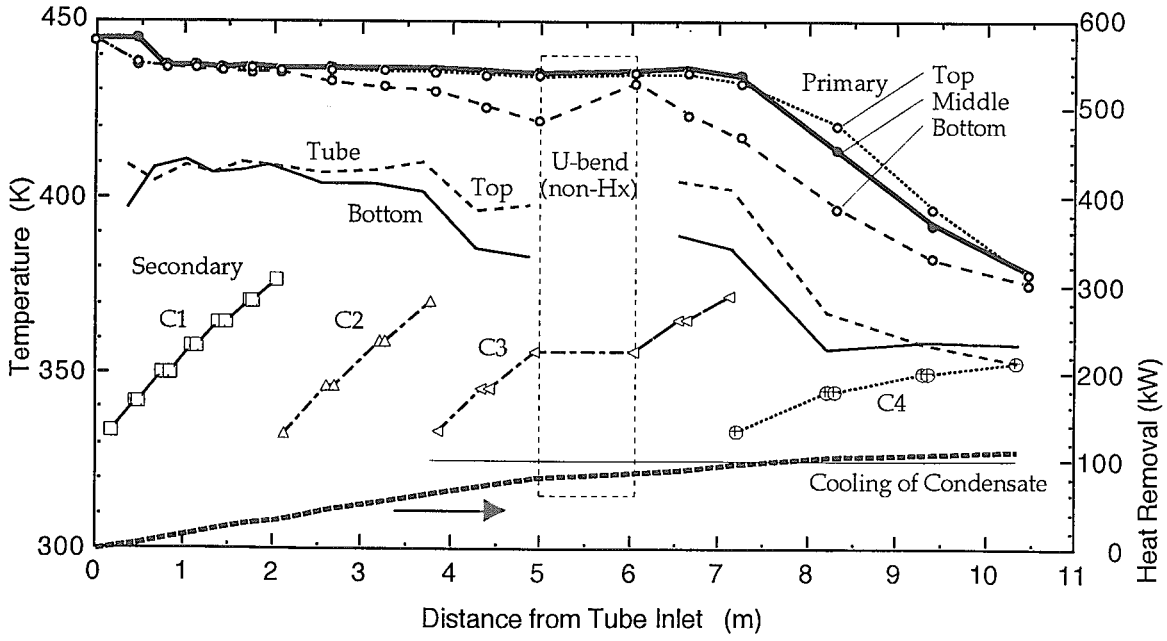



Fig. 5 Typical Temperature Data (Shakedown Test for 31.8 mm o.d. tube)

## 4. Preliminary Code Analysis

### 4.1 Calculation Conditions

Preliminary pre-test analyses of the condensation heat transfer in a simulated horizontal U-tube were performed using RELAP5/MOD3.2.1.2 code[21] to expect the experimental outcomes. The code employs Nusselt, Shah and Chato correlations[9-11] for the prediction of steam condensation respectively under laminar and turbulent flow conditions and a modification to Nusselt for laminar film flow in a horizontal tube. A correlation to predict condensation degradation because of non-condensable gas by Ueno et al.[14] was incorporated into the code, while a correlation in the original code; Colburn-Hougen,[22] was not used. The correlation by Ueno et al. is based on experiments simulating a horizontal steam generator of NP-21 as a part of the passive safety features during accidents/transients, thus for low pressure (< ~0.4 MPa) and small-diameter (~19 mm) tube conditions.

The code analyses were performed for the conditions noted in **Table 1.**

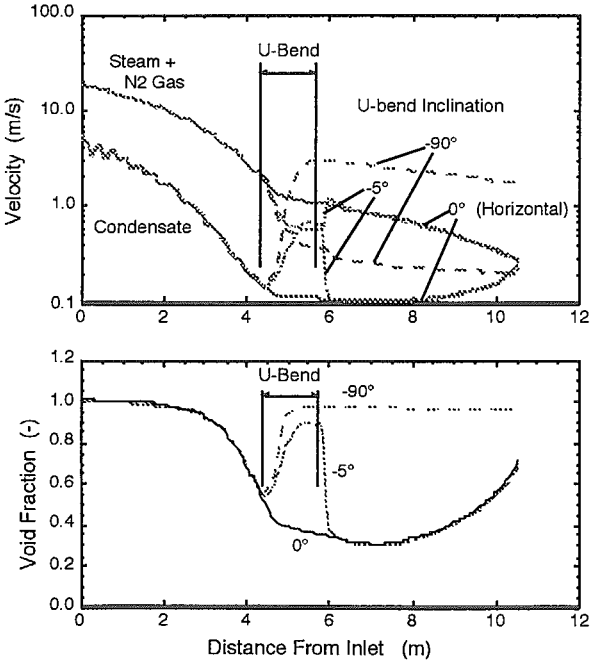



Fig. 6 Comparison of Calculated Fluid Velocities and Void Fractions for Different U-bend Inclinations (31.8 mm tube)

### 4.2 Calculated Results

**Figure 6** compares the calculated gas and liquid velocities and void fractions in terms of distance from tube inlet obtained for three U-bend inclinations; 0°, -5° and -90°. There was no difference in the upstream horizontal leg among three cases. Velocities of both phases decreased monotonically along the length of the tube for both phases. Maximum velocity of condensate film was ~6 m/s at the tube inlet while gas velocity was ~20 m/s. In the upstream horizontal leg, liquid level of condensate reached almost to the tube axis around the connection to U-bend in the two "inclined" cases. Liquid velocity increased as well as the void fraction in the "inclined" cases because of the acceleration in the U-bend. In the "horizontal" U-bend case, on the other hand, these two parameters continued to decrease monotonically. Gas phase velocity in the "inclined" cases decreased in the downstream of the U-bend, because the cross sectional area increased and steam condensation almost completed in the upstream leg, thus gas phase is mostly composed of non-condensable gas.

In the downstream leg, liquid level increased, and started to decrease after the void fraction recorded the minimum of ~0.3 in horizontal and -5° inclined cases because of gravity drain towards the tube exit. In the -5° inclined case, the condensate velocity increased being accelerated in the U-bend temporarily, but decreased suddenly to the value of the horizontal case around the downstream leg inlet. This response looks similar to hydraulic jump. The small inclination of U-bend has little effect onto the hydraulic behavior. In the -90° inclined case, on the other hand, the condensate velocity increased very much** in the U-bend and decreased gradually in the downstream leg by the wall friction until the tube exit as super-critical flow that Froude number exceeds well 1.0. This result indicates that fluid acceleration in the U-bend has no influence to the upstream leg behavior, but controls the flow condition in the downstream leg, depending on elevation change between the upstream and downstream legs.

** Note that velocity in Fig. 6 is presented in semi-Log co-ordinate.

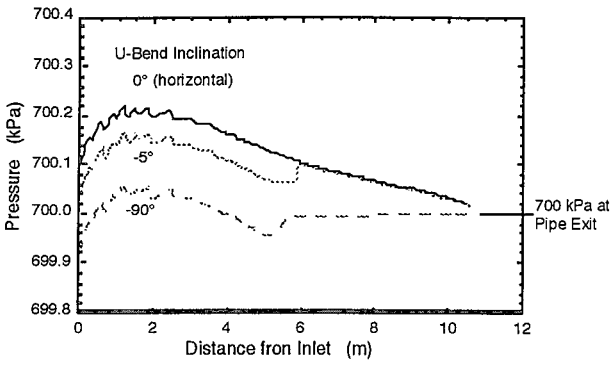



Fig. 7 Comparison of Calculated Static Pressures for Different U-bend Inclinations (31.8 mm tube)

**Figure 7** compares the static pressures in terms of distance from the tube inlet. The calculated pressures first increased around the tube inlet probably because of significant condensation, while they decreased monotonically afterwards in the upstream leg. In -5° inclined case, a sudden increase in the pressure occurred at the sudden level increase around the inlet of the downstream leg because of acceleration of gas flow. In -90° inclined case, decrease in the pressure in the downstream leg was small because gas flow velocity is very small; smaller than liquid velocity. This result indicates that the condensate acceleration in the U-bend with large level difference between upstream and downstream legs is favorable to suppress the pressure loss in the heat exchanger.

In summary, the preliminary calculations suggest that the horizontal U-tubes would be promising to use for the PCCS heat exchanger by the complete steam condensation with small differential pressure across the unit under an assumed severe accident condition.

## 5. Conclusions

JAERI and JAPC started a verification study for the performance of a horizontal heat exchanger type PCCS for next-generation BWR as a cooperative study in 1998. A test facility with a horizontal single U-tube was constructed in JAERI in July, 1999 to investigate fundamental in-tube condensation behavior in the horizontal heat exchanger. Major experimental parameters are tube diameter, primary pressure, steam flow rate, composition and amount of non-condensable gas and secondary cooling conditions. Preliminary test results obtained under assumed accident conditions; steam generation rate ≈ 1% core power, concentration of $N_2$ gas of 1% and containment vessel pressure of 0.7 MPa, indicated a total steam condensation in ~6 m from the tube inlet a 31.8 mm o.d. test section.

Preliminary pre-test analyses were performed using RELAP5/ MOD3.2.1.2 code to expect the experimental outcomes. A correlation by Ueno et al. was incorporated to predict degradation of steam condensation by non-condensable gas. The calculated results indicated that the PCCS using horizontal U-tubes is promising with a small differential pressure between inlet and outlet plenum.

Experimental data will be accumulated, and models and correlations will be developed for a better prediction of condensation and degradation by non-condensable gas in the horizontal heat exchanger for PCCS based on the experimental data. System and multi-dimensional analyses will be performed using computer codes with the developed models and correlations. Large-scale experiments will then be performed to clarify the total responses of the horizontal heat exchanger including multi-dimensional phenomena that are necessary for system response analyses.

## References

[1] H.A. Upton et al., 'Simplified Boiling Water Reactor Passive Safety Features,' Proc. of ICONE-2, San Francisco CA (1993), Vol. 1, pp. 705.

[2] J. Dreier et al., 'The PANDA Tests for the SWR 1000 Passive Containment Cooling System,' Proc. of ICONE-7, Tokyo (1999), ICONE-7316.

[3] M. Huggenberger et al., 'ESBWR Related Passive Decay Heat Removal Tests in PANDA,' Proc. of ICONE-7, Tokyo (1999), ICONE-7322.

[4] P. Masoni et al., 'Tests on Full-Scale Prototypical Passive Containment Condenser for SBWR's Application,' Proc. of ICONE-3, Kyoto (1995), Vol. 2, pp. 1023.

[5] H. Oikawa et al., 'Safety System Improvement for the Nest Generation BWR,' Proc. of ICONE-5, Nice (1997), ICONE5-2538.
[6] H. Nagasaka et al., 'Heat Removal Tests of Isolation Condenser Applied as a Passive Containment Cooling System,' Proc. of ICONE-1, Tokyo (1991), vol. 1, pp. 257.
[7] Y. Kataoka et al., 'Heat Removal Capacity and System Pressure of The Water-Wall Type Passive Containment Cooling System,' Proc. of ICONE-2, San Francisco CA (1993), Vol. 1, pp. 691.
[8] The ROSA-IV Group, 'ROSA-IV Large Scale Test Facility (LSTF), System Description for Second Simulated Fuel Assembly,' JAERI-M 90-176.
[9] W. Nusselt, 'Die Oberflachenkondensation des Wasserdampfes,' Ver. Deutsch. Ing., 60 (1916) pp. 541.
[10]J.C. Chato, 'Laminar Condensation inside Horizontal and Inclined Tubes,' American Soc. Heating, Refrig. & Air Cond. Engnrs. (ASHRAE) J., 4 (1962) pp. 52.
[11]M.M. Shah, 'A General Correlation for Heat Transfer during Film Condensation inside Pipes,' Int. J. Heat & Mass Trans., 22 (1979) pp. 547.
[12]A.C. Bannwart et al., 'Condensation of Vapour with Incondensables: An Improved Gas Phase Film Model Accounting for the Effect of Mass Transfer on Film Thickness,' Int. J. Heat Mass Trans., Vol. 33(7) (1990) pp. 1465.
[13]I.K. Huhtiniemi et al., 'Condensation in the Presence of Noncondensable Gases,' Nucl. Engng. Des. 141 (1993) pp. 429.
[14]T. Ueno et al., 'Thermal-Hydraulic Test on Mitsubishi Simplified PWR,' 9th Proc. of Nucl. Thermal Hydraulics, ANS Winter Wtg., SF, CA (1993) pp. 193.
[15]S. Alt et al., 'Steam Condensation Processes in Horizontal Tubes with Presence of Noncondensing Gases,' Proc. of ICONE-5, Nice, (1997) ICONE-5-2435.
[16]M.K. Dobson et al., 'Condensation in Smooth Horizontal Tubes,' J. Heat Trans., Trans ASME, 120 (1998) pp. 193.
[17]G. Breber et al., 'Prediction of Horizontal Tubeside Condensation of Pure Components using Flow Regime Criteria,' J. Heat Transfer, Trans. ASME, Vol. 102 (1980) pp. 471.
[18]R.G. Sardesai et al., 'Flow Regimes for Condensation of Vapour inside a Horizontal Tube,' Chem. Engng. Sci. Col. 36 (1981) pp. 1173.
[19]T.N. Tandon et al., 'A New Flow Regimes Map for Condensation Inside Horizontal Tubes,' J. Heat Transfer, Trans. ASME, Vol. 104 (1982) pp. 763.
[20]M.M. Rahman et al., 'Flow Pattern Boundaries during Condensation: New Experimental Data,' Canadian J. Chem. Engng. Vol. 63 (1985) pp. 547.
[21]The RELAP5 Development Team, 'RELAP5/MOD3 Code Manual,' NUREG/CR-5535, INEL-95/0174, Vol. 1 & 4 (1995).
[22]A.P. Colburn and O.A. Hougen, 'Design of Cooler Condensers for Mixtures of Vapours with Non-Condensable Gases,' Ind. & Engng. Chem., 26 (1934) pp. 1178.

A paper for SARJ-99

JP0150108



# 8.2 ANALYSIS OF CONTAINMENT VENTING FOLLOWING A CORE DAMAGE AT A BWR MARK I USING THALES-2

Surip WIDODO
Nuclear Safety Technology Development Center,
National Nuclear Energy Agency (BATAN),
Puspiptek, Serpong, Tangerang, INDONESIA 15310
Ph.: 62-21-7560912 Fax.: 62-21-7560913
E-mail: suripw@batan.go.id

Jun ISHIKAWA, Ken MURAMATSU
Japan Atomic Energy Research Institute
2-4 Shirakata Shirane Tokai-mura, Naka-gun, Ibaraki-ken, 319-11, JAPAN

Toru SAKAMOTO
Toshiba Advanced System Co.
1-2-4 Isogo, Kawasaki-ku, Kawasaki-shi, Kanagawa-ken, 210, JAPAN

**ABSTRACT**

Analysis of containment venting following a core damage at a boiling water reactor (BWR) Mark I using THALES-2 was performed. In this analysis, the effect of various parameters, namely,

- the areas of the vent path,
- containment venting pressure, and
- accident sequences

on the containment thermodynamic response, and radionuclide transport and release in the containment venting at a BWR was examined. The code THALES-2B developed by the Japan Atomic Energy Research Institute (JAERI) was used in this analysis. The model plant in this analysis was the Browns Ferry plant. From this analysis was found that the 4-inch pipe of containment venting flow path is sufficient to maintain the containment pressure in the specified range if the containment was pressurized by the decay heat power. The entrainment by the pool swelling as well as by the flashing was not occurred during the containment venting. The source terms are not sensitive to the variation of containment venting flow path area. The containment venting pressure operation setting point has important rule in the containment venting. In the containment venting, the source terms are not sensitive to the accident sequence, except for Sr source term. In order to get better understanding on the containment venting strategy, the following analyses are necessary. Analyses of accident sequence which has a high power such as anticipated transient without scram are necessary, as well as analyses of accident sequence which pressurize the containment before the core damage.

## 1. Introduction

Containment venting has been recognized as an important accident management tool for Boiling Water Reactor (BWR) Mark I containments[1]. It is used to prevent uncontrolled containment failure by providing a controlled release of containment atmosphere if the containment pressure equals or exceeds a specified limit. After core damage, venting via a path through the suppression pool will provide considerable radionuclide scrubbing and reduce

release. Important issues for containment venting are the containment venting pressure, the areas and flow capacities of the vent paths, and the structural capability of vent paths.

Ishikawa, et al.[2] performed analyses of containment venting at a BWR using THALES-2 code[3]. The purposes of analyses were aiming at obtaining better understanding on the controlling factors of the source terms of containment venting and demonstrating the usefulness of THALES-2 code for planning or reviewing of containment venting strategies. Further study on the THALES-2 code applications to examine effect of various parameters (i.e. set point pressure for opening, set point pressure for closing, accident sequences) on the containment venting at a BWR was recommended by them.

Based on above circumstances it is necessary to study furthermore on the containment venting at a BWR.

The objective of this analysis is to examine effect of various parameters, namely,

- the areas of the vent path,
- containment venting pressure, and
- accident sequences

on the containment thermodynamic response, and radionuclide transport and release in the containment venting at a BWR using THALES-2 code.

## 2. Analytical Method

The THALES-2B code, a BWR version of THALES-2, was used in this analysis. The integrated severe accident analysis code THALES-2 code, was originally developed by JAERI under the cooperation of Japan N.U.S. Co. Ltd. and Toshiba Advanced System Co. The code covers major physical phenomena that would occur in the severe accident condition. Figure 2.1 and 2.2 show the control volume model in the THALES-2B and the fission product transport model of the ART module, respectively.

The Browns Ferry plant[4] was used as a reference plant in this analysis. This plant is a General Electric BWR4 Mark I, with thermal power 3,440 MWt. Since this study is not intended to provide a plant-specific analysis, various assumptions were made because sufficiently detailed information was not obtained from the Final Safety Analysis Report

The input data was prepared by JAERI.

The analytical assumptions were as follows:

- venting from wetwell using hardened vent paths,
- successful closure of vent line after depressurization,
- pool scrubbing model by Kaneko et al.,
- revaporation of deposited aerosol was considered

The calculation cases in the analyses were as follows:

for the area of the vent path sensitivity study

Case 1 (base case) : TQUV sequence (loss of feed water + no injection to core + no containment spray), flow path area 16" pipe, open at 1.5x design pressure, close at design pressure.

Case 2 : same as case 1 except use flow path area 8" pipe.

Case 3 : same as case 1 except use flow path area 4" pipe.

for the containment venting pressure sensitivity study

Case 4 : same as case 1 except open at containment failure pressure

Case 5 : same as case 4 except close at (failure pressure - 0.5 design pressure)

for the accident sequence sensitivity study

Case 6 : same as case 1 except for S2E sequence (small break at loop B + no containment spray).
Case 7 : TQUV sequence, no containment venting, containment fails in the drywell.

## 3. Analytical Result

### 3.1 Containment Thermodynamic Response

Sequence of events and their timing of occurrence for both TQUV and S2E accident sequences are summarized in Table 3. The Figure 3.1 shows the containment pressurization prior to the containment was vented. It was found that both accident sequences pressurized the containment significantly after the core was damage. In the S2E accident sequence, it was found a pressure spike in the containment just following the vessel breach.

Figure 3.2 shows containment pressures for cases 1, 2, and 3. We found that in all cases the containment pressure can be maintained in the specified pressure range.

Figure 3.3 shows the wetwell temperature of cases 1, 4 and 5. It found that the liquid temperature was remaining in the sub cooled until the end of simulation, therefore the flashing was not happen. The Figure 3.4 shows the wetwell mixture level for cases 1, 4 and 5. It found that the pool swelling due to the containment venting was not enough to produce entrainment through containment venting line.

### 3.2 Radionuclide Transport and Release

Figure 3.5 shows the CsI mass in the wetwell (WW) gas space for both TQUV and S2E accident sequences. This figure indicates that both accident sequence give a difference CsI mass before the containment venting started to operate. The higher containment venting setting pressure operation has more time to remove CsI naturally from the WW gas space than the lower containment venting setting pressure operation has.

The comparison for other species of fission product released to the environment is depicted in the Figure 3.6 in the form of normalized for case 1. The percentage in the parentheses in the figure 3.6 represents source terms for case 1. It was found that the high setting pressure of opening containment venting could extend time for fission product to be removed from WW gas space naturally. Therefore the high setting pressure of opening containment venting will produce a smaller fission product released to the environment than the low setting pressure of opening containment venting has. However the wide range of containment venting operation pressure will produce a higher fission product released to the environment than the narrow range of containment venting operation pressure has. It also was found that the only the Sr was sensitive to the accident sequence.

## 4. Conclusions and recommendation

### 4.1 Conclusions

1. The 4-inch pipe of containment venting flow path is sufficient to maintain the containment pressure in the specified range if the containment was pressurized by the decay heat power.
2. The entrainment by the pool swelling as well as by the flashing was not occurred during the containment venting.
3. The source terms are not sensitive to the variation of containment venting flow path area.
4. The containment venting pressure operation setting point has important rule in the containment venting.
5. The source terms are not sensitive to the accident sequence, except for Sr source term.

## 4.2 Recommendation

The various analyses described in this paper not only confirmed to the conclusions described in the previous section but also identified several areas where additional analyses would give better understanding on the containment venting strategy. It is recommended that analyses of accident sequences which has high power such as anticipated transient without scram are necessary as well as accident sequence which pressurized the containment before the core damage to investigate the capability of venting flow path area for maintaining containment pressure. There is a pressure spike in the containment due to vessel breach. Therefore, this pressure spike is necessary to be considered in the decision on the determination of the starting point of containment venting pressure operation.

## Acknowledgement

One of authors (Surip Widodo) would like to gratefully acknowledge the Japan Atomic Energy Research Institute (JAERI) for giving an opportunity to perform the research through Scientist Exchange Program of Science and Technology Agency (STA) of Japan.

## References

1. US. Nuclear Regulatory Commission "Individual Plant Examination Program: Perspectives on reactor Safety and Plant Performance", NUREG-1560 Volume 2, Parts2-5, December 1997.
2. J. Ishikawa, et al., "A scooping analysis of containment venting at a BWR using THALES-2", Proceedings of the workshop on severe accident research held in Japan (SARJ-97), JAERI-Conf-98-009 513 pp. 389-394/ May 1998
3. M. Kajimoto, et al., Private Communication, 1994.
4. TENNESSE VALLEY AUTHORITY, "Browns Ferry Nuclear Power Plant, FSAR", DOCKET 50259, 1970.

**Table 3 Sequence of Events and its Timings of Occurrence**

| EVENTS | TQUV Time (min.) | S2E Time (min.) |
|---|---|---|
| Accident | 0 | 0 |
| Automatic Depressurization System (ADS) open | 8.25 | NA[a)] |
| Core Uncovery | 14.82 | 17.55 |
| Core Melt Initiation and Relocation | 44.67 | 63.65 |
| Core Support Failure | 61.05 | 87.25 |
| Core Collapse | 88.95 | 88.92 |
| Vessel Failure | 101.92 | 124.53 |
| Containment Pressure reaches the design pressure (4.97E4 $kg_f/m^2$) | 215.4 | 277.5 |
| Containment Pressure reaches 6.94E4 $kg_f/m^2$ | 303.0 | 369.0 |
| Containment Pressure reaches the limit pressure (9.2594E4 $kg_f/m^2$) | 398.0 | NA[b)] |

Notes

a) : It was not modeled in this analysis.

b) : It was not simulated in this analysis.

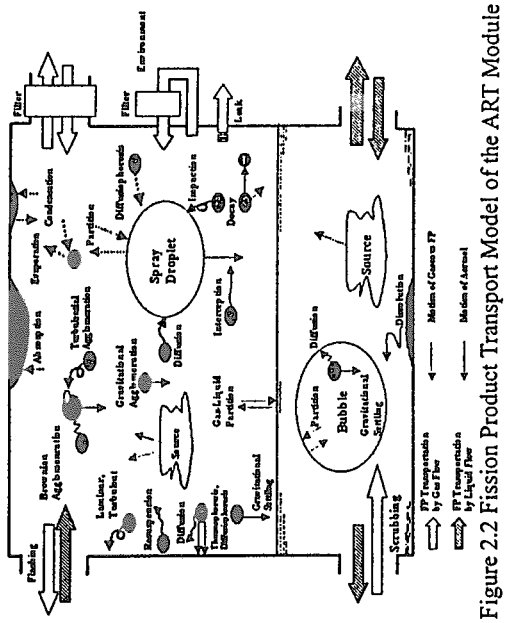



Figure 2.2 Fission Product Transport Model of the ART Module

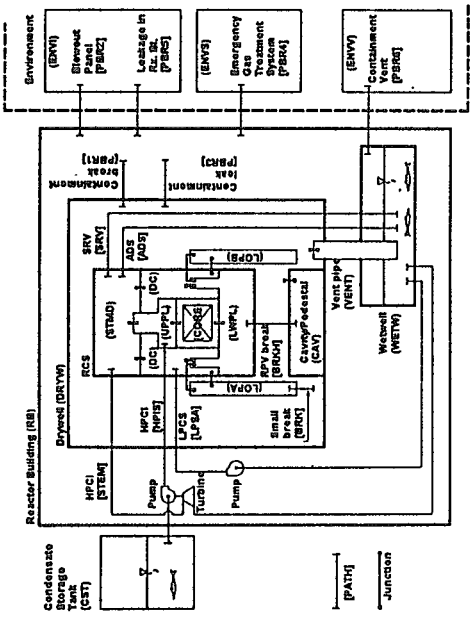



Figure 2.1 Control Volume Model in THALES-2B

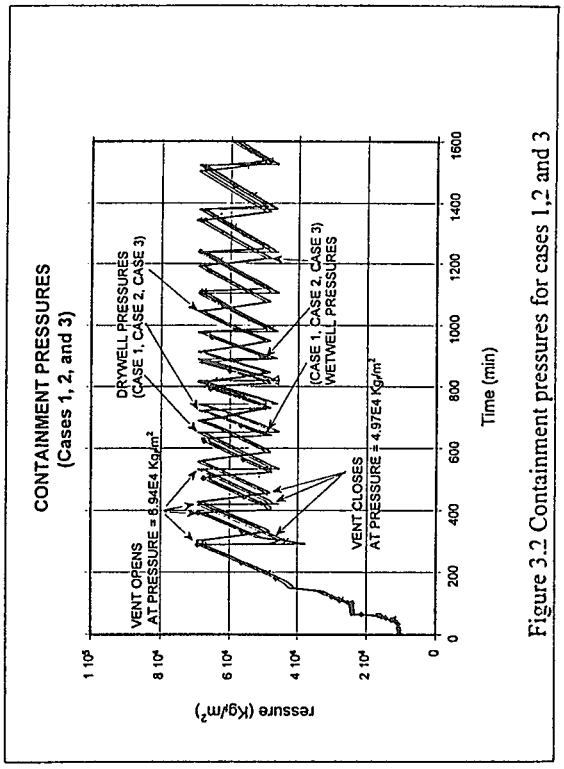



Figure 3.2 Containment pressures for cases 1,2 and 3

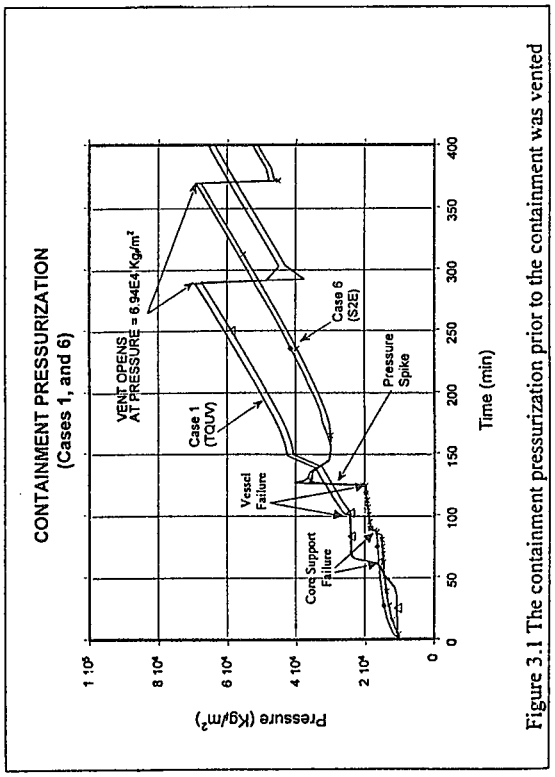



Figure 3.1 The containment pressurization prior to the containment was vented

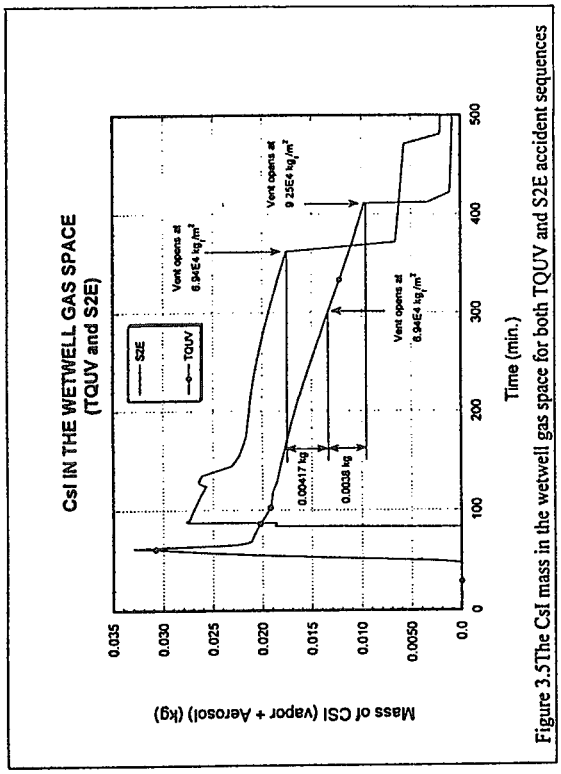



Figure 3.5The CsI mass in the wetwell gas space for both TQUV and S2E accident sequences

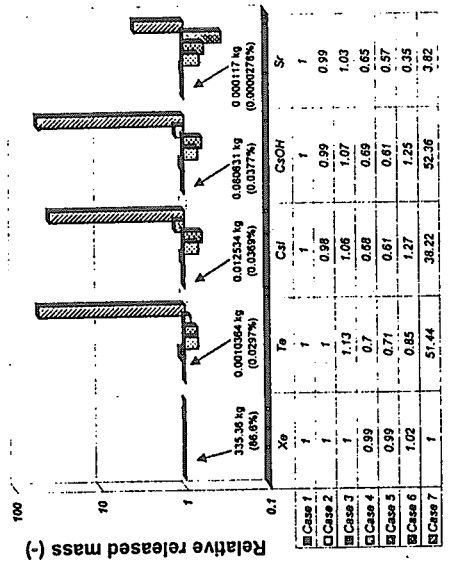



Figure 3.6 Relative Fission Product released mass to the Environment for Case 1 (base case) at 1600 minutes into the accident

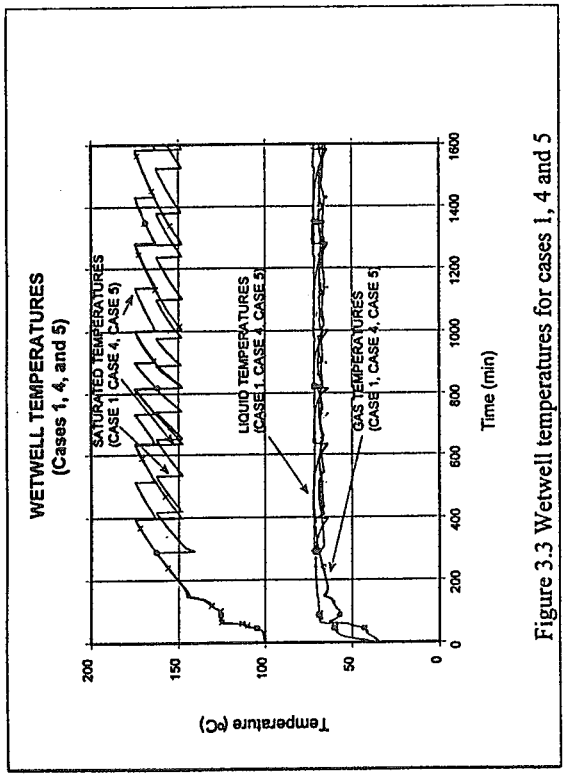



Figure 3.3 Wetwell temperatures for cases 1, 4 and 5

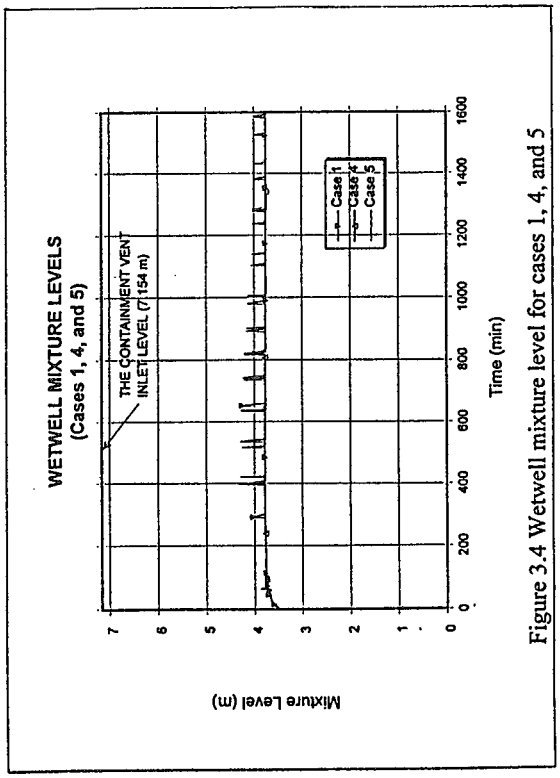



Figure 3.4 Wetwell mixture level for cases 1, 4, and 5

# 9. Session 8

# Fission Product Behavior I

Chairperson:

A. Jones (JRC)

A. Watanabe (NUPEC)

This is a blank page.

JP0150109

JAERI－Conf 2000－015

# 9.1 Current Status of VEGA Program and a Preliminary Test with Cesium Iodide

A. Hidaka, T. Nakamura, T. Kudo, R. Hayashida, J. Nakamura, T. Otomo and H. Uetsuka

Dept. of Reactor Safety Research
Japan Atomic Energy Research Institute
Tokai-mura, Naka-gun, Ibaraki-ken, 319-1195, JAPAN
Tel: +81-29-282-6778, Fax: +81-29-282-5570
E-mail: hidaka@sarl.tokai.jaeri.go.jp

**Abstract**

The VEGA program has been performed at JAERI to clarify the mechanism of FP release from irradiated PWR/BWR fuels including MOX fuel and to improve predictability of the source term. The principal purposes are to investigate the release of actinides and FPs including non-volatile radionuclides from irradiated fuel at 3000 ℃ under high pressure condition up to 1.0 MPa. The short-life radionuclides will be accumulated by re-irradiation of test fuel just before the experiment using the JAERI's research reactor such as JRR-3 or NSRR. The test facility was installed into the beta/gamma concrete No.5 cell at RFEF and completed in February, 1999. Before the first VEGA-1 test in September, 1999, a preliminary test using a cold simulant, cesium iodide (CsI) was performed to confirm the fundamental capabilities of the test facility. The test results showed that the trapping efficiency of the aerosol filters is about 98 %. The amount of CsI which arrived at the downstream pipe of the filters was quite small while a small amount of $I_2$ gas which can pass through the filters was condensed just before the cold condenser as expected in the design.

**Key Words:** *Severe Accident, Radionuclide Release, VEGA Program, Non-Volatile Fission Products, Source Term, Cesium Iodide, $I_2$ gas, Aerosol, Condensation, Deposition*

## 1. INTRODUCTION

The release of radionuclides such as fission products (FPs) and actinides from fuels is one of key issues for precisely estimating the source terms in hypothetical severe accidents[1]. A lot of experimental researches such as ORNL/HI-VI (USA)[2], CEN Grenoble/HEVA-VERCORS (France)[3] and CRL/HCE-HCL (Canada)[4] tests have been conducted so far. However, the number of the tests and the covering test conditions were limited. Thus, considerable uncertainties still remain, especially in the areas under high temperature and/or high pressure conditions and the behavior of short half-life FPs. For example, the ambient atmosphere such as oxidizing or inert condition could affect the chemical form of released radionuclides which depends on the volatility. The bundle material such as control rod could react chemically with the released radionuclides and could change their volatility. The FP release from very high burnup fuel could be enhanced compared with that from low burnup fuel. The FP release rate could become small as the pressure increases[5]. There is no data from MOX (mixed-oxide fuel).

Moreover, recent VERCORS tests[6] showed that Sr is less volatile than Ba although the both elements were classified in the same group in the CORSOR-Booth model[7]. Moreover, it was pointed out that large amount of Ba release would result in approximately 20% decrease in residual decay power of degraded core during severe accidents[8]. Accordingly, the Ba release behavior could delay the accident progression as well as the change of FP source term.

In order to solve these uncertainties and to investigate the releases of FPs and actinides from irradiated fuel at 3000 ℃ under high pressure condition up to 1.0 MPa, an experimental program, VEGA (Verification Experiments of radionuclides Gas/Aerosol release) has been performed at Japan Atomic Energy Research Institute (JAERI)[9),10),11]. The summary of previous studies and target of VEGA program are shown in **Table 1**. In the VEGA program, a first priority is made for the release of volatile/non-volatile FPs and actinides under high temperature above 2700 ℃ and high pressure conditions. One of special features of this program is to investigate the effect of ambient pressure on the radionuclide

release from fuel which has never been examined in previous studies. In the experiment, the irradiated PWR/BWR fuels including MOX will be used as the test sample. The other objective of this program is to investigate the effect of oxidized/unoxidized conditions on the radionuclide release/transport behavior in reactor core and coolant systems.

## 2. OUTLINES OF VEGA FACILITY

The test facility was installed into the beta/gamma concrete No.5 cell at the Reactor Fuel Examination Facility (RFEF) and completed in February, 1999. Schematic of VEGA facility is shown in **Fig.1**. The facility mainly consists of a steam/gas supply system, high-frequency induction furnace, thermal gradient tubes (TGTs), aerosol/charcoal filters, cascade impactor and on-line gamma measurement system. The test section is pressurized up to 1.0 MPa between the gas supply system and the valves just after the aerosol filter. During the experiment, one of three valves will be opened depending on the fuel temperature. The valve of cascade impactor line will be opened for several minutes to measure the aerosol size distribution. The temperature of piping between the furnace and TGTs is maintained at 750 ℃ to avoid CsI aerosol deposition. The temperature at TGTs is decreased linearly from 750 to 200 ℃ to obtain the FP deposition data as a function of temperature and to identify the chemical form of deposited FPs.

Depending on the maximum temperature of induction furnace and the oxidized/unoxidized carrier gas conditions, the materials used in the VEGA furnace will be changed as shown in **Table 2**. In the case of the maximum temperature below 2200℃, $ZrO_2$ will be used as crucible materials. In the case of the maximum temperature above 2200℃ and unoxidized condition, tungsten (W) will be used while $ThO_2$ will be used under oxidized condition.

The latest design of furnace for oxidized condition is shown in **Fig. 2**. The induction coil is located just outside of alumina tube. Only the material which has an electric conductivity in circumferential direction can be heated by induction coil. In this design, graphite cylindrical susceptor can be heated. The inner tube is a pressure boundary and there is no steam flow near graphite susceptor to avoid oxidation of graphite. The furnace is surrounded by thermal insulator made of carbon felt and carbon powder. Temperatures of furnace are measured by two pyrometers. One pyrometer measures temperature at crucible bottom while the other one measures the side of susceptor as the backup. In order to keep gas flow path, lateral holes were made on the stand pipe and crucible. Moreover, a cap was covered above crucible to help carrier gas to come into crucible and to sweep released FPs. The fundamental design of W furnace for unoxidized condition is basically the same as that of $ZrO_2$ or $ThO_2$ furnace. One of special features of W furnace is that there is no graphite susceptor and instead W inner tube is directly heated by induction coil.

The fabrication study of $ThO_2$ tubes is being performed. Since $ThO_2$ is a nuclear material, the handling is not so easy. JAERI has conducted the fabrication of $ThO_2$ tube by using the centrifugal slip casting, rubber pressing or metal mold techniques. Recent study showed that the $ThO_2$ powder size growth (about 1 $\mu$ m) by heating up to 1,500 ℃ is very important for improvement of the mold strength.

**Photograph 1** shows the VEGA facility taken through a lead grass of concrete cell. The furnace and induction coil are located inside the right-hand chamber. **Photograph 2** shows the gaseous FP trap device which is set at the isolation room next to the hot cell. The carrier gas including released FPs enters, at first, condenser and gaseous iodine is removed by charcoal at 0℃. Then, the carrier gas is delivered to dryer and noble gas trap and the noble gas is removed by charcoal cooled by Fluorinert (compound of fluorine) less than -70℃. Emitted gamma rays from the inside condenser and noble gas trap are measured by the Ge semiconductor detectors.

## 3. EXPERIMENTAL CONDITIONS

The maximum size of test sample is 6 cm long and the diameter is 14.3 mm. The weight of test sample with or without cladding is about 100 g. The samples used in the VEGA experiments are irradiated PWR, BWR or MOX fuels of which burnup varies from 26 to 61 GWd/tU. In order to accumulate the short-life radionuclides such as I-131, re-irradiation of test fuel just before the experiment will be done using JAERI's research reactor such as JRR-3 or NSRR (Nuclear Safety Research Reactor). The maximum temperature of

test fuel can be raised up to 3,000 ℃ and the ambient pressure will be changed from 0.1 to 1.0 MPa. In order to investigate the effect of ambient gas species on the FP release behavior and the chemical form of released FPs, helium, hydrogen, air, steam or the mixed gas of them will be used. Moreover, the effect of control rod materials (such as Ag, In, Cd and boron) or the fuel burnup on the FP release behavior will be examined.

## 4. MEASUREMENTS AND CHEMICAL ANALYSES

The transport and deposition behaviors of released FPs will be studied by chemically measuring the deposition masses onto pipings such as TGTs under well characterized flows of steam/$H_2$/He/air atmosphere monitored by on-line oxygen/hydrogen sensors. On-line gamma measurement will be done for aerosol filters, cascade impactor, charcoal and cooled charcoal traps. Radionuclides such as Cs-137, I-131, Ba-140 and La-140 will be trapped and measured at aerosol filters and cascade impactors. Gaseous I-131 will be captured at charcoal trap. Noble gases such as Kr-85 and Xe-133 will be trapped at cooled charcoal trap. On-line measurement of $O_2$/$H_2$ concentrations will be done at just after aerosol filters. Off-line gamma spectrometry will also be performed after the experiment for most of downstream pipings including crucible in furnace.

The analyses with SEM/EPMA (Scanning Electron Microscope/Electron Probe X-Ray Micro Analyzer) will be performed to identify elements deposited onto piping. The analyses with SIMA (Secondary Ion Micro Analyzer) and ICP-AES (Inductively Coupled Plasma Atomic Emission Spectrometer) will also be conducted for measurement of inorganic materials in solution.

The radioactivity of various nuclides calculated by the ORIGEN-2 code[12] is shown in **Table 3**. The calculated fuel is PWR MOX of which weight is 104 g$UO_2$ and its burnup is 56 GWd/t. The cooling duration is 1 year. The reason for use of this PWR MOX in the calculation is that radioactivity becomes the highest among expected candidates for fuel specimens. It was also assumed that NSRR re-irradiation with linear heating rate of 0.065 W/m is performed for 9 hours and after that, the sample is cooled for 3 days. Kr-85 and Cs-137 will not be accumulated in sample fuel pellet by NSRR re-irradiation because their yield mass are small. On the other hand, relatively large amount of short half-life radionuclides such as I-131, Xe-133m, Ba-140 and Np-239 will be accumulated and their radioactivities will become large enough for measurement.

## 5. TEST MATRIX

Preliminary VEGA test schedule is shown in **Table 4**. The shakedown of test facility was finished by the beginning of FY1999 and first VEGA-1 test was performed in September 9, 1999. The maximum temperature of experiment will be gradually increased. The re-irradiation of test sample using JAERI's research reactor will be done for one experiment a year. Three experiments a year are scheduled after FY2000. In near future, radionuclide release from MOX will be investigated. This is because there is a difference in yield-mass between U-235 and Pu-239. Moreover, plutonium is very poisonous compared with uranium.

## 6. PRELIMINARY TEST WITH CESIUM IODIDE

Before the VEGA-1 test, a preliminary test using a cold simulant, CsI instead of irradiated fuel was performed to confirm the fundamental capabilities of the test facility[11]. Prior to the CsI test, several coupons were set at three different locations to measure CsI deposition onto them. The location of SUS316 coupons for CsI test is shown in **Fig. 3**. It is noted that two coupons were set at the same place to confirm reproducibility of measurement. Moreover, aerosol deposition onto 4 inner SUS tubes which are inserted in TGTs were measured. Again, by measuring CsI deposition at different places inside VEGA facility, an attempt was made to obtain trapping efficiency of aerosol filter and to confirm almost no arrival of CsI aerosol at condenser as expected in the design.

The furnace temperature of CsI test is shown in **Fig. 4**. Temperature was increased at a rate of about 1 ℃/s. A small plateau was made at 1,350℃ because the pyrometer had to be changed from monochromatic to two color for higher temperature measurement. After that, temperature was raised and maintained at 1,500℃ for 30 min and was decreased mostly in the same manner. The deposited mass distribution and

temperature at 60 min are shown in **Fig. 5**. The temperature simply decreased as the distance becomes far from fuel.

The cesium and iodine masses deposited onto the coupons were measured separately by using the ion meter and the liquid ion chromatography. The deposition masses of cesium and iodine increased at downstream of TGTs and decreased by two orders of magnitude at filter. This result indicates that the trapping efficiency of filter is about 98 %. Moreover, deposition masses of cesium and iodine were almost the same at the piping between TGTs and filters. Therefore, it can be said that most of CsI was vaporized, transported and deposited as the original chemical form of CsI.

However, there was an obvious difference in deposited mass just before condenser between cesium and iodine. This is considered that small amount of CsI was dissolved due to impurities such as humidity and formed $I_2$ gas which can pass through the filters was condensed just before the cold condenser. However, these results indicates that any aerosol did not arrive at condenser as expected in design. The test results also showed that a relatively large amount of CsI may be deposited at the outlet piping of furnace in the case that the flow rate is not kept high enough. Since the gamma measurement at that portion is difficult for present design due to its structural reason, the design will be changed in future experiments.

## 7. CONCLUSIONS

The VEGA program has been performed at JAERI to clarify the mechanism of FP release from irradiated PWR/BWR fuels including MOX and to improve predictability of the source term. The principal purposes of this research are to investigate the release of actinides and FPs including non-volatile radionuclides from irradiated fuel at 3000 ℃ under high pressure condition up to 1.0 MPa. The test facility was completed in February, 1999. Before the first VEGA-1 test in September, 1999, a preliminary test using a cold simulant, CsI instead of irradiated fuel was performed to confirm the fundamental capabilities of the test facility. The test results showed that the trapping efficiency of the aerosol filters is about 98 %. The amount of CsI which arrived at the downstream pipe of the filters was quite small while a small amount of $I_2$ gas which can pass through the filters was condensed just before the cold condenser as expected in the design.

## REFERENCES


1) U. S. Nuclear Safety Commission, "Severe Accident Research Program Plan Update," NUREG-1365 Rev.1 (1992).
2) M. F. Osborne, et al., "ORNL Studies of Fission Product Release under LWR Accident Conditions," Nuclear Safety Vol.33, No.3 (1992).
3) J. P. Leveque, et al., "The HEVA Experimental Program," Nucl. Technol., 108, 33 (1994).
4) B. J. Lewis, et al., "Release Kinetics of Volatile Fission Products under Severe Accident Conditions," Nucl. Technol. Vol.99, pp.330-342 (1992).
5) R. B. Bird, et al., "Transport Phenomenon," John Wiley and Sons, New York (1960).
6) G. Ducros, et al., "Fission Product Release and Fuel Behavior under Severe Accidental Conditions; Synthesis of the VERCORS 1 to 6 Experimental Program," Proc. of ANS International Topical Meeting on LWR Fuel Performance, Park City (2000).
7) M. Ramamurthi, et al., "Refinement of CORSOR - An Empirical In-Vessel Fission Product Release Model," U. S. Nuclear Regulatory Commission (1990).
8) K. Froment, et al., "Physico-Chemistry and Corium Properties for In-Vessel Retention," Proc. of OECD/CSNI Workshop on In-Vessel Core Debris Retention and Coolability, NEA/CSNI/R(98)18, pp.163-171, Garching (1998).
9) T. Nakamura, et al., "Research Program (VEGA) on the Fission Product Release from Irradiated Fuel," JAERI-Tech 99-036 (1999).
10) A. Hidaka, et al., "Current Status of VEGA Program," JAERI-Conf 99-005, pp.211-218 (1999).
11) A. Hidaka, et al., "Outlines of VEGA Program and A Test with Cesium Iodide for Confirmation of Fundamental Capabilities of the Experimental Facility," JAERI-Research 99-066 (1999).
12) A. G. Croff, "ORIGEN2: A Versatile Computer Code for Calculating the Nuclide Compositions and Characteristics of Nuclear Materials," Nucl. Technol. Vol. 62, 335 (1983).

Table 1 Previous studies and target of VEGA

| Parameters / Radionuclides | <2700℃ | ≧2700℃ | Pressure | Ambient gas |
|---|---|---|---|---|
| Volatile FP | ○ | × | × | △ |
| Non-volatile FP | △ | × | × | △ |
| Actinide (Mox fuel) | △ | × | × | × |
| Short-life FP | △ | × | × | × |

○ ;Sufficient data, △ ; Insufficient data, × ; No data

First priority of VEGA　Second priority of VEGA

Table 2 Requirement for furnace material

| | M.P. > 3000℃ | Stability under oxidizing condition |
|---|---|---|
| $ThO_2$ | ○ (3370℃) | ○ |
| W | ○ (3382℃) | × |
| $ZrO_2$ | × (2677℃) | ○ |

Table 3 Gamma measurement

(ORIGEN-2 calculation)

| Nuclide | E-gamma (MeV) | Half life (day) | I-gamma (%) | LWR*1) (Ci) | Re-irradiation in NSRR*2) (Ci) | Total (Ci) |
|---|---|---|---|---|---|---|
| Kr-85 | 0.514 | 3912.8 | 0.434 | 8.91E-01 | - | 8.91E-01 |
| I-131 | 0.364 | 8.04 | 81.2 | - | 8.07E-02 | 8.07E-02 |
| Xe-133m | 0.233 | 2.19 | 10.3 | - | 1.32E-02 | 1.32E-02 |
| Cs-137 | 0.662 | 10950 | 85.2 | 1.74E+01 | - | 1.74E+01 |
| Ba-140 | 0.537 | 12.75 | 24.39 | 4.99E-02 | 1.21E-01 | 1.71E-01 |
| Np-239 | 0.278 | 2.36 | 14.1 | - | 1.00E-01 | 1.00E-01 |

*1) PWR MOX fuel (104g$UO_2$, Burnup; 56GWd/t, Cooling duration : 1 year)

*2) NSRR re-irradiation ; 0.065W/m for 9hrs and cooling for 3days

Table 4 VEGA test schedule

| | 1999 | 2000 | 2001 | 2002 | 2003 | 2004 | 2005 |
|---|---|---|---|---|---|---|---|
| $ThO_2$ tube fabrication | | | | | | | |
| Shakedown | | | | | | | |
| Inert condition | | | | | | | |
| Oxidizing condition | | | | | | | |
| Pressure effect (+burnup) | | | | | | | |
| Short-life FP | | | | | | | |
| MOX fuel test | | | | | | | |

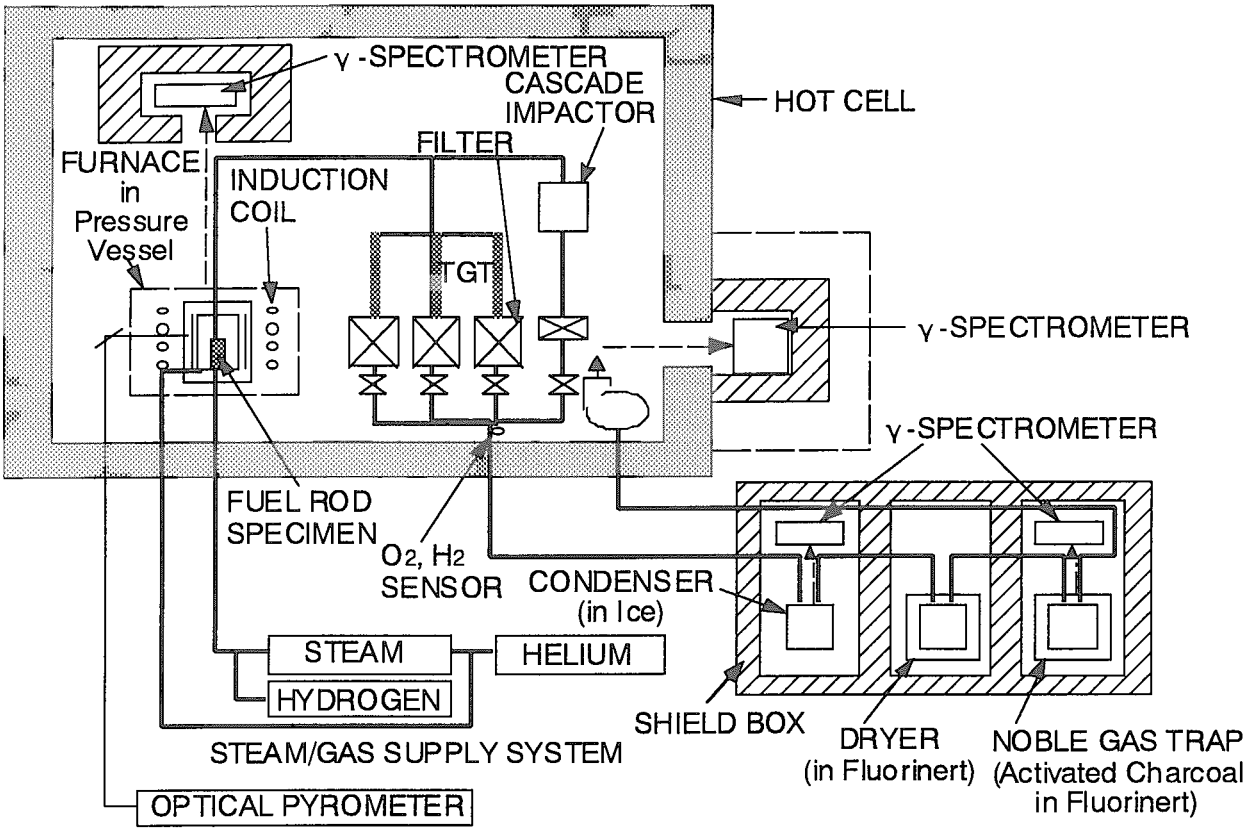



Fig.1 Schematic of VEGA facility

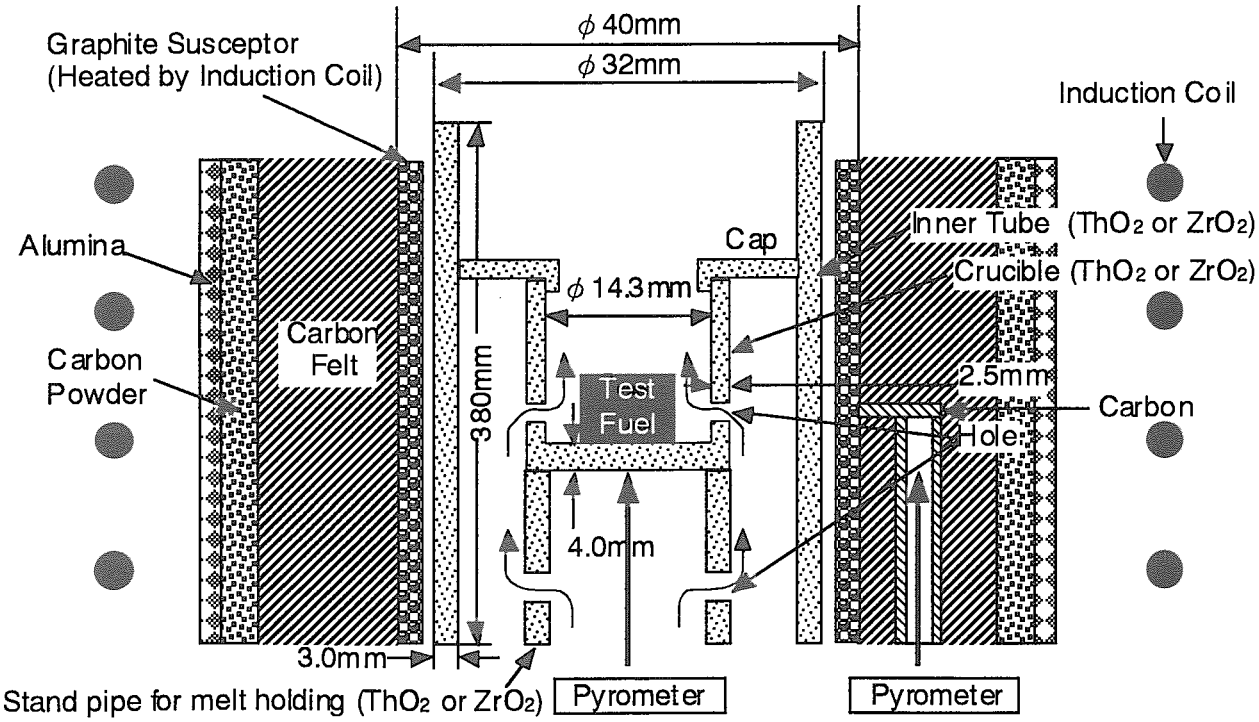



Fig.2 VEGA furnace for oxidized condition

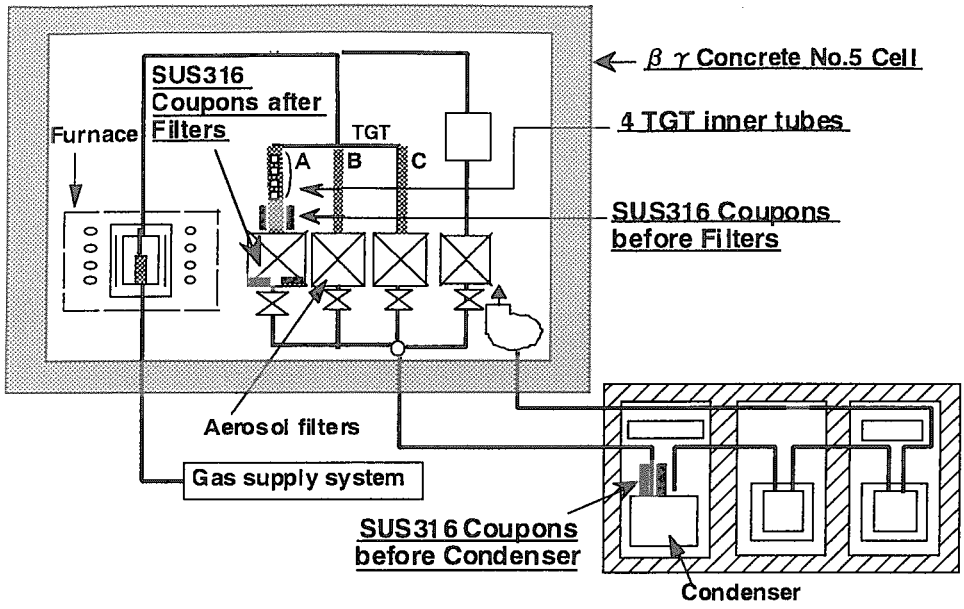



Fig.3 Location of SUS316 coupons for CsI test

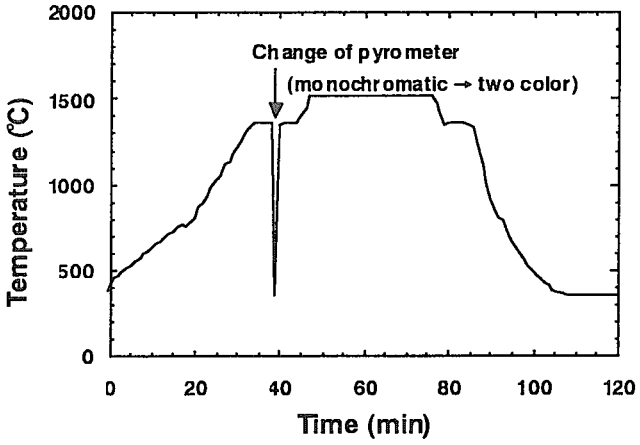



Fig.4 Furnace temperature of CsI test

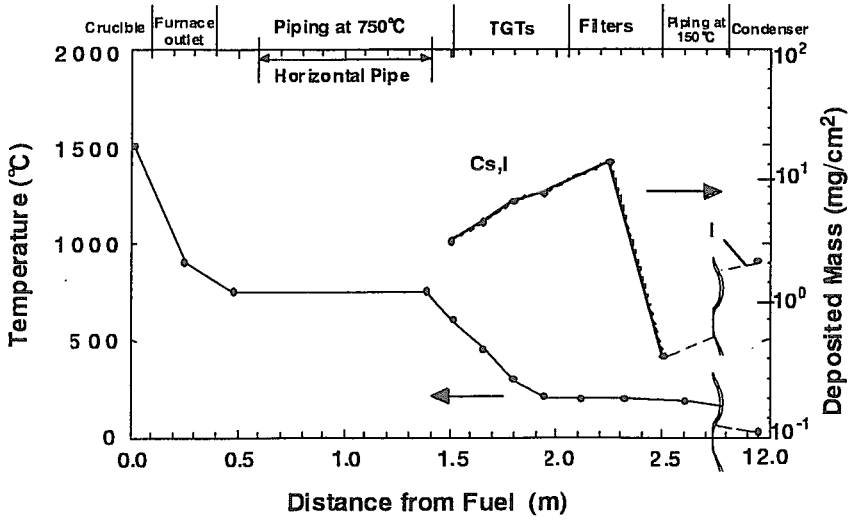



Fig.5 Deposited mass and temperature at 60 min

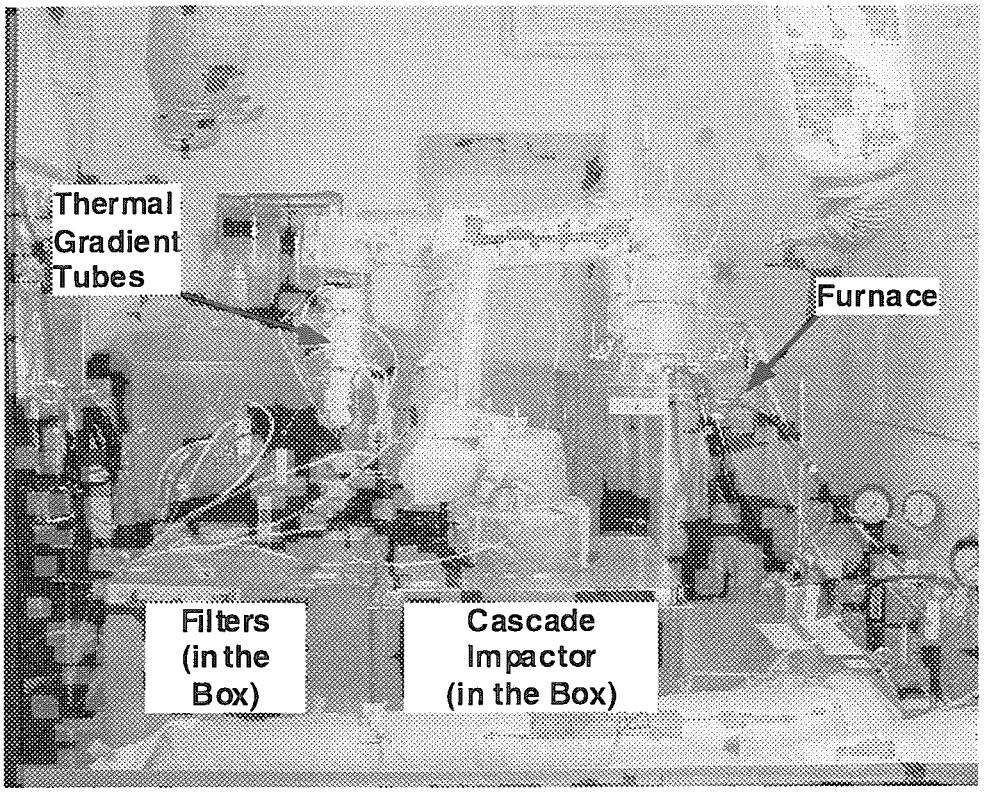



Photo.1 VEGA Facility

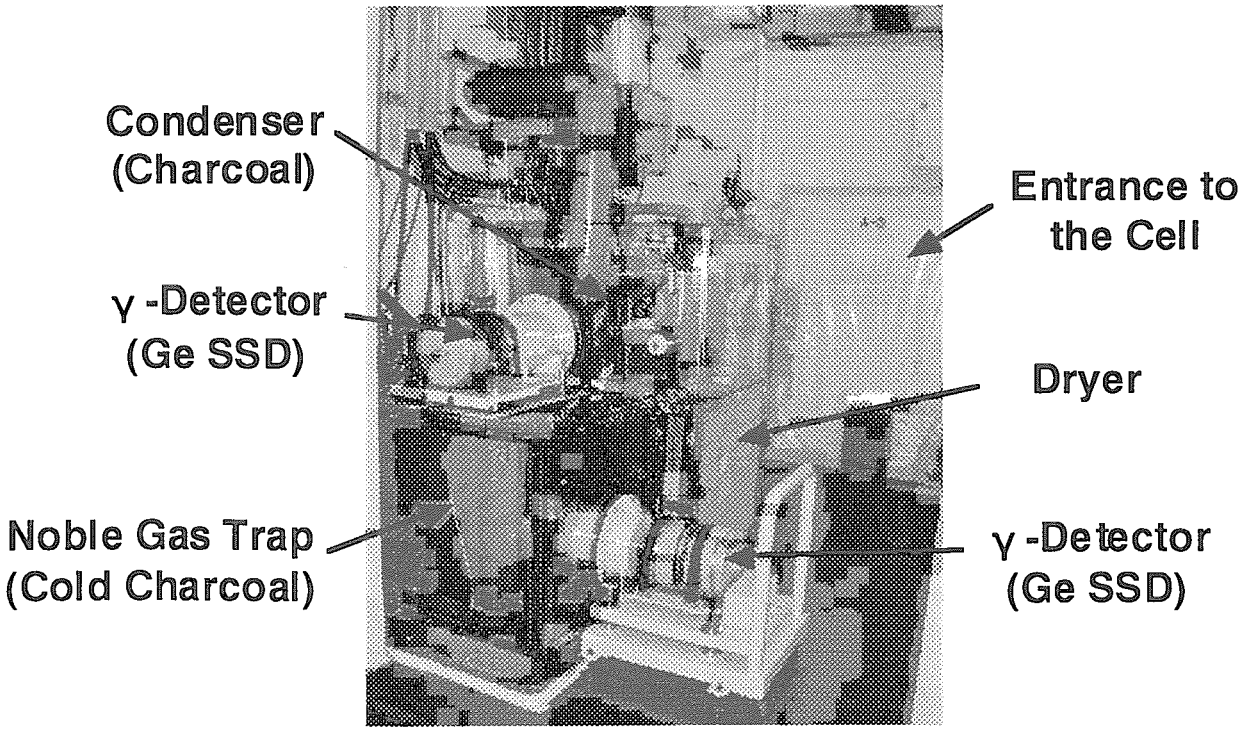



Photo.2 Gaseous FP trap device

JP0150110



# 9.2 Quick Look of First VEGA Test and Fabrication Study of Thoria Components

Takehiko NAKAMURA, Akihide HIDAKA, Tamotsu KUDO, Retsu HAYASHIDA,
Takashi OHTOMO, Jinichi NAKAMURA and Hiroshi UETSUKA

Fuel Safety Research Laboratory
Japan Atomic Energy Research Institute
Tokai-mura, Naka-gun, Ibaraki-ken
phone : (+81) 29-282-5955
fax : (+81) 28-282-6160
e-mail : take@nsrr.tokai.jaeri.go.jp

## ABSTRACT

The first fission product release test VEGA-1 was conducted on September 9, 1999 in the Reactor Fuel Examination Facility (RFEF) of JAERI Tokai using two PWR pellets at burnup of 47GWd/tU. The fuel pellet of about 10g without cladding tube was heated up to 2500℃ for 10min in an inert helium atmosphere at 0.1MPa, following two other plateaus at 1727℃(20min) and 2027℃(20min). The release of radioactive fission products was on-line measured by 4 gamma sensors watching at the fuel in a furnace, at trapped aerosols in filters, at a condenser, and at noble gases in a charcoal trap.

Gamma intensity of the fuel, which was dominated by Cs-134 and Cs-137, started to decrease, when the furnace temperature started to rise to the first plateau of 1727℃ from a conditioning stage at 1350℃. Following the decease, the intensity at the filters, which was located about 2.5m downstream of the furnace following thermal gradient tubes (TGTs) to collect the aerosols, started to increase. At about the same time, the counting rate on Kr-85 at the charcoal trap at –60℃ started to rise. Preliminary releases of Cs-134, Cs-137, and Ru-106, etc. were estimated from changes of gamma-ray spectrum before/after the heating test. Total releases of the nuclides, however, will be evaluated later, by comprehensive off-line measurement of the apparatus, e.g. gamma scanning, leaching and gamma spectroscopy of pipes, the TGTs, and the filters.

Development of thoria components in the VEGA furnace has been progressing for the use in high temperature tests under oxidizing atmosphere. Three kinds of slip casting techniques, i.e. centrifugal casting, drain casting and solid casting, were

successfully applied to fabricate inner tubes, crucibles and caps, respectively. Calcination of the thoria powder was conducted to optimize slip characteristics for casting and sintering. Fabrication of test pieces has finished, expecting for two to four sets of the components being ready for heating tests in year 2000.

## 1. Introduction

In order to evaluate consequence and influence of severe accidents (SAs) of light water reactors (LWRs), amount, timing and chemical/physical forms of radionuclide release (source terms) are needed be known under wide range of the accident conditions. With the better understanding on the source terms, more accurate probabilistic safety assessment (PSA) and more effective accident management (AM) could be realized, which would improve safety and reliability of LWRs. Release behavior of radioactive fission products and actinides from the over heated fuel under the SA conditions gives primary source terms in the SA evaluations.

A new experimental program VEGA (Verification Experiments of radionuclides Gas / Aerosol release)[1, 2] was initiated in Japan Atomic Energy Research Institute (JAERI), in order to supply reliable source term data. A short fuel specimen of 6cm long (max.) is induction heated under steam/hydrogen, air and/or helium atmosphere up to 3,000℃. The test can be done under high pressure of up to 1.0MPa to see the influence of the system pressure on the release. In order to realize the high temperature condition under chemically active steam conditions, development of thorium oxide (thoria: $ThO_2$) components has been made as one of the key elements of the project.

## 2. Test Conditions

The first test VEGA-1 was conducted September 9, 1999 at peak fuel temperature of 2,500℃ under inert helium atmosphere, using two PWR pellets at burnup of 47GWd/tU. The de-cladded fuel pellet of about 10g was heated up to 2500℃ for 10min in an inert helium atmosphere at 0.1MPa, following two other plateaus at 1727℃(20min) and 2027℃(20min). Fission product inventories of the test fuel estimated with ORIGEN2 code[3] are listed in Table 1. Isotopes of which gamma rays are identified in the pre test gamma spectrometry are marked gray in the table.

Table 1 Fission product Inventory In the PWR fuel at burnup of 47GWd/tU used in test VEGA-1.

| Nuclide | Inventory | | Half life | γ ray | Intensity |
|---|---|---|---|---|---|
| | mol | Bq | days | keV | 1/s |
| Kr-85 | 2.25E-06 | 3.80E+07 | 3.9E+03 | 514 | 1.65E+05 |
| Sr-90 | 6.54E-05 | 4.07E+08 | 1.1E+04 | | |
| Tc-99 | 1.01E-04 | 8.58E+04 | 7.8E+07 | | |
| Ru-106 | 1.14E-07 | 2.05E+07 | 3.7E+02 | | |
| Rh-106 | 1.07E-13 | 2.05E+07 | 3.4E-04 | 512 | 4.25E+06 |
| Pd-107 | 3.08E-05 | 8.59E+02 | 2.4E+09 | | |
| Ag-110M | 7.11E-11 | 1.88E+04 | 2.5E+02 | 884.67 | 1.37E+04 |
| | | | | 937.48 | 6.46E+03 |
| | | | | 1384.27 | 4.64E+03 |
| Sb-125 | 2.18E-07 | 1.42E+07 | 1.0E+03 | 427 | 4.19E+06 |
| Te-125M | 3.04E-09 | 3.48E+06 | 5.8E+01 | 109.27 | 9.59E+03 |
| Sn-126 | 3.03E-06 | 5.50E+03 | 3.7E+07 | 87.57 | 2.02E+03 |
| I-129 | 1.91E-05 | 2.21E+02 | 5.7E+09 | 39.58 | 1.66E+01 |
| Cs-134 | 1.27E-06 | 1.12E+08 | 7.5E+02 | 605 | 1.09E+08 |
| | | | | 796 | 9.55E+07 |
| Cs-137 | 1.00E-04 | 6.07E+08 | 1.1E+04 | 662 | 5.17E+08 |
| Ce-144 | 3.31E-08 | 7.71E+06 | 2.8E+02 | 133.5 | 8.55E+05 |
| Pr-144 | 1.40E-12 | 7.73E+06 | 1.2E-02 | 696 | 1.04E+05 |
| Pm-146 | 2.90E-10 | 9.58E+03 | 2.0E+03 | 747 | 3.54E+03 |
| Eu-154 | 2.47E-06 | 5.22E+07 | 3.2E+03 | 723 | 1.03E+07 |
| | | | | 1274 | 1.85E+07 |
| Total | 4.02E-03 | 2.38E+09 | | | 7.41E+08 |

* Inventory is calculated with ORIGEN2 code.

* Nuclides whose gamma rays were identified by the measurements are marked gray.

The radioactivity of the fuel was on-line measured by a pure Ge detector, which looked to the furnace through a changeable collimator. The released radionuclides from the fuel go through/or trapped at thermal gradient tubes (TGTs), filters, a condenser, a dryer and a cold charcoal trap, as illustrated in Fig. 1. Temperature of the pipes were kept 750℃ from the furnace to TGT inlet, then deceased linearly to 200℃ in the TGTs. The temperature of the filters to trap aerosols and pipes down steam was kept 200℃ till condenser which was 0℃. The charcoal trap was kept at –60 to trap fission gas Kr. Three sets of TGTs and filter packages are operated sequentially to separate the releases from the three temperature plateaus, as illustrated in Fig. 2. The filters, condenser, and charcoal trap were on-line measured by the gamma sensors.

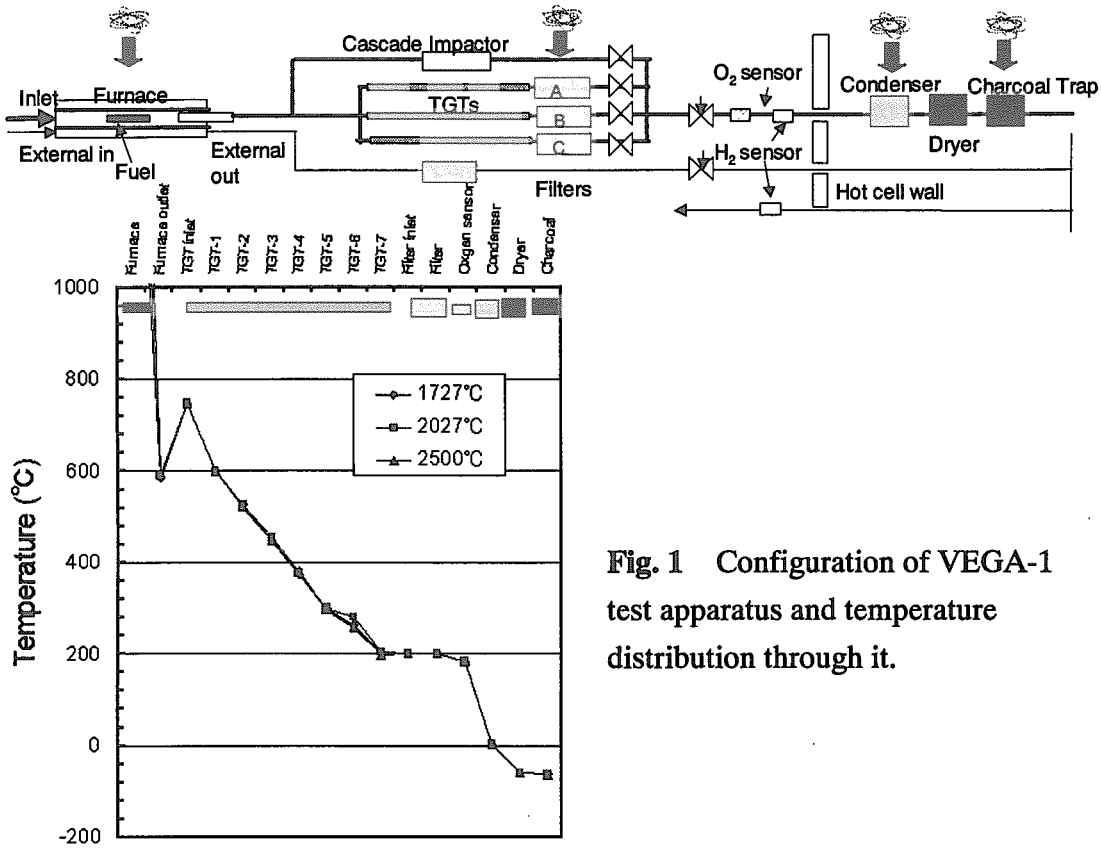



**Fig. 1** Configuration of VEGA-1 test apparatus and temperature distribution through it.

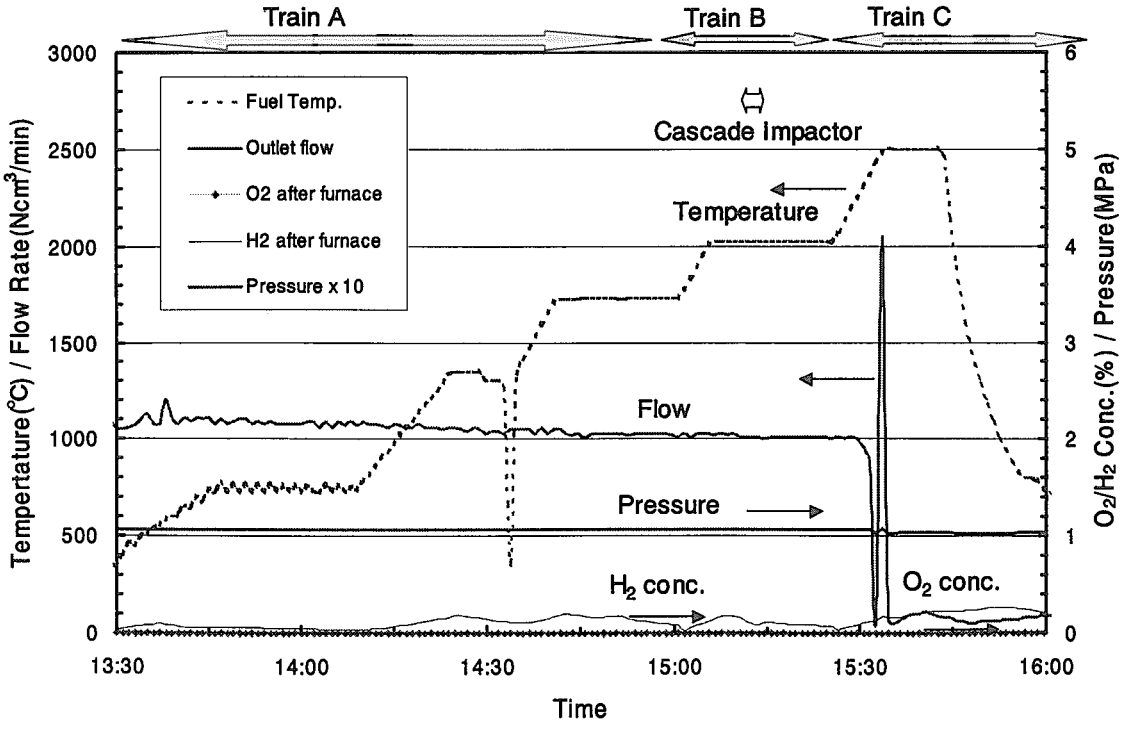



**Fig. 2** Time histories of temperature, flow, pressure and $H_2/O_2$ concentration in test VEGA-1.

## 3. Test Results

Gamma intensity of the fuel, which was dominated by Cs-134 and Cs-137, started to decrease, when the furnace temperature started to rise to the first plateau of 1727℃ from a conditioning stage at 1350℃ as shown in Fig. 3. Following the decease, the intensity at the filters, which was located about 2.5m downstream of the furnace and TGTs started to increase. At about the same time, the counting rate on Kr-85 at the charcoal trap started to rise. Preliminary releases of Cs-134, Cs-137, Ru-106, Ce-144, Sb-125, and Ag-110m were estimated from changes of gamma-ray spectrum before/after the heating test, as listed in Table 2. The releases are compared with those obtained in test VI-3, which was conducted in ORNL under steam atmosphere at a comparable temperature of 2,427℃ for 20min. The releases of Cs, Sb and Ag are similar in the two tests. The release of Ru and Ce, though, shows a large difference. The difference in the test atmosphere and/or cladded/uncladded test fuel might have caused the difference. The gamma peaks from Ce-144, Sb-125 and Ag-110m, however, are so small that the preliminary release estimation for the nuclides has larger uncertainties. Thus, the total releases of the nuclides will be re-evaluated later, by comprehensive off-line measurement of the apparatus, e.g. gamma scanning, leaching and gamma spectroscopy of pipes, the TGTs, and the filters.

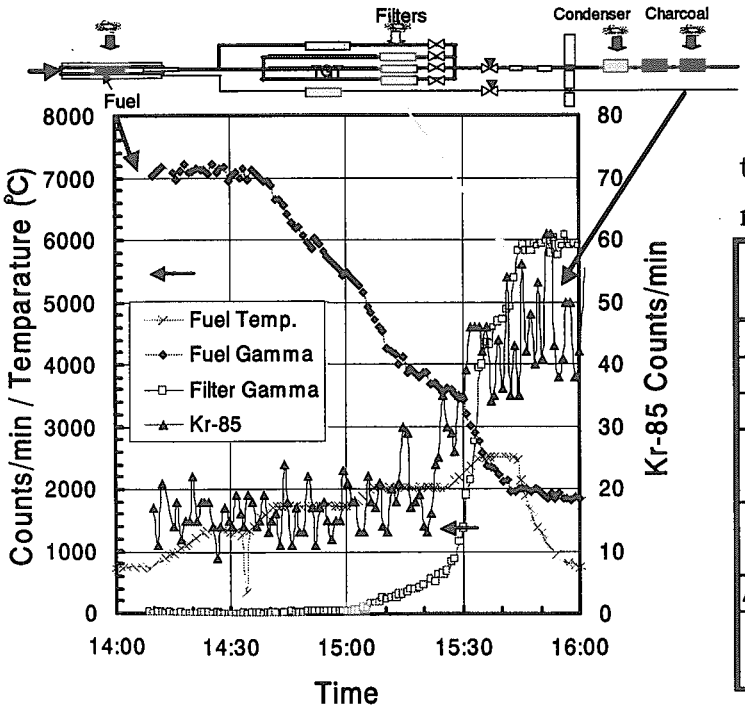



Table 2 Preliminary releases in test VEGA-1, assuming no Eu release

| Nuclide | γray | Release | VI-3* |
|---|---|---|---|
| | keV | % | % |
| Sb-125 | 429 | 96 | 99.2 |
| Cs-134 | 605 | 91 | 99.9 |
| Cs-137 | 662 | 87 | |
| Ru-106 | 622 | 70 | 5 |
| (Rh-106) | 1051 | 65 | |
| Ce-144 | 696 | 61 | <0.2 |
| (Pr-144) | 2186 | - | |
| Ag-110m | 885 | 71 | 84 |
| Eu-154 | 724 | 0 | <0.01 |
| | 1275 | 0 | |

**Fig. 3** Online gamma measurement results in VEGA-1.

## 4. Thoria Fabrication

In order to realize high temperature enough to melt $UO_2$ fuel, development of the furnace components, which stands for the high temperature up to 3,000℃ under chemically active steam/air atmosphere, is essential. Development of tubes and crucible of thorium dioxcide ($ThO_2$) have been made for the use in the VEGA furnace. Schematic configuration and thoria components needed in the furnace are illustrated in **Fig. 4**. An inner tube of 385mm long, which separate the test atmosphere to the inert susceptor atmosphere, a crucible, a cap, and a support of the crucible, were fabricated for the use in preliminary heating tests. Centrifugal slip casting technique for the inner tube, drain casting for the crucible, and solid casting for the cap are selected for the fabrication after trial with the dry rubber press technique[4]. Outline of the fabrication flow of the slip casting is illustrated in **Fig. 5**.

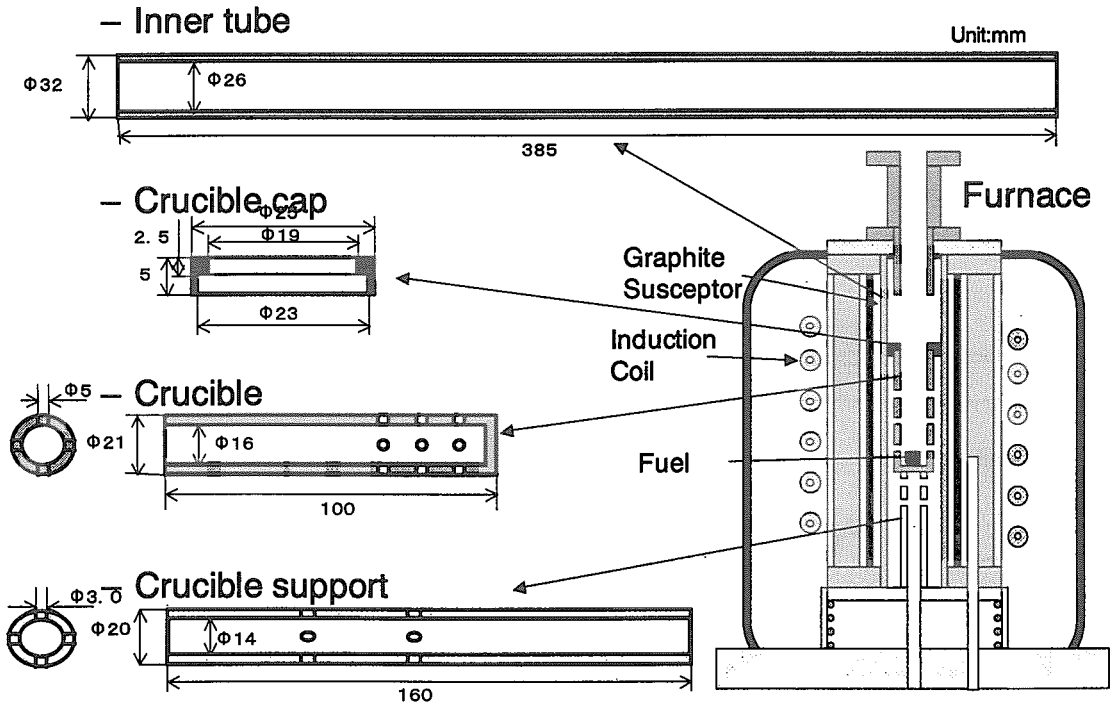



**Fig. 4** Schematic configuration of VEGA furnace and thoria components needed.

In order to optimize characteristics of the thoria powder for slip casting, pre-heating process of the powder, which is called calcination, was taken at the first stage of the fabrication. With the calcination of the powder, size of the primary particle glows larger to improve the slip stability and castability. As is shown in **Fig. 6**, the sintered density decreases as the calcination temperature becomes higher. Thus, it

is important to optimize these characteristics of the powder by adjusting the calcination temperature. In the test fabrication, calsination temperature of 1,500℃ was taken to achieve sintered density larger than 9g/cm$^2$ and specific surface of the powder about 1m$^2$/g.

The powder was mixed with water and defloculant to be homogeneous slip. The content of the thoria was adjusted to be 40vol.%, in order to have proper viscosity for the casting. The cast components was, then, sintered at 1,700-1,750℃ under air atmosphere to have densities about 9.4g/cm$^3$. Specifications and appearance of the crucible are shown in **Fig. 7**. Heating tests using the test pieces are planned in July 2000 prior to the actual use in the fission product release tests.

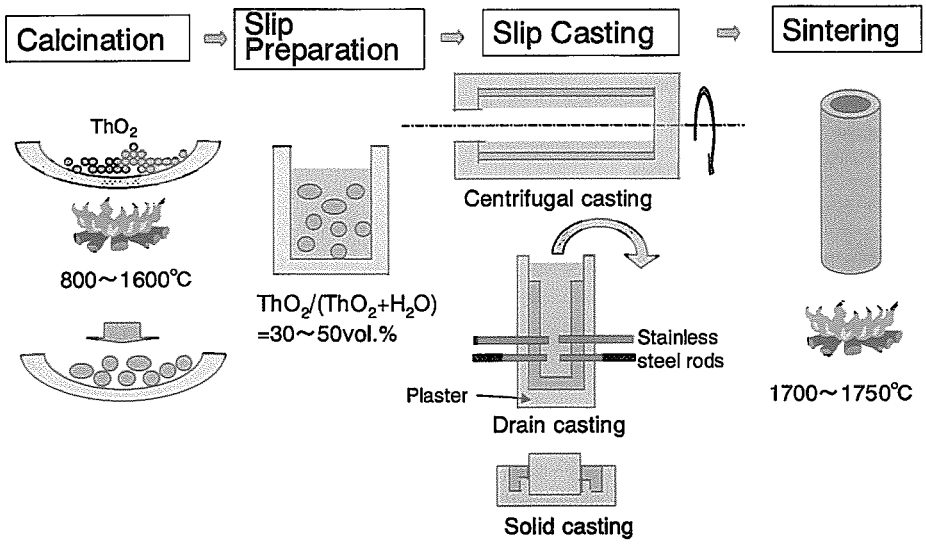



**Fig. 5** Flow of thoria fabrication by slip casting techniques.

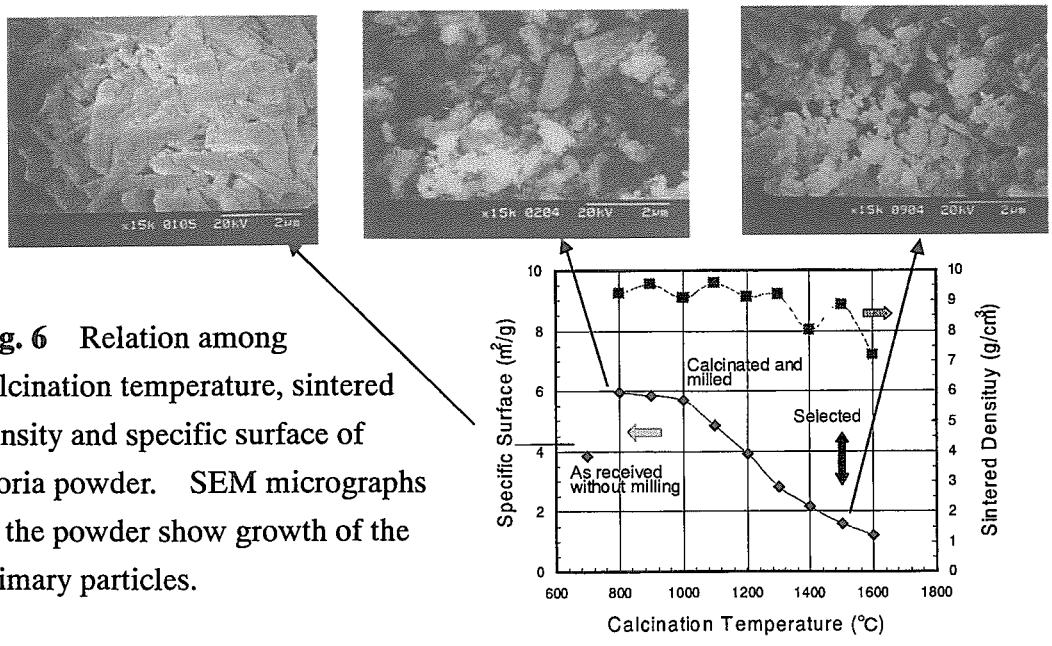



**Fig. 6** Relation among calcination temperature, sintered density and specific surface of thoria powder. SEM micrographs of the powder show growth of the primary particles.

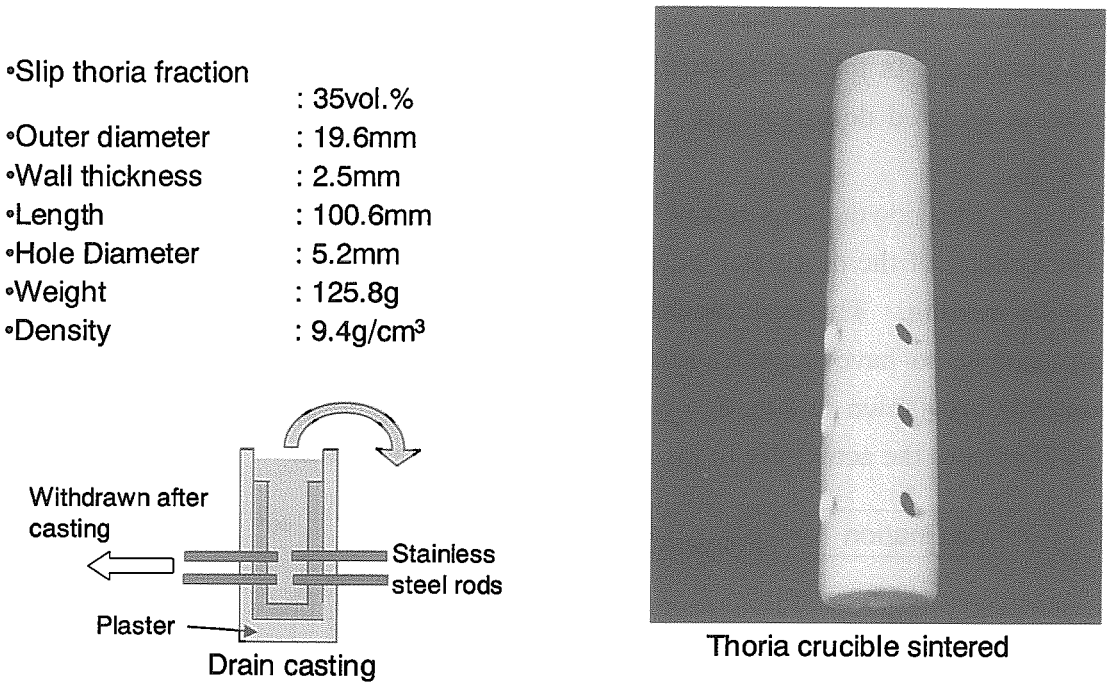



**Fig. 7** Specification and appearance of thoria crucible made by slip casting.

## 5. Summary

The first heating test to investigate the fission product release behavior under accident conditions, VEGA-1, was successfully conducted in Sep. 9, 1999. Two PWR fuel pellet without the cladding tube was heated to 2,500℃ under inert helium atmosphere at a pressure of 0.1MPa. Considerable releases of Cs-137, Cs-134, Sb-125, Ru-106, Ce-144, and Ag-110m were preliminary evaluated from the pre/post gamma spectrometry. The limited counting rates for the isotopes other than those of Cs, however, made the uncertainty fairly large. Post test gamma scanning and quantitative gamma measurement of the leached solution of the test apparatus are necessary to have total release evaluation with a better accuracy. The second test, VEGA-2, will be conducted at the identical test conditions except for the system pressure, i.e. 1MPa in test VEGA-2. The pressure effects on the releases are to be studied in the first two VEGA tests.

Development of thoria component for the VEGA furnace has mostly completed. The components made with slip casting techniques will be used for heating tests, prior to the use in the actual VEGA tests under the oxidizing atmosphere at high temperatures.

## Acknowledgement

The authors are grateful to JAERI colleagues at the Reactor Fuel Test Facility lead by Mr. T. Kodaira. They would like to acknowledge Messrs. I. Takahashi, T. Kushida H. Ohuchi, M. Anzo, T. Nakamura for assisting the reliable and safe operation of the VEGA experiment. The fuel sample was supplied from Kansai Electric Power Company, Inc. for a collaboration program between JAERI and Nuclear Fuel Industries, Ltd. Noticeable assistance was obtained from Mr. S. Goto of Mitsubishi Kakoki Kaisha, Ltd and Mr. A. Tsuchihashi of Daiichi Kiden, Ltd. for the installation and characterization of the VEGA facility, prior to the first test.

## References

[1] T. Nakamura, et al., JAERI-Tech 99-036 (1999).
[2] A. Hidaka, et al. JAERI-Research 99-066 (1999) (in Japanese).
[3] A. G. Croff et al., Nucl. Technol. Vol.62 (1983).
[4] M. F. Osborne, et al., Nucl. Safety Vol. 33[3], (1992).
[5] T. Nakamura, et al. JAERI-M 93-222 (1993) (in Japanese).

JP0150111



## 9.3 Phebus FPT4: Test Conditions and First Results

F. Serre, F. Arreghini, C. Ktorza, M-C Anselmet, F. Jeury
*Institut de Protection et Sûreté Nucléaire (IPSN)*
*Département de Recherches en Sécurité (DRS)*
*CEA Cadarache, F- 13108 St Paul-Lez-Durance, France*

## ABSTRACT

The Phebus Fission Product program is a worldwide cooperative project, managed by the IPSN, designed to address issues associated with the fission product (FP) behavior in Light Water Reactors (LWR) under severe accident conditions. The last experiment FPT4 is devoted to the study of releases of low volatile FPs and transuranic elements from an irradiated debris bed or a molten pool.
The in-pile test section was composed of a rubble bed and a set of filters. The rubble bed composition is close to the one observed in the TMI2 debris bed. Five filters were located above the debris bed to collect the aerosols released from the experimental fuel.
The test package was subjected to neutronic heating in the Phebus reactor to take the debris bed in steps up to its melting temperature to form a molten pool under a vapor-hydrogen flow. The five filters were operated sequentially during the transient to collect the released aerosols.
Preliminary results show that the target debris bed temperatures defined in the test protocol were reached leading to a melt pool formation at the end of the transient. The filters present high activities when gamma scanned 24 hours after the test.

## I. INTRODUCTION

The Phebus Fission Product program is designed to address issues associated with the fission product (FP) behavior in Light Water Reactors (LWR) under severe accident conditions. Its objectives is to investigate through a series of in-pile integral experiments key phenomena such as core degradation up to fuel liquefaction and pool formation, the subsequent release of fission products and structural materials, their transport in the primary circuit including the steam generator and their behavior in the containment with special emphasis on iodine behavior [1].
The Phebus FP experiments are carried out in the Phebus facility. It is composed of a driver core to reirradiate the experimental fuel to re-build the short-lived fission products during a reirradiation phase, and to heat-up the fuel up to its liquefaction during the experimental phase. It is also composed of simulators at a reduced scale (1/5000) of a LWR primary circuit with a steam generator U-tube and of LWR containment with a sump.
Within the frame of the Phebus FP program, 6 experiments have to be performed.
To date three experiments have been carried out. The first two experiments were performed with an experimental fuel rod bundle (10kg of fuel) under oxidizing conditions (steam environment). Trace-irradiated fuel was used in the first test FPT0, while the FPT1 test was performed with 23GWd/tU fuel. They provided information on FP releases up to fuel liquefaction and on FP behavior in LWR primary circuit and containment [2]. The fuel liquefaction occurred at a relatively low temperature due to material interactions.
The following test was the FPT4 test performed on July 22$^{nd}$, 1999. It will be described in this paper.
The further tests FPT2, FPT5 and FPT3 will be similar to FPT1, changing respectively the chemical environment (reducing atmosphere or air) or changing the experimental control rod made of SIC by an $B_4C$ control rod).
This program is managed by the French Institut de Protection et Sûreté Nucléaire, Electricité de France and the European Commission in close cooperation with, and funded by, the USNRC (US), NUPEC and JAERI (Japan), COG (Canada), KAERI (South Korea), PSI and HSK (Switzerland).

## II. FPT4 TEST OBJECTIVES

The main objective of the FPT4 test is to study the releases of low volatile fission products and transuranic elements from a debris bed as well as the fuel vaporization. Such kind of fuel configuration was observed in the Three Miles Island 2 reactor vessel, which underwent a severe accident. It results from a thermal chock on the reactor core following the restart of the primary pumps and the arrival of cold water of the oxidized fuel rods. This fuel geometry, compared to bundle geometry, promotes the release of low volatile fission products and transuranic elements. This is due to the larger specific area (ratio of the surface of the particle to its volume) of FP emission of the rubble bed particles compared to the bundle geometry. As well, the steam oxidizes the fuel particles promoting the FP diffusion in the fuel matrix as well as the fuel vaporization. This last phenomenon can enhance the release of FP trapped in the fuel matrix.
The uncertainties of low volatile FP and uranium releases from a debris bed are very large: the data base is poor due to the need to carry-out experiments at very high temperature (T~2400°C).
The secondary objectives of the test is to study the heat transfer in the debris bed, the physical transition from debris bed to molten pool and the aerosol releases from the molten pool. Releases from the debris bed and from the molten pool will be compared. It is expected to have fewer releases with the molten pool due to a smaller specific emission area of the pool.
Because in the FPT4 test package the experimental fuel is not cladded (see §III), it is not possible to reirradiate the irradiated fuel. The cooling water flowing in the rubble bed would be contaminated in case of reirradition. Therefore the $^{131}I$ inventory will be low and radiochemistry would not take place in the containment due to the low activity. It was then decided to skip the primary circuit and containment objectives for the FPT4 test. To have a better mass balance of the aerosol released from the rubble bed, it was decided to collect the released elements in filters located just above it.

## III. FPT4 TEST DEVICE

### *Debris bed*

The in-pile test section is composed of a rubble bed enclosed in a Zircaloy canister and layers of melt barriers and thermal insulation encompassed in a pressure tube (figure 1). The rubble bed consists of two distinct zones. The upper zone is similar to the debris bed observed in the TMI2 reactor: same material composition is used. It is composed of a mixture of PWR fuel pellet fragments with an average burn-up of around 33 GWd/tU mixed with oxidized Zircaloy cladding shards. It is 24 cm long and has a diameter of 7 cm. The porosity of the debris bed is close to 50% leading to a mass of irradiated fuel of 3.2 kg and a Zirconia mass of 0.8kg. This upper zone is named 'active bed'. The fuel-cladding debris mixture sits on a 12 cm-thick layer of depleted $UO_2$ (Figure 2). The objective of the lower zone is to limit the downward progression of a molten pool. This zone is named 'passive bed'.

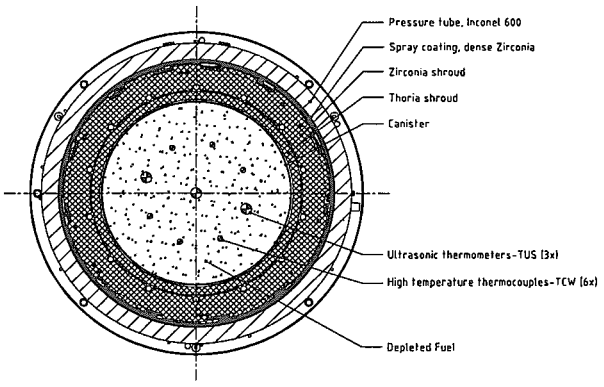



Figure 1: Radial cut of the test package

To limit the radial progression of the molten materials, Thoria sleeves surround the debris bed. Porous Zirconia sleeves provide the thermal insulation of the test package. The debris bed with its melt and thermal barriers is enclosed in a pressure tube externally cooled by a water flow and internally coated by a flame-sprayed Zirconia. In the lower part of the depleted bed, the Zirconia sleeves have been replaced by a neutron shield made of Hafnia to limit the power generated at this level and therefore to limit the downward progression of a molten pool.

## Filtration set

Above the debris bed is located the filtration device designed to collect the aerosol released by the experimental fuel during the test (Figure 2). This filtration device is composed of 2 stages of filtration. The first stage is composed of 5 parallel channels equipped with filter cartridges and deposition coupon cartridges. Downstream the first stage of filtration is located a large capacity filter (back-up filter). Plugging of the first stage of filters has been envisaged. In that case a parallel void channel can be used to bypass the first filtration stage and collect the aerosols in the back-up filter. The gas flowing out of this last filter is directed toward the containment simulator (named REPF 502).

The filters of the first stage are used sequentially by operating pneumatics remote valves. Due to the high technology of these valves, qualification tests have been performed by PSI. Also the characteristics of filter loading have been performed there (loading versus pressure drop, maximum loading).

## Instrumentation

In order to pilot the test and to get experimental measurements for test analyses, the test package was equipped with a large number of detectors.

The debris bed is instrumented with 6 W/Re TC at various axial locations and 3 ultrasonic thermometers (UTS). Each of these UTS is design to give debris bed temperature at 7 different axial location. Because it was expected to lose the debris bed instrumentation when the temperature reach temperature as high as 2300°C, the shroud of the test package was also instrumented with three sets of thermocouples: one set of thermocouple in between the Thoria layer and the porous Zirconia, one set in the porous Zirconia, and one set in between the porous Zirconia and the pressure tube. Additionally, a melt through detector, made of wires of thermocouples wrapped on the external face of the porous Zirconia was implemented.

The filtration device was equipped with thermocouples at the inlet and the outlet of the first filtration stage, pressure sensors upstream and downstream the filtration device as well as pressure drop sensors. Four on-line gamma spectrometers are implemented along the outlet line of the filtration device and in the containment simulator.

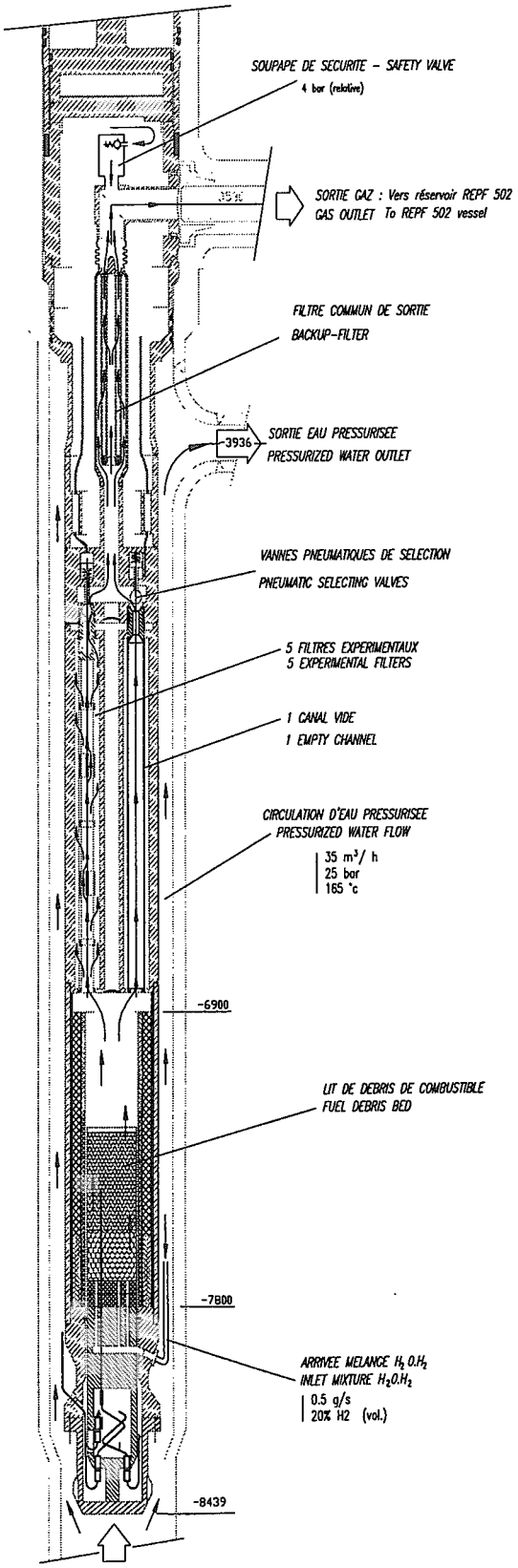



Figure 2: In-pile test section: axial cut

# IV. TEST PROTOCOL

The FPT4 test protocol has been defined in order to simulate the reactor conditions during a severe accident during the phase following the debris bed formation. Therefore, it was decided to inject a mixture of steam and hydrogen during the phase of aerosol releases. To steady the releases at various temperatures with solid debris bed geometry or from a molten pool, it was decided to heat up the debris bed by steps, alternating power-increased periods with steady-state periods. The five sequential filters are sequentially opened during this different periods. The test protocol is given figure 3 (dash line). It is divide into 3 phases: a calibration phase, a bed release phase, a molten pool phase and a cooling phase.

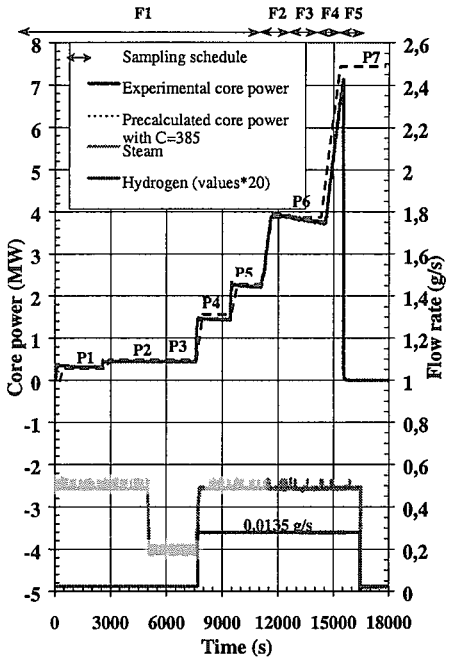



Fig 3: Power, steam and H2 injection histories & sampling schedule

During the calibration phase, one checks the thermal response of the test package by increasing the power deposited in the debris bed or varying the steam flow rate to study the steam convection in the debris bed. As well, the instrumentation response is checked. Target temperatures at the hottest point of the debris bed are 600°C, 800°C, 920°C and 1627°C (1900K) for a short period. During this phase low aerosol release are expected. Therefore only one sequential filter is used.

The bed release phase includes two temperature plateaus, named P5 and P6, at 1927°C (2200K) and 2427°C (2700K) of respectively 15 and 30mn. During the P5 plateau, 50% of the volatile FP inventory is expected to be released while only few percent will be released during the calibration phase. Therefore, it was planned to continue to use the first filter up to the end of the P5 plateau. During the P6 plateau, 10% of the low volatile FP inventory is expected to be released. The second filter will be used during the transient from P5 to P6 plateaus and the third filter during the P6 plateau to collect the low volatile FP released at a stabilized temperature of the debris bed.

The following phase was dedicated to the study of the molten pool formation and the release from this molten pool. The pool formation is obtained by nearly doubling the heat deposition in the experimental fuel (P7) compared to the P6 plateau. The fourth filter is planned to be used during the transient from P6 to P7. It is then planned to open the last filter during the steady state period with the molten pool.

At the end of the molten phase, the driver-core will be scrammed leading to the cooling of the test package. During this cooling phase, it was foreseen to drive the gas flow through the empty channel of the first filtration stage directly in the back-up filter.

Analyses of the aerosol deposited in the sequential filter will give information on releases during the periods when they were opened.

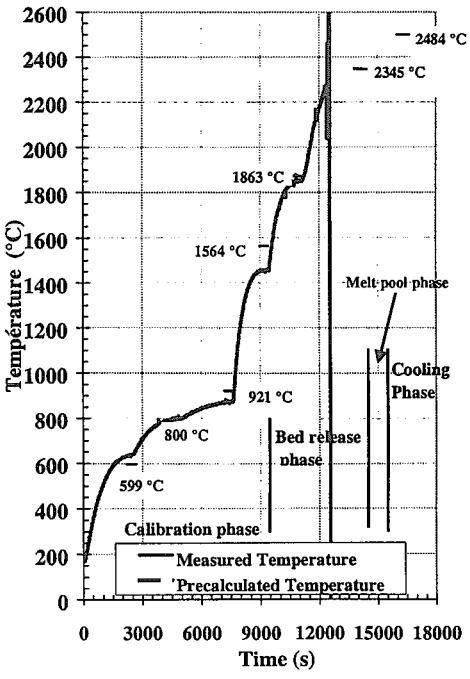



Fig. 4: Bed temperature evolution

## ACTUAL TEST SCENARIO

The test was conducted on July 22nd 1999 according to the protocol up to nearly the end of the power ramp from the P6 to P7 plateau. At that time the power shut-down criteria where reached leading to the scram of the driver core.
Target temperatures of the different power plateaus were reached with a maximum error of 100°C by correcting the precalculated driver core power according to the temperature reached during the previous power plateau. The power correction never exceeds 7%. During the P5 plateau, the maximum temperature measured by the hottest TC is 1844°C for a precalculated temperature of 1863°C. During the P6 plateau the estimated temperature is about 2400°C.
The sequential filters were operated as planned up to the scram of the reactor. Because the fifth sequential filter was not used for measurement of releases from a stabilized melt pool, it was opened during the cooling phase.

## V. PRELIMINARY TEST RESULTS

### *Debris bed behavior*

Up to the beginning of the P6 plateau, the behavior of the debris bed was as expected. However, a relatively high fuel heat-up in the depleted zone of the debris was detected. This might be due to an underestimation of the heat deposition in this zone in the pretest calculation.
Concerning the test package instrumentation, it worked very well up to the beginning of the P6 plateau. However the ultrasonic thermometers showed signals very noisy; only one UTS has been used on-line.
When the thermocouples located in the active bed reached about 2300°C during the P6 plateau, they failed as expected. The thermal behavior of the debris bed was then monitored using the shroud thermocouples.
At the end of the P6 plateau one noticed a deformation of the axial temperature profiles (figure 5). At the same time, it was pointed out a decrease of the temperature in the upper part of the active debris bed and an increase of the temperature in the lower part of this region. Such temperature evolution might be due to material motion from the upper part of the active bed to the lower part. This movement would lead to increase the density of the lower part of the debris bed and therefore increase the heat deposition in this zone. On the contrary in the upper part of the debris bed where the fuel porosity would increase, the heat deposition is lower. Because most of the power deposited at one elevation of the debris bed is lost through the shroud radially, the temperature measured at one location gives the thermal flux through the shroud and therefore the heat deposited at this elevation. Therefore, an axial temperature deformation might indicate a modification of the fuel distribution in the debris bed.

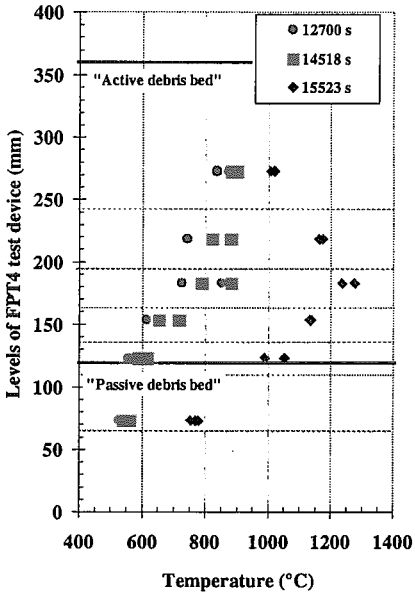



Fig. 5: Axial shroud temperature profile

A material movement during the P6 plateau at temperatures close to 2400°C was not expected despite the oxidation of the fuel by the steam, which lower the liquefaction temperature of an $UO_2$-$ZrO_2$ mixture (2527°C). Also the ACRR MP experiments showed that the mixture started to relocate only when reaching the fusion of the Zirconia (2700°C) [3].

During the power ramp from P6 to P7, a significant fuel displacement was on line detected by monitoring the axial profile deformation (figure 5). It was concluded on line that a molten pool was formed. This result was confirmed by the non destructive examination of the test package (X radiography and gamma-scanning, figure 6). One can see that the particles left the upper part of the test section and downward relocated leading to a cavity formation in the upper part of the debris bed

and a pool formation in the lower part of the active bed. This pool penetrated in the passive bed as calculated in the pretest calculation at the end of the P7 power plateau [4]. Also a vault can be observed at the top of the debris bed as already seen in the ACRR MP experiments and precalculated.
The shut-down criteria were obtained on the melt-through detector. They are based on the detection of a hot temperature on the internal face on the pressure tube. It should indicate that hot materials penetrate through the shroud. However, non destructive examinations (300 tomographies at the present time) did not show any shroud degradation and melt penetration. Wrong use of the melt-detector signal is suspected.

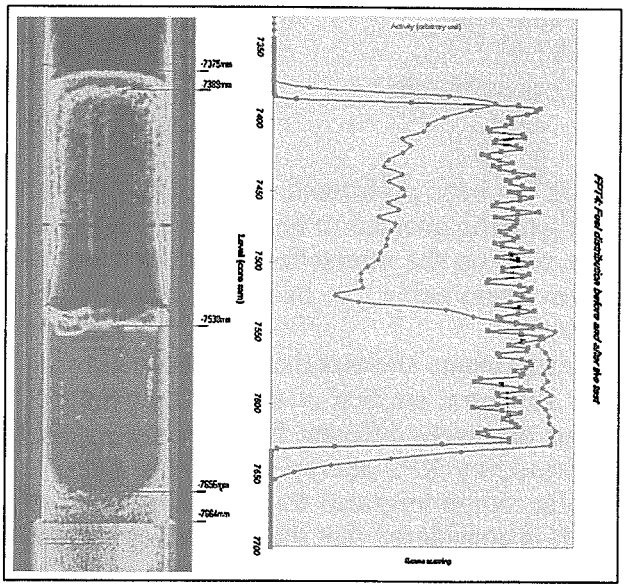


Fig 6: X radiography and γ-scans

Also, at the same time the shut-down criteria were obtained on TCs located in the mid-elevation of the passive bed. This indicates that the molten pool penetrates in the passive bed. The penetration given by the post-test examinations showed that the pool bottom was located at about 4 cm above the TCs.

### *Aerosol releases*

Few results are now available. The analyses of the pressure drop across the sequential filters, based on the qualification tests performed at PSI, shows that their loadings were relatively low. However, first activity measurements of the sequential filters 24 hours after the test were higher than expected. It must be pointed out that low volatile FPs such as $^{106}Ru$, $^{141}Ce$, $^{154}Eu$ have been detected.

## VI. CONCLUSION

The FPT4 test was successfully performed, with conditions as defined in the test protocol. The test was stopped when shut-down criteria were reached as specified in the test procedure.
The objective regarding the fuel degradation (melt pool formation) were reached as shown by the first non destructive package examination. As well the objective concerning the measurement of the released aerosols from the test package in the sequential filters during the different phase of the transients was fulfilled.
The preliminary results show that the fuel motion might be occurred at temperatures lower than expected (2400°C instead of 2500°C).
Concerning the aerosols released, the loading of the sequential filters show that the aerosol were released according a scenario of low test package releases. However the activity measured 24 hours after the test was higher than expected.
Non destructive examination of the filters are now under way and further post-test analysis on collected aerosols will be performed in various laboratories around the word. These analyses will allow determining the mass and species released during the different phase of the test.

## References

[1] M. Schwarz et al., The Severe Accident Research Programme PHEBUS FP, 1995 WRSM Meeting
[2] P. von der Hardt et al., Results of the First Phebus FP Experiments, 1998 TOPSAFE'98
[3] R.O. Gauntt et al., The MP2 Experiment in ACRR, 1993 USNRC CSARP Meeting
[4] F. Serre et al., Phebus FPT4: Test Description and PreTest and Calculations, 1997 SARJ Meeting

JP0150112



# 9.4 Studies on Interaction between Cesium Iodide and Type 316 Stainless Steel in WIND Project

T. KUDO, Y. MARUYAMA, H. SHIBAZAKI, A. HIDAKA,
H. NAKAMURA, E. CHINO, Y. YUCHI and K. HASHIMOTO
Severe Accident Research Laboratory
Japan Atomic Energy Research Institute
Tokai-mura, Naka-gun, Ibaraki-ken
phone : (+81) 29-282-5166
fax : (+81) 28-282-5323
e-mail : kudo@sarl.tokai.jaeri.go.jp

## ABSTRACT

A test series on FP/structural material interaction has been performed in WIND project at Japan Atomic Energy Research Institute to investigate the interaction between CsI and type 316 stainless steel, and the CsI instability. Three tests on the interaction of cesium iodide with type 316 stainless steel were performed under steam/noble gas, hydrogen/steam/noble gas and air/steam/noble gas atmospheric conditions.

In the test with air ingress condition, EDX measurements showed that the retained mass of cesium was larger than that of iodine in the structural surface at a high temperature. Retained cesium might have taken chemical forms that were different from cesium iodide. However, the cesium compounds were not confirmed by XPS analysis. In all the tests, it was confirmed by XPS analysis that the molecular iodine migrated to a depth of 100 nm maximum of the surface layer of stainless steel. It is considered that the amount of cesium and iodine retained in the type 316 stainless steel surface was too small to influence the source term evaluation. It was also found that a decomposition rate of cesium iodide in the air ingress condition was higher than that in the hydrogen injection condition.

## KEY WORDS

Severe Accident, Cesium Iodide, Type 316 Stainless Steel, Decomposition, Reactor Coolant System, WIND Project

## 1. INTRODUCTION

During a severe accident of a light water reactor, fission products (FPs) are released from fuel and transported to the reactor coolant system (RCS) and the containment. Some of FPs are deposited on the piping in the RCS and may chemically interact with piping structural materials. A change of FPs chemical form influences the source term of a severe accident. Therefore, it is important to investigate the interaction between FPs and structural materials.

Previous studies [1), (2)] related to the FP/structural materials interaction were performed under atmospheric condition of steam and hydrogen. However, the influence of the air ingression on FP behavior in the RCS has not been well understood. It is possibility that the air ingression into RCS occurs during a PWR accident.

In order to investigate the interaction between cesium iodide and structural materials, and the cesium iodide stability in an air ingress condition, a test series on FP/structural materials interaction has been performed in WIND (Wide range piping INtegrity Demonstration) project at Japan Atomic Energy Research Institute.

## 2. OUTLINE OF FP/STRUCTURAL MATERIALS INTERACTION TESTS

### 2.1 TEST FACILITY AND TEST PROCEDURE

The schematic diagram of FP/structural materials interaction tests is shown in Fig. 1.

Cesium iodide (CsI) as a FP simulant is put on the FP generation section heated by electric heaters. The generated CsI gas and/or aerosol is brought into the FP mixing section by an inert gas and mixed with a specified carrier gas there to be introduced into the test section. The test section, which has 0.085 m in inner diameter and 1.5 m in length, is divided into the constant temperature section and the thermal gradient section having 0.5 m and 1.0 m in length, respectively. The piping of FP generation/mixing section and test section are made of quartz glass and enclosed in a stainless steel pipe. Two sample coupons were installed in the test section as structural material. One is for temperature measurement, and the other is for chemical analyses of deposited compounds. The sample coupon is 20 mm in width and 500 mm in length for constant temperature test section and 1000 mm in length for thermal gradient test section. During a test, the atmosphere was sampled at the upstream and downstream of the test section. The sampled atmosphere was passed through the quartz glass U-tubes in the water bath and the dry ice bath to condense volatile iodide species. After each test, the hydrazine solution, which reduced the molecular iodine, was put into the grass U-tubes. This solution was supplied for IC analysis.

The sample coupon was sectioned for chemical analyses. Ion chromatography (IC), scanning electron microscopy (SEM), energy dispersive X-ray spectroscopy (EDX) and X-ray photoelectron spectroscopy (XPS) were used to quantify the cesium and iodine deposited mass, to observe the morphology of deposits, to specify the existent elements and to identify the chemical form, respectively.

## 2.2 TEST CONDITIONS

The test conditions are summarized in Table 1. The tests designated as FSI-1, FSI-2 and FSI-3 simulated the atmosphere of super heated steam/noble gas, hydrogen/steam/noble gas and air/steam/noble gas, respectively. In FSI-3, the ratio of air and steam was based on the analysis by MELCOR for a station blackout accident of Surry plant [3]. The mass of vaporized cesium iodide in the FP generation section was 171 to 243 g that were the difference between the initial and remained CsI. The flow rate of carrier gas in the test section at 1000 °C was 0.00057 $m^3/s$, which corresponded to a superficial velocity of 0.1 m/s in all the tests. The duration while CsI was introduced into test section was 65 min in FSI-1 and 90 min in other tests. The temperature of the thermal gradient test section was linearly decreased from 1000 °C to 300 °C. The oxygen potential was derived from Ellingham diagram.

Table 1 Experimental Conditions

| Exp. | FP Simulant | Generation Mass (g) | Carrier Gas | | | Piping Temp. (°C, Constant/ Gradient) |
|---|---|---|---|---|---|---|
| | | | Composition (Volume Ratio) | Flow Rate (m/s) | $\mu_{O2}$* (kJ/mol) | |
| FSI-1 | CsI | 171 | He (0.1)<br>Ar (0.86)<br>Steam (0.04) | 0.1 | -287 | 1000/1000-300 |
| FSI-2 | CsI | 243 | He (0.92)<br>$H_2$ (0.04)<br>Steam (0.04) | 0.1 | -390 | 1000/1000-300 |
| FSI-3 | CsI | 175 | He (0.2)<br>Air (0.5)<br>Steam (0.3) | 0.1 | -19 | 1000/1000-300 |

* : Oxygen potential at 1000 °C

## 3. RESULTS AND DISCUSSION

The mass of cesium and iodine deposited on the coupon surface of FSI-3 analyzed by IC are shown in Fig. 2 along with the temperature profile of the coupon and the carrier gas. The deposition mass increased when the carrier gas temperature became higher than the coupon temperature. This implied that the deposition of the both elements was dominated by the condensation of CsI vapor and thermophoresis of CsI aerosol. The elemental analysis of FSI-3 coupon surface by EDX is shown in Fig. 3. The deposition mass of cesium and iodine was almost the same each other at 0.7 m from the entrance of the test section. However, the atomic ratio of cesium was larger than that of iodine at 0.3 m from the entrance where the temperature of the coupon was estimated to be 950 °C. It was considered that cesium iodide was decomposed and some cesium compounds was formed at high temperature region.

The XPS analysis was performed to identify chemical forms of cesium and iodine compounds (at coupon No. 4, 8 and 14 which corresponded to 0.3 m, 0.7 m and 1.3 m from the entrance). The analysis was performed from the surface to a deeper inner layer up to 100 nm (10 nm intervals). Spence et al. [4] showed that cesium iodide reacted with $Cr_2O_3$ solid aerosol. Bowsher [5] noted that this precise form of the chromate is not known with confidence but one possible reaction is given below.

$$2Cr_2O_3 + 5O_2 + 8CsI = 4\ Cs_2CrO_4 + 4\ I_2$$

Figure 4 shows the result of XPS analysis for chromium compounds in the FSI-3 at No. 4 coupon. The cesium compounds were lower than detection limit and not confirmed.

The results of XPS analysis for iodine compounds are shown in Fig. 5. The molecular iodine ($I_2$) was detected in all the tests, and reached to 100 nm maximum (FSI-3 at No. 8 coupon). This showed that some amount of CsI was decomposed in all the tests. At the surface layer, the nickel iodide ($NiI_2$) was detected (for example, FSI-1 at No.8 coupon). $NiI_2$ could be produced by a reaction of $I_2$ and nickel hydroxide ($Ni(OH)_2$). However, above about 200°C, $Ni(OH)_2$ is decomposed into NiO and $H_2O$. Therefore, $NiI_2$ may be produced during a cool-down phase of the tests. The iodine mass ratio of FSI-3 No. 8 coupon surface layer, where $I_2$ was existed until 100 nm in depth, was 0.58 %. By using some assumptions (coupon was not oxidized, X-ray of XPS was reached until 2 nm, and retained iodine concentration was the same until 100 nm in depth), retained $I_2$ mass concentration within the coupon was 0.46 $\mu g/cm^2$. Moreover, the cesium compound was less than detection limit. It was considered from the above consideration that the amount of CsI decomposed on the type 316 stainless steel was very small. This indicated that the chemical interaction of CsI and type 316 stainless steel could give a limited influence to the source term evaluation.

Figure 6 shows the mass of cesium and iodine captured in U-tubes of the atmosphere sampling systems in FSI-3. The mass of iodine was larger than that of cesium at both sampling systems. Since the chemical interaction of cesium and the coupon was hardly occurred, it indicated that cesium iodide was decomposed in the atmosphere at air ingress condition. In FSI-2 test, a significant decomposition of CsI was not found in the analysis of the sampled atmosphere. The decomposition rate was evaluated as follows,

$$D = C_I * 100 / C_{CsI}$$

$$C_I = M/E$$

D : decomposition rate [%]
$C_I$ : mole concentration of iodine produced by decomposition [mol/m$^3$]
$C_{CsI}$ : mole concentration of CsI in the test section [mol/m$^3$]
M : mole concentration of the captured iodine [mol/m$^3$]
E : capture efficiency of iodine at U-tube [-]

The decomposition rate of CsI in the air ingress condition was 0.3 %. The capture efficiency of iodine at U-tube was 1.0 in this case. In the future, we will perform the evaluation test on capture efficiency of iodine at the U-tube.

## 4. CONCLUSIONS

Studies on the interaction between CsI and type 316 stainless steel, and CsI stability under the several atmosphere conditions were performed in WIND project.

The interaction between the cesium and the type 316 stainless steel surface was not confirmed. It was observed that the $I_2$ retained within the stainless steel surface. Since the amount of CsI decomposed on the type 316 stainless steel was very small, it is considered that the chemical interaction of CsI and type 316 stainless steel hardly influences the source term evaluation.

The CsI tend to decompose under the air ingress condition in comparison with the $H_2$ injection condition, which indicated CsI was less stable in the air atmosphere.

## ACKNOWLEDGMENTS

This work was performed under a contract between the Atomic Energy Bureau in Science and Technology Agency of Japan and Japan Atomic Energy Research Institute. We wish to acknowledge Messrs. H. Ito, H. Osaki, K. Komori and T. Kiuchi of Safety Engineering Service Division of Japan Atomic Energy Research Institute and staffs of Nihon Advanced Technology Co., Ltd. led by Mr. N. Sonobe for their technical assistance on experiments.

## REFERENCES

(1) R. M. Elrick, et al., "Reaction Between Some Cesium-Iodine Compounds and the Reactor Materials 304 Stainless Steel, Inconel 600 and Silver, Volume II Cesium Iodide Reactions," NUREG/CR-3197/2 of 3, SAND83-0395, Sandia National Laboratories, Albuquerque, New Mexico, June 1984.

(2) B. R. Bowsher, "Fission-Product Chemistry and Aerosol Behaviour in the Primary Circuit of a Pressurized Water Reactor under Severe Accident Conditions," Progress in Nuclear Energy, Vol. 20, No. 3, pp. 199-233, 1987.

(3) L. Kmetyk, "Air Ingression Calculations for Selected Plant Transients Using MELCOR," SAND93-3808, Sandia National Laboratories, Albuquerque, New Mexico, January 1994.

(4) R. D. Spence, et al., "The Importance of Fission Product/Aerosol Interactions in Reactor Accident Calculations," Nuclear Technology, Vol. 77, pp. 150-160, 1987.

(5) B. R. Bowsher, "Fission-Product Chemistry and Aerosol Behaviour in the Primary Circuit of a Pressurized Water Reactor under Severe Accident Conditions," Progress in Nuclear Energy, Vol. 20, No. 3, pp. 199-233, 1987.

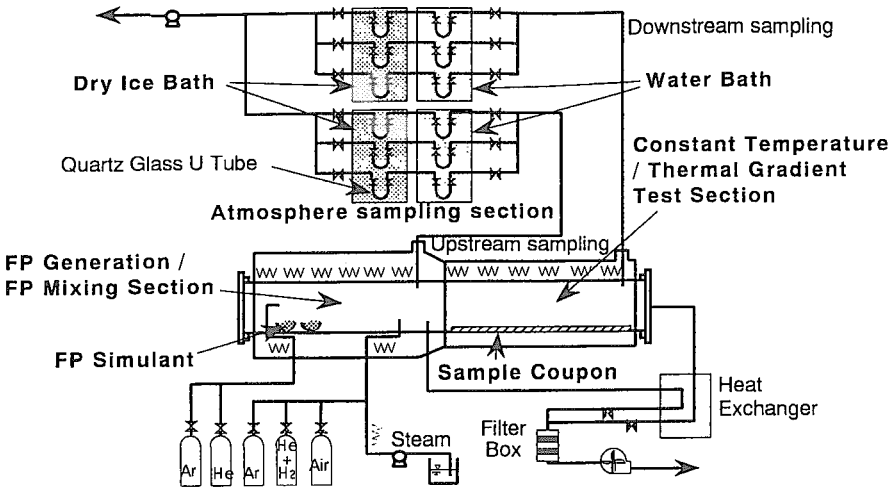



Fig. 1 Schematic Diagram of FP/Structural Materials Interaction Tests

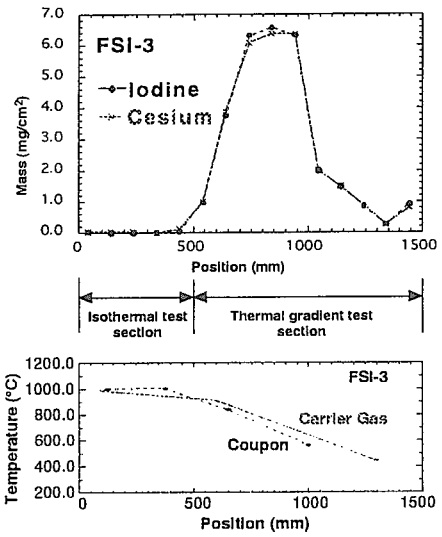



Fig. 2 Deposited Mass on Coupon

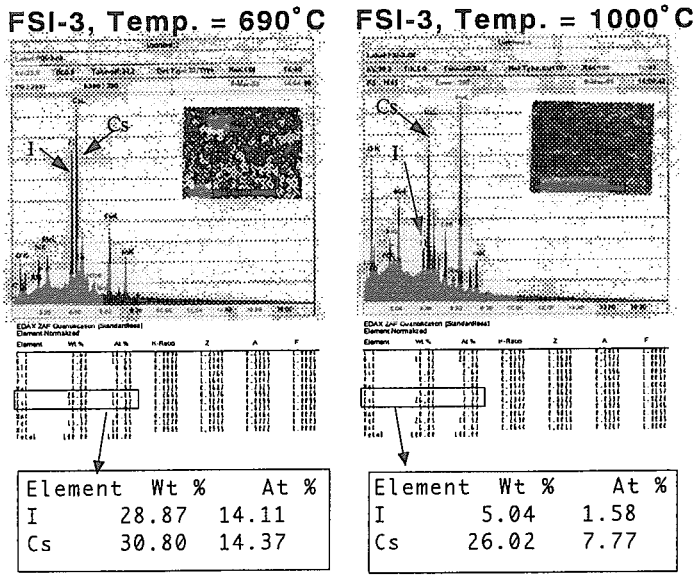



Fig. 3 Elemental Analysis of Coupon Surface by EDX

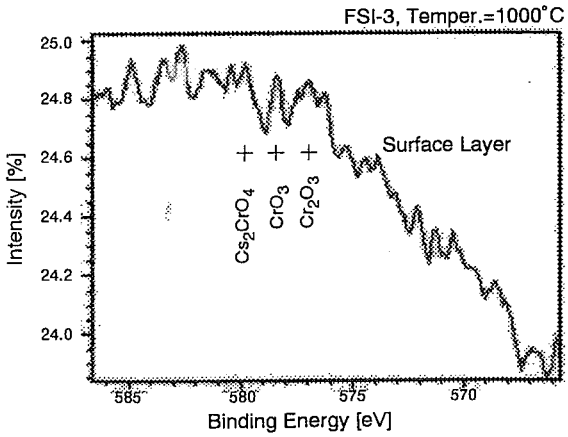



Fig. 4 Analysis of Cr Compounds by XPS

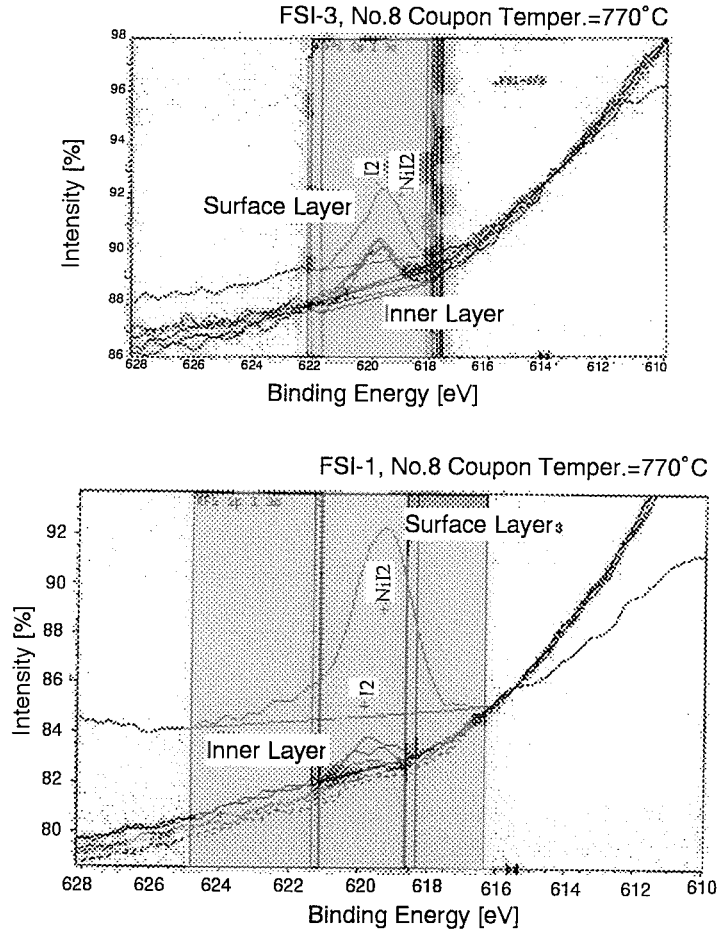



Fig. 5 Analysis of I Compounds by XPS

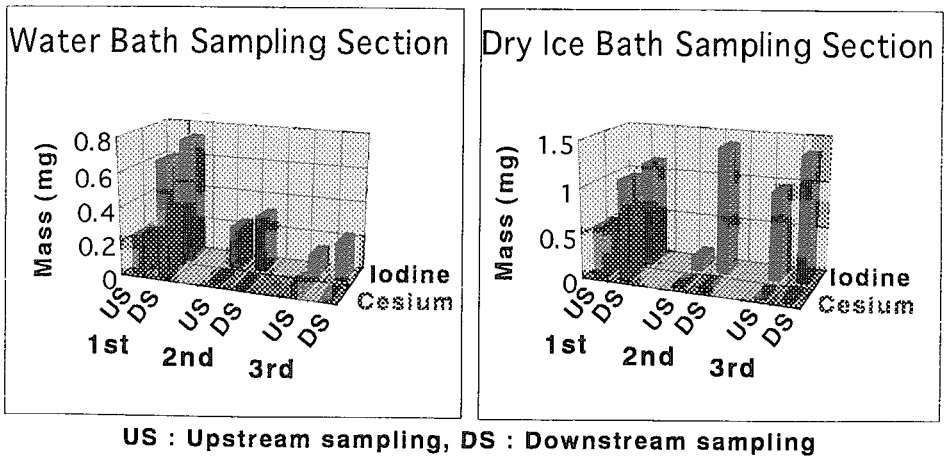



Fig. 6 Analytical Results of Atmosphere Sampling (FSI-3)

This is a blank page.

# 10. Session 9

# Fission Product Behavior II

## Chairperson:

P. Bottomley (ITU)
K. Hashimoto (JAERI)

This is a blank page.

JP0150113



# 10.1 EXPERIMENTAL STUDY ON EFFECTS OF BORIC ACID ON AEROSOL REVAPORIZATION IN WIND PROJECT

**Hiroaki Shibazaki, Yu Maruyama, Tamotsu Kudo, Yoko Yuchi, Eiichi Chino, Hideo Nakamura, Akihide Hidaka and Kazuichiro Hashimoto**
Severe Accident Research Laboratory
Department of Reactor Safety Research
Japan Atomic Energy Research Institute
Phone: +81-29-282-6163
Fax : +81-29+282-5570
Email : shiba@sarl.tokai.jaeri.go.jp

## ABSTRACT

The revaporization of the once-deposited FPs onto surfaces of reactor coolant piping is being investigated in WIND (Wide Range Piping Integrity Demonstration) project at JAERI. The objectives of the present study are to characterize the aerosol revaporization from piping surfaces under various thermal-hydraulic conditions and to investigate the effects of boric acid on aerosol revaporization. Cesium iodide was introduced into the test section on which metaboric acid was/was not placed in advance. After quantifying the deposited mass of cesium and iodine, the test section was heated to realize the revaporization. The revaporized materials were deposited onto another test section with an axial temperature gradient located in downstream. In the cases that metaboric acid was placed on the test sections, it was found that the mole ratio of iodine to cesium deposited onto wall became gradually small as the wall temperature increased up to 500°C. Chemical analyses with XPS suggested that chemical reaction of deposited cesium iodide with metaboric acid would result in formation of borate, cesium oxide and molecular iodine. In the revaporization phase, the experiments showed that the once-deposited cesium and iodine compounds were mostly revaporized when the temperature exceeded 500°C.

## KEY WORDS

Severe accident, Reactor coolant piping, Aerosol deposition, Revaporization, Boric acid, Cesium iodide, WIND project

## 1. INTRODUCTION

During a severe accident of a light water reactor (LWR), fission products (FPs) with a physical form of vapor and aerosol are released from a degraded reactor core. They are transported into a reactor coolant system (RCS) and deposited onto the inner surface of the RCS piping. The deposited FPs might react on boric acid included in primary coolant and the chemical form of the deposited FPs might be changed. The once-deposited FPs onto the surface of the RCS piping might be revaporized due to decay heat. Therefore, it is very important to characterize the revaporization of the once-deposited FPs for estimating the source term of LWR severe accidents.

The previous studies such as the revaporization of cesium from stainless steel[1], the revaporization phenomena in control rod alloy aerosols[2] and theoretical assessments to understand the revaporization behavior of cesium[3] were performed.

Japan Atomic Energy Research Institute (JAERI) initiated aerosol behavior test in Wide Range Piping Integrity Demonstration (WIND) project[4] to clarify FP aerosol behavior in the RCS piping. Aerosol revaporization test series is currently underway in the aerosol behavior tests of WIND project. The objectives of the present study are to characterize the revaporization of FPs from piping surfaces and to understand the effects of boric acid included in primary coolant.

## 2. OUTLINE OF AEROSOL REVAPORIZATION TEST SERIES

### 2.1 Test Facility

Figure 1 shows the schematic diagram of the aerosol behavior test facility of WIND project. The facility mainly consists of an argon gas supply system, a steam generator, aerosol generators, an aerosol chamber, two test sections in series and an aerosol sampling system. Two types of aerosol generators are installed, namely an induction heating type and a nebulizer type. The induction heating type aerosol generator vaporizes FP simulants filled in an inductively heated graphite crucible. The vaporized simulants are nucleated in a cooler downstream region to form fine aerosol particles. In order to stabilize initial aerosol conditions, the aerosol chamber with an inner volume of $0.12m^3$ is placed between the aerosol generators and the test sections.

The test sections are composed of upstream test section (UTS) and downstream test section (DTS). The two test sections are connected by connection pipe (CP). Each test sections are made of stainless steel (type 304) straight pipes having 2.0m in length and 0.1063m in inner diameter. The test sections are surrounded with eleven individually controllable electric heaters to establish a desired axial temperature profile of the test section wall. Eleven type-K thermocouples are placed on the outer surface of each test section for the control of the heater. For the measurement of the carrier gas temperature, type-K thermocouples are possible to set in the inner volume of the test sections. The temperature of the carrier gas is separately measured in thermal-hydraulic tests under identical conditions as the aerosol revaporization test series without CsI introduction.

The aerosol sampling system is mainly composed of diluters, dilution gas heaters, cascade impactors, a thermostatic oven to install the cascade impactors and several flow meters. The system is controlled to realize isokinetic sampling. Aerosol of CsI is sampled through sampling nozzles with an inner diameter of 15mm located at the inlet of the UTS and the outlet of the DTS.

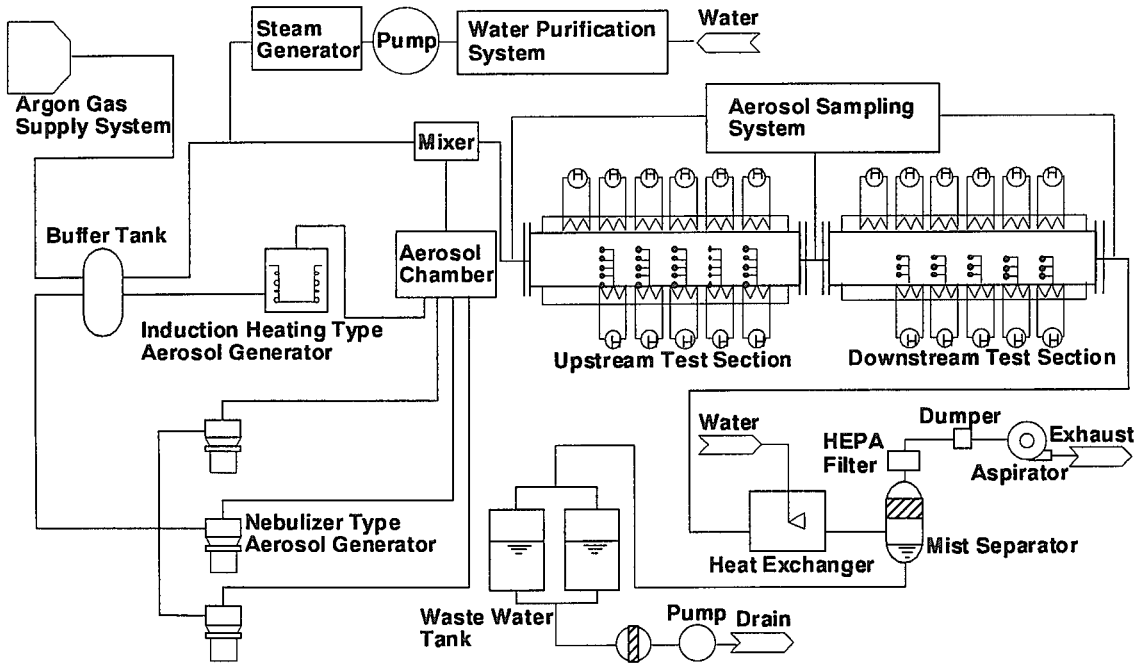



Fig. 1 Aerosol behavior test facility of WIND project

## 2.2 Test Procedure

The aerosol revaporization test series consists of deposition and revaporization phases. In the deposition phase, the steady state thermal-hydraulic condition was established, then vapor and aerosol of CsI were introduced into the test sections from the induction heating type aerosol generator. After CsI aerosol was deposited onto the surface of the test sections in the deposition phase, the test sections were cooled down to the room temperature and the DTS was clean up and UTS remained for the revaporization phase. In the revaporization phase, UTS, where CsI aerosol was deposited during the deposition phase, was heated to revaporize the deposited CsI without introducing CsI aerosol from the aerosol generator. The deposition coupons made of stainless steel (type 316) with 20mm in width and 2m in length were welded on the surface of the floor, side wall, ceiling area of the test sections. After deposition and revaporization phases, the deposition coupons were removed from the test section and sectioned in order to use for observation by scanning electron microscope (SEM) and a post-test elemental analysis. The sectioned coupons excluding small specimen for the SEM observation were soaked in pure water for 12 hours to dissolve deposited materials into the water. A quantitative analysis for cesium and iodine was conducted with a liquid ion chromatography. The other sectioned specimen was analyzed with X-ray photoelectron spectroscopy (XPS) to specify the chemical compounds of deposited materials.

## 2.3 Test Conditions

The thermal-hydraulic and CsI aerosol conditions of the aerosol revaporization test series are summarized in Table 1. Letters of D and V added to the end of run ID indicate the deposition and revaporization phases, respectively. In the UTS of the revaporization phases, the axial temperature profile of the test section wall was uniform and was increased stepwise to 800°C in WAV1-V and WAV2-V, 700°C in WAV4-V. Each temperature step was held for 20 minutes except for last temperature step. A mixture of superheated steam and argon was used as a carrier gas in the deposition phases. The volumetric percent of superheated steam and argon was the same. In the revaporization phases, only superheated steam was supplied into the test section. Reynolds number at the inlet of the test section was set from approximately 100 to 1000 in all the runs indicating laminar flow regime. In order to clarify the effects of boric acid included in primary coolant, metaboric acid ($HBO_2$) was placed in advance on the deposition coupons of floor area of the test sections in WAV2-D, WAV3-D and WAV4-D. It was assumed that a mass of boric acid included in primary coolant was uniformly distributed onto the inner surface of the test section.

**Table 1** The thermal-hydraulic and CsI aerosol Conditions

| Run ID | Carrier gas | Carrier gas flow rate (g/s) | Max. Temp. of test section wall (°C) UTS / DTS | Aerodynamic Mass Median Diameter (μm) | Mass Concentration ($g/m^3$) | Metaboric acid |
|---|---|---|---|---|---|---|
| WAV1-D | Steam + Argon | 2.6 | 1000 / 700 | 2.2 | 2.1 | × |
| WAV1-V | Steam | 0.28 | Stepwise / 800 | --- | --- | × |
| WAV2-D | Steam + Argon | 2.6 | 430 / 900 | 2.2 | 2.7 | ○ |
| WAV2-V | Steam | 0.28 | Stepwise / 800 | --- | --- | ○ |
| WAV3-D | Steam + Argon | 2.6 | 983 / 650 | 0.5 | 1.4 | ○ |
| WAV4-D | Steam + Argon | 2.6 | 368 / 893 | 1.2 | 5.4 | ○ |
| WAV4-V | Steam | 0.28 | Stepwise / 802 | --- | --- | ○ |

## 3. RESULTS AND DISCUSSION

Figure 2 shows the axial temperature profile of the outside wall and carrier gas in WAV1-D. Figure 3 shows the deposition mass of cesium onto each area of the inner surface of the test section in WAV1-D. The deposition densities of cesium and iodine were almost identical. In outlet part of the UTS and DTS and in the CP, the measured carrier gas temperature was higher than the wall temperature. The deposition mass onto floor, wall and ceiling area was almost uniform in outlet part of the UTS. On the other hand, the deposition mass onto ceiling area was dominant in middle part of the DTS. In the DTS, carrier gas temperature gradient near the ceiling area in cross section was steeper due to natural convection. Therefore, it is considered that CsI was condensed on the wall in outlet part of the UTS and was mainly deposited onto ceiling area by thermophoresis in middle part of the DTS.

The comparison of the deposition densities of cesium and iodine onto the floor area and the axial temperature profile of the test section wall in WAV2-D are shown in Fig. 4. Metaboric acid was placed in advance on the floor area of the test section in this case. In inlet part of the UTS, the deposition density of cesium was larger than that of iodine. As the wall temperature decreased gradually, the deposition density of iodine increased. At high temperature region in the DTS, only cesium was deposited. Metaboric acid could be transformed to boric oxide ($B_2O_3$) above 300°C. It is supposed that CsI reacted with $B_2O_3$ and was decomposed into cesium and iodine.

Figure 5 shows the relationship between the mole ratio of iodine to cesium in the deposition phases with metaboric acid and the outside wall temperature of the test section. At the location where the outside wall temperature was approximately 300°C, mole ratio of iodine to cesium was almost 1.0. Mole ratio of iodine to cesium decreased as the outside wall temperature increased. At the location where the outside wall temperature was above approximately 500°C, mole ratio of iodine to cesium was almost 0. Therefore, a part of CsI reacted with $B_2O_3$ above 300°C, then CsI was decomposed into cesium and iodine. Above 500°C, CsI was decomposed into cesium and iodine completely, then only cesium was deposited onto the inner surface of the test section. It is supposed that molecular iodine was ejected from the test section.

Figure 6 shows the final axial temperature profile of the outside wall in WAV2-V. Figure 7 shows the deposition mass of cesium onto each area of the inner surface of the test section in the revaporization phase with metaboric acid (WAV2-V). In the UTS, once-deposited materials were almost revaporized. There were two peaks of the deposition mass of cesium in the floor area of the DTS. In the first peak (from 3m to 4m), iodine was not deposited because the wall temperature was very high. In the second peak (from 4.5 to 5m), the deposition mass of cesium and that of iodine were almost identical. It is supposed that the deposited material is CsI in the second peak. The wall temperature of the first peak was approximately 800°C and that of the second peak was approximately 450 °C. The materials, which revaporized at 800 °C and 450 °C in the UTS, were deposited at the same temperature region of the DTS. Therefore, the deposited material in the first peak might be less volatile material than CsI.

Figures 8 and 9 show the identified chemical form by chemical analyses with XPS, the deposition density profile of cesium and iodine, the outside wall temperature profile and the points of chemical analyses in WAV4-D and in WAV4-V, respectively. In WAV4-D, molecular iodine ($I_2$), cesium oxide ($Cs_2O$) and boric acid ($H_3BO_3$) were detected in the UTS and $Cs_2O$ and borate were detected in the DTS. It indicates that CsI reacted with $B_2O_3$ above 300°C then $Cs_2O$ and borate were produced. $B_2O_3$, which could not react with CsI in the UTS, was transformed to $H_3BO_3$ because $B_2O_3$ absorbed water ($H_2O$) after the experiment. In the DTS, $B_2O_3$ was vaporized completely because the wall temperature was very high. In the WAV4-V, $I_2$, $Cs_2O$ and borate were detected in the UTS. The reason why $H_3BO_3$ was not detected was similar to that in WAV4-D.

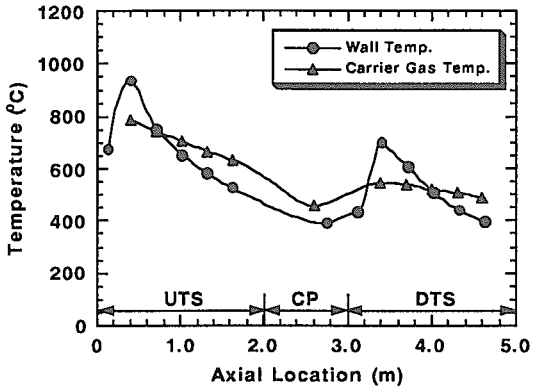



Fig. 2 The axial temperature profile of the wall and carrier gas in WAV1-D

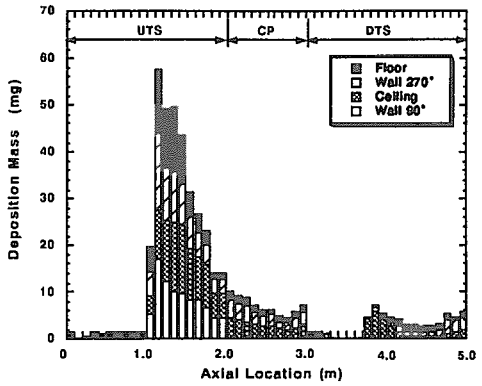



Fig. 3 The deposition mass of cesium in WAV1-D

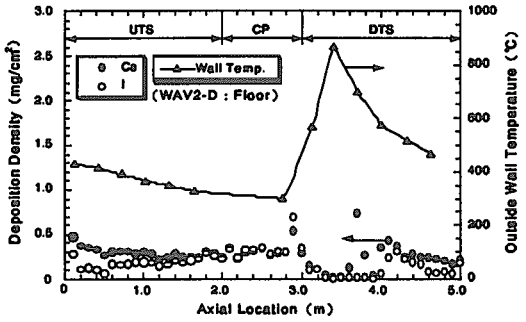



Fig. 4 The deposition density of Cs and I in WAV2-D

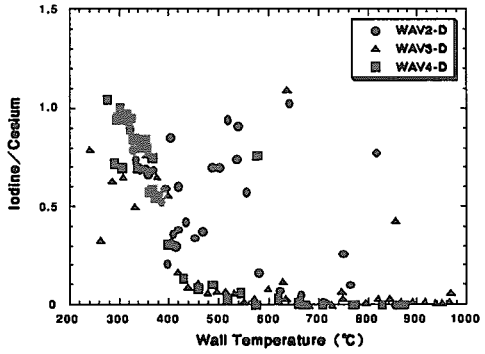



Fig. 5 Mole ratio of iodine to cesium in the deposition phase with metaboric acid

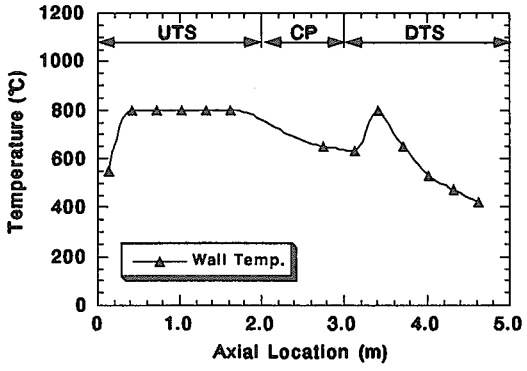



Fig. 6 The axial temperature profile of the test section wall in WAV2-V

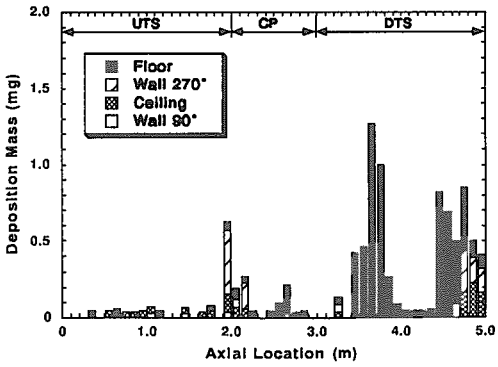



Fig. 7 The deposition mass of cesium in WAV2-V

| WAV4-D | ① | ② | ③ |
|---|---|---|---|
| I | $I_2$ | $I_2$ | — |
| Cs | $Cs_2O$ | $Cs_2O$ | $Cs_2O$ |
| B | $H_3BO_3$ | $H_3BO_3$ | Borate |

| WAV4-V | ① | ② | ③ |
|---|---|---|---|
| I | $I_2$ | — | — |
| Cs | $Cs_2O$ | $Cs_2O$ | $Cs_2O$ |
| B | Borate | Borate | Borate |

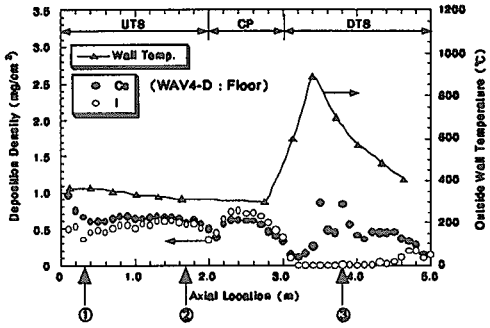



Fig. 8 Identified chemical form by chemical analyses with XPS in WAV4-D

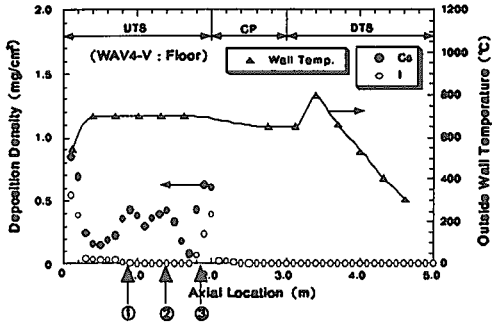



Fig. 9 Identified chemical form by chemical analyses with XPS in WAV4-V

## 4. CONCLUSIONS

Revaporization of once-deposited CsI aerosol are being investigated in WIND project, including the effects of boric acid deposited on the inner surface of reactor coolant piping. The following findings were obtained through the aerosol revaporization tests.

- Once-deposited CsI was mostly revaporized when the test section was heated up to 800°C.
- The decomposition of CsI occurred when $HBO_2$ was placed in the test section and temperature of the test section wall was above 300°C.
- As the wall temperature became high, more CsI was decomposed. Deposited CsI was mostly decomposed at the temperature exceeding approximately 500°C.
- It was presumed that, based on the chemical analyses, CsI reacted with $HBO_2$ to form less volatile materials.

## ACKNOWLEDGMENTS

Authors wish to express sincere gratitude to Mr. H. Ito, Mr. H. Osaki, Mr. K. Komori and Mr. T. Kiuchi of Safety Engineering Service Division of JAERI and staffs of Nihon Advanced Technology Co., Ltd. led by Mr. N. Sonobe for their excellent technical assistance on the performance of tests and maintenance of the test facility.

## REFERENCES

(1) Dickinson, S., UKAEA Report AEEW-R 2473, 1989 (also included in CEC Report EUR 12844 EN, 1990).

(2) Benson, C. G., et al., 1988, "Physical Resuspension and Revaporization Phenomena in Control Rod Aerosols," AEA Report AEEW-R 2427.

(3) Powers, D. A., et al., Proc. Symp, "Chemical Phenomena Associated with Radioactivity Releases During Severe Nuclear Plant Accidents," Anaheim, California, 9-12 September 1986, Editor: Niemczyk, S. J., US NRC Report, NUREG/CP-0078, p 3-67, 1987.

(4) Hashimoto, K., et al., 1994, "WIND Project, (1) Aerosol Behavior Test and High Temperature Test," Transactions, 1994 Fall Mtg. of Atomic Energy Soc. of Japan, Vol. 1, pp. 114, Sapporo, Japan (in Japanese).

JP0150114

JAERI－Conf 2000－015

# 10.2 Analyses of CsI Aerosol Deposition Tests in WIND Project with ART and VICTORIA Codes

Y.Yuchi*, H.Shibazaki*, T.Kudo*, A.Hidaka*, Y.Maruyama*, E.Chino*, H.Nakamura*, T.Yoshino**, K.Suzuki** and K.Hashimoto*

*: Severe Accident Research Laboratory
Japan Atomic Energy Research Institute
Phone:(+81)29-282-6466
Fax:(+81)29-282-5570
**: Toshiba Advanced Systems Co. Ltd.

## ABSTRACT

Deposition behavior of cesium iodide (CsI) was analyzed with ART and VICTORIA-92 codes for a test of the aerosol re-vaporization test series performed in WIND project at JAERI. In the test analyzed, CsI aerosol was injected into piping of test section where metaboric acid ($HBO_2$) was placed in advance on the floor area. It was confirmed in the present analysis that similar results on the CsI deposition were obtained between ART and VICTORIA when influences of chemical interactions were negligibly small. The analysis with VICTORIA agreed satisfactorily with the test results in analytical cases that cesium metaborate ($CsBO_2$) was injected into the test section instead of CsI to simulate the pre-existence of $HBO_2$ effect.

Keywords : Severe accident, Aerosol, Deposition, ART code, VICTORIA-92 code, Cesium iodide, Boric acid

## 1. Introduction

During a LWR (Light Water Reactor) severe accident, FPs (fission products) are released from a reactor core and transported into RCS (Reactor Coolant System) piping. Aerosols and vapors of FPs deposit on the RCS piping and a part of the deposited FPs is revaporized by own decay heating. Due to the complicated phenomena, large uncertainties still exist in FP aerosol behavior in the RCS piping especially in the revaporization phenomena, which result in the late phase release of FPs (1). As a research item of WIND (Wide range piping INtegrity Demonstration) project at JAERI, the investigation of the FP aerosol behavior in the RCS piping under sever accident conditions is in progress (2). The aerosol revaporization test series is being performed in this project. The deposition behavior of the aerosol revaporization test series was analyzed by ART (3) and VICTORIA-92(4) codes in order to confirm the capabilities of the both codes. ART code is being developed at JAERI for the analyses of the FP behavior in the RCS and the containment vessel. VICTORIA code has been developed at SNL for the analyses of FP release and transport in the RCS.

## 2. Description of Aerosol Revaporization Test Series Analyzed

The schematic diagram of test sections is shown in Fig. 1. Upstream and downstream test sections and connecting pipe are placed in series. The test

sections are fabricated from straight stainless steel pipes of about 0.1m in inner diameter. A length of each test section and connecting pipe are 2.0m and 1.0m, respectively. Each test section is covered with 11 electric heaters to form desired temperature profile of the test section wall. Thermocouples are set on the outer surface to measure the pipe wall temperatures. Aerosol of FP simulants was injected into the test sections with a carrier gas of Ar and superheated steam mixture to realize the deposition onto the inner surface (deposition phase). After the deposition phase, the test sections were reheated in order to investigate the revaporization of the once deposited materials.

Primary coolant of a PWR includes boric acid. Fission products could react with boric acid, and affect the FP transportation. In some of the aerosol revaporization tests, $HBO_2$ was placed on the deposition coupon at the floor area prior to conducting the deposition phase. In the present study, the deposition phase of one of the revaporization tests (designated as WAV4-D) with $HBO_2$ was analyzed.

Temperature of the carrier gas separately measured after the revaporization tests by installing thermocouples in the test sections as shown in Fig.1.

### 3. Conditions of Analyses

The analytical conditions of WAV4-D test, based on the measurement, are shown in Table1. Temperature of aerosol was assumed to be equal to the carrier gas temperature. Concentration of aerosol in a node was assumed to be uniform. Axial temperature profiles of the carrier gas and the test section wall used for analyses are shown in Fig. 2. The wall temperature was around 300℃ for the upstream test section and the connecting pipe. The maximum wall temperature was approximately 900℃ for the downstream test section and linearly decreased to approximately 300℃ at the exit. The temperature of the carrier gas plotted in this figure was measured at the center of the test sections. As shown in Fig.1, the test sections and connecting pipe was divided into 20 axial nodes and 1 cross-sectional node.

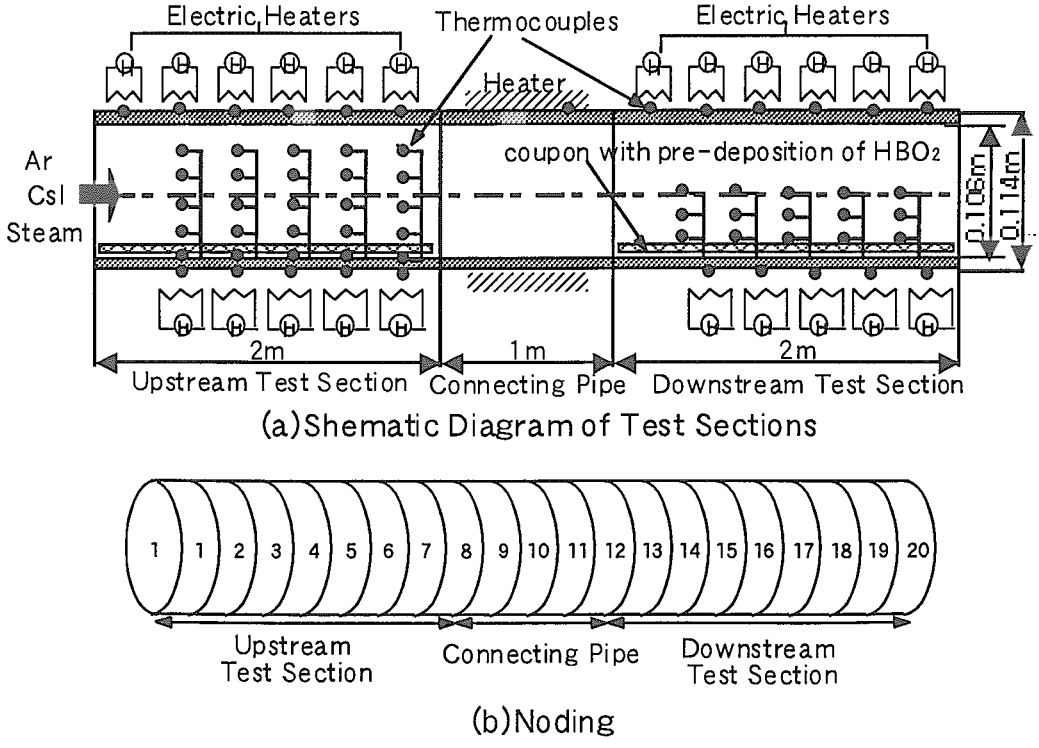



Fig.1 Schematic Diagram of Test Sections and Noding of Analyses

Table1 Analytical Conditions

| Condition at Inlet of Upstream Test Section | | |
|---|---|---|
| Aerosol Source Species | | CsI |
| Aerosol | AMMD* | 1.2 $\mu$ m |
| | GSD** | 2.0 |
| Aerosol Concentration | | 5.4g/m$^3$ |
| Carrier Gas Species | | Argon<br>Steam |
| Carrier Gas | Velocity | 0.7m/sec |
| | Reynolds Number | 725 |
| | Temperature | 600℃ |
| Duration of Deposition | | 3000sec |

* AMMD : Aerodynamic Mass Median Diameter
**GSD : Geometric Standard Deviation

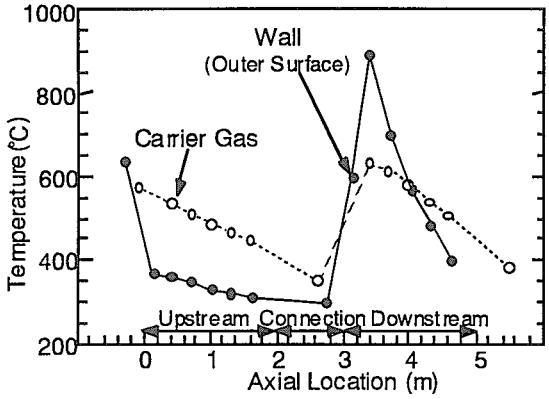



Fig.2 Temperature of Carrier Gas and Test Section Wall

## 4. Results of Analyses

### 4.1 Comparison between ART and VICTORIA-92 codes

VICTORIA-92 code has a capability of calculating thermodynamic chemical equilibrium. On the other hand, the chemistry is not sufficiently modeled in ART code. In WAV4-D test, $HBO_2$ was placed on the floor area of the test section in advance, and it was expected that chemical reaction between CsI and $HBO_2$ occurred. For the purpose of the comparison between the both codes, the first analysis with VICTORIA-92 was performed without thermodynamic chemical equilibrium model.

The calculated deposition density of cesium and iodine is shown in Fig.3 together with the test results. The major deposition mechanisms identified in the analyses are shown in Fig.4. It was found that the similar analytical results were obtained from the analyses with ART and VICTORIA-92. Thermophoretic deposition and gravitational settling of CsI aerosol were estimated as dominant deposition mechanisms in the both codes.

However, the test result on the deposition

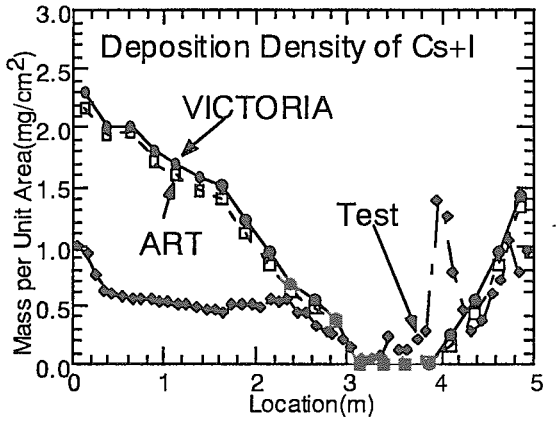



Fig.3 Comparison of Deposition Density of Cesium and Iodine between ART and VICTORIA -92

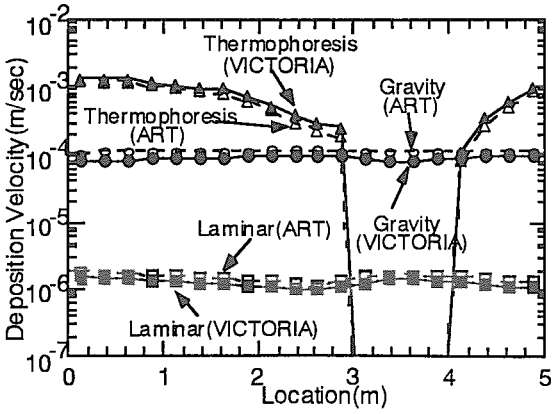



Fig.4 Comparison of Deposition Mechanisms between ART and VICTORIA-92

density was largely overestimated by the both codes for the upstream test section. In addition, a deposition peak at the mid of the downstream test section was not predicted in the both analysis.

### 4.2 Analyses with VICTORIA-92 Considering $HBO_2$ Effect

The analysis with VICTORIA-92 code taking the effect of $HBO_2$ into account was performed. It was difficult to model the pre-existence of $HBO_2$ in VICTORIA-92 code. Therefore, $CsBO_2$ aerosol was assumed to enter into the test sections in the analysis. The comparison for the deposition density of cesium between the test and the VICTORIA-92 analyses is shown in Fig.5. The difference between the test and the analysis became smaller in case of the $CsBO_2$ injection.

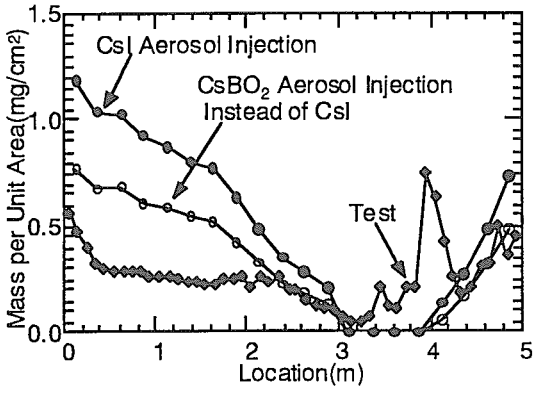



Fig.5 Comparison for Deposition Density of Cesium between Test and VICTORIA-92 Analyses

### 4.3 Effects of Temperature Distribution

The deposition peak of CsI was observed at the mid of the down stream test section in the test, which was not predicted by the analysis. The more detailed test results on the deposition are shown in Fig.6, for floor, ceiling and wall areas of the test sections. The observed deposition peak in the downstream test section was dominated by the selective deposition on the ceiling area. The location, where the deposition peak was observed, agreed with that the carrier gas temperature became higher than the temperature of the test

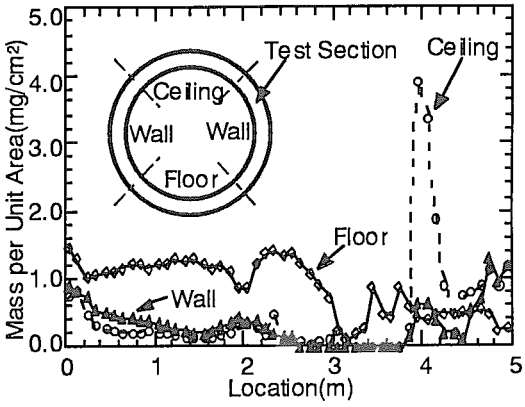



Fig.6 Test Results on Spatial Distribution of Deposition of Cesium and Iodine

section wall as shown in the Fig.2.

The temperature profile of the carrier gas in the downstream test section calculated with WINDFLOW is shown in Fig.7. WINDFLOW is a three dimensional thermo-fluiddynamic analysis code which is being developed at JAERI. At the vicinity of the location where the deposition peak was found in the test, the carrier gas temperature in the ceiling area was predicted to be higher than the wall temperature. It was supposed that vapor condensation or thermophoretic aerosol deposition of CsI occurred onto the ceiling of the mid of the downstream test section.

The excess vapor pressure of CsI based on the temperature profile of the carrier gas predicted with WINDFLOW is shown in Fig.8. The excess vapor pressure was defined in the present study as

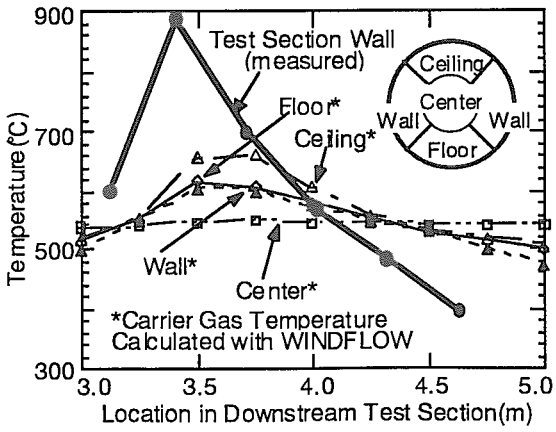



Fig.7 Axial Profile of Carrier Gas Temperature in Downstream Test Section

the difference between saturated vapor pressures of CsI at temperature of the carrier gas and the test section wall. It was found that the excess vapor pressure in the ceiling area was higher than the other areas at the mid of the downstream test section. The localized deposition could not be reproduced by the analyses with ART and VICTORIA-92 code since a representative of the carrier gas temperature was used.

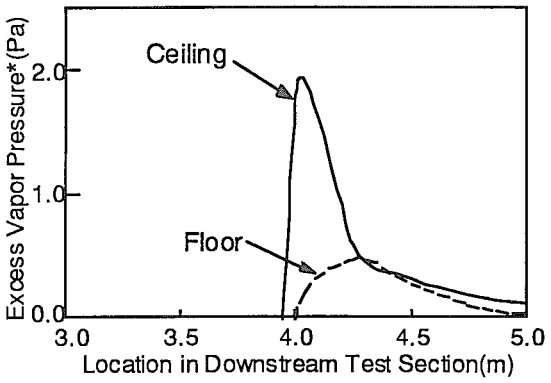



Fig.8 Excess CsI Vapor Pressure Based on Temperature of Carrier Gas Predicted with WINDFLOW

## 5. Conclusions

The deposition phase of aerosol revaporization test series, designated as WAV4-D, was analyzed with ART and VICTORIA-92 codes. The influence of boric acid on the CsI aerosol deposition was investigated in WAV4-D. The following conclusions were obtained from the present analyses.

(1) In terms of aerosol deposition without chemical interactions, the results of the analyses were in good agreement between ART and VICTORIA-92 codes.

(2) The results of the analysis showed that the reproducibility of VICTORIA-92 was improved when $CsBO_2$, instead of CsI, was assumed to be injected into the test sections.

(3) Cross sectional temperature distribution of the carrier gas should be taken into account in order to increase the predictability for the localized deposition.

## 6. Acknowledgement

Authors would like to express their sincere gratitude to Mr. H. Ito, Mr. K. Komori, Mr. T. Kiuchi of JAERI and to Mr. H. Somobe, Mr. T. Iwabuchi, Mr. H. Takaizumi, Mr. H. Kuribayashi of NAT for their technical assistance on WIND experiment.

## References

(1) Kudo,T., et al., 1998,"Analyses of CsI Aerosol Deposition in Aerosol Behavior Tests in WIND Project", JAERI-Conf. 99-005.

(2) Sugimoto,J., 1998,"OVERVIEW OF SEVER ACCIDENT RESEARCH AT JAERI", JAERI-Conf. 99-005.

(3) Ishigami, T., et al., "User's Manual of ART code for Analyzing Fission Product Transport Behavior during Core Meltdown Accident", JAERI-M 88-093, 1988

(4) Heames, T. J., et al., NUREG/CR-5545, 1992

JP0150115



# 10.3 Effects of Radiation and Impurities on Gaseous Iodine Behavior in a Containment Vessel

Masato Takahashi, Atsushi Watanabe, Takashi Hashimoto
Nuclear Power Engineering Corporation, Japan
m-takahashi@nupec.or.jp a-watanabe@nupec.or.jp t-hashimoto@nupec.or.jp

ABSTRACT

In order to estimate the effect of impurities and radiation on gaseous iodine behavior in containment vessel, NUPEC has improved IMPAIR-3 code developed by PSI. Several modifications on the iodine oxidation by radiolysis and the production of nitric acid, the existence of boric acid, and the reaction of silver particle with iodine were newly added in evaluating the effect of radiolysis and impurities. pH change resulting from presence of boric acid, nitric acid production by radiolysis of air, and sodium hydroxide addition by AM operation, was also considered. The code verification for pH change was performed using the RTF experimental results. Additionally, the effects of boric acid and silver impurities on gaseous iodine behavior were evaluated by the sensitivity analysis.

As a result, the experimental results of iodine concentration transient under pH change were well simulated. The following results were also obtained from the sensitive analysis. The gaseous iodine behavior was not affected by the existence of boric acid. In the case of silver existence in liquid phase, the gaseous iodine concentration rapidly decreased because a large amount of iodine changed into AgI species in liquid phase. The restraint effect of silver on gaseous iodine production was larger than that of pH change.

*Keywords : gaseous iodine, iodine, radiolysis, impurity, pH, severe accident, containment vessel*

## 1. INTRODUCTION

In PHEBUS tests (FPT-0 and FPT-1), gaseous iodine produced under acid sump conditions with radiation field and the production was mitigated by the presence of silver. Therefore, it is important to evaluate the effect of impurities and change of sump pH condition by accident management (AM) on gaseous iodine behavior.

Several modifications on the nitric acid production and iodine oxidation by

radiolysis, the presence of boric acid and the reaction of silver particle with iodine were newly added to IMPAIR-3 code[1] developed by PSI. The code verification for radiation effect and pH change was performed using the RTF experimental results[2]. Additionally, the effects of boric acid and silver impurities on gaseous iodine production were evaluated by the sensitivity analysis.

## 2. MODELING OF RADIATION AND IMPURITIES EFFECTS

### 2.1 Effect of radiation

The radiolytic chemical processes considered in this work were iodine oxidation and nitric acid production. In IMPAIR-3 code, the global iodide oxidation by radiolysis is prepared as follows (Eq.1).

$$2I^- + h\nu \xrightarrow{k(1)} I_2 + 2e^- \quad (1)$$

The iodine production equation and reaction rate constant k(1) in Eq.(1) were assumed by Eqs.(2) and (3) depending the pH and dose rate based on several experimental results. [3]

$$d[I_2]/dt = 1/2 \cdot k(1) [I^-]^{1-n} [H^+]^n \cdot D \qquad (n=0.3) \quad (2)$$

$$k(1) = 0.042/(kGy) \quad (3)$$

where D is dose rate (kGy/h).

Nitric acid production resulting from radiolysis of air is due to pH change in sump as well as sodium hydroxide addition by AM operation and $H_3BO_3$ control materials. Production rate of nitric acid is calculated using the following Eq.(4).

$$d[HNO_3]/dt = 1.22\times10^{-7} G_g D_g V_g / V_W + 1.036\times10^{-4} f_N G_W D_W \quad (4)$$

where G, D and V are G-values, dose rate (kGy/s) and volume, respectively. Subscript g and w denote gas and liquid phase, respectively. And $f_N$ is solubility of $N_2$ gas in liquid phase. The adopted G-values of nitrogen ion production were 0.007 in the gas phase and 2.4 in the liquid phase, respectively. [4),5)]

### 2.2 Effect of impurities

Boric acid and silver, used as the core control material and transported to the containment vessel, react with iodine chemical species. It is considered that boric acid reacts with several iodine species, and accelerates the reaction of Eq.(5). [6)]

$$3HOI \xrightarrow{k(2)} IO_3^- + 2I^- + 3H^+ \quad (5)$$

Acceleration reactions with boric acid through the intermediate species were assumed by Eqs.(6) and (7).

$$H_3BO_3 + IO^- \xrightarrow{kA1} B(OH)_3OI^- \quad \text{(intermediate)} \tag{6}$$

$$B(OH)_3OI^- + HOI \xrightarrow{kA2} IO_2^- + I^- + H^+ + H_3BO_3 \tag{7}$$

The reaction rate constant k(2) in Eq.(5) was regulated by Eq.(8) as a function of boric acid concentration.

$$k(2) = k_0 + k_A[H_3BO_3] \tag{8}$$

where $k_0$ and $k_A$ are reaction rate constants without and with boric acid, respectively.

The reaction of iodine with silver in containment sump has major impact on iodine volatility from solution. The reaction of silver with soluble iodide or dissolved molecular iodine leading to the formation of non-volatile silver iodide is important in containment condition during severe accident. The silver moved into containment exist not only silver metal (Ag) but also oxidized silver ($Ag_2O$). The reaction of oxidized silver with soluble iodide depend on pH was newly considered in Eq.(10), in addition to reaction between Ag and $I_2$ in Eq.(9).

$$2Ag + I_2 \rightarrow 2AgI \tag{9}$$

$$Ag_2O + 2I^- + 2H^+ \xrightarrow{k(3)} 2AgI + H_2O \tag{10}$$

## 3. ANALYTICAL RESULTS

### 3.1 Code verification

The comparison between the analysis by IOCAP code and AECL/RTF3b experiment under different pH conditions was performed. Table 1 shows the conditions of RTF3b test.[2] Iodine concentration changes in gas and liquid phase were calculated in Figs.1 and 2. As a result, the behavior of organic ($CH_3I$) and inorganic ($I_2$) iodine concentrations in gas phase, and the behavior of the $I_2$ and $I^-$ concentrations in liquid phase, associated with pH change, were well simulated.

### 3.2 Sensitivity analysis in actual plant scale

Three cases of the parametric analysis were performed using IOCAP code under the actual plant radiation conditions in order to evaluate the effect of radiation and impurities on iodine behavior. Table 2 shows the calculating conditions of actual plant scale. The initial condition of iodine and impurities concentrations in each case are shown in Table 3 (case 1 is no impurities condition, case 2 is condition with boric acid, and case 3 is condition with silver and boric acid). The initial components of each element were estimated based on 25GWd/t fuel burnup core inventory, considering core

control materials components of typical LWR plant. From thermochemical calculation, boric acid ($H_3BO_3$) and metallic silver were assumed as the chemical forms of boron and silver in containment vessel, respectively. The ratio of the concentration (Ag/I) in case 3 approximately corresponded to PHEBUS-FPT1 test result. pH change from acid to alkaline at 260,000 second was simulated by NaOH injection in sump. Impurities and radiation models were used and molecular iodine/ozone reaction in the gas phase were excluded in this analysis.

Figure 3 shows the result of iodine concentration change in gas phase of case 1. The dominant gaseous iodine species in gas phase was molecular iodine. The pH slowly decreased by production of nitric acid. The rapid increase in pH (acid to alkaline) at 260,000 second induced the large concentration change of iodine species. The gaseous iodine in gas phase strongly depended on the pH condition in sump, and the concentration of gaseous iodine species ($I_2$ and $CH_3I$) which indicate the nearly constant in acid condition decreased rapidly after pH change at 260,000 second. Figure 4 shows the comparison of iodine species concentration in liquid phase between case 1 and 2. The effect of boric acid on iodine behavior was small in this model. Figures 5 and 6 show the iodine behavior with boric acid and silver (case 3) in gas phase and liquid phase. In gas phase, the gaseous iodine species ($I_2$ and $CH_3I$) extremely decreased by existence of silver. All concentration of iodine species except AgI in case 3 were much smaller than that in case 1, because a large amount of iodine changed into AgI species in liquid phase. Figure 7 shows the comparison of $I_2$ and $CH_3I$ concentrations under pH change between with and without silver. The molecular iodine concentration in gas phase decreased by the trapping of inorganic iodine followed by AgI formation. The restraint effect of silver on gaseous iodine production was larger than that of pH change. The dominant gaseous iodine species under presence of silver changed inorganic into organic iodine.

## 4. CONCLUSION

The simulation results by IOCAP code for RTF3b experimental data well reproduced the experimental results. The following effects on gaseous iodine behavior were obtained by the sensitivity analysis using the IOCAP code.

- The effect of boric acid on the gaseous iodine production was small in this model.
- Gaseous iodine concentration decreased irrespective of acid and alkaline conditions under silver existence in liquid phase, because a large amount of iodine changed into AgI species.
- Silver had larger effect on mitigation of molecular iodine production than pH control.

5. ACKNOWLEDGEMENT

This work was sponsored under the contract by the Ministry of International Trade and Industry, Japan.

6. REFERENCE

1) Salih Güntay and Robin Cripps, A computer program to analyze the Iodine behavior in multi-compartment of a LWR containment, ISSN 1019-0643, 1992.

2) Evans G.J. and Palson A.S., The absorption of $I_2$ vapour by Epoxy Paint at 80℃, ACE-TR-B11, 1991, Research Chemistry Branch, AECL, Whiteshell Nuclear Research Establishment, Pinawa, Manitoba, Canada.

3) Burns, W.G., et al., The Thermal and Radiolytic Oxidation of Aqueous $I^-$ and the Hydrolysis and Disproportionation of Aqueous $I_2$, AERE/R- 10767 (1986).

4) Beahm,E.C. et al., Iodine Evolution and pH control, NUREG/CR-5950, December 1992.

5) H.Karasawa and M.Endo, Proceedings of the fourth CSNI workshop on the chemistry of Iodine in Reactor Safety Effect of Nitrogen and Oxygen on Radiolysis of Iodine Solution, PSI Report Nr.97-02 (1996)NEA/CSNI/R(96)6, pp.123-129.

6) Buxton,G.V., et al., Radiation induced redox reactions iodine species in aqueous solution, 1985. J. Chem. Soc., Faraday Trans.I, 81,449-471.

Table 1 The experimental condition of RTF3b test

| Parameter | Condition |
|---|---|
| Initial Iodine Concentration | $10^{-5}$ mol $dm^{-3}$ |
| Temperature | 60 ℃ |
| Pressure | Atmosphere |
| Aqueous Volume | 35 $dm^3$ |
| Gas Volume | 350 $dm^3$ |
| pH | 5.5 → 9.0 |
| Dose Rate | 2 kGy/h |
| Surface Type | Epoxy |

Table 2 Actual plant scale condition

| Parameter | Condition |
|---|---|
| Gas phase volume | 70000 $m^3$ |
| Liquid phase volume | 1700 $m^3$ |
| Gas/water boundary surface area | 250 $m^2$ |
| Temperature | 333 K |
| Initial pH | 5.5 |
| Dose rate | 50 kGy/hr |
| Painted vessel wall surface area in gas phase | 5500 $m^2$ |
| Steel vessel wall surface area in gas phase | 500 $m^2$ |
| Concrete vessel wall surface area in gas phase | 300 $m^2$ |
| Painted vessel wall surface area in water phase | 2.0 $m^2$ |
| Steel vessel wall surface area in water phase | 450 $m^2$ |
| Concrete vessel wall surface area in water phase | 50 $m^2$ |

Table 3 Initial concentration of iodine and impurities

| Element | Case 1 | Case 2 | Case 3 |
|---|---|---|---|
| I * (mol/l) | $5.88 \times 10^{-4}$ | $5.88 \times 10^{-4}$ | $5.88 \times 10^{-4}$ |
| Ag (mol/l) | 0 | 0 | $2.53 \times 10^{-2}$ |
| $H_3BO_3$ (ppm) | 0 | 2870 | 2870 |

*Initial chemical form is $I^-$

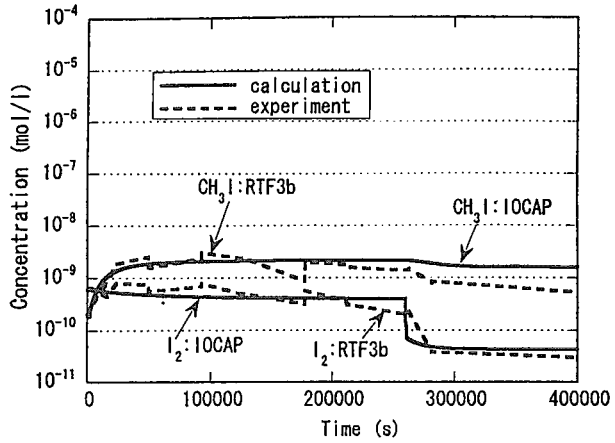



Fig. 1. Comparison of $I_2$ and $CH_3I$ concentration in gas phase between calculation and experimental results.

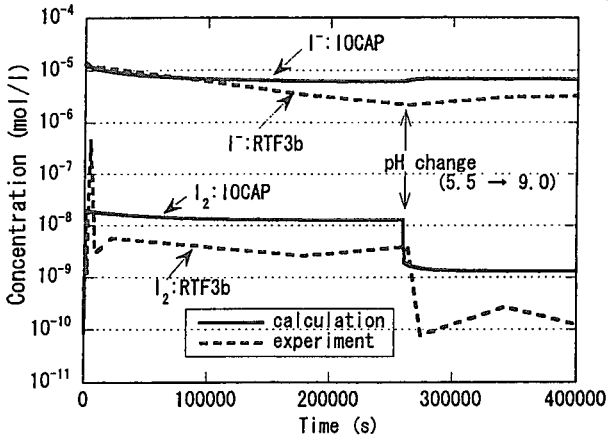



Fig. 2. Comparison of $I_2$ and $I^-$ concentration in liquid phase between calculation and experimental results.

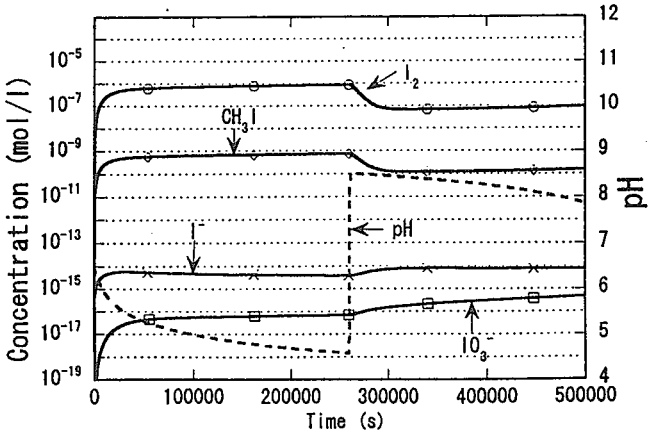



Fig. 3. Iodine behavior in gas phase under the condition without boric acid and silver conditions (case 1)

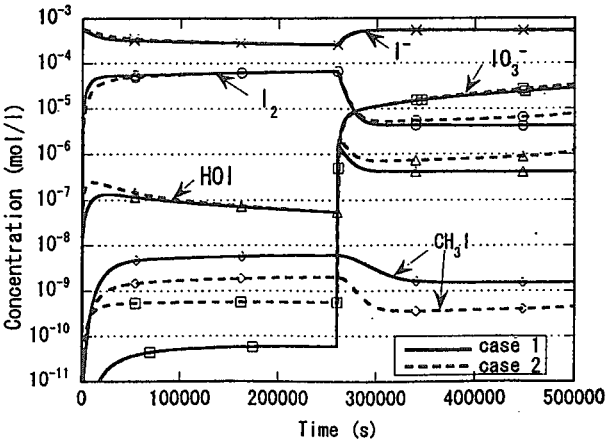



Fig. 4. Effect of boric acid on iodine behavior in liquid phase.

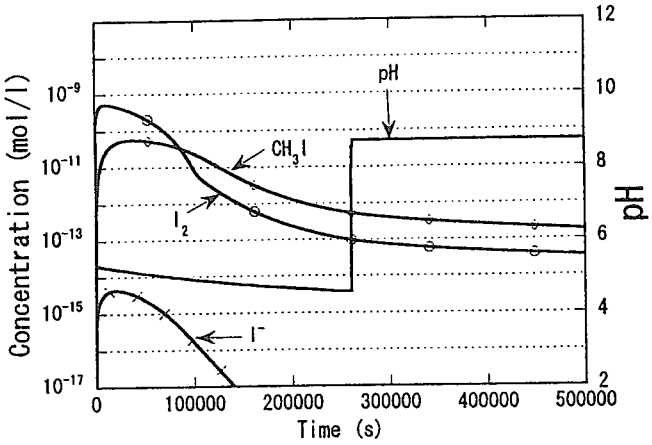



Fig. 5. Iodine behavior in gas phase under the condition with boric acid and silver (Case 3)

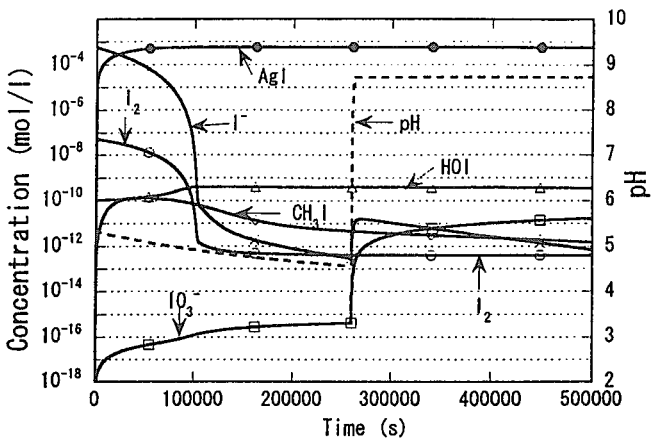



Fig. 6. Iodine behavior in liquid phase under the condition with boric acid and silver (Case 3)

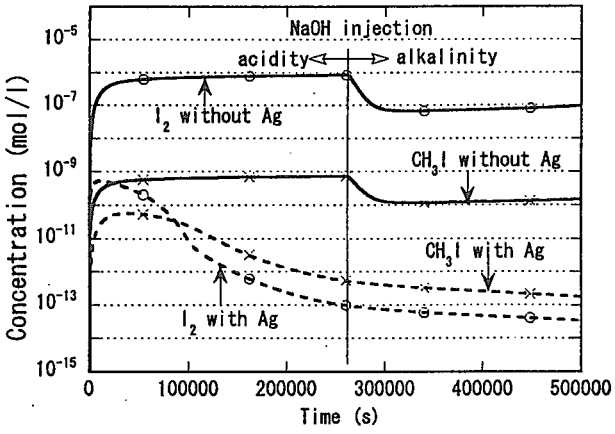



Fig. 7. Gaseous iodine concentration change in gas phase before and after NaOH injection under conditions with and without silver

JP0150116



# 10.4 Fission Product Aerosol Removal Test by Containment Spray under Accident Management Conditions(3)

Atsushi WATANABE, Hideo NAGASAKA
Systems Safety Department, Nuclear Power Engineering Corporation, Japan
tel: 03-4512-2587 a-watanabe@nupec.or.jp, tel: 03-4512-2571 h-nagasaka@nupec.or.jp

Seiichi YOKOBORI, Makoto AKINAGA
Nuclear Engineering Laboratory, Toshiba Corporation, Japan
tel: 044-288-8130 seiichi.yokoboro@toshiba.co.jp, tel: 044-288-8165 makoto.akinaga@toshiba.co.jp

## ABSTRACT

In order to demonstrate the effective FP aerosol removal by containment spray under Japanese AM conditions, two system integral tests and two separate effect tests were carried out using a full-height simulation test facility. In case of PWR LOCA, aerosol concentration in the upper containment vessel decreased even under low spray flow rate. In case of BWR LOCA with water injection into RPV, the aerosol concentration in the entire vessel also decreased rapidly after aerosol supply stopping. In both cases, the removal rate estimated from the NUREG-1465 was coincided with test results. The aerosol washing effect by spray was confirmed to be predominant by conducting suppression chamber isolation test. It turned out that the effect of aerosol solubility and density on aerosol removal by spray was quite small by conducting insoluble aerosol injection test. After the modification of aerosol removal model by the spray and hygroscopic aerosol model in original MELCOR 1.8.4, calculated aerosol concentration transient in the containment vessel agreed well with the test data.

*Keyword: severe accident, accident management, containment spray, fission product, aerosol removal, MELCOR*

## 1. INTRODUCTION

As Japanese accident management (AM), containment spray is adopted to suppress pressure and temperature increase, and to remove fission product (FP) from the containment air space. To demonstrate the validity of the AM procedure, the FP removal characteristics and the thermal-hydraulic behavior in the containment have been studied. The AM conditions inside containment are characterized as follows:

- Larger water droplets due to low spray flow rate, affecting steam condensation rate
- High humidity condition due to steam generation as a result of debris cooling
- Continuous supply of fresh water from outside of containment reflecting the AM procedure

Although a few tests on FP aerosol removal characteristics by spray were conducted[(1),(2)], the test conditions did not simulate above mentioned AM conditions.

The objectives of the test program are to provide data demonstrating the effective aerosol removal by the containment spray under several AM conditions using the full-height containment vessels and to provide the data for qualification and modification of system integral codes such as MELCOR for analysis of FP transport behavior inside containment. Cesium iodide (CsI) aerosol was used as a typical FP aerosol in the tests.

In the previous SARJ meetings, several tests focusing on the effects of spray flow rate, non-condensable gas partial pressure and FP release location (simulating LOCA sequence) on aerosol removal effect were clarified by selecting BWR TQUV sequence as a reference case. Analyses of the tests by modifying aerosol model by spray in MELCOR 1.8.3 were also conducted.

This paper dealt with following four tests results on aerosol removal effects by spray and analytical results by modified FP removal model in MELCOR 1.8.4. Two system integral tests under other typical SA scenarios (PWR LOCA condition and water injection into RPV in BWR) and two separate effect tests (isolation of BWR suppression chamber and insoluble aerosol (polystyrene LATEX) injection) were conducted by measuring the aerosol concentration transient in the containment vessel.

## 2. TEST FACILITY

Figure 1 shows the outline of the test facility. The facility consists of three separate vessel components, simulating BWR drywell (D/W) or PWR containment vessel (C/V), a suppression chamber (S/C) and a reactor pressure vessel (RPV). The C/V volume and its height are 12.2 $m^3$ and about 18 m, respectively. Its volumetric scaling ratio is about 1/720 to a typical BWR or about 1/5900 to a typical PWR. An actual spray nozzle for typical BWR and a simulator nozzle for typical PWR were used.

In order to satisfy the characteristic features of AM conditions mentioned above, generated steam associated with ex-vessel debris cooling, generated FP aerosol resulting from re-evaporation inside reactor pressure vessel and spray water were supplied continuously to the C/V as transient boundary conditions. Heat loss from each test vessel was compensated by heaters wrapped on the outer surface of the vessel.

## 3. TEST CONDITION AND TEST PROCEDURE

Containment spray was initiated immediately after the simulation of RPV failure. Initial conditions of total pressure, steam partial pressure, non-condensable gas partial pressure, temperature and aerosol concentration were determined from level-2 PSA analysis results. Aerosol and steam corresponding to decay heat power were supplied from the bottom C/V. The boundary conditions of spray flow rate, steam generation rate and aerosol injection rate were scaled down to the volume ratio of the C/V.

As a typical FP aerosol, CsI and polystyrene LATEX particle were selected for soluble aerosol and insoluble aerosol, respectively. Aerosol was supplied by a newly developed atomizing system which was a two-fluid nozzle type using superheated steam. The aerosol solution was well entrained by two high speed steam flows. Both aerosol diameter and its concentration were measured under steam environment by two sets of optical particle counters, which were moved up and down by an elevator. In order to obtain the axial distribution of aerosol concentration in the C/V, the three measuring locations (top, middle and bottom part of the C/V) were selected. In order to evaluate the data scattering, measurement was repeated three times at each location. The total measuring interval at one location was about 30 minutes.

## 4. TEST RESULTS AND DISCUSSION

### (1) PWR LOCA sequence

In PWR LOCA condition, where additional FP release by re-evaporation from reactor pressure vessel could be neglected because of flooding of RPV bottom and steam cooling of core regions as a result of corium falling into water pool. Hence this case is characterized by no CsI additional release. Spray flux of this case is one order lower than typical BWR because of one order smaller scaling ratio.

CsI aerosol concentration transient in the C/V is shown in Fig. 2 together with the results of natural removal test and the estimation result using NUREG-1465 model[3] which had developed under design basis accident conditions. Aerosol concentration in the upper C/V decreased within 2

hours exponentially after the spray initiation even under low spray flow rate. The aerosol removal rate during initial spray period was about 3 times larger than the natural removal rate. Aerosol removal rate estimated from the equation in NUREG-1465 was coincided with the test result.

**(2) Simulation of water injection into RPV in BWR**

When water is injected into reactor pressure vessel in addition to containment spray in BWR, FP release into the D/W by re-evaporation will be reduced and terminated about 2hours after accident by MELCOR analysis. This case is characterized by the limited 2 hours of CsI additional release.

Measured CsI aerosol concentration transient in the D/W is shown in Fig. 3 together with the results of estimation from NUREG-1465. During CsI supply period, CsI concentration transient in the entire D/W was similar to the reference case because of same test conditions. After CsI supply stopping, the concentration decreased rapidly and reached to zero, which was similar to PWR case. Aerosol removal rate estimated from the equation in NUREG-1465 was coincided with test result.

**(3) Isolation of BWR S/C**

In this case, test conditions are identical to the reference case except for the S/C isolation. Hence the contribution of the S/C in reference case to aerosol removal is evaluated from these tests.

CsI aerosol concentration transient in the D/W is shown in Fig. 4 comparing with the results of reference case. As shown in this figure, overall aerosol concentration transient in the entire D/W was similar to the reference case. That is, basically no aerosol removal in the S/C in reference test conditions was confirmed.

**(4) Insoluble aerosol (LATEX particle) injection**

In this case, test conditions are identical to the reference case except for aerosol solubility and density. Hence the effect of aerosol solubility and density on aerosol removal by spray is evaluated by comparing these two tests. In this test, volumetric concentration (count concentration) instead of mass concentration was used for the comparison of aerosol size distribution because of the difference of aerosol density.

CsI aerosol concentration transient in the D/W is shown in Fig. 5 comparing with the results of reference case. As shown in this figure, the effect of aerosol solubility on aerosol removal by containment spray was small. The effect of CsI aerosol growth associated with steam condensation and larger density favorable to gravitational settling was negligible. Diffusiophoresis in the upper D/W and interception and impaction in the middle and the lower D/W were main aerosol removal mechanisms.

## 5. ANALYTICAL RESULTS

Several test data for CsI aerosol concentration transient in the C/V were compared with the analytical results using original MELCOR 1.8.4 and modified MELCOR 1.8.4.

During the verification study for aerosol removal model by spray in original MELCOR, the following inadequacy was found. Firstly, since aerosol collection efficiency by diffusiophoresis was artificially set to be 1.0 under pure steam condition in original MELCOR, calculated aerosol removal effects by spray was overestimated. Secondly, since the steam condensation was only considered on one spray droplet in the evaluation of the aerosol collection efficiency in original MELCOR, calculated aerosol removal effects by spray was underestimated. That is, the value of the aerosol collection efficiency was calculated based on the definition equation of aerosol removal rate. Hence the value of whole spray droplet was used for steam condensation rate in the modified analysis.

Figures 6 and 7 show the analytical result of CsI aerosol concentration transient in the C/V of reference case and PWR LOCA case, respectively. In these calculations, hygroscopic aerosol model of

MELCOR 1.8.4 was not used. As shown in these figures, calculated CsI aerosol concentration transients by modified MELCOR better predicted the test data comparing with original MELCOR in both cases. In original MELCOR, calculated aerosol removal effects by spray was overestimated in the reference case under pure steam condition and was underestimated in the PWR LOCA case under non-condensable gas existence.

In the next step, hygroscopic aerosol model was assessed for the analysis of PWR LOCA test case because its effect became more clearly. Figure 8 shows the analytical result considering the hygroscopic model comparing with the test data and hygroscopic model neglecting case. Since the hygroscopic model in original MELCOR used the material property of NaOH aerosol, CsI material property was used in this calculation. As shown in the figure, calculated concentration transient agreed well with test data by adopting the hygroscopic model.

## 6. CONCLUSIONS

In order to demonstrate the effective FP aerosol removal by containment spray under Japanese AM conditions, two system integral tests and two separate effect tests were carried out using a full-height simulation C/V test facility.

Under the PWR LOCA condition, where additional FP release by re-evaporation from RPV could be neglected, aerosol concentration in the upper C/V decreased within 2 hours exponentially after the spray initiation even under low spray flow rate. The aerosol removal rate during initial spray period was about 3 times larger than the natural removal rate.

In case of water injection into RPV in BWR, FP release into the D/W by re-evaporation will be terminated about 2hours after accident. Under this condition, aerosol concentration in the entire D/W decreased rapidly after FP supply stopping similar to PWR case.

The removal rate estimated from the equation used in NUREG-1465 evaluation was coincided with test result, which justified NUREG model even under SA conditions.

From the test of isolation of BWR S/C, it was confirmed that the aerosol washing effect in the D/W during spray period was very predominant. The effect of aerosol solubility on aerosol removal by containment spray was quite small based on the test result using insoluble aerosol (polystyrene LATEX particle).

After the modification of aerosol removal model by the spray and hygroscopic aerosol model in original MELCOR 1.8.4, calculated aerosol concentration transient in the C/V agreed well with the test data.

## ACKNOWLEDGMENT

This work was sponsored under the contract by the Ministry of International Trade and Industry, Japan.

## REFERENCES

(1) R. K. Hilliard, et al., "Removal of Iodine and Particles by Sprays in the Containment Systems Experiment," Nuclear Technology, Vol. 10, pp. 499-519, April 1971.

(2) M. Tanaka, et al., "Performance on Containment Sprays for Light Water Reactors and Evaluation of the Heat Transfer," Nuclear Technology, Vol. 54, pp. 54-67, July, 1981.

(3) L. Soffer, et al., "Accident Source Terms for Light-Water Nuclear Power Plants", NUREG-1645, 1992.

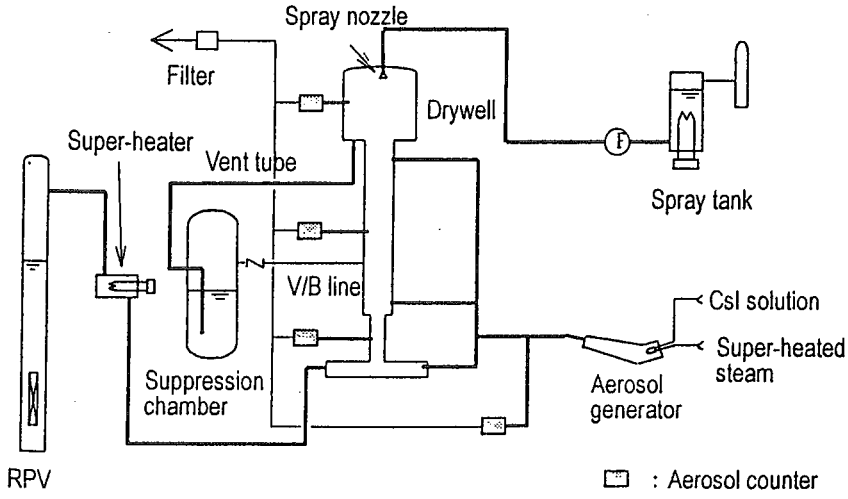



Fig. 1 Schematic Diagram of Test Facility

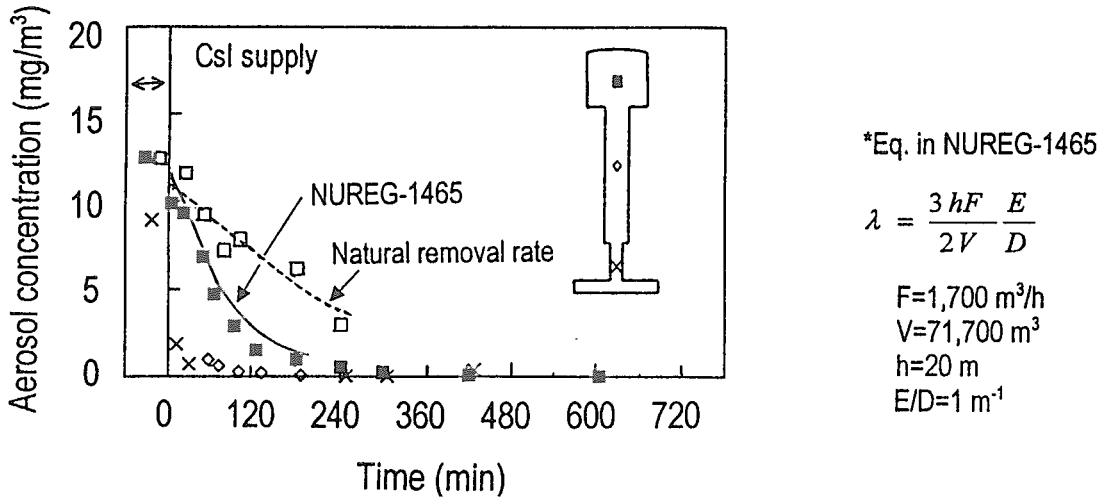



Fig. 2 Aerosol Concentration Transient in the C/V (PWR LOCA sequence)

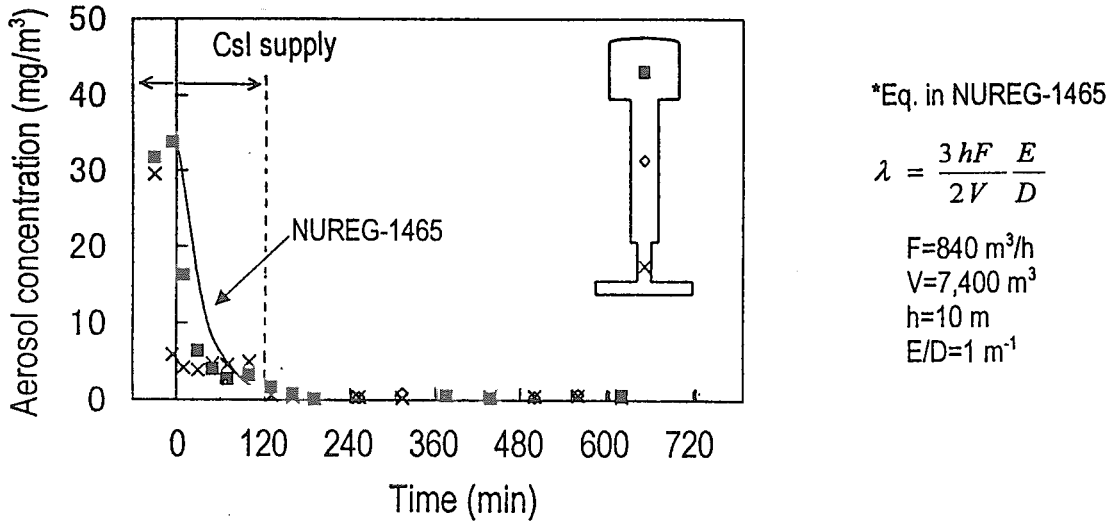



Fig. 3 Aerosol Concentration Transient in the D/W (Water injection into RPV in BWR)

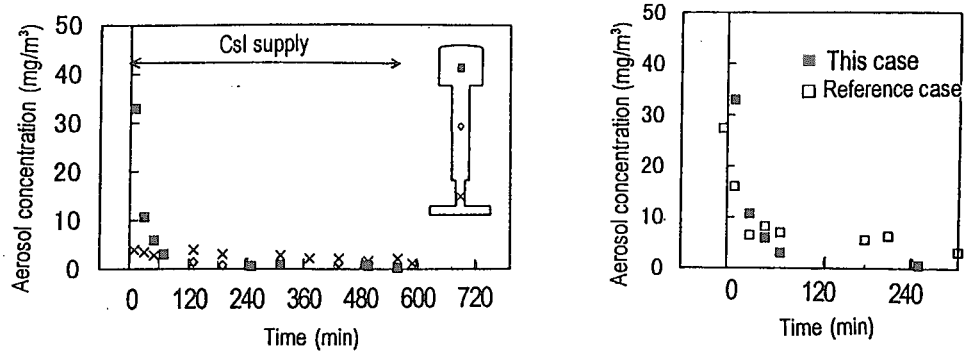



Fig. 4 Aerosol Concentration Transient in the D/W (Isolation of BWR S/C)

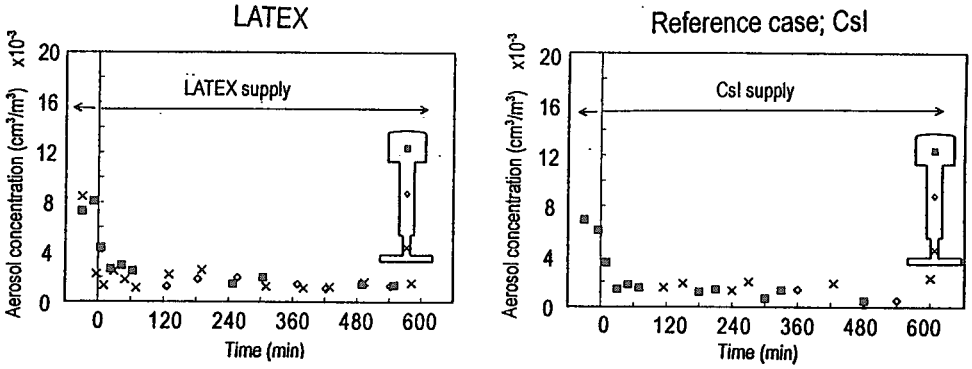



Fig. 5 Aerosol Concentration Transient in the D/W (Insoluble aerosol (LATEX) injection)

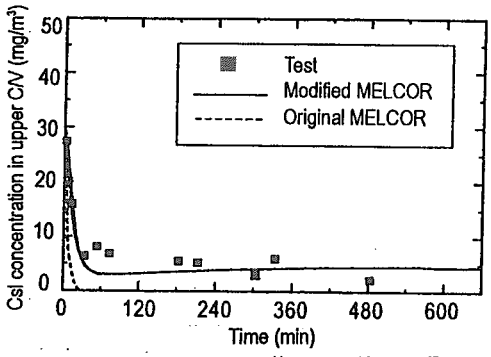



Fig. 6 MELCOR Analysis of Aerosol Concentration with or without hygroscopic model (BWR TQUV sequence)

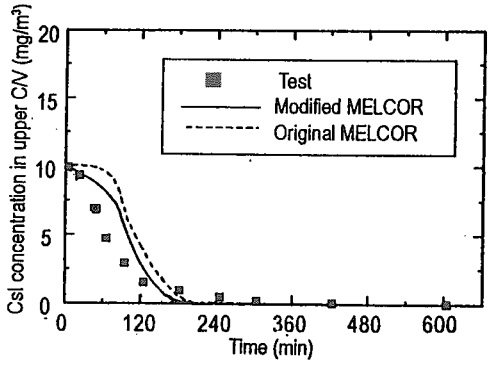



Fig. 7 MELCOR Analysis of Aerosol Concentration with or without hygroscopic model (PWR LOCA sequence)

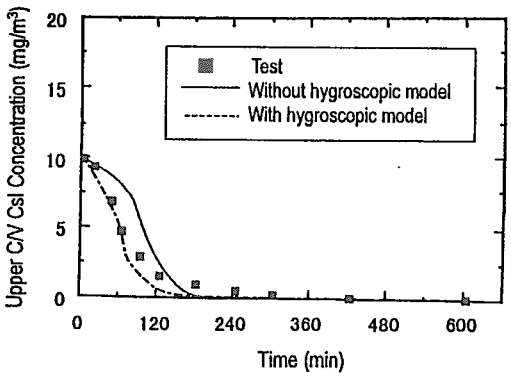



Fig. 8 MELCOR Analysis of Aerosol Concentration with hygroscopic model (PWR LOCA sequence)

This is a blank page.

# 11. Session 10

# Research Reactors

## Chairperson:

T. Hashimoto (NUPEC)
K. Hashimoto (JAERI)

This is a blank page.

JP0150117



# 11.1 MINT RESEARCH REACTOR SAFETY PROGRAM

**Mohamad Idris bin Taib**
Intelligent System Group
Division of Special Project
Malaysian Institute for Nuclear Technology Research (**MINT**)
Bangi,
43000 KAJANG, SELANGOR.
MALAYSIA
http://www.mint.gov.my
E-mail: Idris@mint.gov.my

## ABSTRACT

Malaysian Institute for Nuclear Technology Research (MINT) Research Reactor Safety Program has been done along with Reactor Power Upgrading Project, Reactor Safety Upgrading Project and Development of Expert System for On-Line Nuclear Process Control Project. From 1993 up to date, Neutronic and Thermal-hydraulics analysis, Probabilistic Safety Assessment as well as installation of New 2MW Secondary Cooling System were done. Installations of New Reactor Building Ventilation System, Reactor Monitoring System, Updating of Safety Analysis Report and Upgrading Primary Cooling System are in progress. For future activities, Reactor Modeling will be included to add present activities.

# INTRODUCTION

Malaysian Institute for Nuclear Technology Research (MINT) has TRIGA MARK II Reactor and became critical for the first time on June 28th 1982. This 1MW MINT Research Reactor (MRR) is pool-type and has 1300MW pulsing capacity. Past utilization of MRR are emphasized solely on the operation, maintenance and management of MRR. Research and development activities were geared towards applications in industrial, agricultural and medical fields, with MRR being used as a neutron source and producer of radioisotopes. Initially, MRR was operated by a group of staff from Reactor Department.

In 1993 Reactor Upgrading Project was initiated. Several activities such as Neutronic and Thermal-Hydraulic Analysis Probabilistic Safety Assessment, Updating Safety Analysis as well as Installation of New 2MW Secondary Cooling System were done.

In 1996 MINT used new structure of management and Reactor Department staffs were distributed to several group namely Reactor Operation, Reactor Upgrading Project, MINT Scientific Computing Center, Intelligent System and Policy and Strategic Planning Group. Reactor operation and maintenance were handle by Reactor Operation Group and Reactor related project was handle by Reactor Upgrading Project Group. Almost these two group resource are used for MRR related activities. Other three groups have expertise and skill, however their resource only partially use for MRR related activities. For that year also, Development of Expert System for On-Line Nuclear Process Control Project was carried. On 1997 MINT has change Reactor Power Upgrading Project to Reactor Safety Upgrading Project due to lack of funds and personnel. During these time Updating Safety Analysis Report are continued and Installation of New Reactor Building Ventilation and Upgrading Primary Cooling System are initiated.

# REACTOR PROJECT

## REACTOR POWER UPGRADING PROJECT AND REACTOR SAFETY UPGRADING PROJECT

Reactor Power Upgrading Project was started on 1993. That project has two main goal: upgrading of reactor power from 1MW to 2MW and to produce local group of expertise to cater for the needs of possible Malaysian nuclear power development program, in general. Under this upgrading project, the local group of expertise, capable of performing the design and analysis of research reactor, was expected to be established in duration of this upgrading project. The area of expertise should cover pertinent aspects of reactor design, including reactor physics, thermal-hydraulics, instrumentation and control, accident analysis, system reliability analysis, quality assurance as well as construction and installation of research reactor. This expertise could then directed towards the continuation of analysis and upgrading of reactor facilities to meet the needs of an increasingly sophisticated local scientific and research community. The expertise developed could also be used in non-nuclear areas, especially in enhancing the safety and reliability of a system operation, as well as process control in industrial plants in this country, such as in the petrochemical industries.

On 1997 MINT has change Reactor Upgrading Project to Reactor Safety Upgrading Project. So, the scope of the project has been modified due to lack of funds and personnel. Maintaining safety and the operational capability of the MRR at 1 MW are main priority. Several components such as the Reactor Building Ventilation System, the Primary Cooling System, including the Heat Exchangers and the Reactor Instrumentation and Control System need to be changed or upgrade.

## DEVELOPMENT OF EXPERT SYSTEM FOR ON-LINE NUCLEAR PROCESS CONTROL

That project was started on 1996, to develop very large microcomputer software for nuclear process control, including Artificial Intelligence and Nuclear Reactor Software. The initial objective of that project was to combine Process Control, Intelligent Control (Fuzzy Logic, Neural Networks, Noise Diagnostics etc.) as well as Nuclear Software (Neutronic and Thermal-Hydraulic) to control MRR intelligently. On 1998 that project was structured to Reactor Monitoring System and Reactor Control System Modeling.

# REACTOR ACTIVITIES

## NEUTRONIC ANALYSIS

The main softwares were used to evaluate the safety of the upgraded core configuration. TRIGAM was used to evaluate the effective multiplication factors. TRIGAM was also used to estimate the power generation in each fuel element. TRIGAM also plots the average fast and thermal spectrum in each ring. TRIGAM can also be used evaluate the possibility of extended operation under xenon poisoning and to assess the safety of the upgraded core at accident conditions of 2.2MW. PULDTRIM is used to evaluate the power pulsing capabilities of the upgraded core. WINS-D/4 is used to estimate the 69-group neutron spectrum in the central thimble. The software also calculates various 69 or less number of group cross section values for the central thimble. WIMS-D/4 can also be used to generate the flux values in the fuel element. Calculations proved that the presently available fuel elements are adequate for the first 2MW core at least for the first year of operation. It was also found that the 2o uranium weight-percent fuel element should not be positioned in the central rings due to high power peaking factors.

From the design calculation, tentative decision have been made for the first 2MW operation, core configuration will be maintained, existing fuel stock adequate and safety during pulse operation. The use of 20% and 12% standard fuel elements in the present core loading pattern will provided experience in handling these types of fuels. The behavior of the 2MW reactor can be calculated and estimated based on the present core using the computer code available. For the first 2MW core, a mixture of fuels, i.e. 8.5% w/o, 12% w/o and 20% w/o will be used due to optimize utilization of fuel. Safety of pulsing operation should guaranteed by means of limiting the maximal fuel temperature and maximal peak power achieved.

## THERMAL-HYDRAULIC ANALYSIS

Analysis of thermal-hydraulic aspect of the reactor upgrading will give detail analysis the behavior of the reactor's coolant and indication on the adjustment needed to keep the bulk water temperature below the safety limits, under full 2MW operating power. Based on this analysis, the cooling and demineralizer system will be upgraded as required. In-pool delay tank was also designed. PARET code was successfully used to simulate the natural convection flow through the TRIGA core and concluded that can be used to predict transient flow characteristics in pool-type research reactors cooled by natural convection. Such capability is extremely useful in determining the feasibility and safety of a power increase while maintaining the core-cooling mode.

### PROBABILISTIC SAFETY ASSESSMENT

Probabilistic Safety Assessment (PSA) for MRR first introduced in 1995. The main reasons are to be used for Development of Expert System for On-Line Nuclear Process Control as well as updating Safety Analysis Report. Some work has been done to use PSA for Reliability Analysis of Reactor Instrumentation and Control System as well as Accident Analysis. For that time MINT also plan to promote PSA to other MINT facilities focused on maintenance purposed. Beyond MINT for industrial process especially petrochemical industry.

### SAFETY ANALYSIS REPORT

After MRR has been operated more than fifteen year and several modification has been made, updating of Safety Analysis Report (SAR) are required. The new SAR also required making compliance with new SAR new format. Neutronic and thermal-hydraulics analyses as well as PSA definitely are required.

### REACTOR MONITORING SYSTEM

Reactor Monitoring System (RMS) is a part of Development of Expert System for On-Line Nuclear Process Control Project. The main objective of RMS is to enable several MINT staff that has own Reactor expertise and skill to get on-line Reactor parameter during operation via Computer Networking. Beside Reactor Operation Group, other group in MINT also have expertise and skill in Reactor field. On the other hand RMS gather Reactor parameters especially in-core and pool temperature for analysis. For the future in-core on-line flux measurement are planned.

### OTHER ACTIVITIES

On November 1995 installation of New 2MW Secondary Cooling System (SCS) was successfully completed to replace 1MW previously Secondary Cooling System. Those activities involve changing Cooling Tower and Piping System. Before installation of New SCS, Reactor only can be operated up to 800kW due to maintain water pool temperature. Installation of New Reactor Building Ventilation System is started this month. That new system will be operable at the middle next year. At the same time, installation of Deminelizer System, a part of Primary Cooling System is also being done and will complete within several months.

## FUTURE ACTIVITIES

Updating of Safety Analysis will be main priority of MINT. More activity on Neutronic and Thermal-Hydraulic Analysis as well as PSA will be done. With the limitation of facilities and manpower, those activities are more toward calculation, modeling and analysis. Measurement and experiment will be done with present facilities only. Reactor Modeling and Reactor Monitoring System also have interested by MINT researchers due to applicability to other field.

JP0150118



# 11.2 Measurements of Radiation Dose Level Around 3W1 Beamline of Beijing Electron-Positron Collider

Qingbin Wang, Ming Zhao, Jianping Li, Yueli Tang, Baozhong Dong

Division of Radiation Protection
Institute of High Energy Physics, Chinese Academy of Sciences
P.O.Box 918-13 Beijing 100039 PR CHINA
Tel. +86-10-68235895 Fax.+86-10-68213374
Email: wangqb@alpha02.ihep.ac.cn

## Abstract

This paper describes the possible radiation sources and their characteristics around 3W1 beamline of Beijing Electron-Positron Collider (BEPC). A homemade monitoring system is used to measure the dose level around 3W1 beamline. The obtained results show that the radiation field depends on the BEPC operation status. During the normal storage operation, the radiation field is a slowly changing field close to a constant. The dose level is proportional to the beam intensity. However when electrons are injected into the storage ring, the radiation field becomes a fast changing field with a very high dose level. Furthermore our results indicate that accidentally the beam loss occurred near to 3W1 beamline, which led to the fast increase of dose level.

**Keywords:** Radiation, Dose, Beamline, Electron-Positron Collider

## Introduction

In the upgrade program of the BSRF, a new permanent-magnetic wiggler, two beamline and related experimental stations have been installed and operated since the end of 1996. 3W1 is a permanent-magnetic wiggler installed at quadrant III of the BEPC storage ring, as illustrated in Figure 1. The operation parameters are as follows: total length of straight section, 7.5m; period number, 5; gap, 4.3; magnetic field, 1.43 T; critical energy, 4.6keV; deflection coefficient, 40. It can be operated in either the dedicated or parasitic mode of the BEPC. The photon beam from the front end is separated into two beamlines at an angle of 6.3 mrad. 3W1A is a white-radiation beamline with an acceptance of 1 mrad, and -1 mrad with respect to the wiggler axes. 3W1B is a monochromatic focusing soft X-ray beamline with an acceptance of 1 mrad. and +5.3 mrad with respect to the wiggler axes. Fig. 2 shows a sketch of beamlines 3W1A and 3W1B.

However the design of 3W1 beamline lacked of the consideration of radiation shielding and only had a safety shutter. When the experiment is done and the safety shutter is open, the dose level near 3W1 beamline is very high. After the operation of

3W1 beamline. The relative high dose level is reduced by means of adding a lot of local shielding.

Our work aims at determining the radiation field distribution of 3W1 beamline in order to determine the possible radiation sources and to take appropriate protection measures. In addition, the field distribution is significant for other beamline of BEPC designs too.

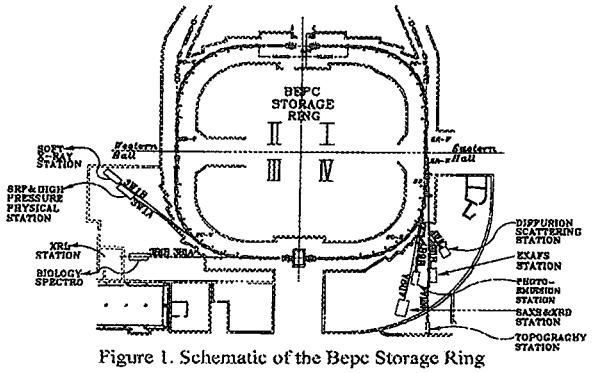



Figure 1. Schematic of the Bepc Storage Ring

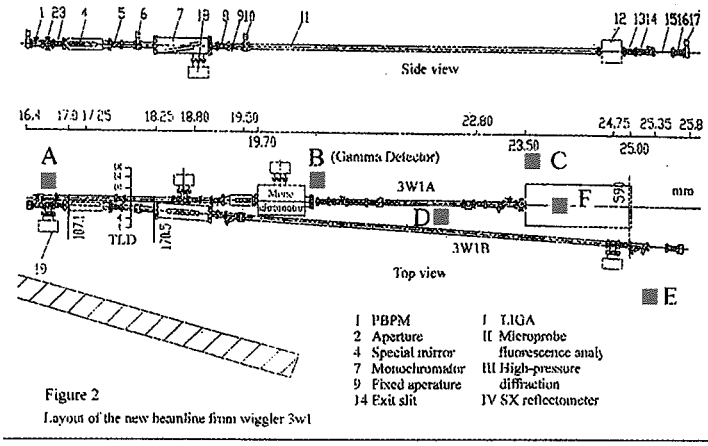



Figure 2
Layout of the new beamline from wiggler 3w1

# Radiation sources and characteristics

The radiation field around 3W1 beamline behaves very differently depending on the operation status of the storage ring. At the beam injection stage, the field is a transiently changing field occupying a small space with a high radiation dose level while it is a slow changing field close to a constant field at the normal beam storage stage. The radiation dose level at the normal storage stage is proportional to the beam intensity in the storage ring. A sudden beam loss can result in great increase in dose level. The following section gives a more detailed description about the radiation dose level at varieties of operation stages.

- **Beam lost during electron beam injection into storage ring**

3W1 beamline locates at the west experimental hall of the synchrotron radiation facility that is near to the positron injection spot. The thickness of the concrete shielding between the beamline and the storage ring is 50 cm (see Figure 1). At the injection stage, a lot of injected electrons are lost in the vicinity of the injection spot due to the injection efficiency. Therefore the dose level around 3W1 beamline which is behind the positron injection spot is obviously higher than other experimental halls during the positron injection. However the electron injection has little influence on the dose level.

- **Gas bremsstrahlung**

The gas bremsstrahlung is produced by the interaction of the storage ring positron or electron with residual gas molecules in the ring vacuum chamber. Such interactions are one of the sources of stored beam losses that result in beam decay. Gas bremsstrahlung interactions take place all around the storage ring, But are a particular in the straight sections for the Insert Device. Gas bremsstrahlung is produced in a very narrow beam ($1/\gamma$) that sums for the entire section length. The 3W1 Insert Device straight sections are 7.5 m in length. The characteristic scattering angle of the gas bremsstrahlung is [1]:
$\theta = 0.511 \times E^{-1}$ (radian), $E$ is the electron energy within the storage ring in unit of *MeV*.

The radiation dose equivalent rate (*DER*), in the forward direction due to the direct gas bremsstrahlung beam is proportional to[2]:

$$DER \propto \frac{E_0^{2.67} \cdot ipl}{d(l+d)}$$

$E_0$: the storage ring energy　　$i$: the storage ring current
$P$: the storage ring pressure　　$l$: the length of the effective straight section
$d$: the distance from the end of straight section to the observation point

The gas bremsstrahlung produced in the straight section migrates along the beam pipe. During the migration, it radiates the pipe shell and the optical components inside, which produces the second radiation. The mixture of the primary and the secondary radiation can penetrate the pipe shell and the shielding wall (50 cm) forming a radiation field with fairly high dose level.

- **Sudden beam lost within storage ring**

The physical reason for sudden beam loss is too complex to discuss. Here only the dose measurement results are given.

# Experimental

The radiation field around 3W1 beamline was studied under a variety of storage ring operation and shielding conditions. The dose level at the sampled spots was recorded by our monitoring system consisting of γ-monitor and Digital Data Logger All the instruments are introduced as follows:

The homemade γ-monitor adopts a cylinder ionization chamber aerified argon gas as the detector. The sensivity is $2.58\times10^{-10}$ C/Kg Pulse. The output is a current circle being of 20 mA in intensity and 800 μs in time interval. This output form has a strong resistibility to electromagnetic disturbances.

The CPU of the Digital Data Logger (DDL) is a high speed CMOS chip produced by Motorola Company. There are 16 channels at the DDL inlet. The input is carried out by means of photoelectric coupling which provides a reliable signal transmitting among the monitors at a variety of distances. The software programmed in assembly and C language can realize the functions such as data acquisition and storage for γ-monitor, parameter setting, plotting, printing and alarming and so on. The memory (RAM) inside the DDL can reserve the data acquired within ten days.

The γ monitors are located at A, B, C, D, E and F points around 3W1 beamline in the forward direction, as illustrated in Figure 2. The dose equivalent rate at several points were measured under three operation stage of the storage ring: injection stage, storage stage, beam loss stage. The measurement result are listed in Table1:

A typical figure of variety of the beam current in storage ring is presented in Figure 4.

**Table 1. Dose Equivalent Rate around 3W1 Beamline**

| Stage / Position | Injection | Storage | Beam Loss |
|---|---|---|---|
| A | 12.5 | 8.0--2.0 (50--20mA) | 52.0 |
| B | 3.0 | 1.3--0.6 (65--20mA) | 30.0 |
| C | 0.8 | 0.3--0.16 (60--20mA) | 32.0 |
| D | 6.0 | 4.0--1.2 (65--20mA) | 96.0 |
| E | 1.0 | 0.32--0.16 (60--20mA) | 20.0 |
| F | >12900 | >12900 | |

Unit: uSv/hr

Figure 5 demonstrated the detection result of the dose rate at A spot, which correspond with the beam current in Figure 5. There are a lot of downward hackles in the figure, these are caused by that, when the experimental personal shut off the safety shutter , the dose rate decreased sharply. According to this figure, the beam current decreased slowly during the beam storage stage and the dose rate decreased slowly too. Accidentally the beam loss occurred near to 3W1 beamline, which led to the fast increase of dose rate.

The thermoluminescent dosemeter used in the experiments is a $^{7}$LiF-TLD produced by China Nuclear Radiation Monitoring Institute. Its energy response is from 30 KeV to

4 MeV within the measurement range between 0.1 μ Sv and 12Sv, [4]. In our experiments the TLD is used as a relative measurement tool which gives the accumulated γ-dose value at a specified position during a time period. As shown in Figure2, TLD chips were arranged behind the light target A point, in the level of the beamline, which is vertical to the beamline, the distance between every two chips is 4.6 cm. The cumulative was detected during 1998/7/1/9:00--7/4/18:00. Figure 3 presents the result and show that the cumulative dose is higher at the point near the beamline.

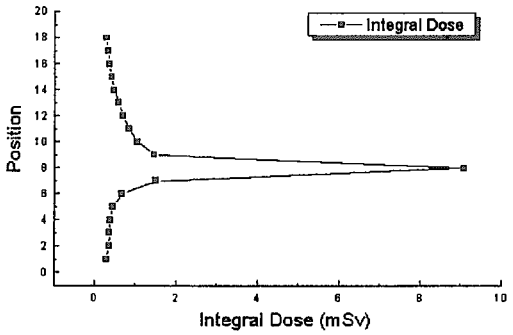



Figure 3. Integral Dose vs Position

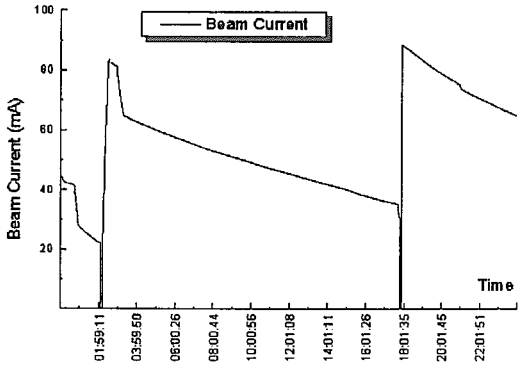



Figure 4. Beam Current vs Time

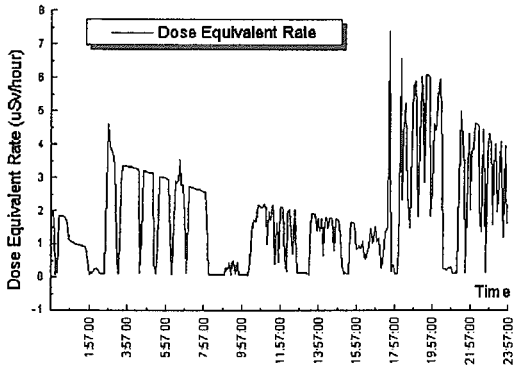



Figure 5. Dose Equivalent Rate vs Time

# Conclusions

Finally, following conclusions can be drawn from our measurement results:

- The dose level along the exit direction of 3W1 beamline relates to the operation stage in storage ring and the exit angle. Specially when in injection stage The year integral dose can reach the limit value 3/10 allowed for radioactive personnel within a certain angle scope if the safety optical shutter is open and the Wiggler is inserted. This angle scope is called controlled area which boundary should be labelled by a radiation mark or equipped with a shielding net.
- Under the synchrotron operation, the dose equivalent rate near to the light target along the direction of the observation window can reach 8.0 μ Sv/hr if the safety shutter is open and Wiggler is inserted. Therefore it is absolutely forbidden to observe the facula with eye in the direction along the observation window.
- Under the synchrotron operation, the dose equivalent rate has exceeded measure range (12900 μ Sv/hr) of γ-monitor inside the experimental hutch which will` exceed the limit value allowed for radioactive personnel if the safety shutter is open, photo shutter is off, and Wiggler is inserted. In this case, nobody is allowed to work in the hutch.
- During the beam injection, the measured maximum values of the dose equivalent rate in 3W1A work area C spot and in 3W1B work area E spot are 0.8 μ Sv/hr and 1.0 μ Sv/hr respectively. The radiation dose level is very high relatively. Therefore we suggest all the working staffs leave the 3W1 work area during the beam injection.
- Under the synchrotron operation, in the normal beam storage stage, the measured maximum values of the dose equivalent rate in 3W1A work area C spot and in 3W1B work area E spot are 0.3 μ Sv/hr and 0.32 μ Sv/hr respectively. Both values are under the safety dose level and staffs are allowed to work in 3W1 work area.
- The area near to the observation window of the light target is a high radioactive area. Furthermore it directly faces to 3B1 area which radiation dose level is very high too. The observation window should be shielded with Pb plate in general case.
- The radiation dose level at the vacuum pipeline outlet behind the hutch of 3W1A is relative high for the scattering experiments. More shielding should be added in the area.

# References

[1] A.Ferrari, M.Pelliccioni, and P.R.Sala, "Estimate of Fluence Rate and Absorbed Dose Rate Due to Gas Bremsstrahlung from Electron Storage Rings," LNF-93/016 P, INFN, Frascati, Italy(1993).

[2] N.Ipe, D.R.Haeffner, and E.E.Alp, "Guide to Beamline Radiation Shielding Design at the Advanced Photon Source," ANL/APS/TB-7, SLAC TN 93-5.

[3] Yueli.Tang, and Jianping.Li, Nuclear Electronics and Nuclear Detect Technology, 4(1998), 244.

This is a blank page.

# 12. Session 11

# Ex-Vessel Phenomena

## Chairperson:

S. Koshizuka (Univ. of Tokyo)
H. Nagasaka (NUPEC)

This is a blank page.

JP0150119



# 12.1 Analysis of Containment Direct Heating (DCH) For 300MWe Nuclear Power Plant

Jinghui Gao

29 Hong Cao Road, 200233, Shanghai, China
Tel: (021) 64850457
Email: jingh_gao@hotmail.com

【Abstract】

The expulsion of high temperature core debris from the reactor cavity into the containment atmosphere has been identified as an important potential contributor to containment failure in the event of a severe accident[1]. Experiments and analyses have shown failure of reactor vessel under high pressure of primary system can result in the rapid discharge of molten core debris into the cavity. Gas from blowdown of the coolant system may then entrain the debris as fine particulate that may be carried out of the cavity region. Containment loading can result from combustion of hydrogen produced by interaction of the debris with steam from the primary system and from thermal and chemical energy transferred from the debris to the atmosphere. This phenomenon has become known as Direct Containment Heating (DCH). In this article, the progression of DCH is simulated under Station Blackout condition for 300MWe Nuclear Power Plant using MELCOR code. Comparison of the results among different nuclear power plants under DCH conditions is presented as well.

【Key Words】

Severe Accident, Station Blackout, Containment Direct Heating

## 1 Physics Model

### 1.1 Modeling of Systems

Nodalizations of primary system and secondary system are shown in Fig. 1. Multi-volume simulation is applied in containment building.

### 1.2 Core Damage Modeling

After occurrence of a severe accident, core will damage by degrees. Two different models exist theoretically, i.e. melt pool model and non-melt pool model. Fig. 2 shows the mechanism of melt pool model that was found in core region in TMI accident. SCDAP/RELAP5 can model this progression. Fig. 3 gives the mechanism of non-melt pool model that can be simulated by MELCOR[2].

Because MELCOR has no capability for modeling the melt pool model, control functions are applied to simulate this type of core damage as a conservative approach, thereafter to evaluate the DCH phenomenon.

## 2 Selection of Cases for Calculation

Selection of Cases for DCH calculation shows in Table 1, where case 1 stands for base case, that follows the assumptions described in section 4. Case 2 to 9 is selected for sensitive analyses under DCH condition.

## 3 Initial Conditions and Assumptions

Before occurrence of the accident, the plant remains at full power operation condition, where vital parameters of the plant keep nominal values.

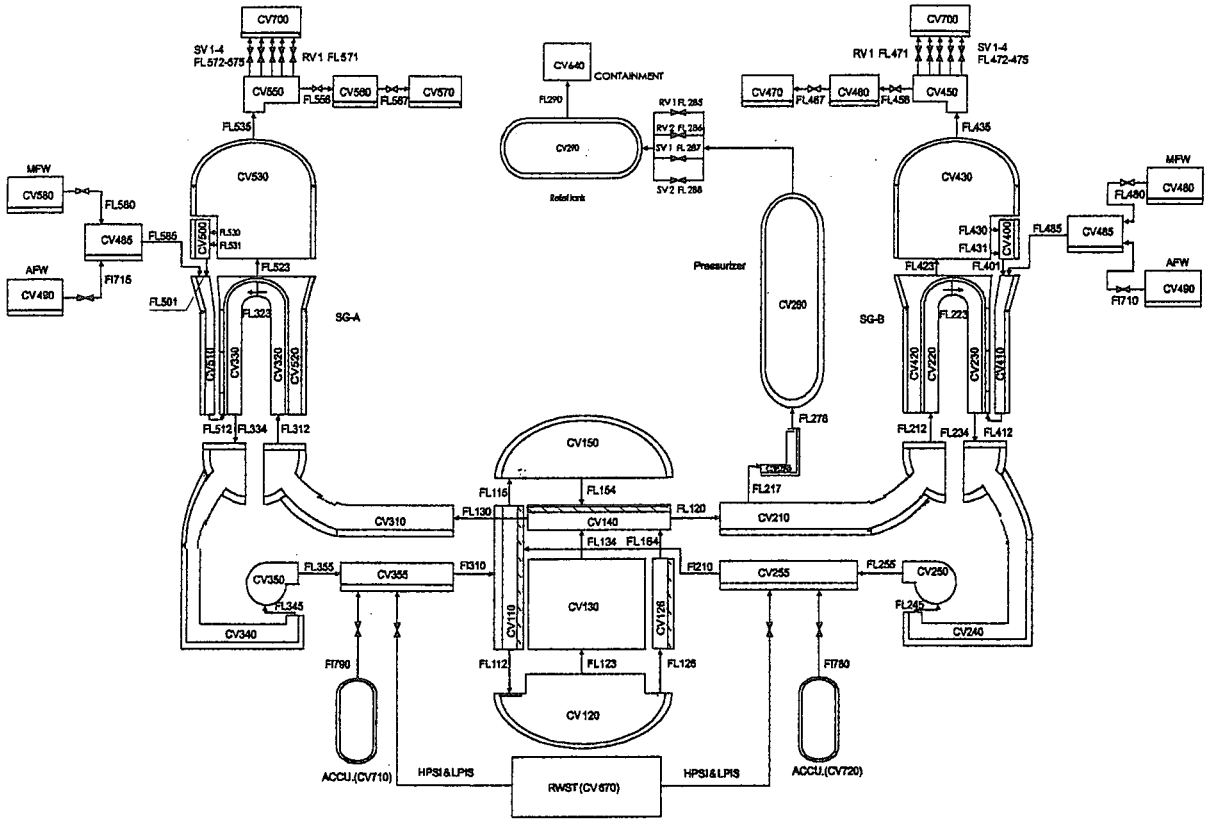



Fig. 1 RCS and Secondary System Nodalization for MELCOR Simulation

Under case 1, SBO occurs at 0.0sec, leading to a series of response in the plant, such as reactor trip, turbine trip and main coolant pumps trip as well. Assumptions of the accident are as follows:

1) Relief valves and safety valves of Pressurizer/ Steam Generators available,
2) Auxiliary Feedwater Systems unavailable, ECCS unavailable (Accumulators available), Containment Spray System unavailable.

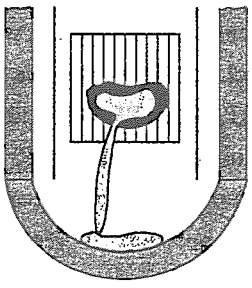


Fig. 2 Melt Pool Model

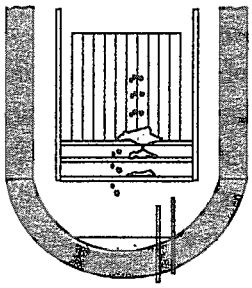


Fig. 3 Non-Melt Pool Model

## 4 Results Analyses and Discussions

### 4.1 Results of Case 1

According to MELCOR calculation, main events timing of case 1 is indicated in table 2.

After the occurrence of SBO, due to loss of heat sink in core region, core suffers uncovery on the top at 8500 seconds, successively, undergoes a series of core damage, including core heatup, core melt, metal water reaction and core slumping, etc. Heat transfer in core region deteriorates when core dryouts at 14020 seconds. At 17422 seconds, penetration failure in lower head occurs, leading to high pressure melt ejection. About 2.5 tons of corum and 1.8 tons of coolant blowdown into reactor cavity. DCH occurs immediately in

containment.

During the process of HPME, peak pressure of containment is only 2.31 bar, increasing only 0.7 bar of pressure in containment. DCH lasts about 7 seconds.

Table 1 Case Selections

| Cases | Assumptions |
|---|---|
| 1 | Base case, Station Blackout occurs. |
| 2 | On case 1, melt fraction ratio of melt mass to corium inventoryf (R) is 10%, melt temperature (T): 2000K, UCHB, etc. |
| 3 | On case 2,R : 20%, HB unavailable |
| 4 | On case 2, R: 50%, UCHB |
| 5 | On case 2, R: 90%, UCHB |
| 6 | On case 5, limited speed of melt ejection is 0.1m/s. |
| 7 | On case 2,R: 100%, T is 2500K. |
| 8 | On case 2, R: 100%, UCHB unavailable |
| 9 | On case 2, R: 100%,T is 2000K, 20% of melt on cavity basemat. |

Table 2 Timing of main events in case 1

| Main Events | Time (sec) |
|---|---|
| SBO occurs | 0.0 |
| SG water inventory dryout | 3270.0 |
| PORVs of PRZ Open | 6270.0 |
| Disk rupture of Relief Tank | 6720.0 |
| Uncovery of core in the top | 8500.0 |
| Control rods begins to melt | 10270.0 |
| Zr-$H_2O$ reaction occurs | 10330.0 |
| Rupture of fuel rod cladding | 12470.0 |
| Uncovery of core on the bottem | 14020.0 |
| Failure of core support plate | 17306.0 |
| Failure of lower head of RPV | 17422.0 |
| DCH begins | 17422.0 |
| Accumulators start pulling water | 17422.0 |
| DCH ends | 17429.0 |
| Containment reaches peak pressure | 17429.0 |
| End of calculation | 20000.0 |

## 4.2 Parameters Effects to DCH

Table 1 gives cases selection of sensitive analyses for SBO-induced DCH. Up to 8 cases are included. Mainly, some vital factors such as melt mass, melt temperature, condition of hydrogen burning, DCH triggering limit, etc. are under consideration. In Figs. 4 and 5, core melt ejection occurs at 0 second, CVH-P.650 refers to pressure of containment hall, (2) stands for case 2, and so on.

From case 2 to 5, calculations have been carried out to evaluate the results of different ratio of core ejection mass out of corium inventory with 10%, 20%, 50%, 90%, respectively. Shown in Fig. 3, peak pressure in containment hall will reach 4.75bar, 3.18bar, 6.6bar, 7.3bar, respectively. Hydrogen burning contributes greatly to the increasing of containment pressure. DCH lasts about 8 seconds. The more core melt mass ejected, the higher pressure containment reaches with the exception of case 3. Main reason is that in case 3, no hydrogen burning is simulated. As a result, we can estimate that hydrogen burning could contribute to 1.5 bar of pressure increasing in the containment that is quite similar to the result in reference[3] 2, about 1.5-2.0 bar.

Compared case 6 with case 5, only speed limit of core melt ejection is relaxed. Results show that DCH extends to 60 seconds. Peak pressure is 7.82 bar (Fig. 4) after DCH loads. Totally, the limit only change the duration of DCH occurrence, not pressure.

Compared case 7 with case 5, ejection ratio of core melt inventory is 100%, with 2500K temperature. Core melt ejection lasts 26 seconds, and DCH lasts 28 seconds. At 20 seconds, nearly 20 tons of water in cavity dry out. About 430 Kg of hydrogen is generated in core before ejection. Peak pressure of

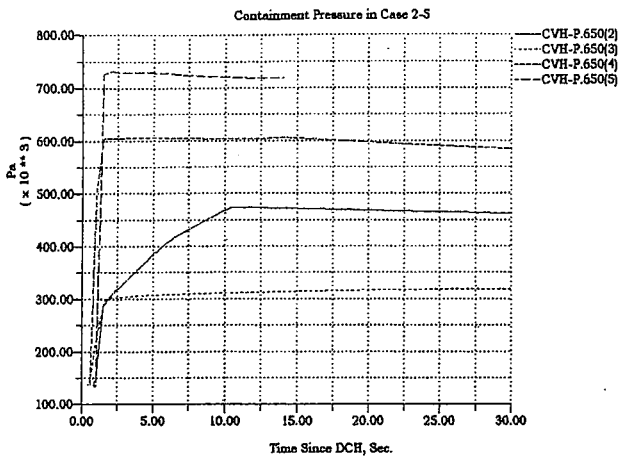



Fig. 4 Containment Pressure in Case 2-5

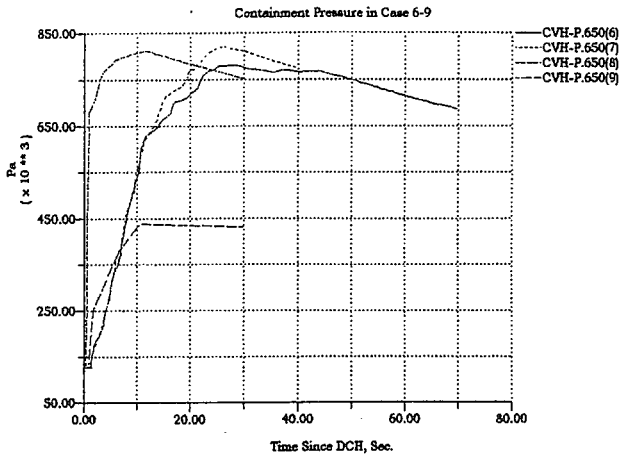



Fig. 5 Containment Pressure in Case 6-9

containment reaches 8.2bar.

In case 8, it is assumed that 100% of core mass is melted and ejected out of vessel, with temperature of 2000K. Melt mass blowdown lasts 5 seconds, and DCH lasts 8 seconds. At 11 seconds, peak pressure of containment appears, about 8.12 bar (Fig. 4). Containment atmosphere temperature reaches 2300 K.

In case 9, it is assumed that 100% of corium inventory with temperature of 2000 K, ejects into containment, 20% of that settle on the basemat of reactor cavity. HPME lasts 5 seconds and DCH 8 seconds. At 11 seconds, peak pressure of containment atmosphere reaches, to 4.8bar (Fig.4). Because there are about 20% if core mass deposit on the heat structure in cavity and containment, great amount of steam generated, containment pressure increases 3.5 bar within 2 seconds.

### 4.3 DCH Result Comparison with Other Different NPP

Table 3 gives vital parameters and DCH results for SURRY、BELLEFONTE、ZION as well as 300MWe NPP[4]. Due to its own nature of DCH, there is quite large uncertainty to simulate DCH.

Compared with other nuclear power plants, 300Mwe NPP has its own character, e.g. relatively larger free volume of containment, so it has a smallest value of ratio of thermal power to containment free volume, and smallest value of ratio of corium inventory to containment free volume. It is a good advantage of 300Mwe NPP to prevent early containment failure. The most conservative calculation shows that only 8.2 bar of peak pressure is found in case 7 where, no credit is taken for accumulation of core mass settlement and deposition in the cavity basemat, moreover, absorption of fission product fine particulate by heat structure in containment is not considered.

Reference 2 shows that if there are 25% of core mass accumulated in the reactor cavity, pressure of containment will decrease about 0.7 bar, and if absorption of heat structure in containment is taken into account, another 0.7 bar of pressure decrease will be got. Due to above conservative assumptions, the possibility of DCH-induced containment failure will be very low.

## 5 Conclusions

For 300Mwe NPP, some conclusions could be obtained as follows:

1) For 300Mwe NPP, due to specific configurations of its reactor core and reactor pressure vessel,

Table 3 Comparison of vital parameters and DCH results of different nuclear power plants

| Parameters \ Plant | SURRY | BELLE-FONTE | ZION | 300Mwe NPP | Remarks |
|---|---|---|---|---|---|
| Thermal power MWt | 2441 | | 3250 | 998.6 | (1) Corium inventory accounted between lower core plate and upper core plate is about 58 tons. |
| Total corium ton | 113 | 177 | 138 | 68[1] | |
| Free volume of containment m3 | 49200 | 93500 | 75850 | 51000 | |
| Ratio of thermal power to containment free volume kWt/m3 | 48.0 | | 42.8 | 19.6 | (2) Corium ejection time is 10 seconds, UCHB, burning time is 1 second, no water layer in cavity. |
| Ratio of corium inventory to containment free volume kg/m3 | 2.30 | 1.89 | 1.82 | 1.33 | |
| Containment failure pressure bar | 6.9-10.9 | >10. | 10.3 | 8.6 | (3) Corium ejection time is 10 seconds, UCHB, no water layer in cavity. |
| Ejection fraction | 0.5 | 0.5 | 1.0 | 1.0 | |
| Initial corium temperature K | 2550 | 2550 | 2550 | 2500 | (4) Corium ejection time is 6 seconds, UCHB, no water layer in cavity. |
| Pressure spectium of DCH induced high pressure bar | 5.5-12.3 | 5.7-8.3 | 7.4-14.3 | 4.8-8.2 | |
| Peak pressure under DCH bar | 9.7[2] | 8.3[3] | 9.9[4] | 8.2[5] | (5) Corium ejection time is 8 seconds, UCHB, no water layer in cavity. |
| Codes used | CONTAIN 1.04 | CONTAIN 1.04 | CONTAIN -DCH | MELCOR | |

after core suffers the loss of heat sink and coolant, few tons of core debris will heat the lower head, consequently result in penetration failure in lower head. Insufficient ejection mass under high pressure will cause containment direct heating, and a small peak pressure that would not pose threat to the integrity of containment.

2) If the entire core materials (about 58 tons) are assumed to eject under high pressure with temperature of 2500 K, under UCHB, then, the severest DCH case is observed. As a result, containment will reach high pressure of 8.2 bar that is 0.4bar smaller than the failure pressure of the containment.
3) Calculations show that, DCH lasts from 8 seconds to 1 minute.
4) UCHB will give a certain contribution to the increasing of containment about 1.5 to 2.0 bar.
5) With comparison of SURRY NPP, etc. 300Mwe NPP is shown to have the capability to prevent DCH-induced early failure of containment relatively, owing to the fact that DCH would occur with quite low possibility.

## Reference

[1] Severe Accident Risks: An Assessment for Five U.S. Nuclear Power Plants, NUREG-1150, December 1990.

[2] MELCOR Computer Code Manuals Version 1.8.3, NUREG/CR-6119, SAND93-2185, September 1994.

[3] Estimation of Containment Pressure Loading Due to DCH for Zion Plant, NUEG/CR-5282, March 1991.

[4] Containment Loads Due to Direct Containment Heating and Associated Hydrogen Behavior, Analysis and Calculations with the CONTAIN Code, NUREG/CR-4896, Sandia NL, May 1987.

JP0150120



# 12.2 Improved Hydrogen Combustion Model for Multi-Compartment Analysis

Masao Ogino and Takashi Hashimoto
Systems Safety Department, NUPEC
Phone: 03-4512-2589, Facsimile: 03-4512-2599
e-mail: ogino@nupec.or.jp, T-HASHIMOTO@nupec.or.jp

## ABSTRACT

NUPEC has been improving a hydrogen combustion model in MELCOR code for severe accident analysis. In the proposed combustion model, the flame velocity in a node was predicted using six different flame front shapes of fireball, prism, bubble, spherical jet, plane jet, and parallelepiped. A verification study of the proposed model was carried out using the NUPEC large-scale combustion test results following the previous work in which the GRS/Battelle multi-compartment combustion test results had been used. The selected test cases for the study were the premixed test and the scenario-oriented test which simulated the severe accident sequences of an actual plant.

The improved MELCOR code replaced by the proposed model could predict sufficiently both results of the premixed test and the scenario-oriented test of NUPEC large-scale test. The improved MELCOR code was confirmed to simulate the combustion behavior in the multi-compartment containment vessel during a severe accident with acceptable degree of accuracy. Application of the new model to the LWR severe accident analysis will be continued.

*Keywords: lumped-parameter code, hydrogen, combustion model, containment vessel*

## 1. INTRODUCTION

In order to simulate the hydrogen mixing and combustion behavior in a containment vessel two kinds of analytical model have been considered. One is the multi-dimensional (or field) model, applied in GASFLOW[1] and CFX-F3D[2] for example, which allows simulating the local hydrogen behavior mechanistically. But it requires considerable CPU resources, as well as memory resources, which makes the precise multi-dimensional simulation of the complete containment geometry be difficult. The other is the lumped-parameter model, applied in MELCOR[3] and RALOC[4] for example, which has an advantage that a complete geometry can be represented by a series of nodes and junctions, and that the simulation can cover the whole physical time of a severe accident in a limited CPU time. However, due to the limitations of the model, it is generally difficult to simulate the local hydrogen behavior in a node, such as the flame propagation. For example, MELCOR hydrogen combustion model, which consists of empirical models based on experimental data from single-chamber premixed combustion tests, can not track a propagating flame front in a node. That is, the burning rate is defined as the flame velocity multiplied by the constant cross sectional area and the time lag for flame propagation between adjacent nodes, specified as user input. Thus the calculated pressure as well as burning time in a node (compartment) is depending

on the input data of time lag arbitrarily specified.

Therefore NUPEC proposed a new model MCFLASH (Multi-Compartment Flame Shape Model) which replaced a combustion model in MELCOR code to simulate local combustion behavior in a multi-compartment containment vessel with acceptable accuracy and CPU time. In the previous work, the proposed model was already verified by premixed test of GRS/Battelle [5]. To verify the model installed in MELCOR code, the NUPEC scenario oriented large-scale combustion test results as well as premixed test results were used.

## 2. COMBUSTION MODEL

### (1) Node geometry

The proposed model calculates the laminar and turbulent burning velocity. The burning rate is defined as the flame velocity multiplied by the front surface of the growing fire shape, considering the three dimensional geometry of the nodes and the connection junctions.

Figure 1 shows the node geometry of the combustion model. The node geometry is rectangular, in which flame is generated and propagates. The node dimensions are characterized by length (L), height (H), and width (W) and the node is interconnected by several junctions to other nodes. The location of an igniter and the flame front are specified by Cartesian coordinate of X, Y and Z.

### (2) Flame propagation model

The flame velocity in each node is predicted using six different flame front shapes of fireball, prism, bubble, spherical jet, plane jet, and hypothetical parallelepiped, as shown in Fig.2.

Figure 3 summarizes schematically the flame propagation in six different shapes described above. The upward flame front velocity $S_r$ of the fireball is the sum of the propagation velocity, the upward velocity $U_{bl}$ and the expansion velocity caused by combustion. The upward velocity $U_{bl}$ is determined by a force balance as follows:

$$\frac{dU_b}{dt} = g\left(\frac{\rho_u}{\rho_b} - 1\right) - \frac{3}{8} C_D \frac{\rho_u}{\rho_b} \frac{U_b^2}{r_b}$$

where, $\rho_b$: burned gas density　　$C_D$: drag coefficient

$\rho_u$: unburned gas density　　$r_b$: radius of the fireball

The prism, contacted with a ceiling, has two flame propagation velocities $S_h$ and $S_d$ in horizontal and downward directions. The horizontal velocity $S_h$ includes the expansion velocity and the spreading velocity due to the buoyancy force. The downward velocity $S_d$ includes the expansion velocity and the upward velocity due to buoyancy force. In the bubble flame, the upward and downward velocities $S_u$ and $S_d$ are determined by the expansion velocity and the upward velocity $U_b$ expressed as follows:

$$U_b = 0.48\left(gR\frac{(\rho_u - \rho_b)}{\rho_u}\right)$$　　R: hydraulic radius

The shape of spherical jet and plane jet is determined by the upper stream gas conditions mainly dependent on junction velocity $U_J$.

Propagated flame coming from a compartment into a large free volume, which is divided to small nodes and connected each other with paths, changes into a parallelepiped flame. The parallelepiped flame is characterized by gas conditions in the node and the upper stream gas velocity. The vertical velocity $S_u$, $S_d$ include the expansion velocity and the upward velocity due to buoyancy force. The horizontal velocity $S_h$ includes the expansion velocity and the spreading velocity due to the buoyancy force in addition to an average fluid velocity in the node.

(3) Burning velocity

In the combustion model, a laminar burning velocity derived from experiments[6] and the turbulent burning velocity reported by AECL[7] are adopted. This turbulent burning velocity consists of the laminar burning velocity $S_u$ and multiplier of the turbulence intensity factor $\phi$, as follows:

$$\phi = \sqrt{1 + B\left(\frac{u'}{S_u}\right)^2} + \frac{u''}{S_u}$$

where,

$\phi$ : turbulence intensity factor

$S_u$: laminar burning velocity

B: constant value of 16

u': turbulence velocity of the flame front

u": turbulence velocity generated by the flame

$$u'' = \frac{S_u}{\sqrt{3}}\left(1 - e^{-\frac{u'}{S_u}}\right)\left(\frac{\rho_u}{\rho_b} - 1\right) \quad [m/s]$$

## 3. NUPEC LARGE-SCALE COMBUSTION TEST

For the validation of the proposed model, the results of the NUPEC Large-scale hydrogen combustion test were used. Figure 4 shows the NUPEC model containment vessel and the compartment configuration. The model containment vessel is spherical (inner diameter: 8m, free volume: 270m$^3$) and has eleven compartments. The selected test cases for the study were the premixed test B-4-6, and the scenario-oriented test B-11-3 and B-11-4.

Table 1 shows the test conditions. In the premixed test B-4-6, the gas composition was hydrogen-air mixture, and the initial temperature and pressure were room temperature and atmospheric pressure, respectively. A spark type igniter was installed at the lower general compartment and actuated at the beginning of the test. In the scenario-oriented test B-11-3 and B-11-4, the initial gas compositions and the hydrogen and steam mixture gas release rates were arranged simulating the accident scenario of small LOCA and transient, respectively. Model containment spray and four igniters (glow-plug type) were continuously actuated during the test.

## 4. ANALYTICAL RESULTS

Figure 5 shows the nodalization of the large-scale test facility for the premixed test B-4-6. The model containment vessel and compartments were divided into 78 nodes in axially symmetrical in two-dimension. The heat sink of the spherical vessel and the internal structure were considered. The calculated results by the proposed model were compared with the NUPEC test results focussed on the pressure behavior in the compartments. Figure 6 shows the calculation results of B-4-6 in comparison with the test results. The calculated pressure was slightly higher than the measured data.

Figure 7 shows the nodalization of the large-scale test facility for the scenario-oriented test B-11-3 and B-11-4. The model containment vessel and compartments were divided into 113 nodes in axially symmetrical in two-dimension. Figure 8 shows the calculation results of B-11-3 in comparison with the test results. Ignition occurred at $H_2$ concentration of about 5.5 vol % at the upper vessel (①) and then the flame shifted down to the gas injection region (③) and remained there. No combustion occurred in the torus regions(②). The proposed model could predict sufficiently the combustion behavior of the scenario-oriented test B-11-3. Figure 9 shows the calculation results of B-11-4 in comparison with the test results. Since the steam flow rate and steam concentration was relatively high in test B-11-4, ignition occurred at relatively high $H_2$ concentration of about 7.5 vol % at the upper vessel (①) and the flame remained there until $H_2$ gas flow rate was decreased to nearly zero. No combustion occurred in the torus regions(②). Though slightly underestimated the $H_2$ concentration, the proposed model could predict sufficiently the combustion behavior of the scenario-oriented test (B-11-4).

## 5. CONCLUSIONS

- NUPEC proposed a new combustion model to simulate combustion behavior in a multi-compartment containment vessel.
- The improved MELCOR code replaced by the NUPEC model (MCFLASH) for the combustion model could predict sufficiently both results of the premixed test and the scenario-oriented test of NUPEC large-scale test.
- The improved MELCOR code was confirmed to simulate the combustion behavior in the multi-compartment configuration.
- Application of the new model to the LWR severe accident analysis will be continued focused on the sensitivity analysis of a number of nodes.

## ACKNOWLEDGMENT

This work was sponsored under the contract by the Ministry of International Trade and Industry, Japan.

REFRENCES

(1) J. R. Travis, K. L. Lam, and T. L. Wilson, "GASFLOW: A Three-Dimensional Finite-Volume Fluid-Dynamics Code for Calculating the Transport, Mixing, and Combustion of Flammable Gases in Geometrically Complex Domains," LA-UR-94-2270, July 11, 1994.

(2) CFX-F3D (Version 4) User Manual, AEA Technology, Harwell, UK

(3) Summers, R.M., et al, 1994, "MELCOR Computer Code Manuals", NUREG/CR-6119, SAND93-2185.

(4) H. Jahn et al., 1988, "Description of the RALOC/FIPLOC family Part 2:physical modeling of thermal hydraulics and integration methods," Technical report, GRS-A-1426.

(5) Heitsch, M., 1994, "A Model of Vented Hydrogen Deflagrations in a Containment," Proceedings Int. Conf. on New Trends in Nuclear System Thermohydraulics, Pisa, Italy, May 30th - June 2nd, Vol. 2, pp. 133-142.

(6) Liu, D., and MacFarlane, R., 1983, "Laminar Burning Velocities of Hydrogen-Air and Hydrogen-Air-Steam Flames," Combustion and Flames, Vol. 49, pp. 59-71.

(7) Koroll, G. W., Kumar, R. K., and Bowles, E.M., 1993, "Burning velocities of Hydrogen-Air Mixtures," Combustion and Flames, Vol. 94, pp. 330-340.

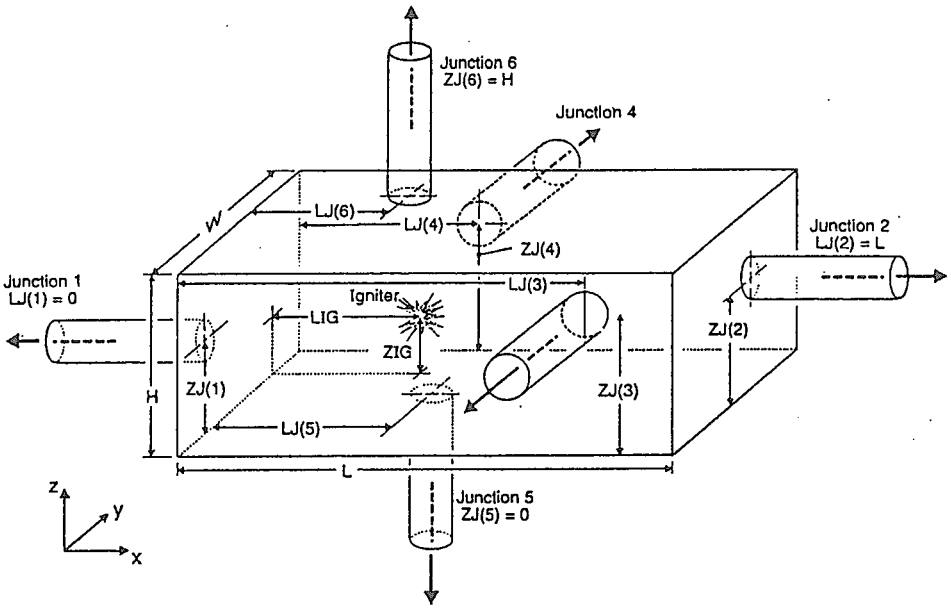



Fig. 1 Node model of the proposed combustion model

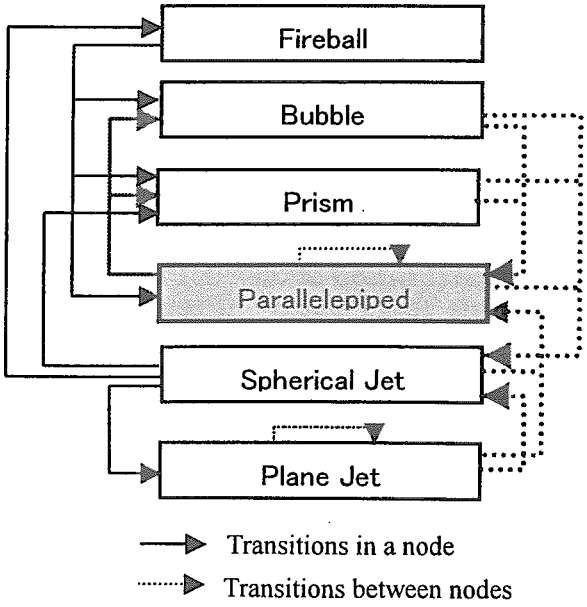



Fig. 2 Transitions of six different flame shapes

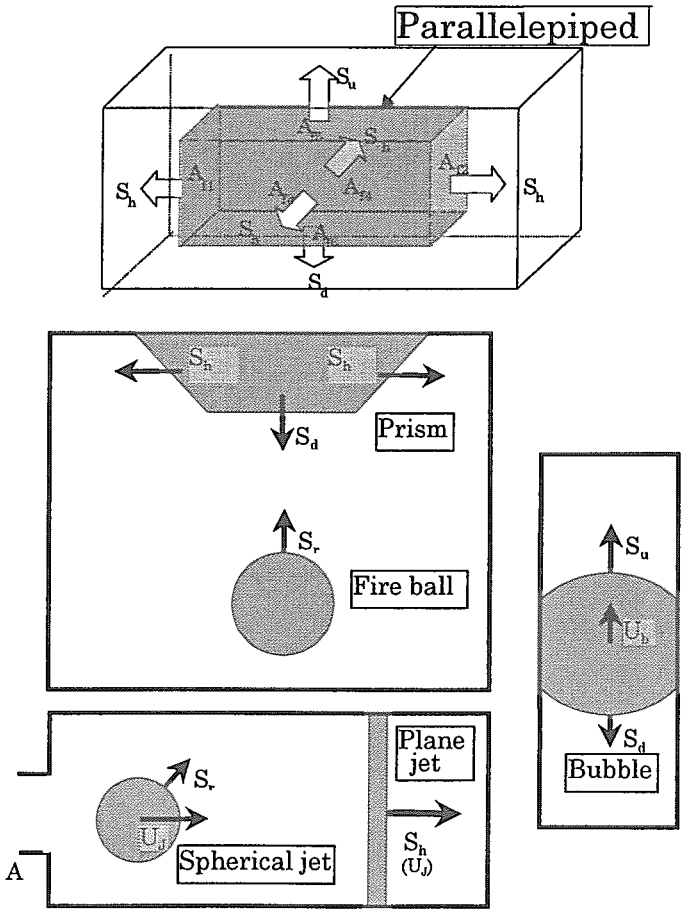



Fig. 3 Schematic of six different flame propagation model

Table 1 Test conditions

| Test case | Premixed homogeneous conditions | Scenario-oriented (LOCA with spray) | Scenario-oriented (Transient with spray) |
|---|---|---|---|
| Initial temperature | 40 ℃ | 85 ℃ | 85 ℃ |
| Initial pressure | 101 kPa | 140 kPa | 125kPa |
| Initial $H_2$ concentration | 15 vol% | 0 vol% | 0 vol% |
| $H_2$ flow rate | — | 0～0.94 g/s | 0～1.2 g/s |
| Steam flow rate | — | 20～0 g/s | 107～25 g/s |
| Spray flow rate | — | 4.3 $m^3$/h | 4.3 $m^3$/h |
| Ignition point | Lower general compartment: Ig-2 (Spark type) | Four points: Ig-1～Ig-4 (glow plug type) | Four points: Ig-1～Ig-4 (glow plug type) |
| (Note) | RUN B-4-6 | RUN B-11-3 | RUN B-11-4 |

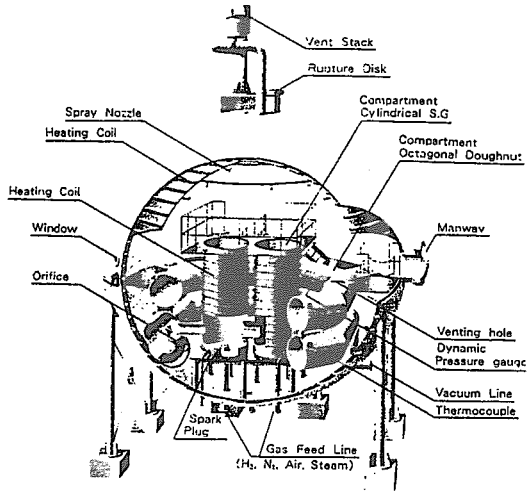
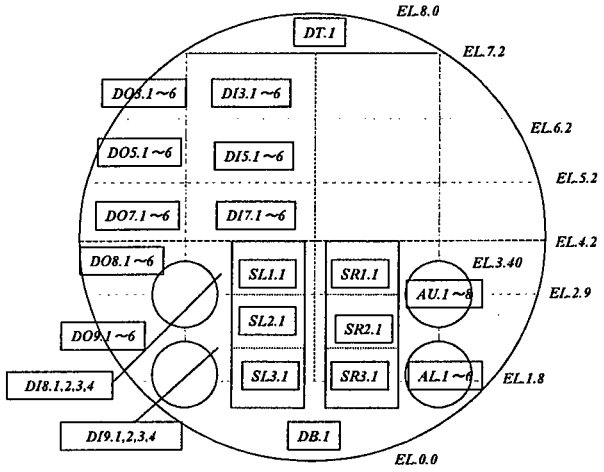



Fig. 4 NUPEC model containment vessel




***Total: 78 nodes***

- ***Upper region: 37nods***
- ***Lower region: 41nods***

Fig. 5 Nodalization of the NUPEC Large-scale Test Facility (Premixed test)

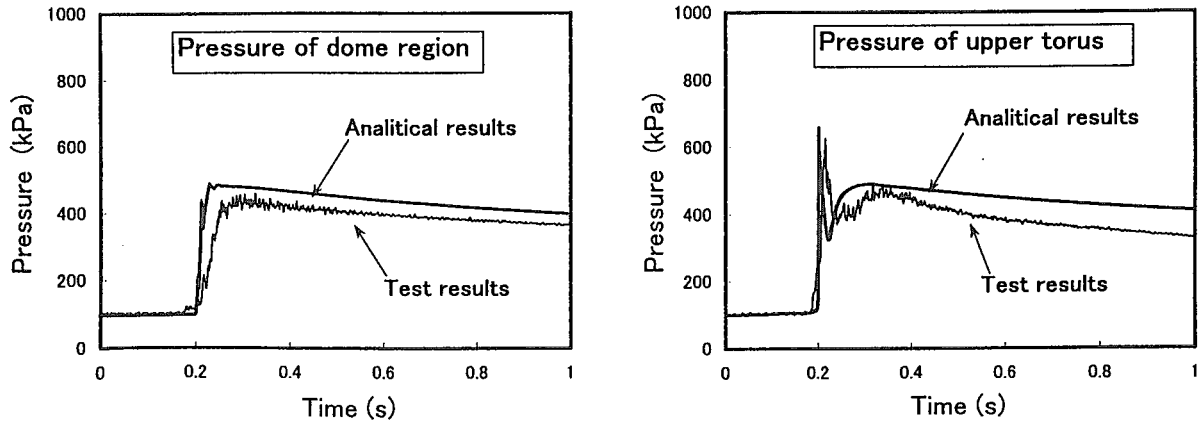



Fig. 6 Analytical results comparing with test results (B-4-6)

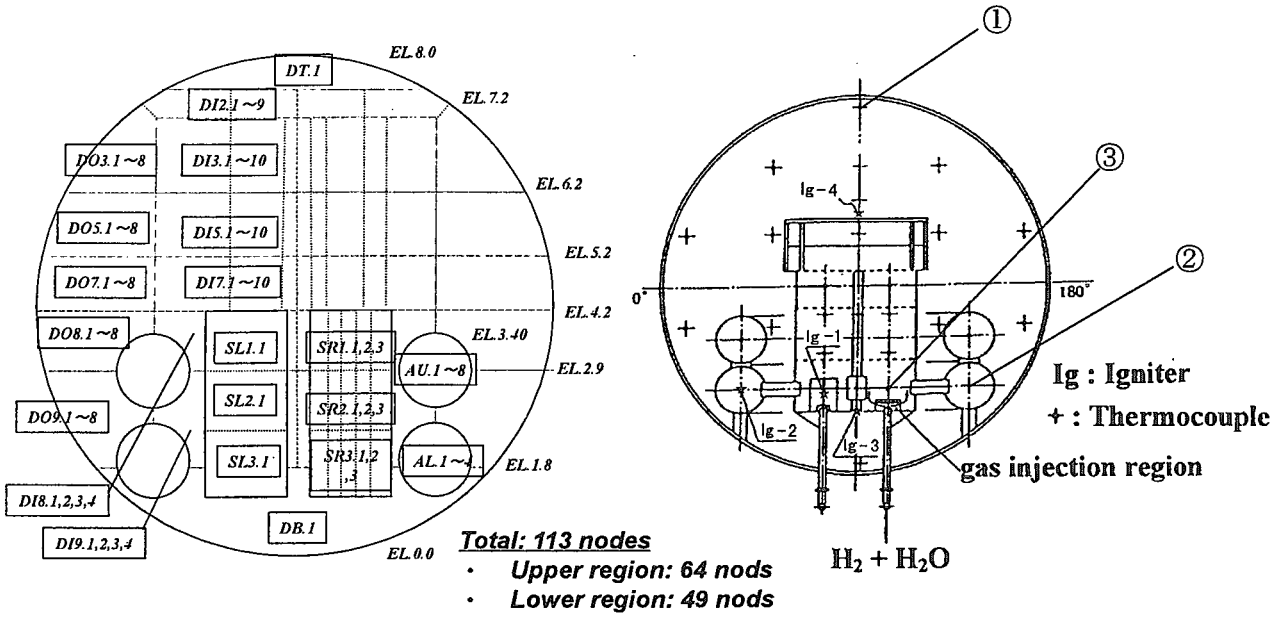



Fig. 7 Nodalization of the NUPEC Large-scale Test Facility (Scenario-oriented test)

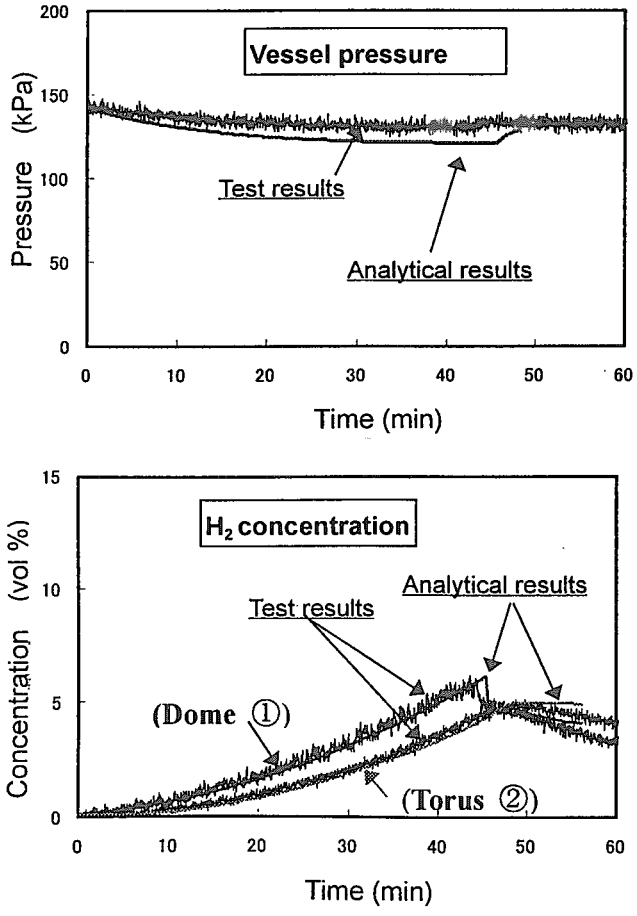



Fig. 8 Analytical results comparing with test results (B-11-13)

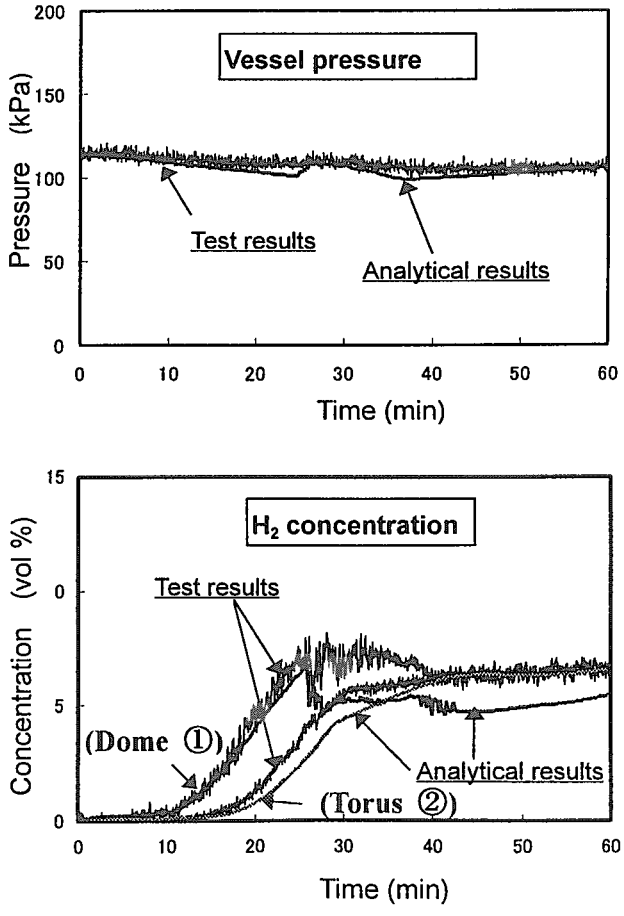



Fig. 9 Analytical results comparing with test results (B-11-14)

JP0150121



# 12.3 Evaluation of Upward Heat Flux in Ex-vessel Molten Core Heat Transfer using MELCOR

Soo Y. Park, Jong H. Park, See D. Kim, Dong H. Kim, Hee D. Kim
Thermal Hydraulic and Safety Research Team,
Korea Atomic Energy Research Institute
P.O.Box 105, Yusong, Taejon, KOREA, 305-600
Tel:82-42-868-8298 Fax:82-42-868-8256 E-mail:sypark@nanum.kaeri.re.kr

**Abstract**

The purpose of this study is to share experiences of MELCOR application to resolve the molten corium- concrete interaction (MCCI) issue in the Korea Next Generation Reactor (KNGR). In the evaluation of concrete erosion, the heat transfer modeling from the molten corium internal to the corium pool surface is very important and uncertain. MELCOR employs Kutateladze or Greene's bubble-enhanced heat transfer model for the internal heat transfer. The phenomenological uncertainty is so large that the model provides several model parameters in addition to the phenomenological model for user flexibility. However, the model parameters do not work on Kutateladze correlation at the top of the molten layer. From our experience, a code modification is suggested to match the upward heat flux with the experimental results. In this analysis, minor modification was carried out to calculate heat flux from the top molten layer to corium surface, and efforts were made to find out the best value of the model parameter based on upward heat flux of MACE test M1B. Discussion also includes its application to KNGR.

**Keywords**

Molten Core Concrete Interaction, MCCI, Severe Accident, Molten Pool Heat Transfer

## 1. Introduction

A molten corium-concrete interaction analysis has been performed for licensing purpose using the MELCOR computer program. This phenomenon is recognized as an important aspect in severe reactor accidents. The potential hazard of MCCI is the integrity of the containment building due to the possibility of a basemat melt-through, containment overpressurization by non-condensable gases, or oxidation of combustible gases. The containment integrity is largely affected by the basemat melt-through or containment over-pressurization[1]. Basemat melt-through refers to the process of concrete decomposition and destruction associated with a corium melt interacting with the reactor cavity basemat. Concerning to MCCI, the NRC staff recommends that both the evolutionary and passive light water reactor designs meet the following criteria[2]:

- provide reactor cavity floor space to enhance debris spreading
- provide a means to flood to reactor cavity to assist in the cooling process
- protect the containment liner and other structural members with concrete, if necessary ensure that the best estimate environment condition (pressure and temperature) resulting from concrete interactions do not exceed Factored Load Category for concrete containment, for approximately 24 hours.

The purpose of this study is to share experiences of MELCOR application to resolve the molten corium- concrete interaction issue in the KNGR.

## 2. Review of Code Modeling for Ex-vessel Debris Pool

As there are so many uncertainties in phenomena of molten core-concrete interaction (MCCI), the typical integrated severe accident programs such as MELCOR 1.8.4 and MAAP4 have different models for the treatment of debris layering and mixing, concrete ablation, and gas generation. The cavity(CAV) package in MELCOR models the attack on the basemat concrete by molten core materials. The package consists of models taken from the CORCON-MOD3 code together with all necessary interfaces to the MELCOR. In the mean time, the DECOMP is a phenomenology subroutine in MAAP to calculate the concrete ablation rate and subsequent gas release due to the presence of molten core material. A concrete ablation is largely affected by the heat flux from the core debris to the concrete. The MAAP model calculates the concrete ablation based on the user specified heat transfer coefficients, while the MELCOR allows this interfacial heat flux to be calculated using either a gas film or a slag film model. Five possible types of debris layers (light oxide, light oxide-metal mixed phases, metal, heavy oxide-metal mixed phases, heavy oxide) are considered in MELCOR, which is discussed in reference[3]. Three options are available for the treatment of layering and mixing of debris: (1) enforcement of complete mixing, (2) enforcement of complete stratification, and (3) mechanistic modeling of the entrainment and separation processes. On the contrary, the MAAP assumes that all the debris is homogeneously mixed. Followings are description of molten pool heat transfer.

### 2.1 MELCOR

A multi-layered pool model is employed, for which it is convenient to consider heat transfer one layer at a time. The model allows for several possible configurations in each layer. The layer may be completely molten, it may have a solid crust, or it may be completely solid. Here, heat transfer in a liquid layer or the liquid portion of a partially-solidified layer will be addressed. Heat transfer coefficients are required from the interior of a liquid layer to its surfaces. If the layer were a right circular cylinder type, there would be three such coefficients, that is, to the upper, lower, and radial surfaces. Models are included for gas injection at the bottom surface of the melt, and gas agitation along the sides of the melt.

For the bottom interface of the melt pool, where gas bubbles may be injected from the incoming concrete, the heat transfer coefficient for a liquid layer is calculated using the correlation devised by Kutateladze. The Kutateladze correlation[4] is given by

$$Nu_a = 1.5\times10^{-3} Ku^{2/3} f(\eta) \qquad (1)$$

where $Nu_a$ is the Nusselt number, Ku is the dimensionless number ,and is the dimensionless gas velocity

For liquid layers within the melt pool, a correlation devised by Greene is used to calculate the heat transfer coefficient in each layer, except for the uppermost melt layer. Greene's correlation[5] is

$$h = 1.95k(\mathrm{Re\ Pr})^{0.72} / r_b \qquad (2)$$

where k is the thermal conductivity, Re is the Reynolds number for the liquid based on the characteristic length $r_b$ and the superficial gas velocity $j_g$, Pr is the Prandtl number for the liquid, and $r_b$ is the average bubble radius in the layer.

For the uppermost melt layer (adjacent to the atmosphere or coolant), the heat transfer coefficient is calculated using a modified form of the Kutatelaze correlation, which accounts for the greater surface area of the unstable surface. For the upper melt surface, the Kutatelaze correlation is simply multiplied by an area enhancement derived by Farmer,M.T.[6]:

$$A = 1 + 4.5\frac{j_g}{U_b} \qquad (3)$$

where A is the area enhancement factor, $j_g$ is the superficial gas velocity, and $U_b$ is the bubble rise velocity.

## 2.2 MAAP

The debris pool has a single lumped energy and a mass balance capability for up to 50 condensed phase compounds from the standard MAAP list. The debris pool consists of molten liquid and three independent crusts, the lower, side, and upper crust. The bottom and side crust thickness may be different from each other because the convective heat transfer coefficients for sideward and downward may be different. The upper crust is treated separately because its energy is transferred by radiation to the cavity wall and convection to the gas. Due to the internal heating, three independent crusts are assumed to have parabolic temperature profiles. For example, the temperature profile within the lower crust which can be expressed by the steady-state expression[7].

$$\frac{T-T_i}{T_{F,m}-T_i}=1-\left(\frac{x}{x_c}\right)^2 \qquad (4)$$

where $T_{F,m}$ is the corium mixture melting point, $T_i$ is the interface temperature of the crust and the concrete, and $x_c$ is crust thickness. $T_i$ is assumed to equal the concrete surface temperature.

For those cases where the corium-concrete mixture pool is too deep to transfer the energy generated by thermal conduction, the central region of the pool would be molten. Under these conditions, the heat flux from the molten central region to the crust can transferred out of the crust using the conduction equation ;

$$q'' = -kF\frac{dT}{dx}\Big)_{x=xc} \qquad (5)$$

## 3. Cavity Design of Reference Plant

The reactor cavity is configured to promote retention of the postulated core debris and to remove decay heat by a cavity flooding system during a severe accident, thus serving several roles in accident mitigation. The large cavity floor area allows for spreading of the core debris, enhancing its coolability within the reactor cavity region. The cavity includes approximately 566m$^3$(20,000 ft$^3$) of free volume. This large volume benefits the plant design when cavity pressurization issues are considered. Large and well vented volumes are not prone to significant pressurization resulting from vessel breach or during corium quench processes. It has been designed to maximize the unobstructed floor area available to the spreading of corium debris. The cavity floor is free from obstructions and comprises an floor area available for corium debris spreading of approximately 80.36m$^2$(865 ft$^2$).

The reactor cavity is designed to satisfy the URD[8] requirement that the distance between the floor elevation and the embedded portion of the containment shell is a minimum of 0.91meter. An additional 3.35 meter of concrete is available below the linear elevation.

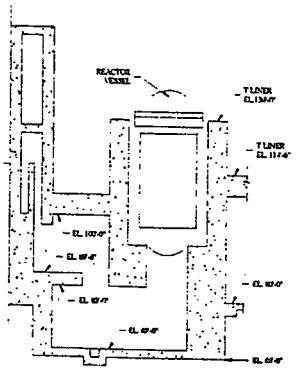


Figure 2-1 Section-view of Cavity

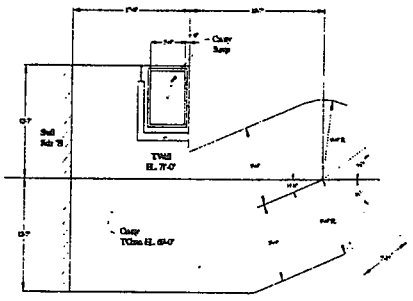


Figure 2-2 Plane-view of Cavity Floor

## 4. Concrete Erosion Analysis

The erosion was calculated using MAAP and MELCOR codes. After a hypothetical accident scenario was simulated by MAAP, the conditions of molten corium in the reactor cavity such as mass, temperature or decay heat at the time of reactor vessel failure were used as initial conditions of MELCOR. By doing this, two codes would have the similar initial conditions for the erosion calculations in the cavity.

### 4.1 Analyzed Case Description

The sequence simulated is a 6 inch-diameter-break loss of coolant accident (LOCA). Following a LOCA , the reactor trips and high pressure safety injection systems are not available to deliver water from the refueling water storage tank to the cold legs. The only water available to make up the primary side is the inventory of four safety injection tanks. As the water inventory in the reactor coolant system decreases, the core becomes uncovered. The reactor vessel eventually fails and 195,630 kilograms of corium discharged into the cavity. Since the pressure of the primary system has already decreased enough, all the discharged corium is captured in the reactor cavity.

Calculations of five cases were carried out to investigate the concrete erosion and the upward heat flux. The first case was calculated by MELCOR with default model parameter values (Case 1-MEL). Forced mixed layer option and slag film model was used. Parameter value of HTRINT was set to zero, which is default CORCON-Mod3 model. HTRINT is one of model parameters which controls the debris-to-pool heat transfer. The second case(Case 1-MAAP) was calculated by MAAP with default model parameter values. FCHF, which is a flat plate critical heat flux Kutateladze number that controls the pool boiling heat flux, was set to zero. The third case(Case2-MEL) was the same as Case 1-MEL except that HTRINT value has been changed to 10 in order to increase the upward heat flux artificially. The next case (Case 2-1-MEL) was the same as Case 2-MEL but the code was modified because the parameter change did not work properly. The final case (Case 2-MAAP) was the same as Case 1-MAAP except that FCHF value has been changed from 0.9 to 0.015 in order to decrease the upward heat flux artificially. In the cases of Case 2-1-MEL and Case 2-MAAP, we tried to match the upward heat flux to the MACE test of M1B results. M1B result shows that initial melt/water heat flux reached to about 3.6 $MW/m^2$ followed by a plateau at about 1.6 $MW/m^2$ which lasted about 6 minutes. Thereafter, the heat flux gradually decreased to 200 $kW/m^2$ at 200 minutes after water was added [9]

### 4.2 Calculation Results

- Case1-MEL & Case 1-MAAP

Figure 3 and Figure 4 shows the erosion depth and upward heat flux, respectively. Axial/Radial erosions reach to 1.12m/ 0.65m at 24 hours following Rx trip in MELCOR results and the erosions are negligible in MAAP. It results from the difference of upward heat flux from molten debris to the overlying water pool. The heat flux of Case 1-MEL is much lower than test M1B and that of Case 1-MAAP is much higher than M1B.

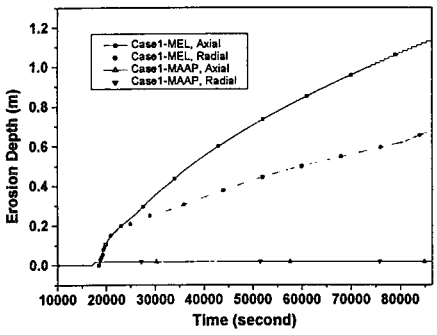



Figure 3. Concrete erosion depth for Case1-MEL & Case 1-MAAP

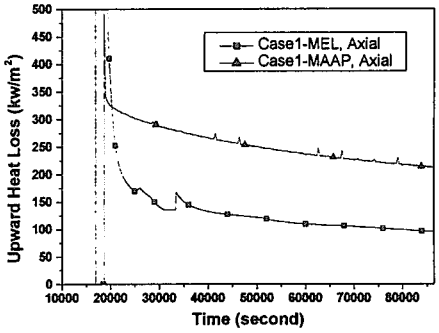



Figure 4. Upward heat flux for Case1-MEL & Case 1-MAAP

- Case2-MEL & Case 2-1-MEL

HTRINT has been changed to 10 in Case2-MEL in order to increase the upward heat flux to the M1B test results, but MELCOR did not work properly. As shown in Figure 5 & Figure 6, the erosion and heat flux did not changed. Model parameters of HTRBOT, HTRINT, HTRSIDE are not applied to Kutateladze's correlation in current coding. Therefore minor code modification is needed to increase the heat flux artificially. Axial/Radial erosions reach to 0.79m/ 0.27m at 24 hours following Rx trip in modified MELCOR results.

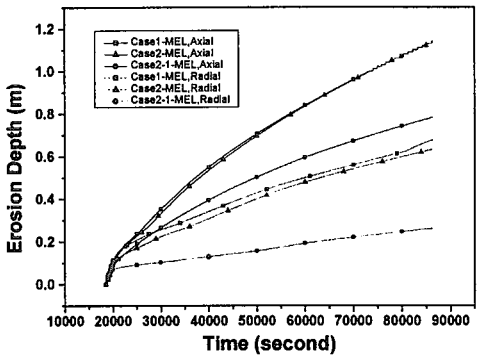



Figure 5. Concrete erosion depth for Case2-MEL & Case2-1-MEL

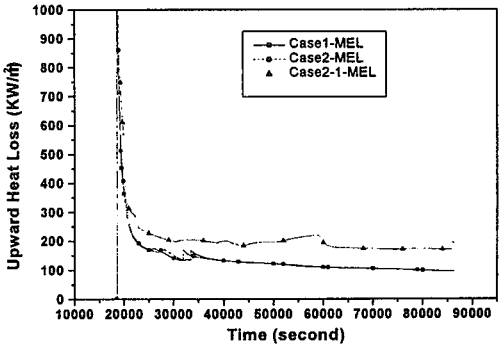



Figure 6. Upward heat flux for Case2-MEL & Case2- 1-MEL

- Case2-MAAP

FCHF has been changed from 0.09 to 0.015 in Case2-MAAP in order to decrease the upward heat flux to the M1B test results. As shown in Figure 8, initial high melt/water heat flux of about 1500 seconds, which result in complete debris quenching in Case1-MAAP, has disappeared in Case2-MAAP. And long term heat flux of about 200 KW/m$^2$ meets the liner protection requirement. Axial/Radial erosions reach to 0.89m/ 0.78m at 24 hours following Rx trip (Figure 7).

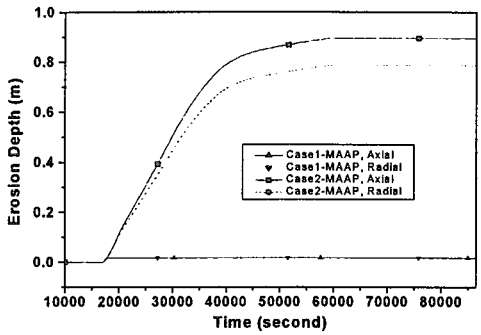



Figure 7. Concrete erosion depth for Case 2-MAAP

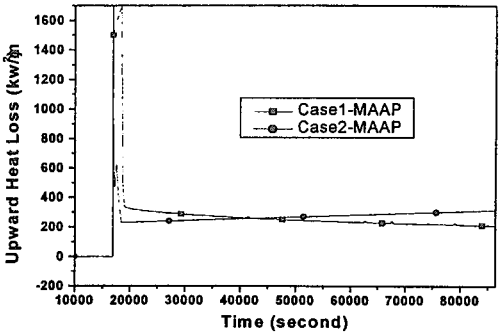



Figure 8. Upward heat flux for Case 2-MAAP

## 5. Summary

Following observations are made from this analysis;

- MELCOR with default parameter value tends to under-estimate the upward heat transfer compare to the MACE experimental result. And MAAP tends to over-estimate it.
- MELCOR with HTRINT=10 and MAAP with FCHF=0.015 result in similar upward heat transfer rate to the MACE experimental result.
- Minor code modification of MELCOR is needed for user flexibility to increase the heat flux from debris pool into overlying water pool when the mixing option is selected
- Long term upward heat flux of 200-350 kw/m$^2$ in ex-vessel debris meets the liner protection requirement of SECY-93-087 for the KNGR

## ACKNOWLEDGE MENTS

This Project has been carried out under the Nuclear R&D Program by MOST.

## REFERENCES

1. J.W. Park et al., study on the Influence Diagrams for the Application to Containment Performance Analysis, Journal of Korean Nuclear Society, Vol.28, Number2, April 1996, pp.129-136.
2. SECY-93-087, olicy, Technical, and Licensing Issues Pertaining to Evolutionary and Advanced Light Water Reactor Designs April, 1993
3. Summers, R.M., and al., ELCOR Computer Code Manuals, NUREG/CR-6119, September 1994.
4. Kutateladze,S.S., and I.G.Malenkov, oiling and Bubbling Heat Transfer Under Conditions of Free and Forced Convection, 6th Internal Heat Transfer Conference,Toronto,Canada.1978
5. Green,G.A., and T.F. Irvine, eat Transfer Between Stratified Immiscible Liquid Layers Driven by Gas Bubbling Across the Interface, in ANS Proceedings of the 1988 National Heat Transfer Conference,Houston, TX, July 24-27, 1988.
6. Farmer,M.T., J.J.Sienicki, and B.W.Spencer, ORQUENCH: A Model for Gas Sparging-Enhanced Melt-Water, Film Boiling Heat Transfer, ANS Special Session on Thermal Hydrolics of Severe Accidents, November 11-15,1990.
7. FAI , odular Accident Analysis Program, May,1994.
8. EPRI, Advanced Light Water Reactor Requirement Document, 1992.
9. Presentation material, verview of MACE Test M1b B.W. Apencer, ANL, 1992. June.

JP0150122



# 12.4 COTELS Ex-Vessel Debris Coolability Tests

Isao Sakaki, Masami Kato and Hideo Nagasaka
Systems Safety Department, Nuclear Power Engineering Corporation, Japan
Phone:+81(3)4512-2575, Facsimile:+81(3)4512-2599, E-mail:sakaki@nupec.or.jp

Vladimir S. Zhdanov, Aleksander A. Kolodeshnikov and Yuri S. Vasilyev
Institute of Atomic Energy, National Nuclear Center, Republic of Kazakhstan

## ABSTRACT

Test C in COTELS project was performed to investigate molten core concrete interaction (MCCI) under water injection onto molten corium. After 60kg $UO_2$ corium mixture was melted in electric melting furnace (EMF), the corium was fallen into concrete trap. The molten corium in the trap was re-heated to simulate decay heat. Debris was cooled after water injection and MCCI was suppressed. In 6 tests out of 10 tests, particulate debris bed was formed above continuous ingot debris. The size distribution of the particulate debris was well correlated by Rosin-Rammler equation. Cross section of concrete trap along with solidified debris tested in COTELS Test C, in which the interaction among core melt, water and concrete was simulated, were structurally investigated. Large amount of smallest diameter particles was obtained due to the entrainment of molten corium, decomposed concrete and oxidation of metallic components in corium associated with MCCI generated gas. Favorable debris cooling observed in the Test C was attributed to the existence of remaining porosity inside corium due to simulation of falling process, water ingression via eroded concrete side wall clearance and channels, and the interruption of further concrete floor erosion due to the existence of pebble bed, decomposed from concrete, below the debris.

***Keywords : COTELS, Ex-Vessel Debris Coolability , $UO_2$ Corium, MCCI, AM***

## 1. INTRODUCTION

Suppression of MCCI by water injection onto molten debris accumulated on a containment floor is one of the most important accident management (AM) to prevent containment failure during a severe accident. However, the suppression of MCCI by water injection has not been observed in former MCCI tests, such as SWISS[1], WETCOR[2] and MACE[3,4] tests.

Test C in COTELS project[5] was performed to investigate MCCI under continual water injection onto molten debris. Main features of this test are simulation of $UO_2$ corium falling, usage of basaltic concrete and simulation of side wall made of concrete. Debris cooling and suppression of MCCI after water injection were observed for the first time in COTELS Test C[6]. The particulate debris bed was formed above the ingot debris in 6 tests out of 10 tests in the Test C.

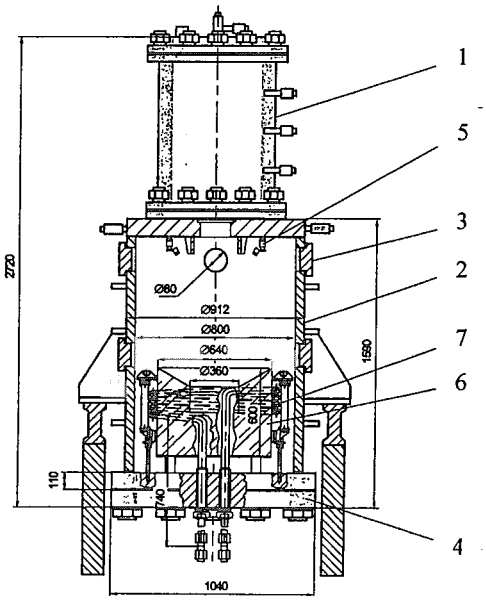
This paper summarizes the data evaluation results focussed on long term debris cooling mechanism by analyzing the geometry of cross section of solidified debris and eroded concrete trap, and the structural investigation of the solidified debris and the eroded concrete focused on the mechanism of the particulate debris bed formation.

## 2. TEST FACILITY AND TEST PARAMETERS

Test C was conducted using LAVA-M facility shown in Fig.1. In this test, 60kg maximum mixture of $UO_2$, stainless steel, $ZrO_2$ and Zr was melted in EMF by electrical induction heating, located above a concrete trap. The corium was fallen onto the concrete trap inside a test vessel in order to simulate a realistic situation of a severe accident. The accumulated corium in the trap was heated to simulate decay heat by another electrical induction heater surrounding the concrete trap. Water was injected onto the molten debris by spray type or jet type nozzle. Steam condensation system to measure generated steam flow rate after the water injection and gas sampling system to evaluate gas composition due to MCCI were equipped. Temperatures and pressures of ambient gas in a test vessel were measured.

Two types of concrete trap were used in the tests. One type was 36cm inner diameter trap and the aspect ratio of accumulated corium (ratio of height to diameter) was 0.19, corresponding to a typical LWR severe accident condition, and another type was 26cm inner diameter and the aspect ratio was 0.5. These concrete trap were made of basaltic concrete, simulating Japanese plant cement composition, pebble size distribution and composition, strength, and field curing. Thirty five thermocouples in 36cm trap and 43 thermocouples in 26cm trap were arranged spirally inside concrete trap to measure concrete temperature transient.

As shown in Table 1, mixture composition, concrete trap diameter, power input to debris, water injection method, timing and flow rate, and differential pressure between EMF and test vessel to adjust corium falling velocity were varied. For all tests, melt mass was about 60kg, melt temperature was about 3200K slightly above $UO_2$ melting temperature and initial ambient gas pressure was 0.3MPa, corresponding to reactor containment pressure during a severe accident, and water temperature was room temperature. Corium type A corresponds to the mixture composition obtained from TMI-2 accident[7], while corium type B includes more metallic compositions, considering the existence of metal structures in lower plenum of reactor pressure vessel. Seventy five kW net heat power input corresponds to 11W/cm$^3$ (about 11 times larger than decay heat), which was determined by obtaining similar transient of vertical concrete erosion depth (defined by 1650K) between reference plant and test facility based on two-dimensional unsteady heat conduction analysis. Two l/min is the minimum water injection rate to remove 75kW heat power input.




1:EMF, 2:Test vessel, 3:Instrumentation nozzle, 4:Removable bottom, 5:Water injection nozzle, 6:Concrete trap, 7:Induction heater

Fig. 1 LAVA-M test facility

Table 1 Test C conditions

| Varied Parameter | Test No. | | | | | | | | | |
|---|---|---|---|---|---|---|---|---|---|---|
| | C-4 | C-6 | C-9 | C-5a | C-5 | C-8 | C-7 | C-2 | C-3 | C-10 |
| Corium type* | B | | | | | | | A | B | |
| Concrete trap diameter, cm | 36 | | | 26 | 36 | | | | | |
| Power input to debris, kW | 75 | ~0 | 75 | ~0 | 75 | | | | | |
| Condition of water injection | | | | | | | | | | |
| - Injection method | Jet | | Spray | - | Jet | | | | | Jet |
| - Flow rate, l/min | 2.0 | | 2.0 | 0 | 2.0 | | | | | 2.0 |
| - Temperature, K | room | | room | - | room | | | | | room |
| - Injection timing delay, min. | 8 | | 8 | - | 8 | | | | | 15 |
| Δ P (EMF - test vessel), MPa | 0 | | | | | 0.1 | 0.15 | 0 | | |

Note) *Corium composition (weight %) Type A : $UO_2$-78, Stainless Steel-5, $ZrO_2$-17, Zr-0
Type B : $UO_2$-55, Stainless Steel-15, $ZrO_2$-5, Zr-25

## 3. EVALUATION OF TEST RESULTS

### 3.1 Effect of Several Parameters on Concrete Trap Temperature Transient

Figure 2 compares a cross section of continuous solidified debris (ingot debris) and concrete trap between Test C-5a and C-5 after removing particulate debris bed formed above the ingot debris. Debris heating period was 6min in Test C-5a, while 75min in Test C-5. Large cavities as a result of the impingement of falling corium jet on concrete trap were remained in C-5a due to short heating period. In Test C-5, such large cavities were vanished and molten debris core region was extended due to re-melting during long term heating process. In fact, the concrete in the vicinity of the ingot debris was decomposed completely and larger amount of particulate debris formed due to MCCI in Test C-5. These observations confirmed the re-melting of debris by another induction heating.

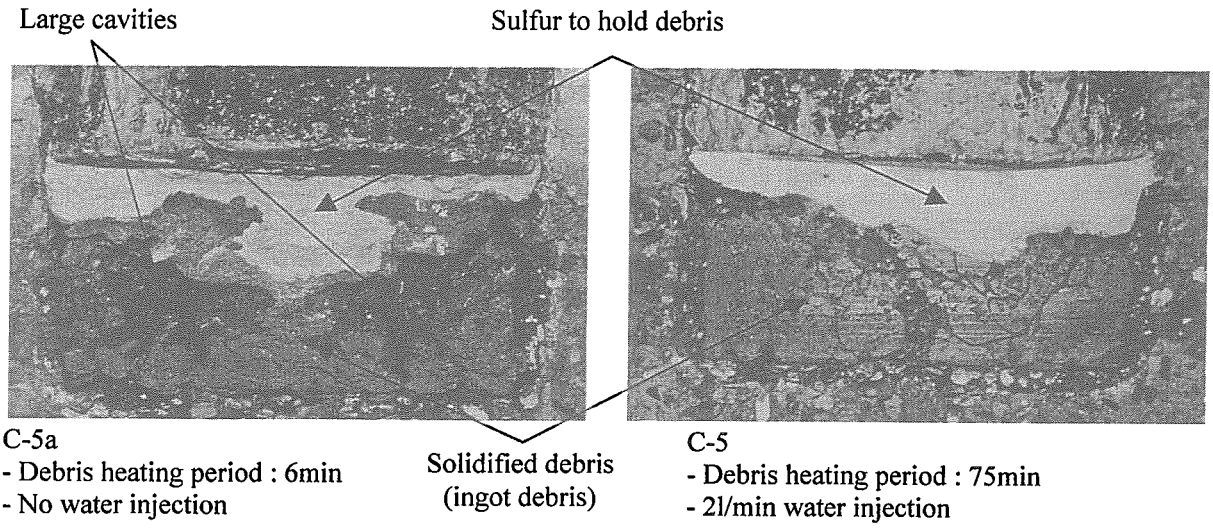



Fig.2 Confirmation of debris re-heating by induction heating

Figure 3 shows the effect of aspect ratio on concrete trap temperature transient, comparing Test C-5 with C-9. Faster increase in concrete temperature and higher maximum temperature in C-5 (larger aspect ratio of 0.5) was observed. Figure 4 shows the effect of integrated power $P_I$, before water injection after corium falling, on the concrete temperature transient, comparing C-3 ($P_I$=71.2MJ) with C-9 ($P_I$=26.2MJ). Faster increase in concrete temperature and higher maximum temperature in C-3 was confirmed. The effect of corium type on concrete temperature transient was small. Higher temperature test cases of Test C-5 and C-3 produced large amount of particulate debris above ingot debris due to MCCI. However, the concrete temperature decreased gradually after water injection and MCCI was suppressed in any test cases.

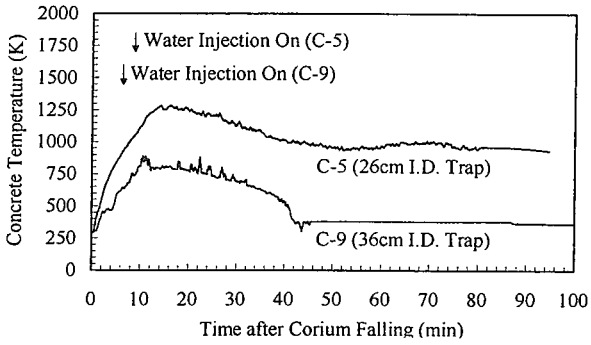



Fig.3 Effect of aspect ratio on concrete temperature (C-5 and 9)

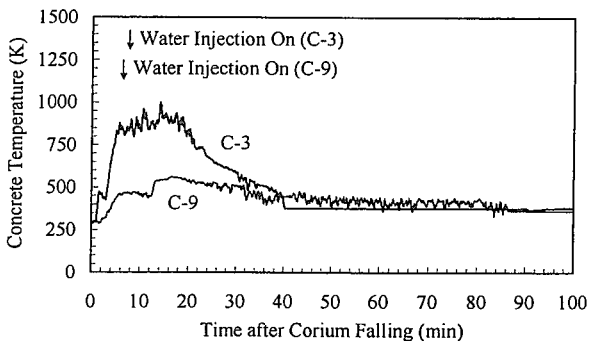



Fig.4 Effect of integrated power on concrete temperature (C-3 and 9)

### 3.2 Cooling Mechanism of Debris

Table 2 summarizes solidified debris and eroded concrete conditions. The test results were classified, depending on the amount of particulate debris bed formed above lower ingot debris, into three groups: case (1) formation of particulate debris bed, 20 to 40% of total solidified debris (case (1a) for 26cm concrete trap and case (1b) for 36cm concrete trap), case (2) formation of particulate debris bed, 70 to 80% and case (3) no formation of particulate debris bed. It is understood from this table that deeper concrete erosion was observed in the test cases with larger amount of the particulate debris bed formation.

Heat removal rate from the debris in concrete trap under nearly constant pressure condition in the test vessel was evaluated by energy balance neglecting heat loss from the vessel and assuming saturated water reaching to pool surface. The heat removal rate per unit upper surface of solidified debris was ranged from 0.2 to 0.7MW/m$^2$ which was close to SWISS, WETCOR and MACE results.

Table 2 Solidified debris and eroded concrete conditions

| Classification / Items / Test No. | Case (1) (1a) C-5a | Case (1) (1a) C-5 | Case (1) (1b) C-4 | Case (2) C-2 | Case (2) C-3 | Case (2) C-10 | Case (3) C-6 | Case (3) C-7 | Case (3) C-8 | Case (3) C-9 |
|---|---|---|---|---|---|---|---|---|---|---|
| Solidified debris conditions | | | | | | | | | | |
| -Total mass* (kg) | 47 | 56 | 56 | 45 | 46 | 58 | 53 | 52 | 42 | 51 |
| -Particulate debris bed (kg/%) | 9/19 | 21.5/38 | 19/34 | 35/78 | 33/72 | 48/83 | None | None | None | None |
| Stone like debris** (kg) | 0 | 0 | 6 | 0 | 0 | 18 | - | - | - | - |
| Sand like debris*** (kg) | 9 | 21.5 | 13 | 35 | 33 | 30 | - | - | - | - |
| Median diameter of sand like debris (mm) | 0.6 | 0.8 | 2.2 | 1.5 | 1.0 | 0.4 | - | - | - | - |
| -Lower ingot debris (kg) | 38 | 34.5 | 37 | 10 | 13 | 10 | 53 | 52 | 42 | 51 |
| Eroded concrete conditions | | | | | | | | | | |
| -Max. erosion depth (mm) Side/bottom | 13/28 | 10/25 | 25/22 | 15/15 | 15/20 | 48/40 | 8/15 | 10/18 | 8/15 | ~0/10 |
| -Max. thick. of pebble bed (mm) | 12 | 15 | 21 | 18 | 15 | 15 | 10 | 12 | 12 | 5 |
| -Max. thick. of discolored concrete region (mm) | 40 | 55 | 65 | 40 | 34 | 35 | 32 | 35 | 30 | 20 |

Note) * : Total mass of accumulated debris after test, ** : Particles larger than 16mm diameter, *** : Particles smaller than 16mm diameter

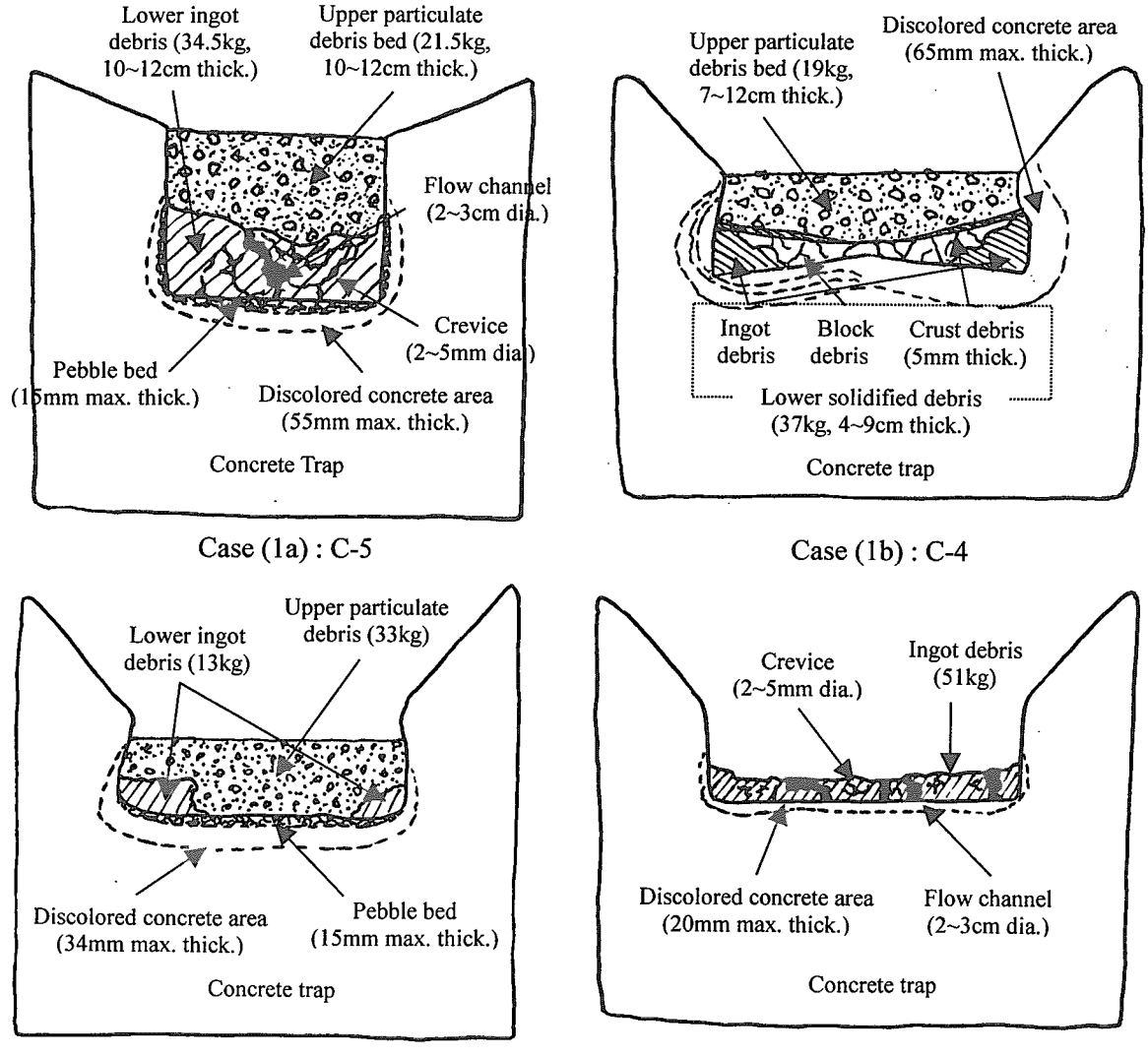



Fig.5 Typical cross section of solidified debris and concrete trap

Figure 5 shows the cross section of solidified debris and concrete trap for typical test number, corresponding to each case mentioned above. In all cases concrete side wall as well as concrete floor were eroded and pebble bed decomposed from concrete, surrounding continuous solidified ingot debris, was observed. As concrete erosion depth (defined as the elevation difference between original concrete floor and the bottom elevation of ingot debris) increased, the pebble bed became deeper. A discolored concrete region existed surrounding the pebble bed, due to free water evaporation and chemical reactions in the concrete.

In C-5 (case (1a)) where the initially accumulated corium on the concrete trap was relatively not coolable condition due to larger aspect ratio, 10 to 12cm thickness particulate debris bed was formed as a result of longer MCCI period, above 10 to 12cm thickness ingot debris. There were crevices and channels penetrating from bottom to top surfaces of ingot debris. The inner surface of the channels and crevices were smooth and their color was brown, which suggested the oxidation of metallic components due to steam flow through them. Small pebbles were also observed inside ingot debris due to the entrainment associated with MCCI generated gas.

In C-4 (case (1b)) where water injection was stopped from 26 to 56min under continual heating of debris, 34% particulate debris bed was formed in spite of smaller aspect ratio due to re-melting of partially solidified debris. The particulate debris consisted of stone-like debris larger than 16mm and sand-like debris similar to those observed in any other tests. Larger mass median diameter of this particulate debris is confirmed in Table 2. The particulate debris bed (7 to 12cm thickness) was separated from lower debris (4 to 9cm thickness) by a hard crust debris less than 5mm. The lower debris consisted of ingot debris in peripheral region and block debris in central region. The above observation suggested the outflow of stone-like debris as a result of hard crust rapture at central region associated with the reduction of crust thickness and increasing pressure below hard crust debris. In fact, slight pressure increase was observed at 68min, though steam condensation system was turned on during this period, as shown in Fig.6. Concrete temperature(T/C-9B) at 1cm below from initial concrete floor still increased at 68min, which confirmed the heating of the debris.

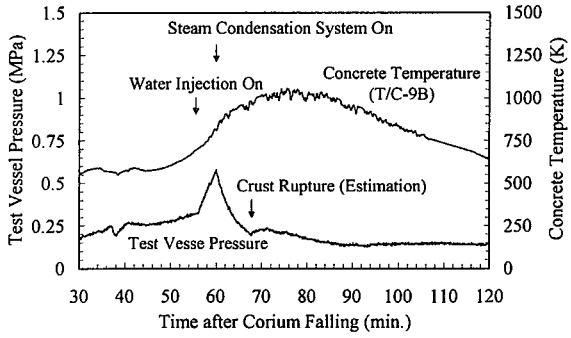



Fig.6 Test vessel pressure and concrete temperature (C-4)

In C-3 (case (2)) where the integrated power to debris before water injection was about 2.5 times larger than that in case (1) and (3), most of debris was particulated and only small amount of ingot debris (28%) was remained in the peripheral region of concrete trap due to violent MCCI. Lager amount of decomposed cement with white color was embedded in the ingot debris.

In C-9 (case (3)) where smaller integrated power before water injection was applied in smaller aspect ratio concrete trap, no particulate debris bed was formed. There were several channels penetrating bottom to top surfaces. The concrete bottom erosion depth was only 1cm.

The above observation of solidified debris condition, combined with the measured concrete temperature transients, shown in Figs.3 and 4, suggested that the favorable cooling was attributed to the remaining porosity of debris due to simulation of debris falling process and water penetration via eroded concrete side wall clearance in peripheral region and channels in central region. Besides the accumulated pebble bed decomposed from the concrete, as a large thermal and flow resistances, interrupted the further concrete erosion.

### 3.3 Eroded Concrete Conditions

The concrete erosion and degradation condition for both side wall and floor was similar in all test cases, irrespective of the particulate debris bed formation. The difference was only in erosion depth and the thickness of discolored concrete region. The maximum erosion depth of concrete floor was 48mm in Test C-10, where largest integrated power before water injection was adopted. However, the maximum erosion depth was still smaller than the results of SWISS, WETCOR and MACE.

Figure 7 represents the typical discolored region of concrete in Test C-4 as an example. Region I (5 to 7mm thickness) neighboring to the ingot debris was friable mass of solidified concrete compositions which had melted at the first contact between molten corium and concrete. The void fraction in this region was quite high. The second region II (12 to 20mm thickness) was dark-gray color compared with original concrete color and included many pebbles. The temperature in this region reached above 750K corresponding to a chemical reaction of $CaCO_3 \rightarrow CaO + CO_2$[8]. The pebble bed was defined as region I plus region II, which had a large thermal resistance due to high porosity. Visually it looked like apparent increasing of pebble concentration due to partial or absolute absence of binding substance of cement between pebbles. Since cement and sand ingredients were melting out, partial dipping of corium and penetration of cooling water into region I and II occurred. The thin layer (3 to 5mm thickness) of region III was white and had low porosity. The temperature in this region reached about 650K corresponding to a chemical reaction of $Ca(OH)_2 \rightarrow CaO + H_2O$[8]. The last region IV (15 to 20mm thickness) was solid concrete of light-gray color and the boundary between region IV and undamaged concrete was not definite. The temperature in this region reached about 400K corresponding to the evaporation of free water in the concrete[8].

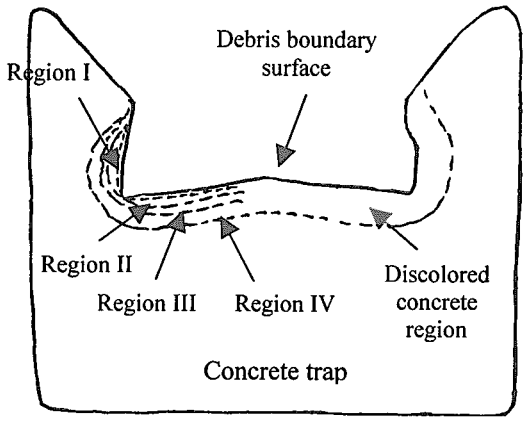



Fig.7 Discolored Concrete Region (C-4)

### 3.4 Structural Investigation of Solidified Debris

In order to clarify the mechanism of the particulate debris bed formation, size distribution of the particulate debris bed was evaluated. The particulate debris bed was removed layer by layer from the concrete trap to evaluate the vertical size distribution difference. The free fragments of each layer were divided into 12 sizes according to the cross section dimension by using sieve method. Figure 8 shows the result of size distributions for Test C-3. The basic difference of the size distributions among upper, middle and lower layers was more mass of the smallest particles in the upper layer.

The measured size distributions for total layers were well correlated nearly by one set of Rosin-Rammler distribution[9] constants irrespective of case (1a) (C-5) and (2) (C-3), as shown in Fig.9. However, the distribution was completely different from the size distribution obtained in Test A-6[10], for example, where molten corium was fallen into water pool. In general larger amount of smallest diameter particles was contained in Test C.

In this Fig.9, the size distribution of C-4, where a thin hard crust above the ingot debris was ruptured during re-heating process under no water injection period, was also included. The different size distribution in Test C-4 was resulting from the combined effects of MCCI and fuel coolant interaction associated with the crust rupture.

Figure 10 compares the size distribution for the two test cases with and without water injection. In C-5a no water was injected, while 2l/min was injected in C-5. Similar size distribution in both tests, irrespective of the amount of the particulate debris bed, suggested the continuation of MCCI even after water injection.

The amount of the particulate debris bed was strongly affected by the integrated induction power before water injection. Figure 11 shows mass of the particulate debris bed versus the integrated power for

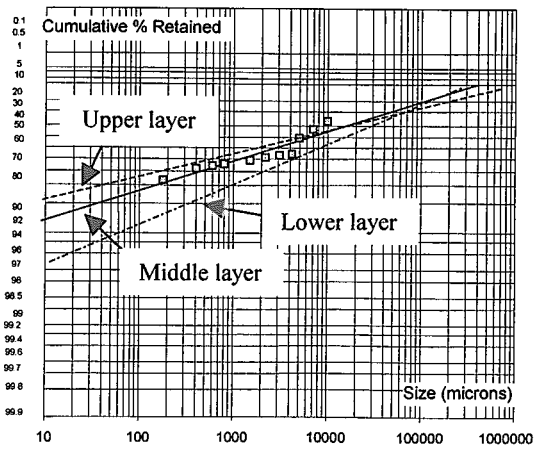



Fig.8 Vertical elevation difference of particulate debris size distribution (C-3)

all 36cm concrete trap tests. Larger amount of the particulate debris bed was formed in C-2, 3 and 10 even in the concrete trap with smaller aspect ratio of 0.19. As the integrated power was increased, the more mass was observed. C-4 was exceptional due to long term interruption of water injection, mentioned above.

In the course of burden heating in the EMF up to complete melting of materials, the material components were interacted to form eutectic and ceramic alloys[11]. During this process, oxides contained in initial burden lost its oxygen partially. Since, during the heating process, gaseous components were discharged to avoid overpressure of the EMF, oxidation reactions of metal components inside EMF was less likely to occur. Thus, it should be noted that most of the metal mixture of materials remained as metal and drained into the test vessel.

During the early stage of MCCI before water injection, melted and partially vaporized concrete components tended to penetrate to the melt upper surface due to its smaller density as a result of the entrainment effect by MCCI generated gas. The entrainment to the upper surface was confirmed by the existence of channels and crevices and small cavities including pebbles, as shown in Fig.5. During this process, the above mentioned metal components in corium was oxidized by $H_2O$ and $CO_2$ decomposed from concrete, and the metal oxides was entrained. The molten corium was also entrained. Similar phenomena occurred in the clearance between the eroded side wall of concrete and the ingot debris. Thus, the particulate debris bed consisting of small particles was formed above the ingot debris due to the entrainment of molten corium and decomposed concrete, and oxidation components of metal associated with MCCI generated gas.

During the corium dilution with concrete components, net specific energy release in the corium was reduced, which resulted in gradual decreasing of average temperature in the entire melt volume and slowing down of concrete erosion process. Such a situation will be expected also in a severe accident of LWR. The measured pebble melting point of about 2730K, used as concrete filling compound, was remarkably higher than melting point of binding components (mortar) of about 1520K. This fact suggested that the erosion of pebble bed was controlled as long as the binding components were completely released. The pebble bed played the role of both thermal insulation and flow resistance against invasion of molten debris. The further erosion was possible only after melt entering to a new concrete layer still containing binding components.

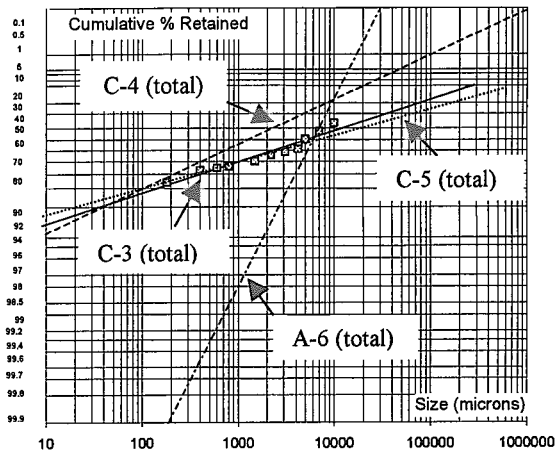



Fig.9 Rosin-Rammler correlation fitting of particulate debris size distribution compared with that in FCI test (A-6)

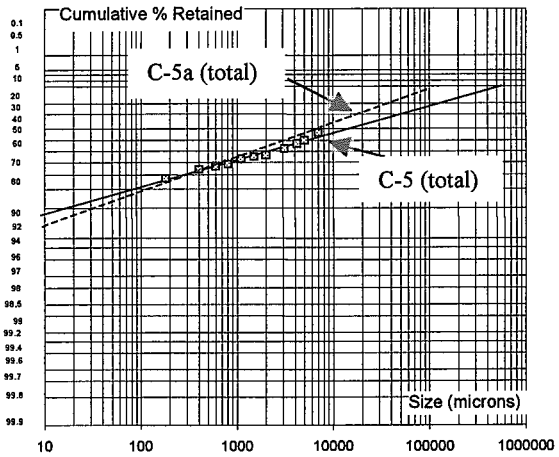



Fig.10 Effect of water injection on particulate debris size distribution (C-5a and 5)

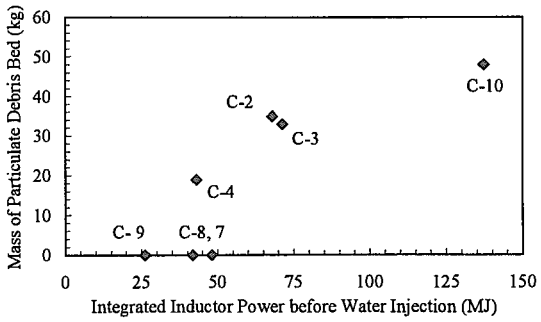



Fig.11 Mass of particulate debris bed vs integrated power

## 4. CONCLUSION

1) Re-heating of molten $UO_2$ mixture debris in concrete trap by induction heating was confirmed.
2) Debris, in which a decay heat generation was simulated, was cooled after water injection and MCCI was suppressed in all test cases.
3) Steady state heat removal rate from upper surface of solidified debris to water pool ranged 0.2 to 0.7MW/m$^2$, consistent with SWISS, WETCOR and MACE results.
4) Particulate debris bed was formed above ingot debris in 6 tests out of 10 tests. The size distributions of the particulate debris bed were well correlated by nearly one set of Rosin-Rammler distribution constants.
5) The formation of particulate debris bed was governed primarily by stored energy in corium before water supply on the melt surface. Large amount of smallest diameter particles was obtained due to the entrainment of molten corium, decomposed concrete and oxidation components of metal in corium associated with MCCI generated gas.
6) Favorable debris cooling observed in COTELS Test C was attributed to the remaining porosity of debris due to simulation of corium falling process, water penetration via eroded concrete side wall clearance and channels and the interruption of further concrete floor erosion due to the existence of accumulated pebble bed decomposed from concrete below the debris.

## ACKNOWLEDGEMENTS

This work was sponsored under the contract by the Ministry of International Trade and Industry, Japan.

## REFERENCES

1) Blose, R.E., et al., 'SWISS : Sustained Heated Metallic Melt/Concrete Interaction with Overlaying Water Pools', NUREG/CR-4727, July 1987.
2) Blose, R.E., et al., 'Core-Concrete Interaction with Overlying Water Pools : The WETCOR-1 Test', NUREG/CR-5907, November 1993.
3) Spencer, B.W., et al., 'MACE Scoping Test Data Report', Argonne National Laboratory Report, MACE-TR-D03, June 1991.
4) Farmer, M.T., et al., 'MACE Test M1B Data Report', Argonne National Laboratory Report, ACE-TR-D6, September 1992.
5) Nagasaka, H., et al., 'COTELS Project (1) : Overview of Project to Study FCI and MCCI during Severe Accident', OECD Workshop on Ex-Vessel Debris Coolability, November 1998 (to be published).
6) Sakaki, I., et al., 'Ex-Vessel Debris Coolability Tests using $UO_2$ Mixture under AM Conditions', JAERI-Conf 99-005, P.310-314, July 1999.
7) Akers, D.W., et al. 'Physical and Radiochemical Examination of Debris from the TMI-2 Lower Head', NUCLEAR SAFETY, Vol.35, No.2, P.288-300, July-December 1994.
8) Bradley, D.R., et al., 'CORCON-MOD3: An Integrated Computer Model for Analysis of Molten Core-Concrete Interactions', NUREG/CR-5843, October 1993.
9) Brown, W.K., et al., 'Derivation of the Weibull Distribution Based on Physical Principles and its Connection to the Rosin-Rammler and Lognormal Distributions', Ken Wohletz Recent Publications, Los Alamos National Laboratory.
10) Kato, M., et al., 'Fuel Coolant Interaction Tests using $UO_2$ Corium under Ex-vessel Conditions', JAERI-Conf 99-005, P.304-309, July 1999.
11) Hofmann, P., et al., 'Reactor Core Materials Interaction at Very High Temperatures', Nuclear Technology, vol. 87, P.146-185, August 1989.

JP0150123



# 12.5 Numerical Analysis of Molten Core-Concrete Interaction Using MPS Method

S. Koshizuka[1], M. Sekine[1], Y. Oka[1] and H. Obata[2]

(1) The University of Tokyo
2-22 Shirane, Shirakata, Tokai-mura, Naka-gun, Ibaraki 319-1106, Japan
telephone: +81-29-287-8441, facsimile: +81-29-287-8488, e-mail: koshi@tokai.t.u-tokyo.ac.jp

(2) The Japan Atomic Power Company
1-6-1 Otemachi, Chiyoda-ku, Tokyo 100-0004, Japan

Moving particle semi-implicit (MPS) method uses particles for discretization of fluids. Governing equations are transformed to particle interactions. Grids are not necessary. This enables us to analyze multi-fluid and multi-phase flows with large deformation of interfaces. In the present study, a two-dimensional code is developed for molten core-concrete interaction (MCCI) based on the MPS method. Heat transfer is calculated without any specific correlations. Solid is simply represented by fixed particles. A particle can be changed to a moving (fluid) or fixed (solid) particle corresponding to its enthalpy. The developed code is applied to SWISS-2 experiment. The calculation geometry is x-y two dimensions though the experiment was r-z two dimensions. Nucleate boiling and radiation heat transfers are considered between the melt and the water pool. Only heat conduction is assumed among the melt pool, concrete and MgO (side walls). Natural convection in the melt pool is considered using Boussinesq's approximation. Gas release and volume contraction accompanied by the concrete ablation are ignored. Calculated heat flux to the water pool agrees well with the experiment, though the ablation speed in the concrete is a little slower. A stable crust is formed in a short time after water is poured in and the heat flux to the water pool rapidly decreases. The shape of the crust is like a bridge due to the natural convection in the melt pool.

**key words**: MPS, MCCI, crust, severe accident, molten core, SWISS

## 1. INTRODUCTION

If a molten core breaches the reactor pressure vessel, the melt spreads on the containment concrete basemat. The concrete ablation continues while the core debris temperature is above about 1500K. Decomposition gas is released by the ablation and this leads to overpressurization in the containment vessel.

In most of the past experiments, the concrete ablation was not terminated by pouring water on the core debris. This is because stable crust, which was supported by the side wall, was formed between the debris and the water pool. Heat flux to the water pool was reduced by the heat conduction in the crust. However, the scales of such experiments were much smaller than that of the real plants. The crust may be unstable without the support if the scale is larger. The experiment of the real scale is almost impossible.

Computer codes have been developed for the molten core-concrete interaction (MCCI); such as DECOMP, CONTAIN and DCRA in IMPACT. In these codes, the phenomena are treated as zero- or one-

dimensional. Thus, multi-dimensional behavior cannot be analyzed. In order to analyze MCCI in the real scale, we have to consider the multi-dimensional effect. Specific correlations which are needed for the integral codes are also limiting the applicability. Therefore, we need a multi-dimensional code based on fundamental governing equations without the specific correlations for the purpose of unrestricted application to the wide range of parameters including the real plant scale in the MCCI analysis.

In the present study, a two-dimensional code is developed for MCCI using moving particle semi-implicit (MPS) method. Governing equations are transformed to particle interactions in the MPS method. Large deformation of interfaces and phase change processes are easily analyzed because grids are not necessary. Fragmentation of a melt drop in vapor explosions was analyzed and the fragmentation process was clarified in the past studies [1-6]. As a verification, water jet impingement on a fluorinert pool was analyzed and good agreement with MUSE experiment carried out in the Japan Atomic Energy Research Institute (JAERI) was obtained [7]. Numerical models for boiling and solidification have already been developed to be incorporated into the MPS method [8].

The developed code is applied to SWISS-2 which is a typical MCCI experiment carried out in the Sandia National Laboratory (SNL) [9].

## 2. NUMERICAL METHOD

In the MPS method, particle interaction models are prepared with respect to the differential operators: gradient, divergence and Laplacian. All the interactions are limited among the neighboring particles within a finite distance (Fig.1). Mass, momentum and energy conservation equations, which involve such differential operators, are transformed to particle interaction equations. Grids are not necessary. The particles move in Lagrangian description, so that the convection terms are not calculated. Thus, numerical diffusion does not occur. This is preferable to keep the interfaces clear. Incompressibility is calculated by a semi-implicit algorithm where the pressure field is implicitly solved using Poisson equation while the other terms are explicitly calculated.

Melting and solidification are modeled in the manner of particle motion. Each particle has variables of enthalpy, temperature and liquid fraction. When a particle is at the melting point, the liquid fraction is linearly changed according to the enthalpy. The particle moves as liquid when the liquid fraction is above a certain value and it is fixed as solid when the liquid fraction is below the certain value.

The concrete particle melts when the liquid fraction reaches 1.0 and it changes to a debris particle. This implies that the melted concrete is uniformly mixed in the melt pool and change of the debris properties is ignored. Decomposition gas release and volume contraction of the concrete are not considered. The latent heat for the melting is concentrated at the ablation temperature. Actually, dehydration and decarboxylation occur at different temperatures.

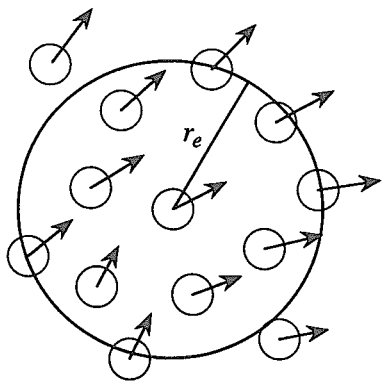


Fig.1 Concept of particle interaction models in MPS

The debris particle is solidified when the liquid fraction is below a critical value of 0.45 and melted when the liquid fraction is above the critical value. This critical value of 0.45 is tentatively chosen from a melt spreading experiment using stainless steel [10]. The solidified debris particle is fixed if another fixed particle exists in the neighborhood. This implies that the solidified particle sinks without the support. MgO and concrete

particles are regarded as fixed. Natural convection in the melt pool is calculated using Boussinesq's approximation.

Nucleate boiling heat transfer is considered on the interface between the core debris and the water pool. A general correlation that the heat transfer is proportional to the third power of the temperature difference is employed. The coefficient is determined to provide a critical heat flux of $1.5 \times 10^6 W/m^2$ at $\Delta T = T_w - T_{sat} = 17.17K$. When the water subcooling is 45K, this is the case of SWISS-2 experiment, the critical heat flux is increased to $4.7 \times 10^6 W/m^2$. The heat flux is limited by this critical value. Transition and film boiling are not considered. Radiation heat transfer to the water pool is also considered. No special models are used and only heat conduction is considered among the core debris, the bottom concrete and the side MgO.

## 3. ANALYSIS OF SWISS-2

### 3.1 Calculation Conditions

The MPS code developed here is applied to the analysis of SWISS-2 experiment. The geometry is depicted in Fig.2. The calculation is x-y two-dimensional though the experiment was r-z two-dimensional. The width of the melt pool in the calculation is the same as the diameter in the experiment. At the moment, cylindrical coordinates cannot be used in MPS method. The core debris, concrete and MgO are initially represented by 513, 783 and 2025 particles, respectively.

Thermophysical properties in the report [9] are used. The initial melt temperature is 1850K which is a 150K superheat. Heat source is initially fixed at 1.6W/g and it decreases as the debris particles increase due to the melting of concrete. The total heat input is kept constant except for twice stops for short periods. The power supply starts at 25sec and the water is poured at 99sec, which are the same timings as the experiment.

Two calculations are carried out. One is neglecting the natural convection in the melt pool in order to use a long time step. This calculation reached the end of the experiment. The other is considering the natural convection though the time step is by far limited due to the Coulant condition. In this case, the calculation did not reach the end of the experiment.

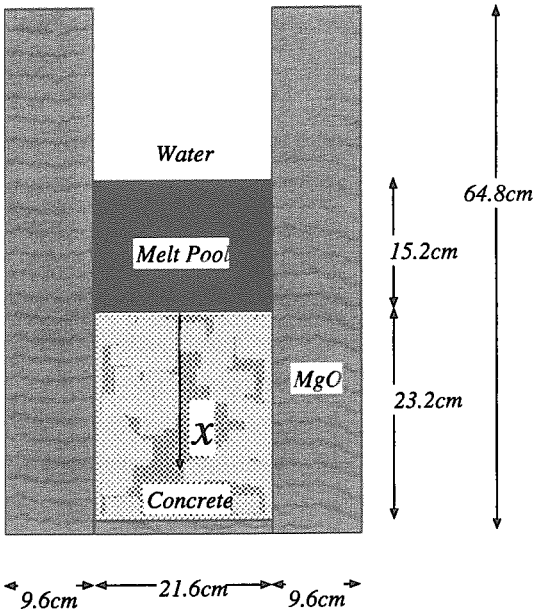



Fig.2 Calculation geometry for SWISS-2

### 3.2 Analysis Neglecting Natural Convection in Melt Pool

Calculated temperature distributions are depicted in Fig.3. We can see the melt pool is heated up and the pool moves downward with ablating the concrete. The side walls are also heated to some extent. Figure 4 shows the solidified debris particles. Some debris particles are solidified on the side MgO at 60sec. These particles are melted again at 500sec and a layer of the solidified particles appears at the top of the melt pool. This is the stable crust supported by the side walls. The shape of the crust is almost flat. The

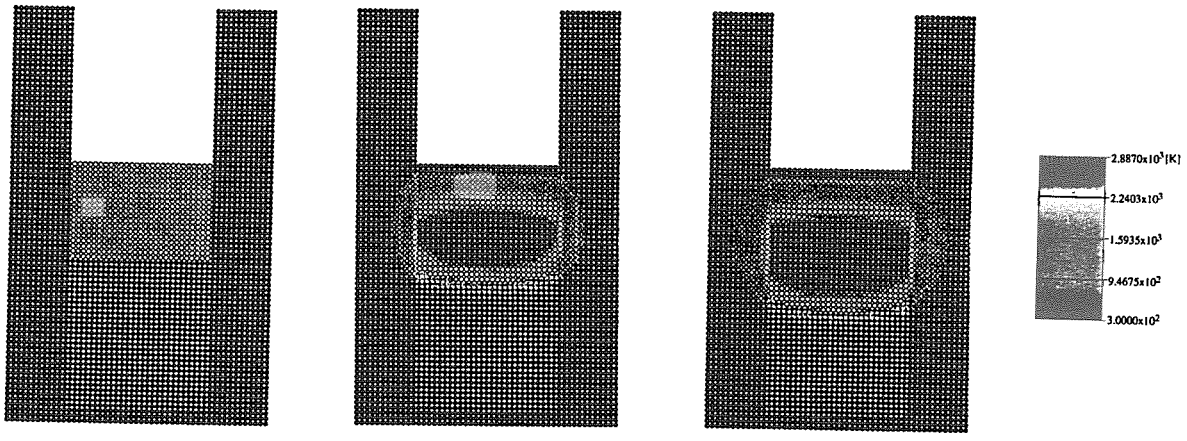



Fig.3 Temperature distribution

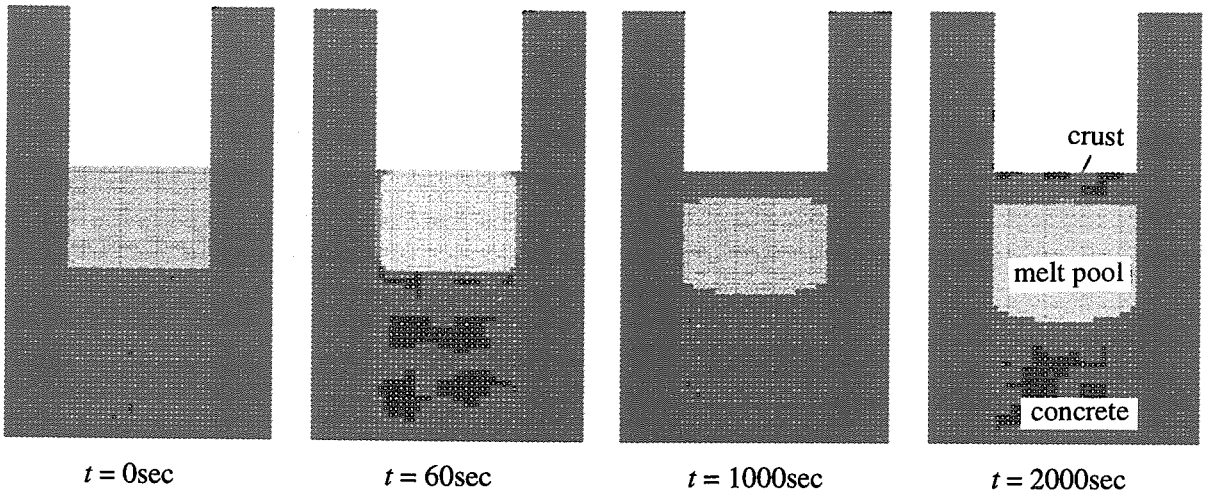



Fig.4 Solidified debris particles

thickness of the crust is constant till the end. There is no space between the melt pool and the crust. This is because the volume contraction is neglected when the concrete is melted. In [9], they presumed that the decomposition gas causes pool swell and that contact between the melt pool and the crust was established during the experiment.

The ablation front in the concrete is shown in Fig.5. The ablation does not appear till 300sec because the core debris is cooled by cold concrete at first. This is also found in the experiment. After 300sec, we can see that the calculated ablation speed is slower than that of the experiment. This is due to the heat flux to the concrete is smaller in the calculation. The calculated temperature of the melt pool is much above the melting point because the natural convection is not considered. Some heat is stored in the melt pool instead of transferred to the concrete.

The heat flux to the water pool is compared in Fig.6. A very high heat flux of $6x10^6 W/m^2$ is observed in the calculation though it was not so high in the experiment. One reason is that the heat transfer is not properly calculated. The calculated peak is the sum of the critical heat flux to subcooled water and the radiation heat transfer. Transition or film boiling might be realized in the experiment.

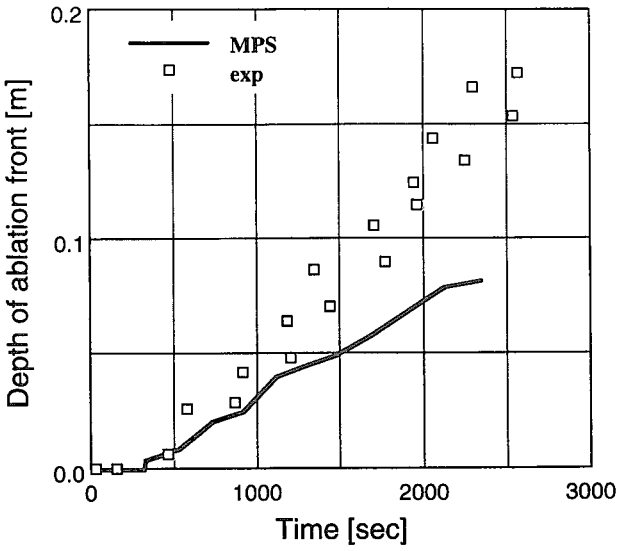



Fig.5 Ablation front in concrete

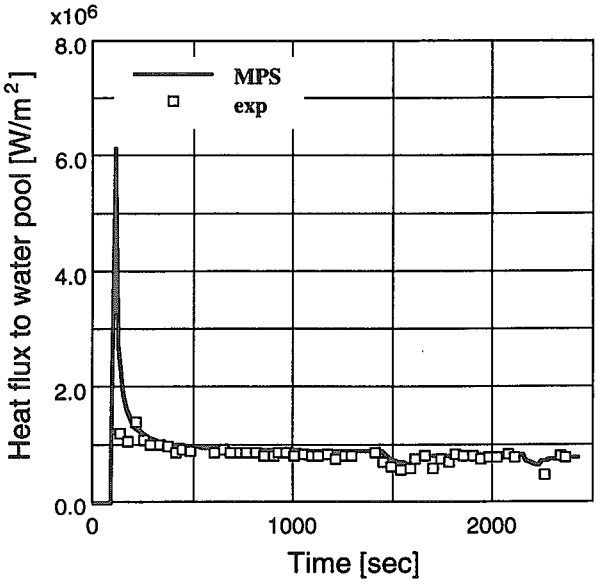



Fig.6 Heat flux to water pool

Another reason is that the experimental data of the heat flux were evaluated from the water temperature difference between the inlet and the outlet of the water pool. This implies that the short peak was not detectable in the experiment. The heat flux rapidly decreases after the initial peak due to the stable crust. The decreased heat flux is about 0.8MW/m$^2$ which is in good agreement with the experiment. The heat flux drops twice at about 1500 and 2200sec when the power input is lost as the experiment was so.

### 3.3 Analysis with Natural Convection in Melt Pool

The time step must be much smaller than the previous case because of the Courant condition. Thus, the calculation does not reach the end of the experiment. The concrete ablation speed and the heat flux to the water pool are almost the same as those of the previous case.

Figure 7 shows pictures of the melt pool. A thin crust grows from the side walls in about 10sec. At 670sec, the center of the crust is thinner and the sides are thicker. This shape is formed by the natural convection in the melt pool. Hot melt rises in the center, which makes the crust thinner. This is not found in the previous calculation neglecting the natural convection. The bridge-like shape of crust was also found in the experiment.

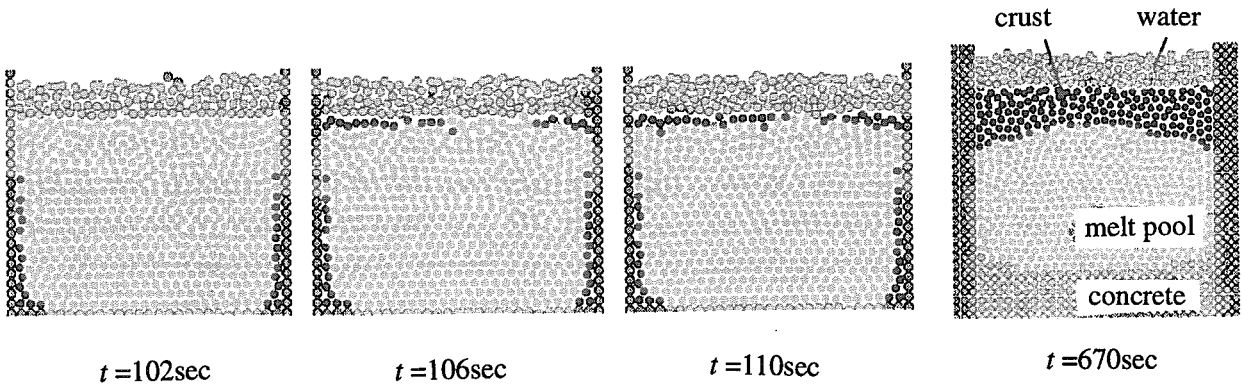



Fig.7 Crust formation

## 4. CONCLUSIONS

A two-dimensional MPS code for MCCI analysis is developed without the specific correlations. Melting and solidification are modeled as the manner of particle motion. The developed code is applied to SWISS-2 experiment. The calculated ablation speed of concrete is slower than that of the experiment. The heat flux to the water pool shows a peak when the water is poured and it rapidly decreases due to the stable crust. The decreased heat flux is in good agreement with that of the experiment. The stable crust grows from the side walls in 10sec and finally the bridge-like shape is created because of the natural convection in the melt pool.

The present code successfully analyzed multi-dimensional behavior of MCCI without the specific correlations. We will test the code for the case of corium melt and effect of the scale is next investigated.

## REFERENCES

[1] S. Koshizuka, H. Ikeda and Y. Oka, "Numerical Analysis of Fragmentation Processes in Vapor Explosions" Proc. Workshop on Severe Accident Research in Japan (SARJ-96), JAERI-memo 09-142, Tokyo, October 28-30, 1996, p.86-91 (1997)

[2] S. Koshizuka, H. Ikeda and Y. Oka, "Numerical Analysis of Fragmentation Mechanisms in Vapor Explosions" Proc. OECD/CSNI Specialists Meeting on Fuel-Coolant Interactions, May 19-21, 1997, Tokai, JAERI-Conf 98-009, p.722-731

[3] S. Koshizuka, H. Ikeda and Y. Oka, "Effect of Spontaneous Nucleation on Melt Fragmentation in Vapor Explosions" Proc. Int. Seminar on Vapor Explosions and Explosive Eruptions (AMIGO), Sendai, May 22-25, 1997, p.185-192

[4] S. Koshizuka, H. Ikeda and Y. Oka, "Numerical Simulation of Fragmentation Processes in Vapor Explosions Using Moving Particle Semi-implicit Method" Proc. Int. Meet. Advanced Reactors Safety (ARS'97), Orlando, June 1-5, 1997, p.872-879

[5] H. Ikeda, F. Matuura, S. Koshizuka and Y. Oka, "Numerical Analysis of Fragmentation Processes of Liquid Metal in Vapor Explosions Using Moving Particle Semi-implicit Method" Trans. JSME(B) **64**, 2431-2437 (1998)

[6] S. Koshizuka, H. Ikeda and Y. Oka, "Numerical Analysis of Fragmentation Mechanisms in Vapor Explosions" Nucl. Eng. Des. **189**, 423-433 (1999)

[7] H. Ikeda, S. Koshizuka, Y. Oka, H. S. Park and J. Sugimoto, "Numerical Analysis of Water Jet Dynamics in Coolant Injection Mode of Fuel-Coolant Interactions" Proc. 7th Int. Conf. Nucl. Eng., Tokyo, April 19-23, 1999, ICONE-7113

[8] H. Ikeda, S. Koshizuka and Y. Oka, "Boiling and Solidification Models for Particle Method to Analyze Molten Core Behavior in Severe Accidents" Proc. 6th Int. Conf. Nucl. Eng. (ICONE-6), San Diego, May 10-15, 1998, ICONE-6233

[9] R. E. Blose, J. E. Gronager, A. J. Suo-Anttila and J. E. Brockmann, "SWISS: Sustained Heated Metallic Melt/Concrete Interactions with Overlying Water Pools" NUREG/CR-4727, SAND85-1546 (1987)

[10] H. Suzuki, T. Matsumoto, T. Mitadera M. Matsumoto, I. Sasaki and T. Zama, "Fundamental Experiment and Analysis for Melt Spreading on Concrete Floor" Proc. ASME/JSME Nucl. Eng. Conf., 1993, Vol.1, p.403-407

This is a blank page.

# 13. Session 12

## Structural Integrity

Chairperson:

N. Miyazaki (Kyusyu Univ.)

Y. Maruyama (JAERI)

This is a blank page.

JP0150124



# 13.1 POST-TEST CREEP ANALYSIS OF PIPING FAILURE TESTS IN WIND PROJECT

**E. Chino, Y. Maruyama, Y. Yuchi, H. Shibazaki, H. Nakamura, A. Hidaka, T. Kudo, K. Hashimoto, and A. Maeda***

*Severe Accident Research Laboratory*
*Department of Reactor Safety Research*
*Japan Atomic Energy Research Institute*
*Tokai-mura, Naka-gun, Ibaraki-ken, 319-1195 Japan*
*Phone: +81-29-282-6466, Fax: +81-29-282-5570*
*E-mail: chino@sarl.tokai.jaeri.go.jp*

**Applied and Scientific Systems Department*
*MRI Systems Inc.*

Thermal and structural responses of the reactor coolant piping under elevated temperature and pressure conditions are being investigated in piping failure tests in WIND (Wide Range Piping Integrity Demonstration) project at JAERI (Japan Atomic Energy Research Institute) . The elasto-plastic creep analysis was performed with ABAQUS code for the test using a nuclear grade type 316 stainless steel pipe, which had an outer diameter of 114.3*mm* and a wall thickness of 13.5*mm*. The major material properties at elevated temperature needed for the analysis were measured for specimen sectioned from the test pipe. Based on the measured creep data, a creep constitutive equation including the tertiary stage was developed and incorporated into ABAQUS code. We compared the results of the three-dimensional analysis with those of two-dimensional analysis and the piping failure test. The comparison showed that the piping failure timing and deformation of pipe obtained from the three dimensional analysis underestimated the test results, and that temperature history at the elevated temperature should be adequately considered.

**Keywords** WIND Project, Creep analysis, Severe accident, Piping failure, Piping integrity

## 1 INTRODUCTION

In a severe accident of a light water reactor, high temperature gases generated in a reactor core region could flow into the piping, and a large amount of fission products (FPs) released from fuel rods will deposit on the inner surface of reactor coolant piping. In such conditions the piping might be subjected to thermal loads due to the heat transfer from the high temperature gases and the decay heat released from the deposited FPs together with an internal pressure load. These thermal and pressure loads could threaten the integrity of the piping. A failure of a hot leg or a pressurizer surge line of a pressurized water reactor (PWR), for example, has been concerned in high pressure accident sequences (Chambers et al., 1989, Hidaka et al., 1996).

Thermal and structural responses of the reactor coolant piping under elevated internal pressure and temperature conditions are being investigated in piping integrity tests of WIND project at JAERI (Hashimoto et al., 1995, Nakamura et al., 1996, Maeda et al., 1998). Several piping failure tests have been performed using steel pipes which simulate a part of reactor coolant piping. In parallel with conducting the tests, post-test analyses are in progress with a commercial finite element method code, ABAQUS (Hibbitt, Karlsson & Sorensen, Inc. 1989), to assess analytical models for the creep deformation and failure of the piping in the tests. This paper describes the results of two and three-dimensional elasto-plastic creep analyses and comparison of the analyses with the piping failure test.

## 2 PIPING FAILURE TESTS IN WIND PROJECT

### 2.1 Test Facility

A schematic diagram of the piping integrity test facility of WIND project is shown in Fig. 1. The facility consists of a test section, nitrogen supply system, an internal heating system, a safety enclosure, a heat exchanger, and an exhaust line. A straight pipe as the test section is pressurized with nitrogen gas, and locally heated by an internal electric heater. Several types of pipe are used as the test section. Structure and major dimensions of small diameter test pipe are illustrated in Fig. 2. The small

diameter test pipe has a length of 2000 *mm*, an outer diameter of 114.3 *mm*, and a wall thickness of 13.5 *mm*. The internal electric heater is made of silicon carbide (SiC) and a heat generating part of the heater is located at the center of the test pipe. The test pipe is surrounded with a thermal insulator layer to form a nearly adiabatic boundary condition at the outer surface. Temperature is measured with thermocouples distributed over the test pipe.

Fig. 3 shows a method of measurement of enlargement in piping diameter. Two sets of wires are used for measurement of vertical and horizontal diameter enlargement. For vertical direction, one side of wire is connected with the top or the bottom of the pipe at the center of heated area and another side is hung with weight. Displacement of the weight is measured with laser displacement measurement system. Diameter enlargement of the test pipe is measured throughout the test.

### 2.2 Test Conditions

The major test conditions are listed in Table 1. A cold drawn type 316 stainless steel of nuclear grade pipe with an outer diameter of 114.3 *mm* was used in WPH3, WPH6 and WPH15. These three tests were performed with constant internal pressures of 9.8, 4.9, or 14.7 MPa, respectively. In WPH4 test, a cast stainless steel pipe with an outer diameter of 114.3 *mm* was used and the internal pressure was maintained at 9.8 MPa. In other tests, middle diameter test pipes with an outer diameter of 355.6 *mm* were used. A hot extrusion type 316 stainless steel pipe was used in WPH11 and WPH17, and a hot extrusion carbon steel pipe was used in WPH13. The maintained internal pressures were 9.8 MPa in WPH11, 14.7 MPa in WPH17 and 7.4 MPa in WPH13, respectively. The pipe was locally heated with a temperature increase rate of 130 °C/h. In WPH15, which was analyzed in the present study, the test pipe was failed when the temperature of heating area was sustained at 970 °C for 1 hour. Histories of internal pressure and temperature at top of piping outer surface of WPH15 are shown in Fig. 4.

An axial displacement was constrained at the pipe end and the free axial displacement was allowed at another end.

### 2.3 Test Results

The conditions in all the tests at the failure are summarized in Table 2, including the maximum temperature, a ratio of outer diameter before and after test, and a ratio of wall thickness at upper part of piping before and after test. In these tests except WPH4, the test pipes were remarkably enlarged and the wall thickness was remarkably reduced. The major difference in test conditions between WPH3, WPH6 and WPH15 is internal pressure. The internal pressure was 9.8 MPa in WPH3, 4.9 MPa in WPH6 and 14.7 MPa in WPH15. Thus, piping failure occurred at higher temperature in WPH6 than in WPH15.

Figs. 5 and 6 show the temperature distribution observed in WPH15 when the temperature was sustained at 970 °C. Fig. 5 shows the axial temperature distribution along the top of outer surface. Fig. 6 shows the circumferential temperature distribution at the center of heating area of pipe outer surface. The temperature difference between the top and the bottom was caused by the natural convection of nitrogen in the piping.

## 3 POST-TEST ANALYSIS

### 3.1 Material Properties

In parallel with the piping failure tests, the measurement for mechanical and thermal properties of the pipe materials at elevated temperature is in progress in WIND project. The measured properties were used in the present analyses. These material properties include creep characteristics, yield and tensile strength, Young's modulus, Poisson's ratio, density, specific heat, thermal diffusivity and thermal expansion coefficient.

### 3.2 Analytical Models

Two-dimensional (2D) and three-dimensional (3D) elasto-plastic creep analyses were conducted for WPH15 with the finite element method code, ABAQUS. Due to a symmetric geometry to a vertical bisection plane, one half of the cross section at the center of the heating area of the test pipe was modeled for the 2D model, and a half cylinder with a half length of the test pipe was modeled for the 3D model as shown in Fig. 7. In the 2D model, the cross section was divided into 15 layers in radial direction and 90 sections in circumferential direction. The 3D models were divided into 5 layers in radial direction, 45 sections in circumferential direction and 30 sections in axial direction. For the 2D and 3D analyses, it was assumed that the internal pressure was constant at 14.7 MPa. The temperature distribution was based on the test results.

The following creep constitutive equation based on the modified θ projection concept (Maruyama et al., 1987, 1990) with the measured creep data was developed and incorporated into ABAQUS code.

Maruyama et al. developed the simplified θ projection concept:

$$\varepsilon = \varepsilon_0 + A\{1-\exp(-\alpha t)\} + B\{\exp(\alpha t)-1\} \quad (1)$$

$$t_r = (1/\alpha) \times \ln\{(\varepsilon_r-\varepsilon_0-A)/B\} \quad (2)$$

where $\varepsilon$ is creep strain, $\varepsilon_0$ and A are material constants depending on stress, $\alpha$ and B material constants which depend on temperature and stress, $t_r$ rupture time, and $\varepsilon_r$ rupture strain. The material constants were determined by the least square's fit of the measured creep data and upper and lower bounds were determined by $1\sigma$ (standard deviation) for each material constant. Second term of Eq.(1) indicates primary creep and third term indicates tertiary creep.

The approximate expressions of the material constants which was calculated by use of creep data shown as follows.

$$\varepsilon_0 = -2.3181e\text{-}4 + 3.7358e\text{-}5\,\sigma - 8.4995e\text{-}7\,\sigma^2 + 7.3644e\text{-}9\,\sigma^3 \quad (3)$$

$$A = -1.6681e\text{-}2 + 4.5476e\text{-}3\,\sigma - 3.5937e\text{-}5\,\sigma^2 + 8.3663e\text{-}8\,\sigma^3 \quad (4)$$

$$\alpha = 123161\,\sigma^{5.2645} / \exp(48750/T) \quad (5)$$

$$B = 0.0045\,\sigma^{-1.2138} / \exp(8150/T) \quad (6)$$

Figure 8 shows predicted rupture time by Eq.(2) and the measurement. The upper bound was approximately 1.7 times longer and the lower bound is approximately 0.6 times shorter than the predicted values. In the present analysis, the following model on the accumulation of creep damage definition was used,

$$Dc = \Sigma\,(\Delta t/tr) \quad (7)$$

where Dc is creep damage at time t (if the value is 1.0, the structure has failed), $\Delta t$ time step at current problem time.

In present analyses, we considered three kinds of procedure which were '2D analysis with constant temperature distribution of piping'(Case A), '2D analysis considering temperature history of piping'(Case B), and '3D analysis with constant temperature distribution of piping'(Case C).

### 3.3 Analytical Results

The timing that the creep damage reached 1.0 from the initiation of temperature sustaining in the heating area at 970 °C in the 2D creep analysis is 50 minutes at the top of piping outer surface. The observed failure time was 60 minutes after temperature was sustained at 970 °C. The piping failure timing obtained from the analysis agreed well with the test result. The analytical result slightly overestimated the failure time, probably due to two-dimensional limitations. The final results from test and analysis with constant temperature distribution were summarized in Table 3. The diameter and the wall thickness obtained from the 2D analysis agreed well with the test results. Figs. 9 and 10 show the comparison of inverse of vertical diameter. In Fig. 9, vertical diameter increase was compared between the test and 2D and 3D analysis with the constant temperature distribution of the piping. Time 0 in Fig. 9, in table 3, and in Fig. 10 were set at the time when the temperature at the top of the test pipe reached 970 ℃ . It was found that the 2 D analysis well reproduced the deformation of the piping observed in the test. However, it was not possible to conclude that the 2D analysis was sufficient, because the constraint on the deformation resulted from the development of the axial temperature profile was not taken into account in the 2D analysis. Therefore, we carried out the 3D analysis. The results of 3D analysis was underestimated the test results. Table 3 shows the summary of the result of the 2D and 3D analysis. We thought this underestimation came from that which the creep damage accumulated before piping temperature reached 970℃ was ignored. To confirm this consideration, we carried out the analysis considering the temperature history and compared with the test results and the analytical results using constant temperature distribution. We chose 2D analysis to examine the influence of the temperature history, since 3D analysis using fine analysis with solid elements is very time consuming. Figure 10 shows the comparison among the test and 2D analysis for the increase of vertical diameter. Case A is the result of analysis using constant temperature distribution. Case B is the result of analysis considering temperature history. The case B analysis performed for the period after the piping temperature became approximately 900℃. As shown in Fig. 10, the results of case B largely overestimated the history of diameter increase obtained from the test and case A analysis. The comparison between case A and case B indicated that the damage on the piping material at elevated temperature must be adequately taken into account. An initial value of the analytical diameter increase, about 2 *mm*, is caused mainly by thermal expansion.

The deformation of pipe at 120 minutes are shown in Fig. 11. The 3D creep analysis qualitatively reproduced the enlargement at the heating area and the axial distribution of the enlargement. However, the failure time and the extent of enlargement were underestimated. The predicted failure time was 109 minutes, which is close to the upper bound of Eq.(3). Finally, Fig. 12 shows the history of circumferential

stress at failure location in 2D analysis which is considering temperature history and comparison with membrane stress. The initial membrane stress imposed on the piping due to the internal pressure is also plotted in Fig. 12, and compared with the analytical results. The reason why we compared these two stress was that the membrane stress could be one of candidates for the representative stress used in system level codes such as MELCOR and THALES. It was found that the circumferential stress from the analysis was slightly higher than the membrane stress, but the both were at same level.

## 4 CONCLUSIONS

Post-test creep analyses for one of piping failure tests in WIND project have been performed with ABAQUS code. The following findings were obtained from the analyses. All 2D and 3D analyses reproduced the failure location and the acceleration of piping deformation by applying the creep equation taking tertiary creep into account. Predicted failure time depended on the conditions used in the analyses. However, it was within the deviation range evaluated from the comparison between the specimen tests and the predictions. The stress at the failure location was predicted to be slightly higher than the membrane stress created by the internal pressure. The analytical results implied that creep deformation and failure were significantly influenced by the axial temperature profile and the creep damage accumulated before the piping reached the failure temperature. Based on the finding from the analyses, 3D analysis considering the effect of the temperature history is now underway.

## ACKNOWLEDGMENTS

This work was performed under a contract between the Atomic Energy Bureau in Science and Technology Agency of Japan and Japan Atomic Energy Research Institute. The authors wish to express their appreciation to the members of WIND project, Mr. K. Komori, and Mr. T. Kiuchi, in Safety Facility Engineering Services Division of JAERI headed by Mr. H. Itoh for maintaining the facility and for conducting the tests, and staff of Nihon Advanced Technology Co., Ltd. led by Mr. N.Sonobe for their excellent technical assistance on the performance of tests and the maintenance of test facility.

## REFERENCES

Chambers, R., et al.: "Depressurization to mitigate direct containment heating," Nucl. Technol. Vol.88, 239 (1989).

Hashimoto, K., et al.: Proc. 3rd Int. Conf. on Nuclear Engineering, Vol.3, 1241 (1995).

Hibbitt, Karlsson & Sorensen, Inc.: "ABAQUS User's Manual, Version 5.4," Providence, Rhode Island, (1995).

Hidaka, A., et al.: Proc. International Topical Meeting on Probabilistic Safety Assessment, Vol.3, 1548 (1996).

Maeda, A., et al.: Proc. 5th Int. Conf. on Nuclear Engineering, ICON5, 2088 (1995).

Maruyama, K. el al.: Trans. ASME, J.Press. Vess. Technol., 109, 142 (1987).

Maruyama, K., el al.: Trans. ASME, J. Press. Vess. Technol., 112, 92 (1990).

Nakamura, N., et al.: Proc. 4th Int. Conf. on Nuclear Engineering, Vol.3, 199 (1996).

R. W. Evans, el al.: "Recent Advances in Creep and Fracture of Engineering Materials and Structures", Ed. By B. Wilshire and D. R. J. Owen, Pineridge Press, Swansea, 135 (1982).

R. W. Evans, et.al.: "Creep of Metals and Alloys", The institute of Metals, London, 197 (1985).

Table 1 Major conditions of piping integrity tests

| Test No. | Outer Diameter (mm) | Wall Thickness (mm) | Piping Material | Internal Pressure (MPa) | Circumferential Stress* |
|---|---|---|---|---|---|
| WPH3 | 114.3 | 13.5 | SUS316(N) | 9.8 | 31.7 |
| WPH6 | | | | 4.9 | 15.9 |
| WPH15 | | | | 14.7 | 47.6 |
| WPH4 | | | CF8M | 9.8 | 31.7 |
| WPH11 | 355.6 | 35.7 | SUS316 | 9.8 | 39.0 |
| WPH17 | | | SUS316 | 14.7 | 58.6 |
| WPH13 | | 27.8 | STS410 | 7.4 | 39.9 |

*Calculated value by " Internal pressure x Inner radius / Wall thickness "

SUS316(N) : Nuclear Grade Type 316 Stainless Steel (cold drawing), CF8M : Cast Stainless Steel
SUS316 : Type 316 Stainless Steel (hot extrusion), STS410 : Carbon Steel (hot extrusion)

Table 2 Maximum temperature and deformation characteristics of piping at failure

| Test No. | Internal Pressure (MPa) | Maximum Temperature (°C) | Ratio of Outer Diameter before and after Test | | Wall Thickness Ratio at Top of Pipe before and after Test |
|---|---|---|---|---|---|
| | | | Vertical | Horizontal | |
| WPH3 | 9.8 | 1070 | 1.31 | 1.24 | 0.44 |
| WPH6 | 4.9 | 1130* | 1.47 | 1.40 | 0.48 |
| WPH15 | 14.7 | 970 | 1.31 | 1.20 | 0.36 |
| WPH4 | 9.8 | 1000 | 1.06 | 1.02 | 0.88 |
| WPH11 | 9.8 | 1040 | 1.28 | 1.19 | 0.66 |
| WPH17 | 14.7 | 960 | 1.32 | 1.19 | 0.42 |
| WPH13 | 7.4 | 820 | 1.31 | 1.29 | 0.64 |

* Estimation from surrounding thermocouples (thermocouple at highest temperature area failed)

Table 3 Summary of final results from test and analysis with constant temperature distribution (WPH15)

| | Failure Time (min) | Failure Location | Vertical (mm) | Horizontal (mm) |
|---|---|---|---|---|
| Test | 60 | Top | 146.8 | 136.6 |
| 2D | 50 | Top | 143.0 | 130.9 |
| 3D | 97 | Top | 136.9 | 132.1 |

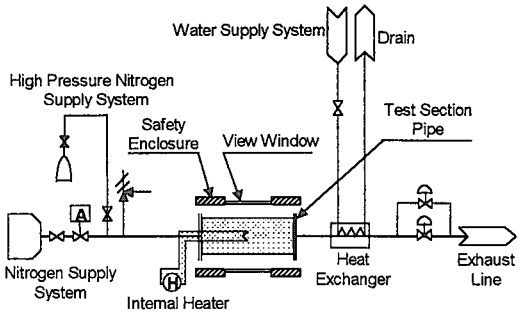



Fig.1 Schematic of piping integrity test facility

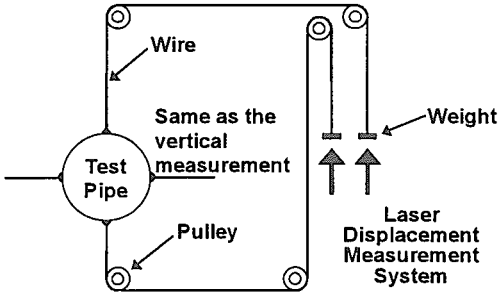



Fig.3 Measurement of enlargement in piping diameter

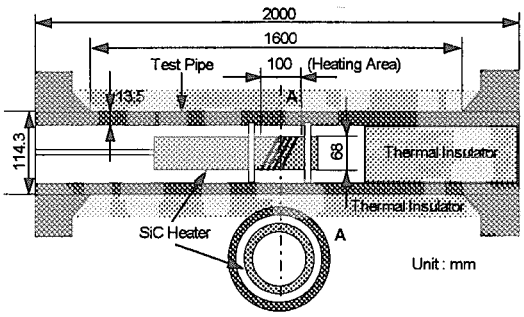



Fig.2 Structure of small diameter test pipe

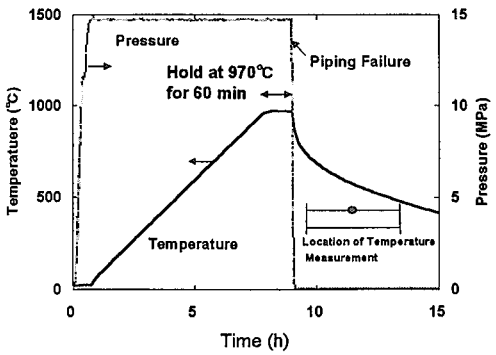



Fig.4 Histories of internal pressure and temperature at top of piping outer surface in WPH15

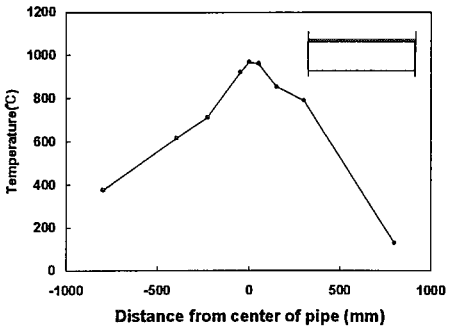



Fig.5 Axial temperature distribution along the top outer surface of pipe (WPH15)

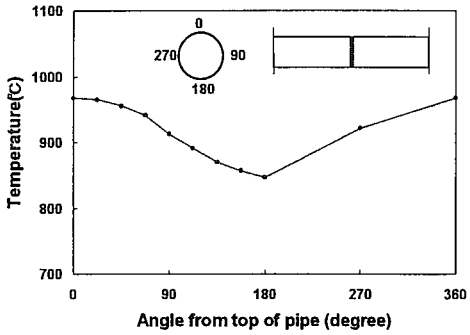
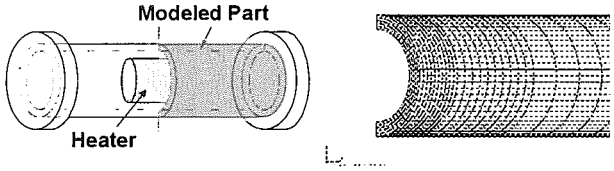



Fig.6 Circumferential temp. distribution at the center of heating area of pipe outer surface (WPH15)




**(Radial 5 ×Circumferential 45 ×Axial 30)**

Fig.7 Model and mesh for 3D analysis

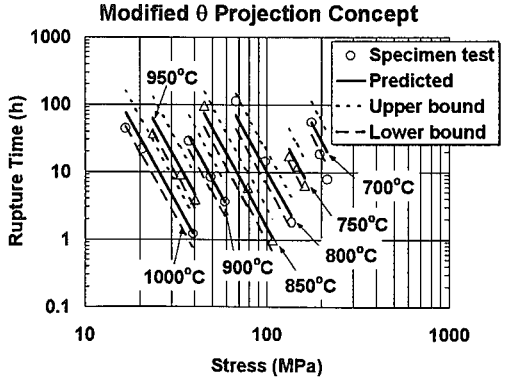



Fig.8 Predicted and observed rupture time

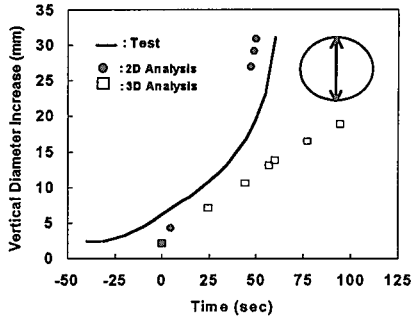
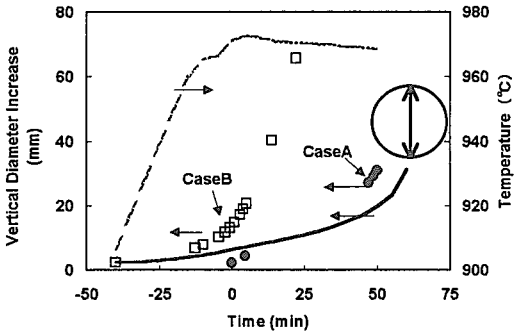



Fig.9 Comparison of increase of vertical diameter between the 2D and 3D analysis (WPH15)




CaseA: Constant Temperature Distribution
CaseB: Considering Temperature History

Fig.10 Comparison of increase of vertical diameter between the 2D analysis and test (WPH15)



Magnification 1

Fig.11 Pipe deformation obtained from the 3D analysis

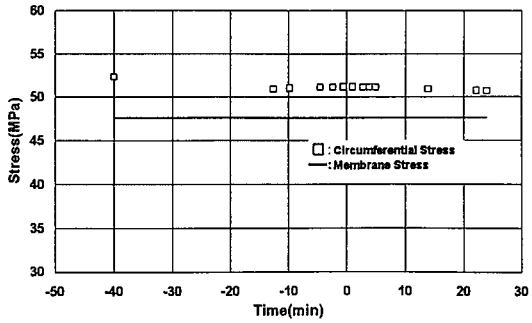



Fig.12 History of circumferential stress at failure and comparison with membrane stress (CaseB) (WPH15)

JP0150125



# 13.2 Modeling of Hot Tensile and Short-Term Creep Strength for LWR Piping Materials under Severe Accident Conditions

Y. HARADA[1], Y. MARUYAMA, A. MAEDA[2], E. CHINO, H. SHIBAZAKI,
T. KUDO, A. HIDAKA, K. HASHIMOTO, J. SUGIMOTO

Japan Atomic Energy Research Institute (JAERI), Department of Reactor Safety Research
Tel. +81-29-282-5854, Fax. +81-29-282-5570, E-mail: maruyama@sarl.tokai.jaeri.go.jp
[1] Mitsubishi Heavy Industries, Ltd. (MHI), Nuclear Fuel & Core Safety Engineering Department
Tel. +81-78-672-3354, Fax. +81-78-672-3347, E-mail: yuhei harada@kind.kobe.mhi.co.jp
[2]MRI Systems Inc., Applied and Scientific Systems Department
Tel. +81-3-3356-5844, Fax. +81-3-3532-3769, E-mail: maeda@mrisys.co.jp

**Abstract**

The analytical study on severe accident shows the possibility of the reactor coolant system (RCS) piping failure before reactor pressure vessel failure under the high primary pressure sequence at pressurized water reactors. The establishment of the high-temperature strength model of the realistic RCS piping materials is important in order to predict precisely the accident progression and to evaluate the piping behavior with small uncertainties. Based on material testing, the 0.2% proof stress and the ultimate tensile strength above 800℃ were given by the equations of second degree as a function of the reciprocal absolute temperature considering the strength increase due to fine precipitates for the piping materials. The piping materials include type 316 stainless steel, type 316 stainless steel of nuclear grade, CF8M cast duplex stainless steel and STS410 carbon steel. Also the short-term creep rupture time and the minimum creep rate at high-temperature were given by the modified Norton's Law as a function of stress and temperature considering the effect of the precipitation formation and resolution on the creep strength. The present modified Norton's Law gives better results than the conventional Larson-Miller method. Correlating the creep data (the applied stress versus the minimum creep rate) with the tensile data (the 0.2% proof stress or the ultimate tensile strength versus the strain rate), it was found that the dynamic recrystallization significantly occurred at high-temperature.

**Keywords:** light water reactor, severe accident, reactor coolant piping, stainless steel, carbon steel, tensile strength, creep rupture time, minimum creep rate, microstructure, dynamic recrystallization

## 1. Introduction

The analyses by Pilch et al.[1] and Hidaka[2] with the SCDAP/RELAP5[3] code showed that failure of the hot leg or pressurizer surge line resulting in the depressurization of the reactor coolant system (RCS) could occur prior to the reactor pressure vessel (RPV) meltthrough at lower head for short-term station blackout scenarios for PWR in severe accident. In such scenarios, the temperature of RCS pipings significantly increased by superheated steam from the degraded reactor core due to countercurrent flows in the hot leg. Therefore, U. S. NRC concluded that the issue of containment failure by direct containment heating (DCH) in PWR, had been mostly resolved. Moreover, the U. S. NRC[4] recently concluded that the pressure- and temperature- induced failure of the steam generator tubes never occur before the failure of the hot legs or surge line in the high pressure severe accident with secondary system depressurization. These important conclusions were made based on the thermal-hydraulics and the creep failure times for each component predicted by using the SCDAP/RELAP5. The model for creep rupture of the structural component in SCDAP/RELAP5 was based on the Larson-Miller theory or the Manson-Haferd theory.

The Larson-Miller and the Manson-Haferd theories using the first degree equation of the logarithms of stress, are used to calculate the creep damage and nearness to rupture of RCS components in best estimate transient simulation

of RCS during a severe accident. The Larson-Miller and the Manson-Haferd theories are applicable to extrapolation of creep rupture data using a linear time temperature relationship. If the creep rupture data for the time frame of interest in severe accidents, however, are obtained from the short-term creep tests, the model for creep rupture can be evaluated by interpolation of creep rupture data. It is important to evaluate the model of the high-temperature tensile and creep strength using data obtained from real RCS piping materials in order to assess the risk of severe accident-induced RCS piping failure with small uncertainties.

The present paper describes the high-temperature tensile and creep data for the RCS piping materials. These specimen tests have been performed to obtain the hot tensile properties, the short-term creep rupture time and the minimum creep rate under WIND (Wide Range Piping Integrity Demonstration) project at Japan Atomic Energy Research Institute (JAERI). Before and after the specimen testing, the microstructures were examined by the metallography. The experimental formula of the 0.2% proof stress and the ultimate tensile strength are developed. Also the model of the rupture time and the creep rate are developed by the modified Norton's Law taking into account the microstructural change during the testing. The correlation between the creep data (the applied stress versus the minimum creep rate) and the tensile data (the 0.2% proof stress or the ultimate tensile strength versus the strain rate) are investigated to predict the tensile behavior at high-temperature from its creep behavior using the modified Norton's Law.

## 2. Experiments

The materials of the test pipes are similar as those of RCS piping used in Japanese LWRs as previously reported[5]. The specimen of cold drawn type 316 stainless steel of nuclear grade (here in after, referred to as SUS316(N)), cast duplex stainless steel (CF8M), hot extruded type 316 stainless steel (SUS316) or carbon steel (STS410) were taken circumferentially from as-received pipes, respectively.

The test specimen had the geometry of 30mm in a gauge length and 6mm in a diameter. The tensile and the creep test procedures were reported previously[5]. After creep-rupture testing, longitudinal sections of the gauge and head portions of the specimens were polished, etched in either aqua regia for the stainless steel or 5%$HNO_3$-ethyl alcohol mixture for the carbon steel, and examined by scanning electron microscopy (SEM).

## 3. Results and Discussion

### 3.1 Model of Hot Tensile Strength

The logarithms of the 0.2% proof stress and the ultimate tensile strength above 800℃ are evaluated for CF8M and plotted as a function of the reciprocal absolute temperature in **Fig. 1**. There is a decline of the strength properties with increasing temperature. The conventional model of the 0.2% proof stress, $R_{p0.2}$ (MPa), and the ultimate tensile strength, $R_m$ (MPa), is given by Arhenius equation[5]

$$R_{p0.2} = 0.0233\exp(73.9/RT) \tag{1}$$

$$R_m = 0.0556\exp(70.9/RT) \tag{2}$$

where $R$ is the gas constant of 8.32 J/mol, $T$ (K) the absolute temperature.

On the otherhand, the present model is given by the equation of second degree as a function of the reciprocal absolute temperature

$$LogR_{p0.2} = -14.7 + 3.44(10000/T) - 0.178(10000/T)^2 \tag{3}$$

$$LogR_m = -9.79 + 2.36(10000/T) - 0.116(10000/T)^2. \tag{4}$$

The conventional model slightly underestimates particularly the 0.2% proof stress at 850℃. This is probably due to the effect of a fine precipitation of carbide, $M_{23}C_6$, on the increase of the strength[5]. The prediction by the present model is, however, on the whole in good agreement with the measured stress above 800℃ which is important under severe accident conditions.

### 3.2 Model of Time to Rupture

**Figure 2** plots stress versus logarithmic times to rupture for the tested temperature of CF8M. There is a reduction of the time to rupture with increasing stress. The stress dependence of the time to rupture appears to be split into two regimes: Norton's Law with a linear stress dependence at 600-700℃; and the modified Norton's Law[5] with a nonlinear stress dependence between 800 and 1,000℃. The stress dependence of the time to rupture, $t_r$ (h), at lower temperature is generally expressed as a power law, often called Norton's Law

$$Logt_r = A - nLog\sigma \tag{5}$$

$$A = 0.0904\exp(42.5/RT) \tag{6}$$

$$n = 0.0780\exp(37.2/RT) \tag{7}$$

where $\sigma$ (MPa) is the stress.

The stress dependence of $t_r$ at higher temperature is expressed as the modified Norton's Law

$$Logt_r = a - b(Log\sigma)^2. \tag{8}$$

The logarithmic stress exponent in Eq. (8) is determined between 1 and 5 by the method of least squares. The temperature dependence of the material parameters in Eq. (8), $a$ and $b$, are given by the following equations

$$a = -6.66 + 1.34(10000/T) \tag{9}$$

$$b = 7.90\exp(-15.8/RT). \tag{10}$$

The modified Norton's Law seems to take into account the increase of creep strength by a fine precipitation, the decrease of creep strength by a coarse precipitation and the recovery of creep strength by a resolution of the precipitation, occurring in a short time at high temperature[5]. The equation (8) based on the modified Norton's Law is applicable to the stated change of creep strength caused by the microstructural changes above 800℃.

On the other hand, the master rupture curve for the Larson-Miller parameter at high temperature between 800 and 1,000℃ is given by

$$T(Logt_r + 15)/1000 = 26.6 - 5.08Log\sigma \tag{11}$$

where the parameter constant of 15 is optimized between 10 and 25 by the method of least squares.

The uncertainty in the the modified Norton's Law and the Larson-Miller method was discussed in the previous study[5]. The variance, $s$, about the regression can be estimated from the following equation

$$s = \sqrt{\frac{\sum_i \left( \log t_{r_i} - \overline{\log t_{r_i}} \right)^2}{N}} \tag{12}$$

where $\log t_{r_i}$ is the observed value, $\overline{\log t_{r_i}}$ the value predicted by the the modified Norton's Law or the Larson-Miller theory and $N$ the number of data, 16. **Figure 3** shows the comparison of the variance in the models of $t_r$ for LWR piping materials at high temperature. The variance is smaller in the modified Norton's Law than the Larson Miller method except CF8M. This difference is due to microstructure. The predominant crack occurred on the grain boundary of $\gamma$ phase in SUS316 and on $\delta$ ferrite phase in CF8M. The effect of the microstructural change on creep strength is smaller in $\delta$ ferrite phase of CF8M at 800-1,000℃ than in $\gamma$ phase of SUS316 and SUS316(N) at 800-1,150℃[5].

**Photographs 1** shows the change of microstructure before and after the tests for CF8M. The precipitation are almost free in Photo. 1 (a) because the as-received specimen were finally solution-treated and quenched in water. The precipitation in $\delta$ ferrite phase was evident and extensive precipitation and particle coarsening occurred at 900 and 1,000℃ within the ruptured gauge lengths in Photo. 1 (b) and (c). The morphology of the intragranular particles at 900 and 1,000℃, were different from each other. On the other hand, the precipitation was almost free due to resolution at 1,000℃ within the undeformed specimen heads in Photo. 1 (d). At 1000℃, the resolution took place within the undeformed region in few tens hours. The precipitates at 900 and 1,000℃ is considered to be various carbides and intermetallic phases which were found in CF8M during aging at elevated temperature. The enhancement

of the precipitation occurred by simultaneous creep deformation. The crack occurred in the ferrite phase or along the ferrite/austenite grain boundaries. Therefore, it is considered that the increase of the strength at 850℃ in Fig. 1, is due to the fine precipitation in the ferrite phase or along the ferrite/austenite grain boundaries.

### 3.3 Correlation between Tensile and Creep Data

The stress and temperature dependence of $\dot{\varepsilon}_{min}$ at lower temperature of 600-700℃ in **Fig. 4**, is expressed as Norton's Law

$$Log\,\dot{\varepsilon}_{min} = -c + d Log\sigma \tag{13}$$

$$c = 0.249\exp(34.5/RT) \tag{14}$$

$$d = 0.171\exp(30.6/RT). \tag{15}$$

The stress and temperature dependence of $\dot{\varepsilon}_{min}$ at higher temperature between 800 and 1,000℃ is expressed as the modified Norton's Law

$$Log\,\dot{\varepsilon}_{min} = -c + d\,(Log\sigma)^2 \tag{16}$$

$$c = -6.97 + 1.43(10000/T) \tag{17}$$

$$d = 8.28\exp(-17.0/RT). \tag{18}$$

This prediction is, also, in good agreement with the measured values. The equation (16) using the modified Norton's Law is applicable to the change of the minimum creep rate caused the microstructural changes above 800℃. Also, this prediction of the minimum creep rate is in good agreement with the measured tensile data except the values at 600-800℃. The modified Norton's Law in Fig. 4, is applicable for the tensile and creep data between 850 and 1,000℃. The results for CF8M of this study are in agreement with the effect of dynamic recrystallization on the deformation at high-temperatute[6].

## 4. Conclusions

From the evaluation of the tensile and creep data at high-temperature and short-term time which simulate a time-temperature relation for the reactor coolant pipings failure under severe accident conditions of LWR, the following conclusions were obtained:

(1) The prediction of the 0.2% proof stress and the ultimate tensile strength given by the equations of second degree as a function of the reciprocal absolute temperature considering the strength increase due to fine precipitates, is in good agreement with the measured stress above 800℃ for several piping materials of reactor coolant system.

(2) For the short-term creep rupture time and the minimum creep rate, the modified Norton's Law as a function of stress and temperature considering the effect of the precipitation formation and resolution on the creep strength, predicts well the experiments at high-temperature for the above steels.

(3) The range of uncertainty is smaller in the modified Norton's Law than the Larson-Miller method previously used in severe accident analysis except CF8M duplex stainless steel. The modified Norton's Law is suitable to describe the effect of the very rapid formation and resolution of the precipitation on the creep strength.

(4) Correlation of the creep data (the applied stress versus the minimum creep rate) with the tensile data (the 0.2% proof stress or the ultimate tensile strength versus the strain rate), indicated that dynamic recrystallization occurred significantly at temperatures higher than 850℃.

## ACKNOWLEDGMENTS

This work was performed under a contract between the Atomic Energy Bureau in Science and Technology Agency of Japan and JAERI. Authors would like to express their sincere gratitude to staffs of JAERI and Nihon Advanced Technology Co. Ltd. led by Mr. H. Ito for their technical assistance on WIND experiment. The authors wish to thank Dr. S. Kawasaki (Integrated Technological Information Research Organization) and staffs of Kobe Material Testing Laboratory Co. Ltd. for performing the hot tensile and creep tests.

## - REFERENCES -


(1) Plich, M. M., Allen, M. D., Spencer, B. W., Bergeron, K. D., Quick, K. S., Knudson, D. L., Tadios, E. L., Stamps D. W. : *NUREG/CR-6109* (1995).

(2) Hidaka, A. : *PhD-Thesis, Tohoku University* , p. 149-162 (1998), [in Japanese].

(3) Davis, K. L. : *NUREG/CR-6150, EGG-2720,* vol. 2 (1993).

(4) U. S. Nuclear Regulatory Commission : *NUREG/1570* (1998).

(5) Harada, Y., Maruyama, Y., Maeda, A., Shibazaki, H., Kudo, T., Hidaka, A., Hashimoto, K., Sugimoto, J. : *J. Nucl. Sci. Technol.*, **36**, 10, 923-933 (1999).

(6) Abd El-Azim, M. E. : *J. Nucl. Mater.*, **231**, 146 (1996).

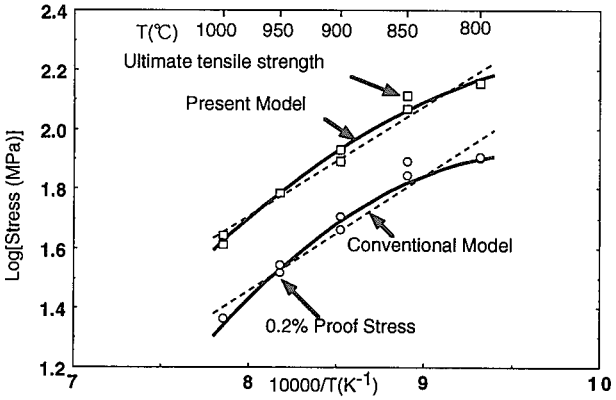




**Fig. 1** Modeling of hot tensile strength for CF8M stainless steel

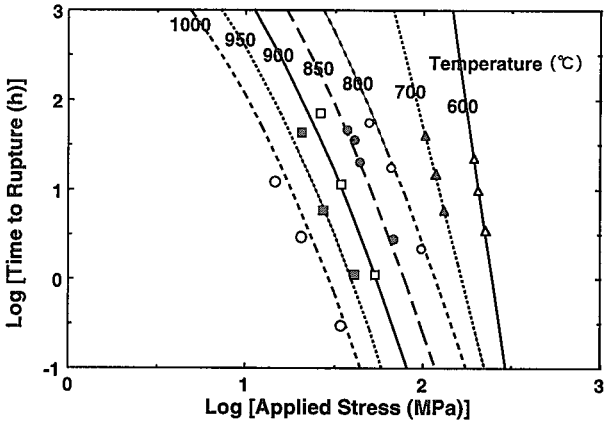



**Fig. 2** Modeling of time to rupture given by modified Norton's Law for CF8M

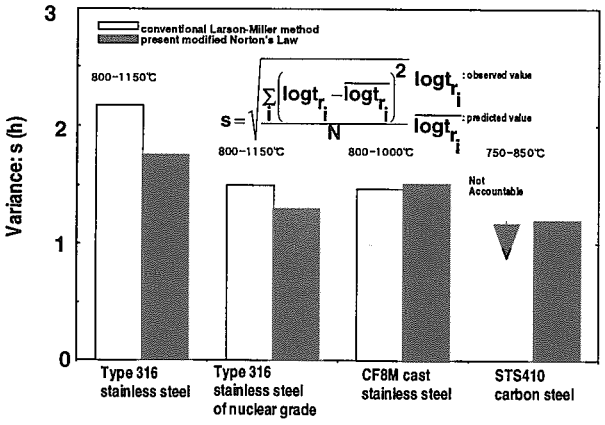



**Fig. 3** Comparison of variance in model s of time to rupture for LWR piping materials

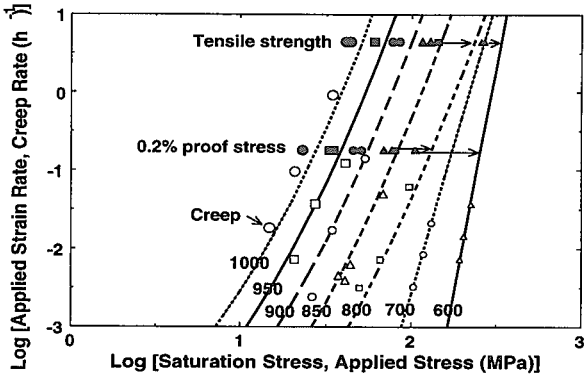



**Fig. 4** Modeling of minimum creep rate given by modified Norton's Law for CF8M

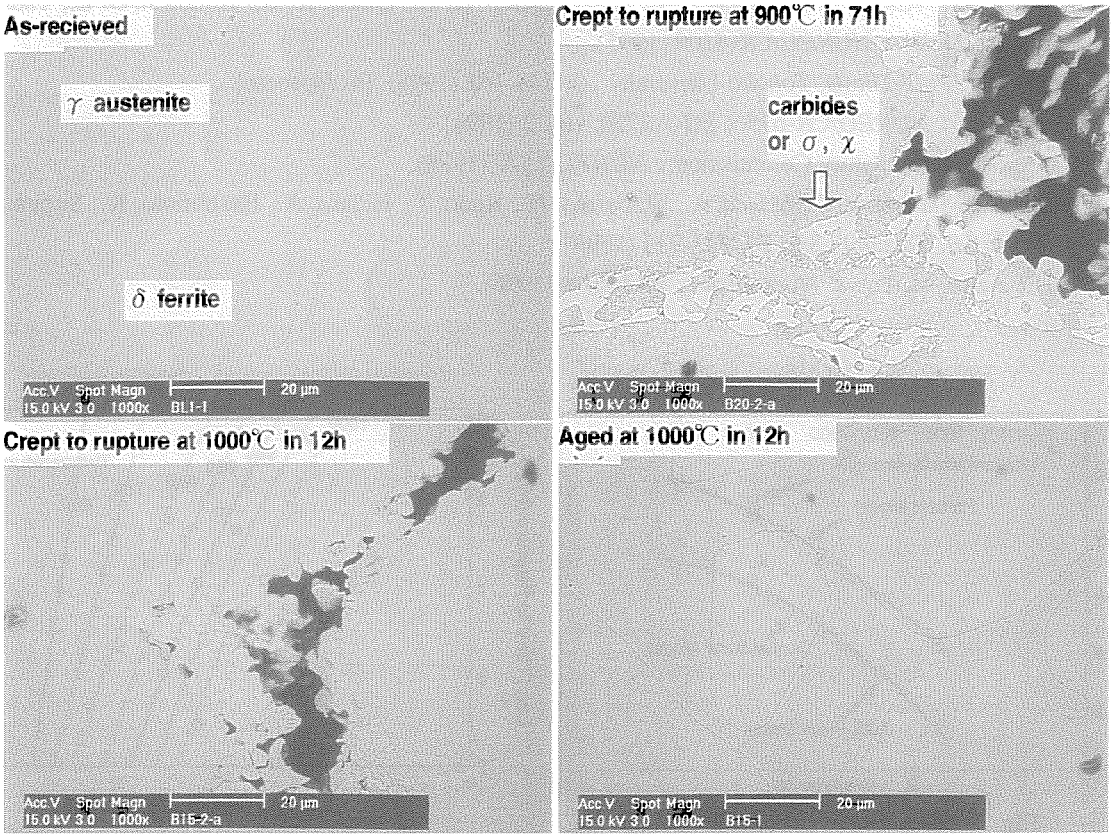



**Photo.1** Microstructural change in CF8M duplex stainless steel at hot-temperature

JP0150126



# 13.3 A Simple Evaluation of Containment Integrity against Ex-Vessel Steam Explosion

Hiroshi NISHIURA
Nuclear Safety Engineering Section,
General Office of Nuclear and Fossil Power Production,
The Kansai Electric Power Co., Inc.

## Abstract

The guideline for consideration to severe accidents on containment design for next-generation LWR was published in 1999. In order to verify the validity of future containment designs, we have developed a method of assessing for the containment integrity against ex-vessel steam explosion. First, we conducted a simple evaluation on an Advanced PWR.

The strength of the reactor cavity wall was assumed to be equivalent to the total strain energy which would accumulate by the time one reinforcing bar element would first reach the failure strain in FEM analyses. As a result, the strength was evaluated to be about 72MJ. The explosion energy was assumed to be a function of the mass of the dropping melted core and the conversion ratio. Assuming the conversion ratio of 1%, it was estimated that the explosion energy would amount to about 1 MJ if the melt mass corresponds to the break of one instrumentation guide tube penetration, and about 40 MJ if the mass corresponds to the simultaneous break of all penetrations.

Therefore, it is expected that the explosion energy would be less than the wall strength; thus, the containment integrity would be maintained even if an ex-vessel steam explosion were to occur.

## Keywords

Containment Integrity, Severe Accident, Steam Explosion, Advanced Pressurized Water Reactor, Cavity Wall

---

This work has been conducted in a joint research project by The Kansai Electric Power Co., Inc., Hokkaido Electric Power Co., Inc., Shikoku Electric Power Co., Inc., Kyushu Electric Power Co., Inc., The Japan Atomic Power Company and Mitsubishi Heavy Industries, Ltd.

# A Simple Evaluation of Containment Integrity Against Ex-vessel Steam Explosion

Hiroshi NISHIURA

Nuclear Safety Engineering Section,
General Office of Nuclear and Fossil Power Production,
The Kansai Electric Power Co., Inc.

This work has been conducted in a joint research project by The Kansai Electric Power Co., Inc., Hokkaido Electric Power Co., Inc., Shikoku Electric Power Co., Inc., Kyushu Electric Power Co., Inc., The Japan Atomic Power Company and Mitsubishi Heavy Industries, Ltd..

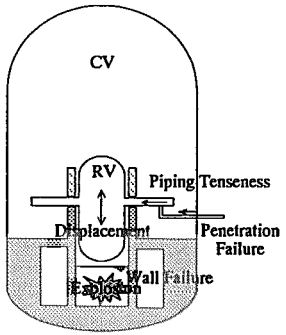
## Objective

- PWRs in Japan utilize the wet cavity formula as an accident management.
- Development of a method of assessing CV integrity against ex-vessel steam explosion is necessary.
- As an initial step, an evaluation of Advanced PWR is conducted.

## Containment Failure Scenario

Explosion Energy Release
↓
Cavity Wall Failure
↓
RV Displacement
↓
Piping Tenseness
↓
CV Penetration Failure

⇨ If Cavity wall remains intact, CV integrity can be secured.




## Previous Assessment Methods

| | Explosion Evaluation | Structural Analysis | Features |
|---|---|---|---|
| Simple Method | Steady Calculation Conversion Ratio  | Static Analysis  | -Simple<br>-Conservative<br>-Depends on input data (melt mass, melt radius, etc.) |
| Detailed Method | Mechanistic Code Analysis  | Dynamic Analysis  | -Detailed<br>-Realistic<br>-Uncertainty of physical model |

## Evaluation Method for Advanced PWR

- The primary purpose is to evaluate whether cavity wall withstands the ex-vessel steam explosion load.
- Detailed analysis of steam explosion phenomena is not pursued, because this estimation is just a reference.
- A workable method for actual plants is preferable.

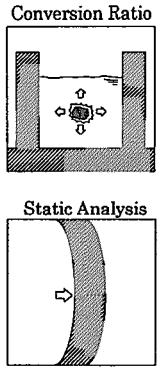
⇨ Use a simple method

## Evaluation Method for Advanced PWR

Simple Method

(1)Explosion Energy
Calculate the mechanical energy from the melt mass, the thermal conditions and the conversion ratio

(2)Wall Strength
Evaluate the strain energy in the reinforcing bar elements up to failure condition using static nonlinear FEM analysis




## Explosion Energy

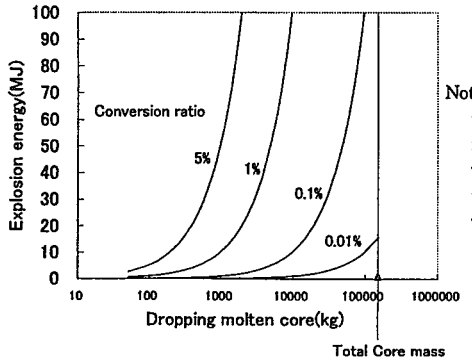
*Steam explosion energy = Conversion ratio ×*
*Melt mass ×* $\{Cp_l\ (T_{melt}\text{-}T_{sol}) + Cp_s(T_{sol}\text{-}T_{w,sat}) + H_{sl}\}$

*Conversion ratio*: 0.01%, 0.1%, 1.0%, 5.0%

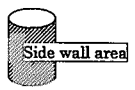
JAERI STX: 0.9-5.7% (press.) ($Al_2O_3$ 20kg)
SNL FITSB: 0-3% (Fe-$Al_2O_3$ max.20kg)
JRC KROTOS: 1.25% ($Al_2O_3$ 1.5kg)
Winfrith(Bird,et al.): max.1.8% ($UO_2$ 0.5kg)
SNL(Buxton,et al.): 0.2-0.5% (Fe-$Al_2O_3$ 5-20kg)
JRC KROTOS: 0.15% ($UO_2$ corium max.5.1kg) (no explosion)

$T_{melt}$, $T_{sol}$ : 2500K (MAAP analyses)
$H_{sl}$ : 352kJ/kg (TMI-2)
$Cp_s$, $Cp_l$ : 480J/kg·K (GE ABWR SSAR)

## Explosion Energy



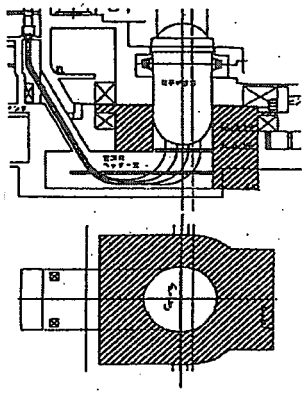

Note:A factor of 0.8 is multiplied to the mechanical energy, which corresponds to the ratio of side wall area



## Wall Strength Analysis

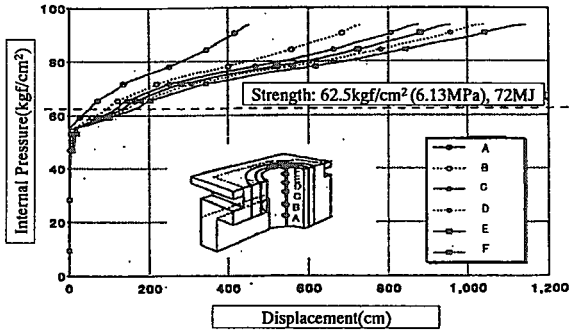
Structural model

- » Primary shield wall
  - – thickness:about 3m
  - – reinforcing:pitch 250mm
- » Under water level (Dashed region)
- » Boundary condition
  - – Lower:fixed
  - – Upper and outside:free
- » Conservative, because the restrictive conditions on the upper and outside parts are neglected.



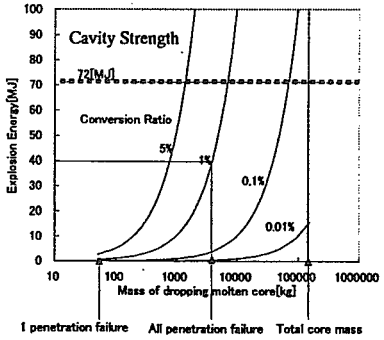
## Cavity Wall Strength

Strength: The strain energy when the strain of a reinforcing bar element first reached 18% was about 72MJ.




## Results

Assuming the conversion ratio of 1%, the explosion energy would be less than the cavity wall strength even if a simultaneous break of all (71) ICIS penetrations were to occur.




## Conclusions

- Using a simple method, CV integrity against ex-vessel steam explosion was evaluated.
- Evaluated cavity wall strength is conservative because the restrictive conditions on the outside and upper parts are neglected.
- It is believed that explosion energy would be less than the strength of cavity wall.
- FP retaining function of CV would be maintained.

JP0150127



# 13.4 AXISYMMETRIC GLOBAL STRUCTURAL ANALYSIS OF PRESTRESSED CONCRETE CONTAINMENT VESSEL BEYOND DESIGN PRESSURE

**Takako Kashiwase**
Systems Safety Department
Nuclear Power Engineering Corporation
Tel:+81(3)3435-3402 Fax:+81(3)3435-3411
Kashiwase@nupec.or.jp

**Masahito Sato**
Lattice Co., Ltd.
Tel:+81(3)5416-8242 Fax:+81(3)5476-8244
sato@lattice-inc.co.jp

## ABSTRACT

NUPEC has been planning the ultimate strength test of PCCV imaging severe accident, in cooperation with USNRC. The test model is 1/4 uniform scale model of Japan actual PCCV in which design pressure is 0.393MPa. It involves an equipment hatch, several penetrations and liner with T-anchors. The pressurization process is achieved by supplying nitrogen to the test model up to containment failure.

This paper describes several techniques to obtain physically reasonable analysis results with better convergence and the summary of preliminary pre-test analysis using axisymmetric global modeling.

## 1. INTRODUCTION

Many techniques of treating post-cracking concrete behavior have been proposed for concrete structure analysis and the analysis modeling itself sometimes depends on the experiences. Although many seismic tests and analyses on reactor containment vessels have been conducted, few tests and analyses, focused on static internal pressure loading beyond design basis condition, have been conducted. As for reactor concrete containment Sizewell B in U.K.[1] and 1/6 scale reinforced concrete containment vessel (RCCV) test in U.S[2] were only available. Sizewell B was internal pressure loading test using 1/10 scale prestressed concrete containment vessel (PCCV) model, which was interrupted because of basemat uplift and could not reach ultimate structural condition. 1/6 RCCV test was conducted up to liner tearing and provided valuable data. However, it did not include the effect of prestressing of tendon.

Considering the above situation, NUPEC has been planning the ultimate strength test of 1/4 uniform scale PCCV imaging severe accident. The pre-test analysis will be compared with measured data and the post-test analysis using this test data will improve analysis model.

This paper describes several techniques to obtain physically reasonable analysis results with better convergence and the summary of preliminary pre-test analysis using axisymmetric global modeling..

## 2. COMPUTATIONAL MODELS

### 2.1 Material properties

The measured average data of concrete Young's modulus, Poisson's ratio, compressive strength, and tensile strength were used based on the trial mix concrete tests after field curing. As for rebars, the average stress-strain curves of each rebar material test were used except dumbbells. The average stress-strain curves obtained from the liner material tests were also used, assuming isotropy of the material. Two-dimensionality of liner material was considered by Mises yield function. The measured stress-strain curve of a tendon material test was used.

### 2.2 Material models

A finite element program ABAQUS/Standard Ver. 5.8 was used to predict the global behavior of 1/4 PCCV test. The stress-strain curve of post-cracking concrete was determined through the following sensitivity study, referring to the displacement data at the cylinder mid point of the 1/6 RCCV test results conducted at SNL.[1] That is, various tension-stiffening curves were adopted under full shear retention model. The tension-stiffening was assumed to be linearly decreased and was reduced to zero at strain values of 10, 20, 30, 40 and 50 times of the concrete crack strain of $1.28 \times 10^{-4}$, considering the simplicity of global analysis. The 10 times model

was the best agreement with 1/6 RCCV data. However this 10 times model induced unstable behavior above 3.0 times design pressure (Pd) condition so that 1 % crack stress was retained even after 10 times of the crack strain.

The reduction of the shear modulus after concrete cracking was determined as follows. The full shear retention model was compared with the model in which shear stiffness under cracking condition was reduced linearly to zero at 10 times of crack strain, similar to the above tension stiffening model. Both models were calculated up to 3.4 Pd where concrete cracking in hoop direction extended to the whole region. The analysis results were almost same so that the full shear retention model was adopted because of the better convergence of calculation.

Non-linear behavior in multi-axial stress field was traced by crack detection surface and compressive surface incorporated in ABAQUS code. Except for the measured ratio of the tensile strength to the compressive strength, defaults values of the surface parameters in ABAQUS were used because of no biaxial test data.

### 2.3 Modeling of 1/4 PCCV test facility

The axisymmetric global analysis was conducted as the first step pre-test analysis. The analytical model included general parts of a dome, a cylinder and a basemat, as shown in Fig. 1. The wall of dome part and cylinder part was divided into 6 elements to evaluate bending behavior. The dome part was divided into 45 elements and the cylinder part was divided into 60 elements. The basemat had 10 vertical elements and 42 radial elements. However, the juncture region between basemat and cylinder had finer elements. The model included the total numbers of 1963 nodes and 1279 elements.

In order to select an element type for the concrete, three solid element types were compared (4-node bilinear (ABAQUS:CAX4), 8-node biquadratic reduced integration (ABAQUS:CAX8R) and 4-node bilinear incompatible mode (ABAQUS:CAX4I)). When 8-node biquadratic reduced integration element and the 4-node bilinear incompatible mode element were used, very high stress occurred in the loading end at about 3.0 Pd and the calculation became divergent. It was supposed that the force directions of some nodes in a element was inconsistent with the direction of element stress in these cases. Since the materials exhibited strong non-linearity and the contact between tendon and concrete was important under high internal pressure condition, 4-node bilinear element was adopted.

Rebar was defined as reinforcement (ABAQUS:REBAR) in solid element. Liner was modeled by shell element (ABAQUS:SAX1) and the liner node was commonly shared with inside node of concrete.

### 2.4 Analytical modeling

Hoop tendon was modeled by rebar bonded to the concrete. Meridional tendon was modeled by shell element and the hoop direction stiffness was made zero in the cylinder part. The hoop direction stiffness was considered only above 45° dome angle, because the meridional tendons in the dome part are arranged as like mesh. Friction was specified between the concrete and the meridional tendon. The meridional tendon was allowed to slide relative to the concrete. Friction coefficient at dome part was 0.2156 which consisted of $\mu$=0.21, average value of the measured friction coefficient, and friction coefficient considering tendon length effect ($\lambda$=0.001 per unit length). For cylinder part, $\mu$=0 and $\lambda$=0.001 were used to stabilize the analysis. Although an empirical friction correlation between tendon and sheath was proposed as a function of loading end load and circumferencial angle,[3] it was not used for the present global axisymmetric analysis. Because hoop tendons don't have a tensile force distribution and meridional tendons are arranged as like mesh.

As a boundary condition, a horizontal direction was fixed along axisymmetric axis to realize axisymmetric condition. Non-linear soil springs were placed at the bottom of basemat to simulate the ground reaction force. The actual ground stiffness was used against compression force and it was zero against tension force. However, the soil springs in non-uplift part had stiffness against tension force, because the vertical displacement became too large when all tensile stiffness of soil springs in non-uplift part were zero. The gravity was considered only at the bottom of basemat as a concentrated force. That is, gravitational force at each node was neglected because of quite smaller force compared with tendon tensile force.

In order to simulate a setting loss condition of tendon, meridional tendon was prestressed with the prescribed value of 503 kN and then loosed to the prescribed value of 470 kN. As for hoop tendon initial stress of 991 MPa, corresponding to the average value of hoop tendon stress, was imposed.

## 3. SENSITIVITY STUDIES FOR THE DETERMINATION OF ANALYTICAL MODELINGS

This section describes the analytical techniques to obtain appropriate analysis results. The main techniques are treatments of dome part meridional tendon, consideration of soil spring and treatment of gravity.

### 3.1 Treatment of dome part meridional tendon

Two modelings of meridional tendon in dome part were compred. The one model simulated hoop stiffness in the meridional tendon above 45° dome angle (model (a)), and the other model simulated hoop stiffness in the meridional tendon above spring line (model (b)). The difference of two models was observed from 2.3 Pd. The apex displacement of model (a) increased in downward direction, while in model (b) it increased in upward direction.

The difference of displacement for two models depended on cracking condition in hoop direction. The difference of cracking condition for the two models became remarkable at 2.4 Pd. In model (a) cracking extended to dome part, while in model (b) it occurred in the cylinder part only.

As mentioned above, the vertical displacement depended on tendon modeling in the dome part. However, the test model failure will occur near penetrations in the middle cylinder part and the strain distribution of the cylinder part for both models were same. The model (a) was finally selected in the present analysis because of the better convergence under higher internal pressure.

### 3.2 Consideration of soil spring

Ground stiffness affects the global deformation behavior via ground reaction force under high internal pressure condition. Therefore, the reaction force of the ground was taken into account by placing soil springs at each node of basemat. The uniform soil spring stiffness values of $1x10^{12}$ N/mm, $1x10^{6}$ N/mm, $1x10^{4}$ N/mm and $1x10^{2}$ N/mm were used for sensitivity analysis. As a result, it was found that soil spring stiffness affected not only deformation behavior but also the convergence under high internal pressure condition. The difference of analysis results under high pressure condition was governed by the uplift condition of the basemat. The stiffness values of $1x10^{6}$ N/mm provided the best convergence which was consistent with the ground stiffness of actual test site of 30 MPa[4]. Therefore, the value of soil spring stiffness was finally distributed in proportion to the node area on the bottom of basemat which provided 30 MPa ground stiffness at each node.

### 3.3 Treatment of gravity

Gravitational force should be considered correctly to evaluate uplift behavior of the model, since actual soil spring of 30 MPa was adopted. Two models were compared. In one case, gravity was considered as concentrated mass at each Gaussian point as usual and in the other case, gravity was considered only at the bottom of the basemat as concentrated force.

Both analysis results were almost same, because vertical force by gravity was negligible compared with tendon tension force. For example, force balance of two elements at the apex of dome was evaluated as follows. Vertical component of the tensile force of meridional tendon was 25 kN. On the other hand, the vertical force by gravity was 0.49 kN, which was only 2 % compared with meridional tendon vertical force. Therefore, the gravity was considered only at the bottom of basemat as concentrated force.

In the ABAQUS model gravity is usually considered as concentrated mass at each Gaussian point and the displacement is calculated by solving equation of motion. Hence, calculation time was longer and the convergence of calculation became worse under large displacement condition.

## 4. ANALYSIS RESULTS

### 4.1 Structural behavior of 1/4 PCCV model

#### (1) Global deformation behavior

Figure 2 shows global deformation behavior for various internal pressures. A slight inward deformation was observed under setting condition due to the influence of prestressing. The cylinder part shape under 1.5 Pd became almost same as that before prestressing. The dome part deformed inward slightly under this pressure. The mid cylinder part begun to deform in outward direction at 2.2 Pd, while the dome part was compressive condition. Outward deformation of the mid cylinder part became remarkable at 3.6 Pd so that the dome part deformed downwards.

#### (2) Local displacement behavior

Figure 3 shows radial displacements versus pressure at various locations. The largest displacement was analyzed at slightly upper region (No. 4) from the mid plane of cylinder part. This was because the constraint force at basemat was larger than that at dome part. The region near the basemat (No. 5) and the dome (No. 2) part had small displacement. The displacements in the cylinder part (No. 3), (No. 4) increased linearly until about 2.1 Pd,

in which concrete cracking occurred in hoop direction as described below. They increased drastically at about 3.5 Pd due to the concrete cracking in meridional direction.

Figure 4 shows vertical displacements versus pressure at various locations. The apex (No. 1) had maximum downward deformation at setting condition due to the existence of mesh-like meridional tendon. Downward displacement of the apex decreased linearly up to about 2.4 Pd and it increased from about 2.4 Pd. However, it deceased from 3.6 Pd again, since vertical concrete cracking crack extended to the whole cylinder part. The displacement at 45° point from spring line (No. 2) had also downward deformation. It was smaller than the displacement at the apex. The displacement at mid part of cylinder part (No. 4) and spring line (No. 3) gradually increased until about 3.2 Pd and increased drastically from 3.5 Pd. The displacement near basemat (No. 5) deformation remained small.

#### (3) Concrete cracking behavior

Figure 5 shows concrete cracking behavior in both hoop and meridional directions. Hoop cracking initially occurred at 2.1 Pd (Fig. 5(a)-2). The hoop cracking caused the non-linear radial displacement as shown in Fig. 3. The hoop cracking extended above spring line at 2.4 Pd (Fig. 5(b)-2). Since the dome part constraint force was large, linear vertical deformation of cylinder part was maintained up to about 2.4 Pd as shown in Fig. 4. The cylinder part deformed outward slightly as shown in Fig. 2(c). Although outer surface cracking in the meridional direction extended to cylinder part at 3.4 Pd, there was no inner surface cracking as shown in Fig. 5(c)-1. Both hoop and meridional cracking almost extended to the whole region at 3.6 Pd (Fig. 5(d)), under which radial displacement increased drastically as shown in Fig. 5. Concrete stiffness became almost zero in both hoop and meridional directions at 3.6 Pd. Hence, vertical displacement in dome part changed from downward direction to upward direction as shown in Fig. 4. Bending behavior was observed in the meridional direction so that meridional cracking mainly occurred outside of concrete wall as shown in Fig. 5(d)-1.

#### (4) Strain distribution

Figure 6 shows hoop liner strains versus pressure at various locations. Hoop liner strain remained negative until about 1.5 Pd due to the tensile force of tendon. The liner strain of mid part (No. 4) of cylinder increased non-linearly from about 2.1 Pd and it increased drastically at about 3.5 Pd. These were closely related to the concrete cracking condition in the hoop direction at 2.1 Pd as shown in Fig. 5(a)-2 and concrete cracking in meridional direction at 3.6 Pd as shown in Fig. 5(d)-1. Although similar strain behavior occurred at spring line (No. 3) and dome part (No. 2), the strain level was lower than that in mid part of cylinder. The strain near basemat (No. 5) was almost zero because of the strong constraint force of the basemat. The hoop stiffness of concrete became almost zero at 3.4 Pd and the rebar in cylinder part was almost yielded at this pressure (yield stress : 459 MPa). That is, the change in liner strain was explained by the changes in concrete and rebar stiffness.

Figure 7 shows the meridional liner strain versus pressure at various locations. The meridional strain near basemat (No. 5) was increased non-linearly from about 2.0 Pd due to the initiation of ballooning of cylinder part as shown in Fig. 2 (c). On the other hand, the strains of other locations were very small up to 3.4 Pd due to the lack of inner surface concrete cracking in meridional direction as shown in Fig. 5(c)-1. The strain of spring line (No. 3) increased drastically from 3.4 Pd, because the spring line deformed outwards remarkably as shown in Fig. 3 and the dome part was tensiled in both hoop and meridional directions. As a result, the strain was concentrated at spring line where structure was discontinuous.

Figure 8 shows the hoop strains of tendon. It exhibited similar behavior as liner strain if the initial prestressing strain condition was considered.

### 2.3.2 Summary of global analysis

Figure 9 shows the distribution relationship of hoop stress of outside concrete, hoop stress of outside rebar and hoop stress of tendon, in contrast with the cracked region in hoop direction and the overall deformation for several values of Pd.

The stress of tendon and outside rebar were almost uniform under 2.0 Pd condition as shown in Fig. 9(a). Because internal pressure was imposed equally on the inner surface of containment and hoop rebar and hoop tendon were not constrained by the vertical force under low pressure condition. The stress of concrete was nearly uniform in the cylinder part except near basemat and spring line, since the constraint forces of dome part and basemat governed the local displacement. The concrete stress decreased along the top of the dome and increased slightly in the apex region. Since hoop stress was proportional to the radius, the membrane stress should reduce to

zero at the apex. However, outside stress increased slightly at the apex region because of the occurrence of bending behavior in the apex region.

Concrete crack initiated at 2.4 Pd, thereby the stress of concrete in the cylinder part decreased as shown in Fig. 9(b). As a result, the stress of rebar and tendon increased remarkably. This clearly demonstrated the role of prestressed concrete, in that the decreasing stress of concrete was supplemented by rebars and tendons.

The stress of concrete became almost zero and the stress of rebar became nearly uniform because of the yielding at 3.7 Pd as shown in Fig. 9(c). The stress of tendon also became nearly uniform in the cylinder part because of the yielding. Hence the displacement increased in the radial direction remarkably.

In summery, concrete cracking governed the global behavior of PCCV. That is, the reduction of concrete stress due to cracking caused the changes in stress distribution of rebars and tendons and resultant global deformation behavior.

## ACKNOWLEDGMENTS

This work is sponsored under the contract by the Ministry of International Trade and Industry, Japan.

## REFERENCES

(1) Twidale, D., and Crowder R., 1991, "Sizewell 'B' - a One Tenth Scale Containment Model Test for the UK Programme," Nuclear Engineering and Design 125 85-93

(2) Horschel, D. S., 1992, "Experimental Results from Pressure Testing A 1:6-Scale Nuclear Power Plant Containment," NUREG/CR-5121, SAND88-0906

(3) Kashiwase, T., and Nagasaka, H., 1997, " Analysis Study on Change of Tendon Tension Force Distribution during the Pressurization Process of Pre-stressed Concrete Containment Vessel, " Proceedings of ICONE-5

(4) Miller, C. M., 1992, "Geotechnical Investigation job No. 1-20904 Containment Technology Test Facility - west Albuquerque, New Mexico," GEO-TEST

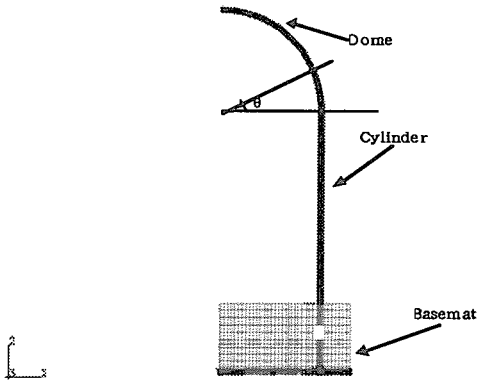



Fig. 1 Axisymmetric global analysis modeling

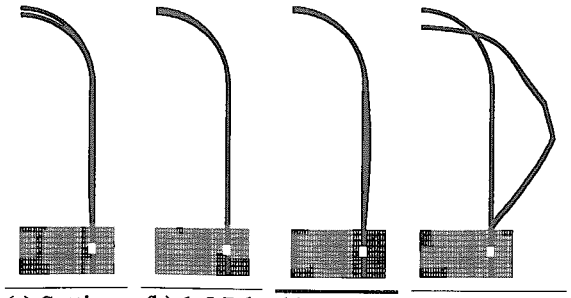



Fig. 2 Deformation of test vessel for various internal pressures

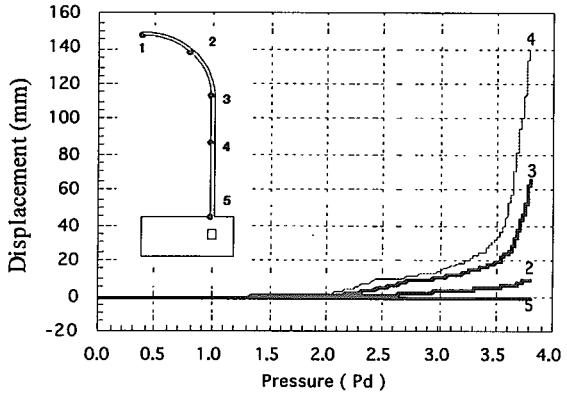



Fig. 3 Radial displacements at various locations

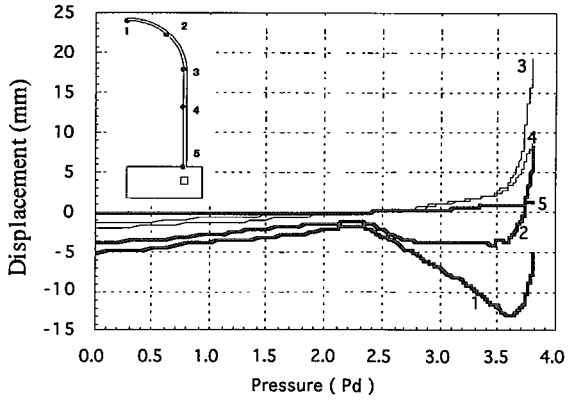



Fig. 4 Vertical displacements at various locations

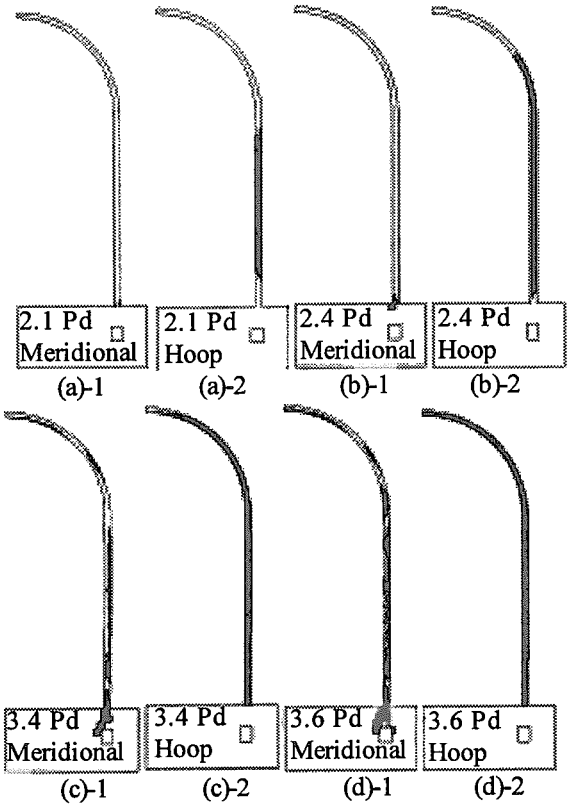



Fig. 5 Concrete cracking behavior in both hoop and meridional directions

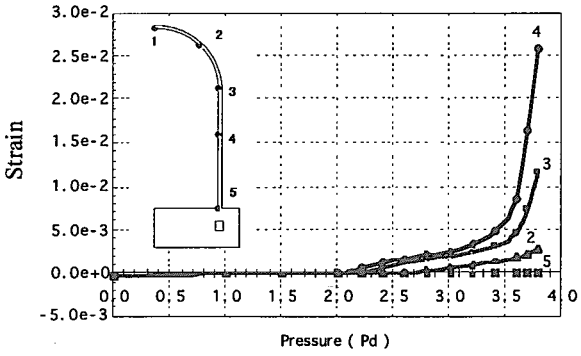



Fig. 6 Hoop liner strains at various locations

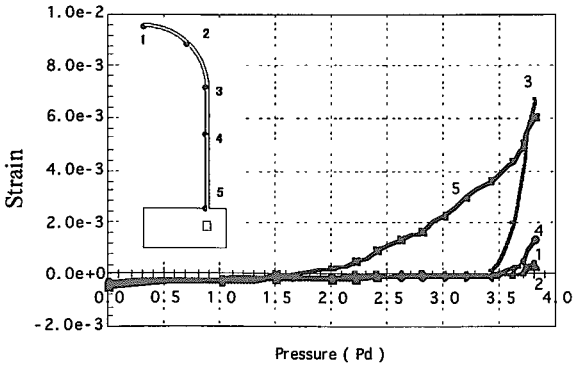



Fig. 7 Meridional liner strains at various locations

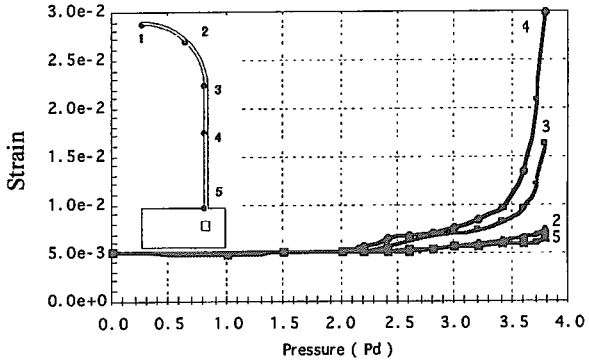
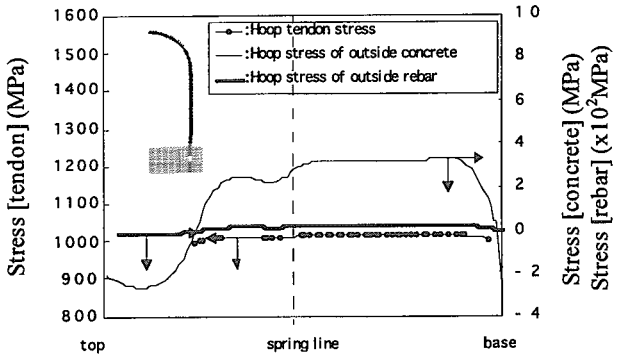
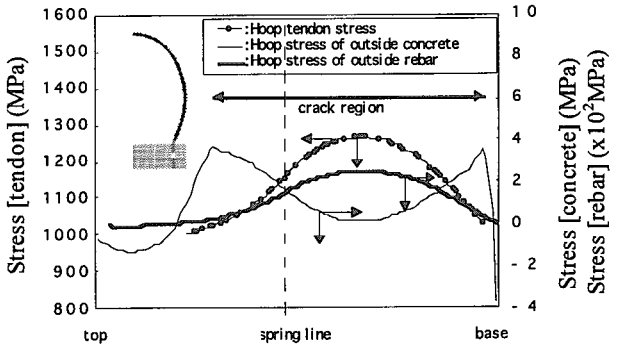


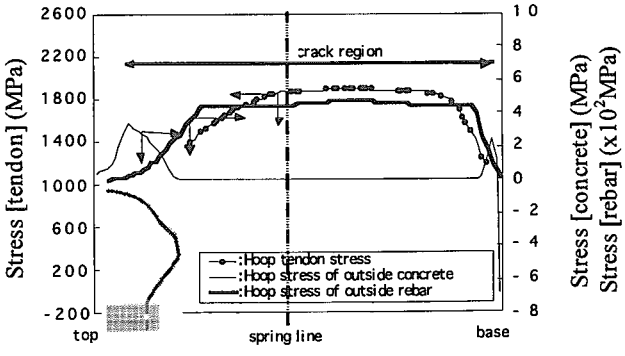

Fig. 8 Hoop tendon strains at various locations




(a) 2.0 Pd




(b) 2.4 Pd




(c) 3.7 Pd

Fig. 9 Relation of several stresses at various internal pressures

# 14. Panel Discussion

# Link of Severe Accident Research Results to Regulation : Current Status and Future Perspective

Chairperson: K. Ishijima (JAERI, Japan)
Panelists: M. Sonnenkalb (GRS, Germany)
A. V. Jones (JRC Ispra, Italy)
H. Nagasaka (NUPEC, Japan)
K. Yahagi (TEPCO, Japan)
J. F. Costello (NRC, USA)

This is a blank page.

# PANEL DISCUSSION

"Link of Severe Accident Research Results to Regulation: Current Status and Future Perspective"

Panelists: Martin Sonnenkalb (GRS, Germany)
Alan V. Jones (JRC/Ispra, Italy)
Hideo Nagasaka (NUPEC, Japan)
Kimitoshi Yahagi (TEPCO, Japan)
James F. Costello (NRC, USA)

Chairperson: Kiyomi Ishijima (JAERI, Japan)

## 1. Opening

Ishijima opened the session of Panel Discussion. He briefly introduced himself and showed the theme of the Panel Discussion. Then each panelist introduced himself on his background and current activities concerning severe accident.

## 2. Summary of Panel Discussion

Ishijima showed the agenda of the Panel Discussion. It consists of two parts; keynote presentation by each panelist and discussion on the specific topics.
As Part I, each panelist was asked to present his views on the following items:

(1) What is the position of severe accident in your domestic regulatory policy?
(2) Do you feel that there are sufficient severe accident research results to reflect them in regulation?
(3) What is your view for the future perspective of link of severe accident results to regulation?
(4) Others.

Sonnenkalb started with the explanation about GRS and the use of severe accident research results in GRS. He mentioned that no definitive

information is available on the current position of severe accident and nuclear energy due to change in German government since September 1998. He pointed out that severe accident research and intensive exchange of results is still needed.

Jones presented his views on each item. According to his viewpoint current research focus is mostly on the containment and measures for its protection. He also emphasized that more precision in modeling and data are needed.

Nagasaka first explained about the chronology of accident management policy in Japan and then he presented his views on molten core concrete interaction. He pointed out that the possibility of ex-vessel debris cooling by water injection should further be investigated in order to avoid premature conclusion.

Yahagi started with the explanation of severe accident management in Japan and then mentioned about consideration of severe accident for future light water reactors. After that he summarized the evaluation of containment integrity against severe accident phenomena.

Costello summarized severe accident research programs at NRC and regulatory implications of severe accident research. He gave MOX and high burnup fuel behavior as examples as future perspectives on severe accident research.

Ishijima indicated the following issues to be discussed among panelists and participants.

(1) What is most important remaining severe accident issues from the point of view of regulation?
(2) Application of severe accident related regulations to the future plant based on the experience of applying severe accident research results to the assessment of measures taking accident management strategies.

The main points of the discussion among panelists and participants are as follows:

(1)Severe accident research has been progressed in the past years and major

phenomena have been clarified, but still there are a lot of phenomena to be resolved.

(2)Among the unresolved severe accident phenomena molten core concrete interaction (MCCI) is most important issue to be investigated. It is pointed out that analytical results for MCCI with existing codes remarkably differ from each other. Interaction between molten material and preexisting water on the floor is also important from the accident management point of view.

(3)Containment bypass and hydrogen risk are also important to be resolved in future severe accident research.

(4)Scaling method for applying the experimental results to actual plant is one of the important issue to be considered.

(5)Severe accident management for existing plants are to be implemented as utility's self-regulatory activity in Japan.

(6)The self regulatory guideline for severe accident consideration for future LWR containment in Japan was summarized in an open document. The guideline is out of regulation. The document will be revised based on new findings obtained through future severe accident research.

(7)The severe accident research results are also important for technical support center staffs for understanding accident phenomena in taking accident management measures.

(8)There will be no possibility of steam explosion during water pouring on molten material on the containment floor. If the water pool on the containment floor is shallow, a steam explosion will not occur when molten material falls into the pool. A steam explosion will occur only when molten material falls into a deep water pool.

(9)Currently the approach to severe accident regulation in each country is different. In future, international harmonization of safety

standards and approach to safety may be necessary. We have to reduce uncertainty on severe accident phenomena through research to get international consensus.

Ishijima made a brief summary of the panel discussion as follows;
Among the severe accident phenomena, molten core concrete interaction is recognized as most important issue. Staff action is important to take proper procedures of accident management for mitigation of severe accident consequences. Integration of severe accident research results is necessary. International collaboration and exchange of available data are important and we have to look for effective way through such as this kind of international conference.
Finally he thanked all the Panelists and participants for their active contribution to the Panel Discussion.

Severe Accident Research in Japan (SARJ-99), November 8-10, 1999
Panel Discussion

# Link of Severe Accident Research Results to Regulation: Current Status and Future Perspective

Dr. Martin Sonnenkalb
Gesellschaft für Anlagen- und Reaktorsicherheit (GRS) mbH
Cologne, Germany

## What organizations are supporting GRS?

- GRS is an independent organization supporting the German Ministries with regard to questions and other topics of the nuclear energy business
- GRS is financed by order of research projects on different aspects not only in the field of nuclear energy
- main employers of GRS are:
  - Federal Ministry for Environment, Nature Conservation and Nuclear Safety (BMU)
  - Federal Ministry for Economics (BMWi)
- other employer of GRS:
  - European Community - EC

## Who is responsible for funding the Severe Accident (SA) research?

- experimental research connected to reactor safety is performed at different Research Centers and supported by BMWi
- investigations for generic plant applications are financed by BMU
- investigations for specific or real plant applications are financed by the industry

## What is the current position of SA and Nuclear Energy in Germany?

- no definitive information available due to change in German government after German election of September 1998
- use of NPP's in Germany
  - limited use of nuclear energy for only several years is foreseen by the new government, but the timing is still under discussion within members of government (socialist democrats and "green people")
  - also ongoing discussions between government and industry to achieve an agreement on the future of the German NPP's
- research with regard to nuclear safety and SA
  - ongoing experimental research with decreasing budgets on main aspects of SA (e.g. core quenching, late phase of core melting, fuel behavior)
  - research at GRS on future reactors (e.g. EPR) funded by German Ministries is already stopped
  - ongoing code development (ATHLET-CD, COCOSYS, ASTEC)
  - ongoing research activities at GRS on SA management and PSA Level 2

## How do GRS use the results of SA research?

- for code development and code validation
  - ATHLET-CD - detailed thermal hydraulic code for DBA and SA analysis
  - COCOSYS - detailed containment code for DBA and SA analysis
  - ASTEC - integral code:
    - common development together with IPSN, France
    - validation within an EC project of 5. Framework Program
- direct use as part of SA management component qualification, e.g. development of a concept of Passive Autocatalytic Recombiners (PAR)
  - investigation of plant specific SA scenarios by integral codes (MELCOR, ATHLET-CD)

  - investigations by detailed codes (COCOSYS) based on integral code results to optimize the plant specific PAR concept
  - additional investigations by FZK with GASFLOW code
  - GRS recommendation of such a system discussed at German Reactor Safety Commission (RSK)
  - PAR system installation recommended by German RSK
  - PAR system licensed plant by plant by local government
  - PAR implementation ongoing in all German plants, finished in 4 of 13 PWRs
- operator training
  - training of plant personal by lectures on SA combined with demonstration by GRS simulator ATLAS (see paper of SARJ 98)

**Are you satisfied with the SA results you have used so far or which are available? YES and NO**

- codes:
  - main improvements of existing codes
  - main phenomena of early phase of SA modeled
  - limitations in late phase (e.g. molten pool formation, crust behavior, FCI, long term MCCI)
  - use of SA codes for accident management have been done (e.g. PAR concept)
- experiments:
  - some of the issues are solved, e.g. hydrogen issue, RPV ex-vessel coolability, principles of MCCI, DCH
  - results with larger uncertainties are existing for other issues, e.g. fission product release and transport, FCI, core quenching, RPV failure mode under different boundary conditions, long term MCCI, ex-vessel melt coolability

**How have such SA research results affected the decision making related to protection against SA?**

- a technical solution related to SA should not be realized in case of large uncertainties for a very sensitive parameter
- SA management measures and new reactor concepts must be simple and robust
- the enhancement of the safety is the overall goal of a measure and have to be demonstrated

**Where and why do you see further need of SA research?**

- properties and chemical reaction kinetics for real plant materials influencing:
  - RPV vessel failure mode -> chemical interaction of corium with RPV wall
  - FCI -> influence on energetic of steam explosion and probability to fail the vessel
  - long-term MCCI
  - debris - or spreaded melt coolability
- long-term slow gas flows and natural convection pattern of gases in RCS and containment:
  - heat up of structures
  - gas- and aerosol distribution
  - fission product re-evaporation
  - source term to the environment
  - SA instrumentation and process indicators to assess the plant status and to initiate SA measures

**Summary**

- The existing international data base of experimental results is large and was never used in total by the experts of the different countries, e.g. due to restrictions in the data exchange agreements.
- In addition research results gained in the past will not satisfy to days requirements e.g. for the verification and use of CFD-tools
- SA research and intensive exchange of results is still needed.

SARJ'99: Panel Session

# Severe Accident Research and Regulation: Current Status and Future Prospects

A.V. Jones
Institute for Systems, Information and Safety - ISIS
European Commission - Joint Research Centre - Italy

**Research**

CSARP, EUROSAFE, FISA, SARJ, CSNI...

**Regulation**

CNRA, Phebus Ad-Hoc Group, STU, VASA...

| Plant | Regulator |
|---|---|
| Design<br>Operating Procedures<br>Maintenance<br>Training<br>Backfits<br>Uprating<br>...<br>so: stimulus to and evaluation of design and operational solutions | Licensing<br>IPRs<br>Lifetime extension requests<br>Incident reviews<br>...<br>so: issues, detailed questions |
| Research<br>Understanding<br>Expertise<br>Tools e.g. integral and detailed codes<br>Data<br>... | |

## Current Status – Regulation

Reduced "demand" from industry
- Higher burnup
- Reduced regulatory burden
- Lifetime extension
- Some new designs and revisited concepts: EPR, HTR, ADS..

Regulators not at centre of political debate
No uniform regulations – more mutual tolerance
Severe accidents almost design basis
Concern about E. Europe

## Current Status – Research

In the EU only F,D still have major experimental programmes
Some focal international projects eg CABRI, PHEBUS FP
Analysis and code development proceeding but no great demand
Difficult to maintain and develop expertise
Negative vibes from the rest of the world
Research focus is mostly on the containment and measures for its protection

- Core melt control
- Hydrogen threat countermeasures
- Dealing with overpressure
- Limiting leaks (including long-term)

## EC's Particular Interests

Harmonisation of safety criteria (single market, civil protection)
Realistic standards for accession countries
Assistance to CIS
International cooperation

## Future Prospects

### The context

Environment and climate-related constraints and world industrialisation vs political coolness towards the nuclear option
OECD's most likely scenario: constant NPP output, declining % of electric power
Even this means resuming construction – life extension is only short-term. Imported reactors in EU?
Goal should be higher economic performance **and** increased safety (cf car, plane industries)

### Regulation

Multi-criteria optimisation means in practice that regulators should press for high weight for safety.
A higher profile for regulators as defenders of public safety would benefit the nuclear debate.

### Research

The optimisation process (safety and economics) needs **more precision** in modelling and data than hitherto.

- Detailed modelling – more sharing with other industries
- Better-instrumented experiments
- But real materials still needed!
- Tools and understanding to evaluate severe accident management measures and procedures

Also need "safety generalists", able to identify emerging issues, guide research strategy, and inform the political debate
Can we act to meet this future fully prepared?

# Link of Severe Accident Research Results to Regulation: Current Status and Future Perspective

## SARJ-99 Panel Discussion

November 10, 1999 Tokyo

H.Nagasaka
Systems Safety Department of NUPEC

## Chronology of Accident Management Policy in Japan

- Recommendation of SA countermeasures (Accident Management) by Japan nuclear safety commission in May 1992
- Directive from MITI to all electric power companies on the future direction of AM in July 1992
- Completion of review on utility AM report by MITI in June 1994
- Completion of review by Japan nuclear safety commission in November 1997
  - Proposed AM appropriate
- Preparation of self-regulatory documents by utility in March 1999

# Major Remaining Issues Directly Related to AM

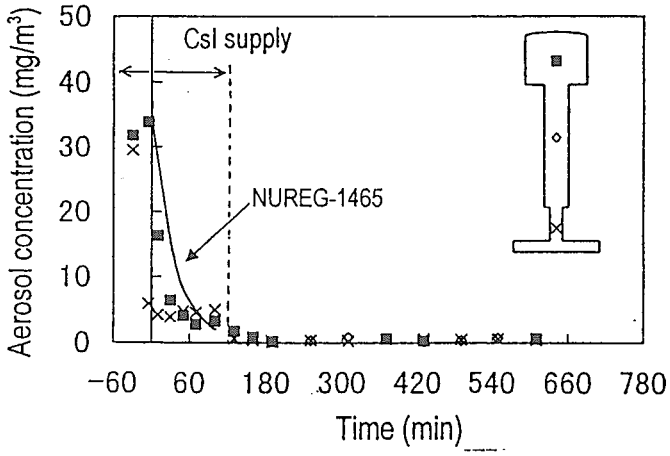
[1] Possibility of Ex-vessel Steam Explosion (SE)
- Low pressure and high subcooling condition under which SE likely to occur
- Few available data ... KROTOS/COTELS

[2] Suppression of MCCI by Water Injection
- Pessimistic Results ... SWISS/WETCOR/MACE
- Optimistic Results ... COTELS

[3] Total Amount of Hydrogen Generation
- 13% hydrogen concentration kept or not
- Uncertainty existed due to MCCI uncertainty

[4] FP Removal by Containment Spray under AM Conditions
- NUREG-1465 developed under DBA conditions
- Few available data

## CsI Mass Concentration in the Drywell (Case 2)




*Eq. in NUREG-1465

$$\lambda = \frac{3hF}{2V}\frac{E}{D}$$

F=840 m³/h
V=7,400 m³
h=10 m
E/D=1 m⁻¹

- Before CsI supply stopping, CsI concentration transient in the entire D/W was similar to the reference case because of same test conditions.
- After CsI supply stopping, the concentration decreased rapidly and reached to zero, which was similar to PWR case.
- The aerosol removal rate estimated from the equation in NUREG-1465 was coincided with test result, which justified NUREG model even under SA condition.

Nupec

## Major Remaining Issues Directly Related to AM (Cont'd)

[5] External Flooding AM of Reactor Pressure Vessel
- Extensive test programs conducted in US, Japan, France, Finland and Russia
- Temperature and melting stratification well not understand
- Applicable to high power rating plant or not

[6] Pursuit of Cooling Mechanism of Corium Falling into Lower Plenum to Expel Simple Conservative Models
- Several test programs on going in Korea, Germany and Sweden
- Interesting results expected

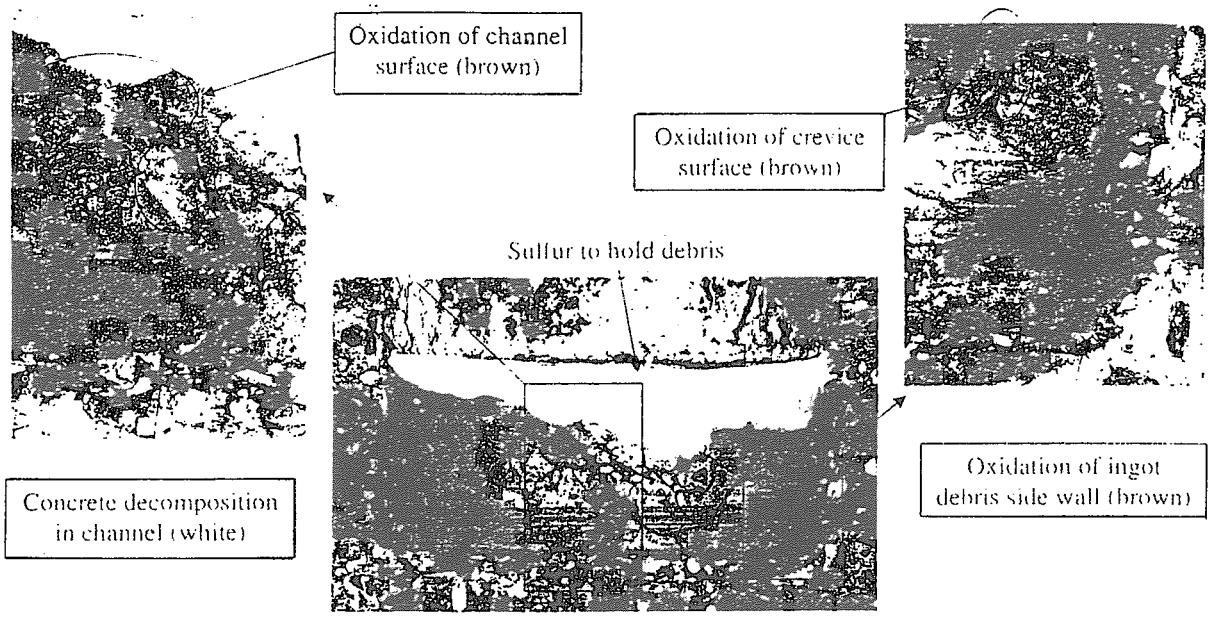
## Suppression of MCCI by Water Injection Possible or Not?

[1] Pessimistic Results ... SWISS/WETCOR/MACE
- Continuation of MCCI
  - Adhesion of upper crust to side wall
  - Existence of large void below upper hard crust

[2] Optimistic Results ... COTELS
- Suppression of MCCI
  - Absence of adhesion of crust to side wall by adopting induction heating
  - Existence of channels in ingot debris formed by the remaining porosity due to simulation of corium falling process and MCCI generated gas
  - Better conditions of water penetration into debris via two flow paths of clearance between eroded side wall and channels in ingot debris
  - Absence of large void
  - Formation of heat resistance of pebble bed below ingot debris

Should avoid premature conclusion and pursue the possibility of ex-vessel debris cooling by water injection

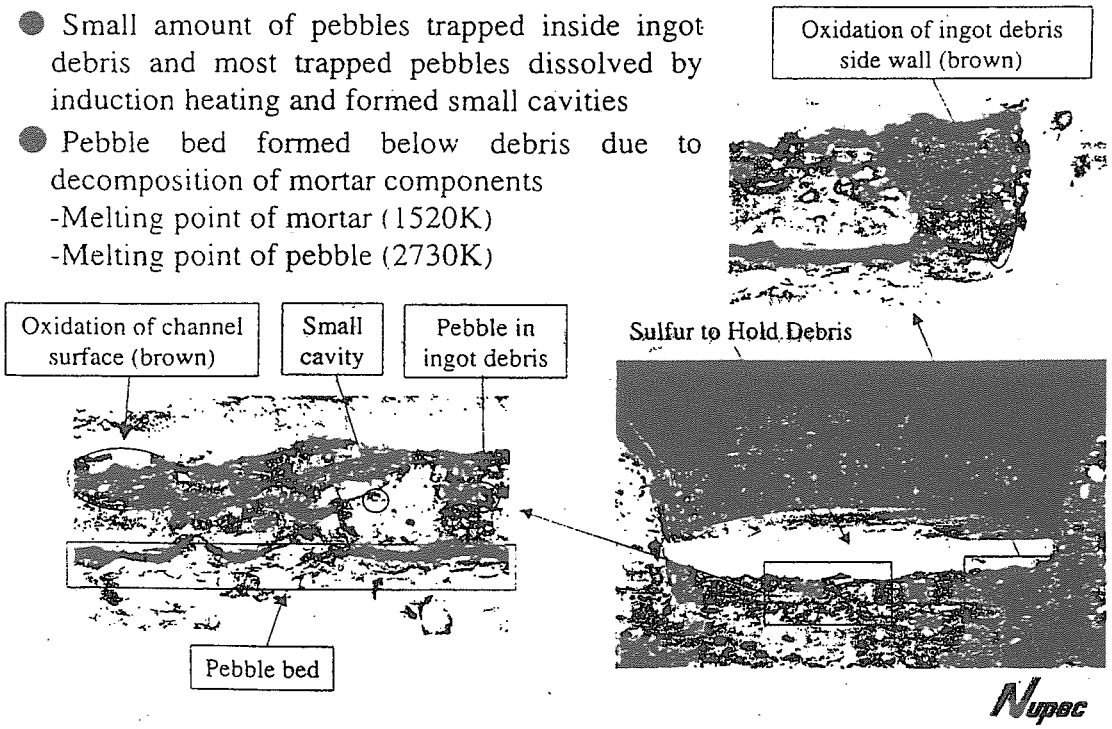
## Evidence of Water Penetration into Channels and Clearances (B/C-5)




Nupec

## Entrainment of Pebbles and Pebble Bed Formation (B/C-9)

- Small amount of pebbles trapped inside ingot debris and most trapped pebbles dissolved by induction heating and formed small cavities
- Pebble bed formed below debris due to decomposition of mortar components
  -Melting point of mortar (1520K)
  -Melting point of pebble (2730K)




Nupec

*The Workshop on Severe Accident Research, Japan (SARJ-99)*
*November 8-10, 1999, Tokyo*

# Consideration of Severe Accident for Future LWRs

Kimitoshi Yahagi
Tokyo Electric Power Company

1

## Severe Accident Management in Japan

- Status of Severe Accident Management (SAM) in Japan
  - NSC & MITI Recommendations (1992):
    - To study on IPE & SAM strategies
  - Utilities Report to MITI (1994/Mar):
    - All LWRs in operation & construction (28 BWRs & 23 PWRs)
    - IPE result, SAM strategy, framework of implementation
  - MITI concluded utilities' report to be appropriate (1994/Oct), and NSC approved MITI's conclusion (1995/Nov)
  - SAM implementation is to complete by 2003 JFY for all existing plants
- Principle of SAM in Japan
  - SAM implemented as utility's self-regulatory activity, no licensing basis
  - For construction plants, it is strongly recommended to report SAM strategy before fuel loading (substantially a part of licensing)

2

## Consideration of SA for future LWRs

- For future LWRs, larger margin for SA expected with systematic and comprehensive consideration of SA in the design phase
  - To enhance safety margin in a cost-effective manner
  - To facilitate AM activities
  - International harmonization of safety standards for future LWRs (ex. IAEA TECDOC-801, EUR, URD)

⇨ Desired to develop the guideline for SA consideration in future LWR containment

3

## Development of the guideline for SA consideration in future LWR containment

- Committee organized in NSRA (Nuclear Safety Research Association) under the sponsorship of utilities (Feb.1996～Mar.1999)
- Chairman: Prof. S. Kondo (Univ. of Tokyo)
- Members: academia, research institutes, utilities & vendors in Japan

⇨ Guideline to be used as self-regulation document for Japanese nuclear industry

4

Nov. 10, 1999 SARJ-99 Panel Discussion (K. Yahagi)

## Structure of the guideline

- Consisting of two approaches
  - Evaluate the conformance to Containment Safety Objectives (CSOs) through PSA
  - Evaluate containment capability to withstand SA phenomena
    - To confirm the capability of containment to SA challenges
    - To facilitate control of SA with design & management

5

## Containment Safety Objectives (CSO)

Safety Objectives

Prevention of core damage: CDF<$10^{-5}$/RY

Containment Safety Objectives
- CSO-1: No need for evacuation (< $10^{-6}$/RY)
- CSO-2: No deterministic health effect & no need for long-term relocation (< $10^{-7}$/RY)
  - These criteria such as "No need for evacuation" are interpreted in CRF (Containment Retention Factor)

Reference Objectives
CCFP < 0.1, Large release earlier than 24hrs < $10^{-7}$ /RY
Containment bypass < $10^{-7}$ /RY

Derived CRFs for each nuclide group

$$CRF = \frac{\text{Release into containment}}{\text{Release to environment}}$$

| | | BWR | | | PWR | | |
|---|---|---|---|---|---|---|---|
| | | noble gas | gaseous iodine | particle | noble gas | gaseous iodine | particle |
| CSO-1 | elevated release | 92 | 290 | 5500 | 92 | 360 | 6800 |
| | ground release | 180 | 1600 | 30000 | 180 | 2000 | 37000 |
| CSO-2 | elevated release | 19 | 3.9 | 720 | 19 | 4.8 | 820 |
| | ground release | 36 | 13 | 3900 | 36 | 16 | 4500 |

6

Nov. 10, 1999 SARJ-99 Panel Discussion (K. Yahagi)

## Evaluation of containment integrity against SA phenomena

- SA phenomena to evaluate
  - Overpressure & Overtemperature · Hydrogen burning (incl. Detonation)
  - MCCI · DCH · FCI · Recriticality · Shell Attack
- Evaluation framework
  - Consideration of likelihood (given core damage, absolute) & seriousness
    - Low likelihood & energetic load (detonation, DCH, FCI)
      - Confirm the prevention of occurrence with design & management
    - High likelihood & non-energetic load (Overpressure & Overtemperature, MCCI)
      - Confirm the capability of containment to withstand the thermal & mechanical load
- Best-estimate approach
  - Best-estimate (non-conservative) evaluation of SA load
  - Credit on realistic structural integrity of containment
  - No single failure criterion
  - Credit on non-safety related SSCs & management

7

## Evaluation for SA phenomena

Overpressure & Overtemperature

Evaluation condition:

- Containment pressure/temperature for representative and significant (in terms of probability) scenarios
- Evaluate under best-estimate condition considering heat & pressure source as follows;
  - Decay heat
  - $H_2$ generation due to metal oxidation
  - Non-condensable gas generation due to MCCI
  - $H_2$ burning

Reference criterion:

- Structural integrity of containment to be retained for 24hrs
  (ex. ABWR-RCCV: based on test data, judged to withstand up to 2Pd & 200℃ realistically)

8

Nov. 10, 1999 SARJ-99 Panel Discussion (K. Yahagi)

## Evaluation for SA phenomena

### Direct Containment Heating (DCH)

Design requirement:

- Reliable RCS depressurization system for prevention of HPME (probability of failure $<10^{-3}$/demand)

Evaluation of DCH prevention

Evaluation condition: RCS pressure for representative & significant scenarios

Reference criterion: RCS pressure < 20kg/cm$^2$ before RPV breach

Evaluation of DCH impact

Reference evaluation for better management & containment configuration (suppressing debris dispersion)

Reference criterion: Containment structural integrity to be retained

9

## Summary

- SA is out of the domain of regulatory requirement, However SA consideration is indispensable for both existing & future plant
  - Probability of SA sufficiently low
  - Containment designed has large margin against SA
- Implementation of SAM was recommended by NSC & MITI
- Guideline for SA consideration in future LWR containment developed on the basis of knowledge obtained from SA research
  - And can be modified with the progress of the knowledge of SA hereafter

10

Nov. 10, 1999 SARJ-99 Panel Discussion (K. Yahagi)

United States Nuclear Regulatory Commission

# LINK OF SEVERE ACCIDENT RESEARCH RESULTS TO REGULATION: CURRENT STATUS AND FUTURE PERSPECTIVES

**Panel Discussion at The Workshop on Severe Accident Research, Japan (SARJ-99)**

**Presentation by**

**James F. Costello**
**Office of Nuclear Regulatory Research**
**U.S. Nuclear Regulatory Commission**

**November 10, 1999**

## SAFETY POLICY TO SUPPORT REGULATORY DECISION MAKING

- Safety policy is based on a defense-in-depth strategy a key element of which is accident prevention
- Existing plants pose no undue risk to public health and safety; no need of generic rulemaking for severe accidents
- However, consideration of severe accidents in regulatory decisions and actions apparent from examples such as siting criteria, Part 100 dose calculations, ATWS and SBO rules, and IPE and IPEEE
- New plants are expected to achieve a higher standard of severe accident performance than prior designs

## SEVERE ACCIDENT RESEARCH PROGRAM AT USNRC

- Severe accident research has focused on understanding phenomena and issues that can challenge reactor pressure vessel and containment integrity
- Research has provided data and analytical tools to support risk assessment, resolve severe accident issues, and evaluate accident management strategies; some issues resolved and others nearing resolution
- Current severe accident research activities include: direct containment heating, fuel-coolant interactions and debris coolability, lower head integrity, fission product behavior, and severe accident codes

Page 3

## REGULATORY IMPLICATIONS OF SEVERE ACCIDENT RESEARCH

- Direct containment heating research has concluded that a PWR containment is unlikely to fail from a high pressure melt ejection event because of inherent design features and capacity of the containment; there is also a high probability that melt ejection may not occur due to depressurization of RCS from hot leg or surge line failure
- Steam explosion research has concluded that the alpha-mode failure is of little or no significance to the overall risk of a nuclear power plant; research has further concluded that reactor core melt has little propensity for explosion and thus, RPV and containment integrity from a steam explosion event may not be as severely challenged as originally estimated
- As a result, no regulatory requirement or burden needs to be imposed on the licensees with regard to the DCH and the alpha-mode issues

Page 4

## REGULATORY IMPLICATIONS OF SEVERE ACCIDENT RESEARCH (continued)

- Hydrogen combustion research investigated potential challenges to containment integrity resulting from various modes of hydrogen combustion during severe accidents, and provided technical basis for the resolution of hydrogen combustion in PWR dry containments; resolution has led to removal of hydrogen recombiners in some nuclear plants

- Revision of the accident source term for light water reactors allowed an increase in actuation time for some engineered safety features and relaxed requirements for some dose mitigation systems

- Revision of source term has the potential to significantly reduce current regulatory burden on the licensees; likewise, curtailing hydrogen management measures without sacrificing safety has the potential to reduce burden as well

Page 5

## REGULATORY IMPLICATIONS OF SEVERE ACCIDENT RESEARCH (continued)

- Core-concrete interaction research has concluded that the likelihood for a Mark I containment liner to survive core melt attack is high provided the containment floor is flooded with water; the results were used by the BWR Owners' Group in developing severe accident management guidelines

- Severe accident research has led to two design-related fixes considered in the backfit category: hardened vent for Mark I containment and implementation of hydrogen control measures

- Severe accident research has also led to an improved understanding of phenomena with implications to accident management for operating reactors and accident prevention for new reactor designs; examples are: in-vessel retention, lower head integrity, etc.

Page 6

## FUTURE PERSPECTIVES ON SEVERE ACCIDENT RESEARCH

- With the transition to a risk-informed regulatory framework, some yet unresolved severe accident issues may be found not to pose as much risk as previously estimated; resolution of other issues may require that phenomenological uncertainties be reduced further and associated analytical tools be more precise

- Emerging issues such as MOX and high burnup fuel behavior and future design issues may create new avenues of severe accident research

# Appendix A Final Program

# *SARJ-99*

## *The Workshop on Severe Accident Research, Japan*

**Hotel Lungwood**
Tokyo, Japan
Phone: +81-3-3803-1234, Fax: +81-3-3803-2843

**November 8-10, 1999**

Organized by

**Japan Atomic Energy Research Institute (JAERI)**
and
**Nuclear Power Engineering Corporation (NUPEC)**

**Chairperson I. Takeshita (JAERI)**
**Co-chairperson H. Ogasawara (NUPEC)**

# Nov. 8 , Toki Room

| | | |
|---|---|---|
| 9:00 | **Registration** | |
| 9:30 | **Opening Remarks** | I. Takeshita (JAERI) |

## Plenary Session
## Overview of Research Activities

**Chairpersons: H. Nariai(Tsukuba Univ.), M. Sonnenkalb(GRS)**

| | | |
|---|---|---|
| 9:45 | Overview of Severe Accident Research at JAERI | K. Hashimoto (JAERI) |
| 10:15 | Present Status of Containment Integrity Tests at NUPEC | H. Nagasaka (NUPEC) |
| 10:45-11:00 | **Coffee Break** | |
| 11:00 | Practical Lessons from the First Three PHEBUS FP Tests | A. Jones (JRC) |
| 11:30 | Overview of Severe Accident Research at KAERI | S. Hong (KAERI) |
| 12:00-13:30 | **Lunch Break** | |

# Nov. 8 , Flower Room

## Session I
## Fuel/Coolant Interaction I

**Chairpersons: S. Miura(NUPEC), K. Moriyama(JAERI)**

| | | |
|---|---|---|
| 13:30 | Overview of KAERI Fuel Coolant Interaction Test | S. Hong (KAERI) |
| 14:00 | Installation for Low Temperature Vapor Explosion Experiment | S. Nilsuwankosit (Chula Univ.) |
| 14:30 | COTELS Fuel Coolant Interaction Tests under Ex-vessel Conditions | M. Kato (NUPEC) |
| 15:00-15:15 | **Coffee Break** | |

## Session II
## Fuel/Coolant Interaction II

**Chairpersons: S. Nilsuwankosit(Chula. Univ.), M. Kato(NUPEC)**

| | | |
|---|---|---|
| 15:15 | Three-Component Melt Jet Breakup Model for FCI Analysis | K. Moriyama (JAERI) |
| 15:45 | Numerical Analysis of Jet Injection Mechanism of Fuel-Coolant Interactions Using MPS | H. Ikeda (Univ. of Tokyo) |
| 16:15 | Study on the Effect of Subcooling on Vapor Film Collapse on High Temperature Particle Surface | D. Tochio (Yamagata Univ.) |
| 16:45 | Scoping Analysis of Steam Explosions in PWR Severe Accidents with JASMINE-pro | Y. Yang (Shanghai Jiao Tong Univ.) |
| 17:15 | **Adjourn** | |

# Nov. 8 , Sue-hiro Room

## Session III
## Accident Analysis and Modeling I

**Chairpersons: G. Bandini(ENEA), A. Hidaka(JAERI)**

| | | |
|---|---|---|
| 13:30 | Status of the Integral Code ASTEC | J. Van Dorsselaere (IPSN) |
| 14:00 | Development Status of Severe Accident Analysis Code SAMPSON | T. Iwashita (NUPEC) |
| 14:30 | ICARE/CATHARE V1: application to a PWR 900 MWe Severe Accident Sequence | M. Zabiego (IPSN) |
| 15:00-15:15 | **Coffee Break** | |

## Session IV
## Accident Analysis and Modeling II

**Chairpersons: J. Van Dorsselaere(IPSN), Y. Maruyama(JAERI)**

| | | |
|---|---|---|
| 15:15 | TMI-2 Accident Analysis with SCDAP/RELAP5 Code | G. Bandini (ENEA) |
| 15:45 | Adaptation of the Severe Accident Codes to VVER-440/V213 and V230 Reactor Unit, Their Comparison and Utilisation of the Results | A. Bujan (VUJE, a.s.) |
| 16:15 | Comparison of MAAP4.03 with RELAP/SCDAPSIM/MOD3.2 | T. Kohriyama (INSS) |
| 16:45 | **Adjourn** | |

# Nov. 9 , Flower Room

## Session V
## In-Vessel Phenomena

**Chairpersons: C. Allison(ISS), S. Hong(KAERI)**

| | | |
|---|---|---|
| 9:30 | Irradiated UO2 Fuel Dissolution by Liquid Zircaloy: Some Results from the SCA Corium Interactions Thermochemistry Project | P. Bottomley (ITU) |
| 10:00 | Analysis for Turbulent Natural Convection Heat Transfer in a Lower Plenum during External Cooling Using the COSMO Code | H. Noguchi (NUPEC) |
| 10:30 | Modeling for Water Penetration into Narrow Gap in CAMP Code | Y. Maruyama (JAERI) |
| 11:00-11:15 | **Coffee Break** | |
| 11:15 | Identification of Gap Cooling Phenomena from LAVA-4 Experiment Using MELCOR | S. Park (KAERI) |
| 11:45 | An Experimental Study on Critical Heat Flux in a Hemispherical Narrow Gap | J. Kim (KAERI) |
| 12:15-14:00 | **Lunch Break** | |

# Session VI
# Accident Management I

**Chairpersons: Y. Abe(Yamagata Univ.), H. Nakamura(JAERI)**

| | | |
|---|---|---|
| 14:00 | Development of Hybrid Hydrogen Control System | H. Nakakura (MHI) |
| 14:30 | Tests on Passive Autocatalytic Recombiner Performance for BWR Application | H. Oikawa (Toshiba) |
| 15:00 | An Experimental Study on Feasibility of Ex-vessel Cooling through the External Guide Vessel | J. Kim (KAERI) |
| 15:30-15:45 | **Coffee Break** | |

# Session VII
# Accident Management II

**Chairpersons: A. Levin(NRC), M. Ogino(NUPEC)**

| | | |
|---|---|---|
| 15:45 | Experimental Investigation of Thermal-Hydraulic Performance of PCCS with Horizontal Tube Heat Exchangers : Single U-Tube Test | H. Nakamura (JAERI) |
| 16:15 | Analysis of Containment Venting Following a Core Damage at a BWR Mark I Using THALES-2 | S. Widodo (BATAN) |
| 16:45 | **Adjourn** | |

**Reception at Toki Room (2F) from 18:00.**
**(All the participants are invited)**

# Nov. 9 , Sue-hiro Room

## Session VIII
## Fission Product Behavior I

**Chairpersons: A. Jones(JRC), A. Watanabe(NUPEC)**

| | | |
|---|---|---|
| 10:00 | Current Status of VEGA Program and a Preliminary Test with Cesium Iodide | A. Hidaka (JAERI) |
| 10:30 | Quick Look of First VEGA Test and Fabrication Study of Thoria Tube | T. Nakamura (JAERI) |
| 11:00-11:15 | **Coffee Break** | |
| 11:15 | PHEBUS FPT4: Test Conditions and First Results | F. Serre (IPSN) |
| 11:45 | Studies on Interaction between Cesium Iodide and Type 316 Stainless Steel in WIND Project | T. Kudo (JAERI) |
| 12:15-14:00 | **Lunch Break** | |

## Session IX
## Fission Product Behavior II

**Chairpersons: P. Bottomley(ITU), K. Hashimoto(JAERI)**

| | | |
|---|---|---|
| 14:00 | Experimental Study on Effects of Boric Acid on Aerosol Revaporization in WIND Project | H. Shibazaki (JAERI) |
| 14:30 | Analyses of CsI Aerosol Deposition Tests in WIND Project with ART and VICTORIA Codes | Y. Yuchi (JAERI) |
| 15:00 | Effects of Radiation and Impurities on Gaseous Iodine Behavior in a Containment Vessel | M. Takahashi (NUPEC) |
| 15:30-15:45 | **Coffee Break** | |
| 15:45 | Fission Product Aerosol Removal Test by Containment Spray under Accident Management Conditions (3) | A. Watanabe (NUPEC) |

## Session X
## Research Reactors

**Chairpersons: T. Hashimoto(NUPEC), K. Hashimoto(JAERI)**

| | | |
|---|---|---|
| 16:15 | MINT Research Reactor Safety Program | T. Mohamad Idris (MINT) |
| 16:45 | Measurements of Radiation Dose Level around 3W1 Beam Line of Beijing Electron-Positron Collider | Q. Wang (IHEP) |
| 17:15 | **Adjourn** | |

**Reception at Toki Room (2F) from 18:00.**
**(All the participants are invited)**

# Nov. 10 , Flower Room

## Session XI
## Ex-Vessel Phenomena

**Chairpersons: S. Koshizuka(Univ. of Tokyo), H. Nagasaka(NUPEC)**

| | | |
|---|---|---|
| 9:00 | Analysis on Direct Containment Heating for 300 MWe NPP | J. Gao (SNERDI) |
| 9:30 | Improved Hydrogen Combustion Model for Multi-Compartment Analysis | M. Ogino (NUPEC) |
| 10:00 | Evaluation of Upward Heat Flux in Ex-Vessel Molten Core Heat Transfer Using MELCOR | S. Park (KAERI) |
| 10:30-10:45 | **Coffee Break** | |
| 10:45 | COTELS Ex-Vessel Debris Coolability Tests | I. Sakaki (NUPEC) |
| 11:15 | Numerical Analysis of Molten Core-Concrete Interaction Using MPS Method | S. Koshizuka (Univ.of Tokyo) |
| 11:45-13:30 | **Lunch Break** | |

# Nov. 10 , Sue-hiro Room

## Session XII
## Structural Integrity

**Chairpersons: N. Miyazaki(Kyusyu Univ.), Y. Maruyama(JAERI)**

| | | |
|---|---|---|
| 9:30 | Current Results of Experimental and Analytical Studies in WIND Project on Creep Failure of Reactor Coolant Piping | E. Chino (JAERI) |
| 10:00 | Modeling of Hot Tensile and Short-Term Creep Strength for LWR Piping Materials under Severe Accident Conditions | Y. Harada (MHI) |
| 10:30-10:45 | **Coffee Break** | |
| 10:45 | A Simple Evaluation of Containment Integrity against Ex-Vessel Steam Explosion | H. Nishiura (KEPCO) |
| 11:15 | Axisymmetric Global Structural Analysis of Prestressed Concrete Containment Vessel beyond Design Pressure | T. Kashiwase (NUPEC) |
| 11:45-13:30 | **Lunch Break** | |

# Nov. 10 , Toki Room

13:30 **Panel Discussion**

**Link of Severe Accident Research Results to Regulation: Current Status and Future Perspective**

Chairperson

Kiyomi Ishijima (JAERI, Japan)

Panelists

Martin Sonnenkalb (GRS, Germany)
Alan V. Jones (JRC/Ispra, Italy)
Hideo Nagasaka (NUPEC, Japan)
Kimitoshi Yahagi (TEPCO, Japan)
James F. Costello (NRC, USA)

| | | |
|---|---|---|
| 15:45 | **Closing Remarks** | H. Ogasawara (NUPEC) |
| 16:00 | **Adjourn** | |

# Appendix B List of Participants

# *SARJ-99*

## *The Workshop on Severe Accident Research, Japan*

| | | |
|---|---|---|
| Kiyoharu Abe | Japan Atomic Energy Research Institute | JAPAN |
| Yutaka Abe | Yamagata University | JAPAN |
| Masaki Adachi | Ship Research Institute | JAPAN |
| Chris Merrill Allison | Innovative Systems Software | U.S.A. |
| Giacomino Bandini | Ente per le Nuove Tecnologie, l'Energia e l'Ambiente | ITALY |
| Paul David William Bottomley | European Commission, Joint Research Center-Institute for Transuranium Elements | GERMANY |
| Albert Bujan | Nuclear Power Plants Research Institute | SLOVAKIA |
| Xuewu Cao | Japan Nuclear Cycle Development Institute | JAPAN |
| Eiichi Chino | Japan Atomic Energy Research Institute | JAPAN |
| James F. Costello | U.S. Nuclear Regulatory Commission | U.S.A. |
| Eiji Doi | Toden Software, Inc. | JAPAN |
| Jean-Pierre Van Dorsselaere | Institut de Protection et Sûreté Nucléaire | FRANCE |
| Alexandre Ezzidi | Computer Software Development Co., Ltd. | JAPAN |
| Hiroaki Fujii | Toshiba Advanced Systems Corporation | JAPAN |
| Toshio Fujishiro | Research Organization for Information Science & Technology | JAPAN |
| Masanori Fukasawa | Nuclear Power Engineering Corporation | JAPAN |
| Kazumi Furuhashi | Toden Software, Inc. | JAPAN |
| Jinghui Gao | Shanghai Nuclear Engineering Research & Design Institute | CHINA |
| Satoshi Haba | Electric Power Development Co., Ltd. | JAPAN |

| | | |
|---|---|---|
| Ryoichi Hamazaki | Toshiba Corporation | JAPAN |
| Yuhei Harada | Mitsubishi Heavy Industries, Ltd. | JAPAN |
| Kazuichiro Hashimoto | Japan Atomic Energy Research Institute | JAPAN |
| Koji Hashimoto | Hitachi, Ltd. | JAPAN |
| Takashi Hashimoto | Nuclear Power Engineering Corporation | JAPAN |
| Shigeo Hayashi | Fuji Electric | JAPAN |
| Akihide Hidaka | Japan Atomic Energy Research Institute | JAPAN |
| Masataka Hidaka | Hitachi, Ltd. Power & Industrial Systems R & D Laboratory | JAPAN |
| Kohei Hisamochi | Energy Research Lab., Hitachi Ltd. | JAPAN |
| Seong Wan Hong | Korea Atomic Energy Research Institute | KOREA |
| Tisako Hosokawa | Nuclear Power Engineering Corporation | JAPAN |
| Kazuaki Igaki | Lattice Co., Ltd. | JAPAN |
| Hirokazu Ikeda | The University of Tokyo | JAPAN |
| Takashi Imada | Fuji EIC | JAPAN |
| Shun-ichi Imai | Tokyo Electric Power Co., Inc. | JAPAN |
| Satoshi Ishiguro | Electric Power Development Co., Ltd | JAPAN |
| Kiyoharu Ishijima | Japan Atomic Energy Research Institute | JAPAN |
| Hideo Itoh | Japan Atomic Energy Research Institute | JAPAN |
| Hiroyuki Itoh | Nuclear Power Engineering Corporation | JAPAN |
| Akiko Iwamoto | Nuclear Power Engineering Corporation | JAPAN |
| Tsuyoshi Iwashita | Nuclear Power Engineering Corporation | JAPAN |
| Alan V. Jones | EC Joint Research Centre | ITALY |
| Takako Kashiwase | Nuclear Power Engineering Corporation | JAPAN |
| Isao Kataoka | Osaka University | JAPAN |

| | | |
|---|---|---|
| Masaharu Kataoka | Japan Atomic Energy Research Institute | JAPAN |
| Etuko Kato | Japan Atomic Energy Research Institute | JAPAN |
| Masami Kato | Nuclear Power Engineering Corporation | JAPAN |
| Yasuharu Kawabe | Institute of Nuclear Safety System, Incorporated | JAPAN |
| Katunori Kawai | Mitsubishi Heavy Industries, Ltd. | JAPAN |
| Masatoshi Kawashima | Toshiba Corporation | JAPAN |
| Seppo Kelppe | Technical Research Centre of Finland | FINLAND |
| Yoshihiro Kikuchi | Hiroshima University | JAPAN |
| Jong Hwan Kim | Korea Atomic Energy Research Institute | KOREA |
| Syouko Kimura | Japan Atomic Energy Research Institute | JAPAN |
| Koji Kitagawa | Shin-Etsu Handotai Co., Ltd. | JAPAN |
| Yasumi Kitajima | Nuclear Power Engineering Corporation | JAPAN |
| Toshio Kiuchi | Japan Atomic Energy Research Institute | JAPAN |
| Tamio Kohriyama | Institute of Nuclear Safety System, Incorporated | JAPAN |
| Yoshihiro Kojima | Toshiba Corporation | JAPAN |
| Keiichi Komori | Japan Atomic Energy Research Institute | JAPAN |
| Seiichi Koshizuka | The University of Tokyo | JAPAN |
| Tamotsu Kudo | Japan Atomic Energy Research Institute | JAPAN |
| Hiroyuki Kusunoki | Electric Power Development Co. Ltd. | JAPAN |
| Alan Levin | U.S. Nuclear Regulatory Commission | U.S.A. |
| Jie Liu | The University of Tokyo | JAPAN |
| Akio Maeda | MRI Systems | JAPAN |
| Tatsuo Makiuchi | Nuclear Power Engineering Corporation | JAPAN |
| Yu Maruyama | Japan Atomic Energy Research Institute | JAPAN |

| | | |
|---|---|---|
| Shiro Matsumoto | Saitama University | JAPAN |
| Tomoyuki Matsumoto | Hitachi, Ltd. | JAPAN |
| Satoshi Miura | Nuclear Power Engineering Corporation | JAPAN |
| Takuya Miyagawa | Toshiba Corporation | JAPAN |
| Kazumi Miyagi | Toshiba Corporation | JAPAN |
| Noriyuki Miyazaki | Kyushu University | JAPAN |
| Hideyuki Moriyama | Nuclear Power Engineering Corporation | JAPAN |
| Kiyofumi Moriyama | Japan Atomic Energy Research Institute | JAPAN |
| Kenji Murakami | Shikoku Electric Power Co., Inc. | JAPAN |
| Ken Muramatsu | Japan Atomic Energy Research Institute | JAPAN |
| Hideo Nagasaka | Nuclear Power Engineering Corporation | JAPAN |
| Masanori Naito | Nuclear Power Engineering Corporation | JAPAN |
| Kotaro Nakada | Toshiba Corporation | JAPAN |
| Takahiro Nakagawa | Toshiba Engineering Corporation | JAPAN |
| Toshio Nakagiri | Japan Nuclear Cycle Development Institute | JAPAN |
| Hiroyuki Nakakura | Mitsubishi Heavy Industries, Ltd. | JAPAN |
| Hideo Nakamura | Japan Atomic Energy Research Institute | JAPAN |
| Masashi Nakamura | Kawasaki Heavy Industrie, Ltd. | JAPAN |
| Takehiko Nakamura | Japan Atomic Energy Research Institute | JAPAN |
| Taeko Naraoka | Japan Atomic Energy Research Institute | JAPAN |
| Hideki Nariai | Tsukuba University | JAPAN |
| Sunchai Nilsuwankosit | Chulalongkorn University | THAILAND |
| Yasuharu Nishino | Japan Atomic Energy Research Institute | JAPAN |
| Hiroshi Nishiura | Kansai Electric Power Co., Inc. | JAPAN |

| | | |
|---|---|---|
| Minoru Nogami | Japan Atomic Energy Research Institute | JAPAN |
| Hironori Noguchi | Nuclear Power Engineering Corporation | JAPAN |
| Katsuya Nomura | The University of Tokyo | JAPAN |
| Shigehiro Nukatsuka | Mitsubishi Heavy Industries, Ltd. | JAPAN |
| Nobuaki Nunogane | Institute of Nuclear Safety System, Incorporated | JAPAN |
| Hideo Ogasawara | Nuclear Power Engineering Corporation | JAPAN |
| Masao Ogino | Nuclear Power Engineering Corporation | JAPAN |
| Nobuyuki Ohnishi | Nuclear Power Engineering Corporation | JAPAN |
| Shuji Ohno | Japan Nuclear Cycle Development Institute | JAPAN |
| Masanori Ohtani | Institute of Nuclear Safety System Inc. | JAPAN |
| Hirohide Oikawa | Toshiba Corporation | JAPAN |
| Tetsuya Oonawa | Japan Atomic Energy Research Institute | JAPAN |
| Motoko Osaka | Nuclear Safety Research Association | JAPAN |
| Hideki Osaki | Japan Atomic Energy Research Institute | JAPAN |
| Jae Won Park | Korea Power Engineering Company, Inc. | KOREA |
| Soo Yong Park | Korea Atomic Energy Research Institute | KOREA |
| Seigo Sakai | Kawasaki Heavy Industries, Ltd. | JAPAN |
| Isao Sakaki | Nuclear Power Engineering Corporation | JAPAN |
| Toru Sakamoto | Toshiba Advanced Systems Corporation | JAPAN |
| Kazuo Sakuramoto | Toden Software, Inc. | JAPAN |
| Yukio Sasajima | Japan Atomic Energy Research Institute | JAPAN |
| Masaki Nakagawa | Marubeni Utility Services, Ltd. | JAPAN |
| Yumiko Sasaki | Marubeni Utility Services, Ltd. | JAPAN |
| Kenichi Sato | Energy Research Lab., Hitachi Ltd. | JAPAN |

| | | |
|---|---|---|
| Masahito Sato | Lattice Co., Ltd. | JAPAN |
| Mayumi Sato | Nuclear Power Engineering Corporation | JAPAN |
| Takashi Sawada | Mitsubishi Heavy Industries, Ltd. | JAPAN |
| Tetsuo Sawada | Tokyo Institute of Technology | JAPAN |
| Akimi Serizawa | Kyoto University | JAPAN |
| Frédéric Olivier Serre | Institut de Protection et Sûreté Nucléaire | FRANCE |
| Satoru Shibata | Nuclear Power Engineering Corporation | JAPAN |
| Hiroaki Shibazaki | Japan Atomic Energy Research Institute | JAPAN |
| Mikiko Shigemoto | Japan Atomic Energy Research Institute | JAPAN |
| Akihiko Shimizu | Nuclear Safety Research Association | JAPAN |
| Kohei Shintani | Taisei Corporation | JAPAN |
| Koki Shiozaki | Ship Research Institute | JAPAN |
| Martin Sonnenkalb | Gesellschaft fur Anlagen-und Reaktorsicherheit mbH | GERMANY |
| Hisao Sonobe | Japan Atomic Energy Research Institute | JAPAN |
| Jun Sugimoto | Japan Atomic Energy Research Institute | JAPAN |
| Kensuke Suzuki | Toshiba Advanced Systems Corporation | JAPAN |
| Mohamad Idris Taib | Malasian Institute for Nuclear Technology Research | MALAYSIA |
| Masato Takahashi | Nuclear Power Engineering Corporation | JAPAN |
| Yukio Takahashi | Toshiba Information Systems Japan | JAPAN |
| Yoshinori Takechi | Mitsubishi Heavy Industries, Ltd. | JAPAN |
| Isao Takeshita | Japan Atomic Energy Institute | JAPAN |
| Ayako Takeuchi | Mitsubishi Heavy Industries, Ltd. | JAPAN |
| Tomohiko Tamaki | Institute of Nuclear Safety System, Incorporated | JAPAN |
| Akira Tani | Nuclear Power Engineering Corporation | JAPAN |

| | | |
|---|---|---|
| Daisuke Tochio | Yamagata University | JAPAN |
| Michiko Tomita | Japan Atomic Energy Research Institute | JAPAN |
| Hiroshi Ujita | Nuclear Power Engineering Corporation | JAPAN |
| Qingbin Wang | Institute of High Energy Physics, Chinese Academy of Science | CHINA |
| Atsushi Watanabe | Nuclear Power Engineering Corporation | JAPAN |
| Fumitoshi Watanabe | Toden Software, Inc. | JAPAN |
| Surip Widodo | National Nuclear Energy Agency | INDONESIA |
| Kimitoshi Yahagi | Tokyo Electric Power Co., Inc. | JAPAN |
| Yusaku Yamada | Toshiba Information Systems Japan | JAPAN |
| Makoto Yamagishi | Mitsubishi Heavy Industries, Ltd. | JAPAN |
| Hiroshi Yanagida | Yamagata University | JAPAN |
| Yanhua Yang | Shanghai Jiao Tong University | CHINA |
| Seiichi Yokobori | Toshiba Corporation | JAPAN |
| Kenji Yonebayashi | Kansai Electric Power Co., Inc. | JAPAN |
| Takehito Yoshino | Toshiba Advanced Systems Corporation | JAPAN |
| Yoko Yuchi | Japan Atomic Energy Research Institute | JAPAN |
| Magali Zabiego | Institut de Protection et de Sûreté Nucléaire | FRANCE |

This is a blank page.

# 国際単位系 (SI) と換算表

表1　SI基本単位および補助単位

| 量 | 名称 | 記号 |
|---|---|---|
| 長さ | メートル | m |
| 質量 | キログラム | kg |
| 時間 | 秒 | s |
| 電流 | アンペア | A |
| 熱力学温度 | ケルビン | K |
| 物質量 | モル | mol |
| 光度 | カンデラ | cd |
| 平面角 | ラジアン | rad |
| 立体角 | ステラジアン | sr |

表2　SIと併用される単位

| 名称 | 記号 |
|---|---|
| 分，時，日 | min，h，d |
| 度，分，秒 | °，′，″ |
| リットル | l，L |
| トン | t |
| 電子ボルト | eV |
| 原子質量単位 | u |

1 eV = 1.60218 × $10^{-19}$ J

1 u = 1.66054 × $10^{-27}$ kg

表3　固有の名称をもつSI組立単位

| 量 | 名称 | 記号 | 他のSI単位による表現 |
|---|---|---|---|
| 周波数 | ヘルツ | Hz | $s^{-1}$ |
| 力 | ニュートン | N | $m \cdot kg/s^2$ |
| 圧力，応力 | パスカル | Pa | $N/m^2$ |
| エネルギー，仕事，熱量 | ジュール | J | N·m |
| 工率，放射束 | ワット | W | J/s |
| 電気量，電荷 | クーロン | C | A·s |
| 電位，電圧，起電力 | ボルト | V | W/A |
| 静電容量 | ファラド | F | C/V |
| 電気抵抗 | オーム | Ω | V/A |
| コンダクタンス | ジーメンス | S | A/V |
| 磁束 | ウェーバ | Wb | V·s |
| 磁束密度 | テスラ | T | $Wb/m^2$ |
| インダクタンス | ヘンリー | H | Wb/A |
| セルシウス温度 | セルシウス度 | ℃ | |
| 光束 | ルーメン | lm | cd·sr |
| 照度 | ルクス | lx | $lm/m^2$ |
| 放射能 | ベクレル | Bq | $s^{-1}$ |
| 吸収線量 | グレイ | Gy | J/kg |
| 線量当量 | シーベルト | Sv | J/kg |

表4　SIと共に暫定的に維持される単位

| 名称 | 記号 |
|---|---|
| オングストローム | Å |
| バーン | b |
| バール | bar |
| ガル | Gal |
| キュリー | Ci |
| レントゲン | R |
| ラド | rad |
| レム | rem |

1 Å = 0.1 nm = $10^{-10}$ m

1 b = 100 $fm^2$ = $10^{-28}$ $m^2$

1 bar = 0.1 MPa = $10^5$ Pa

1 Gal = 1 $cm/s^2$ = $10^{-2}$ $m/s^2$

1 Ci = 3.7 × $10^{10}$ Bq

1 R = 2.58 × $10^{-4}$ C/kg

1 rad = 1 cGy = $10^{-2}$ Gy

1 rem = 1 cSv = $10^{-2}$ Sv

表5　SI接頭語

| 倍数 | 接頭語 | 記号 |
|---|---|---|
| $10^{18}$ | エクサ | E |
| $10^{15}$ | ペタ | P |
| $10^{12}$ | テラ | T |
| $10^{9}$ | ギガ | G |
| $10^{6}$ | メガ | M |
| $10^{3}$ | キロ | k |
| $10^{2}$ | ヘクト | h |
| $10^{1}$ | デカ | da |
| $10^{-1}$ | デシ | d |
| $10^{-2}$ | センチ | c |
| $10^{-3}$ | ミリ | m |
| $10^{-6}$ | マイクロ | μ |
| $10^{-9}$ | ナノ | n |
| $10^{-12}$ | ピコ | p |
| $10^{-15}$ | フェムト | f |
| $10^{-18}$ | アト | a |

（注）

1. 表1－5は「国際単位系」第5版，国際度量衡局 1985年刊行による。ただし，1 eVおよび1 uの値はCODATAの1986年推奨値によった。
2. 表4には海里，ノット，アール，ヘクタールも含まれているが日常の単位なのでここでは省略した。
3. barは，JISでは流体の圧力を表わす場合に限り表2のカテゴリーに分類されている。
4. EC閣僚理事会指令ではbar，barnおよび「血圧の単位」mmHgを表2のカテゴリーに入れている。

換　算　表

| 力 | N(=$10^5$ dyn) | kgf | lbf |
|---|---|---|---|
| | 1 | 0.101972 | 0.224809 |
| | 9.80665 | 1 | 2.20462 |
| | 4.44822 | 0.453592 | 1 |

粘度　1 Pa·s(N·s/$m^2$) = 10 P(ポアズ)(g/(cm·s))

動粘度　1 $m^2/s$ = $10^4$ St(ストークス)($cm^2/s$)

| 圧力 | MPa(=10 bar) | kgf/$cm^2$ | atm | mmHg(Torr) | lbf/$in^2$(psi) |
|---|---|---|---|---|---|
| | 1 | 10.1972 | 9.86923 | 7.50062 × $10^3$ | 145.038 |
| | 0.0980665 | 1 | 0.967841 | 735.559 | 14.2233 |
| | 0.101325 | 1.03323 | 1 | 760 | 14.6959 |
| | 1.33322 × $10^{-4}$ | 1.35951 × $10^{-3}$ | 1.31579 × $10^{-3}$ | 1 | 1.93368 × $10^{-2}$ |
| | 6.89476 × $10^{-3}$ | 7.03070 × $10^{-2}$ | 6.80460 × $10^{-2}$ | 51.7149 | 1 |

| エネルギー・仕事・熱量 | J(=$10^7$ erg) | kgf·m | kW·h | cal(計量法) | Btu | ft·lbf | eV |
|---|---|---|---|---|---|---|---|
| | 1 | 0.101972 | 2.77778 × $10^{-7}$ | 0.238889 | 9.47813 × $10^{-4}$ | 0.737562 | 6.24150 × $10^{18}$ |
| | 9.80665 | 1 | 2.72407 × $10^{-6}$ | 2.34270 | 9.29487 × $10^{-3}$ | 7.23301 | 6.12082 × $10^{19}$ |
| | 3.6 × $10^6$ | 3.67098 × $10^5$ | 1 | 8.59999 × $10^5$ | 3412.13 | 2.65522 × $10^6$ | 2.24694 × $10^{25}$ |
| | 4.18605 | 0.426858 | 1.16279 × $10^{-6}$ | 1 | 3.96759 × $10^{-3}$ | 3.08747 | 2.61272 × $10^{19}$ |
| | 1055.06 | 107.586 | 2.93072 × $10^{-4}$ | 252.042 | 1 | 778.172 | 6.58515 × $10^{21}$ |
| | 1.35582 | 0.138255 | 3.76616 × $10^{-7}$ | 0.323890 | 1.28506 × $10^{-3}$ | 1 | 8.46233 × $10^{18}$ |
| | 1.60218 × $10^{-19}$ | 1.63377 × $10^{-20}$ | 4.45050 × $10^{-26}$ | 3.82743 × $10^{-20}$ | 1.51857 × $10^{-22}$ | 1.18171 × $10^{-19}$ | 1 |

1 cal = 4.18605 J（計量法）

= 4.184 J （熱化学）

= 4.1855 J （15 °C）

= 4.1868 J（国際蒸気表）

仕事率　1 PS（仏馬力）

= 75 kgf·m/s

= 735.499 W

| 放射能 | Bq | Ci |
|---|---|---|
| | 1 | 2.70270 × $10^{-11}$ |
| | 3.7 × $10^{10}$ | 1 |

| 吸収線量 | Gy | rad |
|---|---|---|
| | 1 | 100 |
| | 0.01 | 1 |

| 照射線量 | C/kg | R |
|---|---|---|
| | 1 | 3876 |
| | 2.58 × $10^{-4}$ | 1 |

| 線量当量 | Sv | rem |
|---|---|---|
| | 1 | 100 |
| | 0.01 | 1 |

（86年12月26日現在）